Transactions of the ASME, Journal of Heat Transfer (ISSN 0022-1481) is published monthly by The American Society of Mechanical Engineers, Three Park Avenue, New York, NY 10016. Periodicals postage paid at New York, NY and additional mailing offices. POSTMASTER: Send address changes to Transactions of the ASME, Journal of Heat Transfer, c/o THE AMERICAN SOCIETY OF MECHANICAL ENGINEERS, 22 Law Drive, Box 2300, Fairfield, NJ 07007-2300. **CHANGES OF ADDRESS** must be received at Society headquarters seven weeks before they are to be effective. Please send old label and new address. **STATEMENT from By-Laws.** The Society shall not be responsible for statements or opinions advanced in papers or ... printed in its publications (B7.1, Para. 3).

Journal of Heat Transfer

Published Monthly by ASME

VOLUME 129 • NUMBER 8 • AUGUST 2007 (pp. 929-1106)

HEAT TRANSFER PHOTOGALLERY

TECHNICAL PAPERS

Combustion and Reactive Flows

Evaporation, Boiling, and Condensation

(Contents continued on inside back cover)

This journal is printed on acid-free paper, which exceeds the ANSI Z39.48-1992 specification for permanence of paper and library materials. ♾™
♻ 85% recycled content, including 10% post-consumer fibers.

(Contents continued)

TECHNICAL BRIEFS

(Contents continued on facing page)

ANNOUNCEMENT

The ASME Journal of Heat Transfer is abstracted and indexed in the following:

Applied Science and Technology Index, Chemical Abstracts, Chemical Engineering and Biotechnology Abstracts (Electronic equivalent of Process and Chemical Engineering), Civil Engineering Abstracts, Compendex (The electronic equivalent of Engineering Index), Corrosion Abstracts, Current Contents, E & P Health, Safety, and Environment, Ei EncompassLit, Engineered Materials Abstracts, Engineering Index, Enviroline (The electronic equivalent of Environment Abstracts), Environment Abstracts, Environmental Engineering Abstracts, Environmental Science and Pollution Management, Fluidex, Fuel and Energy Abstracts, Index to Scientific Reviews, INSPEC, International Building Services Abstracts, Mechanical & Transportation Engineering Abstracts, Mechanical Engineering Abstracts, METADEX (The electronic equivalent of Metals Abstracts and Alloys Index), Petroleum Abstracts, Process and Chemical Engineering, Referativnyi Zhurnal, Science Citation Index, SciSearch (The electronic equivalent of Science Citation Index), Theoretical Chemical Engineering

Journal of Heat Transfer

Heat Transfer Photogallery

The Eleventh Heat Transfer Photogallery was sponsored by the K-22 Heat Transfer Visualization Committee for the 2006 International Mechanical Engineering Congress and Exhibition (IMECE) held in Chicago, Illinois, on November 5–10, 2006. The peer-reviewed evaluation process for the presented entries identified the nine entries for publication in the ASME *Journal of Heat Transfer* August issue of 2007.

The purpose of publishing these entries is to draw attention to the innovative features of optical diagnostic techniques and aesthetic qualities of thermal processes. To focus on visualization images and schematics, the text is kept to a minimum and further details should be found directly from the authors. My wish is that the journal readers enjoy viewing these collections, acquire knowledge of the state-of-the-art features, and also promote their participation in the 2007-IMECE Photogallery [http://www.asmeconferences.org/congress07].

The **Call for Photogallery for 2007-IMECE** is also announced in this issue of *Journal of Heat Transfer*.

Kenneth D. Kihm
Department of Mechanical, Aerospace
and Biomedical Engineering,
University of Tennessee,
Knoxville, TN 37996-2210

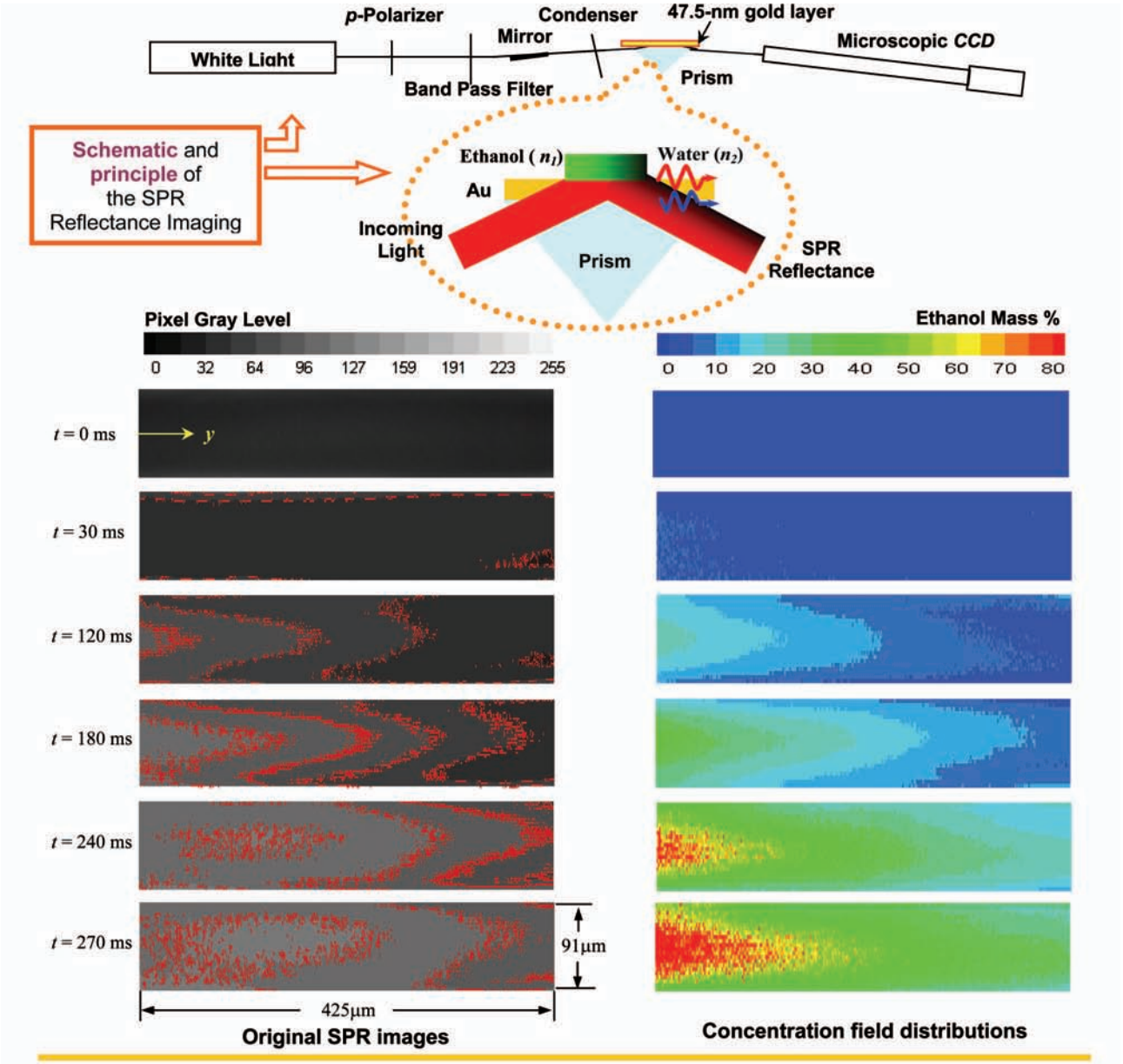

Surface Plasmon Resonance (*SPR*) Reflectance Imaging: A Label-Free/Real-Time Mapping of Microscale Mixture Concentration Fields (Water+Ethanol)

Iltai Kim and Kenneth D. Kihm
Department of Mechanical, Aerospace, and Biomedical Engineering
University of Tennessee, Knoxville, Tennessee

A label-free visualization is successfully conducted for nonintrusive, real-time and full-field mapping of microscale mixture (water+ethanol) concentration fields with surface plasmon resonance (*SPR*) reflectance technique based on Kretschmann's configuration. SPR reflectance is highly sensitive to the refractive index variation of test medium above the thin Au layer with the order of 10^{-5} in the near wall region ($\leq 1\,\mu m$). The Fresnell's equation of *SPR* reflectance intensity correlates with the medium dielectric constant, and thereby the refractive index and mixture concentration fields. The presented results show that ethanol penetrates into pure water stored in microchannel (50μm deep × 91μm wide) by capillary phoretic suction from left to right. The ethanol-water interface rapidly advances to the right inside of the channel and is broadened because of the molecular diffusion progressively occurring during the interfacial advancement.

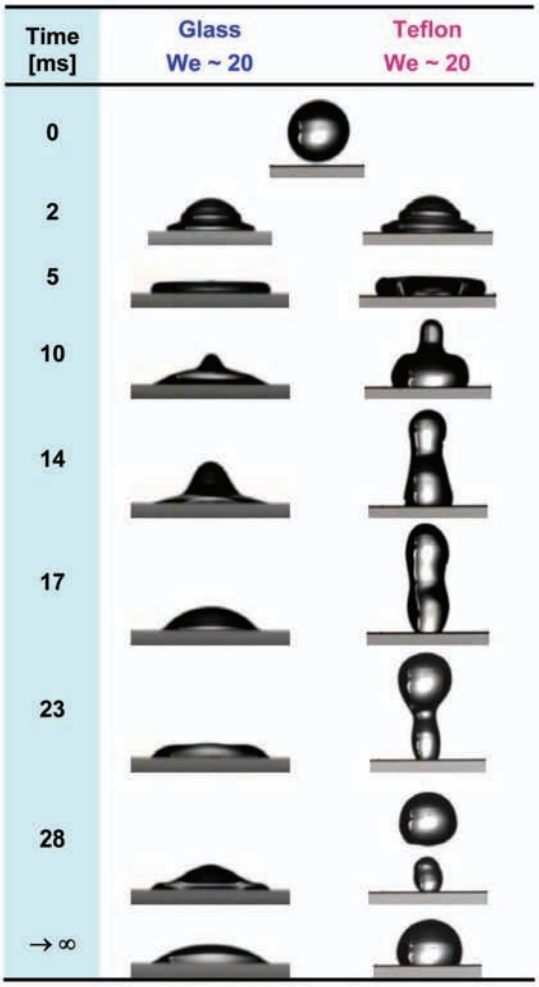

Fig. 1 Water droplet recoil on a glass (hydrophilic) and Teflon (hydrophobic) surface for We ~ 20.

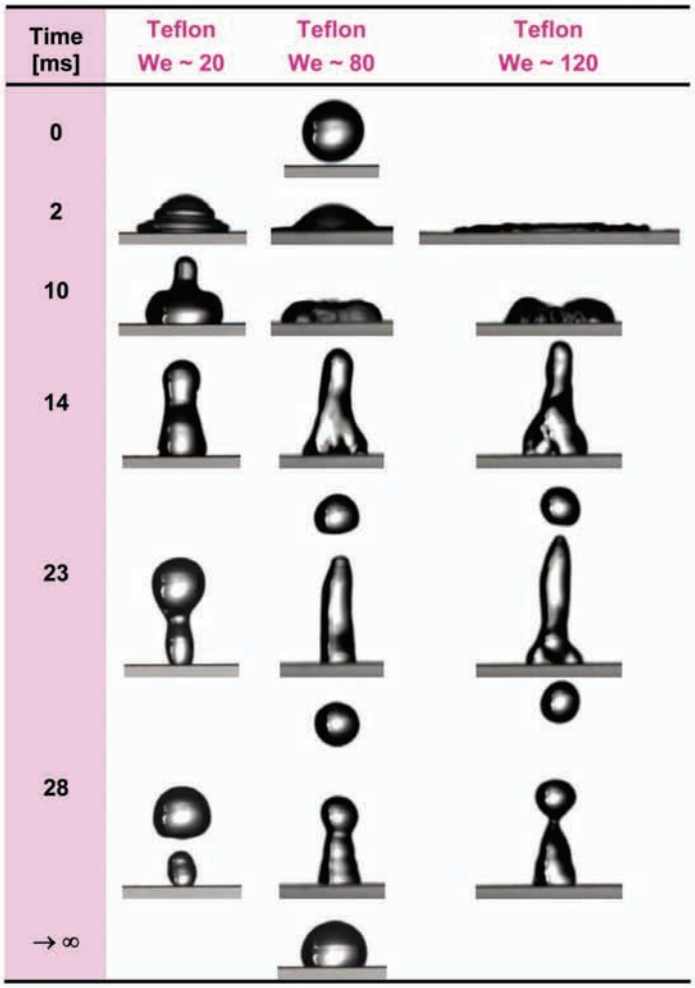

Fig. 2 Variations in water droplet recoil and column fracture behavior with Weber number on a Teflon (hydrophobic) surface.

VISUALIZATION OF FRACTURE DYNAMICS OF DROPLET RECOIL ON HYDROPHOBIC SURFACE

K.P. Gatne, R.M. Manglik, and **M.A. Jog**
Thermal-Fluids & Thermal Processing Laboratory, University of Cincinnati, Cincinnati, OH 45221-0072

The recoil characteristics of liquid droplets generally tend to be altered by the wetting properties of the impacting surface. This is seen in Fig. 1, where with a Weber number of ~ 20 the recoil of a water droplet on a Teflon surface stretches into a column and fractures into two unequal droplets. An identical drop (d_e ~ 3.0 mm) on a glass surface does not display this behavior, as the higher wetting of the glass surface tends to increase the liquid film spread and dampen the recoil. With increasing impact velocity (We ~ 20 → 80 → 120; Fig. 2) there is greater elongation of the recoil column with a tendency to fracture into multiple droplets of different sizes.

This spatial-temporal (millimeter-millisecond scale) evolution of droplet impact, spreading, and recoil/fracture dynamics on a hydrophobic (Teflon) and hydrophilic (glass) surface was captured by using a high-speed (5000 frames per second) digital video camera fitted with a 8× optical zoom lens. The camera was triggered through a computer interface to record continuous high-speed video in real time, from which any desired image frame can be captured by digital-video-processing software; it also allows precise inter-event temporal calculations. The drop size or diameter and liquid film spread at impact were determined by image processing software that employs a saturation-intensity pixel-based area-averaging process. The droplets were generated from a hypodermic needle and their sizes were kept nearly constant at d_e ~ 3.0 mm, and We was varied by changing the free-fall impact velocity. All the experiments were conducted at room temperature (T = 25°C) in a controlled environment that minimized cross-flow effects.

Characteristics of impinging mass will change as the applied voltage is increased

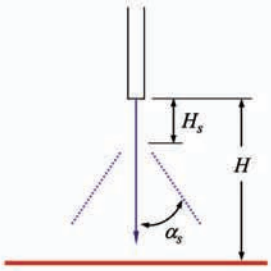

As voltage (V) increases, spray angle (α_s) increases and jet breakup distance (H_s) decreases

Stainless Steel Capillary
$D_o = 0.47$ mm
$D_i = 0.25$ mm

Test Conditions:
$q'' = 10$ W/cm²
$Q = 3$ ml/min,
$H = 0.75$ cm,
$A_s = 0.5$ cm²

Acrylic Capillary
$D_o = 4$ mm
$D_i = 1$ mm

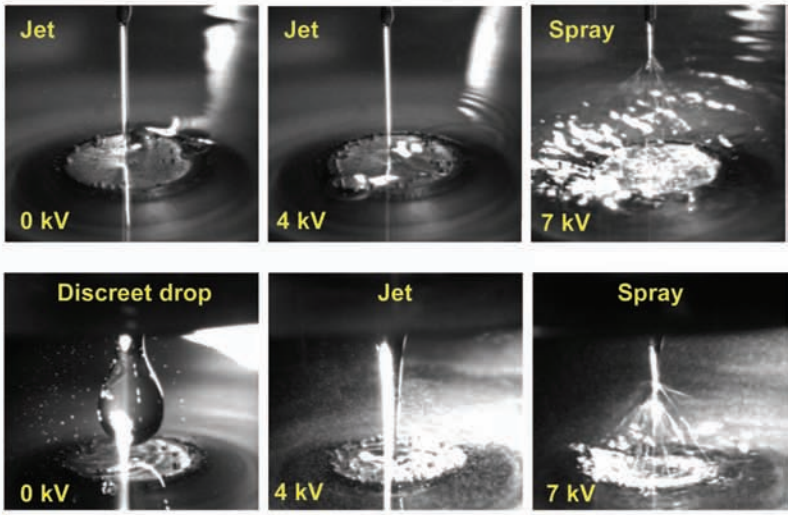

Electric field interaction changes impinging mass characteristics in capillary array

Single 0.47 mm capillary to 1cm² surface

Capillary array of 4 at 0.47mm to 1cm² surface

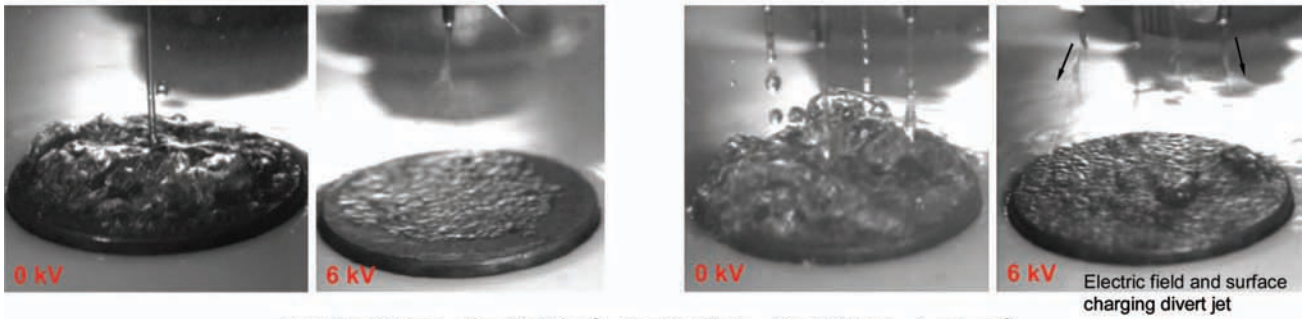

Test Conditions: $q'' = 35$ W/cm², $Q = 3$ ml/min, $H = 0.75$ cm, $A_s = 1$ cm²

Effect of Electric Fields on Two-phase Impingement Cooling

X. Feng and J. E. Bryan
Enhanced Heat & Fluid Transport Laboratory
Mechanical and Aerospace Engineering Department, University of Missouri, Columbia, Missouri

Spray cooling is one method for removing high heat flux and achieving high heat transport. Methods to generate sprays include traditional mechanical methods such as air assisted, swirl nozzles, and even piezoelectric actuation. A new approach is to utilize electric fields to control free boundary flows discreet drops to jets to sprays. The motivation is two-fold: 1) can electric fields be used to better understand the effect of impinging mass characteristics on liquid boiling and evaporation at heated surface; and 2) can electric fields be used to control heat transfer from the surface. Through traditional surface heat transfer measurements and image analysis the effect of electric fields on impingement two-phase heat transfer is being explored. Under the same operating conditions with ethanol it can be seen that the heat transfer is enhanced as the form of the impinging mass to the surface changes from discreet drops to sprays with increasing applied voltage. The form of the free boundary flow produced from the capillary by application of an electric field will depend on operating conditions (flow rate, applied voltage, capillary to heater spacing), fluid properties (thermo-physical and electrical), and capillary geometry (material, size, and shape). If electrical fields are to have application in high flux and high transport processes then arrays of capillaries will be required. The application of an electric field to capillary arrays, as seen in the image sequence, still produces a spray, but the effect of electric field and surface charge from neighboring capillaries distorts and diverts the jet. The change will depend on the relationship between the momentum and electrostatic forces.

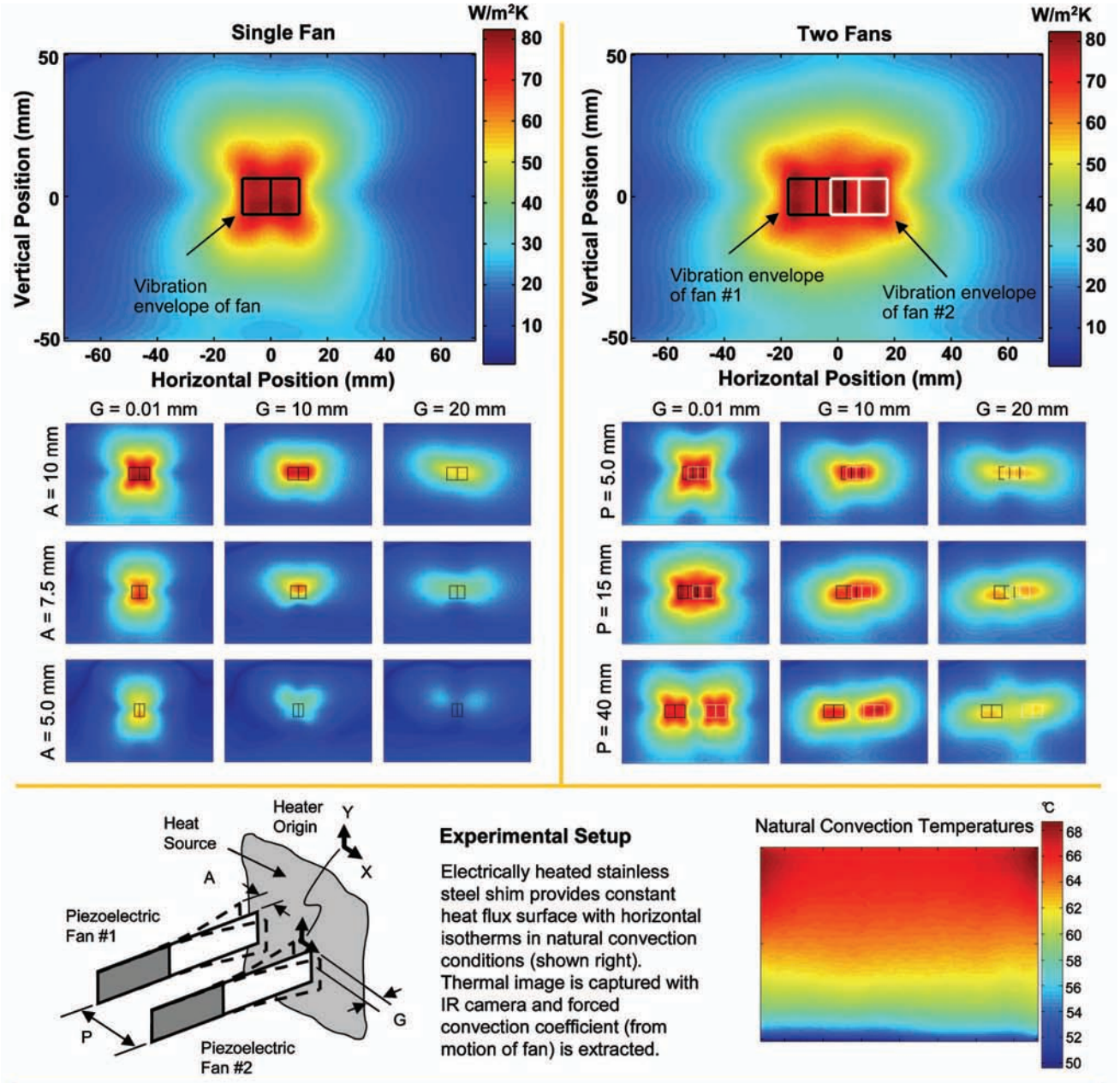

Local Heat Transfer Coefficients Under Flows Induced by Vibrating Cantilevers

Mark Kimber and Suresh V. Garimella
NSF Cooling Technologies Research Center
School of Mechanical Engineering, Purdue University, West Lafayette, Indiana

Piezoelectric fans are flexible vibrating cantilevers and can provide large enhancements in heat transfer over natural convection while consuming very little power. Flows induced by these devices are visualized experimentally by determining local heat transfer coefficients of fans operating near a constant heat flux surface. Behavior of the temperature contours is dependent on vibration amplitude and distance from heater to fan tip (gap). For small gaps, the cooling is nearly uniform within the vibration envelope. An optimal gap based on the stagnation performance is apparent and appears to be dependent on vibration amplitude. With two fans operating simultaneously, the behavior become more complex, and for an intermediate fan pitch, yields constructive interference where the peak local performance shows an increase of approximately 10%.

Numerical prediction with CFD

Case 1: Reynolds number: 800 and heat flux: 80 W/m²

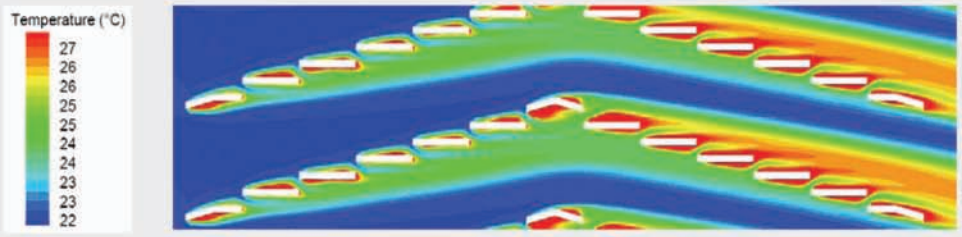

Case 2: Reynolds number: 800 and heat flux: 180 W/m²

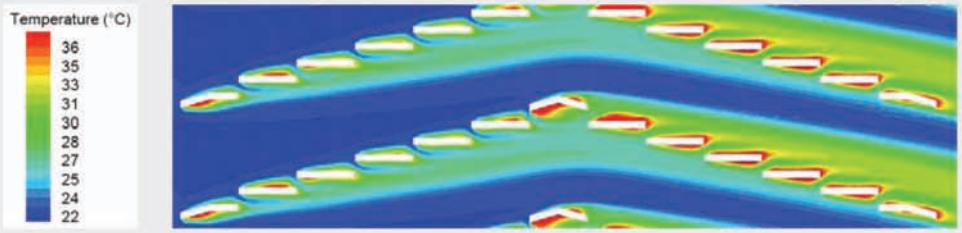

Case 3: Reynolds number: 2000 and heat flux: 80 W/m²

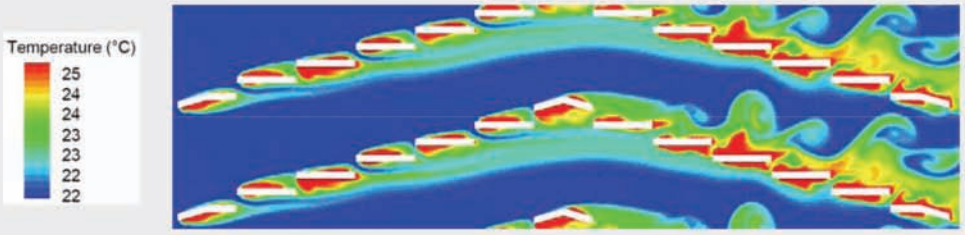

Case 4: Reynolds number: 2000 and heat flux: 180 W/m²

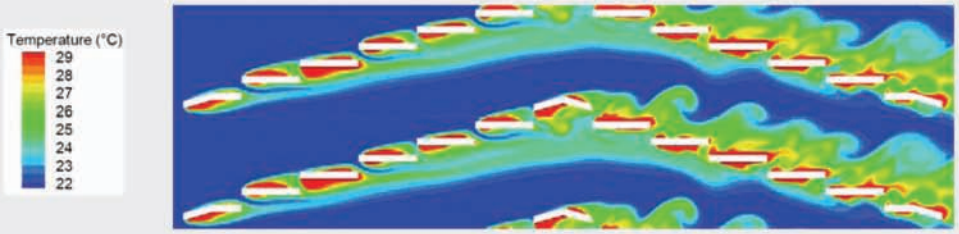

Flow visualisation within inclined louvered fins

C. T'Joen, A. Willockx and M. De Paepe
Department of Flow, Heat and Combustion Mechanics
Ghent University, Belgium

Modern compact fin-and-tube heat exchangers use very complex fin designs on the air side. Common designs include louvered fins, offset strip fins… These corrugated fin types increase the heat transfer rate when compared to plate fins, but also cause a large increase in pressure drop. The 'inclined louvered fin' is a hybrid design between a standard louvered fins and a offset strip fin. It is aimed at improved performance (less pressure drop for a given heat transfer rate) at low Reynolds numbers. To study the flow within the fin array a series of numerical CFD simulations were performed using Fluent. The resulting air temperature profile provides a qualitative image of the flow pattern and shows several distinct flow features: the long cold wake which flows through the array, local hot wakes just downstream of louver (e.g. case 1), hot recirculation zone behind the turnaround section… The flow becomes unsteady for high Reynolds numbers and vortices are being shed by the louvers. This gives rise to a more 'spotted' temperature profile (case 4).

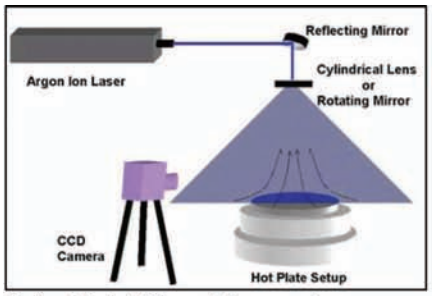

(a) Light Sheet Apparatus

(b) Near Field on Hot Surface

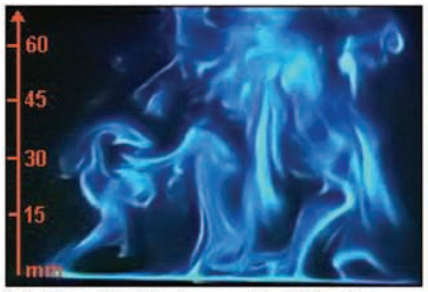

(c) Far Field above Hot Surface

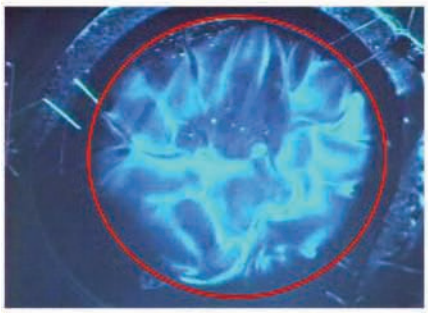

(d) 2 mm above surface

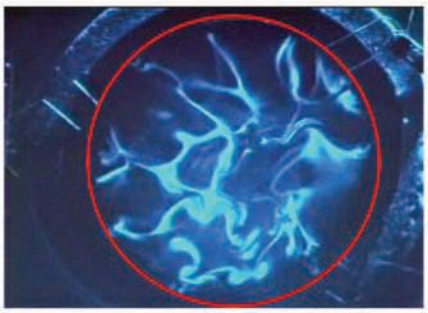

(e) 4 mm above surface

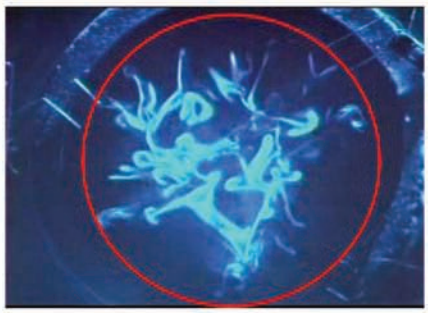

(f) 8 mm above surface

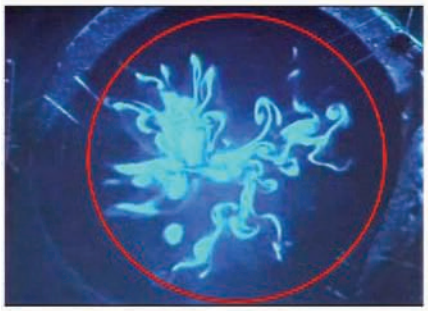

(g) 16 mm above surface

(h) 30 mm above surface

(i) 60 mm above surface

Convective flow field above a heated circular plate

Peter J Disimile [1] & Norman Toy [2]

[1] *C-FEST, Dept of Aerospace Engineering, University of Cincinnati, Ohio 45221(Peter.Disimile@uc.edu)*

[2] *Engineering & Scientific Innovations Inc, Batesville, Indiana 47006 (Dr.Toy@esi-solutionsinc.com)*

Hot surface ignition of flammable fluid is still a major concern in many industrial applications. A Laser light sheet methodology (a) is being used to investigate the flow field above a heated circular flat plate capable of being heated uniformly to 550^0 C. The convective flow has both a near field (b), within approximately 30 mm of the surface, and a far field (c), above 30 mm. Close to the surface at 2 mm (d) cell like structures emanate from the edge of the plate. This is more evident at 4 mm (e) where the cell walls are vortical structures that when 'sliced' appear as mushroom type vortices, (b). At 8 mm (f) the plume is beginning to become more developed and the cells are less distinct in the radial sense. As the plume rises still further at 16 mm (g), the cell like structures disappears although mushroom vortices are still in evidence. These types of vortices are dominant throughout the plume and may be observed in the far field at 30 mm (h) and at 60 mm (i) above the hot surface, even though the flow is much more diffused at these higher levels.

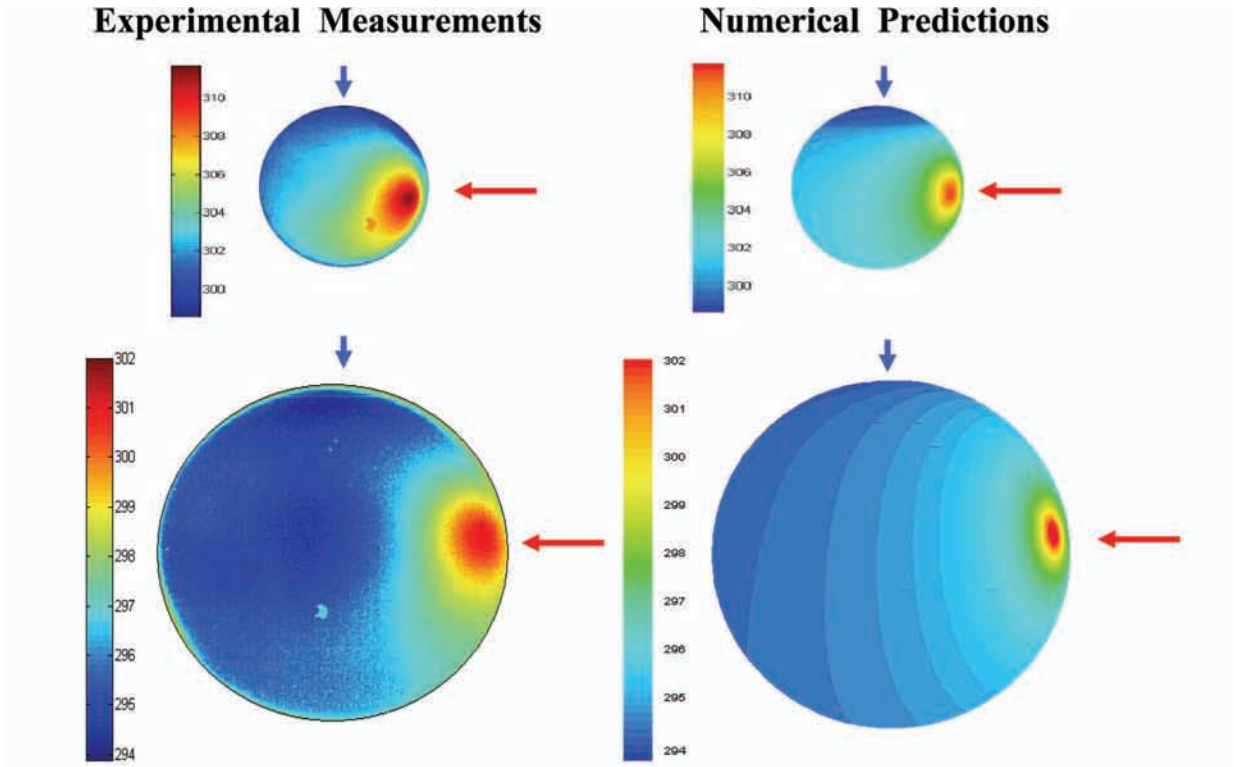

Surface temperature contours on 1mm (top row) and 2mm (bottom row) spheres: Red arrows indicate areas of heating due to focused X-ray beam and blue arrows show lower temperature region due to the coolant flow

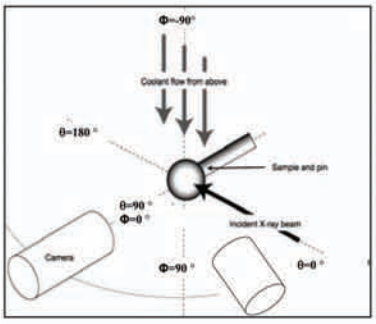

Schematic of system of interest

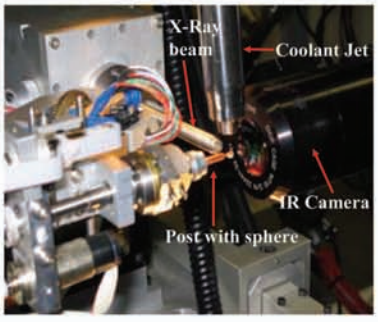

Experimental setup at Advance Photon Source

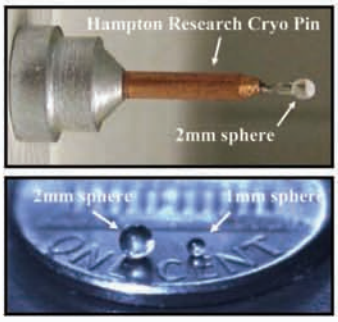

Magnified view of the sample and post

Experimental Measurement of Thermal Heating of Millimeter Sized Spheres using IR Imaging Subjected to Synchrotron X-Ray Beam with Comparison to Theoretical Predictions

M. Kazmierczak, R. Kumar, P. Gopalakrishnan and R. Banerjee

Department of Mechanical, Industrial and Nuclear Engineering, University of Cincinnati, Cincinnati, OH 45221-0072

The temperature rise of 1mm and 2mm glass spheres (sample) exposed to an intense X-ray beam (undulator ID sector 19 X-ray beam of the APS) is measured at high spatial resolution using an Indigo Systems Phoenix thermal imaging camera with a 4x magnification lens (method described in Snell *et al., J. Synchrotron Rad.,* 14, 109-115 (2007)). The sample is cooled in a stream of nitrogen gas (i.e. cryostream) to prevent overheating and minimize thermal damage to the sample. The heat transfer, including external forced convection and internal heat conduction, was also theoretically modeled using CFD to predict the temperature variation throughout and on the sphere. The local surface temperature distribution from the experimental measurements and the numerical predictions are compared side-by-side and show good agreement, both qualitatively and quantitatively, for both sphere sizes and at the two different flow velocities tested using the adjusted beam flux. Over the last decade, sample cooling using cryostream N_2 gas cooling has been routinely used in the field of crystallography for macromolecular structural determination of biocrystals, but heretofore, actual local temperature measurements on small x-ray interrogated samples were unavailable.

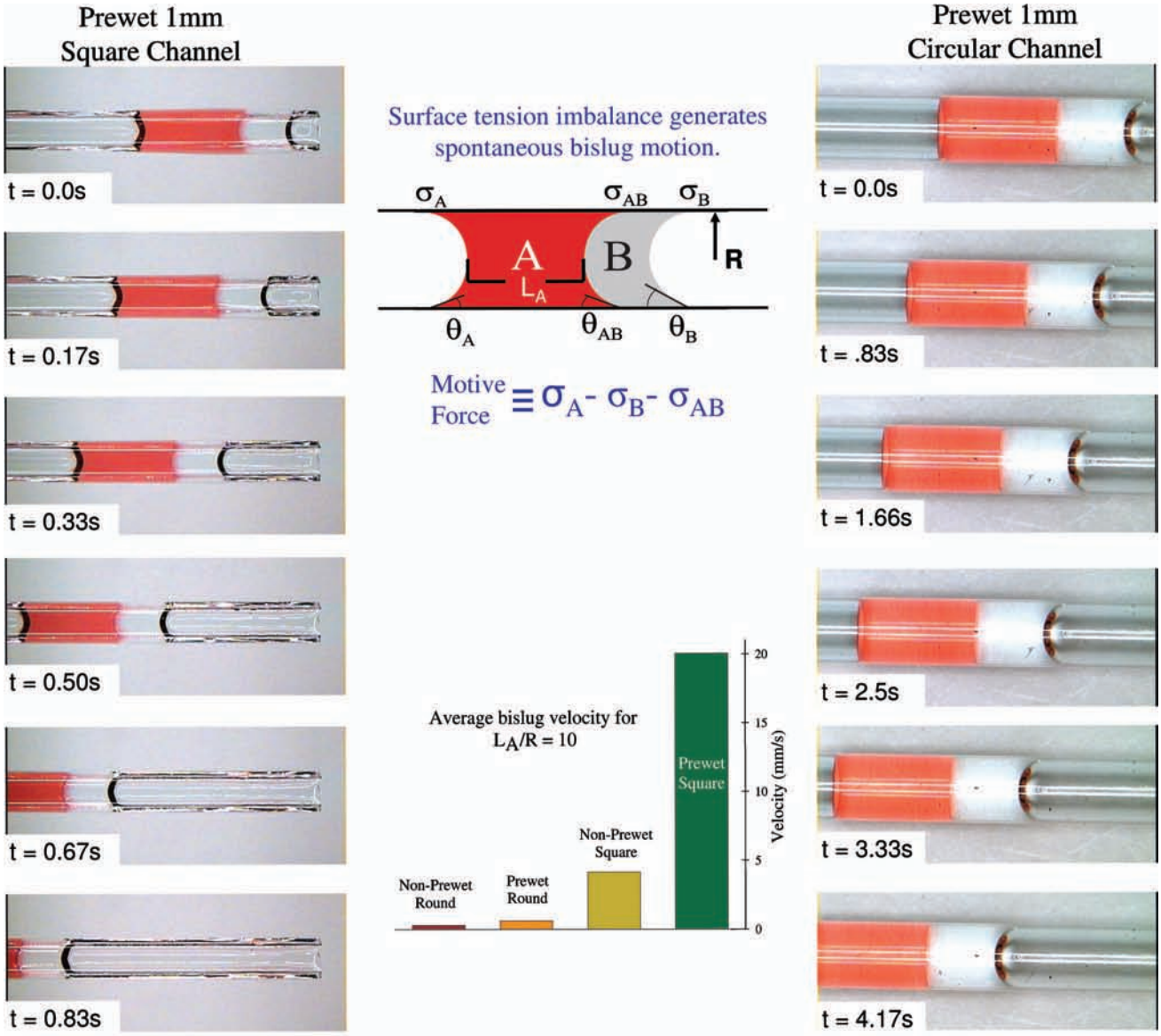

Visualization and Tracking of Spontaneous Liquid-Liquid Slug Flow in Microchannels

Joseph Hernandez & Jeffrey Allen
Microfluidics and Interfacial Transport Laboratory
Michigan Technological University

Spontaneous liquid-liquid slug (bislug) [1] flow in microchannels has been observed for both circular and square cross-sections. Flow is induced via an imbalance in interfacial tensions and curvatures between the two gas-liquid surfaces and the liquid-liquid surface. Liquid A (red) has a higher surface tension than liquid B, the resulting bislug flow occurs in the direction of the higher surface tension. Interface tracking was performed on each of the images to extract the position and time of the slug as it traversed the microchannel. The bar graph shows the average bislug velocities for prewet and non-prewet microchannels of circular and square cross-sections. Bislug velocity in the prewet square microchannel is four times the velocity on the non-prewet square microchannel. The prewet square microchannel has a velocity more than an order of magnitude greater than that found in either the prewet and non-prewet circular microchannels. For the prewet, square microchannels, the Capillary number is greater than that predicted by the laminar flow equation for $L_A/R > 5$, where L_A/R is the length of the fluid A slug and R is the channel radius. The actual Capillary number is much lower than the theoretical Capillary number for the prewet circular microchannels regardless of the bislug aspect ratio, L_A/R, due to dissipation from the menisci motion. Corning wicking reduces the viscous dissipation allowing the bislug to flow faster. When $L_A/R < 5$, hydrodynamic interaction between menisci increases dissipation so that the Ca is less than predicted.

[1] J. Bico and D. Quere. Self-propelling slugs. J. Fluid Mech., 467: 101-127, 2002.

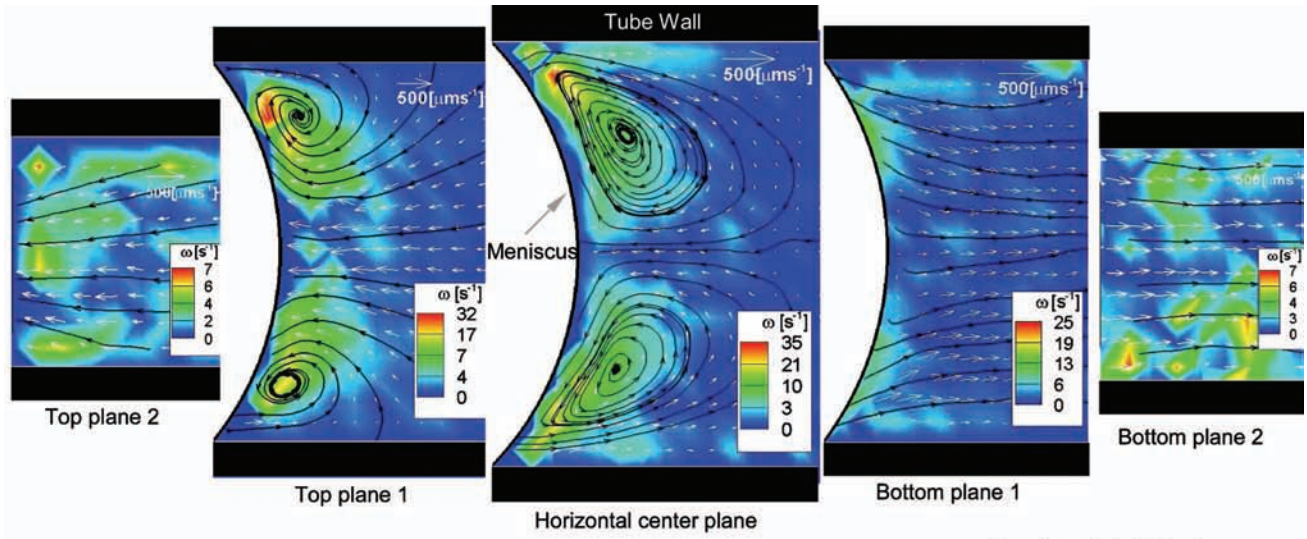

Counter-rotating vortices in the top planes and opposing bulk flow patterns in top and bottom planes indicate the presence of a toroidal vortex near the meniscus.

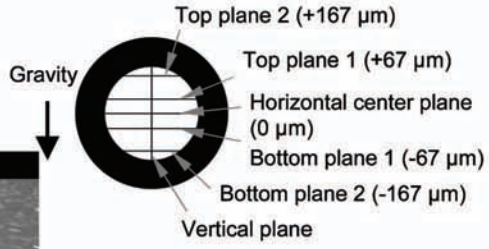

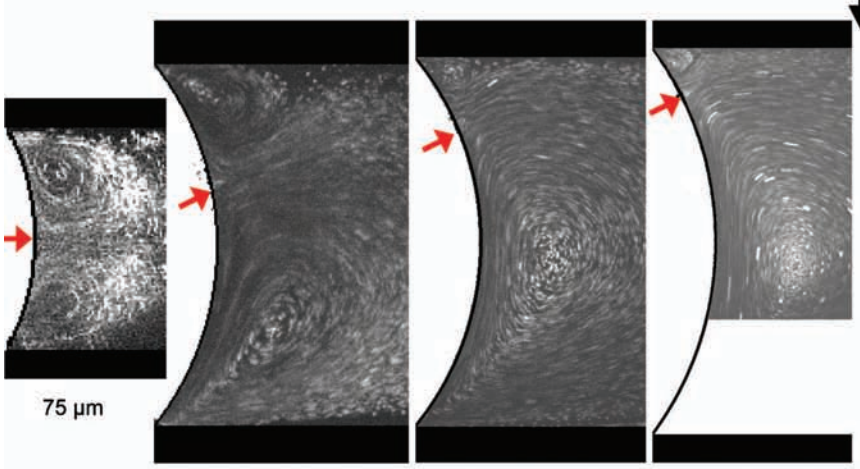

Buoyancy effects set in with increase in tube size.

For the 762 μm tube, only 70% of the tube section is imaged because of the restriction imposed by the field of view of the objective lens.

Thermocapillary Convection Near an Evaporating Meniscus

H. K. Dhavaleswarapu, P. Chamarthy, S. V. Garimella, J. Y. Murthy, and S. T. Wereley
NSF Cooling Technologies Research Center
School of Mechanical Engineering, Purdue University, West Lafayette, Indiana

Differential evaporation is widely known to occur at menisci which are prevalent in many two-phase cooling devices. Thin-film evaporation – the evaporation taking place near a solid-liquid-vapor junction – has long been believed to be the dominant mode of heat transfer in such systems. The intensive heat fluxes near the triple line create a temperature gradient along the meniscus. This results in a surface tension gradient which, coupled with buoyancy effects, causes buoyant-thermocapillary convection. Micro-particle image velocimetry measurements of the convection patterns generated near an evaporating meniscus in horizontally oriented capillary tubes are obtained using polystyrene particles of 0.5 μm diameter suspended in methanol. The velocity vectors at various horizontal measurement planes reveal the three-dimensionality of the flow. The relative influences of buoyancy and thermocapillarity on the flow were also qualitatively investigated by imaging the flow in vertical planes for tube diameters ranging from 75 to 762 μm. These results shed light on the role of thermocapillary convection in heat transfer enhancement in two-phase heat transfer devices.

A Mathematical Model for Heat and Mass Transfer in Methane-Air Boundary Layers With Catalytic Surface Reactions

T. W. Tong
Dean
e-mail: tong@gwu.edu

M. M. M. Abou-Ellail
Visiting Professor
e-mail: abouellail@hotmail.com

Y. Li

School of Engineering and Applied Science,
The George Washington University,
Washington, D.C. 20052

Catalytic combustion of hydrocarbon mixtures involves the adsorption of the fuel and oxidant into a platinum surface, chemical reactions of the adsorbed species, and the desorption of the resulting products. Re-adsorption of some produced gases is also possible. The catalytic reactions can be beneficial in porous burners that use low equivalence ratios. In this case, the porous burner flame can be stabilized at low temperatures to prevent any substantial gas emissions, such as nitric oxide. The present paper is concerned with the numerical computation of heat transfer and chemical reactions in flowing methane-air mixtures over a platinum coated hot plate. Chemical reactions are included in the gas phase and in the solid platinum surface. In the gas phase, 16 species are involved in 49 elementary reactions. On the platinum hot surface, additional surface species are included that are involved in 24 additional surface chemical reactions. The platinum surface temperature is fixed, while the properties of the reacting flow are computed. The flow configuration investigated here is the parallel boundary layer reacting flow. Finite-volume equations are obtained by formal integration over control volumes surrounding each grid node. Up-wind differencing is used to ensure that the influence coefficients are always positive to reflect the physical effect of neighboring nodes on a typical central node. The finite-volume equations are solved iteratively for the reacting gas flow properties. On the platinum surface, surface species balance equations, under steady-state conditions, are solved numerically by an under-relaxed linear algorithm. A non-uniform computational grid is used, concentrating most of the nodes near the catalytic surface. Surface temperatures, 1150 K and 1300 K, caused fast reactions on the catalytic surface, with very slow chemical reactions in the flowing gas. These slow reactions produce mainly intermediate hydrocarbons and unstable species. The computational results for the chemical reaction boundary layer thickness and mass transfer at the gas-surface interface are correlated by non-dimensional relations, taking the Reynolds number as the independent variable. Chemical kinetic relations for the reaction rate are obtained which are dependent on reactants' concentrations and surface temperature.
[DOI: 10.1115/1.2737479]

Keywords: catalytic surface reactions, boundary layer, methane-air chemical reactions, numerical modeling

1 Introduction

Catalysts have been widely used in many industrial applications to control the process of chemical reaction. One of the applications of catalysts is catalytic combustion. With the assistance of catalysts, the ignition temperature of fuel is lower than the ignition temperature of the fuel without catalysts. Combustion of methane at a lower temperature can reduce emissions of pollutants, which is one of the most important advantages of catalytic combustion. Platinum and palladium are common catalysts used to assist combustion. Combustion of several fuels, i.e., NH_3, CH_4, C_3H_8, and NH_3/CH_4 mixture, on a platinum surface in stagnation flow field has been studied experimentally by Williams et al. [1]. In addition, combustion of methane on a platinum surface has been studied numerically by Song et al. [2]. In this work (Song et al., [2]), the surface reaction of methane over platinum has been modeled by a global reaction mechanism. Similarly, combustion of hydrogen on a platinum surface in stagnation flow field and boundary layer flow field have been studied numerically by Warnatz et al. [3]. In their work, the elementary reaction mechanism of the oxidation of hydrogen on a platinum surface, including reactions of absorption/desorption of reactant and products and reactions of surface radical recombination, has been established and used in the model. Thermo-chemical data of surface species involved in the surface reactions have also been published by Warnatz et al. [3]. Later, the elementary surface reaction mechanism of methane with platinum was established by Deutschmann et al. [4]. The detailed surface reaction mechanism has been used by Deutschmann et al. [4] to numerically simulate the experiments of surface combustion of methane over platinum conducted by Williams et al. [1]. It was found that (Deutschmann et al. [4]), the methane is ignited at surface temperature around 1000 K and the reaction is fast between surface temperatures of 1000 K and 1300 K; for surface temperatures below 1000 K, the surface reaction is slow and the methane could not be ignited. Surface coverage of surface species and mole fractions of gas-phase species have been calculated by Deutschmann et al. [4] in their work. Raja et al. [5] use the detailed surface mechanisms for methane combustion (Deutschmann et al., [4]) to model the catalytic honeycomb monolith combustion.

Contributed by the Heat Transfer Division of ASME for publication in the JOURNAL OF HEAT TRANSFER. Manuscript received September 28, 2006; final manuscript received January 9, 2007. Review conducted by Ben Q. Li.

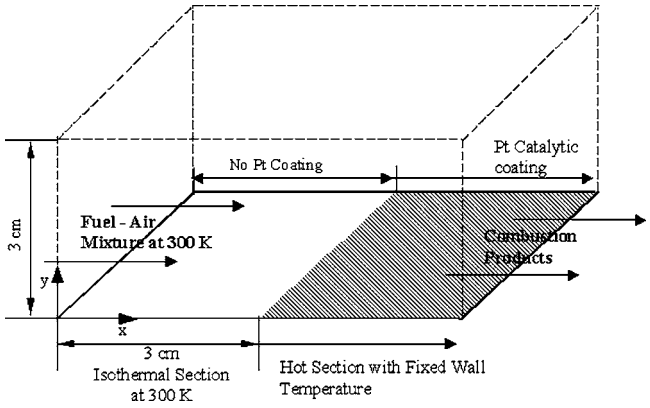

Fig. 1 Layout of the parallel boundary layer flow with surface reactions

In this paper, catalytic combustion of methane over a platinum surface in a boundary layer flow is modeled. The flow configuration is shown in Fig. 1. A parallel flow of methane and air mixture of unity equivalence flows over a flat hot plate. The temperature of the flat plate is kept uniform and constant along the surface. In this flow configuration, the first inert part of the flat plate is for developing the flow hydro-dynamically. The second part of the flat plate is coated with platinum. The present two-dimensional model of boundary layer flow, with surface reactions, is developed mainly for the second part. A multi-step reaction mechanism is adopted for gas phase reaction. It involves 49 elementary reactions and 16 chemical species for methane/air mixtures. The surface reaction mechanism developed by Deutschmann et al. [4] is used in the present work. This surface reaction mechanism, for methane-air mixtures, consists of 24 elementary surface reactions that involve seven gas-phase species and nine surface species. The surface reaction model developed by Coltrin et al. [6] is adopted as a general layout for the present work. Non-dimensional relations are developed to represent the mass transfer boundary layer thickness along the gas-surface interface.

2 Mathematical Model and Solution Procedure

The numerical model for laminar flow, heat transfer, gas phase combustion, and catalytic surface reaction are presented. The flow configuration is shown in Fig. 1. The model can be classified into four main groups of equations as follows:

2.1 Continuity and Momentum Equations. The mass continuity of reacting flow may be written as

$$\frac{\partial(\rho)}{\partial t}+\frac{\partial(\rho u_i)}{\partial x_i}=0 \tag{1}$$

The momentum equation for laminar reacting flow may be written in Cartesian tensor notations as (Abou-Ellail et al. [7])

$$\frac{\partial(\rho u_j)}{\partial t}+\frac{\partial}{\partial x_i}(\rho u_j u_i)-\frac{\partial}{\partial x_i}\left(\mu\frac{\partial u_j}{\partial x_i}\right) =-\frac{\partial(P)}{\partial x_j}+\frac{\partial}{\partial x_i}\left[\mu\left(\frac{\partial u_i}{\partial x_j}-\frac{2}{3}\frac{\partial u_k}{\partial x_k}\delta_{ij}\right)\right] \tag{2}$$

where ρ is the gas density, u_j is the gas velocity along coordinate x_j, and μ is the dynamic viscosity.

2.2 Energy Equations. The energy equation for the reacting flow is

$$\frac{\partial\rho h_g}{\partial t}+\frac{\partial}{\partial x_i}(\rho u_i h_g)-\frac{\partial}{\partial x_i}\left(\Gamma_h\frac{\partial h_g}{\partial x_i}\right)=-\sum_j(\Delta H_j)W_j \tag{3}$$

where h_g is the gas sensible enthalpy, Γ_h is the thermal diffusivity, ΔH_j and W_j are the enthalpy of reaction and reaction rate, respectively, of chemical reaction j of the reaction mechanism involving methane-air mixtures. In the above equations, the subscript g denotes gas phase. The gas temperature, at any point, is directly related to the local gas sensible enthalpy (h_g), gas species mass fractions (Y_j), and constant-pressure specific heats, namely

$$h_g=\int\left(\sum_j C_{pj}Y_j\right)dT \tag{4}$$

The lower limit of the above integration is 298 K, while the upper limit equals local gas temperature, T_g.

2.3 Species Mass Fraction Equations. The species mass fraction for reacting flow in the porous burner may be written as

$$\frac{\partial(\rho Y_l)}{\partial t}+\frac{\partial(\rho u_i Y_l)}{\partial x_i}-\frac{\partial}{\partial x_i}\left(\Gamma_{Y_l}\frac{\partial Y_l}{\partial x_i}\right)=M_l\sum_m\nu_{lm}W_m \tag{5}$$

where Y_l is the mass fraction of species l while Γ_{Y_l} is its molecular diffusivity, M_l is the molecular mass of species l, ν_{lm} is the stoichiometric coefficient of species l in reaction m, while W_m is the reaction rate of the elementary chemical reaction m of the present reaction mechanism. It consists of 49 elementary reactions. The reaction mechanism is based on de-polymerizing the complex molecule of methane into simpler intermediate hydrocarbon molecules. The chemical kinetic mechanism involves 16 species, namely, CH_4, CH_3, CH_2, CH, CH_2O, CHO, CO, CO_2, O_2, O, OH, H, H_2, H_2O, HO_2, and H_2O_2, while the 49 involved elementary reactions are given in detail by Tong et al. [8].

It should be mentioned here that ν_{lm} is taken as a positive value for products and negative for reactants as required for proper summation of the effect of each reaction on the production of a particular species.

2.4 Surface Reaction. For a steady-state problem, the solution has no change with respect to time. Thus, surface coverage of any surface species with respect to time is zero. The variation of the surface coverage with respect to time can be computed from the net production of each surface species. The conservation of the surface coverage of surface species k may be written as (Warnatz et al. [3])

$$\frac{dz_k}{dt}=\frac{\dot{s}_k}{Z} \tag{6}$$

where z_k is the surface coverage of surface species k, Z is the total surface site density, and the surface density used in the present paper is 1.63×10^{15} cm^{-2} (Deutschmann et al. [4]); $\dot{s}_k$ is the net surface production rate, in mole/cm^2/s, of the surface species k.

Since the present reacting flow includes gas-surface interactions, the mass transfer between the gas phase and the catalytic surface needs to be included while solving the species mass fractions of the gas species in the flow. The mass fluxes transferred through convection and the diffusion process at the gas-surface interface of any gas-phase species are balanced by the production or depletion rates of that species by surface reactions. The surface boundary condition of each gas-phase species k based on the mass balance is given by Coltrin et al. [6] as

$$n\cdot[\rho Y_k(V_k+u)]=\dot{s}_k M_k \tag{7}$$

where n is the unit normal vector pointing outward to the surface, u is the bulk fluid velocity, V_k is the diffusion velocity, M_k is the molecular weight of the species k, and $\dot{s}_k$ is the production or

Table 1 Surface reaction mechanism

No.	Reaction	Aj (cm^3 mol s)	Ej (kJ/mol)	Sticking coeff.
1	$H_2+P_t(s)+P_t(s)\rightarrow H(s)+H(s)$			0.046
2	$H(s)+H(s)\rightarrow P_t(s)+P_t(s)+H_2$	1.0×10^{21}	67.4	
3	$O_2+P_t(s)+P_t(s)\rightarrow O(s)+O(s)$			0.023
4	$O(s)+O(s)\rightarrow P_t(s)+P_t(s)+O_2$	1.0×10^{21}	213.2	
5	$H_2O+P_t(s)\rightarrow H_2O(s)$			0.75
6	$H_2O(s)\rightarrow H_2O+P_t(s)$	1.0×10^{13}	40.3	
7	$OH+P_t(s)\rightarrow OH(s)$			1
8	$OH(s)\rightarrow OH+P_t(s)$	1.0×10^{13}	192.8	
9	$CO+P_t(s)\rightarrow CO(s)$			0.84
10	$CO(s)\rightarrow CO+P_t(s)$	1.0×10^{13}	152.5	
11	$CH_4+P_t(s)+P_t(s)\rightarrow CH_3(s)+H(s)$			0.01
12,13	$O(s)+H(s)\leftrightarrow OH(s)+P_t(s)$	1.0×10^{21}	11.5	
14,15	$H(s)+OH(s)\leftrightarrow H_2O(s)+P_t(s)$	1.0×10^{21}	17.4	
16,17	$OH(s)+OH(s)\leftrightarrow H_2O(s)+O(s)$	1.0×10^{21}	48.2	
18,19	$CO(s)+O(s)\leftrightarrow CO_2+P_t(s)+P_t(s)$	1.0×10^{21}	105	
20	$C(s)+O(s)\rightarrow CO(s)+P_t(s)$	1.0×10^{21}	62.8	
21	$CO(s)+P_t(s)\rightarrow C(s)+O(s)$	1.0×10^{18}	156.5	
22	$CH_3(s)+P_t(s)\rightarrow CH_2(s)+H(s)$	1.0×10^{21}	20	
23	$CH_2(s)+P_t(s)\rightarrow CH(s)+H(s)$	1.0×10^{21}	20	
24	$CH(s)+P_t(s)\rightarrow C(s)+H(s)$	1.0×10^{21}	20	

depletion rates of gas-phase species k in surface reactions.

The production rate of each species $\dot{s}_k$, either gas-phase species or surface species, may be written as (Deutschmann et al. [9])

$$\dot{s}_k=\sum_{j=1}^{K_s}\nu_k k_{f_j}\prod_{k=1}^{N_g+N_s}[X_k]^{\nu'_{kj}} \tag{8}$$

where K_s is the total number of elementary surface reactions, ν'_{kj} is the left hand side stoichiometric coefficients of the reaction equation, ν_{kj} is the right hand side minus left hand side stoichiometric coefficients of the reaction equation, k_{fj} is the forward kinetic rate constants, $[X_k]$ is the species concentrations, the units of gas-phase species and surface species concentrations are mol/cm^3 and mol/cm^2, respectively, N_g is the number of gas phase species while N_s is the number of surface species.

A detailed surface reaction mechanism is used to model the gas-surface interaction between fuel and platinum. The surface reaction mechanism adopted in the present work, for methane-air mixtures reacting over platinum coated surfaces, was established by Deutschmann et al. [4]; it is shown in Table 1. The surface chemical species are denoted by a label, (s), as shown in Table 1. The surface reaction mechanism consists of 24 elementary reactions and involves seven gas-phase species, namely, CH_4, CO, CO_2, O_2, OH, H_2, H_2O and nine surface species, namely, $CH_3(s)$, $CH_2(s)$, CH(s), CO(s), C(s), O(s), OH(s), H(s), and Pt(s).The reaction rate constants are described in terms of either an Arrhenius expression or a sticking coefficient, γ. The Arrhenius expression form is

$$k_{fj}=A_j\exp\left(\frac{-E_j}{RT}\right) \tag{9}$$

The sticking coefficient can be converted to the usual kinetic rate constants via the relation given by Coltrin et al. [6]

$$k_{fj}=\frac{\gamma}{1-\gamma/2}\frac{1}{Z^m}\sqrt{\frac{RT}{2\pi M}} \tag{10}$$

where Z is the total surface site concentration, m is the sum of the surface reactants' stoichiometric coefficient, R is the universal gas constant, T is the gas temperature, and M is the molecular weight of the gas-phase species. The thermo-chemical data needed to determine the rate coefficients for the reverse reactions and enthalpies of the surface species are provided by Warnatz et al. [3].

In the present work, steady-state conditions of the flowing gas and the surface species are assumed. Equations (6) and (8), in this case, can be used to compute the surface species mole fractions, given the gas species mole fractions at the interface between the plate surface and the flowing boundary layer. Equations (7) and (8), on the other hand, are used to compute gas species fluxes at the gas-surface interface. Although these fluxes do not appear explicitly in Eq. (5), they are used to impose the proper boundary conditions on the flowing gas species finite-volume equations.

It should be mentioned here that the gas physical properties are computed from temperature dependent relations. At any point in the boundary layer, the density is computed from the ideal gas equation of state, while the viscosity is computed from a temperature polynomial of the third order. The species specific heats are computed from temperature polynomials of the sixth order that are valid for 300–2500 K temperature range [10]. The remaining physical properties are deduced from the above properties and Prandtl and Lewis numbers specified as 0.7 and 1.0, respectively.

2.5 Numerical Solution Procedure. The two-dimensional flow over the catalytic surface, shown in Fig. 1, is overlaid with a finite grid of nodes. At each nodal point, Eqs. (2), (3), and (5) and the pressure correction counterpart of Eq. (1) are formally integrated over a control volume surrounding this nodal point. The time dependent terms of the governing equations were dropped out, since the boundary layer flow considered is under steady-state conditions. The faces of the control volume bisect the distances between the particular node and the four nearest neighbor nodes. The formal integration is performed with due care to preserve the physical meaning and overall balance of each dependent variable. The final form of the finite-volume equations are written as follows (Abou-Ellail et al. [7])

$$\left[\sum(a_n)-S_P\right]\Psi_p=\sum(a_n\Psi_n)+S_u \tag{11}$$

where ψ stands for any of the dependent variables, namely, axial and radial velocity components, gas sensible enthalpy, species mass fractions, or the pressure correction that is used to satisfy both mass continuity and momentum equations simultaneously. The summation (Σ) is over the four neighbors n of a typical node p. The above finite difference coefficients a_n are computed using the hybrid method, such that these coefficients are always nonnegative to give the proper combined effects of convection and diffusion. The above hybrid method is a combination of upwind and central differencing schemes. Each scheme prevails for a par-

ticular range of cell Peclet numbers, as given in detail by Abou-Ellail et al. [7]. S_p and S_u are the coefficients of the integrated source term at node p. Boundary layer flows are parabolic in nature and thus the hybrid scheme is accurate enough to eliminate any false diffusion. In this case, the computational grid directions are aligned along the main flow direction and normal to it.

The solution procedure is based on the line-by-line tri-diagonal matrix algorithm (TDMA). The finite-volume equations (Eq. (11)) for each dependent variable are modified at the boundaries of the solution domain, shown in Fig. 1, to impose the conditions there. On the flat plate surface, the velocity components vanish while all other dependent variables' normal gradients reflect the mass and heat fluxes due to surface reactions. Along the outer edge and exit section of the flow, the normal gradient is equal to zero. At the inlet section, all variables are known from a previous solution of the non-reacting isothermal first part of the flat plate. The numerical solution to the isothermal part of the flat plate was obtained using 301 transverse nodes by 500 axial nodes. Within each computational loop of the gas phase, Eq. (6) is solved iteratively for all surface species concentrations at each transverse plane for steady-state conditions; i.e., $d(z_k)/dt=0$. The validation of the present numerical algorithm is presented by Tong et al. [10] for heat and mass transfer in impinging flows on a hot catalytic surface. Tong et al. [10] compared their results for temperature and species mole fractions in the reacting impinging jet with numerical data of Deutschmann et al. [4]. The agreement they obtained confirms the accuracy of the present numerical procedure [10]. Moreover, standard laminar heat transfer data [11] were also used for validation purposes.

3 Presentation and Discussion of Results

The flow configuration investigated in this paper is a parallel flow of methane-air mixture over a hot plate covered by platinum, as shown in Fig. 1. The height of the computational domain (L), is 3 cm, while the free stream axial velocity (U_∞) is 6 cm/s. In the present numerical model, the first 3 cm long part of the flat plate is for developing the flow hydro-dynamically, at a constant temperature of 300 K. Gas and surface reactions are not included in the first part of the flat plate. After the first 3 cm long part, gas and surface reactions are included in the computational model. As shown in Fig. 1, the surface temperature is constant along the hot section of the flat plate. In order to study the influence of the surface temperature on the surface reactions, two surface temperature values, i.e., $T_s=1150$ K and $T_s=1300$ K, are used. The momentum, heat, and mass transfer of the reacting flow field, as well as the catalytic reaction at the surface, are computed for each surface temperature. First, the numerical results for the surface temperature of 1150 K are presented; second, the results of $T_s=1300$ K are presented. A two-dimensional computational grid, of 301 transverse nodes by 10,000 axial nodes, is used for both surface temperatures. However, the non-dimensional axial increment $\Delta x/L$ is taken as 2.0×10^{-5} for $T_s=1150$ K and 2.0×10^{-6} for $T_s=1300$ K. The finer grid is essential for the higher surface temperature, since the reacting species are highly activated as T_s is increased by 150 K, while the chemical reactions are completed in a much shorter distance.

With a total number of grid nodes of 3.01×10^6, it was necessary to utilize the parabolic nature of the flow. This is done through the use of a line-by-line TDMA scheme to obtain numerical solutions, in such a way as to sweep the solution domain from the inlet section to the exit section. The field values of the dependent variables are stored and then updated during the subsequent iterations. The iterations are stopped when the finite-volume equations of the dependent variables are satisfied with errors less than 0.1%. The above number of grid nodes is sufficient to handle the fast changing gas density and viscosity, both axially and transversely in the thin boundary layer, as well as ensuring a grid-independent solution. The transverse grid nodes are arranged such that 200 nodes lay inside the boundary layer, i.e., in the range $0.0<y/L<0.1$. The rest of the transverse nodes lay in the nearly undisturbed flow outside the boundary layer, i.e., in the range $0.1<y/L<1.0$.

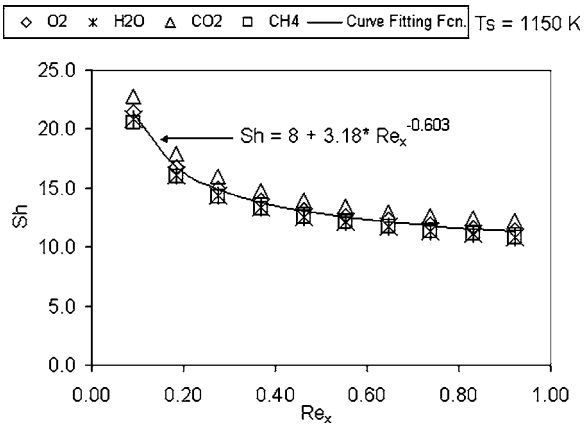

Fig. 2 Sherwood number versus Reynolds number for CH_4, O_2, CO_2, and H_2O at $T_s=1150$ K

It should be mentioned here that the 3 cm length of the isothermal part of the flat plate was chosen as the minimum length that gave a fully developed exit velocity profile, for a free stream velocity of 6 cm/s.

3.1 Results for a Surface Temperature of 1150 K, i.e., $T_s=1150$ K. The computational results are presented in two parts: the gas-surface interactions at the surface and the reacting flow field in the gas phase. The results of heterogeneous surface reactions are plotted in Figs. 2–4. The Sherwood number (Sh) is used to represent the mass transfer of species between the gas phase and the platinum surface in the heterogeneous reaction. The Sherwood number of the major species, O_2, H_2O, CO_2, and CH_4, is computed along the axial direction. Figure 2 shows Sh of the major species versus Reynolds number. The local Reynolds number (Re_x) is based on the local distance from the beginning of the catalytic surface (x), free stream velocity, and physical properties at a temperature of 300 K. This means that, for the same value of the free stream axial velocity, Re_x increases with increasing values of x. The present numerical results show that at a fixed value of the local Reynolds number, the differences among the values of the major species' Sherwood number are small. Thus, at a fixed

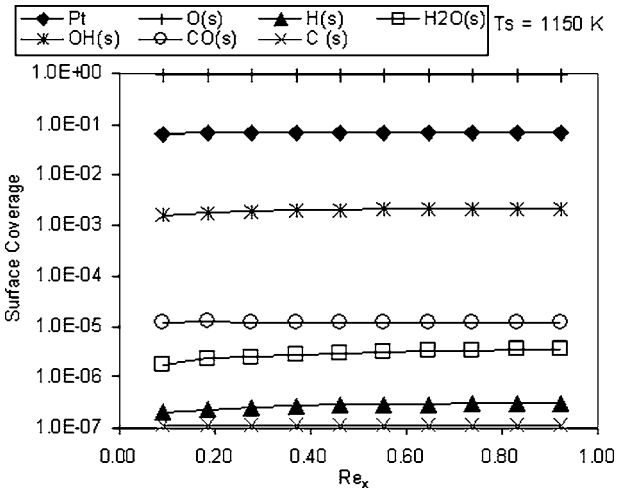

Fig. 3 Surface coverage of surface species versus Reynolds number at $T_s=1150$ K

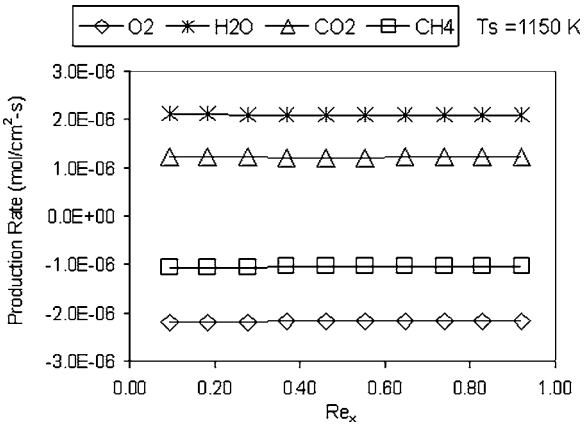

Fig. 4 Production rate versus Re_x for CH_4, O_2, CO_2, and H_2O at T_s=1150 K

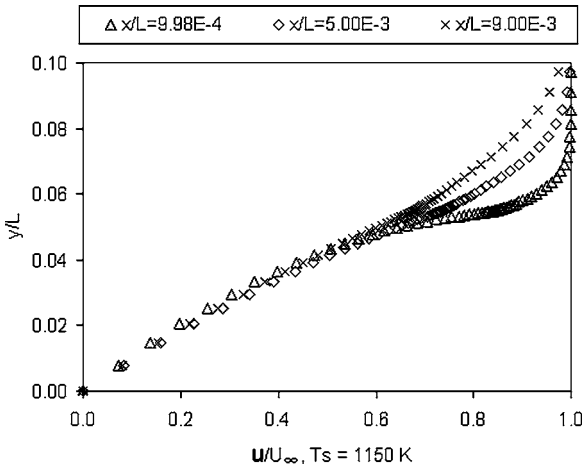

Fig. 6 Transverse profiles of dimensionless axial velocity (u/U_∞) for different axial distances at T_s=1150 K, U_∞=6 cm/s

local Reynolds number, Sherwood numbers of all major species can be approximated by one mean value. With this approximation, the relation between Sh of major species and Re_x can be correlated by a single exponential curve-fitted function. At a surface temperature of 1150 K, the curve-fitted relation between Sh and Re_x reads

$$\mathrm{Sh} = 8.0 + 3.18\ \mathrm{Re}_x^{-0.603} \tag{12}$$

The above correlation is plotted in Fig. 2. For high Reynolds numbers, Sh approaches a value of 8. Figure 3 shows the surface coverage of surface species versus local Reynolds number. It can be seen that most of the platinum sites are covered with O(s) thus reducing considerably the surface reactions. Production rate of major species versus local Re_x is depicted in Fig. 4. The production rates in Fig. 4 are surface reaction rates in mole/(cm^2 s). It is interesting to notice that the production rates decrease very slowly, as can be seen from Fig. 4. Moreover, the production rates of CO_2 and H_2O are essentially mirror images of the reacting species CH_4 and O_2. Also, the ratios of production rates of the main reacting and produced species suggest that these species react according to a one-step chemical reaction, namely, $CH_4 + 2O_2 \rightarrow CO_2 + 2H_2O$. The findings of the present work for the catalytic boundary layer are consistent with the conclusions of Tong et al. [10] for surface reactions of impinging methane-air mixtures.

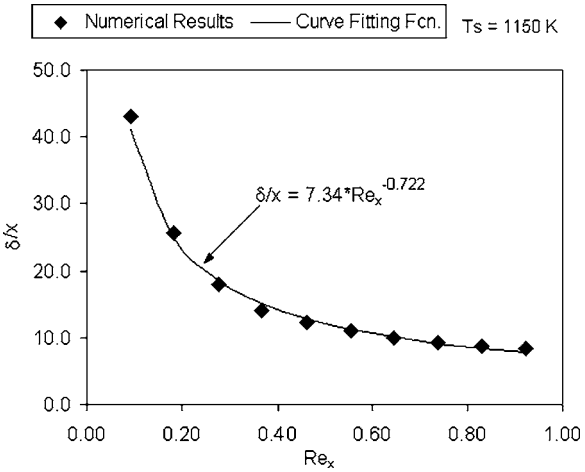

Fig. 5 Combustion boundary layer thickness versus Re_x at T_s=1150 K

The results of the reacting flow field are plotted in Figs. 5–10. The reaction boundary layer thickness of the flowing gases (δ) is determined as the transverse distance above the surface to where the mole fraction of the fuel is 99% of its mole fraction in the free stream. The reaction boundary layer thickness is essentially different from the hydrodynamic one. Figure 5 shows the dimensionless reaction boundary layer thickness δ/x versus local Reynolds number, where x is the axial distance measured from the beginning of surface reactions and not from the leading edge of the flat

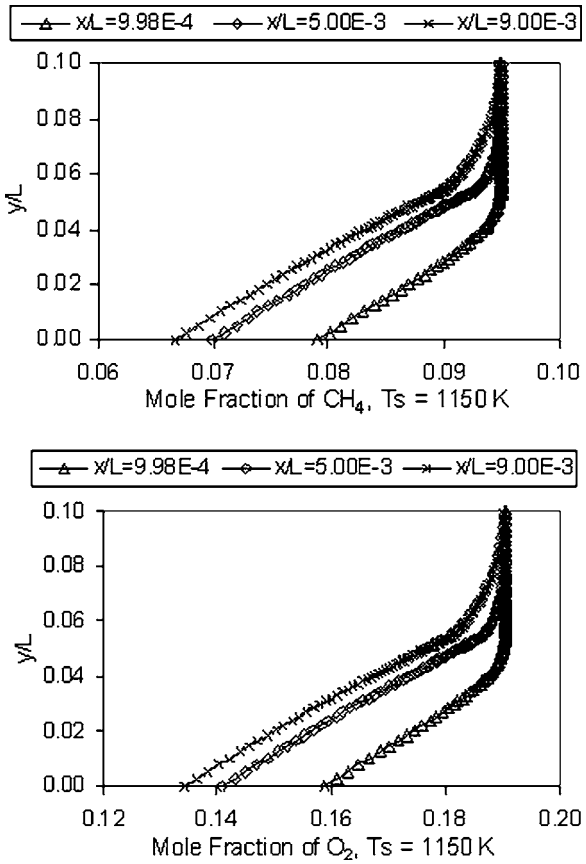

Fig. 7 Transverse profiles of reactants mole fraction for different axial locations at T_s=1150 K

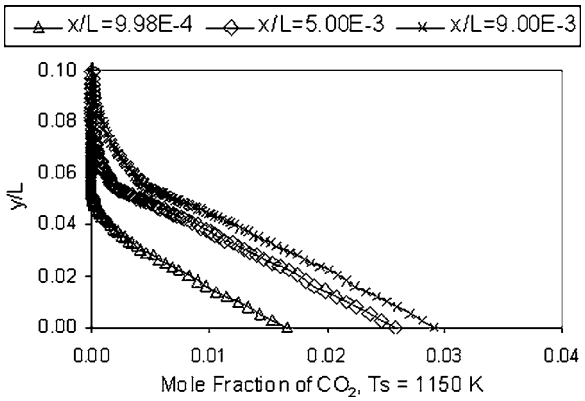

Fig. 8 Transverse profiles of CO_2 mole fraction for different axial locations at T_s=1150 K

plate. Curve fitting is used to establish a relation between δ/x and RE_x.

The correlation between δ/x and the local Reynolds number can be represented by the following numerical equation

$$\delta/x = 7.34\ \mathrm{Re}_x^{-0.722} \tag{13}$$

The obtained equation is plotted in Fig. 5 for comparison with the present numerical results. It can be seen from the above equation that the reaction boundary layer thickness δ is proportional to $(\mathrm{Re}_x)^{0.278}$ and hence increases as Re_x increases. Figure 6 shows the normalized axial velocity profiles along the dimensionless transverse distance above the surface (y/L) at different axial locations in the heated section of the flat plate. At the hot plate inlet section, the axial velocity profile conforms to the fully developed isothermal boundary layer flow. However, for $x>0.0$, the flowing gases have a temperature of 1150 K at the surface, while for $(y/L)>0.08$ the temperature is essentially close to 300 K; this will become obvious from the explanation below of Fig. 9. The large temperature range causes the density and viscosity to increase appreciably at the hot plate surface in comparison to the values at 300 K for $(y/L)>0.08$. At the surface, the density is nearly one-fourth its value for $(y/L)>0.08$, while the viscosity is 2.5 times higher. In this case, the Reynolds number, based on the gas physical properties at the surface, is one-tenth its value at 300 K. As a result of higher friction factors for lower Reynolds numbers, the surface viscous stresses will be much higher in the heated section than in the isothermal section of the plate at 300 K. Consequently, the axial velocity near the surface decelerates to values much lower than the isothermal boundary layer velocity

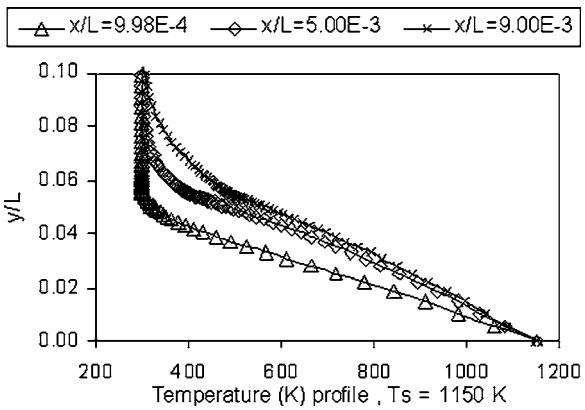

Fig. 9 Transverse gas temperature profiles for different axial locations at T_s=1150 K

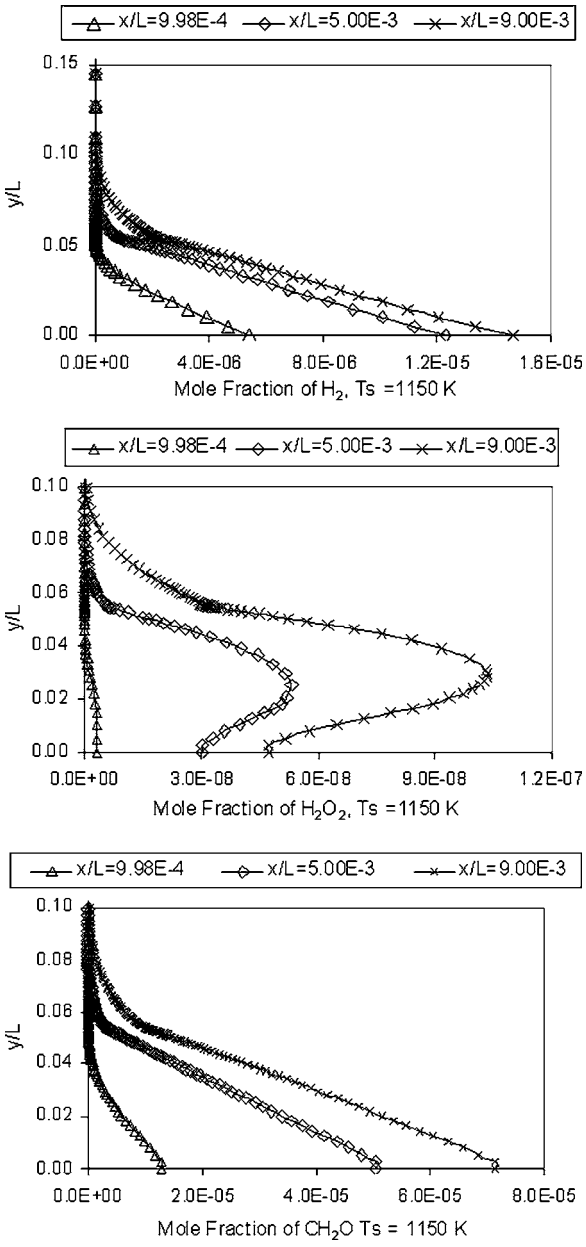

Fig. 10 Transverse profiles of selected rare species for different axial locations at T_s=1150 K

profile, as can be deduced from Fig. 6. On the other hand, the axial velocity, in the outer boundary layer where T is close to 300 K, conforms to the fully developed boundary layer isothermal flow. Figure 7 shows the transverse profiles of the mole fraction of CH_4 and O_2 for different values of x/L. The effect of surface reactions is obvious; the reactants are mainly depleted on the catalytic surface with little chemical activities elsewhere, except for intermediate reactions that produce rare species such as H_2, H_2O_2, and CH_2O, as discussed below. Figure 8 shows the mole fraction transverse profiles of CO_2 along y/L. Figures 7 and 8 show continuous consumption of the reactants and continuous generation of the main products at the catalytic surface as the stoichiometric fuel-air mixture flows downstream. Figure 9 shows the temperature profiles along y/L at different axial locations. Near the surface, at the same transverse location, the temperature monotonically increases along the axial direction. For $(x/L)<0.01$, the temperature variations are essentially limited to dimensionless transverse distances less than 0.08. It can be seen from both Figs.

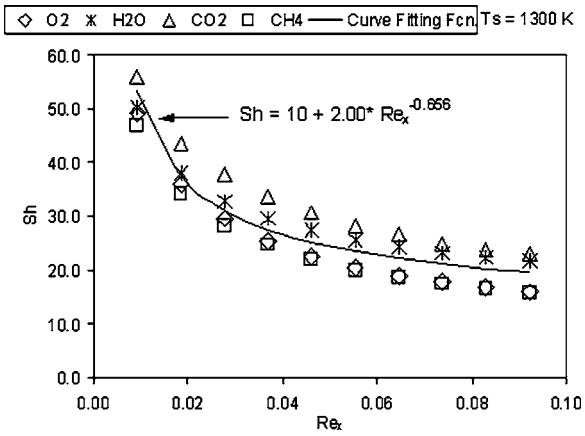

Fig. 11 Sherwood number versus Reynolds number for CH_4, O_2, CO_2, and H_2O at T_s=1300 K

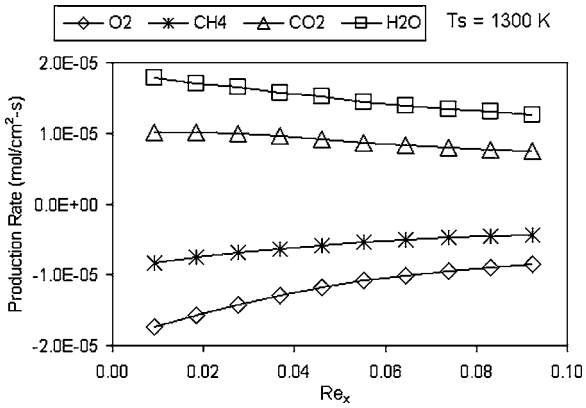

Fig. 13 Production rate versus Re_x for CH_4, O_2, CO_2, and H_2O at T_s=1300 K

9 and 6 that the width of the boundary layer increases with increasing values of (x/L) up to a limiting value of approximately $(L/10)$. The mole fraction transverse profiles of rare species H_2, H_2O_2, and CH_2O are depicted in Figs. 10(*a*)–10(*c*). The maximum values of H_2, CH_2O occur at the surface-gas interface, while the peak of H_2O_2 is shifted towards lower gas temperatures. This is because the production of H_2O_2 involves one reaction $HO_2+HO_2 \rightarrow H_2O_2+O_2$ which is dominant at lower temperatures and has negative activation energy of −5.20 kJ/mol [8]. The production of H_2 and CH_2O involves positive or zero activation energies [8]. Moreover, the mole fractions of the above three species increase as the chemical reactions proceed along the axial direction, as can be seen from Fig. 10.

3.2 Results for a Surface Temperature of 1300 K, i.e., T_s =1300 K. Results of surface reaction are shown in Figs. 11–13. Figure 11 shows the Sherwood numbers of major species versus local Reynolds numbers at the surface temperature of 1300 K. The curve fitted relation between Sh and Re_x at surface temperature of 1300 K reads

$$\mathrm{Sh} = 10.0 + 2.00\mathrm{Re}_x^{-0.656} \tag{14}$$

The above correlation is plotted in Fig. 11. For Re_x from 0.01–0.1, the mean Sherwood number, calculated from the above equation, is 27. Figure 12 shows the surface coverage of surface species versus Re_x. Comparing the surface coverage in Fig. 12 with that at T_s=1150 K, shows a considerable increase in the surface coverage of the active sites of Pt(s) and an appreciable decrease in the surface coverage of O(s). This is because the surface reactions are highly activated at higher surface temperatures. The production rate of major species versus the local Reynolds number is plotted in Fig. 13.

The results of the reacting flow field at surface temperature of 1300 K are plotted in Figs. 14–19. Figure 14 shows δ/x versus local Reynolds number, where δ is the reaction boundary layer thickness of the flowing gases and x is the axial distance measured

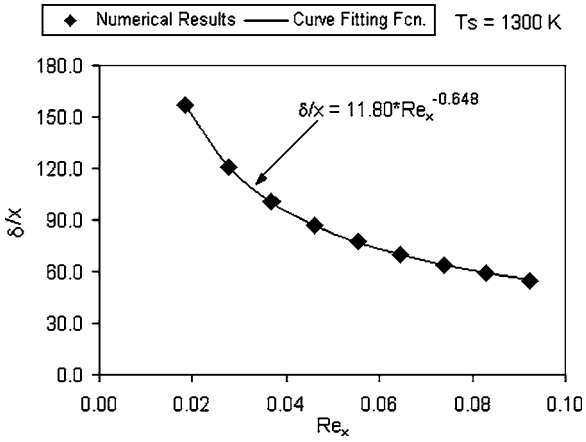

Fig. 14 Combustion boundary layer thickness versus Re_x at T_s=1300 K

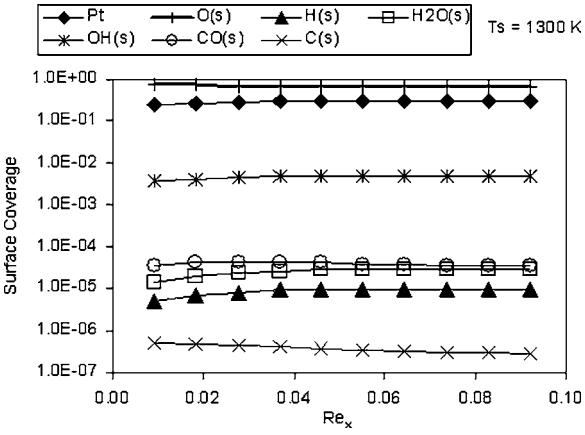

Fig. 12 Surface coverage of surface species versus Reynolds number at T_s=1300 K

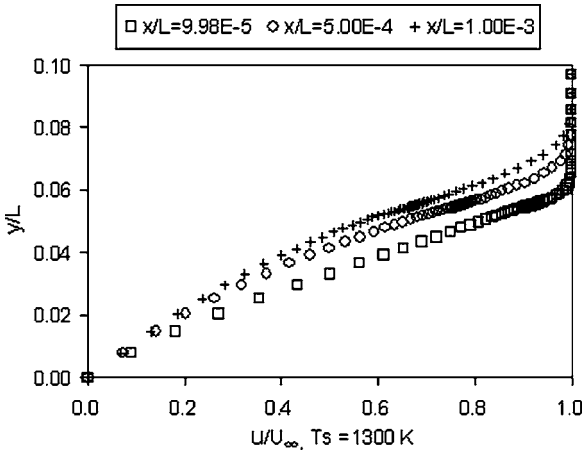

Fig. 15 Transverse profiles of dimensionless axial velocity (u/U_∞) for different axial distances at T_s=1300 K, U_∞=6 cm/s

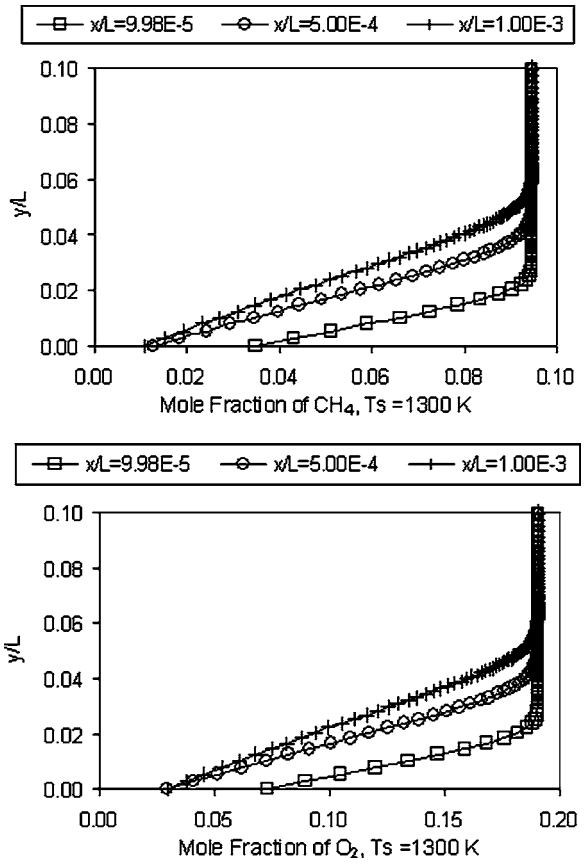

Fig. 16 Transverse profiles of reactants mole fraction for different axial locations at T_s=1300 K

from the beginning of surface reactions. The curve fitting relation between δ/x and Re_x is given by the following numerical equation

$$\delta/x = 11.80\ \mathrm{Re}_x^{-0.648} \tag{15}$$

Equation (15) is plotted in Fig. 14. Here, also, δ increases with increasing values of the local Reynolds number, as dictated by Eq. (15). Figure 15 shows the axial velocity transverse profiles along the dimensionless distance above the surface (y/L) at different axial locations. Here also, the non-isothermal velocity profiles deviate from the analytical solution of isothermal boundary layers [11]. This deviation results from higher resisting shear stresses

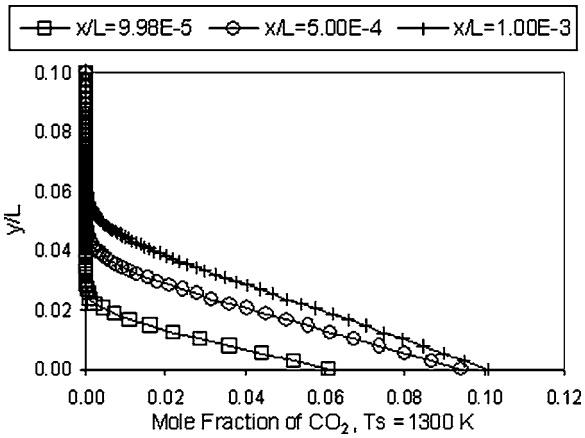

Fig. 17 Transverse profiles of CO_2 mole fraction for different axial locations at T_s=1300 K

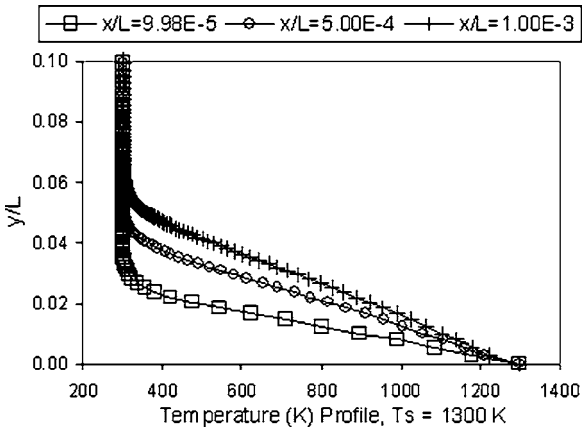

Fig. 18 Transverse gas temperature profiles for different axial locations at T_s=1300 K

and lower axial momentum caused by the higher viscosities and lower densities near the catalytic hot surface compared to the corresponding values in the free stream. Figure 16 shows the mole fraction transverse profiles of CH_4 and O_2 along y/L. Figure 17 shows the mole fraction profiles of CO_2 along y/L. Figure 18 shows temperature transverse profiles along y/L at different axial locations. The analysis of the numerical results of the axial velocity, main species' mole fractions and temperature, reported earlier in this section, is also applicable to the numerical results depicted in Figs. 15–18. Figures 15–18 show clearly the differences in the hydrodynamic, thermal, and surface reactions' boundary layers. However, the different boundary layers have thicknesses that increase with increasing values of the axial distance. Figure 19 shows the mole fraction transverse profiles of selected rare species, namely, H_2, H_2O_2, and CH_2O. In these three species, H_2 is involved in both gas phase reactions and surface phase reactions while H_2O_2 and CH_2O are only involved in gas phase reactions. It can be seen that the maximum values of the mole fractions of these rare species are essentially ten times higher at surface temperature of 1300 K, compared to the values of the same species shown in Fig. 10.

3.3 Catalytic Surface Reaction Rate. The surface production rates, presented in Figs. 4 and 13 for surface temperatures of 1150 K and 1300 K, respectively, suggest that a global one step reaction, between O_2 and CH_4 to produce CO_2 and H_2O, is possible. Therefore, the following catalytic chemical reaction is considered

$$\mathrm{CH_4} + 2\mathrm{O_2} \rightarrow \mathrm{CO_2} + 2\mathrm{H_2O} \tag{R1}$$

Although (R1) is not an elementary reaction, it is possible to represent its reaction rate by the following chemical kinetic equation

$$R_c = A([\mathrm{O_2}][\mathrm{CH_4}])^n \exp\left(-\frac{T_a}{T_s}\right) \tag{16}$$

where T_a and T_s are the activation and catalytic surface temperatures, respectively. The concentrations of the oxygen and methane have units of mole/cm^3, while the surface reaction rate R_c is in mole/(cm^2 s). The above equation can presumably be used for the whole range of the present numerical results for 1150 K and 1300 K surface temperatures. The constants A, n, and T_a are to be computed from the present numerical data. In order to establish the relation between the surface reaction rate and the product of the concentrations of O_2 and CH_4, the production rate of CO_2 is plotted versus $[O_2][CH_4]$ in Fig. 20 for T_s=1150 K and in Fig. 21 for T_s=1300 K. Equation (16) is also plotted in both figures for particular values of constants A, n, and T_a. At 1150 K the numeri-

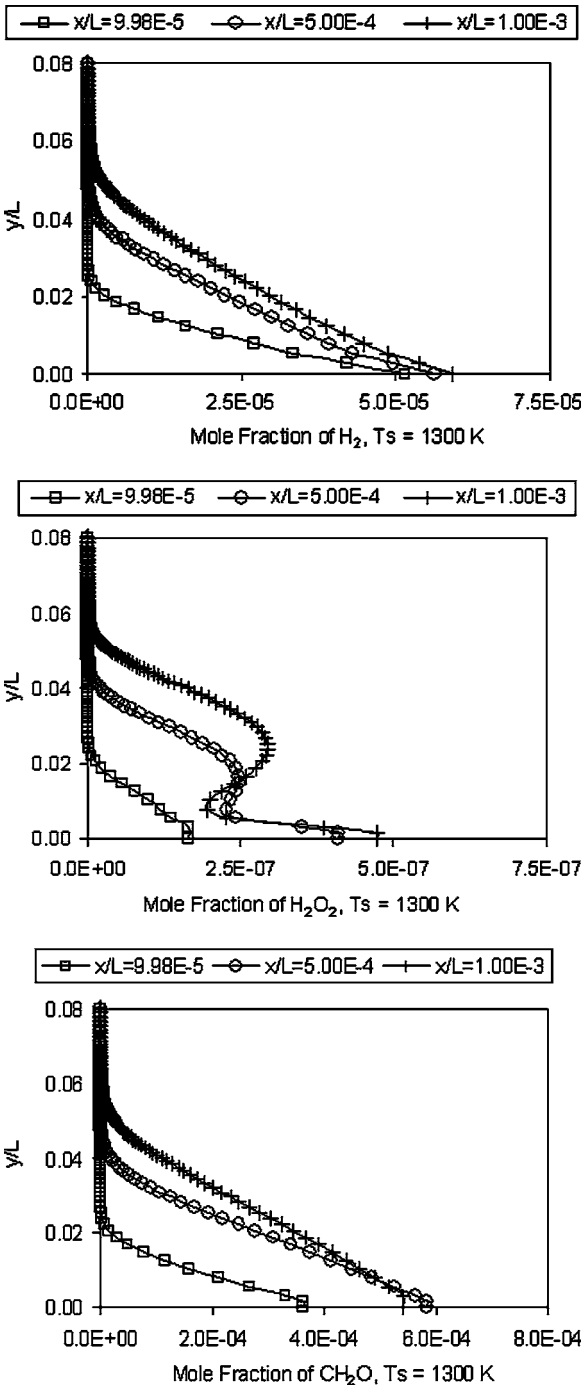

Fig. 19 Transverse profiles of selected rare species for different axial locations at T_s=1300 K

cal results exhibit a single-fold relation, which is consistent with the present data at 1300 K surface temperature and for $[O_2]\times[CH_4]>3.5\times10^{-16}$. For this range of concentrations, A, n, and T_a have unique values to fit the results for T_s=1150 K and 1300 K. However, at lower values of reactants' concentrations, the catalytic surface reaction rate decreases much faster with different set of values for constants A, n, and T_a. The set of constants of Eq. (16) for $[O_2][CH_4]$ higher and lower than 3.5×10^{-16} are given in Table 2. The lower concentration range of surface reactions has an equivalent order of reaction of 2.0, while the higher range is limited to an overall order of reaction of 0.4. On the other hand, the lower range has a lower activation temperature, while

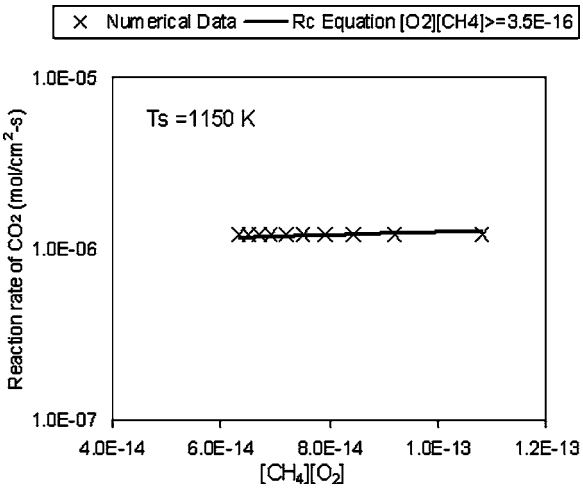

Fig. 20 Surface reaction rate at surface temperature of 1150 K

the higher concentration range is governed by a much higher activation temperature, as can be deduced from Table 2. This means that the higher concentration range is a highly temperature-dependent surface reaction and less dependent on reactants' concentrations, while the lower range is controlled by the reactants' concentrations.

It should be mentioned here that global reaction (R1) is essentially dependent on the total concentration of the platinum catalyst layer. Therefore, the pre-exponential constant values reported in Table 2 reflect only implicitly such dependence. This is because a fixed value is assigned to the total concentration of the active catalytic platinum surface sites.

3.4 Heat Transfer Computations. Heat transfer between the catalyst coated plate and the boundary layer gas mixture is also investigated. The present numerical scheme for laminar heat transfer in boundary layers was validated for a well-known standard case. In this case, the thermal boundary layer and the momentum boundary layer start concurrently at the leading edge. The heat

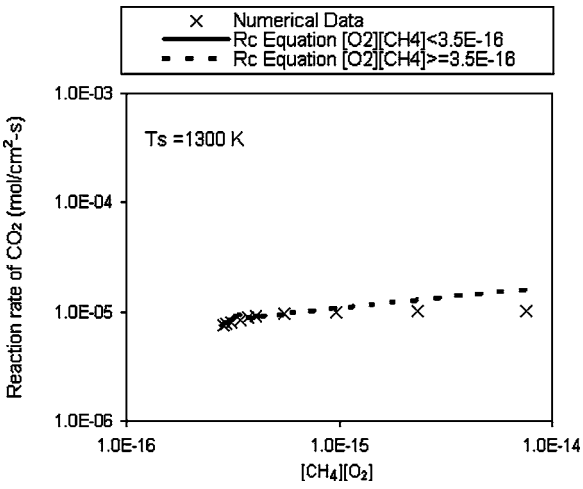

Fig. 21 Surface reaction rate at surface temperature of 1300 K

Table 2 Constants in catalytic surface reaction rate equation

n	A (cm^3 mol s)	T_a (K)
0.2	1.96×10^8	30,699 for $[O_2][CH_4]\geq3.5\times10^{-16}$
1	7.78×10^{13}	10,337 for $[O_2][CH_4]<3.5\times10^{-16}$

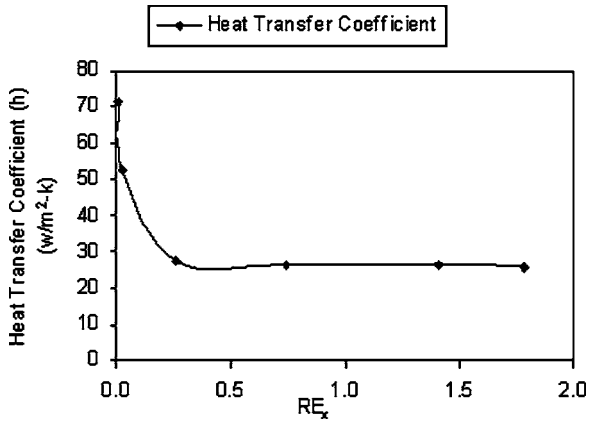

Fig. 22 Heat transfer coefficient versus Reynolds number without chemical reactions

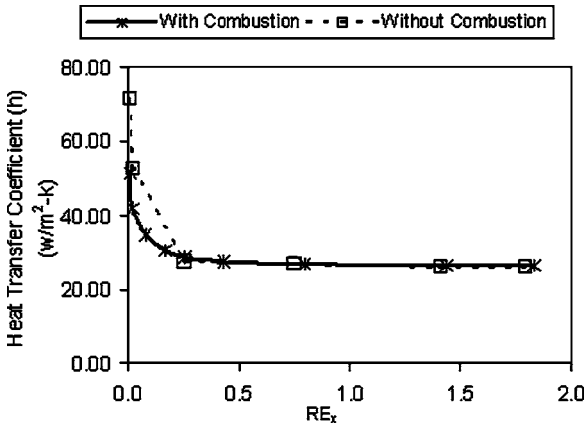

Fig. 24 Comparison of heat transfer coefficient

transfer coefficient (h) and Nusselt number (Nu_x) are calculated. The heat transfer coefficient is plotted against local Reynolds number (RE_x), for a surface temperature of 1150 K, as shown in Fig. 22. It should be mentioned here that the local Reynolds number (RE_x) and Nusselt number are computed based on the gas physical properties at the mean film temperature. For surface and free stream temperatures of 1150 K and 300 K, the present mean film temperature is 725 K. The heat transfer coefficient decreases rapidly near the leading edge up to a local Reynolds number of 0.3 where the decrease in h is much slower, as depicted in Fig. 22. The computed local Nusselt number is plotted versus the local Reynolds number, as shown in Fig. 23. The numerical data of Figs. 22 and 23 were computed for a non-reacting flow for comparison with existing similar correlations. In the same figure, the standard heat transfer correlation for parallel flow over a hot flat plate [11] is also plotted. The Nusselt number correlation [11] for Prandtl number (Pr) ranging between 0.6–10 is given below by Eq. (17)

$$Nu_x = 0.332 Pr^{1/3} RE_x^{0.5} \tag{17}$$

The numerical results presented in Fig. 23 and all other figures in this subsection are computed for a fixed Prandtl number of 0.7. The present computations for the local Nusselt number can be correlated to the local Reynolds number as

$$Nu_x = 0.316 RE_x^{0.520} \tag{18}$$

The present numerical results for $RE_x > 1.0$ slightly over-predicts the local value of Nusselt number, as the present correlation RE_x exponent is 4% higher than its counterpart in Eq. (17). The level of agreement between the above two equations suggests that the present numerical scheme can be used for heat transfer computations with a reasonable accuracy and will thus be used to simulate heat transfer from the catalytic surface to the reacting methane-air mixture reported above in Sec. 3.1.

Figure 24 presents the numerical results for heat transfer in the reacting boundary layer flow over a catalytic surface for surface temperature of 1150 K. In this case, the catalytic surface reactions and heat transfer start 3 cm after the leading edge of the flat plate while the hydrodynamic boundary layer begins exactly at the leading edge, as shown in Fig. 1. The computed heat transfer coefficient of Fig. 22 is also plotted in Fig. 24 for comparison. The non-reacting heat transfer coefficient is higher for Reynolds numbers less than 0.3, and then the reacting heat transfer coefficient becomes higher for RE_x greater than 0.3. It should be mentioned here that both Nu_x and RE_x are based on mean film temperature of 725 K and a characteristic axial distance measured form the beginning of surface reactions, i.e., from a distance of 3 cm after the plate's leading edge. Figure 25 depicts the computed local Nusselt number versus local Reynolds number for reacting boundary layer over a catalytic surface at 1150 K. The standard correlation of laminar heat transfer in an inert boundary layer is also plotted in Fig. 25, for comparison. The relation between Nu_x and RE_x, for heat and mass transfer from a reacting surface, is correlated as

$$Nu_x = 0.327 RE_x^{0.604} \tag{19}$$

Figure 26 shows the correlations between Nu_x and RE_x, as defined

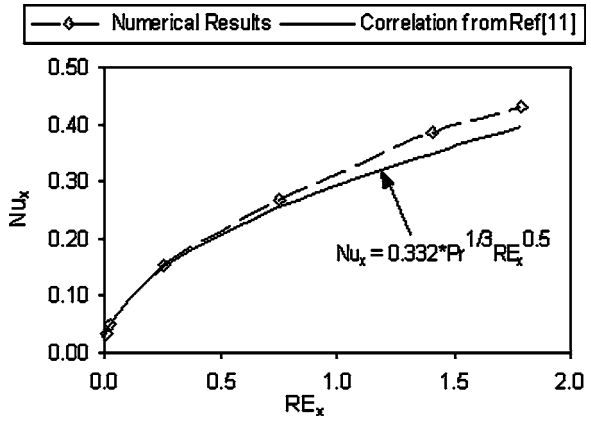

Fig. 23 Nusselt number versus Reynolds number without chemical reactions

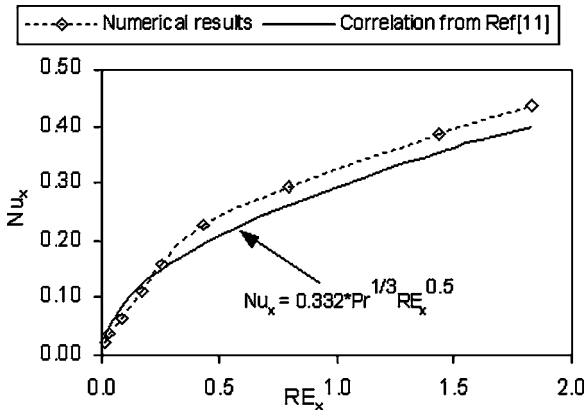

Fig. 25 Nusselt number versus Reynolds number with chemical reactions

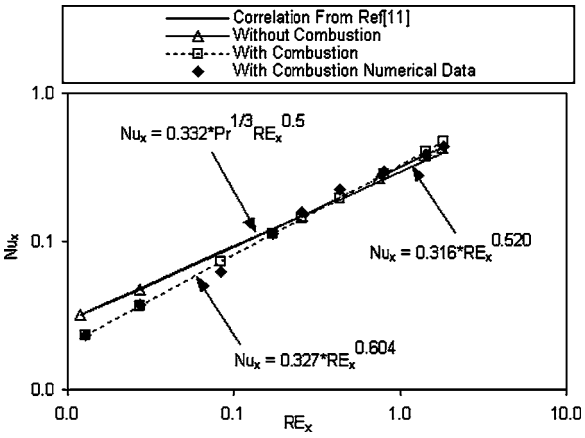

Fig. 26 Comparison of heat transfer correlations

by Eqs. (17)–(19), together with numerical data for selected transverse planes.

The numerical data, present correlations and standard laminar heat transfer data [11] fall in a narrow band suggesting their interlinking coherent relation. However, the reacting flow exhibits higher dependence of Nusselt number on the local Reynolds number. In this case, RE_x is raised to a power 20% higher than standard pure laminar heat transfer correlation [11].

4 Conclusions

The present paper describes a complete computational model for the prediction of the properties of reacting methane-air mixtures flowing over hot catalytic plates. For temperatures 1150 K and 1300 K, the flowing gas mixture reacts mainly on the surface by the active platinum sites. For both temperatures, the non-isothermal boundary layer flow deviates noticeably from its isothermal counterpart as a result of higher viscosity and lower density near the hot catalytic surface. Increasing the surface temperature by 150 K causes the surface reactions to increase by more than one order of magnitude. The computed surface production rates of the flowing gas phase show consistency with the stoichiometric coefficients of the main reacting species, in such a way that the consumption of one mole of CH_4 by two moles of O_2 produces one mole of CO_2 and two moles of H_2O. This shows that the production of the rare species is not important in actual catalytic reactors. The overall one-step reaction was correlated by a general "surface" chemical kinetic equation that is dependent on the product of the concentrations of O_2 and CH_4 and the surface temperature. Two chemical kinetic relations were derived from the present numerical data, distinguishing between a high concentration reaction regime with high activation temperature and a low concentration regime with lower activation temperature. Most of Pt(s) is covered by O(s) at 1150 K, which slows down surface reactions. This reaction inhibition is completely alleviated by the higher surface temperature of 1300 K. New numerical correlations, for the local reaction boundary layer thickness and Sherwood number versus Reynolds number, were deduced. The new correlations could be useful in similar applications involving heterogeneous surface reactions.

Heat transfer correlations between the local Nusselt number and local Reynolds number were first tested against standard correlations for the laminar boundary layer that starts from the leading edge for both heat and momentum transfer. The agreement between the present numerical correlation with no chemical reactions and the standard correlation is acceptable with 4% deviation in Reynolds number exponent. An additional correlation was also obtained for the reacting catalytic surface flow and compared to the non-reacting boundary layer heat transfer relations. The new correlation for catalytic surface heat transfer shows a higher dependence on the local Reynolds number, which is based on the mean film temperature.

Nomenclature

a_n = finite-difference coefficients due to combined convection and diffusion, kg/s
C_p = constant-pressure specific heat, J/kg K
h = heat transfer coefficient, W/m^2 K
h_g = Gas sensible enthalpy, J/kg
L = height of the computational domain, m
M = molecular weight, kg/kmole
Nu = Nusselt number
P = gas pressure, N/m^2
Pr = Prandtl number
R = universal gas constant, J/mole K
Re = Reynolds number based on free stream properties
RE = Reynolds number based on film properties
Sh = Sherwood number
T = temperature, K
u_i = velocity in direction i, m/s
U_∞ = free stream axial velocity, m/s
W_j = reaction rate of reaction j
x = distance along the axial axis, m
x_i = distance along direction i, m
$[X]$ = generalized concentration (gas phase: $mole/cm^3$, surface phase: $mole/cm^2$)
Y = species mass fraction
Z = surface site concentration, $mole/cm^2$
z_k = surface site fraction of k species (surface coverage fraction)

Greek Symbols

δ = chemical reaction boundary layer thickness, m
Γ_h = thermal diffusivity
ρ = density, kg/m^3
γ = sticking coefficient

Subscripts

g = gas
s = surface
x = at a distance x from beginning of surface reactions

References

[1] Williams, W. R., Stenzel, M. T., Song, X., and Schmidt, L. D., 1991, "Bifurcation Behavior in Homogeneous-Heterogeneous Combustion: I. Experimental Results Over Platinum," Combust. Flame, **84**, pp. 277–291.
[2] Song, X., Williams, W. R., Schmidt, L. D., and Aris, R., 1991, "Bifurcation Behavior in Homogeneous-Heterogeneous Combustion: II. Computations for Stagnation-Point Flow," Combust. Flame, **84**, pp. 292–311.
[3] Warnatz, J., Allendorf, M. D., Kee, R. J., and Coltrin, M. E., 1994, "A Model of Elementary Chemistry and Fluid Mechanics in the Combustion of Hydrogen on Platinum Surfaces," Combust. Flame, **96**, pp. 393–406.
[4] Deutschmann, O., Behrendt, F., and Warnatz, J., 1994, "Modeling and Simulation of Heterogeneous Oxidation of Methane on a Platinum Foil," Catal. Today, **21**, pp. 461–470.
[5] Raja, L. L., Kee, R. J., Deutschmann, O., Warnatz, J., and Schmidt, L. D., 2000, "Critical Evaluation of Navier-Stokes, Boundary-Layer, and Plug-Flow Models of the Flow and Chemistry in a Catalytic-Combustion Monolith," Catal. Today, **59**, pp. 47–60.
[6] Coltrin, M. E., Kee, R. J., and Rupley, F. M., 1991, "Surface Chemkin: A General Formalism and Software for Analyzing Heterogeneous Chemical Kinetics at a Gas-Surface Interface," Int. J. Chem. Kinet., **23**, pp. 1111–1128.
[7] Abou-Ellail, M. M., Gosman, A. D., Lockwood, F. C., and Megahed, I. E. A., 1978, "Description and Validation of a Three-Dimensional Procedure for Combustion Chamber Flows," AIAA J., **2**, pp. 71–80; also, published in *Turbulent Combustion*, L. Kennedy, ed., Progress in Aeronautics and Astronautics,

AIAA, New York, 1978, Vol. 58, pp. 163–190.
[8] Tong, T. W., Abou-Ellail, M. M., Li, Y., and Beshay, K. R, 2004, "Numerical Computation of Reacting Flow in Porous Burners With an Extended CH_4–Air Reaction Mechanism," ASME Paper No. HT-FED 2004-56012.
[9] Deutschmann, O., Maier, L. I., Riedel, U., Stroemman, A. H., and Dibble, R. W., 2000, "Hydrogen Assisted Catalytic Combustion of Methane on Platinum," Catal. Today, **59**, pp. 141–150.
[10] Tong, T., Abou-Ellail, M., and Li, Y., 2006, "Mathematical Modeling of Catalytic-Surface Combustion of Reacting Flows," accepted for publication at AIAA Journal of Thermophysics and Heat Transfer; presented at 9th AIAA/ASME Joint Thermophysics & Heat Transfer Conference, San Francisco, CA, AIAA Paper 2006-3815.
[11] Schlichting, H., 1979, *Boundary-Layer Theory*, McGraw-Hill Book Company, New York, Chap. 7.

Direct Numerical Simulation of a Non-Premixed Impinging Jet Flame

Xi Jiang[1]
e-mail: Xi.Jiang@brunel.ac.uk

Hua Zhao

Mechanical Engineering,
School of Engineering & Design,
Brunel University,
Uxbridge UB8 3PH, United Kingdom

Kai H. Luo
School of Engineering Sciences,
University of Southampton,
Southampton SO17 1BJ, United Kingdom

A non-premixed impinging jet flame at a Reynolds number 2000 and a nozzle-to-plate distance of two jet diameters was investigated using direct numerical simulation (DNS). Fully three-dimensional simulations were performed employing high-order numerical methods and high-fidelity boundary conditions to solve governing equations for variable-density flow and finite-rate Arrhenius chemistry. Both the instantaneous and time-averaged flow and heat transfer characteristics of the impinging flame were examined. Detailed analysis of the near-wall layer was conducted. Because of the relaminarization effect of the wall, the wall boundary layer of the impinging jet is very thin, that is, in the regime of viscous sublayer. It was found that the law-of-the-wall relations for nonisothermal flows in the literature need to be revisited. A reduced wall distance incorporating the fluid dynamic viscosity was proposed to be used in the law-of-the-wall relations for nonisothermal flows, which showed improved prediction over the law of the wall with the reduced wall distance defined in terms of fluid kinematic viscosity in the literature. Effects of external perturbation on the dynamic behavior of the impinging flame were found to be insignificant. [DOI: 10.1115/1.2737480]

Keywords: direct numerical simulation, heat transfer, impinging flame, law-of-the-wall, viscous sublayer, wall

1 Introduction

Near-wall fluid flow, heat transfer, and combustion phenomena are encountered in a broad range of practical applications. In almost all of the practical combustion systems, such as combustion engines, gas turbine combustors, and other industrial processes, combustion takes place in a vessel in which flames develop in the vicinity of walls and interact with them. Flame/wall interactions are also encountered in combustion hazards, such as fires. In the context of near-wall combustion, the study of impinging jet flames is of particular interests. In addition to the relevance to many engineering applications, such as industrial burners, metal cutting, glass shaping, and glass melting for fiber-optics production, impinging jet flames are also of great value in fundamental academic studies. The impinging flow configuration is of simple geometry but covers a broad range of important flow phenomena, such as large- and small-scale structures, wall boundary layers with stagnation, large curvature involving strong shear and normal stresses, and wall heat transfer. Impinging flames involve the complex interactions between the wall and the flame. In a turbulent scenario, the flame/wall/turbulence multiway interactions bring many unresolved and challenging issues in combustion modeling [1]. In general, the near-wall flow and heat transfer in reacting flows are not well investigated. For instance, the classical law-of-the-wall models of fluid flow and heat transfer neglected the presence of flame and variable density effects [2], which should be taken into account for combustion applications.

Because of the rich flow phenomena involved and the geometric simplicity, the impinging flame is ideal for development and validation of near-wall models. Over the last several years, near-wall combustion, including impinging flames, has attracted much research interest, e.g., [3–18], to name but a few. However, appropriate law-of-the-wall models for combustion applications have not been investigated in the existing studies. Impinging heat transfer has been an important subject in the context of computational fluid dynamics (CFD) modeling [19]. In many CFD codes for combustion applications, the traditional law of the wall implemented was derived for constant density flows in which temperature variations remain small. This approach could lead to very inaccurate predictions for combustion applications where temperature variations near the wall are normally very large. Moreover, in spite of the various existing efforts, the dynamics of impinging jet flames is still not fully understood due to the complex nature of the problem. The impinging flow contains a broad range of length scales, ranging from the large-scale vortical structure to very thin thermal boundary layers near the wall. The near-wall flow and combustion processes are also highly unsteady. A detailed study of impinging flames requires both spatially and temporally resolved solutions.

Near-wall flow and combustion phenomena deserve more research efforts from both application and fundamental points of view. For impinging flames, it is practically very difficult to investigate the detailed near-wall phenomena using experimental measurements. Among the various approaches, advanced numerical studies, such as DNS, can provide insight into impinging flames by providing both temporally and spatially resolved solutions. In this study, a spatial DNS was employed to investigate the near-wall fluid flow and heat transfer of an impinging jet flame. Since external perturbations, such as acoustic excitation, may significantly affect the impinging flame dynamics [14], the first objective of this study was to examine the effects of external perturbation on the impinging flame dynamics. Because of the lack of appropriate near-wall models for reacting flows, the second objective of this study was, more importantly, to examine the near-wall law-of-the-wall models for flow and heat transfer. Because of its practical importance and theoretical relevance, the impinging flame configuration was used to reveal the law-of-the-wall relations, which is different from the channel flow configuration [4–6]. A comparative DNS study of impinging jet flames was carried out, including reacting impinging flames with and without

[1]Corresponding author.

Contributed by the Heat Transfer Division of ASME for publication in the JOURNAL OF HEAT TRANSFER. Manuscript received April 23, 2006; final manuscript received September 20, 2006. Review conducted by Walter W. Yuen.

external perturbation. A nonreacting impinging hot jet was also computed to illustrate the effects of combustion heat release in the reacting cases.

2 Mathematical Formulation

The physical problem considered was a fuel jet issuing into an open boundary domain from a round nozzle that impinged on a flat surface, where combustion took place when the fuel mixed with the oxidant environment. The impinging jet has two confinement plates, one is the jet nozzle inlet plane and the other one is the impingement plate or the wall. A time-accurate spatial DNS based on high-order finite difference numerical schemes and high-fidelity boundary conditions was performed, using a recently developed code for spatial DNS of reacting and nonreacting jets [20–22]. The wall was considered to be a "cold" wall at the ambient temperature, where flame quenching occurred when the flame front reached the wall. For such a head-on flame quenching on cold walls, the problem was thermally controlled [23,24] and a simple chemistry model may be used [1]. A one-step global reaction $\nu_f M_f + \nu_o M_o \rightarrow \nu_p M_p$ with finite-rate Arrhenius kinetics was considered to be adequate, where M_i and ν_i represent the chemical symbol and stoichiometric coefficient for species i, respectively.

The mathematical formulation of the physical problem included the governing equations, numerical methods for discretization and solution, and boundary and initial conditions. The flow field was described with the compressible time-dependent Navier-Stokes equations in the Cartesian coordinate system (x,y,z), where the z-axis is along the streamwise direction for the head-on impingement and the x-0-y plane is the domain inlet where the jet nozzle exit locates. The nondimensional form of the governing equations was employed [21]. Major reference quantities used in the normalization were the centerline streamwise mean velocity at the jet nozzle exit (domain inlet), jet nozzle diameter, and the ambient temperature, density, and viscosity. The reaction rate, after normalization, takes the form of $\omega_T = \mathrm{Da}(\rho Y_f / W_f)^{\nu_f}(\rho Y_o / W_o)^{\nu_o} \exp[-\mathrm{Ze}(1/T - 1/T_{fl})]$, where W and Y represent species molecular weight and mass fraction, and Da, Ze, and T_{fl} stand for the Damköhler number, Zeldovich number, and flame temperature, respectively. The heat release rate in the energy equation was given by $\omega_h = Q_h \omega_T$ with Q_h representing heat of combustion. The governing equations were supplemented by the ideal-gas law for the mixture. Details of the governing equations can be found in [21].

The equations were solved using a sixth-order accurate compact finite-difference scheme for evaluation of the spatial derivatives [25] in all of the three directions. The finite-difference scheme has spectral-like resolution. It allows flexibility in the specification of boundary conditions for minimal loss of accuracy relative to spectral methods. It is of sixth order at inner points, of fourth order at the next to boundary points, and of third order at the boundary. The time-dependent governing equations were integrated forward in time using a fully explicit low-storage third-order Runge-Kutta scheme [26].

Boundary conditions for the spatial three-dimensional (3D) DNS of impinging jet flames represent a challenging problem. Physical conditions at the jet nozzle exit and the wall must be appropriately represented. In the meantime, open boundary conditions in the jet cross-streamwise direction should allow jet mixing with the ambient and entrainment. The Navier-Stokes characteristic boundary condition (NSCBC) by Poinsot and Lele [27] was utilized for the inflow and wall boundary conditions, whereas the nonreflecting characteristic boundary condition [28] was used to specify the open boundaries. The impinging wall was assumed to be at constant ambient temperature, impermeable with no diffusion across the wall for chemical species, and satisfying the nonslip condition. For the jet nozzle exit (domain inlet), the NSCBC was used to specify the inflow boundary with density treated as a "soft" variable. A soft variable means that the density was allowed to vary according to the characteristic waves at the boundary. In the simulations, the variation of density around the prescribed value was negligible. This treatment is associated with the well posedness of the governing equations [27] and guarantees the numerical stability of the high-order nondissipative numerical scheme near the boundary.

The streamwise mean velocity $\bar{w}$ at the domain inlet was specified as a hyperbolic tangent profile, while the cross-streamwise mean velocity components at the domain inlet were given by $\bar{u}=0$ and $\bar{v}=0$. For the case with external perturbation, unsteady disturbance in a sinusoidal form [14] was artificially added to the mean velocity profile at the domain inlet, given by $u=\bar{u}+A\sin(2\pi f_0 t)$, $v=\bar{v}+A\sin(2\pi f_0 t)$, and $w=\bar{w}+A\sin(2\pi f_0 t)$ with A standing for the amplitude of disturbance that was specified as a percentage of the maximum value of $\bar{w}$. The nondimensional frequency of the unsteady disturbance was $f_0=0.30$, which was chosen to be the unstable mode leading to the jet preferred mode of instability [29]. The fuel temperature at the jet nozzle exit was assumed to be 3, which was chosen to ensure autoignition of the mixture [21]. Ignition occurs automatically above the jet nozzle exit plane when the fuel and oxidizer mix with each other. The inlet temperature profile and streamwise velocity profile were linked with the Crocco-Busemann relation $T=(\bar{w}_0\bar{w}-\bar{w}^2)M^2(\gamma-1)/2+(T_0-T_a)\bar{w}/\bar{w}_0+T_a$, where the subscripts 0 and a represent the centre of the jet nozzle exit and the ambient environment, respectively. The temperature and mass fractions of the species at the domain inlet were kept unchanged during the simulations.

Initially, the pressure field was assumed to be uniform and the flow field was initialized with all variables varying linearly from the conditions at the domain inlet to conditions at the wall. The initial conditions specified did not affect the numerical solutions appreciably after the initial stage of the simulation. For the setup of initial conditions, a no-flow condition with zero initial velocities everywhere in the computational domain was also tested, which showed no difference compared to the initial conditions adopted after the initial flow developing stage. The no-flow initial condition was not adopted, because it required longer simulation time for the flow to develop.

3 Numerical Results and Discussion

Several computational cases were performed for an impinging configuration with nozzle-to-plate distance of two jet diameters. The computational cost related to this relatively small domain was affordable for this study. In applications this shallow configuration has the advantage of reducing the heat losses from the flame to the surrounding environment. In the simulations, the considered jet Mach number was Ma=0.3, which was based on the reference quantities specified in the previous section. The Reynolds and Prandtl numbers used were Re=2000 and Pr=1. The Reynolds number under investigation is in the regime of transitional flow [3]. The ratio of specific heats used was $\gamma=1.4$. The impinging wall temperature was $T_w=1$. The dynamic viscosity was chosen to be temperature-dependent according to $\mu=\mu_a(T/T_a)^{0.76}$ with the reference viscosity taken to be the ambient value. Parameters used in the one-step chemistry were: Damköhler number Da=6, Zeldovich number Ze=12, flame temperature $T_{fl}=6$, and heat of combustion $Q_h=300$, respectively. These values were chosen to give temperatures of the reacting flow typically encountered in many non-premixed flames.

The dimensions of the computational box used were $L_x=L_y=8$ and $L_z=2$. It was tested that extending the domain size in the cross-streamwise directions to $L_x=L_y=12$ did not lead to significant changes in the numerical results, therefore $L_x=L_y=8$ was adopted in the productive runs. A grid system with $208\times208\times104$ nodes was used with uniform grid distribution in each direction. A grid independence test was performed and further refinement of the grid to $240\times240\times120$ did not lead to appreciable changes in the solution. The time step was limited by the Courant-Friedrichs-Lewy (CFL) condition for stability and a chemical re-

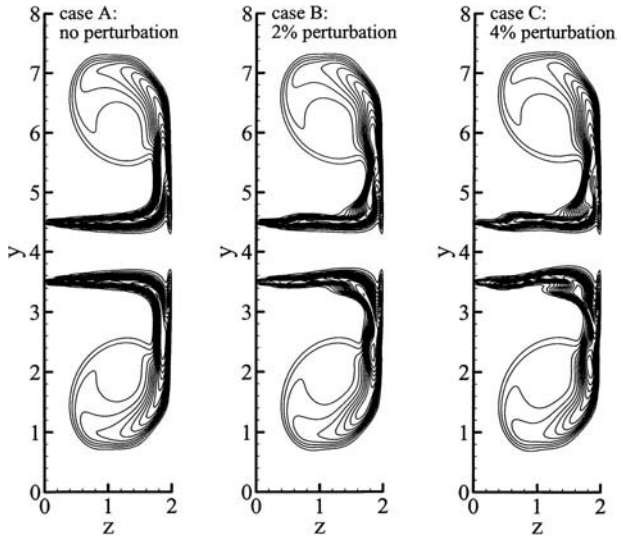

Fig. 1 Instantaneous reaction rate contours in the $x=4$ plane at $t=20$ (15 contours between the minimum and maximum values)

straint [21]. A CFL number of 2 was used in the simulations performed, which also led to time-step independent numerical results. Parallel computations were performed on a 16-processor Beowulf Cluster computer under the MPI environment. The results obtained were considered to be grid and time-step independent. In the following, results will be discussed for four cases that constitute a comparative study: a baseline nonreacting case without external perturbation (case 0) and three reacting cases with no perturbation (case A) and perturbation amplitudes of $A=2\%$ (case B) and $A=4\%$ (case C), respectively. For the nonreacting hot jet, there was a temperature ratio of $T_0/T_a=3$ at the inlet, where subscripts 0 and a represent the center of the domain inlet (jet nozzle exit) and the ambient environment, respectively.

3.1 Instantaneous and Time-Averaged Flow Characteristics. Figure 1 shows the instantaneous reaction rate contours in the $x=4$ plane (the middle of the 3D domain) at $t=20$ of the three reacting cases, respectively. In Fig. 1, it is evident that the non-premixed flame initially formed in the primary jet stream deflects from the wall and then convects along the surface of the wall after the impingement. There is a large head vortex at the end of the wall jet flame. The existence of this large head vortex thickens the wall jet flame significantly. In the meantime, it can be observed that there is a tendency of forming vortical structures in the primary jet stream for the perturbed cases. Vortical structures such as the head vortex are important features of impinging jets [30]. These vortical structures are caused by the Kelvin-Helmholtz-type shear layer instability that can play a significant role in the mixing and entrainment.

In Fig. 1, however, it is noted that the external perturbation does not affect the wall boundary layer of the impinging flame appreciably. For jets, it is well known that there exists a preferred frequency at which an external disturbance receives maximum amplification in the jet column and the jet develops large-scale vortical structures [29]. The results in Fig. 1 indicate that the impinging flame is not significantly affected by the external perturbation. This is mainly associated with the shallow impinging configuration and the relaminarization effect of the wall. An important feature of jet impingement is the wall re-laminarization effect [22]. Upon impingement, the jet streamwise velocity decays to a zero value, meanwhile, the jet spreads over the wall surface in the circumferential direction that forms the wall boundary layer. The viscous effects are important to the wall boundary layer, which has a much larger flow cross-sectional area than that of the jet primary stream. Therefore, the jet velocity decays significantly after the impingement that consequently leads to the relaminarization of the jet flow. Because of this wall relaminarization effect, the external perturbation does not have a significant effect on flow structures of the wall boundary layer. This is consistent with the literature [30], where it was understood that pulsation or perturbation does not always improve the transfer rate because the pulses may not reach up to the wall. In this study, the flow instability induced by the external perturbation does not reach up to the wall boundary layer due to the very small nozzle-to-plate distance of the impinging configuration and the re-laminarization effect of the wall.

Figure 2 shows the instantaneous temperature contours in the $z=1$ plane at $t=20$ of the three reacting cases. It can be seen that the external perturbation does not have a significant impact on the temperature fields in this plane of the computational domain. For all of the three reacting cases, the maximum temperature locates at around two jet diameters away from the centerline of the primary jet stream. Compared to Fig. 1, it can be identified that the maximum temperature zone is located within the head vortex of the impinging jet flame. There are two factors contributing to the formation of this high temperature zone. First, the flow circulation inside the head vortex can enhance the mixing between the fuel and oxidizer. Second, the very low flow speed near the core of the head vortex impedes the convective heat transfer and the heat losses from the flame to its ambient environment. Both factors lead to high temperatures within the head vortex. For all the three reacting cases, the temperature near the core of the head vortex reaches a value higher than 5.2.

For impinging hot jets and impinging flames, the near-wall heat transfer can be measured by the Nusselt number, which is a dimensionless number that measures the enhancement of heat transfer from a surface that occurs in a "real" situation, compared to the heat transfer that would be measured if only conduction could

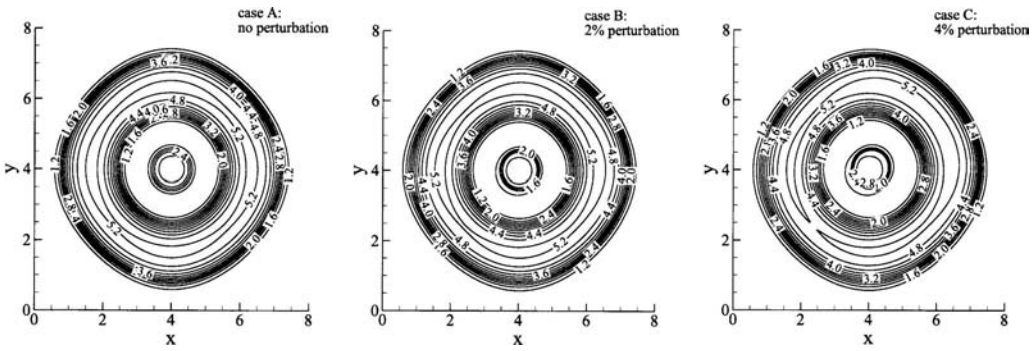

Fig. 2 Instantaneous temperature contours in the $z=1$ plane at $t=20$

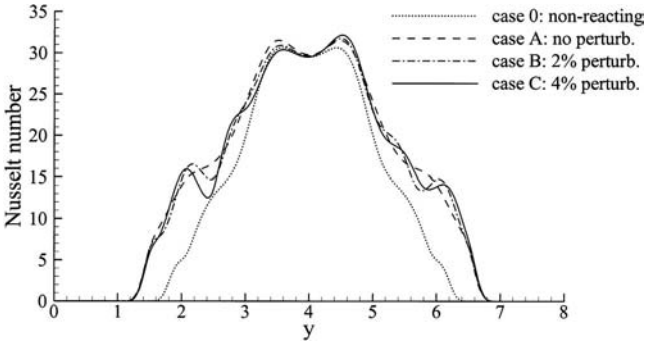

Fig. 3 Instantaneous Nusselt number at the wall in the $x=4$ plane at $t=20$

occur. Typically Nusselt number is used to measure the enhancement of heat transfer when convection takes place. It is defined as $\mathrm{Nu}=hD/k$, where D is the jet nozzle diameter and k is the thermal conductivity of the fluid and h is the heat transfer coefficient defined as $h=-k(dT/dz)/(T_0-T_w)$. Figure 3 shows a comparison of the instantaneous Nusselt number at the wall in the $x=4$ plane at $t=20$ of the four cases, including the nonreacting hot-jet case and the three reacting cases. In Fig. 3, it is evident that the reacting cases have a larger temperature distribution and, consequently, larger heat transfer zone near the wall, compared to the nonreacting case. A close examination of Fig. 3 also reveals that the instantaneous Nusselt number fluctuates at regions near $y=2$ and $y=6$ for the perturbed reacting cases B and C, where the Nusselt number distribution shows small troughs and peaks. This is mainly because of the existence of vortical structures in the perturbed cases. The unsteady vortex separation from the wall in the perturbed cases leads to variations in the Nusselt number distribution due to the changes in the instantaneous thermal boundary layer thickness. The instantaneous Nusselt number in Fig. 3 shows a "bell-shape" distribution, which was reported extensively in the literature [31]. In Fig. 3, it is also noted that the instantaneous Nusselt number at the stagnation point $y=4$ is almost identical for all the four cases and there is no difference between the nonreacting and reacting cases. This is due to the fact that there is no chemical reaction and heat release near the stagnation point, because the fuel has not been mixed with the oxidizer along the jet centerline.

In this study, the time-averaged Nusselt number distribution at the wall was calculated (the results are not included for brevity), in order to validate the numerical simulations. For the time-averaged Nusselt number, the differences between the three reacting cases almost diminish. Similar to the instantaneous Nusselt number shown in Fig. 3, the time-averaged Nusselt number of the reacting cases show a larger distribution near the wall than that of the nonreacting case due to the combustion heat release in the reacting cases. For the nonreacting hot-jet case (case 0), the peak Nusselt number of 30 was reproduced near the stagnation point, which is in close agreement with the experimental value of 31 in the literature [32].

To compare the near-wall structures of different cases, Fig. 4 shows the instantaneous reaction rate, temperature and velocity component v along the line $y=2$ in the $x=4$ plane. From Fig. 4(a), it is observed that the reaction rate has a large distribution across the wall boundary layer due to the existence of the head vortex. The reaction rate in the near-wall jet region is higher than that in the head vortex region. However, the temperature in the near-wall jet region is lower than that in the head vortex region, as shown in Fig. 4(b). This is because that there is a larger heat loss in the near-wall region due to the presence of the "cold" wall. From Fig. 4(b), it is also observed that the reacting cases have much higher temperatures in the near-wall region than the nonreacting case because of the combustion heat release. Because of the very similar near-wall flow structures, the profiles of the three reacting cases in Fig. 4 are almost overlapping. The existence of both negative and positive velocities in Fig. 4(c) is associated with the head vortex, where the flow reverses its direction.

Time averaging of the results was also performed to examine the averaged near-wall flow properties. The time interval used for the averaging is between $t_1=10$ and $t_2=20$, after the flow had reached a developed stage. Figure 5 shows the time-averaged temperature and the velocity component v profiles along the line ($x=4, y=2$). Apparently, the differences between the reacting cases diminish in the time-averaged flow properties. Because of the combustion heat release, the reacting cases have a much larger near-wall layer than the nonreacting case, with higher temperature and wall jet velocity. Because there is virtually no difference between the reacting cases in the time-averaged quantities, only one case will be discussed in the following subsection.

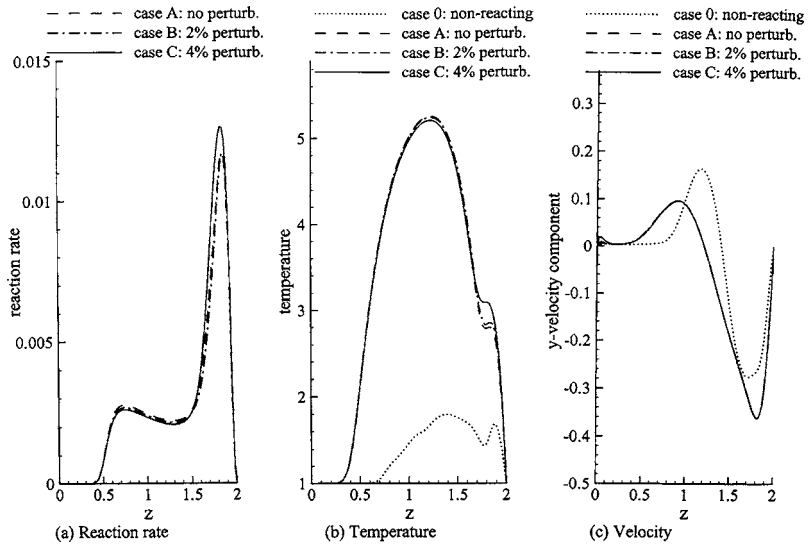

Fig. 4 Instantaneous reaction rate, temperature, and y-velocity component profiles at $t=20$ along the line ($x=4, y=2$)

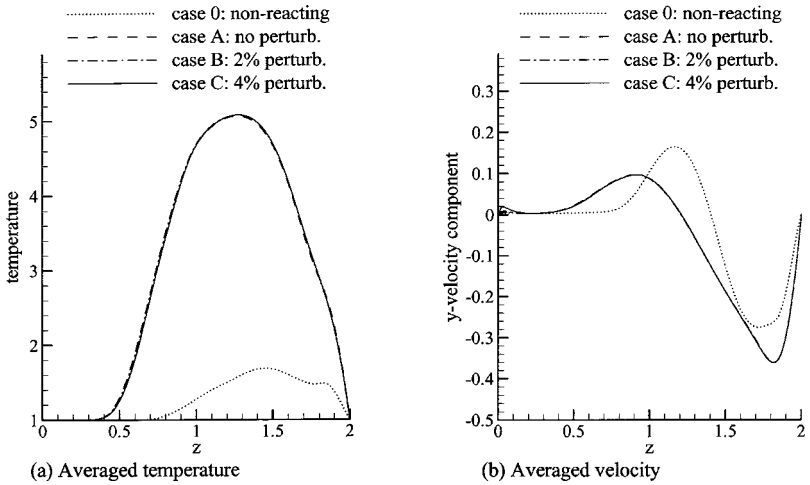

Fig. 5 Time-averaged temperature and *y*-velocity component profiles along the line ($x=4, y=2$)

3.2 Law-of-the-Wall Models for Near-Wall Flow and Heat Transfer. Near-wall models are of great importance in engineering computational fluid dynamics (CFD), including both the Reynolds-averaged Navier-Stokes (RANS) modeling approach and large eddy simulation (LES). The reason behind is that in RANS and LES codes, wall boundary layers are usually too thin to be resolved. The usual technique to overcome this problem is to make assumptions on the flow structure near the wall to avoid having to resolve it. Law-of-the-wall models provide such approximations. Unfortunately, the classical law-of-the-wall models of fluid flow and heat transfer were developed for nearly isothermal flows that neglected the presence of flame and variable density effects [1,2]. There were very few studies devoted to develop law-of-the-wall models for nonisothermal flows encountered in combustion, e.g., [33,34]. In this study, the time-averaged flow quantities in the near-wall boundary layer were analyzed to examining the law-of-the-wall relations.

In the classical law-of-the-wall, all relations are expressed in wall units where distances are scaled by a near-wall characteristic length $\nu_W/\tilde{u}_\tau$, where ν_W and $\tilde{u}_\tau$ are the kinematic viscosity and friction velocity at the wall, respectively. The velocity parallel to the wall is scaled by $\tilde{u}_\tau$ and the temperature by $T_\tau=\phi_W/(\rho C_p \tilde{u}_\tau)$, where ϕ_W is the wall heat flux. Based on boundary layer theory and fits on experimental results, the law-of-the-wall scales the near-wall velocity and temperature with the wall units. Figure 6 shows the calculated scaled velocity (v^+ is used to indicate the boundary layer flow in the y direction) and temperature along the line ($x=4, y=2$) of a reacting case and the nonreacting case, in comparison to the law of the wall in the relevant range of wall distance. Because of the relaminarization effect of the wall and the relatively low Reynolds number considered in this study, the wall boundary layer is within the viscous sublayer where the law-of-the-wall states that $v^+=T^+=z^+$, for unit Prandtl number Pr=1. It can be seen from Fig. 6 that the agreement between the law-of-the-wall and the DNS results is not satisfactory. This is not surprising because the classical law of the wall is valid only for flows in which temperature variations remain small. However, the temperature variation for the reacting case reaches a maximum value around $T/T_W=5$ and a value about 2 for the nonreacting case. Comparing Figs. 6(*a*) and 6(*b*), it can be seen that the reacting case has much larger velocity and temperature profiles in the region close to the wall, which is due to the effects of combustion heat release in the reacting case.

To address the fundamental problem of applying the law of the wall for nearly isothermal flows to combustion applications, few efforts have been made to derive law-of-the-wall relations for nonisothermal flows that can be integrated into CFD codes for combustion. In the literature [1], one approach based on the earlier efforts [33,34] was to assume that law-of-the-wall relations could still be valid, if reduced wall distance, mean velocity, and temperature accounting for temperature changes were used

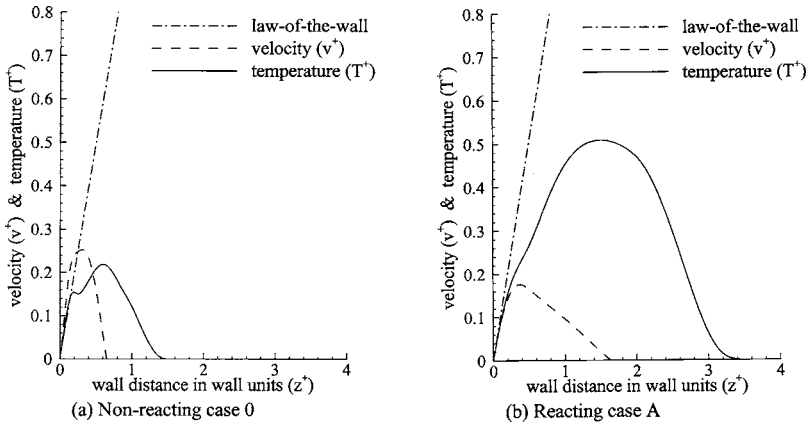

Fig. 6 Comparison with the law-of-the-wall relations for nearly isothermal flows along the line ($x=4, y=2$)

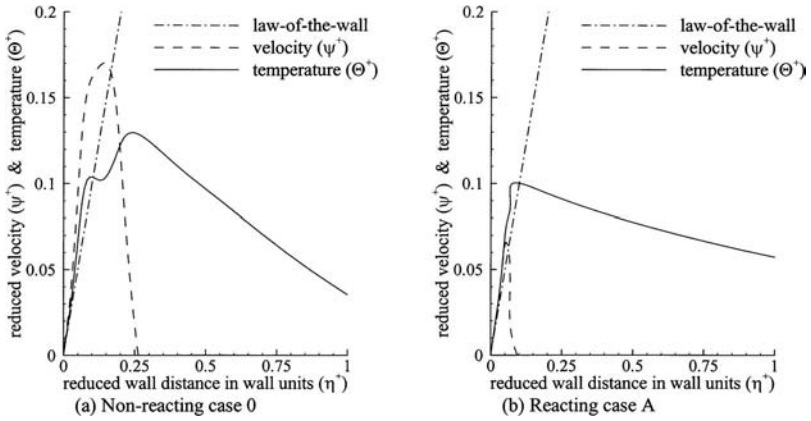

Fig. 7 Comparison with the law-of-the-wall relations for non-isothermal flows along the line ($x=4, y=2$)

$$d\eta^+ = \frac{\nu_W}{\nu} dz^+, \quad d\psi^+ = \frac{\rho}{\rho_W} dv^+, \quad d\Theta^+ = \frac{\rho}{\rho_W} dT^+ \tag{1}$$

where η^+, ψ^+, and Θ^+ are the reduced wall distance, velocity, and temperature, respectively. Figure 7 shows the calculated scaled ψ^+ and Θ^+ with η^+ along the line ($x=4$, $y=2$). However, the comparison between Figs. 6 and 7 is not conclusive, where it is difficult to judge whether the proposed law of the wall for nonisothermal flows better predicts the near-wall flow and heat transfer than the classical law of the wall for nearly isothermal flows. From Fig. 7, it is also noted that the reduced wall distance in wall units is significantly smaller than the classical wall distance shown in Fig. 6. This certainly raises doubts on whether the regimes of different wall boundary layers can still be represented by the same wall distance values as those for the nearly isothermal case [1].

In reacting flows, temperature and velocity equations are intrinsically coupled because temperature controls density and viscosity that are important to momentum transport. This is also the reason that the whole basis of law-of-the-wall models for nearly isothermal flows must be revised for flows with large temperature inhomogeneity. However, an examination of Eq. (1) reveals that it only includes the variable viscosity effect due to temperature inhomogeneity, but not the density effect (as a matter of fact, the $\nu_W/\nu = (\mu_W/\mu)(\rho/\rho_W)$ in $d\eta^+$ cancels out the ρ/ρ_W terms in $d\psi^+$ and $d\Theta^+$). To rectify this, a revised law-of-the-wall model is proposed by readjusting the reduced wall distance from η^+ to ζ^+, which is based on the dynamic viscosity

$$d\zeta^+ = \frac{\mu_W}{\mu} dz^+, \quad d\psi^+ = \frac{\rho}{\rho_W} dv^+, \quad d\Theta^+ = \frac{\rho}{\rho_W} dT^+ \tag{2}$$

Figure 8 shows the calculated scaled ψ^+ and Θ^+ with ζ^+. A close comparison between Figs. 7 and 8 shows that the proposed reduced wall distance ζ^+ based on the dynamic viscosity has improved near-wall flow and heat transfer prediction by the law of the wall. In the meantime, the revised reduced wall distance ζ^+ of the boundary layer is much larger than that of η^+. This implies that the reduced wall distance defined in terms of the dynamic viscosity can potentially improve the law-of-the-wall relations for nonisothermal flows. It is noted that the revised reduced wall distance ζ^+ is smaller than the wall distance z^+ in the classical law of the wall. This is because of the term μ_W/μ in Eq. (2), which takes into account the variable viscosity effect, is normally <1 due to the temperature inhomogeneity near the wall.

The revised law-of-the-wall relations for nonisothermal flows given in Eq. (2) are considered to be better than the law-of-the-wall relations for nonisothermal flows given in Eq. (1) for two reasons: first, the gradients of the revised law-of-the-wall relations shown in Fig. 8 agree much better with the DNS results than the law-of-the-wall relations shown in Fig. 7, where the law-of-the-wall gradients for both velocity and temperature are smaller than the DNS results, and second, the reduced wall distance ζ^+ is much larger than that of η^+ and Eq. (2) takes into account both the variable viscosity and density effects while Eq. (1) takes into ac-

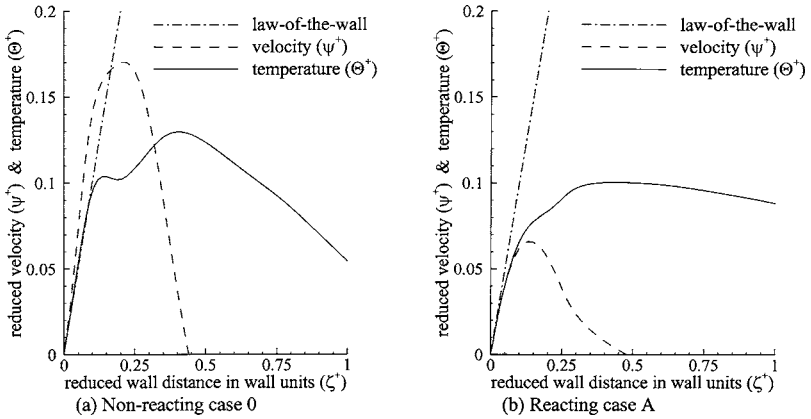

Fig. 8 Revised law-of-the-wall relations for non-isothermal flows along the line ($x=4, y=2$)

count the variable viscosity effect only. The results shown in Fig. 8 are also slightly better than the results shown in Fig. 6, which shows the classical law-of-the-wall relations for nearly isothermal flows and does not take into account the variable viscosity or density effect.

To more fully evaluate the performance of the proposed law-of-the-wall model with reduced wall distance defined upon the fluid dynamic viscosity, averaged temperature and velocity profiles at many locations of the three reacting cases were examined in this study. The trends observed in Figs. 5–8 along the line ($x=4, y=2$) were also observed along the lines of ($x=4, y=1$) and ($x=4, y=3$) and many other locations. For brevity, the results along other locations were not presented, but they are consistent with those discussed above.

4 Concluding Remarks

A non-premixed impinging flame has been numerically explored by solving the compressible Navier-Stokes equations using highly accurate numerical methods. Because DNS can provide detailed information on the near-wall reacting boundary layer, it was used to examine the effects of external perturbation on dynamics of the impinging jet flame. A comparative DNS has been performed, including reacting cases with and without external perturbation and a nonreacting case. The simulations focused on a relatively low Reynolds number $Re=2000$ and a small nozzle-to-plate distance of two jet diameters. Both instantaneous and time-averaged simulation results have been presented. The results showed that the external perturbation does not affect the near-wall combustion significantly due to the wall relaminarization and the shallow impinging configuration.

Based on the time-averaged flow properties, the law-of-the-wall relations for the near-wall flow and heat transfer were examined in this study. It was found that the near-wall boundary layer of the impinging flame is in the flow regime of viscous sublayer. It was also identified that the law-of-the-wall relations for nonisothermal flows in the literature need to be revisited. A reduced wall distance incorporating the fluid dynamic viscosity was proposed to be used in the law-of-the-wall relations for nonisothermal flows, such as those encountered in combustion applications. It showed improved prediction of the near-wall flow and heat transfer over the law of the wall with the reduced wall distance defined in terms of fluid kinematic viscosity in the literature.

The present study represented a challenging application of DNS, which involved chemical reaction, wall, impingement, and a range of flow scales. To reduce the computational costs, the Reynolds number was necessarily low and the computational domain size was relatively small in the impinging direction. However, it is believed that the study revealed the basic features of impinging flames, and increasing the Reynolds number, though desirable, would not give fundamentally different conclusions because a viscous sublayer exists near the wall at any Reynolds number. The revised law-of-the-wall relation proposed for nonisothermal flows in this study is not expected to change if simulations at higher Reynolds numbers are performed. Nevertheless, to fully examine the existing law-of-the-wall relations and to further develop law-of-the-wall models for reacting flows, fully turbulent impinging jet flames at much higher Reynolds numbers need to be investigated. For a fully turbulent flow, quantities such as turbulent Prandtl number and its variation near the wall can be examined. For higher Reynolds numbers and larger nozzle-to-plate distances, the external perturbation may also play an important role in the near-wall flame dynamics. Effects of upstream flow conditions on the near-wall combustion of high Reynolds number impinging jet flames and a full examination of the law-of-the-wall relations for turbulent flows will be topics of further study.

References

[1] Poinsot, T., and Veynante, D., 2001, *Theoretical and Numerical Combustion*, Edwards, Philadelphia, Chap. 7.

[2] Kays, W. M., Crawford, M. E., and Weigand, B., 2004, *Convective Heat and Mass Transfer*, 4th ed., McGraw-Hill, New York.

[3] Viskanta, R., 1993, "Heat Transfer to Impinging Isothermal Gas and Flame Jets," Exp. Therm. Fluid Sci., **6**, pp. 111–134.

[4] Poinsot, T. J., Haworth, D. C., and Bruneaux, G., 1993, "Direct Simulation and Modeling of Flame-Wall Interaction for Premixed Turbulent Combustion," Combust. Flame, **95**, pp. 118–132.

[5] Bruneaux, G., Akselvoll, K., Poinsot, T., and Ferziger, J. H., 1996, "Flame-Wall Interaction Simulation in a Turbulent Channel Flow," Combust. Flame, **107**, pp. 27–44.

[6] Bruneaux, G., Poinsot, T., and Ferziger, J. H., 1997, "Premixed Flame-Wall Interaction in a Turbulent Channel Flow: Budget for the Flame Surface Density Evolution Equation and Modelling," J. Fluid Mech., **349**, pp. 191–219.

[7] Popp, P., and Baum, M., 1997, "Analysis of Wall Heat Fluxes, Reaction Mechanisms, and Unburnt Hydrocarbons During the Head-on Quenching of a Laminar Methane Flame," Combust. Flame, **108**, pp. 327–348.

[8] Zhang, Y., and Bray, K. N. C., 1999, "Characterization of Impinging Jet Flames," Combust. Flame, **116**, pp. 671–674.

[9] Malikov, G. K., Lobanov, D. L., Malikov, K. Y., Lisienko, V. G., Viskanta, R., and Fedorov, A. G., 2001, "Direct Flame Impingement Heating for Rapid Thermal Materials Processing," Int. J. Heat Mass Transfer, **44**, pp. 1751–1758.

[10] Dong, L. L., Cheung, C. S., and Leung, C. W., 2001, "Heat Transfer Characteristics of an Impinging Butane/Air Flame Jet of Low Reynolds Number," Exp. Heat Transfer, **14**, pp. 265–282.

[11] Dong, L. L., Cheung, C. S., and Leung, C. W., 2002, "Heat Transfer from an Impinging Premixed Butane/Air Slot Flame Jet," Int. J. Heat Mass Transfer, **45**, pp. 979–992.

[12] Dong, L. L., Cheung, C. S., and Leung, C. W., 2003, "Heat Transfer Characteristics of a Pair of Impinging Rectangular Flame Jets," ASME J. Heat Transfer, **125**, pp. 1140–1146.

[13] De Lataillade, A., Dabireau, F., Cuenot, B., and Poinsot, T., 2002, "Flame/Wall Interaction and Maximum Wall Heat Fluxes in Diffusion Burners," Proc. Combust. Inst., **29**, pp. 775–779.

[14] Schuller, T., Durox, D., and Candel, S., 2002, "Dynamics of and Noise Radiated by a Perturbed Impinging Premixed Jet Flame" Combust. Flame, **128**, pp. 88–110.

[15] Hsieh, W. D., Hou, S. S., and Lin, T. H., 2005, "Methane Flames in a Jet Impinging Onto a Wall," Proc. Combust. Inst., **30**, pp. 267–275.

[16] Tuttle, S. G., Webb, B. W., and McQuay, M. Q., 2005, "Convective Heat Transfer From a Partially Premixed Impinging Flame Jet. Part II: Time-Resolved Results," Int. J. Heat Mass Transfer, **48**, pp. 1252–1266.

[17] Chander, S., and Ray, A., 2006, "Influence of Burner Geometry on Heat Transfer Characteristics of Methane/Air Flame Impinging on Flat Surface," Exp. Heat Transfer, **19**, pp. 15–38.

[18] Wang, Y., and Trouve, A., 2006, "Direct Numerical Simulation of Nonpremixed Flame-Wall Interactions," Combust. Flame, **144**, pp. 461–475.

[19] Zuckerman, N., and Lior, N., 2005, "Impingement Heat Transfer: Correlations and Numerical Modeling," ASME J. Heat Transfer, **127**, pp. 544–552.

[20] Jiang, X., and Luo, K. H., 2000, "Combustion-Induced Buoyancy Effects of an Axisymmetric Reactive Plume," Proc. Combust. Inst., **28**, pp. 1989–1995.

[21] Jiang, X., and Luo, K. H., 2003, "Dynamics and Structure of Transitional Buoyant Jet Diffusion Flames with Side-Wall Effects," Combust. Flame, **133**, pp. 29–45.

[22] Jiang, X., Zhao, H., and Luo, K. H., 2007, "Direct Computation of Perturbed Impinging Hot Jets," Comput. Fluids, **36**, pp. 259–272.

[23] Huang, W. M., Vosen, S. R., and Greif, R., 1986, "Heat Transfer During Laminar Flame Quenching: Effect of Fuels," Sym. (Int.) Combust., [Proc.], **21**, pp. 1853–1860.

[24] Westbrook, C. K., Adamczyk, A. A., and Lavoie, G. A., 1981, "A Numerical Study of Laminar Flame Wall Quenching," Combust. Flame, **40**, pp. 81–99.

[25] Lele, S. K., 1992, "Compact Finite-Difference Schemes With Spectral-Like Resolution," J. Comput. Phys., **103**, pp. 16–42.

[26] Williamson, J. H., 1980, "Low-Storage Runge-Kutta Schemes," J. Comput. Phys., **35**, pp. 48–56.

[27] Poinsot, T. J., and Lele, S. K., 1992, "Boundary-Conditions for Direct Simulations of Compressible Viscous Flows," J. Comput. Phys., **101**, pp. 104–129.

[28] Thompson, K. W., 1987, "Time-Dependent Boundary-Conditions for Hyperbolic Systems," J. Comput. Phys., **68**, pp. 1–24.

[29] Hussain, A. K. M. F., and Zaman, K. B. M. Q., 1981, "The Preferred Mode of the Axisymmetric Jet," J. Fluid Mech., **110**, pp. 39–71.

[30] Tesar, V., and Travnicek, Z., 2005, "Increasing Heat and/or Mass Transfer Rates in Impinging Jets," J. Visualization, **8**, pp. 91–98.

[31] Chung, Y. M., and Luo, K. H., 2002, "Unsteady Heat Transfer Analysis of an Impinging Jet," ASME J. Heat Transfer, **124**, pp. 1039–1048.

[32] Angioletti, M., Di Tommaso, R. M., Nino, E., and Ruocco, G., 2003, "Simultaneous Visualization of Flow Field and Evaluation of Local Heat Transfer by Transitional Impinging Jets," Int. J. Heat Mass Transfer, **46**, pp. 1703–1713.

[33] Angelberger, C., Poinsot, T., and Delhaye, B., 1997, "Improving Near-Wall Combustion and Wall Heat Transfer Modeling in SI Engine Computations," SAE Technical Paper No. 972881.

[34] Han, Z., and Reitz, R. D., 1997, "A Temperature Wall Function Formulation for Variable-Density Turbulent Flows With Application to Engine Convective Heat Transfer Modeling," Int. J. Heat Mass Transfer, **40**, pp. 613–625.

Yirong Jiang
United Technologies Research Center,
East Hartford, CT 06108

Biswajit Mitra
Carrier Corporation,
Syracuse NY 13221

Srinivas Garimella[1]
e-mail: sgarimella@me.gatech.edu

Ulf C. Andresen

George W. Woodruff School of Mechanical Engineering,
Georgia Institute of Technology,
Atlanta, GA 30332

Measurement of Condensation Heat Transfer Coefficients at Near-Critical Pressures in Refrigerant Blends

This paper presents the results of an experimental study on condensation heat transfer of refrigerant blends R404A and R410A flowing through horizontal tubes of 9.4 and 6.2 mm *inner diameter at nominal pressures of 80% and 90% of the critical pressure. Local heat transfer coefficients were measured for the mass flux range* $200 < G < 800$ kg/m^2-s *in small quality increments over the entire vapor-liquid region. Heat transfer coefficients increased with quality and mass flux, while the effect of reduced pressure was not very significant within this range of pressures. The heat transfer coefficients increased with a decrease in diameter.* [DOI: 10.1115/1.2401618]

Keywords: condensation, heat transfer coefficients, near-critical pressure, experimental, refrigerant blends

Introduction

The use of vapor compression cycles for high-temperature-lift space-conditioning systems and concern about the depletion of the stratospheric ozone level has created an interest in high pressure, zero-ozone-depletion-potential, near-azeotropic refrigerant blends such as R404A and R410A as substitutes for refrigerants such as R22. At the desired high heat rejection temperatures in high-temperature-lift space-conditioning and water heating systems, the saturation pressures of these blends approach and even exceed the critical pressure. Thus, the critical temperature and pressure of R404A are 72.05°C and 3729 kPa, while the corresponding values for R410A are 71.36°C and 4903 kPa, respectively. In comparison, the critical temperature and pressure for R22 are 96.15°C and 4990 kPa, respectively [1]. Phase change at such near-critical pressures in these refrigerant blends is not well understood, as documented in the following section. Much of the literature available for the prediction of condensation heat transfer is at relatively low operating pressures, and the validity of extrapolating these models to near-critical pressures is not well established. This paper presents the results of an experimental study of heat transfer during condensation of refrigerant blends R404A and R410A inside horizontal 9.4 and 6.2 mm I.D. tubes.

Previous Work

Condensation inside horizontal tubes is governed by a combination of gravity forces and interfacial shear stresses, the relative contributions of which change with the geometry and fluid flow conditions. While the annular flow pattern is associated with high vapor shear stresses, stratifying and wavy flows appear when gravity forces dominate. Guo and Anand [2] presented an analytical model for stratified condensation of R-410A at $30 < G < 2200$ kg/m^2-s in a 12.7×25.4 mm horizontal rectangular channel. The heat transfer coefficient was the area-weighted average of the top, bottom, and vertical wall heat transfer coefficients. In particular, for the side walls, they accounted for the combined effects of gravity driven condensation and vapor shear in the axial direction to obtain the film thickness dependent on the axial and vertical location. Chitti and Anand [3] developed a different model for annular flow based on R22 condensing in 8 mm horizontal round tubes. Their model used the Prandtl mixing length theory to obtain the momentum diffusivity. For closure, friction velocity was calculated through the use of a two-phase multiplier. Chitti and Anand [4] extended the experiments to R410A, with various oil concentrations, and pure R-22, primarily in the annular regime. They found a minimal effect ($\sim 10\%$) of condensing temperature on the heat transfer coefficient because the operating conditions (24–38°C) were well below the critical temperature. Heat transfer coefficients for R32/125 mixtures were about 15% higher than those for R-22.

Dobson et al. [5] investigated condensation of R-12 and R-134a in a 4.57 mm horizontal tube at $75 < G < 500$ kg/m^2-s at 35 and 60°C. In annular flow, the heat transfer coefficient increased with mass flux and quality, due to the increased shear and the thinning of the liquid film. In wavy flow, the heat transfer coefficient was independent of mass flux and showed a slight increase with quality, which was attributed to the smaller pool depth at the higher qualities. The heat transfer coefficients for R-134a were about 15% higher at 35°C than at 60°C because of the decrease in the ratio of the densities of the vapor and liquid phases, which leads to lower slip ratios, and also because of a decrease in thermal conductivity at the higher temperature. For wavy flow, they used a Chato [6] type correlation, while for annular flow they used the two-phase multiplier approach. Dobson and Chato [7] extended this work to 3.14 and 7.04 mm tubes, and also to R-22 and R410A. For these revised correlations, they noted that the primary thermal resistance in annular flow is in the laminar and buffer layers. The role of entrainment was also not found to be very significant, because they found that rarely did true mist flow without a thin annular film coating the wall exist. For stratified wavy flow, they accounted for the film condensation at the top of the tube and forced convection in the liquid pool. They recommended that the annular flow correlation should be used when $G > 500$ kg/m^2-s, while for $G < 500$ kg/m^2-s, the annular flow correlation should be used for $\mathrm{Fr}_{so} > 20$, and the wavy flow correlation should be used for $\mathrm{Fr}_{so} < 20$. The applicability of this model was extended for use with R407C by Sweeney [8], who proposed mass flux-based modifications to Dobson and Chato's annular and wavy Nusselt numbers. Boissieux et al. [9] investigated conden-

[1]Corresponding author.

Contributed by the Heat Transfer Division of ASME for publication in the JOURNAL OF HEAT TRANSFER. Manuscript received August 4, 2005; final manuscript received June 22, 2006. Review conducted by Anthony M. Jacobi.

sation of R404A, R407C, and Isceon 59 (a blend of 46.6% HFC-125, 59% HFC-134a, and 3.4% R-600) in a 9.5 mm tube for $150 < G < 400$ kg/m^2-s and $15\,^\circ\text{C} < T_{sat} < 35\,^\circ\text{C}$, and recommended the Dobson and Chato correlation for R404A.

Han and Lee [10] studied heat transfer characteristics of R410A and R22 in smooth and microfin tubes of 7 and 9.52 mm O.D. at 30 and 40 °C for $105 < G < 388$ kg/m^2-s. They attributed the increase in h with x to the thinning of the liquid film around the tube surface at the higher qualities. In addition, they found that h decreased slightly at higher T_{sat} due to the combined effects of decreases in density, thermal conductivity, and latent heat. They noted that the decrease in density causes an increase in liquid film thickness, which causes a higher conduction resistance. They found that the heat transfer coefficients of R410A were 3 to 11% higher than those of R22 due to the higher thermal conductivity of R410A.

Ebisu and Torikoshi [11] also provided heat transfer and pressure drop data for R410A during condensation in a 7 mm tube. For $150 < G < 300$ kg/m^2-s, $T_{sat} = 50\,^\circ\text{C}$, and $0.2 < x < 0.8$, contrary to the results of Han and Lee [10] and Kwon and Kim [12], they found that the heat transfer coefficients for R410A at these conditions were slightly lower than those for R22, particularly for low x. The heat transfer coefficients for $x > 0.4$ were in good agreement with the Haraguchi et al. [13] correlation. Kwon and Kim [12] reported heat transfer coefficients for R22 and R410A in 9.52 mm tubes at $T_{sat} = 31\,^\circ\text{C}$ and $G = 97$, 144, and 202 kg/m^2-s. They developed a model for annular flow including the effects of interfacial shear stress, liquid entrainment, and turbulent eddy viscosity, and found good agreement with the R410A data. In a later study, Kwon et al. [14] presented the predictions of their model with and without liquid entrainment for condensation of refrigerant R22. The predictions for R22 were better than the earlier predictions for R410A.

Cavallini et al. [15–17] obtained heat transfer and pressure drop data for several refrigerants and blends (R-22, R-134a, R-125, R-32, R-236ea, R-407C, and R-410A) condensing in 8 mm horizontal tubes, and developed models to predict their own data as well as data from other investigators for $30 < T_{sat} < 50\,^\circ\text{C}$ and $100 < G < 750$ kg/m^2-s. They noted that the data were often outside the recommended range of applicability for many of the correlations in the literature, especially for the newer high-pressure refrigerants such as R-125, R-32, and R-410A. The predictions of some correlations were also not satisfactory within the stated range of applicability. Therefore, they developed procedures patterned after the approach of Breber et al. [18,19]. For annular flow ($j_g^* > 2.5$, $X_{tt} < 1.6$), they recommended the use of the Kosky and Staub [20] model, which relates the heat transfer coefficient to the frictional pressure gradient through the interfacial shear stress. However, to compute the necessary frictional pressure gradient for this model, they modified the Friedel [21] correlation to apply only to annular flow, whereas it had originally been intended for annular and stratified regimes. For $j_g^* < 2.5$, $X_{tt} < 1.6$, the heat transfer coefficient is a combination of the annular model evaluated at the $j_g^* = 2.5$ boundary and a stratified heat transfer model (a combination of film condensation at the top and forced convection in the liquid pool). They commented that liquid pool heat transfer is significant at high values of p_r. For $j_g^* < 2.5$, $X_{tt} > 1.6$, transition from stratified to intermittent flows starts and occurs at a varying value of X_{tt}, defined by a transition mass flux. For slug flow, they used data from Dobson and Chato [7] and Tang [22] to curve-fit a single-phase correlation. The annular-to-slug transition across $j_g^* = 2.5$ at high X_{tt} was considered unlikely for most applications. In such instances, they recommended interpolation between $h_{annular}$ and h_{LO} based on x. For bubbly flow (high values of j_g^*, X_{tt}, and p_r), they recommended the annular flow correlation.

El Hajal et al. [23] and Thome et al. [24] developed heat transfer correlations based on the work of Kattan et al. [25–27] on flow boiling by fitting data from several investigators. Their basic premise is that void fraction is the most important variable in determining flow regimes, pressure drop, and heat transfer. They represented the void fraction (deduced by relating turbulent annular flow heat transfer data [15–17] to film thickness and then to void fraction) as the logarithmic mean of the Rouhani-Axelsson [28] drift-flux void fraction and the homogeneous void fraction. Liquid-vapor cross-sectional areas are derived from the void fraction to plot flow regime transitions adapted from the corresponding boiling criteria. They state that the maps are applicable for $16 < G < 1532$ kg/m^2-s, $3.14 < d < 21.4$ mm, $0.02 < p_r < 0.8$, $76 < (\text{We/Fr})_L < 884$, for several refrigerants and blends. Although they showed qualitative agreement with some widely used maps, much of the agreement is subject to interpretation and definition of the flow regimes used by various investigators. In particular, an unrealistically large intermittent regime, even for an 8 mm tube, is predicted at x as high as about 45% and $G \geq 1000$ kg/m^2-s. For the heat transfer model, Thome et al. [24] applied the turbulent annular flow heat transfer equation of El Hajal et al. [23] around the perimeter of the tube. For stratified flows, instead of treating the liquid phase as a pool with a flat upper surface at the bottom of the tube, they redistribute it as an annular ring, occupying the portion of the tube circumference that would yield a liquid phase cross-section equivalent to that of the stratified pool. This transformation allows them to use a gravity driven film condensation expression (with zero vapor shear) in the upper part of the tube, coupled with forced convective annular flow for the lower portion of the circumference for what would otherwise be a liquid pool. The rest of the model is a weighted average of the contributions based on the fraction of the circumference occupied by the "stratified" portion. The multiple regimes identified in the first part of the study are handled either as (a) fully annular forced convective or as (b) consisting of varying combinations of upper gravity driven and lower forced convective terms. Intermittent flow is assumed to be predicted by annular flow equations. Mist flow is handled as annular flow, assuming that the liquid entrained in the vapor phase can be viewed as an unsteady annular film. Bubbly flow is not modeled because it is not commonly encountered. The model predicts the database for a wide range of fluids, operating conditions, and diameters well, with 85% of the refrigerant data predicted within 20%. This is about the same level of accuracy as the correlations proposed by Cavallini et al. [16].

It is clear from the above discussion of the literature that most prior investigations have focused on annular flow, pure refrigerants, or refrigerant blends condensing at low reduced pressures. There is little literature available at saturation pressures approaching the critical pressure. As will be demonstrated in this paper, many of the commonly used condensation heat transfer correlations result in significant discrepancies when predicting the heat transfer coefficients for the higher pressures of interest in the present study. The few studies that considered stratified-wavy flow assumed that heat transfer in the liquid pool was negligible compared to the film condensation in the upper portion of the tube, which may not be appropriate at the higher mass fluxes. Thus, the present study investigates heat transfer during condensation of refrigerant blends R410A (in 9.4 and 6.2 mm inner diameter tubes) and R404A (in a 9.4 mm inner diameter tube) at reduced pressures $p_r = 0.8$ and 0.9 using the techniques described in the following section.

Experimental Approach

Heat transfer measurements were conducted in the test facility shown in Fig. 1. Detailed descriptions of this test facility were provided in earlier papers by the authors [29,30]. Subcooled liquid refrigerant is pumped through a tube-in-tube evaporator, in which steam flows counter-current to the refrigerant to boil and superheat it. Temperature and pressure measurements at the superheated state enable determination of the refrigerant enthalpy. The superheated vapor enters one of two precondensers, where city water of the desired (variable) flow rate is used to partially con-

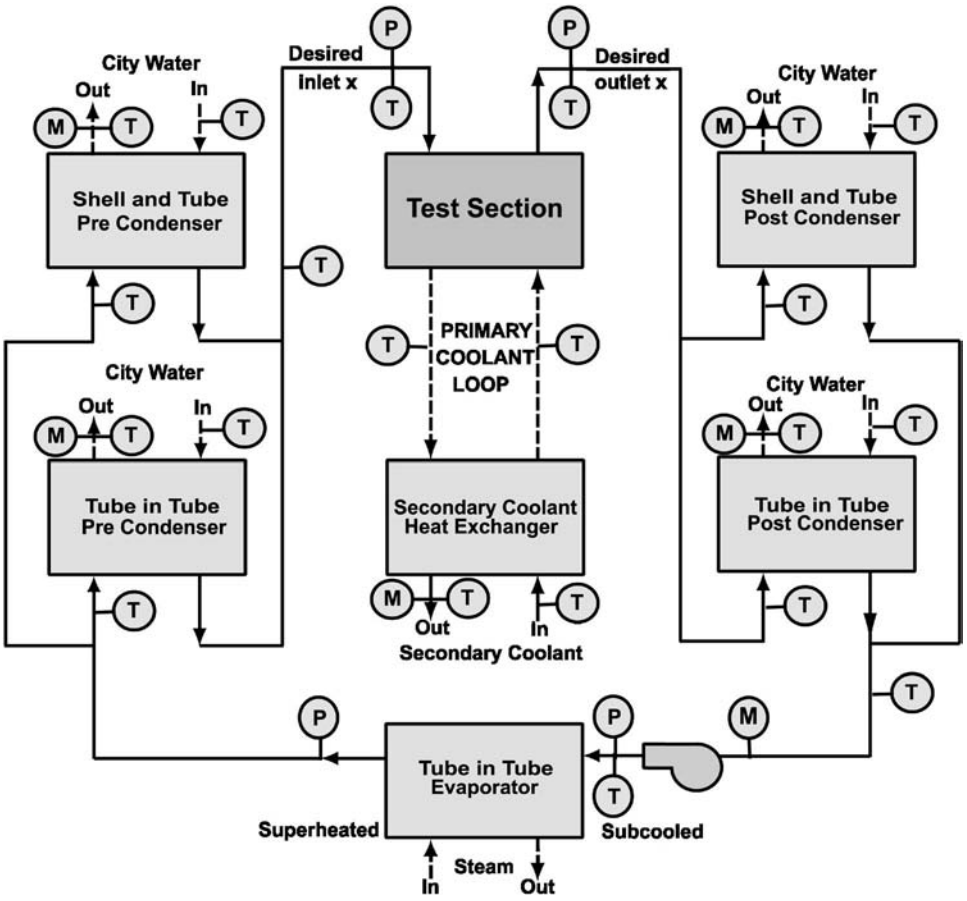

Fig. 1 Test loop schematic

dense the vapor. One of the precondensers is a tube-in-tube heat exchanger, whereas the other is a shell-and-tube heat exchanger. These heat exchangers are switched back and forth during testing depending on the amount of precondensation required. For example, if high test-section qualities are required, the tube-in-tube precooler is used, while for lower qualities, the shell-and-tube heat exchanger, which has a higher cooling capacity, is used. These two precondensers, with their different heat transfer surface areas and variable cooling water flow rates, establish a wide range of refrigerant conditions at the test section inlet. Refrigerant exiting the precondensers enters the test section, which is a counterflow tube-in-tube water-cooled heat exchanger. One of two postcondensers (tube-in-tube or shell-and-tube) downstream of the test section is used to completely condense and subcool the refrigerant. The subcooled refrigerant enthalpy at the exit of the postcondenser and an energy balance on the postcondenser are used to deduce the refrigerant enthalpy and quality at the outlet of the test section. The test section quality is determined from an average of the test section inlet and outlet qualities.

A 292 mm long tube-in-tube heat exchanger was used as the test section. For the 9.4 mm I.D. case, a 12.7 mm O.D., 1.65 mm wall inner copper tube and a 19.1 mm O.D., 1.65 mm wall outer stainless steel tube formed the test section, while for the 6.2 mm case, a 9.5 mm O.D., 1.65 mm wall thickness copper tube and a 15.9 mm O.D., 1.25 mm wall thickness outer stainless steel tube formed the test section. Refrigerant flows through the inner tube, while being condensed by a "primary closed loop coolant" water stream flowing in counterflow (Fig. 1). This primary coolant in turn rejects heat to an open loop city water stream in a shell-and-tube heat exchanger. This arrangement of primary and secondary coolant loops satisfies the requirements for the accurate determination of both the test section heat duty and the refrigerant heat transfer coefficient. Thus, primary coolant flowing at a high flow rate through an annulus with a small gap ensures that the dominant heat transfer resistance in the test section is on the refrigerant side. However, because at the required high flow rate of the primary coolant, the ΔT in this coolant is very small and prone to high uncertainties, secondary coolant flowing at a much lower flow rate is used to obtain a larger ΔT and thus measure the test section Q accurately. Accurate heat duty measurement is particularly important because of low heat duties involved in the determination of local h over small Δx. The secondary coolant flow rate is adjusted as test conditions change to maintain a reasonable ΔT and also small Q in the test section.

This approach depends upon the minimization of spurious heat losses and gains from/to the primary coolant loop $Q_{ambient}$ so that the test section heat duty $Q_{w,test}$ can be calculated accurately from a measurement of the secondary coolant heat load $Q_{w,sec}$. Thus, it is essential that the primary coolant circulation pump heat dissipation Q_{pump} and the $Q_{ambient}$ are small fractions of $Q_{w,sec}$, and also that they be estimated with reasonable accuracy. This ensures that $Q_{w,test}$ is relatively insensitive to Q_{pump} and $Q_{ambient}$, as shown in a subsequent section. Low k insulation and small ΔT's between the primary coolant and the ambient minimize $Q_{ambient}$. Similarly, Q_{pump} is minimized by using a pump with very high efficiency over the range of flow rates and pressure drops encountered; the high efficiency results in an extremely low heat dissipation. This technique of decoupling the determination of Q and h through thermal amplification is described in greater detail in Garimella and Bandhauer [31].

The refrigerant and secondary coolant flow rates were measured using Micromotion Coriolis mass flow meters with ±0.10% and 0.15% uncertainties, respectively. Cooling water flow rates for the

Table 1 Test conditions investigated

	R404A		R410A
Tube I. D., mm	9.4		9.4, 6.2 mm
Pressure, kPa	2983, 3356		3922, 4413
Temperature, °C	~61.8,67.3		~61.1,66.6
Mass flux, kg/m^2-s		200–800	
Quality		0–1	

precondenser were measured using a Rosemount Magnetic flowmeter with a maximum uncertainty of ±0.5%, while the postcondenser water flow rates were measured using banks of Gilmont Accucal rotameters with a maximum uncertainty of ±2%. Pressure transducers with uncertainties of ±0.25% of the span were used to measure pressures of the refrigerant at various locations. Temperatures were measured using a combination of platinum RTDs and Type-T thermocouples. Measured temperatures, flow rates, and pressures were continuously displayed and plotted as a function of time using a data acquisition system to ensure that steady state conditions are reached. Once steady state was achieved, the sight glasses and pressure and temperature readings were inspected to ensure an adequate degree of superheat and subcooling, and the data were recorded. These experiments were conducted for the qualities and mass fluxes in Table 1.

Data Analysis

For each data point, test section inlet and outlet qualities that were used to calculate the average quality were determined using the water-side heat duties of the pre- and postcondensers. An error propagation approach [32] was used to estimate the uncertainty in each calculated quantity. The analysis of a representative data point for R410A condensing in the 9.4 mm tube at $p=0.8\times p_{crit}$, $G=302.4$ kg/m^2-s, and $x=0.658\pm0.053$ is described here. The test section heat duty was calculated using an energy balance for the primary coolant loop (Fig. 1) as follows:

$$Q_{w,test} = Q_{w,\mathrm{sec}} + Q_{ambient} - Q_{pump} \tag{1}$$

To calculate Q_{pump}, the Δp in the primary loop was calculated first to determine the ideal pumping power required for water circulation. The actual power was obtained from the torque and pump rpm. Pump curves available from the vendor provided the torque, rpm, and efficiency for a given combination of flow rate and Δp. Finally, the heat dissipation into the loop was obtained from the efficiency and the actual power. A conservative uncertainty of ±50% was assumed for this calculated Q_{pump}. For this representative case, Q_{pump} was estimated using this procedure to be 22±11 W. For this representative data point, $Q_{ambient}$ was estimated to be 9±4.5 W (once again, with an assumed uncertainty of ±50%). The heat load in the secondary heat exchanger is calculated using the mass flow rate of the coolant (measured using a Coriolis mass flowmeter) and the inlet and outlet temperatures. The thermal amplification provided by the low flow rate of the secondary coolant (1.18×10^{-2} kg/s) is evident from the ΔT in this fluid. Thus, the secondary coolant ΔT for this data point is 11.4°C, while the primary coolant ΔT is only 0.65°C. This ΔT, coupled with the high-accuracy flow rate measurement, yields a low uncertainty in $Q_{w,sec}$, ±6.2%, (561±35 W). Finally, combining the errors in $Q_{w,sec}$, Q_{pump}, and $Q_{ambient}$ using an error propagation technique, the test section heat duty is 547.5±37 W, i.e., an uncertainty of 6.8%. Because the net contribution of the compensating $Q_{ambient}$ and Q_{pump} terms is small by design, the relatively high assumed uncertainties in these terms are not very significant in determining the test section heat duty. From this illustration, it is clear that this technique provides heat duty measurements for such low heat duties with a high degree of accuracy.

The condensation heat transfer coefficient is determined from the measured $Q_{w,test}$, the applicable ΔT, and the other thermal resistances. The test section LMTD and Q of 25.06±0.79°C and 547.5±37 W, respectively, yield an overall UA of 21.85±1.56 W/K. The primary coolant flows through the annulus side of the test section. The heat transfer coefficient for the coolant flowing through this annulus was calculated from laminar and turbulent Nu in annuli reported by Kays and Leung [33]. The transition between laminar and turbulent flow was established based on the lower (transition from laminar) and upper (transition to turbulent) critical Re for different annulus radius ratios reported by Walker et al. [34]. The Nusselt number in the transition region was calculated using a logarithmic interpolation between the Nu at the lower and upper critical Re.

For this representative data point, with a coolant flow rate of 1.146×10^{-4} m^3/s, the Reynolds number Re=7014. With Pr =4.98, the Nusselt number is 55.68, which results in coolant h =11,143 W/m^2-K and a thermal resistance of 7.7×10^{-3} K/W. An uncertainty of 25% was assumed for this coolant-side resistance. The tube wall resistance is 4.12×10^{-4} K/W. The refrigerant-side resistance is calculated from the measured UA of the test section and the coolant-side and tube-wall resistances and, for this case, is 3.77×10^{-2} K/W. This yields a condensation h =3079 W/m^2-K. To estimate the uncertainty in this deduced condensation h, the uncertainty in the UA value discussed above is coupled with an assumed coolant-side heat transfer coefficient uncertainty of ±25%, resulting in an uncertainty of ±10.4% in the refrigerant-side h (3079±320 W/m^2-K). For this representative data point, $R_{refg}/R_{coolant}=4.9$, which ensures that the condensation side presents the governing resistance, and effectively minimizes any sensitivity of the calculated condensation h to the coolant-side R. The resistance ratios ranged from 2.47 to 13.84 for all the data points in this study with an average of 5.8. The uncertainties in h ranged from 4.6% to 19.7%, with an average of 10.2%.

To validate heat transfer coefficients obtained using this thermal amplification technique, wall temperatures of the tested tubes were also measured using thermocouples (3 for the 9.4 mm tube, 6 for the 6.2 mm tube) soldered to the outer wall. The average deviations between the wall-mounted thermocouples for R410A experiments were 1.39°C (range: 0.4–2.9°C) and 0.36°C (range: 0.0–1.3°C) in the 9.4 and 6.2 mm tubes, respectively. For R404A, the average deviation was 0.94°C (range: 0.19–2.06°C). Using the measured tube-wall and refrigerant temperatures (after accounting for the wall resistance), the condensation h for the representative data point under consideration was 2761 W/m^2-K, i.e., 10.3% less than the h of 3079 W/m^2-K determined from the thermal amplification technique. The average difference between the refrigerant heat transfer coefficients for R410A obtained using the resistance ratio and wall temperature methods was 10.7% (5–18% range) and 10.4% (4.8–19.2% range) for 9.4 and 6.2 mm tubes, respectively. Similarly, for R404A, the average difference was 5.39%, with a range of 0–19.4%. It should be noted that these differences are within the uncertainties of obtaining these local heat transfer coefficients, as established above.

Results and Discussion

Experimental Heat Transfer Coefficients. Heat transfer coefficients and uncertainties for the 9.4 mm tube are shown in Figs. 2 and 3. These heat transfer coefficients were obtained over quality increments of about 8–24%. It can be seen from these figures that h increases with an increase in either x or G. The rate of increase in h with G is larger at higher x. At the higher G, shear-controlled condensation leads to the increase in h with x, because of the increase in interfacial shear as the vapor velocity increases and the decrease in film thickness. At low G and x, gravity forces domi-

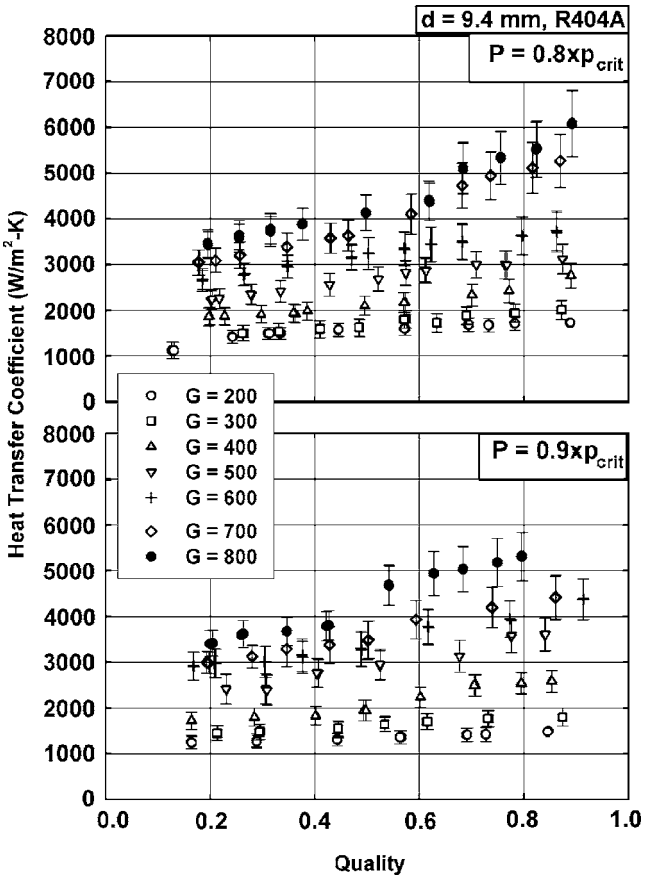

Fig. 2 Measured R404A *h* and uncertainties

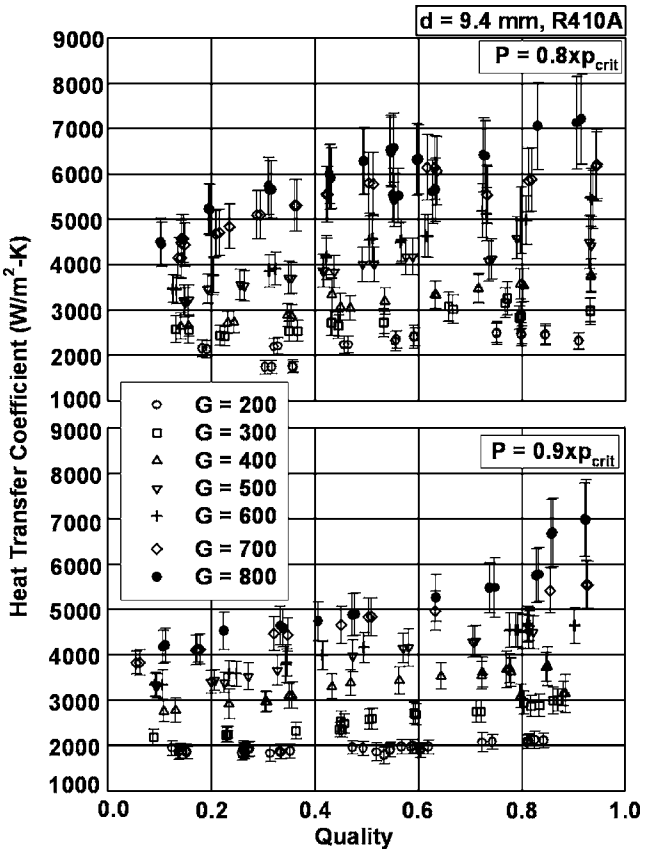

Fig. 3 Measured R410A *h* and uncertainties (9.4 mm tube)

nate, resulting in film condensation at the top of the tube and forced-convective heat transfer in the pool of liquid at the bottom. This explains the relatively lower sensitivity of h to x in this regime.

The effect of p_r on h is shown in Fig. 4. There is a slight decrease in h with an increase in p_r, particularly at high x. This is probably because of the compensating effects of an increase in C_p of the two phases by a factor of about 1.7–1.9, coupled with a decrease in the h_{fg} by a factor of 1.33 as the pressure increases from 0.8 to $0.9 \times p_{crit}$. At low x, where h is insensitive to changes in flow parameters, the effect of p_r is almost negligible. Figure 5 shows a comparison of h of R410A and R404A in the 9.4 mm tube. The heat transfer coefficients for R410A are higher than those of R404A for all cases under similar conditions. This is because of the superior thermophysical properties of R410A for the p_r range under consideration (27% higher Cp_l, 37% higher Cp_g; 41% higher k_l, 14% higher k_g; 28% higher h_{fg}). Figure 6 shows a comparison of h for the 9.4 and 6.2 mm tubes. As expected, the smaller diameter of the 6.2 mm tube leads to larger h under identical G and p_r conditions. Thus, for a constant G and x, the Reynolds number scales linearly with diameter. As the diameter is decreased, Re decreases, which also implies that Nu decreases. While in single phase flows the decrease in Nu can be captured in a single exponent such as $\mathrm{Nu} \propto \mathrm{Re}^{0.8}$, a similar dependence exists in condensation as well, i.e., Nu decreases at a lower rate than Re. The resulting effect is that $h \propto \mathrm{Nu}/D \propto D^n/D$. With n typically <1, h increases with a decrease in D.

Comparison With the Literature. The heat transfer coefficients reported above were first interpreted in terms of the expected flow regimes for the operating conditions investigated in this study. However, due to the absence of maps in the literature for condensation of refrigerant blends at near-critical pressures, the available maps for somewhat similar situations were used to predict the possible regimes. The data were plotted on the Breber et al. [19] map, in which transitions between flow regimes occur at constant Martinelli parameters and dimensionless gas velocities. This map was particularly chosen because it is applicable for a wide range of tube diameters (4.8–50.8 mm), pressures (108–2489 kPa), and refrigerants (R12, R113, steam, n-pentane, R11), and acknowledges that the transitions do not occur abruptly, but over regions with some overlap. It was found that this map predicted a large portion of the data from the present study to be in the annular and mist regions, with some points falling in the transition region between the four primary regimes, and relatively few points in the slug and plug flow regimes (mostly R410A in the 9.4 mm tube). Even though none of the data points fell in the wavy-stratified regions, many data were in the transition region between annular/mist and wavy-stratified flows. The data were also plotted on the flow regime maps developed by Coleman and Garimella [35]. Their maps were developed for condensation of refrigerant R134a in circular, square, and rectangular tubes ($1 < d_h < 5$ mm) for $150 < G < 750$ kg/m^2-s at $p_r \approx 0.34$. The low p_r and slightly lower diameters used in their study might lead to some differences between the regimes predicted by their criteria and those exhibited by R404A and R410A under the conditions of interest in the present study. But these criteria were in fact developed for condensation of refrigerants (rather than boiling experiments or simulations using air-water two-phase flow) and addressed the mass flux range of interest in this study; they were therefore deemed to provide some guidance. Their map showed that the current data would exhibit the discrete and disperse wave flow, and annular flow ($G > 400$ kg/m^2-s and $x > 0.5$) patterns, with a few points at low qualities being in intermittent flow. Thus, the flow regimes predicted by the Breber et al. and the Coleman and Garimella maps were similar, except that the data predicted to

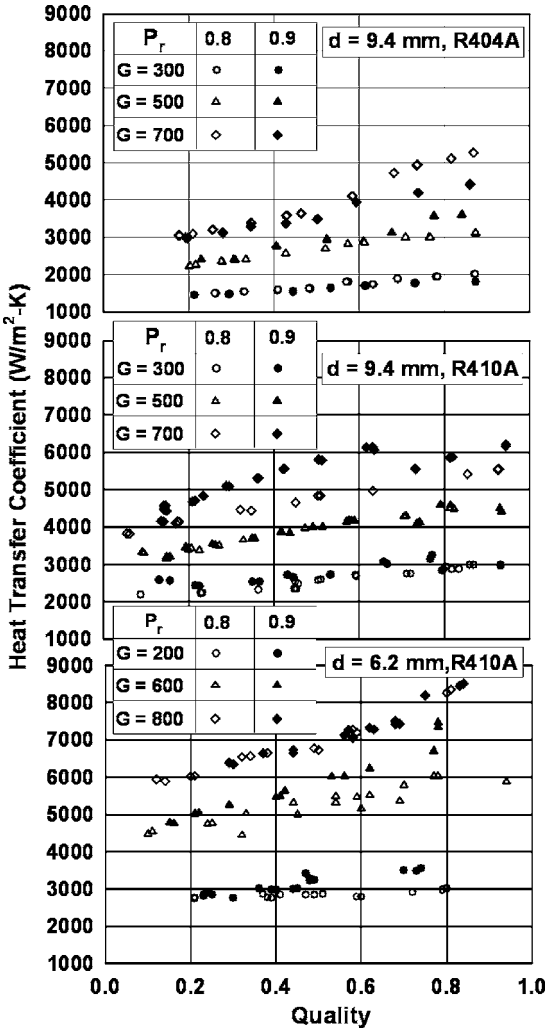

Fig. 4 Effect of reduced pressure on *h*

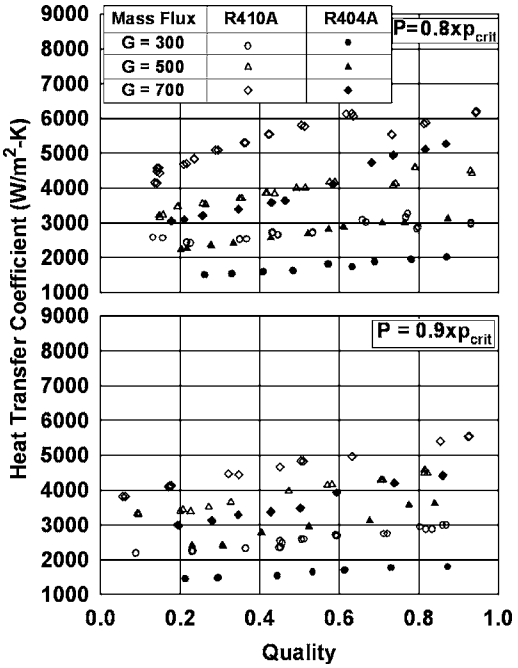

Fig. 5 Comparison of *h* for R410A and R404A (9.4 mm tube)

be in the discrete and disperse wave regimes by Coleman and Garimella appeared in the transition and slug and plug flow regions in the Breber et al. map. Differences in definitions and categorizations of different kinds of flows, details of which are available in the respective papers, could be responsible for some of these differences in the assignment of flow regimes.

With an understanding of the expected flow regimes for the present data, the validity of models in the literature for these high-pressure refrigerant blends operating at near-critical pressures was assessed. (It should be noted that none of the heat transfer models in literature are based on data encompassing conditions under investigation in the present study.) Comparisons with the models of Dobson and Chato [7] are shown in Fig. 7 for the case of R410A condensing in the 9.4 mm tube at p_r=0.9. The average absolute deviation of all the data in the current study from the predictions of this model was 35.3%, with the deviations being higher at the higher p_r. In general, the data from the present study are between the predictions of the annular and wavy-stratified submodels of Dobson and Chato: their annular model strongly overpredicts the current data, while the wavy-stratified model slightly underpredicts the data. This overall result is understandable based on the expectation from the discussion above that the current data are mostly in the discrete and disperse wave regions according to Coleman and Garimella [35] or in the transition regions between the annular and wavy region according to Breber et al. [19]. Even though the models were developed for diameters ($3.14 < d < 7.04$ mm) comparable to present study, it appears that the low reduced pressures ($p_r < 0.57$) in their study contribute to the differences from the present data. The underpredictions of the wavy flow model may be because of the assumption that film condensation is the dominant mechanism and that heat transfer in the bottom of the pool is significant only at high G. They neglect the effect of vapor shear at intermediate quality cases; however, even though the vapor shear is not significant enough to cause annular flow, it may still move some of the condensed film tangentially. The use of the Zivi [36] void fraction model in their correlation may also not be applicable to the present conditions. The abrupt and unrealistic jump in heat transfer coefficient from the wavy-

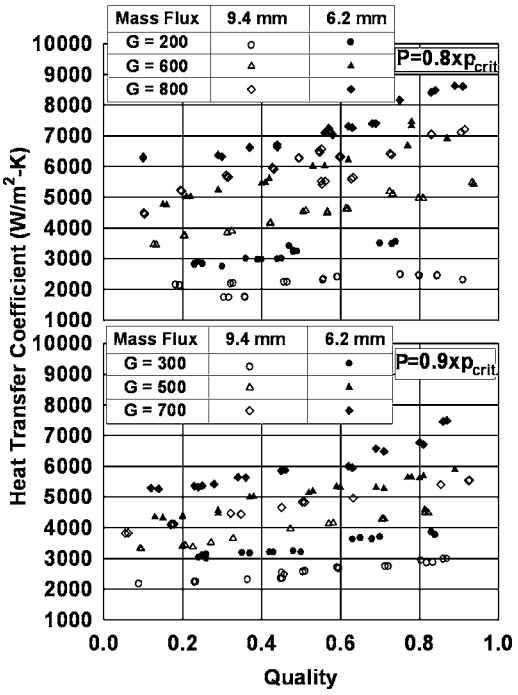

Fig. 6 Effect of diameter on *h* (R410A)

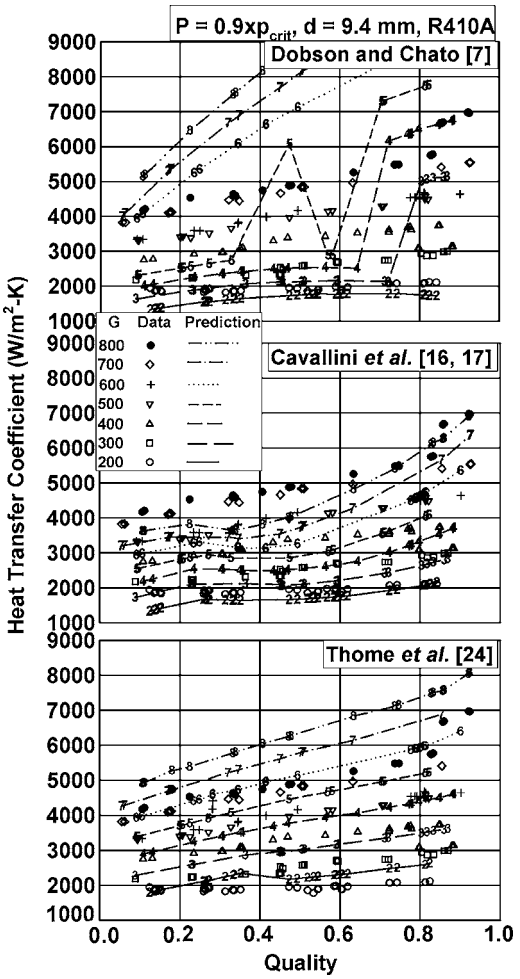

Fig. 7 Comparison of measured h with Dobson and Chato [7], Cavallini et al. [16,17], and Thome et al. [24] model predictions ($P=0.8\times p_{crit}$, R410A, $d=9.4$ mm)

stratified to the annular region predicted by their model limits its usefulness to the conditions under study here. In addition, the Dobson and Chato [7] model predicts an increase in h for an increase in p_r, which appears unrealistic and is different from the trends in the present data (e.g., at $G=800$ kg/m^2-s, $d=9.4$ mm, $x=0.63$ for R410A, for an increase in p_r from 0.8 to 0.9, the predicted h increases from 8989 to 10,113 W/m^2-K, whereas the experimental h decreases from 5647 to 5252 W/m^2-K).

The predictive capabilities of the models of Cavallini et al. [16,17] are also shown in Fig. 7. As stated in the literature review section, these models consist of submodels for annular flow, annular-stratified flow transition, and stratified-slug and slug flow essentially through interpolations between shear and gravity driven models. These predictions are in better agreement (22.9% average absolute deviation) with the present data than the predictions of the Dobson and Chato model. The models underpredict the data with the average absolute deviations ranging from 14.5% for R404A in the 9.4 mm tube to 35.1% for R410A in 6.2 mm tube. The somewhat better predictions of these models are not surprising given that these models are applicable for condensation of halogenated refrigerants in tubes with $3<d<21$ mm, $p_r<0.75$, and $\rho_l/\rho_g>4$. The conditions for the present study, $p_r=0.8$ and 0.9, and $2.69<\rho_l/\rho_g<4.72$, are only slightly outside this range of applicability. Some of the discrepancies in these models may also be due to the fact that the interfacial shear stress (approximated as the wall shear stress) in their model is obtained from a frictional pressure drop model—discrepancies in the pressure drop model might lead to deviations in the heat transfer model.

Figure 7 also shows comparisons with the predictions of the model by Thome et al. [24]. This model predicts the data from the present study fairly well for both refrigerants at $p_r=0.8$ in the 9.4 mm tube (8.8% average absolute deviation for R404A and 10.7% average deviation for R410A). However, for other pressures and diameters, the deviations are high, with the maximum average absolute deviation being 29.6% for R410A in the 6.2 mm tube at $p_r=0.8$. The average absolute deviation for all the data from the predictions of this model is 18.0%. It should be noted that this model predicts an increase in h with an increase in p_r (similar to the model of Dobson and Chato [7]), whereas the trend should show decreases in h as p_r rises. For example, for R410A condensing in a 9.4 mm tube at $G=800$ kg/m^2-s and $x=0.63$, for an increase in p_r from 0.8 to 0.9, the predicted h increases from 5869 to 6832 W/m^2-K, whereas the measured h decreases from 5647 to 5252 W/m^2-K.

Conclusions

Heat transfer during condensation of R404A and R410A in 9.4 and 6.2 mm tubes was investigated. The experiments were conducted at 80% and 90% of the critical pressure for $200<G<800$ kg/m^2-s in small quality increments over entire vapor-liquid region using a thermal amplification technique that measures heat duty accurately while also providing refrigerant h with low uncertainties. The average uncertainties in the heat transfer coefficients were ±10% and 14% for 9.4 and 6.2 mm tubes, respectively. It was found that, due to the compensating variations in properties at near-critical pressures, a change in p_r from 0.8 to 0.9 is not significant enough to cause an appreciable change in heat transfer coefficients. The heat transfer coefficients in the 6.2 mm diameter tubes were higher than those for the 9.4 mm tubes. Also, the heat transfer coefficients for R410A were higher than those for R404A because of the superior thermophysical properties of R410A. The flow regime maps (or transition criteria) developed by Coleman and Garimella [35], Breber et al. [19], and Dobson and Chato [7] all result in a similar categorization of the condensation data into the applicable flow regimes. The data from the present study primarily fell into two flow regimes: wavy-stratified and annular flow. Very few data points were in other regimes such as intermittent and mist flow. None of the available correlations in literature were able to satisfactorily predict the heat transfer coefficients during condensation of refrigerant blends R404A and R410A at such high p_r over the entire range of conditions investigated in this study. The wavy flow model of Dobson and Chato [7] underpredicted the data while their annular flow model overpredicted the data. There were also abrupt changes in h predicted by their models as the flow changed from annular to wavy regimes. The correlations of Cavallini et al. [16,17] and Thome et al. [24] result in better prediction of the data from the present study. It is believed that the present study represents one of the first attempts at measuring local condensation h in refrigerant blends close to the critical region. These results yield insights into the effects of reduced pressure, quality, mass flux, and geometry at near-critical conditions, and will enable more accurate design of refrigerant condensers necessary for the development of high-temperature-lift space-conditioning and water heating systems.

Nomenclature

Cp = specific heat, J/kg-K
d = diameter, mm
Fr = Froude number
G = mass flux, kg/m^2-s
h = heat transfer coefficient, W/m^2-K

h_{fg} = latent heat of condensation, J/kg
j_g^* = superficial gas velocity, dimensionless
k = thermal conductivity, W/m-K
LMTD = log-mean temperature difference, K
Nu = Nusselt number, dimensionless
Pr = Prandtl number, dimensionless
p_r = reduced pressure, dimensionless
Q = heat transfer rate, W
R = thermal resistance, K/W
Re = Reynolds number, dimensionless
T = temperature, °C
UA = overall heat transfer conductance, W/K
We = Weber number, dimensionless
X_{tt} = Martinelli parameter, dimensionless
x = quality, dimensionless
ΔT = temperature difference, °C
Δx = change in quality, dimensionless
ρ = density, kg/m^3

Subscripts and Superscripts

$crit$ = critical
g = gas
l = liquid
LO = liquid only
$refg$ = refrigerant
sat = saturated
so = Soliman
w = water

References

[1] Lemmon, E. W., McLinden, M. O., and Huber, M. L., 2002, *REFPROP Version 7.0, NIST Standard Reference Database 23*, National Institute of Standards and Technology.

[2] Guo, Z., and Anand, N. K., 2000, "Analytical Model to Predict Condensation of R-410A in a Horizontal Rectangular Channel," ASME J. Heat Transfer, **122**(3), pp. 613–620.

[3] Chitti, M. S., and Anand, N. K., 1995, "An Analytical Model for Local Heat Transfer Coefficients for Forced Convective Condensation inside Smooth Horizontal Tubes," Int. J. Heat Mass Transfer, **38**(4), pp. 615–627.

[4] Chitti, M. S., and Anand, N. K., 1996, "Condensation Heat Transfer Inside Smooth Horizontal Tubes for R-22 and R-32/125 Mixture," HVAC&R Res., **2**(1), pp. 79–101.

[5] Dobson, M. K., Chato, J. C., Hinde, D. K., and Wang, S. P., 1994, "Experimental Evaluation of Internal Condensation of Refrigerants R-12 and R-134a," *Proceedings of the ASHRAE Winter Meeting, Jan. 23–26*, New Orleans, LA, Vol. 100, ASHRAE, Atlanta, GA, pp. 744–754.

[6] Chato, J. C., 1962, "Laminar Condensation Inside Horizontal and Inclined Tubes," ASHRAE J., **4**(2), pp. 52–60.

[7] Dobson, M. K., and Chato, J. C., 1998, "Condensation in Smooth Horizontal Tubes," ASME J. Heat Transfer, **120**(1), pp. 193–213.

[8] Sweeney, K. A., 1996, "The Heat Transfer and Pressure Drop Behavior of a Zeotropic Refrigerant Mixture in a Micro-Finned Tube," M.S., thesis, Department of Mechanical and Industrial Engineering, University of Illinois at Urbana-Champaign, Urbana, IL.

[9] Boissieux, X., Heikal, M. R., and Johns, R. A., 2000, "Two-Phase Heat Transfer Coefficients of Three HFC Refrigerants Inside a Horizontal Smooth Tube, Part II: Condensation," Int. J. Refrig., **23**(5), pp. 345–352.

[10] Han, D.-H., and Lee, K.-J., 2001, "Experiments on Condensation Heat Transfer Characteristics Inside a 7 mm Outside Diameter Microfin Tube With R410A," 35th National Heat Transfer Conference, Anaheim, CA.

[11] Ebisu, T., and Torikoshi, K., 1998, "Heat Transfer Characteristics and Correlations for R-410A Flowing Inside a Horizontal Smooth Tube," ASHRAE Trans., **104**(2), pp. 556–561.

[12] Kwon, J. T., and Kim, M. H., 2000, "Modeling and Experiments of In-Tube Condensation Heat Transfer for R22 and Its Alternative Refrigerant," JSME Int. J., Ser. B, **43**(4), pp. 596–601.

[13] Haraguchi, H., Koyama, S., and Fujii, T., 1994, "Condensation of Refrigerants Hcfc22, Hfc134a and Hcfc123 in a Horizontal Smooth Tube (2nd Report, Proposal of Empirical Expressions for the Local Heat Transfer Coefficient," Trans. Jpn. Soc. Mech. Eng., Ser. B, **60**(574), pp. 245–252.

[14] Kwon, J. T., Ahn, Y. C., and Kim, M. H., 2001, "A Modeling of In-Tube Condensation Heat Transfer for a Turbulent Annular Film Flow With Liquid Entrainment," Int. J. Multiphase Flow, **27**(5), pp. 911–928.

[15] Cavallini, A., Censi, G., Del Col, D., Doretti, L., Longo, G. A., and Rossetto, L., 2001, "Experimental Investigation on Condensation Heat Transfer and Pressure Drop of New HFC Refrigerants (R134a, R125, R32, R410A, R236ea) in a Horizontal Smooth Tube (Etude Experimentale sur le Transfert de Chaleur Lors de la Condensation et sur la Chute de Pression des Nouveaux Frigorigenes HFC (R134a, R125, R32, R410A, Et R236ea) dans un Tube Lisse Horizontal)," Int. J. Refrig., **24**(1), pp. 73–87.

[16] Cavallini, A., Censi, G., Del Col, D., Doretti, L., Longo, G. A., and Rossetto, L., 2002, "Condensation of Halogenated Refrigerants Inside Smooth Tubes," HVAC&R Res., **8**(4), pp. 429–451.

[17] Cavallini, A., Censi, G., Del Col, D., Doretti, L., Longo, G. A., Rossetto, L., and Mathur, G. D., 2002, "In-Tube Condensation of Halogenated Refrigerants," 2002 ASHRAE Winter Meeting, Jan 13–16, Atlantic City, NJ, Vol. 108 PART 1, Amer. Soc. Heating, Ref. Air-Conditioning Eng. Inc., pp. 146–161.

[18] Breber, G., Palen, J. W., and Taborek, J., 1979, "Prediction of Horizontal Tube-Side Condensation of Pure Components Using Flow Regime Criteria," Condensation Heat Transfer, 18th Natl. Heat Transfer Conf., Aug 6–8, San Diego, CA, ASME, New York, NY, pp. 1–8.

[19] Breber, G., Palen, J. W., and Taborek, J., 1980, "Prediction of Horizontal Tubeside Condensation of Pure Components Using Flow Regime Criteria," ASME J. Heat Transfer, **102**(3), pp. 471–476.

[20] Kosky, P. G., and Staub, F. W., 1971, "Local Condensing Heat Transfer Coefficients in the Annular Flow Regime," AIChE J., **17**(5), pp. 1037–1043.

[21] Friedel, L., 1979, "Improved Friction Pressure Drop Correlations for Horizontal and Vertical Two Phase Pipe Flow," European Two Phase Flow Group Meeting, Ispra, Italy, Paper No. E2.

[22] Tang, L., 1997, "Empirical Study of New Refrigerant Flow Condensation Inside Horizontal Smooth and Micro-Fin Tubes," Ph.D. dissertation, University of Maryland at College Park.

[23] El Hajal, J., Thome, J. R., and Cavallini, A., 2003, "Condensation in Horizontal Tubes, Part 1: Two-Phase Flow Pattern Map," Int. J. Heat Mass Transfer, **46**(18), pp. 3349–3363.

[24] Thome, J. R., El Hajal, J., and Cavallini, A., 2003, "Condensation in Horizontal Tubes, Part 2: New Heat Transfer Model Based on Flow Regimes," Int. J. Heat Mass Transfer, **46**(18), pp. 3365–3387.

[25] Kattan, N., Thome, J. R., and Favrat, D., 1998, "Flow Boiling in Horizontal Tubes—Part III: Development of a New Heat Transfer Model Based on Flow Pattern," ASME J. Heat Transfer, **120**(1), pp. 156–165.

[26] Kattan, N., Thome, J. R., and Favrat, D., 1998, "Flow Boiling in Horizontal Tubes—Part I: Development of a Diabatic Two-Phase Flow Pattern Map," ASME J. Heat Transfer, **120**(1), pp. 140–147.

[27] Kattan, N., Thome, J. R., and Favrat, D., 1998, "Flow Boiling in Horizontal Tubes—Part II: New Heat Transfer Data for Five Refrigerants," ASME J. Heat Transfer, **120**(1), pp. 148–155.

[28] Rouhani, S. Z., and Axelsson, E., 1970, "Calculation of Void Volume Fraction in the Subcooled and Quality Boiling Regions," Int. J. Heat Mass Transfer, **13**(2), pp. 383–393.

[29] Jiang, Y., and Garimella, S., 2003, "Heat Transfer and Pressure Drop for Condensation of Refrigerant R-404A at Near-Critical Pressures," Technical and Symposium Papers presented at the 2003 Winter Meeting of the ASHRAE, Jan. 26–29, Chicago, IL, Vol. 109 Part 1, Amer. Soc. Heating, Ref. Air-Conditioning Eng. Inc., pp. 677–688.

[30] Mitra, B., and Garimella, S., 2003, "Heat Transfer and Pressure Drop for Condensation of Refrigerant R410A at Near-Critical Pressures," International Mechanical Engineering Congress and RD&D Expo, Washington, DC, Vol. IMECE2003-41807.

[31] Garimella, S., and Bandhauer, T. M., 2001, "Measurement of Condensation Heat Transfer Coefficients in Microchannel Tubes," 2001 ASME International Mechanical Engineering Congress and Exposition, New York, ASME, New York, Vol. 369, pp. 243–249.

[32] Taylor, B. N., and Kuyatt, C. E., 1994, *Guidelines for Evaluating and Expressing the Uncertainty of NIST Measurement Results*, National Institute of Standards and Technology, Gaithersburg, MD.

[33] Kays, W. M., and Leung, E. Y., 1963, "Heat Transfer in Annular Passages: Hydrodynamically Developed Flow With Arbitrarily Prescribed Heat Flux," Int. J. Heat Mass Transfer, **6**, pp. 537–557.

[34] Walker, J. E., Whan, G. A., and Rothfus, R. R., 1957, "Fluid Friction in Noncircular Ducts," AIChE J., **3**(4), pp. 484–489.

[35] Coleman, J. W., and Garimella, S., 2003, "Two-Phase Flow Regimes in Round, Square and Rectangular Tubes During Condensation of Refrigerant R134a," Int. J. Refrig., **26**(1), pp. 117–128.

[36] Zivi, S. M., 1964, "Estimation of Steady-State Steam Void-Fraction by Means of the Principle of Minimum Entropy Production," ASME J. Heat Transfer, **86**, pp. 247–252.

S. W. Paik
Department of Mechanical Engineering,
Texas A&M University,
College Station, TX 77843

K. D. Kihm[1]
Fellow ASME
Department of Mechanical, Aerospace and
Biomedical Engineering,
University of Tennessee,
Knoxville, TN 37996
e-mail: kkihm@utk.edu

S. P. Lee
Department of Mechanical Engineering,
Kyonggi University,
Suwon, Korea

D. M. Pratt
Fellow ASME
AFRL/VAS,
Wright-Patterson Air Force Base,
Dayton, OH 45433

Spatially and Temporally Resolved Temperature Measurements for Slow Evaporating Sessile Drops Heated by a Microfabricated Heater Array

The spatially and temporally resolved evaporation phenomena of a slowly evaporating water droplet are investigated using a microfabricated gold heater array consisting of 32 linear heater elements (100 μm wide and 15 mm long, each). Each of the gold microheater elements works both as a temperature sensor and as a heater. The experiment is performed under a constant voltage mode to examine the spatially resolved temperature history of the droplet contact surface for a period starting at initial contact with the heater and lasting to the point of complete dryout. The raw data obtained from the linear array have been tomographically deconvolved so that the radial temperature profile can be determined assuming a circular droplet contact surface. [DOI: 10.1115/1.2728904]

Keywords: microfabricated heater array, sessile drops, evaporation, temperature measurements, tomography

1 Introduction

Droplet evaporation on a heated surface has a variety of important applications in diverse areas of engineering, including electronics cooling, and thermal management for high heat flux equipment used by nuclear and electronic industries [1,2]. Selected metallurgical industries, such as aerospace industry and liquified natural gas (LNG) shipbuilding, are highly interested in the droplet evaporation phenomena associated with aluminum welding deficiencies [3]. When sophisticated aluminum welding is performed, the quenching of aluminum parts yields nonuniform, mechanical properties that causes a quality problem of surface cracking. Quenching involves exposing the high-temperature part to a liquid quenchant such as condensed water droplets, resulting in a relatively large and rapid fall in the local temperature. Another closely related application is in printer technology [4] where the quality of inkjet printing crucially relies upon the rapid and uniform evaporation of ink droplets. While a number of studies have been made to examine bubble evaporation characteristics, almost all previous studies have concentrated on examining macroscopic measurables.

For the case of planar thin film evaporation, Oron et al. [5] presented the progressive dryout and separation of the thin film in possibly the most comprehensive review article in the field. Their primary focus was on the film spread and contraction, and their contents somewhat share with the present observations. In our case, however, the droplet spreads within a 1 s period and the constant contact angle remains unchanged for the longest evaporation period of several hundred seconds. In addition, they considered varying contact surface areas while we considered a constant contact surface area.

Xiong et al. [6] used thermocouple probes to measure the hot plate bulk temperature and overall heat flux variations during droplet evaporation. This study varies hot plate temperature from film evaporation at relatively low temperatures to the spheroidal vaporization for different test fluids, including water and various hydrocarbon liquid fuels presenting a single averaged value for overall heat flux and bulk temperature.

Bernardin et al. [3] investigated the temperature dependence of the advancing contact angle of a water droplet on an aluminum polished heating surface, using a single thermocouple probe embedded below the heated surface. This experiment presents the temperature information of the heated aluminum surface at a single spatial point that is approximately at the center of the droplet. However, this study lacks spatially resolved thermal data that are necessary to properly characterize droplet evaporation accompanying microscale heat and mass transport.

Makino et al. [7] examined the influence of water droplet evaporation on a heated metal surface by measuring the voltage variations of an electric probe. They used four types of materials for water droplets ranging from 2.54 mm to 4.50 mm in diameter. While this study provides some quantitative data for the voltage variations correlating droplet evaporation, it fails to present meaningful temperature variation or heat flux variation data associated with droplet evaporation.

Crafton et al. [8] measured the heat transfer and evaporation rates of both heptane and water droplets on heated metal surfaces. This team of researchers presented the heat flux data of its experiments by assuming constant droplet evaporation; with this evaporation rate they calculated heat flux. The study also assumes constant temperature inside of the droplet and calculates only one gross heat flux value per droplet. No spatial or temporal heat flux information is given.

Klassen and di Marzo [9,10] used the infrared thermography technique in their first attempt to measure the spatially and temporally resolved temperature distributions for a single evaporating droplet. The major drawback of this study, however, is that the infrared is so excessively absorbed by water that no reliable data could be obtained for the droplet contact surface area. For this reason, useful temperature measurements are available only for the peripheral heated surface outside the droplet contact surface. Dawson and di Marzo [11] again employed the infrared thermography technique in their later study of evaporative cooling. In this

[1]Corresponding author.

Contributed by the Heat Transfer Division of ASME for publication in the JOURNAL OF HEAT TRANSFER. Manuscript received October 5, 2005; final manuscript received October 27, 2006. Review conducted by Yogendra Joshi.

study, they injected multiple water droplets of 10 μL$\pm$1 μL onto a 180°C heated Macor tile. Because of the aforementioned limitation of the infrared thermography technique, measurements were only possible for the surface area outside of the droplet–surface contact.

The model of di Marzo and Evans [12] describing the droplet evaporation life time is based on the assumption that a linear temperature profile prevails inside the droplet and that boundary condition involves both the vapor molar flux and vapor molar fraction. Because di Marzo and Evans take such a different approach to the problem, it is not readily possible to compare this model to the present findings.

Michiyoshi et al. [13] used an electro-probe to measure the variation of heater supply voltage during the evaporation of a single water droplet on various heated plates, including copper, brass, carbon steel, and stainless steel. Based on their experimental observations, only qualitative temperature profiles were presented for the heater surface contacting the droplet. The results identify a sharp drop in temperature upon droplet contact and show a constant temperature drop for almost all of the remaining evaporation period, until dryoff returns it to the dry heater temperature [14].

Using a control volume method, Chandra et al. [15] calculated the temperature history both inside and outside the droplet during evaporation, then attempted to validate their predictions with experimental data from the aforementioned study by Klassen and di Marzo [9]. However, a later publication by Klassen and di Marzo [16] revealed that their published data in Ref. [9] had been unreliable, as the limitation of the infrared thermography technique had been overlooked.

Rule and Kim [17] fabricated two-dimensional, individually controlled 96-heater arrays to study the heat transfer behavior of pool boiling of FC-72 under a constant temperature condition. Since pool boiling behavior is inherently unstable, the heat flux data provided from individual heater arrays reveals large temporal fluctuations and are not interpretative. The primary results of the study, therefore, are presented as averages of either the array or group to derive meaningful temporal heat flux characteristics.

Lee et al. [18] showed the time and space resolved heat transfer characteristics of single droplet cooling using a two-dimensional array of (270 μm$\times$270 μm^2) microheater elements under superheated temperature condition. The heater array used in this study was able to maintain constant temperature with the help of a feedback circuit. The researchers used Wheatstone bridge and OP amp for temperature control. For the experiment, PF-5060 liquid was placed on the heater array and the heater's heat flux variation was measured; however, droplet movement on the microheater arrays made it difficult to evaluate any spatially resolved heat flux and temperature variation.

Hu and Larson [19] found both theoretically and experimentally that the net evaporation rate from the droplet remains almost constant with time for a small initial contact angle, even though the local evaporation flux is higher at the edge than inside of the droplet. Their results qualitatively agree with the present study in that the heater temperature remains the same for most of the entire period of evaporation, and evaporation temperature is higher at the edge of the droplet than inside. Ajaev [20] mathematically calculated the transient contact angle, thickness, radius, and heat flux of a spreading liquid droplet that was dropped from a finite height down to a heater surface. This study predicts fairly well the dynamic behavior of droplet evaporation under geometrical changes.

None of the aforementioned studies yield data that are appropriately resolved enough to measure the mechanism of droplet evaporation. To elucidate this phenomenon, we have fabricated a microscale heater array and achieved spatially and temporally resolved thermal data for evaporating droplets. Each heater works both as a heater and a temperature sensor based on the resistance–temperature relation of a thin, gold deposit heater layer. Direct measurements of heater resistance variations associated with temperature drop of the evaporating droplet allow for determination of the instantaneous surface temperature for each heater with microscale spatial resolution. The microfabricated heater array technique also alleviates the intrinsic problem of the infrared detection technique associated with its absorption in water [10].

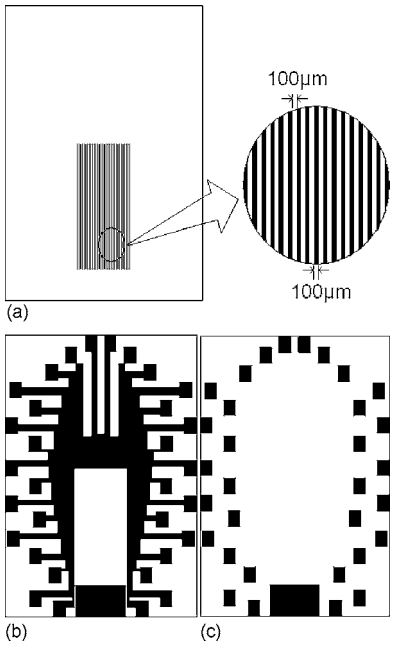

Fig. 1 Three-layered microheater design by AutoCAD

2 Design and Fabrication of Microheater Array

The microheater array design (Fig. 1) consists of three layers: the heater line layer (Fig. 1(*a*)), the connection wiring layer (Fig. 1(*b*)), and the opening layer for power line soldering (Fig. 1(*c*)). Each of the identical 32 line heaters is 100 μm wide with 100 μm spacing, 0.5 μm thick, and 1.5 cm long. Thus, the entire heater array occupies a rectangular heating area of 0.945 cm^2 (0.63 cm $\times$1.5 cm). Our rectangular array design is intended for comprehensive use not only for spherical drops, but also for elongated drops and flat, thin-film boundary, whereas the square design is limited to function only for spherical drops.

All individual wiring layer lines, which connect the line heater ends to the corresponding soldering electrodes, are designed to have an identical resistance value 0.133 times that of the line heater resistance. Each of the wiring layer lines has a surface area 2.885 times larger than that of a single line heater. Under the constant current operation the heating power, i^2R, is linearly proportional to the resistance and, thus, the heat flux from the line heater is 21.70 times (0.133^{-1}*2.885) higher than that from the wiring line. The wiring line resistance varies linearly with its temperature by the linear relation, $R=R_0(1+\alpha(T-T_0))$. Since the temperature rise is proportional to the heat flux, the temperature rise of the line heater is 21.7 times larger than that of the wiring line. For example, for the heater temperature rise of 55°C, the wiring line temperature rises only 2.53°C, which corresponds to a 0.34°C increase of heater temperature. Substituting these values in the resistance–temperature equation shows that the wiring line resistance increase accounts for only 0.096% of the heater resistance. Therefore, the error associated with the resistance variation of the wiring line is considered negligible within acceptable accuracy.

The microheater array was fabricated at the class-1000 clean room located at Texas A&M University. A sputter coater was used to attach the gold seed layer onto a glass substrate. Since gold

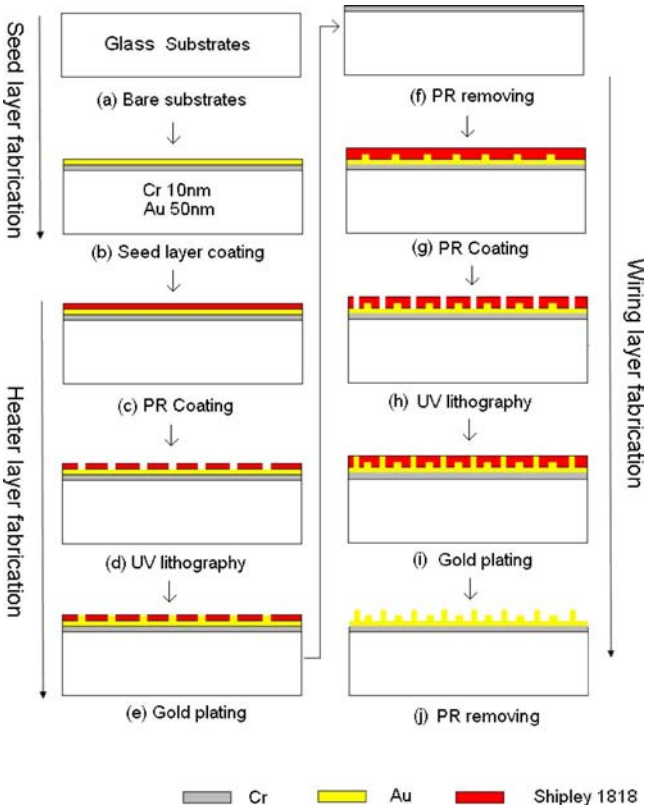

Fig. 2 Schematic illustration of the fabrication process for the three layers: the seed layer (*a*), (*b*) the heater layer (*c*)–(*f*) and the wiring layer (*g*)–(*j*) subprocesses

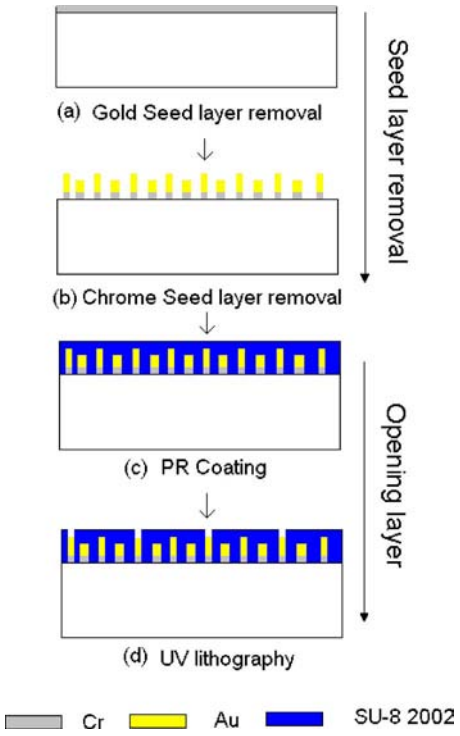

Fig. 3 Seed layer removal and opening layer fabrication procedure

cannot be directly attached to the soda lime glass substrate, a 10-nm-thick chromium–bonding layer was coated to the substrate (Fig. 2(*a*)). Then, the 50-nm-thick gold seed layer was coated over the chromium layer (Fig. 2(*b*)). Figures 2(*c*)–2(*e*) show the heater layer fabricaton. After spin coating PR Shipley 1818 (Fig. 2(*c*)), ultraviolet (UV) lithography was performed, using a mask aligner to carefully align the micropatterned mask (Fig. 2(*d*)). Gold was electroplated under a constant current mode (Fig. 2(*e*)). Then, the remaining PR was removed using isopropyl alcohol and acetone wash (Fig. 2(*f*)). The wiring layer fabrication used the same process shown in Figs. 2(*g*)–2(*j*). Because the gold and chrome seed layers were left covering the entire substrate, the seed layer removal process was conducted by etchant to ensure electrically separated heater lines and connecting wire configurations (Figs. 3(*a*) and 3(*b*)). Then, to physically protect the heater and wiring lines and to prevent electric shorts between them, the entire layer—except for the opening layer electrodes for later soldering—was coated with SU-8 2002 (Figs. 3(*c*) and 3(*d*)). The coating thickness was uniform at 2 μm, i.e., 1.5 μm coating on top of the 0.5 μm heater lines.

For relatively narrow temperature ranges, such as the range tested from 273 K to 400 K, the temperature–resistance relation of gold is nearly perfectly linear as

$$R = R_0(1 + \alpha(T - T_0)) \tag{1a}$$

where the resistance R varies linearly with the slope of temperature–resistance coefficient $\alpha = 0.003715\ \mathrm{K}^{-1}$ for gold. For a single linear resistor element, the resistance–temperature relation can be readily reduced to the resistivity–temperature relation, using $R = \rho^* L/A$, where ρ is the resistivity; L denotes the length of resistor; and A denotes its cross-sectional area

$$\rho = \rho_0(1 + \alpha(T - T_0)) \tag{1b}$$

Equation (1*a*) or Eq. (1*b*) can also be expressed as

$$R = \rho_0[1 + \alpha(T - T_0)]\frac{L}{w \cdot d} \tag{1c}$$

A comparison of the linearized data expressed by Eq. (1*a*) with the actual measured resistivity data [21,22] is shown in Table 1. For the present experiment on slow evaporation of water droplets, the maximum temperature condition will not exceed 80°C, and the linearized relation of Eq. (1*a*) can be used with a linearization error of less than 0.1%.

To minimize heat loss from the backside of the substrate, the 1.5-mm-thick (d_s) glass substrate ($k_s = 1.4$ W/m K) is placed on a 1-cm-thick (d_a) acrylic sheet ($k_a = 0.14$ W/m K). Then, the acrylic sheet is attached to an aluminum block as a heat sink that is maintained at the room temperature 25°C. A one-dimensional heat conduction model is used to estimate the amount of heat loss from the bottom surface of the heater. The total thermal conductivity of the glass substrate and acrylic sheet below the heater array is calculated as $k_{\mathrm{tot}} = 0.159$ W/m K from

Table 1 Comparison between measured gold resistivity [13,14] and the linearized data approximated by Eq. (1)

Temperature (K)	Measured gold resistivity (Ω m)	Calculated gold resistivity by the linearized equation, Eq. (1) (Ω m)	Percentile errors (%)
273	2.051×10^{-8}	2.051×10^{-8}	0.00
293	2.214×10^{-8}	2.214×10^{-8}	0.00
300	2.271×10^{-8}	2.272×10^{-8}	0.03
350	2.685×10^{-8}	2.683×10^{-8}	0.08
400	3.107×10^{-8}	3.094×10^{-8}	0.42

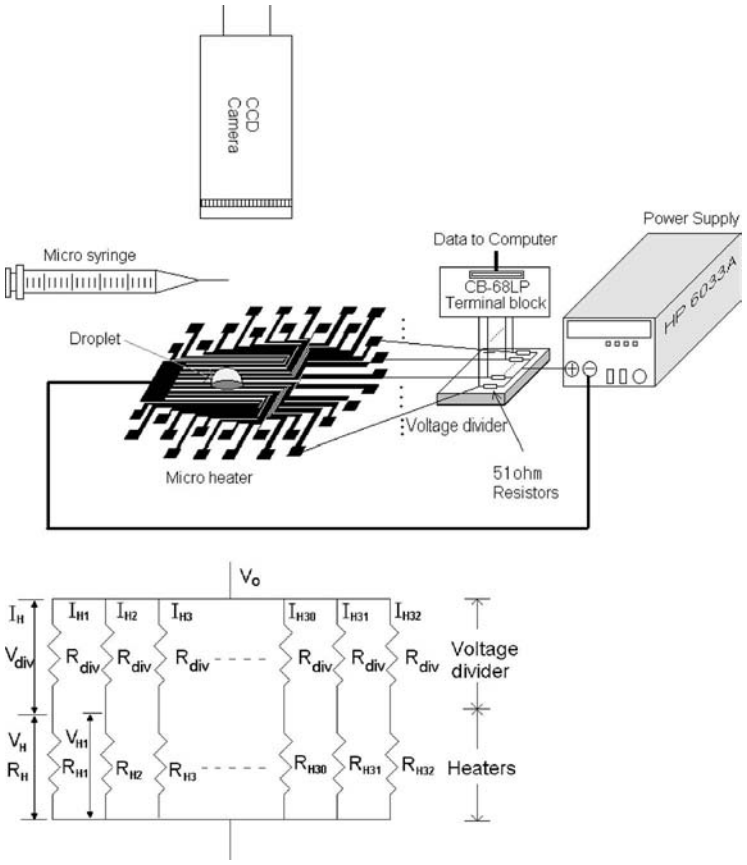

Fig. 4 Schematic illustration of the constant-voltage supply circuit for the microheater array

$$k_{\text{tot}} = \frac{k_s k_a (d_s + d_a)}{k_s d_a + k_a d_s} \tag{2}$$

Then, the heat flux to the aluminum block sink is given as

$$q_b = k_{\text{tot}} \frac{\Delta T}{d_a + d_s} \tag{3}$$

where ΔT denotes the temperature differential between the heater array and the sink; and q_b is calculated to range from 3.3% to 3.9% of the total heat flux of microheater array for the tested range from 40°C to 80°C.

3 Experimental Setup

Figure 4 presents a schematic illustration for the constant–voltage operation of the microheater array. A precision HP 6033A dc power supply powers the heater line array with a constant voltage, specifying a constant dry temperature based on the linearized resistance–temperature relation of gold, Eq. (1*a*). Input voltages of 2.09 V, 3.00 V, and 3.53 V provide the tested dry heater line temperatures of 40°C, 60°C, and 80°C, respectively. The individual data acquisition from the 32 line heaters is achieved using two NI PCI 6013 boards with two CB 68-LP shield connectors. Each line heater with identical resistance approximately at 8 Ω is serially connected to a 51 Ω resistor, as a voltage divider. The measured voltage across the 51 Ω resistor determines the current as $I_H = V_{\text{div}}/R_{\text{div}}(=51\ \Omega)$. The resistance of the line heater is calculated from $R_H = (V_H R_{\text{div}})/V_{\text{div}}$, and the line heater temperature is determined from the resistance–temperature equation, Eq. (1*a*). The heat flux is determined by the power consumption of the line heater, i.e., $I_H^2 R_H$. The NI PCI-6013 board has a 16 bit resolution with a measurement limit from +10 V to −10 V, which is equivalent to 0.31 mV uncertainty. In all, including device uncertainty, intrinsic system temperature uncertainty is approximately ±0.2°C.

All experimental procedures, including data acquisition, are recorded in PC busing the Labview software. Canon Macrolens FD 50 mm captures dynamic images of evaporating droplets. A more comprehensive description of the experimental setup and its operation is available in the leading author's dissertation [23]. A precision 10 μL syringe is used to apply water droplets at three different volumes of 3 μL, 5 μL, and 10 μL, on the heater array surface. Droplets are gently placed by using a precision jack that holds a microsyringe. Once positioned near the heater surface, a specified volume of liquid is slowly injected until the droplet touches the surface at nearly zero velocity. The droplet is not under any advancing or receding motion thereafter, and there is little possibility of effects of different contact angles on the resulting evaporation characteristics.

Before each experiment, the microheater surface is thoroughly cleaned with 99.9% isopropyl alcohol and is then dried for 30 min in a clean environment to ensure a dust-free and stain-free surface. The tested water droplets range from 2.1 mm (3 μL droplet) to 3.24 mm (10 μL droplet) in wet diameter. The experiment is done under the open space of a thermally controlled laboratory. In particular, the room temperature is maintained as 25°C with little variations. The effect of the environmental humidity is expected to be negligibly small, since the experimental time frame was approximately 5% of the total evaporation time for the case of natural evaporation at the laboratory.

When the droplet volume is sufficiently small, surface tension dominates to form its shape upon contact with the solid surface because of negligible gravitational deformation. This assumption is valid when the total droplet volume is less than 1 μL [24]. The

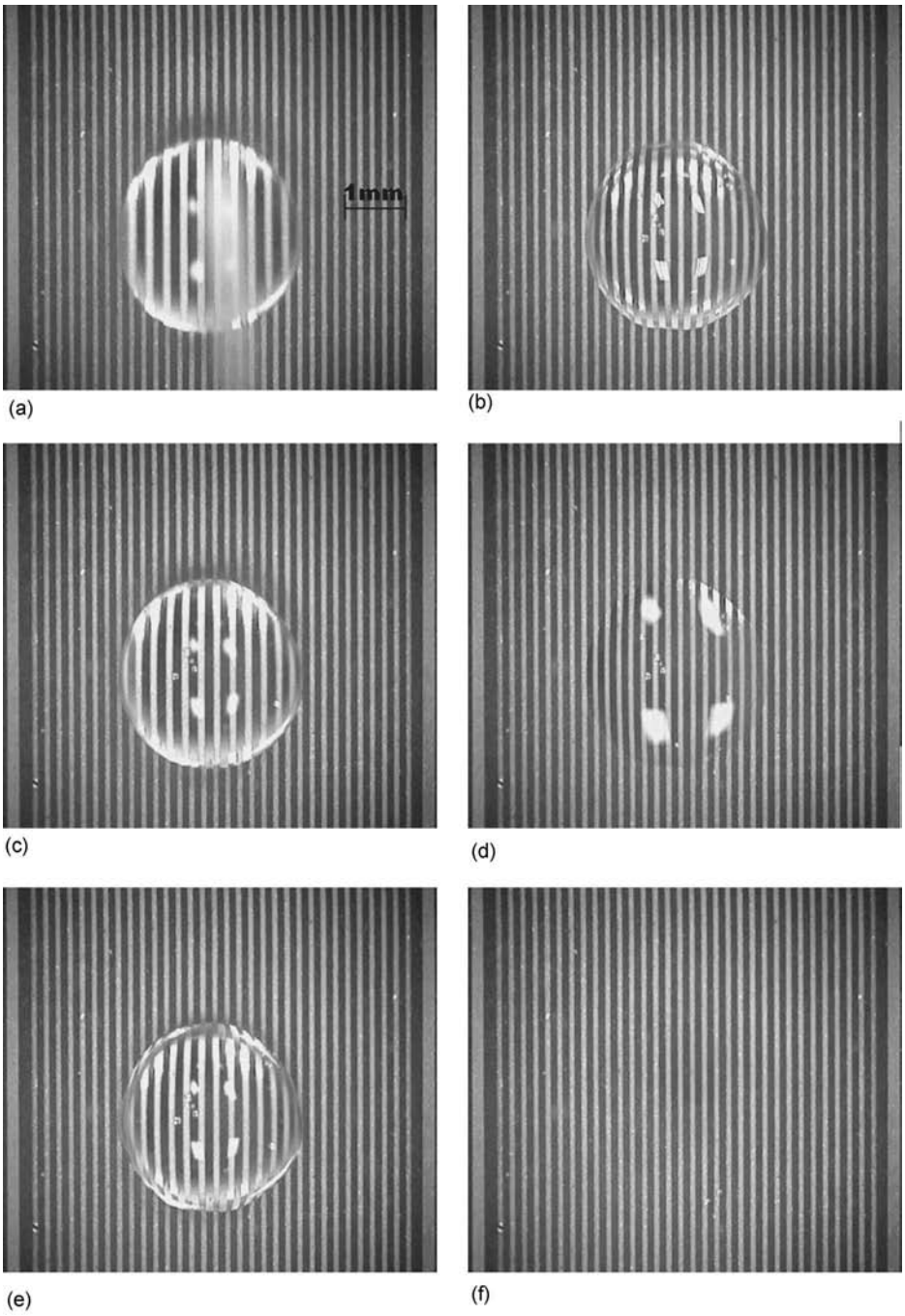

Fig. 5 Sequential images of slowly evaporating water droplets on the microheater array at T_h=60°C

larger droplets are distorted from the spherical cap shape because of gravity and, indeed, the condition for the spherical cap assumption is still in dispute, as published in numerous articles (i.e. Ref. [25]). On the other hand, Padday and Philos [26] proposed an oblate hemi-ellipsoid model, while Erbil and Meric [27] proposed ellipsoidal cap geometry for the droplet shape regardless of its volumetric size.

The spherical cap model [28,29] thus may be applied to determine the initial contact angle (θ) and the height (h) of the spread droplet, which is assumed to have a perfectly spherical "cap" shape

$$\mathrm{Vol} = \frac{\pi r_{\mathrm{wet}}^3 (1-\cos\theta)^2 (2+\cos\theta)}{3\sin^3\theta} \tag{4}$$

$$\tan\left[\frac{\theta}{2}\right] = \frac{h}{r_{\mathrm{wet}}} \tag{5}$$

Using Eqs. (4) and (5), the initial contact angles and heights are calculated as 97.83 deg and 1.204 mm for the 3 μL droplet and as 94.34 deg and 1.748 mm for the 10 μL droplet assuming perfect sphericity.

Zhang and Chao [30] introduced the technique of contact angle measurement with a shadowgraphic method. They utilized the shadow size of the droplet on the screen to measure droplet height, however this method cannot be used in this experiment because the microheater keeps the light from penetrating and does not allow for shadowgraphic imaging. To prevent droplet migration, we did not conduct the boiling experiments. In boiling con-

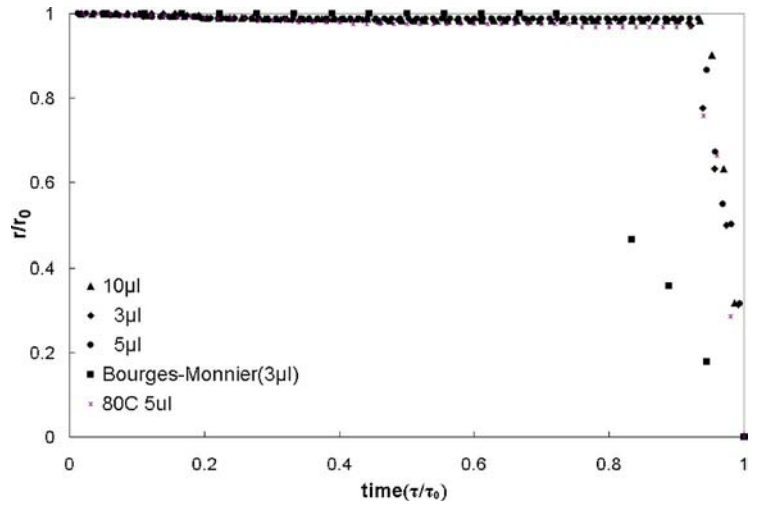

Fig. 6 Nondimensionalized radius variation with nondimensionalized evaporation time on epoxy surface and open chamber

dition, vapor nucleation causes the droplet to move during evaporation. Another factor we consider was heater surface treatment. We treated 100 W oxygen plasma reactive ion etch (RIE) for 1 min to make the surface hydrophilic [31]. With our surface hydrophilic treatment, a water droplet can maintain a constant contact radius for over 90% of its evaporation time, with its initial contact angle exceeding 90 deg.

The results seem to conflict with the generally known fact that the constant contact area evaporation is observed when the contact angle is less than 90 deg [29,32,33]. However, since gravity tends to flatten the spherical shape into an ellipsoid, it is the authors' belief that the calculated results have been somewhat overestimated compared with the actual contact angles and heights. Bourges-Monnier and Shanahan [28] studied the point of contact for a 4 μL water droplet with an epoxy resin surface, presenting a measured, initial contact angle of approximately 88 deg that continued to decrease thereafter. Because the present SU-8 coated contact surface shares similar material characteristics with an epoxy surface [34], the contact angles of the tested droplets are estimated at somewhat less than 90 deg. In addition, Crafton et al. [8] also demonstrated that water droplets under a similar contact surface maintain nearly constant contact area during evaporation while the droplet heights and contact angles both continuously decrease from their initial values.

Figure 5 shows sequential images of the evaporation progress of a 10 μL droplet on a dry heater temperature of 60°C with a dryout time τ=293 sec. At the beginning of evaporation at t/τ =0, water contacts the heater surface and maintains the same contact area until evaporation is nearly complete. Until reaching 94% of evaporation time, the droplet's diameter remains the same before rapidly shrinking. For all tested conditions of three different droplets (3 μL, 5 μL, and 10 μL volume) and three different dry temperatures (40°C, 60°C, and 80°C), constant area evaporation prevails and all three evaporation processes are qualitatively similar.

Figure 6 illustrates the progress of wet radii for the three tested droplet volumes from a captured video image analysis. The data verify constant area evaporation for more than 90% of the total evaporation period. The square symbols indicate the measurements by Bourges-Monnier and Shanahan [28], who allowed a 3 μL water droplet to slowly evaporate on a polished epoxy surface without any heating. Their results show constant area evaporation for less than 80% of the evaporation period. This discrepancy is mainly attributed to the weaker "pinning" of a surface that is less hydrophilic than the present plasma treated SU-8 surface, which was designed specifically for enhanced hydrophilicity and stronger pinning along the contact surface boundary.

The dryout times (Table 2) of the tested droplets persistently increase with increasing droplet volume and decrease with increasing dry-surface temperature. The tested droplet volumes are 3 μL, 5 μL, and 10 μL, and their wetting droplet radii are measured as 1.05 mm, 1.25 mm, and 1.62 mm, respectively. The larger droplet increases the contact area between the droplet and the heater surface, and the increased heated surface accelerates the evaporation rate. While droplet volume increases more than three times from 3 μL to 10 μL, the dryout time increases less than three times, as the contact area increases by 2.4 times. This is attributed to two observations: the evaporation rate increases with the contact surface area, while the contact surface area increase rate is slower than of the droplet volume.

Considering the dryout time as a functional form of the related parameters

$$\tau = f(T_h, T_d, V_d, \tau_0, r_{\text{wet}}) \tag{6a}$$

where T_h and T_d represent the heater temperature and the droplet initial temperature (constant 25°C for all tested cases), respectively, V_d is the droplet volume in μL, and τ_0 refers to the reference evaporation time for the smallest V_d=3 μL droplet under the highest T_h=80°C heater temperature.

Using the Buckingham Pi theorem [35], a dimensionless form of the parametric relation with three unknown parameters is constructed, then linear regressions for the unknown coefficients are performed using an EXCEL program, resulting in

Table 2 Measured dry-out time (τ in seconds) for complete evaporation of droplet for three different droplet volumes and three different dry-surface temperatures

	Droplet Volume (μL) →		
Dry-heater surface Temperature (°C)	3 (1.05 mm wet radius)	5 (1.25 mm wet radius)	10 (1.62 mm wet radius)
40	294	369	724
60	115	163	293
80	71	100	142

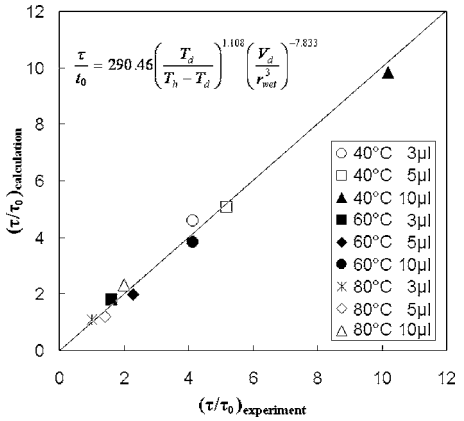

Fig. 7 Comparison of the measured dry-out times with the calculated dry-out times based on the Buckingham-Pi regression analysis for three different tested droplet sizes contacting three different heater surface temperatures

$$\frac{\tau}{\tau_0} = 290.46\left(\frac{T_d}{T_h - T_d}\right)^{1.108}\left(\frac{V_d}{r_{\text{wet}}^3}\right)^{-7.833} \tag{6b}$$

where the regression parameter $R^2=0.9752$ shows an excellent regression fitting. Figure 7 presents a comparison of the measured dryout time data with the calculated dryout times based on the above regression equation for all nine cases tested in Table 1. The comparison reveals highly correlated regression of Eq. (6*b*). According to the equation, total evaporation time is almost proportional to the temperature difference between the droplet and heated surface, which is of great physical importance.

4 Tomographic Deconvolution of Line-Averaged Raw Data

The "line-averaged" data are obtained from direct measurements of the overall resistance variation of each heater line and are recorded as raw data by the PC DAQ board. The value of temperature converted from the line-averaged resistance data is valid only if each heater is imposed to have a uniform temperature at any given instant of time. In reality, however, a substantial temperature gradient exists. The different heat transfer characteristics between dry and wet sections prevail on a single heater surface, and the temperature gradient distribution varies in time as droplet evaporation progresses.

In order to determine the distributed temperature profile accounting for the temperature gradients, tomographic conversion [36–38] is conducted to deconvolve the line-averaged data into radially distributing temperature profiles, assuming axisymmetric evaporation and heat transfer. The volumetric heat capacity of gold is 2.49×10^6 J/m^3 K and that of water is 4.18×10^6 J/m^3 K. The corresponding system heat capacities, defined as the volumetric heat capacity multiplied by the pertinent volume, are calculated to $C_{T\_\text{heater}}=5.132\times10^{-6}$ J/K and $C_{T\_\text{droplet}}=0.0125$ J/K (for the smallest 3 μL droplet). The heat capacity ratio is given as $C_{T\_\text{heater}}/C_{T\_\text{droplet}}=0.00123\%$ or smaller for the other two larger droplets (5 μL and 10 μL). This implies that when the spherical droplet hits the linear heater array, the thermal characteristics of the droplet dominate the nonaxisymmetric effect of the rectangular heater surface, and the temperature distributions on the circular wet surface should largely remain axisymmetric.

Figure 8(*a*) illustrates eight concentric deconvolution zones for the axisymmetric tomographic conversion. Zone I covers only the central region of the middle heater element (A). It was a time-consuming effort to try to coincide the droplet center with the central line heater. The maximum uncertainty for droplet center coincidence is estimated as ±50 μm, one-half of the centerline heater width. This uncertainty is equivalent to less than 2.5% of the wet diameter dimension of the tested droplets. Zone II covers the central regions of the next two left (B) and right (C) heater elements as well as the two subregions of the middle heater. Thus, Zone VIII includes partial regions from all 16 heater elements from A to O. The entire tomographic conversion domain covers the circular region of 6.4 mm diameter, corresponding to the width of the 32-element heater array.[2]

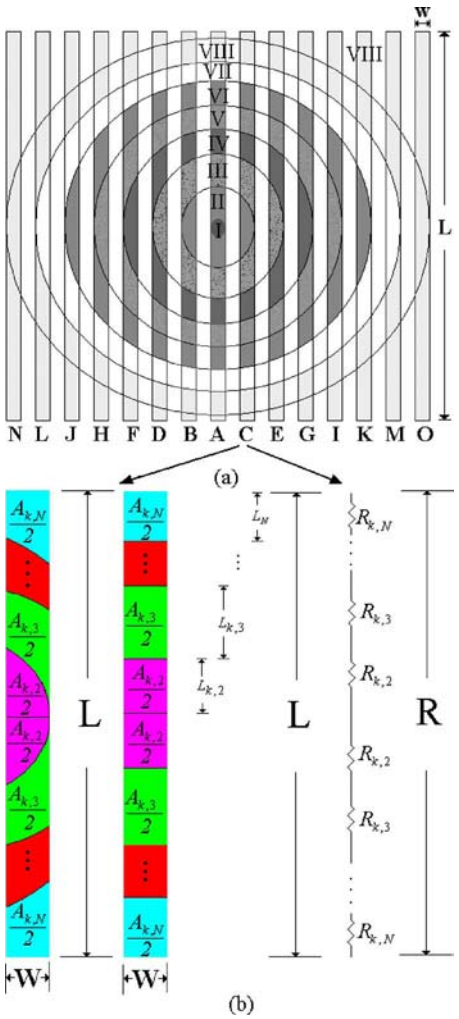

Fig. 8 Tomographic deconvolved temperature zones: (*a*) eight zone tomographic deconvolved heater area and (*b*) zone reconstruction for temperature calculation with electric resistance

The 16 unknown temperatures for the 16 concentric zones, T_i, must be determined from the line-averaged measured temperatures from the 16 line heater elements, $\bar{T}_k$. Thus, 16 linear algebraic equations correlating the line-averaged data with concentric temperature unknowns are established using the linear resistance/resistivity–temperature relations of Eqs. (1*b*) and (1*c*). The kth line heater, represented by the second line heater in Fig. 8(*b*), consists of concentric zones of $i=k, k+1, \ldots, N$ ($N=16$), and its resistance is therefore given as

[2]Sixteen concentric zones are used for the actual tomographic conversion calculations, whereas only eight of the zones are presented in Fig. 8 for simplicity.

$$\bar{R}_k = \sum_{i=k}^{N} R_{k,i}$$

$$= \sum_{i=k}^{N} \rho_0 \frac{L_{k,i}}{w \cdot d} = \sum_{i=k}^{N} \rho_0[1 + \alpha(T_i - T_0)]\frac{L_{k,i}}{w \cdot d}$$

$$= \frac{\rho_0 L}{w \cdot d} + \frac{\rho_0 \alpha}{w \cdot d}\sum_{i=k}^{N} (T_i - T_0)L_{k,i} \tag{7}$$

where w and d are the line heater width and thickness, respectively, and $\Sigma_{i=k}^{N} L_{k,i} = L$.

Assuming a rectangular area for each subzone of the kth heater line, the equivalent heater length of the subzone is given as

$$L_{k,i} = \frac{A'_{k,i}}{w} \tag{8}$$

Substituting Eq. (8) into Eq. (7) gives

$$\bar{R}_k = \frac{\rho_0 L}{w \cdot d} + \frac{\rho_0 \alpha}{w \cdot d \cdot w}\sum_{i=k}^{N} (T_i - T_0)A_{k,i} \tag{9}$$

On the other hand, the measured line-averaged resistance is expressed as

$$\bar{R}_k = \rho_0[1 + \alpha(\bar{T}_k - T_0)]\frac{L}{w \cdot d} \tag{10}$$

where $\bar{T}_k$ represents the line averaged temperature of the kth line heater.

Combining Eqs. (9) and (10), and using a dimensionless area $A_{k,i} = A'_{k,i}/L \cdot w$, gives

$$\bar{T}_k = \sum_{i=k}^{N} T_i A_{k,i} \tag{11a}$$

where the left-hand side presents the measured line-averaged temperature data, and the deconvolved temperature data for each concentric zone, T_k, can be calculated one by one starting from the outmost heater where the heater temperature is uniform and equal to the dry heater temperature. For example, for $k=16$ for the outmost concentric zone

$$T_{16} = \bar{T}_{16} \tag{11b}$$

for $k=15$

$$T_{15} = \frac{\bar{T}_{15} - \bar{T}_{16}A_{15,16}}{A_{15,15}} \tag{11c}$$

and so on. Note that the dimensionless zone area $A_{k,i}$ does not have to be specified by considering the intersection of the droplet edge. After the droplet center location is identified from the droplet image, the concentric zone widths are determined based on the specified number of the zones.

To examine the effect of noncircular wet surface on the tomographic algorithm, the tomographic deconvolution calculations are repeated for various cases of elliptical wet surfaces simulating noncircular situations. In essence, changes in the zone areas (Fig. 8) due to the deviation of the wet surface from a perfect circle to an ellipse are accounted for by the tomographic deconvolution algorithm. For a representative case of 10 μL droplet with a nominal wet diameter of 3.24 mm, the major and minor axes of the equivalent ellipse surface are varied to have their differentials of 100 μm, 200 μm, and 400 μm. Note that the wet surface eccentricity hardly exceeded 400 μm even for the most disturbing cases. The resulting magnitudes of the maximum temperature bias, occurring at the central zone, are calculated to be ±0.3°C, ±0.6°C, and ±1.1°C, respectively.

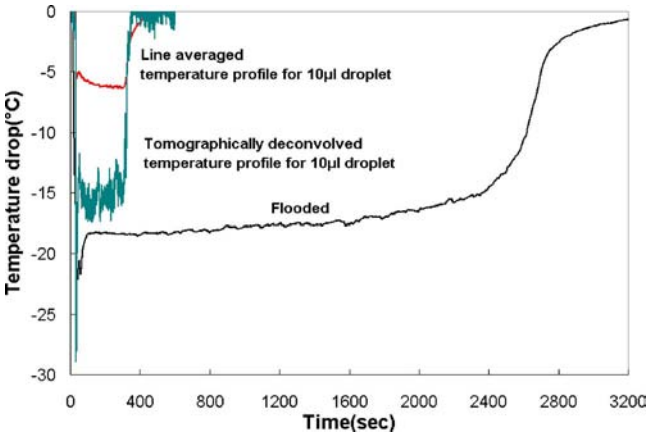

Fig. 9 Temperature variation of droplet center on the microheater (for 10 μL data, both of them are 100 data, moving average method was used)

The temporal developments of the droplet (10 μL) center temperature are shown for the line-averaged profile and for the tomographically deconvolved profile in Fig. 9. Also shown is the temperature variation for the case of flooding (the regular solid black line) at about the same height of the wetted droplet of 10 μL. Droplet evaporation is expected to result in slightly less temperature drop compared with the flooded evaporation, since the droplet is surrounded by a dry heater area, which supplies extra heat through conduction by the glass substrate as well as convection through the nearby air. The line-averaged data, however, unacceptably deviate from the flooded case and fail to predict physically valid temperature history. The overly smoothed line-averaged data also overlook the temperature fluctuations occurring from the fluid motion inside the droplet driven by the interfacial thermocapillary stress and thermally induced buoyancy.

5 Results and Discussion

Figure 10 illustrates temporal development of tomographically deconvolved temperature profiles for 3 μL, 5 μL, and 10 μL droplets for the case of 80°C dry heater temperature. The temperature profiles plotted with normalized radial distance collapse together, showing similar development for all three droplets for practically the entire test period. Upon contact, the largest ΔT, the result of the instantaneous maximum cooling rate (Fig. 10(*a*) for $t/\tau = 0.01$), remains nearly unchanged during evaporation as the latent heat transfer process occurs at a constant temperature (Figs. 10(*b*)–10(*d*) for $0.1 < t/\tau < 0.9$). Then, ΔT returns to the dry heater temperature after completion of evaporation (Fig. 10(*e*) for $t/\tau = 1.1$) and fully recovers to it for $t/\tau = 2.0$ (Fig. 10(*f*)). For the cases of 40°C and 60°C dry heater temperatures, qualitatively similar tendencies were observed, but with relatively less magnitudes of ΔT than were expected. The magnitude of the contacting surface temperature drop and its spatial distribution are independent of the drop volume. The centerline temperature incorporates the uncertainties based on the spatial mismatching of the central heater line with the true center of the droplet wet surface.

Figure 11 shows the temperature fall and recovery history that is tomographically determined at the center of the sessile droplet for the period from droplet impact to the time beyond completion of evaporation. Figures 11(*a*)–11(*c*) show temperature variations for the three 3 μL, 5 μL, and 10 μL tested droplets and for all three dry heater temperatures of 40°C, 60°C, and 80°C. The temporal resolution of the presented data is 100 Hz, with moving

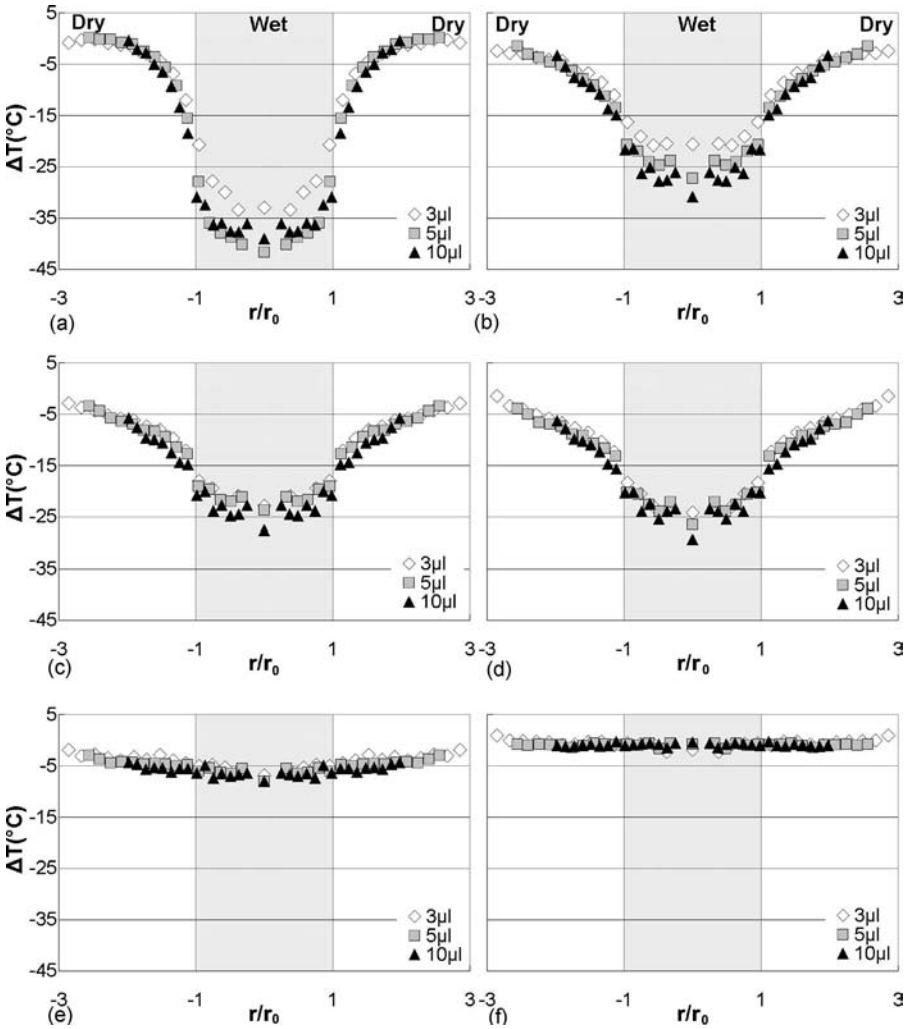

Fig. 10 Microheater temperature drop by the water droplet evaporation with tomographically deconvolved 16 zone model at 80°C: (*a*) $t/\tau=0.01$; (*b*) $t/\tau=0.1$; (*c*) $t/\tau=0.5$; (*d*) $t/\tau=0.9$; (*e*) $t/\tau=1.1$; and (*f*) $t/\tau=2.0$ (τ=dry-out time)

averages of 100 data points.[3] For each of the nine cases shown in Fig. 11, a maximum temperature drop is experienced by the droplet impact at $t=0$, and the amount of temperature drop is basically equivalent to the temperature differential between the dry heater temperature and the cold droplet temperature of 25°C before contact with the heaters. The amount of temperature drop remains nearly constant for the entire evaporation period before it recovers to the dry heater temperature upon completion of the evaporation. Heaters recover to the original dry temperature quickly after evaporation ends.

Note that for the case of the highest heater temperature (Fig. 11(*c*)), sudden temperature drops are apparent at the last moment of evaporation. The large thermocapillary action toward the center results in a rapid contraction of the thin droplet fluid and momentarily increases the liquid mass at the center. In other words, the relatively lower air–water interfacial temperature at the droplet's center increases the local surface tension, so that the surface flow is induced from the droplet rim at relatively high temperature and smaller surface tension, toward the center at relatively low temperature and high surface tension. Thus, at the final stage of the evaporation the center region of water droplet is momentarily cooled, showing a sudden temperature drop before quickly recovering to the dry heater temperature as evaporation is completed. Such dramatic temperature drops are less pronounced for the cases of the lower heater temperatures, as their evaporation develops more slowly and progresses more gradually.

Figure 12 shows temporal variations of temperature drop at four selected radial locations for the case of 80°C dry heater temperature with 10 μL droplet evaporation. The initial temperature drop upon impact is most pronounced at the center ($r/r_0=0$), and the amount of the initial temperature drop diminishes as the droplet boundary is approached ($r/r_0=0.90$). The temperature drop peak exists only on the inside of the droplet, while outside the droplet boundary ($r/r_0=1.16$ or 1.94) the heater surface temperature gradually decreases due to conduction heat loss to the droplet along the heater surface. The sudden temperature drop near the completion of evaporation, as discussed with Fig. 10, is apparent at the center, but the temperature recovers rather gradually as the droplet edge is approached. This is consistent with the conjecture of sudden thickening of the central region driven by the thermocapillary phoresis. Also, the temperature recovery to the dry heater level starts earlier at $r/r_0=0.90$ than at the center. This demonstrates that the dryoff starts from the boundary and completes toward the center. The highly sensitive and fluctuating data

[3]In the 100-point moving average technique, the first 100 data samples are averaged to determine the first data point value. Then, the next 100 data samples (i.e., from data sample No. 2 to data sample No. 101) are averaged to determine the second data point value. This technique was used the tomographic deconvolution.

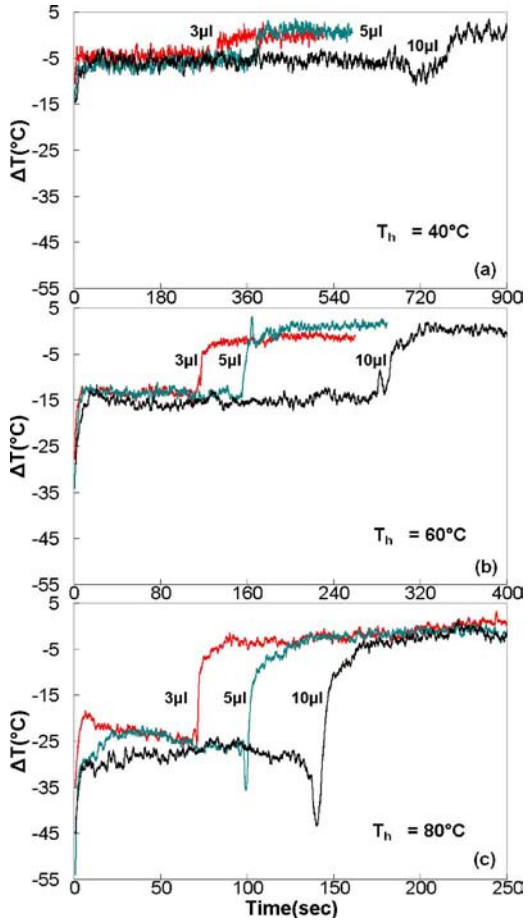

Fig. 11 The center point temperature drop and recovery history: (*a*) 40°C; (*b*) 60°C; and (*c*) 80°C

at the center represent the unsteady and possibly asymmetric nature of the convective heat and mass transfer inside the droplet. The fluctuation magnitudes diminish with increasing radius and the fluctuation disappears farther away from the droplet boundary ($r/r_0=1.94$), where the unsteady nature of evaporation disappears to allow for smooth conductive heat transfer.

The temperature measurement uncertainties are estimated to be better than ±0.12%. Equation (1*a*) is rewritten for temperature as

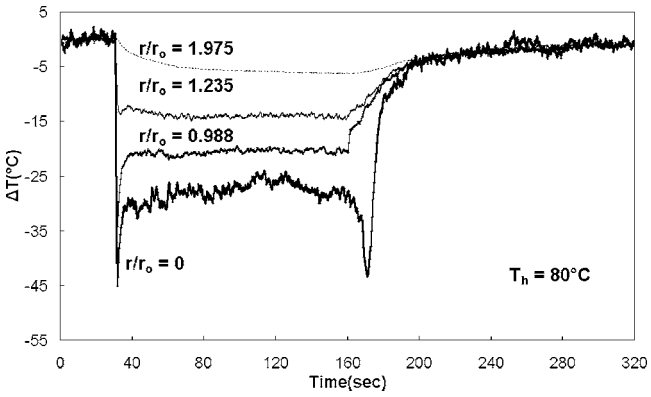

Fig. 12 Temporal temperature variation of microheater at several positions of r/r_0 for T_h=80°C, 10 µL (evaporation started at 30.76 s, ended at 172.99 s)

$$T = f(R_h) = T_0 + \frac{R_h - R_0}{\alpha R_0} \tag{1'}$$

Differentiation of Eq. (1′) gives an expression for temperature uncertainty, based on the Kline–McClintock analysis [39], as

$$u_T = \pm \frac{dT}{T} = \pm \frac{R_h}{R_h - R_0 + T_0 R_0 \alpha} \frac{dR_h}{R_h} = \pm \frac{R_h}{R_h - R_0 + T_0 R_0 \alpha} u_R \tag{12}$$

where R_0=8 Ω, T_0=293 K, and α=0.003715 K^{-1} for gold. The overall uncertainty of the gold resistance, u_R, consists of two parts: the heater resistance uncertainty based on the linearized temperature–resistance correlation, and the uncertainty occurring from the connecting wire resistance. Thus, for a conservative estimation, the maximum values for the two uncertainties are used as 0.08% (see Table 1) and 0.096% (see Sec. 2), respectively, and the overall resistance uncertainty takes the square root of summation of the two uncertainties squared to be u_R=±0.125%. Therefore, the resulting temperature measurement uncertainty u_T is estimated to be ±0.12% from Eq. (12), and the corresponding temperature uncertainties are ranged from ±0.53°C to ±0.60°C for the temperature range tested.

In addition, the accumulated uncertainties occur with the progressive deconvolution calculations associated with the concentric zones. Because the deconvolution calculation equation, Eq. (11), is a linear combination of line-averaged temperature measurements, the accumulated uncertainties are estimated to be a root mean square of the elementary temperature uncertainty of ±0.2°C for individual heater elements, as discussed in Sec. 3. Thus, the uncertainty associated with the progressive tomographic deconvolution ranges from ±0.2°C, for the outmost concentric zone for k=16, to ±0.8°C for the center zone for k=1. By accounting for the aforementioned uncertainty associated with the heater resistance in a similar rms estimation, the overall measurement uncertainties are estimated up to ±1.00°C, including both system bias and the accumulated uncertainties resulting from tomography deconvolution.

6 Conclusions

An array of 32 line heater elements 100 µm wide and 15 mm long was designed and fabricated to study slowly evaporating sessile water droplets under a constant voltage mode heating. Each of the golden heater elements was also used as a temperature sensor with 100 µm spatial resolution. Both spatially and temporally resolved measurements have been conducted to determine the temperature distributions for droplet contacting surfaces with heater elements.

One important implementation for the data analysis was a tomographic deconvolution of the raw data obtained from the linear array heaters using the Abel conversion scheme. This allowed for determination of the radial temperature profiles for the circular droplet contact surfaces.

Upon contact of the droplet with the heater surface, the heater temperature suddenly dropped to the lowest level, then plateaued back to a less pronounced level, where it remained nearly unchanged during the latent heat prevailing evaporation at a constant temperature. The magnitude of initial "negative surge" in temperature increases with increasing droplet volume.

As evaporation is completed, the temperature is recovered to the dry heater values. An interesting point to note is that, at the highest heater temperature (80°C, in particular), the secondary "negative surge" in temperature is observed at the last moment of evaporation. This is believed due to the rapid shrinking at the last stage of the thin droplet, which is primarily driven by the thermocapillary action occurring between the droplet edge and center. The first and second drops in the heater temperature are most pronounced at the droplet center and diminish with increasing radial distance.

Acknowledgment

The authors acknowledge Mr. Cheongsoo Seo of Texas A&M University for his valuable technical advice and helpful discussions, particularly in the beginning stage of the fabrication process, and also Dr. Sangwon Park of University of Texas at Dallas for his help in the seed layer coating process. The authors are grateful to the financial support sponsored by the NASA-Fluid Physics Research Program Grant No. NAG 3-2712 initially to Texas A&M University and transferred to the University of Tennessee. The presented technical contents are not necessarily the representative views of NASA.

Nomenclature

A = heater tomographic sectional area
d_a = acrylic sheet thickness
d_s = soda lime substrate thickness
d = heater thickness, μm
h = droplet height, mm
I = current
k = thermal conductivity
L = heater length, μm
P = power
q = heat flux
r_{wet} = droplet radius on the heater surface, mm
r = radial distance from the center of droplet, mm
r_0 = droplet wet radius at $t=0$
R = resistance, Ω
R_0 = heater resistance at 20°C
t = time, s
T_0 = heater temperature of 20°C
T_r = room temperature (25°C)
T = temperature, °C
$\bar{T}$ = line averaged heater temperature, °C
u = uncertainty
V = voltage
V_d = droplet volume, mm^3
v_{drop} = droplet impact velocity on substrate
w = heater width, μm

Greek Symbols

α = temperature-resistance coefficient
ρ_o = resistivity of gold at temperature 20°C
τ = dryout time, s
τ_0 = dryout time of 3 μL water droplet at 80°C heater temperature as a reference, s
θ = droplet contact angle

Subscripts

d = droplet
div = voltage divider
h = dry heater
H = heater
k = order of heater ($k=1,2,\ldots,32$)
n = order of tomographically deconvolved area ($n=1,2,\ldots,16$)
R = resistance
T = temperature

References

[1] Milke, J. A., Tinker, S. C., and di Marzo, M., 1997, "Effect of Dissolved Gases on Spray Evaporative Cooling With Water," Fire Technol., **33**, pp. 99–114.
[2] Pamula, V. K., and Chakrabarty, K., 2003, "Cooling of Integrated Circuits Using Droplet-Based Microfluidics," *Proceedings of the ACM/IEEE Great Lakes Symposium on VLSI*, Washington, D.C., April 28–29, pp. 84–87.
[3] Bernardin, J. D., Mudawar, I., Walsh, C. B., and Franses, E. I., 1997, "Contact Angle Temperature Dependence for Water Droplets on Practical Aluminum Surfaces," Int. J. Heat Mass Transfer, **40**, pp. 1017–1033.
[4] Tseng, F., Kim, C., and Ho, C., 1998, "A Novel Microinjector With Virtual Chamber Neck," *Proceedings 11th IEEE Workshop on Micro Electro Mechanical Systems Workshop*, Heidelberg, Germany, January 25–29, pp. 57–62.
[5] Oron, A., Davis, S. H., and Bankoff, S. G., 1997, "Long-Scale Evolution of Thin Liquid Films," Rev. Mod. Phys., **69**, 931–980.
[6] Xiong, T. Y., and Yuen, M. Y., 1991, "Evaporation of a Liquid Droplet on a Hot Plate," Int. J. Heat Mass Transfer, **34**, pp. 1881–1894.
[7] Makino, K., and Michiyoshi, I., 1984, "The Behavior of a Water Droplet on Heated Surfaces," Int. J. Heat Mass Transfer, **27**, pp. 781–791.
[8] Crafton, E. F., and Black, W. Z., 2004, "Heat Transfer and Evaporation Rates of Small Liquid Droplets on Heated Horizontal Surfaces," Int. J. Heat Mass Transfer, **47**, pp. 1187–1200.
[9] Klassen, M., di Marzo, M., and Sirkis, J., 1990, "Infrared Thermography of Dropwise Evaporative Cooling," ASME HTD, **141**, pp. 117–121.
[10] di Marzo, M., Tartarini, P., Liao, Y., Evans, D., and Baum, H., 1993, "Evaporative Cooling Due to a Gently Deposited Droplet," Int. J. Heat Mass Transfer, **36**, pp. 4133–4139.
[11] Dawson, H. F., and di Marzo, M., 1993, "Multi-Droplet Evaporative Cooling: Experimental Results," AIChE Symp. Ser., 89, Atlanta, GA, pp. 122–131.
[12] di Marzo, M., and Evans, D. D., 1989, "Evaporation of a Water Droplet Deposited on a Hot High Thermal Conductivity Surface," J. Heat Transfer, **111**, pp. 210–213.
[13] Michiyoshi, I., and Makino, K., 1978, "Heat Transfer Characteristics of Evaporation of a Liquid Droplet on Heated Surfaces," Int. J. Heat Mass Transfer, **21**, pp. 605–613.
[14] Tartarini, P., Liao, Y., Kidder, C., and di Marzo, M., 1993, "Transient Cooling of a Hot Surface by Droplets Evaporation," NIST, Gaithersburg, MD, Final Report No. NIST-GCR-93-623.
[15] Chandra, S., di Marzo, M., Qiao, Y. M., and Tartarini, P., 1996, "Effect of Liquid-Solid Contact Angle on Droplet Evaporation," Fire Saf. J., **27**, pp. 141–158.
[16] Klassen, M., and di Marzo, M., 1990, "Transient Cooling of a Hot Surface by Droplets Evaporation," NIST, Gaithersburg, MD, Report No. NIST-GCR-90-575.
[17] Rule, T. D., and Kim, J., 1999, "Heat Transfer Behavior on Small Horizontal Heaters During Pool Boiling of FC-72," J. Heat Transfer, **121**, pp. 386–393.
[18] Lee, J., Kim, J., and Kiger, K. T., 2001, "Time and Space Resolved Heat Transfer Characteristics of Single Droplet Cooling Using Microscale Heater Arrays," Int. J. Heat Fluid Flow, **22**(2), pp. 188–200.
[19] Hu, H., and Larson, R. G., 2002, "Evaporation of a Sessile Droplet on a Substrate," J. Phys. Chem. B, **106**, pp. 1334–1344.
[20] Ajaev, V., 2005, "Spreading of Thin Volatile Liquid Droplets on Uniformly Heated Surfaces," J. Fluid Mech., **528**, pp. 279–296.
[21] David R. Lide, Editor-in-Chief, 2004, *CRC Handbook of Chemistry and Physics*, 84th ed., Chemical Rubber Co., Cleveland, OH.
[22] R. A. Matula, 1979, "Electrical Resistivity of Copper, Gold, Palladium and Silver," J. Phys. Chem. Ref. Data, **8**, pp. 1147–1298.
[23] Paik, S. W., 2005, "Spatially Resolved Temperature and Heat Flux Measurements for Slow Evaporating Droplets Heated by a Microfabricated Heater Array," Ph.D. dissertation, Texas A&M University, College Station, TX.
[24] Picknett, R. G., and Bexon, R., 1977, "The Evaporation of Sessile or Pendant Drops in Still Air," J. Colloid Interface Sci., **61**, pp. 336–350.
[25] Meric, R. A., and Erbil, H. Y., 1998, "Evaporation of Sessile Drops on Solid Surfaces: Pseudospherical Cap Geometry," Langmuir, **14**, pp. 1915–1920.
[26] Padday, J. F., 1971, "The Profiles of Axially Symmetric Menisci," Philos. Trans. R. Soc. London, Ser. A, **269**, pp. 265–293.
[27] Erbil, H. Y., and Meric, R. A., 1997, "Evaporation of Sessile Drops on Polymer Surfaces: Ellipsoidal Cap Geometry," J. Phys. Chem. B, **101**, pp. 6867–6873.
[28] Bourges-Monnier, C., and Shanahan, M. E. R., 1995, "Influence of Evaporation on Contact Angle," Langmuir, **11**, pp. 2820–2829.
[29] Shanahan, M. E. R., and Bourges, C., 1994, "Effects of Evaporation on Contact Angles on Polymer Surfaces," Int. J. Adhes. Adhes., **14**, pp. 201–205.
[30] Zhang, N., and Chao, D. F., 1999, "A New Approach to Measure Contact Angle and Evaporation Rate With Flow Visualization in a Sessile Drop," Paper No. NASA/TM-1999–209636.
[31] Nordström, M., Marie, R., Calleja, M., and Boisen, A., 2004, "Rendering SU-8 Hydrophilic to Facilitate Use in Micro Channel Fabrication," J. Micromech. Microeng., **14**, pp. 1614–1617.
[32] Birdi, K. S., Vu, D. T., and Winter, A. J., 1989, "A Study of the Evaporation Rates of Small Water Drops Placed on a Solid Surface," J. Phys. Chem., **93**, pp. 3702–3703.
[33] Birdi, K. S., and Vu, D. T., 1993, "Wettability and the Evaporation Rates of Fluids From Solid Surfaces," J. Adhes. Sci. Technol., **7**, pp. 485–493.
[34] Gelorme, J. D., Cox, R. J., and Gutierrez, S. A. R., 1989, "Photoresist Composition and Printed Circuit Boards and Packages Made Therewith," U.S. Patent No. 4,882,245.
[35] Buckingham, E., 1914, "On Physically Similar Systems: Illustration of the Use of Dimensional Equations," Phys. Rev., **4**, 345–376.
[36] Deans, A. R., 1983, *The Radon Transformation and Some of Its Applications*, Wiley, New York.
[37] Kak, A. C., and Slaney, M., 1987, *Principles of Computerized Tomographic Imaging*, IEEE, New York, pp. 275–296.
[38] Kihm, K. D., Okamoto, K., and Ko, H. S., 2004, "Robust Algorithms for Tomographic Reconstruction of Line-of-Sight Thermal Flow Field Images," Adv. Heat Transfer, **38**, pp. 143–202.
[39] Kline, S., and McClintock, F. A., 1953, "Describing Uncertainties in Single-Sample Experiments," Mech. Eng. (Am. Soc. Mech. Eng.), **75**(1), pp. 3–9.

A Flow Boiling Heat Transfer Investigation of FC-72 in a Microtube Using Liquid Crystal Thermography

R. Muwanga

I. Hassan
e-mail: ibrahimH@alcor.concordia.ca

Department of Mechanical and Industrial Engineering,
Concordia University,
Montreal, Quebec H3G 1M8, Canada

This paper presents experimental measurements of boiling heat transfer in a 1.067 mm inner diameter tube, using liquid crystal thermography for wall temperature measurement. The study was motivated by the two-phase microchannel pumped cooling loop, a recent technology proposed for thermal management of tomorrow's high-end electronics. The working fluid was FC-72, which is a dielectric coolant and measurements were obtained in a closed loop test facility. A unique flow boiling onset was observed whereby a large wall temperature gradient travels along the tube. During flow boiling conditions, wall temperature fluctuations have been observed. The use of a thermographic technique has added insight into the flow boiling characteristics and acts as a partial flow visualization method. Local heat transfer coefficients are presented and compared with correlations for both macro- and microchannels. The heat transfer coefficient is found to be influenced by the heat flux at a lower mass flux but only mildly at a higher mass flux. [DOI: 10.1115/1.2728905]

Keywords: boiling, heat transfer, microchannel, thermochromic liquid crystal, microtube, dielectric fluid

1 Introduction

Flow boiling heat transfer in mini- and microchannels has in recent years become a subject of interest, chiefly due to the thermal requirements of emerging high-end electronics. Technologies such as the pumped loop microchannel heat sink, which consists of an array of parallel microchannels, are being developed for thermal management of these emerging electronics. The choice of microchannel is inherent due to the size of the components requiring cooling. Two-phase heat exchangers are desirable due to their effectiveness in providing larger heat transfer rates and improved streamwise uniformity in comparison with their single-phase counterparts [1].

Recent reviews on boiling heat transfer in mini- and microchannels have been presented by Thome [2] and Kandlikar [3]. Kandlikar [3] suggested a channel size criterion whereby 3 mm and greater are conventional (macro) channels, 0.2–3 mm are minichannels, and 0.01–0.2 mm are microchannels. With the exception of the confinement number (N_{conf}), however, no physics based classification of channel sizes has been presented [2]. The confinement number was introduced by Kew and Cornwell [4] and was suggested as a parameter to differentiate between microscale and macroscale boiling phenomena. It is given by

$$N_{\text{conf}} = \frac{[\sigma/(g(\rho_f - \rho_v))]^{1/2}}{D} \tag{1}$$

It was found that for a confinement number greater than 0.5, the macroscale correlations did not predict microchannel results well [4].

It has been generally accepted that both nucleate boiling and convective boiling mechanisms exist in mini- and microchannels, although the dominant mechanism remains inconclusive. Some investigators have shown that there is a decreasing trend in the heat transfer coefficient with mass flux, and so have concluded that forced convection is the dominant mechanism [5,6]. While for macrosize channels, the dominant mechanism is convective boiling, the majority of the mini- and microchannel studies suggest that nucleate boiling is the dominant mechanism, which has been determined by observing the stronger dependence of the heat transfer coefficient with heat flux, and not with mass flux [2].

There have been a number of recent investigations of flow boiling heat transfer in microtubes. Lin et al. [7] investigated the two-phase heat transfer characteristics of R141B in circular tubes of diameter 1.1 mm, 1.8 mm, 2.8 mm, and 3.6 mm. They deduced that there were three boiling regions: a nucleate boiling region whereby the heat transfer coefficient was dominated by the heat flux; a convective boiling region whereby the heat transfer coefficient was independent of heat flux but increased with quality; and a partial dryout region. In the partial dryout region, the heat transfer coefficient was reduced dramatically, and dryout was observed to occur earlier with increasing confinement number as well. Additionally, the heat transfer coefficient was found to have a more marked decrease with quality with decreasing tube diameter. The mean heat transfer coefficient was also independent of mass flux and diameter and dependent only on heat flux in the region before dryout. Recently, Saitoh et al. [8] investigated flow boiling of R-134a in circular tubes of 0.51 mm, 1.12 mm, and 3.1 mm diameter. The two-phase heat transfer coefficient was observed to be governed by convective and nucleation effects, though the convective effects decreased with decreasing diameter. Dryout was observed to occur at a lower quality with decreasing diameter. Through tracking the wall temperature, flow oscillations were observed in the 3.1 mm and 1.12 mm tubes at low quality entry, but not in the 0.51 mm tube. The authors concluded that these were density wave type oscillations due to their period. Grohmann [9] studied the two-phase and single-phase heat transfer characteristics of argon in circular tubes, with nominal diameters of 0.50 mm and 0.25 mm. In the nucleate boiling regime, there was no influence of mass flux or quality on the heat transfer

Contributed by the Heat Transfer Division of ASME for publication in the JOURNAL OF HEAT TRANSFER. Manuscript received November 1, 2005; final manuscript received December 6, 2006. Review conducted by Bengt Sunden.

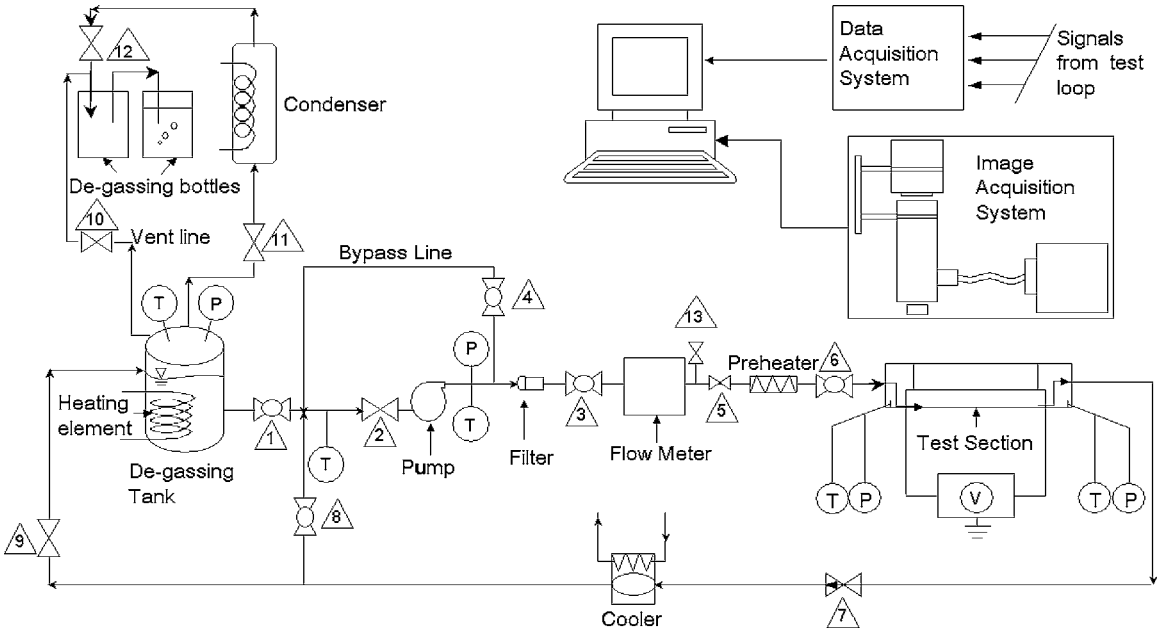

Fig. 1 Test facility

coefficient. Flow condition oscillations were sometimes observed with subcooled entry conditions, however these could be controlled with the entry quality greater than zero.

1.1 Local Wall Temperature Measurement. To determine the wall temperature in flow boiling heat transfer experiments, the majority of researchers use thermocouples mounted on the outer surface of the channel. In addition for local heat transfer data an array of thermocouples are usually mounted on the surface [10,11]. The use of thermocouples, however, limits the spatial data that may be obtained. Thermographic techniques including infrared (IR) thermography and thermochromic liquid crystal (TLC) thermography may be used.

Hapke et al. [12] used infrared thermography for outer wall surface temperature measurements during flow boiling in a 1.5 mm inner diameter circular channel. The study focused on the onset of nucleate boiling and the use of a thermographic technique was key for this objective. Hetsroni et al. [13] similarly utilized IR thermography for investigation of the wall temperature distribution before and after saturation conditions in a 1.0 mm inner diameter tube. As expected, a peak in the wall temperature was observed just before saturation, and due to the use of a thermographic technique, the location and magnitude of the peak could be tracked with varying heat flux. Chin [14] and Lakshminarasimhan et al. [15] used liquid crystal thermography in flow boiling experiments of narrow channels of 2 mm $\times$ 20 mm and 1 mm $\times$ 20 mm, respectively. The authors observed different spanwise wall temperature distributions for laminar versus turbulent flows at onset of boiling, where for laminar flow there was a sharp transition to boiling in comparison to turbulent flow. This observation was enabled due to the use of a thermographic technique. Piasecka et al. [16] also used liquid crystal thermography to investigate the onset of flow boiling in narrow channels (1 mm $\times$ 40 mm). The authors were able to deduce the local heat transfer coefficient around the location of onset through the use of a thermographic technique. Aligoordaz et al. [17] used the liquid crystals in their unencapsulated form to study flow boiling fluctuations in narrow channels of 1 mm $\times$ 2 mm and 2 mm $\times$ 2 mm. Their selection of the unencapsulated form of TLC was primarily due to its increased temporal resolution. The authors faced a number of difficulties in handling the liquid crystals in their unencapsulated form; however, apart from the present work, they are the only other researchers to have used this form for flow boiling experiments.

1.2 Flow Boiling of Dielectric Fluids in Mini- and Microchannels. The fluid type is an important parameter in the heat transfer performance. Although many studies on flow boiling heat transfer in mini- and microchannel have used water or refrigerants, few studies have utilized dielectric fluids. These fluids will typically have lower heat transfer performance than water, however, are advantageous in situations whereby the fluid may be in contact with an electrically charged component. Warrier et al. [18] investigated two-phase heat transfer in an array of five 0.75 mm hydraulic diameter rectangular channels using FC-84 as the working fluid. They compared their heat transfer results with correlations valid for channels ranging in size from 2.4 mm to 32 mm and found none to be in good agreement. The heat transfer coefficient was observed to have a decreasing trend with quality. They developed a correlation relating the saturated flow boiling heat transfer coefficient with quality and boiling number. Yen et al. [10] studied boiling heat transfer in microtubes of 0.19 mm, 0.3 mm, and 0.51 mm inner diameter, using FC-72 and HCFC123. The study was carried out at low mass flux ranging from 145 kg/(m^2 s) to 295 kg/(m^2 s). Local heat transfer coefficient results were only presented for HCFC123. The results showed a decreasing heat transfer coefficient with quality, but independent of mass flux, suggesting nucleate boiling as the dominant mechanism. Recently, Chen and Garimella [19] investigated the effects of dissolved air on the subcooled flow boiling characteristics of FC-77 in an array of ten parallel channels, 0.50 mm wide and 2.5 mm deep. The study showed boiling incipience to occur at lower wall temperatures for the undegassed fluid compared to the degassed fluid. Flow instability fluctuations were larger for the undegassed fluid as well as larger pressure drops were measured. Although the earlier boiling inception caused higher initial heat transfer coefficients for the undegassed fluid, the authors recommended working with a degassed fluid for better predictability and control.

1.3 Flow Boiling Incipience. Important to the safe and reliable design of two-phase heat exchangers with subcooled entry is

the prediction of the wall superheat required to initiate boiling, or inversely, for a given subcooling prediction of the incipient heat flux. Classical approaches for boiling incipience consider a bubble to grow if the minimum temperature surrounding the bubble is equal to or greater than the saturation temperature given by the pressure inside the bubble [20]. The superheat in this case is related explicitly to the heat flux and the pressure. This method tends to underpredict the incipient superheat particularly for well wetting fluids such as refrigerants and perfluorocarbons as it does not consider the fluid–solid contact angle, and it assumes all nucleation sites to be active. Recently, Basu et al. [21] demonstrated a correlation based on adaptations of boiling incipience classical methods, which includes effects of the static contact angle of the fluid–solid system. The correlation showed good agreement with a variety of fluid–solid systems. Qu and Mudawar [22] investigated the incipient heat flux required for boiling in an array of rectangular microchannels. It was shown that this heat flux is dependent on the mass velocity. Additionally, boiling incipience was observed to be different from large channels, in that bubble departure occurred, rather than growth and collapse at incipience. A mechanistic model based on the bubble departure criterion was developed to predict the boiling incipience from the flat surface or a corner and showed good agreement with the experimental results. Regarding single tubes, Kennedy et al. [23] studied boiling incipience in 1.448 mm and 1.168 mm circular copper tubes with water as the working fluid. Their results for the larger tube were in good agreement with macrotube correlations, whereas the smaller tube was underpredicted. An estimation by the present authors of the confinement number for their case, taken at 50°C (from experimental conditions), is calculated to be 0.46 for the larger tube and 0.57 for the smaller tube. Hapke et al. [12] investigated boiling incipience in a 1.5 mm nickel alloy tube with water as the working fluid and mass flux ranges from 100 kg/(m^2 s) to 500 kg/(m^2 s). Their results showed wall superheat dependency at incipience on mass flux. Ghiaasiaan and Chedester [24] developed a model for predicting boiling incipience in microchannels based on the assumption that the thermocapillary force suppressing the bubble plays a crucial role. Their model showed the incipience heat flux to be dependent on channel diameter (results for 0.75–1.45 mm diameter); however, this was not experimentally verified and the results were for turbulent flows. Yen et al. [10] experimentally investigated boiling heat transfer in tubes 0.19–0.51 mm with FC-72 and HCFC123 at low mass fluxes of 50–300 kg/(m^2 s). The wall superheat at incipience was observed to be dependent on both boiling number and mass flux, whereas the maximum wall superheat was dependent on the tube diameter and nucleation site distribution.

1.4 Summary and Present Work.

1 Although recently there has been an increase in the number of studies on flow boiling heat transfer in small diameter channels (<2 mm), due to the complexity of the process, the number of parameters involved and the lack of correspondence to existing larger channel correlations, more data are still required considering a variety of conditions and fluids;
2 From an applied perspective, the characteristics of boiling incipience, including input parameters of influence, the characteristics of the wall superheat, and heat transfer coefficients need to be investigated; and
3 Thermographic techniques, though having limited use, are an effective approach when investigating flow boiling incipience as they can track surface temperatures at varying locations of interest and possibly highlight phenomena not available through discrete methods.

The objective in the present work is to experimentally investigate boiling incipience and heat transfer with a dielectric fluid, in a circular microtube using unencapsulated liquid crystals for wall temperature measurements. The working fluid was FC-72, and a tube inner diameter of 1.067 mm was investigated.

Table 1 FC-72 properties at 25°C and 1 atm

Property	Value
ρ	1680 kg/m^3
μ	0.00064 N s/m^2
σ	0.01 N/m
C_p	1100 J/kg °C
Pr	12.35
T_{sat}	56°C

2 Experimental Facility

A schematic of the main components used in the closed loop test facility is shown in Fig. 1. The working fluid was FC-72 a perfluorocarbon manufactured by 3M, and some relevant properties of FC-72 at room temperature are listed in Table 1. Flow enters the loop from the main tank and is continuously circulated by a magnetically coupled gear pump. The pump is equipped with a variable speed drive allowing for a flow range up to 300 mL/min, with a maximum pressure of 517 kPa (75 psi). A nutating digital output flowmeter provided by DEA Engineering was used to monitor the flow rate. This meter outputs a 5 V square wave signal at a frequency proportional to the time for the nutator to complete one cycle. The flowmeter was calibrated using the weighing method, and has a reliable range from 10 mL/min to 250 mL/min. Upstream of the flowmeter is a 15 μm filter which is used to remove any accumulating particles. In addition, a preheater is located at the inlet of the test section for additional flow temperature control. It consists of a 2.743 m (9 ft) length of 12.7 mm (0.5 in.) o.d. serpentined copper piping, with three 0.914 m (3 ft) rope heaters rated at 125 W, wrapped around the piping. Power to the preheater is controlled by a variac providing a stable inlet temperature setpoint. At the exit of the test section is a water-cooled heat exchanger, which is used to restore the temperature of the fluid.

The test section is a circular stainless-steel tube with a nominal inner diameter 1.067 mm (0.042 in.). Its hydraulic length is 152 mm, with a corresponding hydrodynamic developmental length of 23.5 mm, while the heated length is 105 mm. A schematic of the circular tube test module is shown in Fig. 2. A transparent polycarbonate sheet was machined to produce the measurement chambers for pressure and temperature and provided minor flow visualization. The tube is connected to these chambers using standard 0.0625 mm (1/16 in.) stainless-steel compression fittings with specialty ferrules to accommodate the small diameter tubing. The ferrule material is a composite of graphite and polymide, which has a high electrical resistance. The advantages of the compression fittings are that they are resealable and can withstand high pressures (~690 kPa rating). Copper stranded wire (14AWG) was soldered to the tube to provide the electrical lead connection. Close to the tube exit a 0.254-mm-diameter type T unsheathed thermocouple was embedded with an electrically isolating epoxy for auxiliary temperature measurement.

2.1 Instrumentation. Two 1.5-mm-diameter Type-T (Omega special error limits material) thermocouples were placed in each plenum chamber to measure the bulk fluid temperature. Two pressure transducers tracked the gauge pressure in the inlet and outlet plenums and they are Omega model PX01C1 (inlet) and PX02C1 (outlet) with ratings of 517 kPa (75 psig) and 345 kPa (50 psig), respectively. A Vaisala PTB220 barometer was used to obtain the absolute pressure of the surroundings. The output from these and other sensors was monitored through an automated data acquisition system using the LabVIEW software. The data acquisition hardware consisted of National Instrument's SCXI 1000 signal

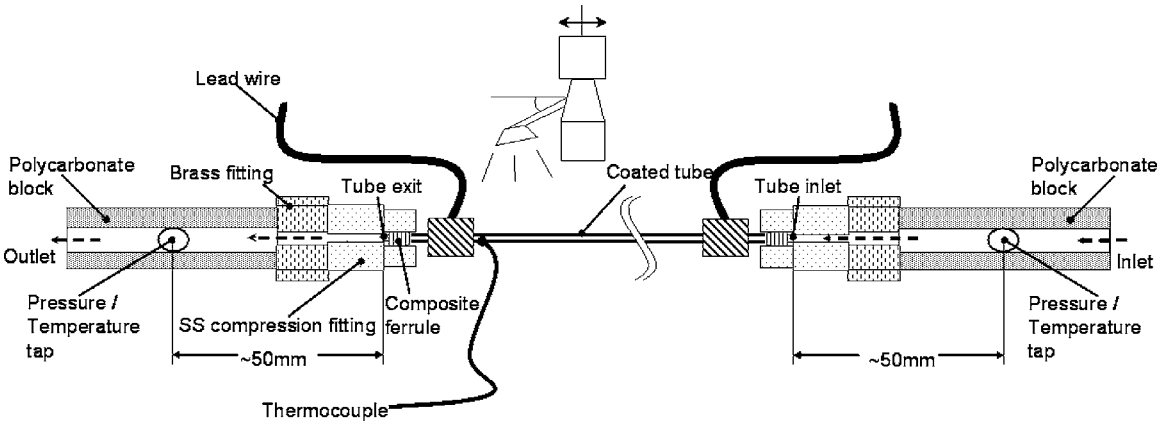

Fig. 2 Test section module

conditioning unit, with the appropriate modules as well as the NI 6052E 16-bit 333 kHz data acquisition card. A schematic of the data acquisition system is presented in Fig. 3.

Heater power was provided by two dc power supplies. One was a BK Precision switch mode power supply (Model 1692) with a voltage range of 2.7–15 V and a maximum current rating of 40 A. The second was a Good Will (GW) Instruments power supply (Model GPC-1850) with a voltage range of 0–5 V and a maximum current rating of 20 A.

2.2 Measurement With Thermochromic Liquid Crystals. The unencapsulated liquid crystal material used was provided by LCR-Hallcrest. Two TLC mixtures were utilized at separate occasions, with nominal red starts of 70°C and 75°C and both with a bandwidth of 20°C. To obtain quantitative thermal data from the TLC response, a calibration of the material is required, which involves quantitatively relating the observed color to the material temperature. Different methods are available for quantifying the color observed and in the current work, the hue angle is taken as the color descriptor. The hue to temperature conversion is similar to that outlined by Muwanga and Hassan [25]. In summary, localized calibration curves of third to fifth order are determined, relating the wall temperature to the hue angle based on a calibration. A calibration based on circulating the fluid through the channel was selected due to its ease of incorporation into the setup; however, due to the high wall temperature calibration required (up to 100°C), water instead of FC-72 was used as the calibrating fluid. The water was only circulated through the tubing test section portion of the test setup. The water was heated at a rate of approximately 2°C/min and inlet and outlet temperatures were maintained to within 0.4°C of each other. After calibration the water was purged from the test-tube test section by running an air stream for 1–2 h.

Image acquisition was achieved using a Sony 3-charge-coupled device (CCD) analog camera connected to a variable zoom microscopic video lens. The camera and lens were mounted onto a three-axis traverse through variable length stages each with approximately a 1 μm resolution. This allowed for the length of the channel to be monitored through traversing the entire length. The lateral and vertical axis stages allow for fine tuning of the position and focusing. A fiber optic line was fixed onto the zoom lens at a

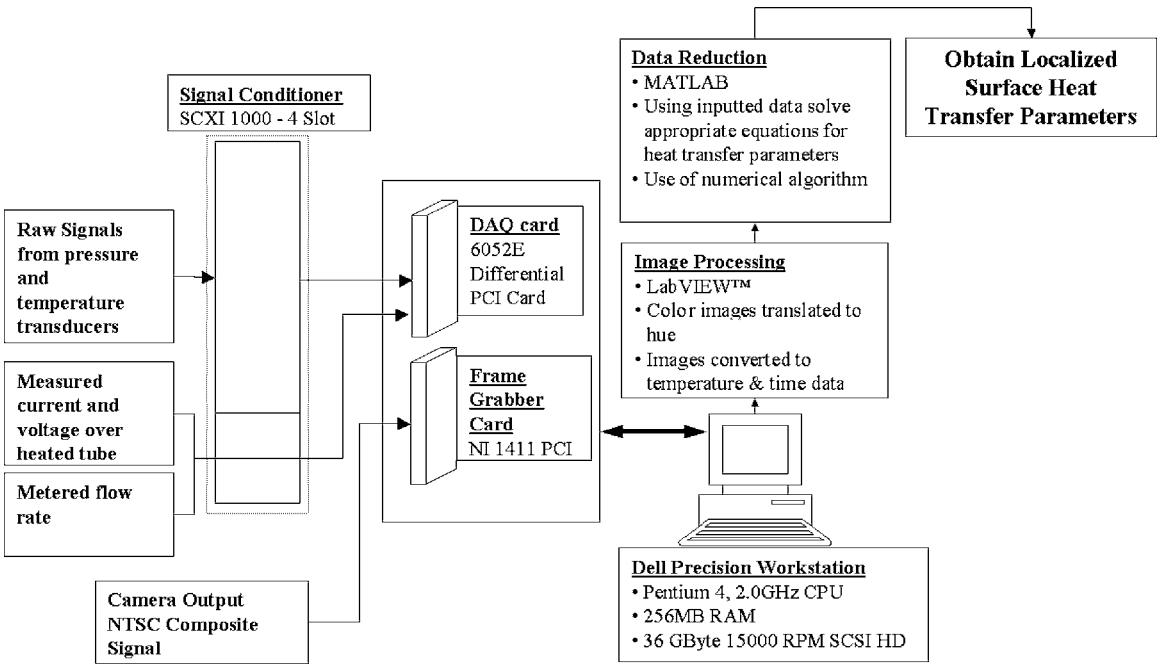

Fig. 3 Schematic of the data acquisition system

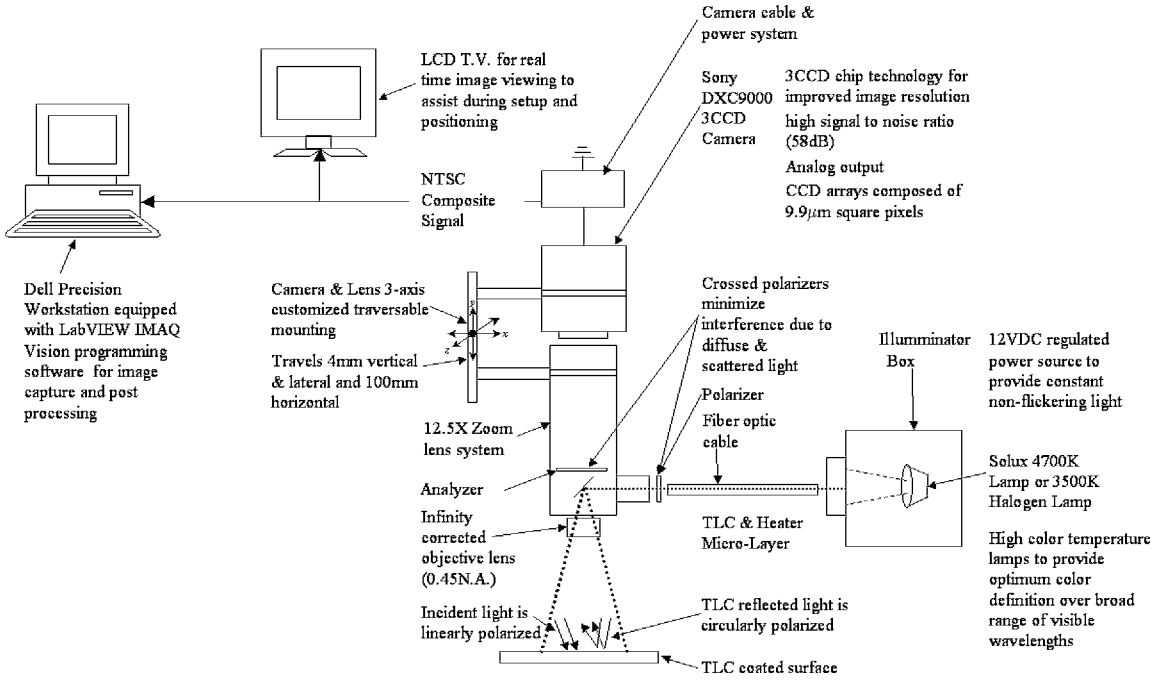

Fig. 4 Schematic of the image acquisition system

fixed angle and directly illuminated the surface. A schematic of this setup is shown in Fig. 4. The configured magnification provided a field of view of 10.233 mm × 7.671 mm, which translates into 15.528 μm/pixel. Images were captured at a speed of 30 frames/s. The best images by visual inspection were selected for final data reduction.

3 Procedure

Prior to measurement, the fluid is degassed to purge the system of noncondensables, particularly oxygen. The fluid is circulated through the system and the degassing tank at a flow rate of 150 mL/min. The degassing tank is heated until the fluid in the tank boils. With reference to Fig. 1, Valves 11 and 12 are open, allowing for the vapor to travel through the condenser and condense. The air escapes as bubbles through the second degassing bottle, which is filled with water. This acts as a visual technique to track the process and is similar to the degassing process of Ammerman [26]. The fluid is circulated for 1 h after the temperature in the degassing tank has exceeded 50°C. The preheater is turned on to maintain the fluid at this high temperature throughout the system. This duration, coupled with the flow rate, allows for the entire fluid in the system to pass through the degassing tank. After this time duration bubbling in the degassing bottles is practically nonexistent. At this point Valve 11 (Fig. 1) is closed and the system is shut off from the environment. The flow rate is lowered to the desired setpoint, and the tank heater is adjusted to maintain the tank temperature between 50°C and 56°C. The fluid in the tank therefore remains in a two-phase state throughout the experiment, and the system pressure may be adjusted by adjusting the tank's temperature. After degassing, the TLC material was calibrated as described in the previous section. To begin measurements, the flow rate is set by adjusting the motor speed and the preheater was adjusted to obtain the desired subcooling at test section entry.

4 Data Reduction

The local heat transfer coefficient (h_z) was obtained using

$$h_z = \frac{Q/A_h}{(T_{w,zy} - T_{b,z})} \tag{2}$$

The heat flux to the fluid was calculated based on the power applied to the tube and corrected for losses to the environment. The internal wall temperature was calculated considering a hollow cylinder and assuming steady, one-dimensional (1D) radial heat conduction through the wall with internal heat generation. The boundary conditions applied were at the outer radius, the temperature was equal to that measured by the TLC, and at the outer radius the conduction out of the wall was equal to the convective transport at the surface. The external heat transfer coefficient was obtained from tests with no fluid circulating and a constant power applied to the tube. The difference between inner and outer wall temperatures was minor and typically less than 0.3°C.

In order to determine the local heat transfer coefficient, the local bulk temperature is required. In the single phase region it is based on an energy balance from the inlet, whereas in the saturated flow boiling region, it is determined from the local saturation pressure. This method is similar to that adopted by many recent works [6,10,5,27]. The local quality is then calculated as

$$x(z) = \frac{Q/A_h \pi D(z - z_0)}{\dot{m} h_{fg}} \tag{3}$$

4.1 Uncertainty. The uncertainty in the TLC temperature was calculated using similar methods discussed in Muwanga and Hassan [25]. Typical uncertainties in TLC temperature measurement were estimated to be ±1.1°C and are similar to that of other researchers [14]. Uncertainties in pressure drop measurement were ±0.73 kPa, based on instrument specifications and ±0.71°C, for fluid temperature measurement based on manufacturer specifications of the combined measurement system. Typical uncertainty in the two-phase heat transfer coefficient was estimated to be ±9.9%.

5 Results and Discussion

5.1 Measurement Scope. Measurements were carried out at three flowrates, two low flowrates in the laminar regime, and a high flowrate in the turbulent regime. For the low flowrates, the mass flux was nominally 770 kg/(m^2 s) and 1040 kg/(m^2 s) with inlet subcooling ranging from 7°C to 18°C. For the high flow-

Table 2 Measurement conditions

Volumetric flow rate (mL/min)	Descriptor	Nominal mass flux (kg/(m^2 s))	T_{in} (°C)	ΔT_{sub} (°C)	P_{out} (bar)	N_{conf}
68 mL/min	$\Delta T_{sub,low}$	2050	59	5.2	1.25	0.66
	$\Delta T_{sub,med}$		56	9.9	1.33	0.55
	$\Delta T_{sub,high}$		46	18.4	1.26	0.70
			48	16.3	1.26	0.69
26 mL/min	$\Delta T_{sub,low}$	770	56	6.7	1.20	0.55
	$\Delta T_{sub,high}$		48	17.8	1.32	0.69
35 mL/min	$\Delta T_{sub,low}$	1040	55.5	7.8	1.21	0.64

rate, the mass flux was nominally 2050 kg/(m^2 s) and the inlet subcooling ranged from 5 °C to 18 °C. Details of the conditions investigated are listed in Table 2.

At the high mass flux, onset of nucleate boiling characteristics such as increased pressure drop and large wall temperature drop, were not observed for the heat flux range covered. Additionally, with increased heat flux the exit fluid temperature could sustain temperatures higher than the saturation temperature for small time periods before dropping to the saturation temperature. With a drop in the exit fluid temperature to its saturation temperature, vapor was observed in the tubing downstream of the test section. However, the wall temperature and pressure drop characteristics were virtually unchanged. Figures 5(*a*)–5(*d*) compare the wall temperature and pressure drop characteristics at different levels of inlet subcooling for both the high and low mass fluxes. These figures show the differences in initiating boiling at a mass flux of 770 kg/(m^2 s) and 2050 kg/(m^2 s). It is important to note that the temperature for these plots is measured by the thermocouple bonded to the tube wall close to the exit. This temperature is not representative of the actual wall temperature, due to the thermal resistance of the electrically resistive epoxy used. However, it is presented since it effectively highlights the wall temperature trend. The TLCs are not presented at this point since the wall temperature was not always within their active range. In Fig. 5(*a*), for the low mass flux, the wall temperature increases in the single-phase regime until about 30 kW/m^2 when boiling is initiated. At this point, there is a large wall temperature drop. With increased heat flux the wall temperature rises slightly with increased heat flux. At a high heat flux of about 42 kW/m^2 for the high subcooling case and 80 kW/m^2 for the low subcooling case, further increase in heat flux causes a drastic wall temperature rise. The wall temperature through a large part of the boiling region fluctuates and is likely the reason for some of the scatter in the data at lower heat flux. Although the cause of the large temperature rise appears to be due to a critical heat flux condition, it needs to be investigated further as the trend is counter to the trends observed in many other works. That is, if it is a critical heat flux condition, the lower critical heat flux should be observed in the lower subcooled case [28]. Figure 5(*b*) shows the pressure drop characteristics at the low mass flux case. The pressure drop slightly decreases with increasing heat flux in the single phase regime, as would be expected. At onset of boiling, the pressure drop increases, though this increase is more significant for the low inlet subcooling case.

Figure 5(*c*) shows the wall temperature characteristics for the

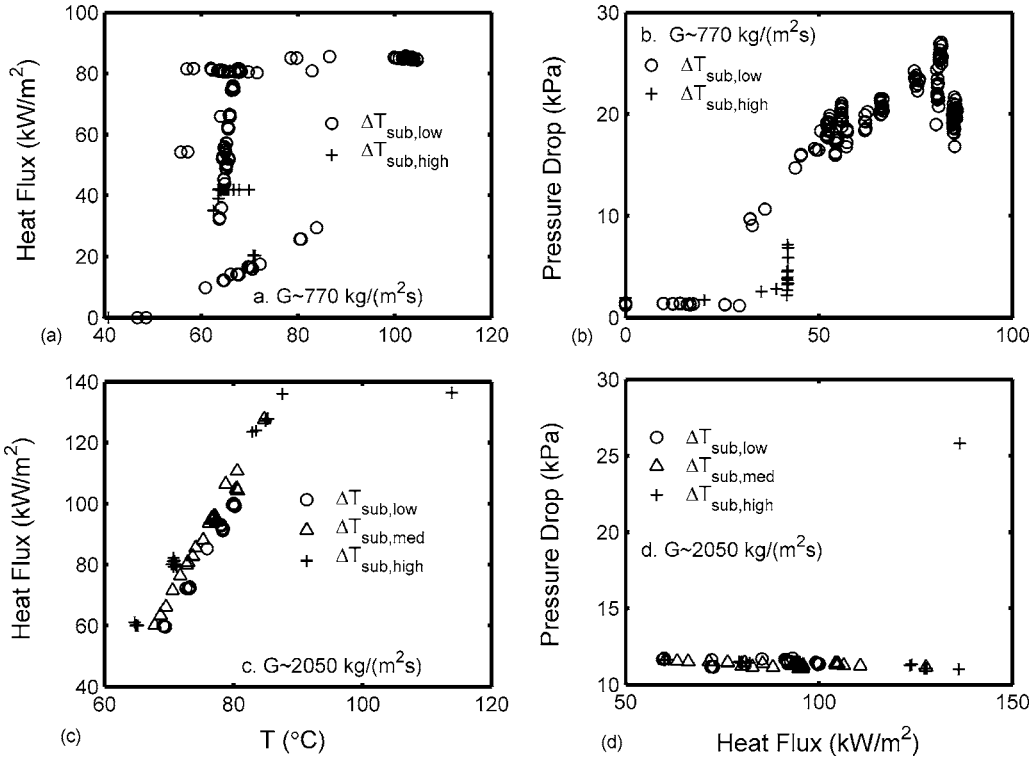

Fig. 5 (*a*), (*c*) Heat flux versus wall temperature, measured by embedded thermocouple; and (*b*), (*d*) pressure drop versus heat flux

high mass flux case. Unlike the low mass flux case, increased heat flux continually increases the wall temperature at an almost constant rate. For the case of high inlet subcooling, a threshold heat flux was observed, at which point further increase in heat flux caused a wall temperature jump. As the setup was not configured for critical heat flux experiments, power to the system was immediately shut down to prevent damage to the tube. Figure 5(*d*) shows the wall pressure drop characteristics for the high mass flux case. Similar to what is observed for single phase flows, the pressure drop slightly decreases with increasing heat flux for the range covered. For the high inlet subcooling case at a threshold heat flux of about 138 kW/m^2, a significant rise in pressure drop is observed, signifying two-phase or superheated flow.

For the wall thermocouple temperature measurements presented above, a wall temperature of 87°C signifies a tube outer wall temperature greater than 100°C. This high temperature caused vaporization of the TLC coating and long periods at this temperature would completely eliminate the TLC coating. This highlights one of the two drawbacks in utilizing unencapsulated TLCs for boiling measurements. That is, when using the material in conditions that require high wall superheats to initiate boiling, there is a potential that the wall temperature can be too high for the TLC material and thus erode or completely eliminate the coating. The second drawback is related to effectively utilizing the TLC active range. The measurements were restricted to a system pressure that would provide wall temperature conditions in the active TLC range during boiling. This range was determined through a number of trials and is not an effective approach for a full parametric study.

From the above, boiling was only initiated at the low mass flux conditions. Detailed experimental measurement and analysis were therefore carried out at these conditions and more specifically at the low inlet subcooling condition. The remainder of this section provides results from these test conditions of low mass flux and low inlet subcooling.

5.2 Boiling Onset at Low Mass Flux. Flow boiling was initiated by incrementing the applied heat flux, while in single phase, the wall temperature constantly rose and this was observed with the TLC color changing from red to blue at a given location. With further increase of heat flux downstream locations of the tube past the clearing point of the TLC and wall temperature monitoring was restricted to the thermocouple embedded close to the tube end. The demarcation to the clearing point was a long smooth color change implying a low temperature gradient. With further increase, the TLC clearing point moved further upstream signifying an increased wall temperature. No bubbles or vapor were observed in the tubing downstream of the test section or in the outlet instrumentation chamber. At a threshold heat flux, a fast moving front with a large temperature gradient was observed to travel toward the exit of the tube. Additionally, just prior, the TLC coating was observed to partially vaporize, suggesting an instantaneous wall temperature rise. A sample of this fast moving front is shown in Fig. 6. The red region is the cooler temperature region, whereas the black is the higher temperature region since it is past the TLC clearing point. The velocity of the front was estimated to be approximately 1.4 to 1.7 m/s, which is higher than all the liquid fluid velocity of 0.58 m/s and much lower than all the vapor velocity of 47.95 m/s. Immediately following the front, the wall temperature is significantly lower than under single-phase conditions, and remains relatively constant over the two-phase length. The location of this front initiation was not identified exactly on the tube, but was approximately 1/5 to 1/4 downstream of the inlet. The large temperature spike at onset suggests a transition from all liquid to significant vapor flow. The moving wall temperature gradient further suggests that this condition is unstable, causing an immediate purging of the high vapor region by a two-phase region with better heat transfer characteristics. This onset phenomenon was found to be repeatable over the same experimental run by turning on and off the power to the tube, and was also observed on different experimental days. Its occurrence is a likely function of the tube's inner surface, the tube diameter, and the working fluid characteristics. Further studies are recommended to clearly identify this phenomenon.

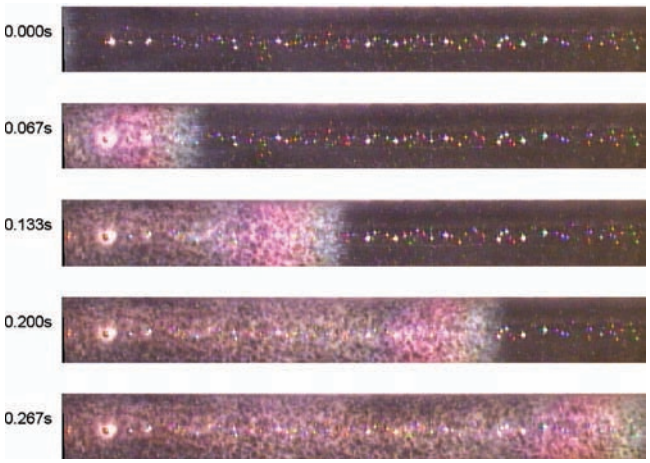

Fig. 6 (Color) TLC wall temperature visualization over time during boiling onset, 79–88 z/D, $Q/A_h \sim 30.4$ kW/m^2, $G \sim 770$ kg/(m^2 s). Red is lower temperature region, and flow is from left to right

5.3 Wall Temperature Visualization and Measurement During Flow Boiling. With boiling initiated at a low heat flux, the wall temperature remained stable. The TLC color was at the red start of the bandwidth and hence it was difficult to obtain measurements at this condition. With an increase in heat flux the wall temperature slightly increased and the TLC color response was clearly in the red range. With further increase in heat flux wall temperature oscillations were observed. Far downstream the oscillations were in the red range signifying a low wall temperature and far upstream they were in the yellow to green range signifying a higher wall temperature. With further increase in heat flux, a large increasing wall temperature gradient was observed downstream, past the clearing point of the TLC in the form of a front. This front would periodically oscillate and its color would fluctuate.

Figure 7 presents sample data of these oscillations taken at a

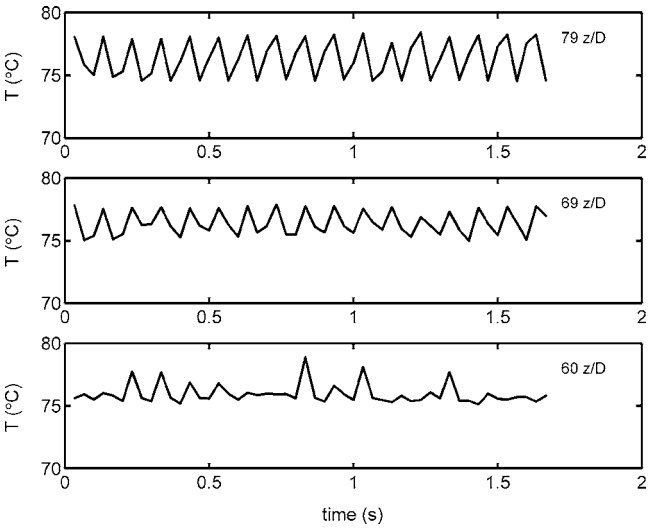

Fig. 7 TLC wall temperature time trace—three separate locations imaged at separate time instants, $Q/A_h \sim 50.7$ kW/m^2, $G \sim 770$ kg/(m^2 s)

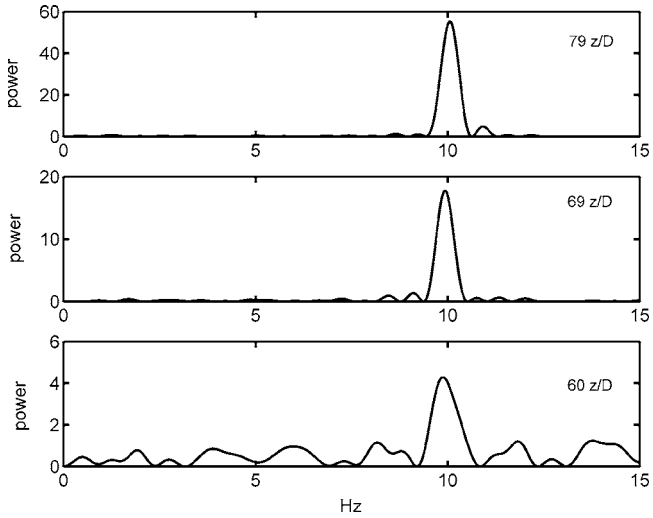

Fig. 8 Typical power spectrum of oscillating wall temperature as measured by TLC, for corresponding wave forms in Fig. 7, $Q/A_h \sim 50.7$ kW/m^2, $G \sim 770$ kg/(m^2 s)

low heat flux and at a far downstream location of 60–79 z/D. The time traces are produced from considering the median value of a region of 20 pixels in the streamwise direction and 72 pixels in the circumferential direction. Prior to this the images are filtered to exclude pixels that appear white or black based on consideration of their intensity, hue, and saturation. The wall temperature fluctuations in Fig. 7 are observed to be semi-periodic with amplitudes ranging from 1 °C to 5 °C. Based on this figure and other data, it was not clear if variable distance influenced the amplitude at a given heat flux. Figure 8 shows a frequency spectrum of the signal typical of a variety of far downstream locations along the tube. The fundamental frequency is approximately 10 Hz. With the temporal resolution available, a constant frequency was observed across the length of the tube for a fixed heat flux.

With increased heat flux, there is a threshold at which a significant rise in wall temperature and a large fluctuating wall temperature gradient front is observed at far downstream locations. Figure 9 shows a sample of this front over a time period of 0.3 s. From 0 s to 0.167 s wall temperature fluctuations are observed within the range of the TLC. The wall temperature gradient at this point is mild. From 0.2 s to 0.3 s a rapid rise in temperature is observed as the clearing point of the TLC is exceeded. This signifies a large temperature gradient. These conditions are observed at the point where the wall temperature begins to increase after the constant wall temperature region in Fig. 5. With a further increase in heat flux the large temperature gradient front continues to move further upstream. This large temperature gradient front suggests conditions of partial dryout inside the tube in the vicinity of the front.

An important point to note during these oscillations is that there were no oscillations in mass flux, and the fluid bulk temperature at inlet and outlet remained relatively constant. The pressure, however, fluctuated at relatively small amplitude. The low-pressure drop fluctuations, as well the lack of mass flow fluctuations, suggest that these are neither pressure drop nor density instabilities. Ding et al. [29] presented the various dynamic instabilities that may be present in a horizontal tube. Their discussion on thermal oscillations suggests that high wall temperature fluctuations will be present. Additionally, the characteristics of the thermal oscillations are initiated at the transition from a thin liquid film to an all vapor region that may oscillate due to frequent impulses of purged vapor slugs from upstream. Although at upstream locations the wall temperature oscillations are on the order of 10 °C at maximum, at the oscillating front the wall temperature gradient is likely greater than 20 °C, which is high and therefore more representative of thermal oscillations. This suggests that the mechanism responsible for the oscillations is similar to that for thermal oscillations, whereby there exists a thin film of liquid that oscillates due to bubbles being purged at the interface. This is corroborated by the fact that just upstream of the interface the wall temperature fluctuates, suggesting a passing vapor slug. These observations, however, need further verification by means such as flow visualization. Nevertheless, the advantage of a thermographic technique has been highlighted in the present measurements. The spatial correspondence of discrete fluctuating signals (pixels) over time could be observed and their relationship identified as a likely vapor liquid interface. Therefore the TLCs have inadvertently provided a means of flow visualization.

5.4 Two-Phase Heat Transfer Coefficient. In order to determine the two-phase heat transfer coefficient, accurate wall and fluid bulk temperature measurements are required. As mentioned earlier, determination of the fluid bulk temperature in the two-phase region is based on a linear pressure drop assumption. Additionally, accurate determination of the zero quality location requires an effective energy balance. Figures 10(*a*)–10(*e*) present samples of the wall temperature, as well as the calculated fluid bulk temperature at incremental levels of heat flux and at a mass flux of ~770 kg/(m^2 s). The wall temperature is a spanwise average of 72 pixels and has been down sampled for presentation. It is compiled from snapshots at a number of locations along the tube with each location spanning 640 pixels or ~10 diameters. Identified in the figure is the zero quality location calculated based on an energy balance. Typical in all figures is an almost constant but slightly decreasing wall temperature in the two-phase region. In the single-phase region of Figs. 10(*d*) and 10(*e*), the wall temperature rises then falls, typical of what is seen during onset of

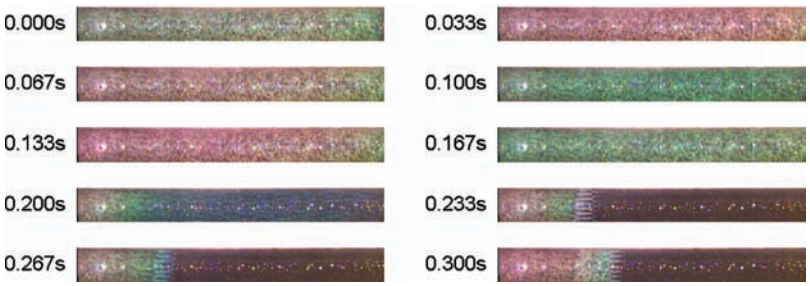

Fig. 9 (Color) Wall temperature fluctuations highlighting oscillatory behavior and high wall temperature gradient front. Red is cool and blue is hot, black is high temperature past the clearing point of the TLC. Covering a time span of 0.3 s, at 78–88 z/D and $Q/A_h \sim 79$ kW/m^2, $G \sim 770$ kg/(m^2 s), and flow is from left to right.

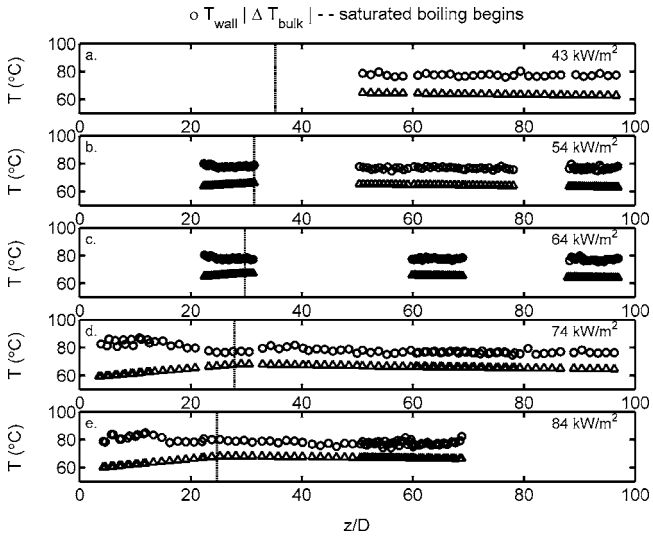

Fig. 10 Circumferentially averaged wall temperature measurement and calculated fluid bulk temperature along tube for varying heat fluxes, $G \sim 770$ kg/(m^2 s)

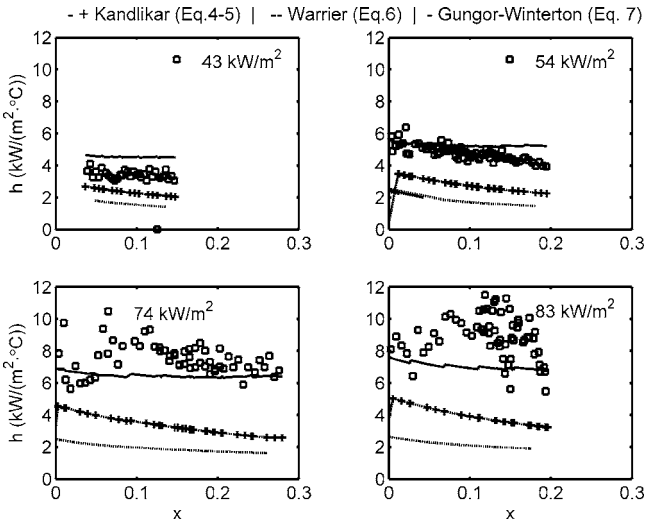

Fig. 12 Local heat transfer coefficient, comparison with correlation at various heat fluxes, $G \sim 770$ kg/(m^2 s)

subcooled boiling. There is scatter within the data and this is partially due to the time variance of the data. The data during high heat flux when significant wall temperature variations were present and where the liquid crystal clearing point was exceeded are not included.

Figure 11 presents the heat transfer coefficient at two different heat fluxes and mass fluxes as a function of quality. Similar to the wall temperature measurements, they are determined by a spanwise average of 72 pixels and down sampled for presentation. In the region leading up to the zero quality location, the heat transfer coefficient rises rapidly. With increasing heat flux, the heat transfer coefficient increases when the quality is greater than zero. The increase for $G \sim 1043$ kg/(m^2 s) is not as significant for as for the lower case of $G \sim 770$ kg/(m^2 s). With the exception of the low mass flux, the high heat flux case ($Q/A_h \sim 83$ kW/m^2, $G \sim 770$ kg/(m^2 s)), the heat transfer coefficient has a mild decrease with increasing quality. Finally at a given heat flux, the influence of mass flux is mild. For the low heat flux case, the heat transfer coefficient increases slightly with increased mass flux, whereas for the high heat flux case there is a slight decrease in the heat transfer coefficient with increased mass flux. However, at this high heat flux case, there is significant scatter in the data set, and looking back at the wall temperature trend in Fig. 10(*e*), it is expected that the heat transfer coefficient should be displaying the same trend as the other higher mass flux dataset.

In observing the trends of the lower mass flux case ($G \sim 770$ kg/(m^2 s)), these data suggest a nucleation dominated region at low quality, with the heat transfer coefficient being a strong function of the heat flux and a weak function of the mass quality. These trends were typical for the other heat flux values at this mass flux. For the higher mass flux case ($G \sim 1040$ kg/(m^2 s)), the heat flux influence on the heat transfer coefficient is less significant however, and this was typical for other heat flux cases at this mass flux. It is noted that the data obtained during the large temperature gradient fronts are not presented as they are out of range of the TLC, as well would be accompanied with significant time variance. However, if wall temperature measurements were available they would show a significant decrease in the heat transfer coefficient in the range of quality greater than 0.35.

Figures 12 and 13 compare the measured heat transfer coeffi-

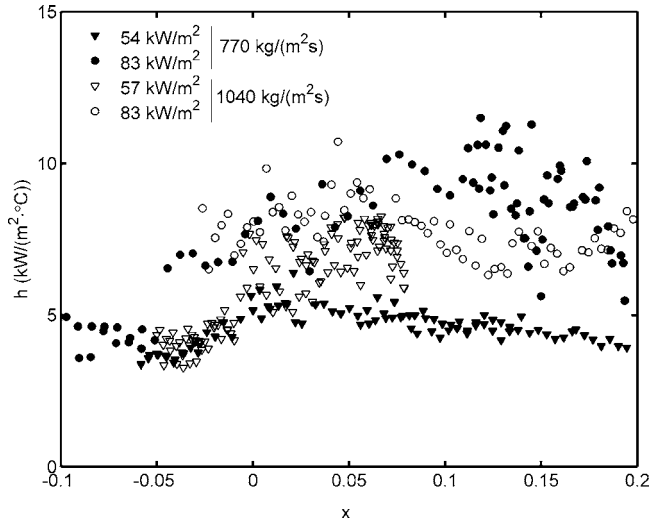

Fig. 11 Local heat transfer coefficient as a function of quality, effect of heat flux, and mass flux

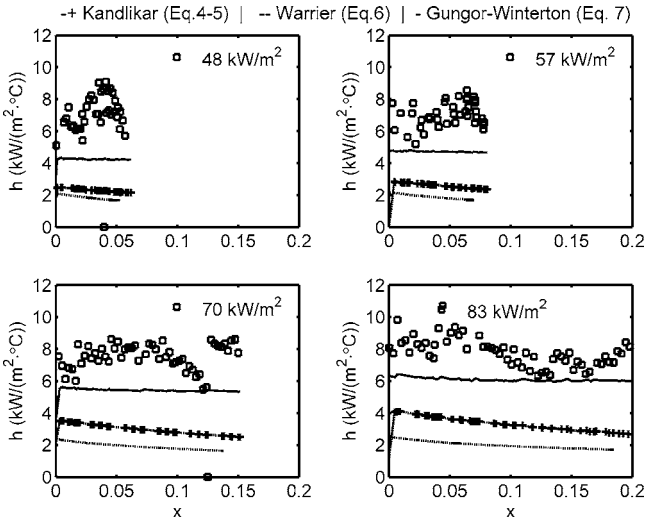

Fig. 13 Local heat transfer coefficient, comparison with correlation at various heat fluxes, $G \sim 1043$ kg/(m^2 s)

cient with three different correlations. The first correlation is given by Kandlikar [30] and Kandlikar and Balasubramanian [31]. It is based on a variety of working fluids and working conditions, and for channel diameters ranging from 4 mm to 32 mm [3]. It has been modified from its original form to account for flow in minichannels ($0.20\ \text{mm} \leqslant D \leqslant 3.0\ \text{mm}$) in the laminar and transitional range [31]. Flow is considered in the transitional range if $1600 \leqslant \text{Re}_f \leqslant 3000$, which are the conditions of the presented data. The correlation is

$$h_{\text{tp}} = \text{larger of}(h_{\text{tp, NBD}} \text{ and } h_{\text{tp, CBD}}) \tag{4}$$

where NBD denotes nucleation boiling dominated and CBD denotes convection boiling dominated. Each term is

$$h_{\text{tp,NBD}} = 0.6683\text{Co}^{-0.2}(1-x)^{0.8}h_f + 1058.0\text{Bo}^{0.7}(1-x)^{0.8}F_{\text{Fl}}h_f$$

$$h_{\text{tp,CBD}} = 1.136\text{Co}^{-0.9}(1-x)^{0.8}h_f + 667.2\text{Bo}^{0.7}(1-x)^{0.8}F_{\text{Fl}}h_f$$

$$\text{Co} = \left(\frac{1-x}{x}\right)^{0.8}\left(\frac{\rho_v}{\rho_f}\right)^{0.5} \tag{5}$$

where F_{Fl} is a fluid to surface relating term and for stainless steel tubes with any fluid is 1.0 [31]. For the transitional regime, it is recommended to use a single-phase heat transfer coefficient based on a linear interpolation between laminar and turbulent flow. In the present work, h_f has been taken as that based on the analytical solution for laminar thermally developing flow [32].

The second correlation by Warrier et al. [18] was selected as it is based on a working fluid with similar chemical structure, FC-84. However, the geometry used in the study was composed of five parallel rectangular channels of 0.75 mm hydraulic diameter. The correlation is given by

$$\frac{h_{\text{tp}}}{h_f} = 1 + 6.0\text{Bo}^{1/16}[-5.3(1-855\text{Bo})]x^{0.65} \tag{6}$$

The single-phase, liquid heat transfer coefficient (h_f) is for fully developed flow, however, it was taken as the thermally developing value for the present.

The third correlation by Gungor and Winterton [33] is based on a database covering a variety of fluids for channel diameters ranging from 2.95 mm to 32.00 mm, and under a variety of channel orientations. It is

$$h_{\text{tp}} = Eh_f + Sh_{\text{ncb}}$$

$$h_{\text{ncb}} = 55P_r^{0.12}(-0.4343\ln(P_r))^{-0.55}M^{-0.5}(Q/A)^{0.67}$$

$$E = 1 + 24{,}000\text{Bo}^{1.16} + 1.37\left(\frac{1}{X_{tt}}\right)^{0.86}$$

$$S = (1 + 1.15 \times 10^{-6}E^2\,\text{Re}_f^{1.17})^{-1}$$

$$X_{tt} = \left(\frac{1-x}{x}\right)^{0.9}\left(\frac{\rho_v}{\rho_f}\right)^{0.5}\left(\frac{\mu_f}{\mu_v}\right)^{0.1} \tag{7}$$

The parameter E is an enhancement factor of the single-phase heat transfer and S is a suppression factor for the pool boiling term. The single-phase heat transfer coefficient (h_f) is defined based on the Dittus–Boelter correlation [33] for turbulent flow. However, in the present as with the previous cases, it has been modified with the thermally developing laminar flow analytical solution. Due to lack of data on vapor phase viscosity of FC-72, this term was taken as 1.0.

As shown in Figs. 12 and 13, both the correlation of Eqs. (4) and (5) and Eq. (6) underpredict the heat transfer coefficient for all cases of heat fluxes, although Eqs. (4) and (5) are closer in magnitude. The trends presented by both correlations, however, are very similar to that observed in the data of Fig. 12 ($G \sim 770\ \text{kg/(m}^2\,\text{s)}$), showing a slight decrease in heat transfer coefficient with increasing quality. For this lower mass flux case, the correlation by Eqs. (7) also provides a good measure of the magnitude of the heat transfer coefficient for the middle range of heat fluxes; however, it overpredicts and slightly underpredicts the data for the low and high heat flux cases, respectively. For the higher mass flux case shown in Fig. 13, however, the correlation from Eq. (7) consistently slightly underpredicts the heat transfer coefficient. The correlation of Eqs. (4) and (5) contains a nucleate boiling dominated form ($h_{\text{tp,NBD}}$) and a convective boiling dominated form ($h_{\text{tp,CBD}}$). For the conditions in the present work it was found that the nucleate boiling dominant form of the equation prevailed for the majority of the instances, particularly at the lower mass flux case ($770\ \text{kg(m}^2\,\text{s)}$). On the other hand, the correlation in Eq. (7) contains a nucleate boiling component (Sh_{ncb}) and a convective boiling (Eh_f) component and in general had the best agreement with the results in terms of magnitude. It was found that the total heat transfer coefficient from this correlation was dominated by the convective boiling component which accounted for 60–70% of its value. The lack of correspondence of the correlations confirms that additional studies are still required as has been mentioned by many other researchers, and additionally with a variety of fluids to expand the correlation versatility as has been demonstrated by the lack of fit with present data.

6 Conclusions and Recommendations

The investigation of flow boiling heat transfer of FC-72 in a 1.067 mm tube through use of liquid crystal thermography has been presented. Local heat transfer data are presented for a low mass flux of ($G \sim 770\ \text{kg/(m}^2\,\text{s)}$ and $G \sim 1040\ \text{kg/(m}^2\,\text{s)}$) and a low inlet subcooling partially because boiling initiation was not observed at other conditions. At these low mass flux cases, a unique phenomenon at boiling onset was observed, whereby a large temperature gradient front moved toward the exit of the tube with a cooler wall temperature behind it. This observation was enabled due to the use of a thermographic technique for wall temperature measurement. Additional investigations are recommended to provide further understanding of this observation.

Under two-phase conditions the wall temperature was observed to oscillate for a wide range of heat fluxes. The amplitude was on the order of $1-7\,^\circ\text{C}$ for low heat flux and the frequency around 10 Hz. At a high heat flux large oscillatory wall temperature gradients were observed through the form of a wall temperature gradient front. The nature of these large gradient oscillations suggests an oscillating partial dryout regime. Although flow visualization was not directly performed, the use of a thermographic technique has inadvertently provided a means for partial flow visualization.

Local heat transfer coefficient data were presented for a quality up to approximately 0.3. In the range of heat flux covered, the heat transfer coefficient is dependent on heat flux, but only mildly influenced by quality at a lower mass flux of $\sim 770\ \text{kg/(m}^2\,\text{s)}$. At a higher mass flux of $\sim 1040\ \text{kg/(m}^2\,\text{s)}$, the heat transfer coefficient is less dependent on heat flux. When compared with some relevant correlations, none can accurately predict the observed magnitude and trend over the entire range of heat fluxes. In conclusion, although there has been an increase of work in the area of two-phase flow in mini- and microchannels, much work still remains in order to provide good predictability of the phenomena. To aid this work, researchers should consider thermographic approaches such as thermochromic liquid crystal thermography, as they may provide an added perspective on the phenomena.

Nomenclature

A = area, m^2
Bo = boiling number
C_p = specific heat, kJ/(kg K)
D = inner tube diameter, m
f = friction factor
g = gravity, m/s^2
G = mass flux, $\text{kg/(m}^2\,\text{s)}$

h = heat transfer coefficient, $W/(m^2\,K)$
h_{fg} = latent heat of vaporization
k = thermal conductivity, W/(m K)
L = length, m
$\dot{m}$ = mass flow, kg/s
n = index
N_{conf} = confinement number
Nu = Nusselt number $h_z D/k_{f,z}$
P = pressure, N/m^2
Pr = Prandtl number
P_r = reduced pressure
Q = heat to fluid, W
Re = Reynolds number, with respect to tube inner diameter
T = temperature, K
x = quality
z = streamwise location, m
z^* = $z/\mathrm{Re}\,\mathrm{Pr}\,D$

Greek

ρ = density, kg/m^3
σ = surface tension, N/m
μ = viscosity, Ns/m^2

Subscripts

0 = zero quality location
∞ = free stream condition
b = fluid bulk condition
bi = boiling incipience
CBD = convection boiling dominated
f = liquid phase
fd = fully developed
fluid = fluid condition
h = heated
in = inlet condition
i = inner wall
loc = local condition
NBD = nucleate boiling dominated
out = outlet condition
sat = saturation conditions
sub = subcooled conditions with respect to entry
TLC = thermochromic liquid crystal
tp = two-phase
v = vapor phase
w = wall
y = spanwise direction
z = streamwise direction

References

[1] Hassan, I., Phutthavong, P., and Abdelgawad, M., 2004, "Microchannel Heat Sinks: An Overview of the State-of-the-Art," Microscale Thermophys. Eng., **8**, pp. 183–205.
[2] Thome, J. R., 2004, "Boiling in Microchannels: A Review of Experiment and Theory," Int. J. Heat Fluid Flow, **25**, pp. 128–139.
[3] Kandlikar, S. G., 2002, "Fundamental Issues Related to Flow Boiling in Minichannels and Microchannels," Exp. Therm. Fluid Sci., **26**, pp. 389–407.
[4] Kew, P. A., and Cornwell, K., 1997, "Correlations for the Prediction of Boiling Heat Transfer in Small-Diameter Channels," Appl. Therm. Eng., **17**, pp. 705–715.
[5] Lee, H., and Lee, S. Y., 2001, "Heat Transfer Correlation for Boiling Flows in Small Rectangular Horizontal Channels With Low Aspect Rations," Int. J. Multiphase Flow, **27**, pp. 2043–2062.
[6] Qu, W., and Mudawar, I., 2003, "Flow Boiling Heat Transfer in Two-Phase Micro-Channel Heat Sinks: Part I: Experimental Investigation and Assessment of Correlation Methods," Int. J. Heat Mass Transfer, **46**, pp. 2755–2784.
[7] Lin, S., Kew, P. A., and Cornwell, K., 2001, "Flow Boiling of Refrigerant R141B in Small Tubes," Transactions of IChemE, **79**, Part A, pp. 417–424.
[8] Saitoh, S., Daiguji, H., and Hihara, E., 2005, "Effect of Tube Diameter on Boiling Heat Transfer of R-134a in Horizontal Small-Diameter Tubes," Int. J. Heat Mass Transfer, **48**, pp. 4973–4984.
[9] Grohmann, S., 2005, "Measurement and Modeling of Single-Phase and Flow-Boiling Heat Transfer in Microtubes," Int. J. Heat Mass Transfer, **48**, pp. 4073–4089.
[10] Yen, T., Kasagi, N., and Suzuki, Y., 2003, "Forced Convective Boiling Heat Transfer in Microtubes at Low Mass and Heat Fluxes," Int. J. Multiphase Flow, **29**, pp. 1771–1792.
[11] Yu, W., France, D. M., Wambsganss, M. W., and Hull, J. R., 2002, "Two-Phase Pressure Drop, Boiling Heat Transfer, and Critical Heat Flux to Water in a Small-Diameter Horizontal Tube," Int. J. Multiphase Flow, **28**, pp. 927–941.
[12] Hapke, I., Boye, H., and Schmidt, J., 2000, "Onset of Nucleate Boiling in Minichannels," Int. J. Therm. Sci., **39**, pp. 505–513.
[13] Hetsroni, G., Gurevich, M., Mosyak, A., Pogrebnyak, E., Rozenblit, R., and Yarin, L. P., 2003, "Boiling in Capillary Tubes," Int. J. Multiphase Flow, **29**, pp. 1551–1563.
[14] Chin, Y., 1997, "An Experimental Study on Flow Boiling in a Narrow Channel: From Convective to Nucleate Boiling," Ph.D dissertation, University of Houston, Houston, TX.
[15] Lakshminarasimhan, M. S., Hollingsworth, D. K., and Witte, L. C., 2000, "Boiling Incipience in Narrow Channels," *Proceedings of the ASME Heat Transfer Division, ASME IMECE*, Vol. **4**, ASME, New York, pp. 55–63.
[16] Piasecka, M., Hozejowska, S., and Poniewski, M. E., 2004, "Experimental Evaluation of Flow Boiling Incipience of Subcooled Fluid in a Narrow Channel," Int. J. Heat Fluid Flow, **25**, pp. 159–172.
[17] Aligoodarz, M. R., Yan, Y., and Kenning, D. B. R., 1998, "Wall Temperature and Pressure Variation During Flow Boiling in Narrow Channels," *Heat Transfer 1998*, Proceedings of the 11th IHTC, Vol. 2, pp. 225–230.
[18] Warrier, G. R., Dhir, V. K., and Momoda, L. A., 2002, "Heat Transfer and Pressure Drop in Narrow Rectangular Channels," Exp. Therm. Fluid Sci., **26**, pp. 53–64.
[19] Chen, T., and Garimella, S. V., 2005, "Effects of Dissolved Air on Subcooled Flow Boiling of a Dielectric Coolant in a Microchannel Heat Sink," *Proceedings of the 3rd International Conference on Microchannels and Minichannels (ICMM2005)*, p. 8.
[20] Collier, J. G., and Thome, J. R., 1999, *Convective Boiling and Condensation*, 3rd ed., Oxford Science Publications, Oxford, UK.
[21] Basu, N., Warrier, G. R., and Dhir, V. K., 2002, "Onset of Nucleate Boiling and Active Nucleation Site Density During Subcooled Flow Boiling," ASME J. Heat Transfer, **124**, pp. 717–728.
[22] Qu, W., and Mudawar, I., 2002, "Prediction and Measurement of Incipient Boiling Heat Flux in Micro-Channel Heat Sinks," Int. J. Heat Mass Transfer, **45**, pp. 3933–3945.
[23] Kennedy, J. E., Roach, G. M., Dowling, M. F., Abdel-Khalik, S. I., Ghiaasiaan, S. M., Jeter, S. M., and Quershi, Z. H., 2000, "The Onset of Flow Instability in Uniformly Heated Horizontal Microchannels," ASME J. Heat Transfer, **122**, pp. 118–125.
[24] Ghiaasiaan, S. M., and Chedester, R. C., 2002, "Boiling Incipience in Microchannels," Int. J. Heat Mass Transfer, **45**, pp. 4599–4606.
[25] Muwanga, R., and Hassan, I., 2006, "Local Heat Transfer Measurements in Microchannels Using Liquid Crystal Thermography: Methodology Development and Validation," ASME J. Heat Transfer, **128**(7), pp. 617–626.
[26] Ammerman, C. N., 1997, "Experimental Investigation of Enhanced Convective Boiling in Small Channels," Ph.D. dissertation, The University of Texas at Arlington, Arlington, TX.
[27] Tran, T. N., Wambsganss, M. W., and France, D. M., 1996, "Small Circular- and Rectangular-Channel Boiling With Two Refrigerants," Int. J. Multiphase Flow, **22**, pp. 485–498.
[28] Bowers, M., 1994, "High Heat Flux Dissipation Using Small Diameter Channels," Ph.D dissertation, Purdue University, West Lafayette, IN.
[29] Ding, Y., Kakaç, S., and Chen, X. J., 1995, "Dynamic Instabilities of Boiling Two-Phase Flow in a Single Horizontal Channel," Exp. Therm. Fluid Sci., **11**, pp. 327–342.
[30] Kandlikar, S. G., 1990, "A General Correlation for Saturated Two-Phase Flow Boiling Heat Transfer Inside Horizontal and Vertical Tubes," J. Heat Transfer, **112**, pp. 219–228.
[31] Kandlikar, S. G., and Balasubramanian, P., 2004, "An Extension of the Flow Boiling Correlation to Transition, Laminar, and Deep Laminar Flows in Minichannels and Microchannels," Heat Transfer Eng., **25**, pp. 86–93.
[32] Shah, R. K., and London, A. L., 1978, "Laminar Flow Forced Convection in Ducts," *Advances in Heat Transfer*, Academic, New York.
[33] Gungor, K. E., and Winterton, R. H. S., 1986, "A General Correlation for Flow Boiling in Tubes and Annuli," Int. J. Heat Mass Transfer, **29**, pp. 351–358.

A Generalized Diffusion Layer Model for Condensation of Vapor With Noncondensable Gases

Y. Liao
e-mail: liao2@ecn.purdue.edu

K. Vierow
e-mail: vierow@ne.tamu.edu

Department of Nuclear Engineering,
Texas A&M University,
3133 TAMU,
College Station, TX 77843-3133

The diffusion layer model for condensation heat transfer of vapor with noncondensable gases was originally derived on a molar basis and developed from an approximate formulation of mass diffusion, by neglecting the effect of variable vapor–gas mixture molecular weights across the diffusion layer on mass diffusion. This is valid for gases having a molecular weight close to that of the vapor or for low vapor mass transfer rates, but it may cause serious error if a large gradient in the gas concentration exists across the diffusion layer. The analysis herein shows that, from the kinetic theory of gases, Fick's law of diffusion is more appropriately expressed on a mass basis than on a molar basis. Then a generalized diffusion layer model is derived on a mass basis with an exact formulation of mass diffusion. The generalized model considers the effect of variable mixture molecular weights across the diffusion layer on mass diffusion and fog formation effects on sensible heat. The new model outperforms the one developed by Peterson when comparing with a wide-ranging experimental database. Under certain limiting conditions, the generalized model reduces to the one developed by Peterson.
[DOI: 10.1115/1.2728907]

Keywords: condensation heat transfer, diffusion layer model, noncondensable gas

1 Introduction

Condensation with noncondensable gases occurring in passive containment cooling systems of future nuclear light water reactors plays a key role in removing decay heat from the containment building. An accurate model for condensation with noncondensable gases is essential for the design of heat exchangers in passive containment cooling systems. This paper discusses development of a model for condensation with noncondensable gases and validation against a comprehensive experimental database covering the operation range of passive containment cooling systems. The model is valid for any heat exchanger with vapor/gas mixtures condensing inside tubes.

The theoretical analysis of condensation of vapor–noncondensable gas mixtures using the stagnant film model was first presented by Colburn and Hougen [1] for vapor–air mixtures. In their method, the overall heat transfer conductance between the condenser tube wall and vapor–air mixture is comprised of the conductance of the condensate film and the gas boundary layer where the air accumulates. The heat transfer through the gas boundary layer includes sensible and latent heat transfer. The latent heat transfer is evaluated by using the stagnant film model combined with the heat and mass transfer analogy. Because this calculation method requires the convergence of two unknown variables, the interface temperature and air mole fraction, the methodology is cumbersome to use in engineering applications, requiring extensive iterations to match the condensation mass flux to the heat transfer through the condensate film. Although Colburn and Hougen [1] never derived an expression for the conductance of the gas boundary layer, they suggested that for saturated mixtures the mass transfer coefficient in the stagnant film model could be converted to a corresponding heat transfer coefficient by using the Clausius–Clapeyron equation. The diffusion layer model [2] was based on this principle.

Peterson et al. [2] introduced the concept of a "condensation thermal conductivity" in developing the diffusion layer model, wherein the overall gas-side conductivity is formulated as a combination of the condensation thermal conductivity for latent heat transfer and the standard thermal conductivity for sensible heat transfer. The advantages of diffusion layer modeling are depiction of the mass transfer in a form as simple as that for the sensible heat transfer, and rapid convergence in numerical calculations, since the condensation thermal conductivity is only a weak function of the interfacial temperature.

Due to the model's simplicity, calculation methods utilizing the diffusion layer model have been applied to analyze condensation with noncondensables in heat exchangers designed for nuclear systems [3,4]. These calculation methods often underpredict experimental data, with standard deviations of theoretical predictions from the experimental data by Vierow [5] and Siddique [6] in the range from about 40% to 70%. This paper discusses an improvement of the original diffusion layer model and presents a methodology for heat transfer prediction of condensation with noncondensables, which has improved prediction capabilities for heat exchangers in passive containment cooling systems.

Peterson's [2] diffusion layer model can be improved further by considering the effects of fog formation, suction, and condensate film waviness. Brouwers [7] introduced fog correction factors for both sensible and latent heat transfer. Under operating conditions of passive containment cooling systems, fog formation enhances the sensible heat transfer and the fog correction factor for the sensible heat transfer ranges from 1 to 3, while fog formation reduces the latent heat transfer and the fog correction factor for the latent heat transfer is virtually 1. Therefore, the effects of fog formation are more important for higher noncondensable gas concentration regions where the sensible heat transfer is comparable to the latent heat transfer. The "suction" effect of condensation promotes better heat transfer by pulling vapor to the condensation surface. The suction factor for the latent heat transfer has already been included in Peterson's [2] diffusion layer modeling of mass transfer [7,8], therefore, only the suction factor for the sensible heat transfer needs to be considered herein. Film waviness enhances both heat and mass transfer by increasing the interfacial surface roughness. A film waviness factor of 1.2 correlated from

Contributed by the Heat Transfer Division of ASME for publication in the JOURNAL OF HEAT TRANSFER. Manuscript received September 30, 2005; final manuscript received September 11, 2006. Review conducted by N. K. Anand.

experimental data for the latent heat transfer was reported [2]. The film waviness should affect the sensible heat transfer to the same extent by the heat and mass transfer analogy.

The condensation thermal conductivity in Peterson's [2] diffusion layer model was derived from a formulation of mass diffusion by using quantities and Fick's law of diffusion on a molar basis, a conventional formulation for analysis. Peterson's [2] diffusion layer model may be extended by formulating the condensation thermal conductivity on a mass basis. Although the formulation on a mass basis becomes more complicated than that on a molar basis, it is more appropriate to use when the condensation thermal conductivity is coupled with the heat and mass transfer analogy to evaluate the latent heat transfer.

The theoretical basis underlying the analogies between momentum, heat, and mass transfer is that the original as well as the transformed conservation equations for momentum, heat, and species mass continuity have similar mathematical forms. Mass-based quantities such as mixture density and mass-averaged velocity are used in conservation equations for multicomponent flow systems. Rohsenow [9] pointed out the distinction between the molar and mass-based formulations of the convective mass diffusion. If the molecular weights of the two species in the gas mixture are quite different, the molar-averaged mixture velocity deviates from the mass-averaged mixture velocity. Since the mass-averaged mixture velocity is the velocity used in conservation equations for multicomponent systems, and for turbulent flow where momentum is important in controlling the structure of the gas boundary layer, the use of mass-based quantities is more appropriate when applying the analogies between momentum, heat, and mass transfer. Therefore, formulating convective mass diffusion on a mass basis is preferred in this analysis.

The effects of variable mixture molecular weights across the diffusion layer on vapor diffusion provide another motivation for selecting the mass-based formulation. The effects of mixture molecular variations that result from large concentration differences through the boundary layer prove to be very substantial and serious error can be introduced if they are ignored [10]. Fick's law of diffusion on a molar basis will be shown to neglect the effects of variable mixture molecular weights across the diffusion layer on mass diffusion. Even for a slight bulk noncondensable gas fraction, the noncondensable gas may accumulate at the condensation interface and attain a large gas fraction. Therefore, neglecting the change of the mixture molecular weight may cause serious error if a large gradient of gas concentration exists across the diffusion layer.

The stagnant film model proposed by Colburn and Hougen [1] and the diffusion layer model proposed by Peterson [2] were shown to be equivalent to each other [8] and both of them rely on the heat and mass transfer analogy to calculate latent heat transfer. Both the stagnant film model and diffusion layer model neglect the longitudinal flow acceleration, which is unrealistic for most applications. Solving boundary layer equations with a numerical method for the gas and liquid phases can take into account the longitudinal flow acceleration [11,12]. However, the neglect of the longitudinal flow acceleration makes it possible to obtain an analytical solution which is simple to use in engineering applications and provides results not far from the rigorous boundary layer analysis. The stagnant film model has been formulated on a molar and a mass basis and the mass-based approach tends to provide higher values of mass flux than the molar-based approach [13]. Ambrosini [13] noted that recent progress in the modeling is minimal even though the models that underpredict heat transfer continue to be widely used. One of the objectives of the current work is to formulate the diffusion layer model on a mass basis and compare the diffusion layer models on a molar basis and on a mass basis.

Herein a generalized diffusion layer model pursued on a mass basis is developed and differences of the mass and molar-based formulations in their approximations are discussed. Under limiting conditions, the generalized model is identical to the model developed by Peterson [2]. A calculation methodology using the new model was developed and validated against a wide-ranging experimental database. In the methodology, the effects of variable mixture molecular weights across the diffusion layer on the latent heat transfer are taken into account, and the effects of fog formation and suction on the sensible heat transfer are calculated with a mechanistic model developed by Brouwers [7]. The new method gives better predictions for a variety of experimental data than other methods using molar-based diffusion layer models.

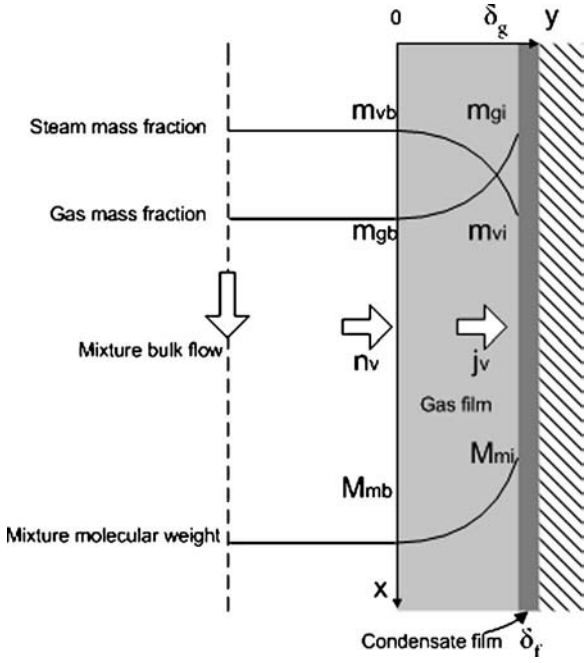

Fig. 1 Coordinate system for condensation of vapor–gas mixture

2 A Generalized Diffusion Layer Model

Treating the gas film as a diffusion layer, Peterson [2,14] derived a condensation thermal conductivity in the diffusion layer model on a molar basis

$$k_c^p = \frac{1}{\phi}\frac{h'_{fg}h_{fg}PDM_v^2}{R^2\bar{T}^3}$$

$$\phi = \frac{\ln[(1-x_{gb})/(1-x_{gi})]}{\ln(x_{gi}/x_{gb})} \tag{1}$$

where k_c^p is the condensation thermal conductivity. Using the concept of condensation thermal conductivity, the Sherwood number for condensation takes a simple form, $\mathrm{Sh}=h_cL/k_c^p$, which is analogous to the Nusselt number for sensible heat transfer, $\mathrm{Nu}=h_sL/k$. Then the total heat transfer coefficient is conveniently given by combining the parallel gas-side latent heat transfer and sensible heat transfer coefficients in series with the liquid-side heat transfer coefficient

$$\frac{1}{h_t} = \frac{1}{h_c+h_s} + \frac{1}{h_f} = \frac{L}{\mathrm{Sh}\cdot k_c + \mathrm{Nu}\cdot k} + \frac{\delta_f}{k_f} \tag{2}$$

Figure 1 shows the coordinate system used to develop the diffusion layer model on a mass basis. Since the liquid–vapor interface is impermeable to gas, the mass balance requires that the absolute noncondensable gas mass flux normal to the interface is zero, $n_g=0$; the absolute vapor mass flux n_v normal to the interface is the sum of a convective and a diffusive component

$$n_v = m_v(n_v + n_g) - \rho_m D \frac{dm_v}{dy} \tag{3}$$

where Fick's law of diffusion on a mass basis is employed. Equation (3) can be simplified to

$$n_v = \rho_m D \frac{d\ln(1-m_v)}{dy} \tag{4}$$

Letting δ_g be the effective thickness of the diffusion layer, integration of Eq. (4) over the diffusion layer leads to

$$\int_0^{\delta_g} n_v\, dy = \int_{m_{vb}}^{m_{vi}} \rho_m D\, d\ln(1-m_v) \tag{5}$$

To conserve mass, the absolute vapor mass flux, n_v, must be constant through the diffusion layer. It is noted that in Peterson's [2,14] diffusion layer model, the molar average mixture velocity has to be constant following the assumption of a constant molar density through the diffusion layer. In general, the molar density is going to be more uniform in the boundary layer than the mass density, if the molecular weights of the two species are quite different. This provides motivation to select the molar-based formulation by Peterson [2,14]. For the mass-based formulation in Eq. (5), since the mixture density, ρ_m, is a decreasing function of temperature ($\sim T^{-1}$), and the mass diffusivity, D, is an increasing function of temperature ($\sim T^{1.5}$) that nearly compensates, $\rho_m D$ is a weak function of temperature. Consequently, if $\rho_m D$ is evaluated at an average temperature and considered a constant, no significant error is introduced and a convenient analytical solution can be obtained. Therefore, the absolute vapor mass flux can be evaluated from Eq. (5) as

$$n_v = \frac{\bar{\rho}_m D}{\delta_g} \ln \frac{1-m_{vi}}{1-m_{vb}} \tag{6}$$

The latent heat transfer coefficient is expressed by using Eq. (6) as

$$h_c = n_v h'_{fg}/(T_b - T_i) = \frac{h'_{fg}\bar{\rho}_m D}{\delta_g (T_b - T_i)} \ln \frac{1-m_{vi}}{1-m_{vb}} \tag{7}$$

The Sherwood number, $\mathrm{Sh} = L/\delta_g$, can be recast by substituting δ_g from Eq. (7) as

$$\mathrm{Sh} = \frac{h_c L}{h'_{fg}\bar{\rho}_m D/(T_b - T_i)} \frac{1}{\ln[(1-m_{vi})/(1-m_{vb})]} = \frac{h_c L}{k_c} \tag{8}$$

Therefore, the condensation thermal conductivity derived on a mass basis is

$$k_c = \frac{h'_{fg}\bar{\rho}_m D}{T_b - T_i} \ln \frac{1-m_{vi}}{1-m_{vb}} \tag{9}$$

In Appendix A, the condensation thermal conductivity derived on a mass basis is recast to a form comparable to that derived on a molar basis [2] by using the Clausius–Clapeyron equation and the ideal gas law. The final result is

$$k_c = \frac{\phi_2}{\phi_1} \frac{h'_{fg} h_{fg} P D M_v M_g}{R^2 \bar{T}^3}$$

$$\phi_1 = \frac{\ln[(1-m_{gb})/(1-m_{gi})]}{\ln(m_{gi}/m_{gb})}$$

$$\phi_2 = \frac{\bar{M}_m^2}{M_{mb} M_{mi}} \tag{10}$$

ϕ_1 in Eq. (10) appears similar to ϕ in Eq. (1) and takes into account the effects of noncondensable gas and suction on vapor condensation. ϕ_2 is a new factor, which takes into account the effects of variable mixture molecular weights on vapor diffusion that result from large concentration differences through the diffusion layer.

By the definition of the suction factor [10], $\ln(1+B_m)/B_m$, which is a function of the mass transfer driving force, $B_m = (m_{vb} - m_{vi})/(m_{vi} - 1)$, ϕ_1 can be converted to

$$\frac{1}{\phi_1} = \frac{\bar{m}_v}{m_{gi}} \frac{\ln(1+B_m)}{B_m} \tag{11}$$

The mechanism responsible for the degrading effects of the noncondensable gas on vapor condensation is accumulation of the noncondensable gas at the interface. As the gas accumulates at the interface and the gas fraction at the interface m_{gi} approaches unity, the log mean vapor mass fraction $\bar{m}_v$ approaches zero and the condensation thermal conductivity k_c decreases toward zero. Consequently, the condensation heat transfer is nearly completely inhibited and the total heat transfer coefficient in Eq. (2) is given by the serial combination of only the sensible gas-side heat transfer and liquid-side heat transfer coefficients. On the other hand, as the gas fraction at the interface approaches zero, the condensation thermal conductivity approaches infinity. Consequently, the total heat transfer coefficient is identical to the liquid-side heat transfer coefficient, which is the case of pure vapor condensation. For intermediate gas fractions, the suction factor always augments the condensation heat transfer. Therefore, the definition of the condensation thermal conductivity clearly shows the effects of noncondensable gases and suction on condensation.

If the mixture molecular weight M_m in Fick's law of diffusion is considered a constant across the diffusion layer, as an approximation used by the diffusion layer model on a molar basis [2,14], then either there is a uniform vapor–gas composition through the diffusion layer or the gas molecular weight is approximate to the vapor molecular weight. Since there is mass transfer it cannot be true that there is a uniform vapor–gas mixture composition, so it must be true that the gas molecular weight is approximate to the vapor molecular weight, $M_g \approx M_v$. It follows that $\phi_2 \approx 1$, $\phi_1 \approx \phi$, and Eq. (10) is identical to Eq. (1). Therefore, the diffusion layer model based on Eq. (10) is a generalized one, and the diffusion layer model on a molar basis is for a specific case.

3 Comparison of Molar and Mass-Based Diffusion Layer Models

Fick's law of diffusion for two-component systems is generally expressed either on a molar basis or a mass basis. On a molar basis, the diffusive vapor molar flux is

$$J_v = -CD\nabla x_v \tag{12}$$

On a mass basis, the diffusive vapor mass flux is

$$j_v = -\rho D \nabla m_v \tag{13}$$

Without demonstration, Mills [15] stated that the mass fraction is more suitable than the mole fraction for formulating the driving potential in Fick's law of diffusion. The next paragraphs demonstrate that Eq. (13) is indeed the more appropriate mathematical form for describing mass diffusion for binary gas mixtures by using the results from the kinetic theory of gases, although the expressions in Eqs. (12) and (13) are algebraically identical.

Using $m_v = x_v M_v / M_m$, the diffusive vapor mass flux in Eq. (13) may be represented in terms of molar fractions as $j_v = -\rho D M_v \nabla (x_v/M_m)$. This can be expanded for a one-dimensional geometry as

$$j_v = -\rho D M_v \left(\frac{\nabla x_v}{M_m} - \frac{x_v \nabla M_m}{M_m^2} \right) \tag{14}$$

From Eq. (14), it is noticed that if the mixture molecular weight is assumed constant through the diffusion layer, $\nabla M_m = 0$, Fick's law of diffusion can be expressed by either Eq. (12) or (13). Otherwise, Fick's law of diffusion should be expressed by Eq. (13) in

accordance with the kinetic theory of gases on mass diffusion. Using $M_m = x_v M_v + (1-x_v) M_g$, it follows that $\nabla M_m = M_v \nabla x_v - M_g \nabla x_v$ and Eq. (14) can be recast as

$$j_v = -\rho D M_v \frac{M_g \nabla x_v}{M_m^2} \tag{15}$$

Using $C = \rho / M_m$, Eq. (15) is equivalent to

$$j_v = -\frac{C^2}{\rho} D M_v M_g \nabla x_v \tag{16}$$

Equation (16) is exactly the formulation of mass diffusion for two-component systems according to the kinetic theory of gases, if the concentration gradient is the only driving force for diffusion [16]. Therefore, Fick's law of diffusion for two-component systems should be expressed on a mass basis and Fick's law of diffusion on a molar basis neglects the variation in mixture molecular weights. The form on a molar basis, assuming a constant mixture molecular weight across the diffusion layer, is a good approximation if the vapor concentration is small as in low mass transfer situations ($M_m \approx M_g$), or the molecular weights of the two components in the system are very close to each other ($M_v \approx M_g$).

It is useful to compare the vapor mass flux predicted by the molar and mass-based formulations of mass diffusion. On a molar basis, by using Eq. (12) the diffusive condensation mass flux is

$$j_v = M_v J_v \tag{17}$$

While on a mass basis, by using Eq. (14) the diffusive condensation mass flux can be represented as

$$j_v = M_v J_v + \rho D M_v \frac{x_v \nabla M_m}{M_m^2} \tag{18}$$

Comparing Eqs. (17) and (18) shows that for condensation of vapor–air mixtures, the diffusive condensation mass flux predicted on a mass basis is different from that predicted on a molar basis. Since the air accumulates at the liquid–vapor interface and causes a variation of the mixture molecular weight M_m across the diffusion layer, the second term on the right hand side of Eq. (18) contributes to an additional condensation mass flux. This effect is taken into account by the condensation thermal conductivity in the generalized diffusion layer model with the factor ϕ_2 in Eq. (10), which is greater than unity due to the variation of the vapor–air mixture molecular weight across the diffusion layer.

The ratio of the condensation thermal conductivity k_c in Eq. (10) from the current derivation and k_c^p in Eq. (1) from Peterson [2] is

$$\frac{k_c}{k_c^p} = \frac{M_g \overline{M}_m^2}{M_v M_{mb} M_{mi}} \frac{\ln(m_{gi}/m_{gb})}{\ln[(1-m_{gb})/(1-m_{gi})]} \frac{\ln[(1-x_{gb})/(1-x_{gi})]}{\ln(x_{gi}/x_{gb})} \tag{19}$$

For a prescribed total pressure, this ratio is a function of the gas molar fraction in the bulk fluid (x_{gb}) and the interfacial gas molar fraction (x_{gi}) as determined by the temperature difference ($\delta T = T_b - T_i$) between the bulk fluid and the liquid–vapor interface. Figure 2 shows this ratio versus x_{gb} for air. The computation of this ratio was performed at a total pressure of 200 kPa. The temperatures were assumed equal to the saturation temperatures corresponding to the vapor partial pressure in the bulk and at the interface. Figure 2 shows that the new theory predicts a higher condensation thermal conductivity and therefore higher latent heat transfer rates. The enhancement of the latent heat transfer comes from the effects of the variation of the mixture molecular weight across the diffusion layer. These effects can increase the total heat transfer significantly, because the latent heat transfer is much larger than the sensible heat transfer, especially for the lower noncondensable gas concentration region near the inlet of the condensation tubes. Since calculation methods based on Peterson's [2] diffusion layer theory generally underpredict experimental data, the calculation method based on the new theory is shown to have better prediction capabilities.

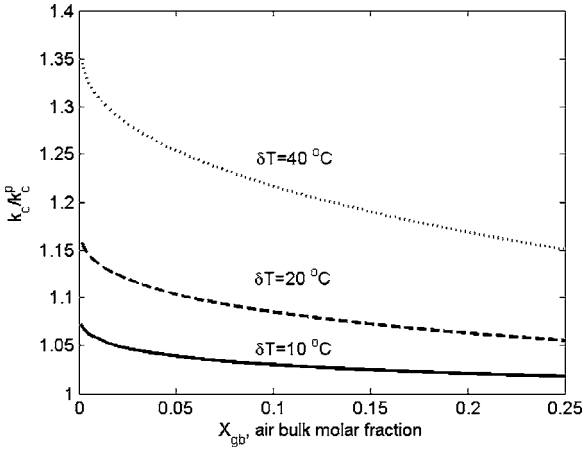

Fig. 2 Dependence of k_c/k_c^p on air fractions and temperature differences (P=200 kPa)

4 Results and Discussion

The generalized diffusion layer theory has been validated against local heat transfer coefficient data for condensation with a noncondensable gas. The data were taken from Vierow's [5], Siddique's [6], and Kuhn's [17] experiments on condensation of vapor–air forced convection flows inside vertical tubes. The database was comprised of 17 steady-state runs with 204 data points from Vierow's [5] data, 52 runs with 393 data points from Siddique's [6] data, and 79 runs with 627 data points from Kuhn's [17] data. The database covers a variety of test parameters, with the inlet air mass fraction ranging from about 1% to 40%, steam–air mixture Reynolds number ranging from about 500 to 45,000, and total pressure ranging from about 100 kPa to 500 kPa.

The test section is divided into axial elements of equal size Δz centered at axial location z_j. The total heat transfer coefficient defined in Eq. (2) was calculated at each axial location z_j. For each run in the experimental database, the inputs were the inlet air molar fraction, inlet mixture Reynolds number, and total pressure. At each axial node, the tube inner wall temperature was prescribed by the measured data in the experiments; the latent heat was evaluated with the generalized diffusion layer model developed herein; and the sensible heat was evaluated by considering the suction and fog formation effects using multiplying factors derived from a basic analysis of combined heat and mass transfer [7,18]. The calculation procedure at each axial location z_j of the tube is comprised of ten steps as shown in Appendix B.

Figure 3 shows a comparison of the theoretical and experimental data. The standard deviation of the predictions from the experimental data is defined as

$$\text{std} = \sqrt{\sum_{i=1}^{N} \left(\frac{h_{\text{theory}}}{h_{\text{exp}}} - 1 \right)_i^2 \Big/ (N-1)}$$

where N is the number of data points in the experimental data sets. The predictions are in good agreement with the experimental data, considering the measurement error in the experiments was about 20%. Table 1 compares the standard deviations of the current calculation method and two other methods using the molar-based diffusion layer models [3,4] for three experimental data sets [5,6,17]. Although the data sets are more comprehensive in the

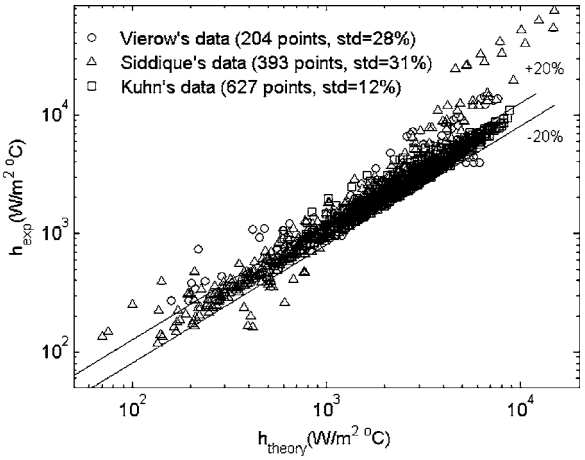

Fig. 3 Comparison of theoretical and experimental local heat transfer coefficients

current calculations than those used in Kageyama's [3] and Herranz's [4] calculations, the performance of the current method is much better.

In the present model, Peterson's [2] diffusion layer model has been extended by considering the effects of variable mixture molecular weights, which notably increase the latent heat transfer especially for low air concentration regions, and the effects of fog formation [7], which significantly increase the sensible heat transfer especially for high gas concentration regions. As noted by Brouwers [7], approximations have been made to conveniently derive an analytical condensation thermal conductivity in the molar-based model. The water vapor saturation line was replaced by the Clausius–Clapeyron equation and the acceleration of the axial flow has been neglected. These approximations are still used in the new mass-based model.

In the calculation method the film waviness effects have not been considered since a good and simple mechanistic model compatible with the current methodology is unavailable. Numerical simulations [19,20] showed that film waviness can enhance heat transfer due to thinning of the film thickness and increasing of the interfacial shear stress. It is observed from Fig. 3 that greater data scattering happens for predictions of smaller local heat transfer coefficients ($h<500$ W/m^2 °C). Low heat transfer rates commonly occur at the downstream end of condensation tubes, where the film thickness is larger and the film waviness effects are more significant. Another factor contributing to the discrepancy is the neglect of buoyancy effects in the calculations. Significant buoyancy effects come into play when the mixture Reynolds number is small and the mixture density at the interface is much larger than that in the bulk flow. The data points with very high heat transfer coefficients ($h>20{,}000$ W/m^2 °C) in Fig. 3 were taken from Siddique's [6] experimental data. These data were measured at the inlet of the exchange tube ($z=0$), where the entrance effect resulting from the developing flow prior to a fully developed gas boundary layer on heat transfer is quite large [6]. The current calculations have not considered entrance effects.

Since the liquid-side heat transfer coefficient plays a secondary role in determining the total heat transfer coefficient in the presence of noncondensables [21], the liquid-side heat transfer coefficient was evaluated with the classic Nusselt film theory to simplify calculations. For condensation of pure vapor flows, the liquid-side heat transfer coefficient could be evaluated with a more rigorous model.

5 Conclusions

A generalized diffusion layer model for condensation of vapor from vapor/noncondensable gas mixtures was developed by formulating the mass diffusion on a mass basis. The condensation thermal conductivity derived for this model considers the effects of noncondensable gas and suction on condensation heat transfer. The effect on vapor diffusion of variable mixture molecular weights across the diffusion layer have been taken into account in the new model, which significantly increases the latent heat transfer, especially for low noncondensable gas concentration regions. The generalized model is reduced to the original one developed by Peterson [2] with the assumption of constant mixture molecular weights across the diffusion layer. Comparisons with a variety of experimental data show that the generalized diffusion layer model can better predict the data than molar-based diffusion layer models.

Nomenclature

B_m = $(m_{vb}-m_{vi})/(m_{vi}-1)$, mass transfer driving force
C = molar density (kmol/m^3)
c_p = constant pressure specific heat (J/kg K)
D = diffusivity (m^2/s)
h = heat transfer coefficient (W/m^2 K)
h_{fg} = latent heat of vaporization (J/kg)
h'_{fg} = $h_{fg}+c_p(T_b-T_i)$
J = diffusive molar flux (kmol/m^2 s)
j = diffusive mass flux (kg/m^2 s)
k = thermal conductivity (W/m K)
L = characteristic length (m)
Le = Sc/Pr, Lewis number
M = molecular weight (kg/kmol)
M_m = $x_vM_v+(1-x_v)M_g$, mixture molecular weight (kg/kmol)
$\overline{M}_m$ = $\bar{x}_vM_v+(1-\bar{x}_v)M_g$, average mixture molecular weight (kg/kmol)
m = mass fraction
$\overline{m}$ = $(m_b-m_i)/\ln(m_b/m_i)$, log mean mass fraction
n = absolute mass flux (kg/m^2 s)

Table 1 Comparison of standard deviations by different calculation methods

	Current method		Kageyama[d]		Herranz[e]	
Data set	Number of data points	Standard deviation (%)	Number of data points	Standard deviation (%)	Number of data points	Standard deviation (%)
Vierow[a]	204	28	129	71	144	48.5
Siddique[b]	393	31	141	40	—	—
Kuhn[c]	627	12	—	—	—	—

[a]See Ref. [5].
[b]See Ref. [6].
[c]See Ref. [17].
[d]See Ref. [3].
[e]See Ref. [4].

P = absolute pressure (Pa)
R = universal gas constant (J/kmol K)
St^* = $\mathrm{Nu}^*/\mathrm{RePr}$
T = absolute temperature (K)
$\bar{T}$ = $(T_b+T_i)/2$, average temperature (K)
v_{fg} = phase specific volume change (m^3/kg)
x = mole fraction
$\bar{x}$ = $(x_b-x_i)/\ln(x_b/x_i)$, log mean mole fraction
y = coordinate normal to interface
δ = film thickness (m)
ρ = density (kg/m^3)
$\bar{\rho}$ = average density (kg/m^3)
υ_f = liquid viscosity (m^2/s)

Subscripts

b = bulk
c = condensation (latent) heat transfer
f = condensate film
g = noncondensable gas
i = liquid-vapor interface
m = vapor-gas mixture
s = sensible heat transfer
t = total
v = vapor

Appendix A: Derivation of Condensation Thermal Conductivity

By using the Clausius–Clapeyron equation, $(P_{vb}-P_{vi})/(T_b-T_i)=h_{fg}/(T\upsilon_{fg})$, and the approximation $\upsilon_{fg}\approx 1/\bar{\rho}_v=1/(\bar{m}_v\bar{\rho}_m)$ where the log mean vapor mass fraction is $\bar{m}_v=(m_{vb}-m_{vi})/\ln(m_{vb}/m_{vi})$, Eq. (9) can be recast as

$$k_c=\frac{h'_{fg}h_{fg}\bar{\rho}_m^2 D}{\bar{T}}\frac{m_{vb}-m_{vi}}{P_{vb}-P_{vi}}\frac{\ln[(1-m_{vi})/(1-m_{vb})]}{\ln(m_{vb}/m_{vi})} \tag{A1}$$

Using $(P_{vb}-P_{vi})/P=x_{vb}-x_{vi}$, and assuming ideal gas behavior $\bar{\rho}_m=\bar{M}_m P/(R\bar{T})$, Eq. (A1) leads to

$$k_c=\frac{h'_{fg}h_{fg}PD\bar{M}_m^2}{R^2\bar{T}^3}\frac{m_{vb}-m_{vi}}{x_{vb}-x_{vi}}\frac{\ln[(1-m_{vi})/(1-m_{vb})]}{\ln(m_{vb}/m_{vi})} \tag{A2}$$

By the definition of mass fraction $m_v=x_vM_v/(x_vM_v+(1-x_v)M_g)=x_vM_v/M_m$, the second term on the right hand side of Eq. (A2) can be recast as

$$\frac{m_{vb}-m_{vi}}{x_{vb}-x_{vi}}=\frac{M_vM_g}{M_{mi}M_{mb}} \tag{A3}$$

Combining Eqs. (A2) and (A3), the condensation thermal conductivity is derived on a mass basis as

$$k_c=\frac{h'_{fg}h_{fg}PDM_vM_g}{R^2\bar{T}^3}\frac{\bar{M}_m^2}{M_{mb}M_{mi}}\frac{\ln[(1-m_{vi})/(1-m_{vb})]}{\ln(m_{vb}/m_{vi})}$$
$$=\frac{h'_{fg}h_{fg}PDM_vM_g}{R^2\bar{T}^3}\frac{\bar{M}_m^2}{M_{mb}M_{mi}}\frac{\ln(m_{gi}/m_{gb})}{\ln[(1-m_{gb})/(1-m_{gi})]} \tag{A4}$$

Appendix B: Calculation Methodology for Local Total Heat Transfer Coefficients

1. Initialize the first node with test inlet conditions;
2. Guess an interfacial gas molar fraction, $x_{gi}=x_{gb}+0.01$;
3. Calculate $M_m=x_vM_v+(1-x_v)M_g$, $m_g=x_gM_g/M_m$, and fluid properties;
4. Calculate the gas-side latent heat transfer coefficient h_c from $\mathrm{Sh}=h_cL/k_c$; k_c is evaluated with Eq. (10); Sherwood number is evaluated with the heat and mass transfer analogy

$$\mathrm{Sh}=\begin{cases}0.023\,\mathrm{Re}^{0.8}\,\mathrm{Sc}^{0.35}, & \mathrm{Re}\geq 2300\\ 48/11, & \mathrm{Re}<2300\end{cases} \tag{B1}$$

5. Estimate the condensation mass flux based on the calculated condensation heat transfer coefficient, $\dot{m}''=h_c(T_b-T_i)/h_{fg}$, where the temperatures are assumed equal to the vapor saturation temperatures corresponding to the vapor partial pressures; update the node-wise condensate mass flow rate per unit length (Γ) with $\dot{m}''$; update the node-wise vapor–gas mixture Reynolds number and gas molar fraction at the bulk fluid accordingly;
6. Calculate the gas-side sensible heat transfer coefficient with

$$\mathrm{Nu}^*=\begin{cases}0.023\,\mathrm{Re}^{0.8}\mathrm{Pr}^{0.35}, & \mathrm{Re}\geq 2300\\ 48/11, & \mathrm{Re}<2300\end{cases} \tag{B2}$$

The Nusselt number for sensible heat transfer should be corrected by a suction factor θ_t and a fog formation factor θ_{tf} [7]

$$\mathrm{Nu}=\mathrm{Nu}^*\theta_t\theta_{tf}$$

$$\theta_t=\frac{\frac{c_{pv}}{c_p}\frac{\mathrm{Sh}_l}{\mathrm{Nu}_l}\ln\left(\frac{1-x_{vb}}{1-x_{vi}}\right)}{\exp\left[\frac{c_{pv}}{c_p}\frac{\mathrm{Sh}_l}{\mathrm{Nu}_l}\ln\left(\frac{1-x_{vb}}{1-x_{vi}}\right)\right]-1}$$

$$\theta_{tf}=\frac{1+\frac{h_{fg}}{c_p\mathrm{Le}}\frac{x_{vb}-x_{vi}}{T_b-T_i}\frac{\mathrm{Sh}_l}{\mathrm{Nu}_l}}{1+\frac{h_{fg}}{c_p\mathrm{Le}}\left.\frac{dF}{dT}\right|_{T_i}} \tag{B3}$$

where $\mathrm{Sh}_l/\mathrm{Nu}_l=\mathrm{Le}^{0.35}$, and $F(T)=P_v(T)/P_t$ represents the saturation line of water vapor and an error in the denominator of θ_t has been corrected with respect to the analysis given by Brouwers [22];

7. Calculate the liquid-side heat transfer coefficient with $h_f=k_f/\delta_f$; δ_f is evaluated from the Nusselt film condensation theory

$$\delta_f=\left(\frac{3\upsilon_f\Gamma}{(\rho_f-\rho_g)g}\right)^{1/3} \tag{B4}$$

8. Update the interfacial temperature using

$$(T_b-T_i)(h_c+h_s)=(T_b-T_w)h_t=(T_b-T_w)\Big/\left(\frac{1}{h_c+h_s}+\frac{1}{h_f}\right) \tag{B5}$$

9. Calculate the vapor partial pressure at the interface assuming the interfacial temperature equal to the vapor saturation temperature; update the interfacial gas molar fraction x_{gi} using $x_{gi}=1-P_i/P_t$; and
10. If x_{gi} converges by some predefined criterion, store results and go to Step 2 for the next node. Otherwise, go to Step 3 and repeat until x_{gi} converges.

References

[1] Colburn, A. P., and Hougen, O. A., 1934, "Design of Cooler Condensers From Mixtures of Vapours With Noncondensing Gases," Ind. Eng. Chem., **26**, pp. 1178–1182.
[2] Peterson, P. F., Schrock, V. E., and Kageyama, T., 1993, "Diffusion Layer Theory for Turbulent Vapor Condensation With Noncondensable Gases," ASME J. Heat Transfer, **115**, pp. 998–1003.
[3] Kageyama, T., Peterson, P. F., and Schrock, V. E., 1994, "Diffusion Layer Modeling for Condensation in Vertical Tubes With Noncondensable Gases," Nucl. Eng. Des., **149**, pp. 313–321.
[4] Herranz, L. E., Munoz-Cobo, J. L., and Verdu, G., 1997, "Heat Transfer Modeling in the Vertical Tubes of the Passive Containment Cooling System of the Simplified Boiling Water Reactor," Nucl. Eng. Des., **178**, pp. 29–44.
[5] Vierow, K. M., 1990, "Behavior of Steam-Air Systems in Cocurrent Vertical Downflow," M.S. thesis, University of California, Berkeley, CA.

[6] Siddique, M., 1992, "The Effects of Noncondensable Gases on Steam Condensation Under Forced Convection Conditions," Ph.D. thesis, Massachusetts Institute of Technology, Cambridge, MA.
[7] Brouwers, H. J., 1996, "Effect of Fog Formation on Turbulent Vapor Condensation With Noncondensable Gases," ASME J. Heat Transfer, **118**, pp. 243–245.
[8] Ghiaasiaan, S. M., and Eghbali, D. A., 1997, "On Modeling of Turbulent Vapor Condensation With Noncondensable Gases," ASME J. Heat Transfer, **119**, pp. 373–376.
[9] Rohsenow, W. M., and Choi, H. Y., 1961. *Heat, Mass and Momentum Transfer*, Prentice–Hall, Englewood Cliffs, NJ.
[10] Kays, M. K., and Crawford, M. E., 1993, *Convective Heat and Mass Transfer*, 3rd ed., McGraw–Hill, New York.
[11] Sparrow, E. M., and Lin, S. H., 1964, "Condensation Heat Transfer in the Presence of Noncondensable Gas," ASME J. Heat Transfer, **86**, pp. 430–436.
[12] Minkowycz, W. J., and Sparrow, E. M., 1974, "Local Nonsimilar Solutions for Natural Convection on a Vertical Cylinder," ASME J. Heat Transfer, **96**, pp. 178–183.
[13] Ambrosini, W., Forgione, N., Manfredini, A., and Oriolo, F., 2006, "On Various Forms of the Heat and Mass Transfer Analogy: Discussion and Application to Condensation Experiments," Nucl. Eng. Des., **236**, pp. 1013–1027.
[14] Peterson, P. F., 2000, "Diffusion Layer Modeling for Condensation With Multicomponent Noncondensable Gases," ASME J. Heat Transfer, **122**, pp. 716–720.
[15] Mills, A. F., 1999, *Basic Heat and Mass Transfer*, 2nd ed., Prentice–Hall, Englewood Cliffs, NJ.
[16] Hirschfelder, J. O., Curtiss, C. F., and Bird, R. B., 1954, *Molecular Theory of Gases and Liquids*, Wiley, New York.
[17] Kuhn, S. Z., 1995, "Investigation of Heat Transfer From Condensing Steam-Gas Mixtures and Turbulent Films Flowing Downward Inside a Vertical Tube," Ph.D. thesis, University of California, Berkeley, CA.
[18] Brouwers, H. J., 1992, "A Film Model for Heat and Mass Transfer With Fog Formation," Chem. Eng. Sci., **47**, pp. 3023–3036.
[19] Miyara, A., 2001, "Flow Dynamics and Heat Transfer of Wavy Condensate Film," ASME J. Heat Transfer, **123**, pp. 492–500.
[20] Wang, C., and Chen, C., 2002, "Combined Free and Forced Convection Film Condensation on a Finite-Size Horizontal Wavy Plate," ASME J. Heat Transfer, **124**, pp. 573–576.
[21] Corradini, M. L., 1984, "Turbulent Condensation on a Cold Wall in the Presence of a Noncondensable Gas," Nucl. Technol., **64**, pp. 186–195.
[22] Brouwers, H. J., 1991, "An Improved Tangency Condition for Fog Formation in Cooler-Condensers," Int. J. Heat Mass Transfer, **34**, pp. 2387–2394.

Heat Transfer Enhancement of Steam Reformation by Passive Flow Disturbance Inside the Catalyst Bed

Paul Anders Erickson
e-mail: paerickson@ucdavis.edu

Chang-Hsien Liao

Mechanical and Aeronautical Engineering Department,
University of California, Davis,
One Shield Avenue,
Davis, CA 95616

Because of the potential for high efficiency and low emissions, hydrogen powered systems are considered to be the next generation power source for both stationary and transportation applications. Providing a hydrogen source is a critical challenge. Steam reforming processes are demonstrated for producing hydrogen for fuel cell and other applications. Generating hydrogen via steam reformation requires that heat energy be transferred to the reactants to support the endothermic reaction. For a cylindrical steam-reforming reactor, large thermal gradients between the heat source (reactor wall) and reactor centerline create a nonideal condition for complete conversion. This gradient is caused by insufficient heat transfer inside the catalyst bed. Passive flow disturbance inside the catalyst bed is a potential method to enhance the heat and mass transfer in the steam-reforming process. This paper presents experimental research that investigates the effect of changing the flow pathway inside the reactor to improve the heat and mass transfer and thus enhance fuel conversion. Based on the experimental results, a 14% increase of methanol fuel conversion was achieved via the passive flow disturbance enhancement. The tradeoff was an extra pressure drop of 2.5 kPa across the reactor. A 30 h experimental run does not show a significant change in degradation rate for the passive flow disturbance. The results of this study contribute to the improvement of reformer design for better fuel processing system performance. [DOI: 10.1115/1.2728906]

Keywords: hydrogen, methanol, reformer, flowpath

Introduction

Hydrogen fuel cells have attracted attention because of the potential for high energy efficiency and eco-friendly emissions. In transportation applications, fuel cells are also considered as a candidate to replace the conventional internal combustion engine. Providing a hydrogen source for fuel cells is a critical challenge. Steam reformation, partial oxidation, and autothermal reformation are three general fuel processing methods studied for generating hydrogen. Each processing pathway has its advantages and disadvantages, and has been widely discussed [1,2]. The overall fuel processing system's long startup and shutdown time due to the warmup and cooldown periods [3] are also issues that need to be addressed. In existing prototype vehicle designs, steam reformation is the most widely used fuel processor in generating hydrogen-rich gas. In stationary hydrogen generating facilities, steam reforming is also the most often used process because of a high H_2 concentration in the output gas and lower required temperatures with the aid of catalysts. Since steam reformation is an endothermic reaction, as demonstrated in catalytic converters [4,5], the corresponding response time, size, temperature gradient inside the catalyst bed, and the fuel conversion are all used to determine the efficiency or performance of the steam reformer. Methane, methanol, ethanol, and gasoline are common fuels to investigate in a steam-reforming process. In this study, methanol fuel was used. For theoretical stoichiometric methanol steam reformation, 75% of hydrogen concentration can be achieved for the dry gas. In practice, extra water is usually used to prevent coking in the reformation process.

Current practice in stationary hydrogen production is to use multiple fixed bed tubes as the chemical reactor for steam reformation. The common size of a single tube is 10.16 cm i.d. and 1140 cm length, filled with reforming catalyst with no other obstruction (communication with Air Products and Chemicals Inc., 2006). This study utilizes devices known as "bluff" or "blunt" bodies to create a passive flow disturbance inside a catalyst bed to increase the overall efficiency of a methanol-steam reformer. Even though this strategy is a well known enhancement in the heat transfer field, the application in a fixed-bed cylindrical hydrogen producing reactor has not been performed previously. It is shown that via this methodology, the overall efficiency in producing hydrogen for steam reformers can be improved. The penalty of this enhancement strategy results in higher pressure drop in the system.

Limiting Steps in the Reformation Process

An ideal reforming system should have characteristics of high reforming capacity, short transient response time, and long catalyst lifetime. These characteristics are largely affected by the flow rate of reactants, heat transfer rate, diffusion or mass transport, chemical kinetics, and the catalyst degradation rate.

Due to the endothermic nature of the reaction, a catalytic steam reformer requires that heat energy be transferred from an external heat source to the reaction site. Equation (1) presents the overall methanol steam-reforming reaction

Contributed by the Heat Transfer Division of ASME for publication in the JOURNAL OF HEAT TRANSFER. Manuscript received January 11, 2006; final manuscript received October 6, 2006. Review conducted by Minking Chyu. Paper presented at the 2005 ASME Heat Transfer Summer Conference (HT2005), San Francisco, CA, USA, July 15–22, 2005.

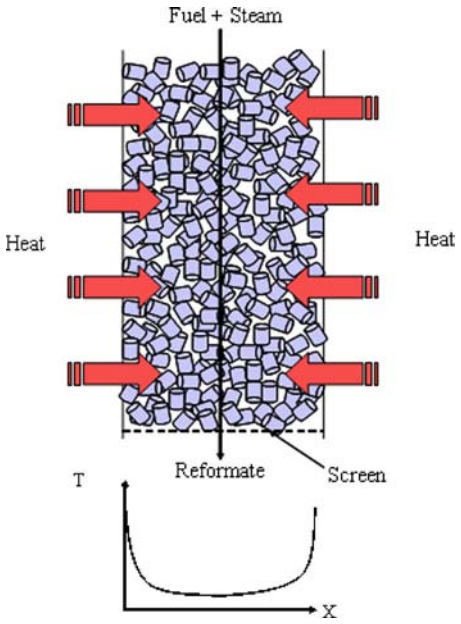

Fig. 1 Simplified schematic of heat conducting into a nonobstructed cylindrical catalyst bed and a typical temperature profile in the radial direction

$$CH_3OH_{(g)} + H_2O_{(g)} \xrightarrow{\text{catalyst}} 3H_2 + CO_2 \quad (\Delta h = +49 \text{ kJ/mol}) \quad (1)$$

There are three modes of heat transfer available including radiation, conduction, and convection. Due to the relatively low local temperature difference, radiation is usually negligible. In a packed-bed cylindrical reformer, as shown in Fig. 1, heat conduction from the external heat source is limited by the point-to-point contact between the catalyst pellets, while conduction can be more significant at the catalyst bed-housing wall. The small contacting area limits the heat conduction within the catalyst bed. Therefore, heat is mainly transferred via bulk fluid convection.

Due to an irregular packing configuration and the endothermic nature of the steam-reforming process, a cylindrical packed-bed reactor typically suffers in a severe nonisothermal environment [6]. This large thermal gradient inside the catalyst bed results in a nonideal condition for steam reformation, thus lowering fuel conversion. It also increases the risk of catalyst degradation due to the uneven temperature distribution. Some numerical analyses and models of the heat transfer phenomenon inside cylindrical packed beds have been carried out [7–9]. The poor convective heat transfer inside the catalyst bed limits a steam reformer's performance. Increasing the size of the reformer for a larger convection area can enhance the heat transfer. However, a large volume reformer represents a higher capital investment and is not ideal for transportation applications.

Aside from the heat transfer limitation, the mass transfer limitation also can affect the overall reformer performance. Figure 2 represents the overall steps with this diffusion process.

Typically these steps can be classified into three categories including external diffusion (Steps 1 and 7), internal diffusion (Steps 2 and 6), and surface reaction (Steps 3–5). The surface reaction rate is governed by the chemical kinetics shown in Eq. (2)

$$\frac{d[CH_3OH]}{dt} = -k_f \cdot [H_2O] \cdot [CH_3OH] \quad (2)$$

$[CH_3OH]$, $[H_2O]$, and k_f are the concentrations of methanol, water, and the reaction rate constant, respectively. Based on the Arrhenius mechanism, the reaction rate constant can be expressed as an exponential function of the reacting temperature T

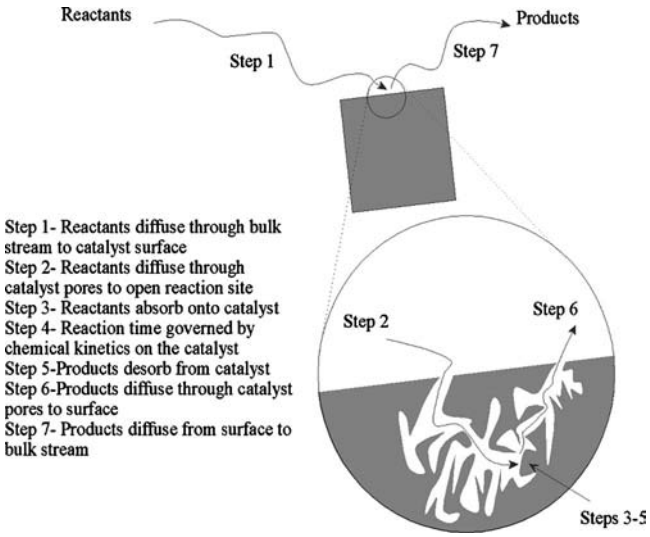

Fig. 2 Steps required within the catalytic steam-reformation process [6]

$$k_f(T) = a \cdot \exp(-E_a/R_u T) \quad (3)$$

Coefficient "a" is a constant designated as a preexponential factor with units of $[\text{mol}/(\text{s kg bar})]$. E_a is the activation energy, and R_u is the universal gas constant.

The diffusion (mass transfer) rate depends on three factors: velocity, particle size, and temperature. Table 1 summarizes the dependence of different limitations on these three factors.

From Table 1, one can see that temperature has a strong effect on the two diffusion limitations and the surface reaction (exponential dependence). Therefore, elevating temperature can effectively reduce the diffusion limitations. Table 1 also shows that particle diameter has an inverse relationship to both external and internal diffusion. Reducing the particle size by crushing the catalyst pellet can shorten the diffusion time between bulk stream and open catalyst sites. This method can effectively increase the overall active area without having to increase the reactor's size.

Compensation for the diffusion limitation can also be achieved by increasing the amount of catalyst. Increasing the catalyst amount is equivalent to decreasing the flow rate or space velocity. The definition of space velocity is shown in Eq. (4)

$$\text{space velocity} = \frac{\text{volumetric flow rate}}{\text{reactor volume}} \quad (4)$$

Table 1 indicates that reducing the space velocity decreases the external diffusion rate. It is also undesirable in reformer design since that would decrease the reforming capacity for a specified reformer volume or require a larger reforming processor. Past studies have shown that space velocity plays an important role in reformation systems [11–13]. However, a previous study showed that space velocity is not sufficient to characterize reformer system performance [14]. A recent study has also demonstrated that the reactor geometry (the aspect ratio of a cylindrical type reactor) also has large effects on fuel conversion in reformation [15].

Table 1 Diffusion rate dependence on factors[a]

	Variation of reaction rate with:		
Type of limitation	Velocity	Particle size	Temperature
External diffusion	$U^{1/2}$	$(d_p)^{-3/2}$	~ Linear
Internal diffusion	Independent	$(d_p)^{-1}$	Exponential
Surface reaction	Independent	Independent	Exponential

[a]See Ref. [10].

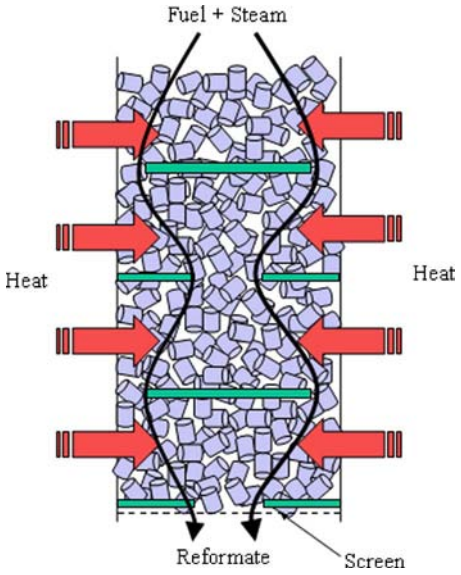

Fig. 3 Schematic of catalyst bed obstructed with two packages of bluff bodies

As deduced from the above discussions, elevating the overall temperature to a proper level could minimize the limiting influences in a reformation process. But as a severe temperature gradient usually exists within the catalyst bed, the reactor cannot be brought up to proper temperature at all locations because of overheating the catalyst near the heat source. Several options have been introduced to improve heat transfer of an internal flow within a pipe. These options include placing coil springs, swirl tape, longitudinal fins, and helical ribs inside the tube [16]. For a steam-reforming reactor, some previous studies have reported to enhance the heat transfer in an endothermic reformation reaction [6,17]. In a previous study [6], applying an acoustic field inside a fixed bed can raise the average conversion by up to 4% over the nonoscillating cases for the flow rate of 2.0 liquid hourly space velocity of methanol (LHSV-M). Another study [17] shows that using an internal corrugated metal heater supported with catalyst evens out the temperature in the reaction region. The study presented in this paper is another method to enhance the reforming process.

Mechanisms of Enhancement by Introducing Flow Obstruction

The enhancement method presented in this study was enabled by placing bluff body packages inside the catalyst bed. One bluff body package was composed of a thin disk and a thin ring. A simple schematic of two bluff body packages inside a catalyst bed is shown in Fig. 3. Three possible mechanisms by which these bluff or blunt bodies might enhance the entire reforming process are as follows:

1. Enhancing heat transfer via conduction and convection;
2. Enhancing mass transfer by increasing the effective path length; and
3. Flow disturbance (i.e., redirected channeling).

Enhancing Heat Transfer via Conduction and Convection. The main heat transfer mode inside the catalyst bed is convection, which can be expressed as Eq. (5)

$$Q = h \cdot A \cdot \Delta T \tag{5}$$

Without bluff body rings, A in Eq. (5) is the internal wall area inside the pipe. In Fig. 3, the two bluff body rings act as two radial fins. Aside from enabling the heat conduction from the heated wall into the cold center region, these fins also increase the convection area A in Eq. (5). By increasing the number of rings, the heat transfer is also expected to increase. Some empirical studies indicate that the Nusselt number in a packed bed has a positive exponent correlation with Reynolds number (Re) [9,18]. Because the Nusselt number (Nu_D) is the ratio of the convection coefficient (h) and characteristic diameter (D) to the conductivity (k) of the fluid, it can be expressed as Eq. (6)

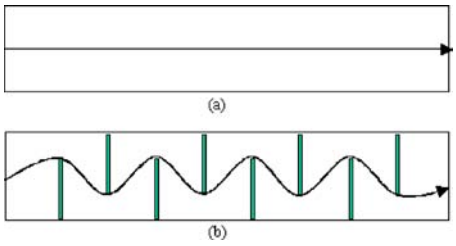

Fig. 4 Scheme of minimum path length inside: (*a*) nonobstructed reactor; and (*b*) reactor with bluff bodies

$$\mathrm{Nu}_D = \frac{h \cdot D}{k} \propto \mathrm{Re}_D^X \tag{6}$$

X is a positive value and Reynolds number is proportional to the stream velocity. Without changing D and k, the convection coefficient, h, is a velocity based function. Increasing the local velocity can effectively increase the local convection rate coefficient. As shown in Fig. 4, the minimum stream line in a nonobstructed reactor (a) is shorter than the minimum stream line in the equivalently sized obstructed reactor (b). Under a fixed space velocity condition, the local speed in a bluff body-filled reactor is larger than the local speed in a nonobstructed reactor. Therefore, introducing bluff bodies must raise the local velocity increasing the convective heat transfer rate coefficient shown in Eq. (5),

Increasing Effective Path Length in Reactor

Single Catalyst Particle. At the boundary surface of a catalyst particle, the molar flux of species A, (W_A), of a first-order reaction equals the rate of reaction on the surface ($-r''_{\mathrm{As}}$) in steady state and can be written as Eq. (7) [10]

$$W_A = -r''_{\mathrm{As}} = \frac{k_c k_f C_A}{k_c + k_f} = k_{\mathrm{eff}} C_A \tag{7}$$

where k_c is a function of temperature, pressure, velocity of fluid (V), and particle size (d_p), and k_f is independent of V but may depend on d_p for a porous catalyst. Figure 5 shows the reaction rate of a single particle as a function of particle size and local velocity flow through the particle. This figure shows that increasing the local velocity of the fluid as well as decreasing the particle diameter is expected to increase the molar flux to the surface of the catalyst (external diffusion) for diffusion limited reactions. The dimension of (V/d_p) is a reciprocal of time. As increasing the velocity or reducing the diameter of the particle, the diffusion time decreases to a minimum value and drives the overall reaction to a

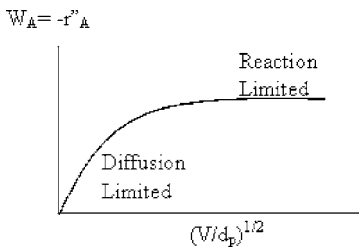

Fig. 5 Regions of mass transfer-limited and reaction-limited reactions for a single particle [10]

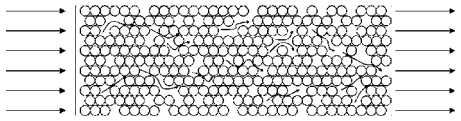

Fig. 6 Potential channeling effect inside a catalyst bed

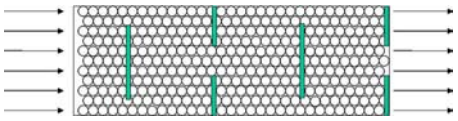

Fig. 8 Decreasing channeling effect by introducing flow obstruction

reaction-limited regime. As seen in the figure, it is preferable to operate the system toward a reaction-limited regime so that a maximum reaction rate can be achieved. Tonkovich's data [19] show that an intrinsic contact time for 25 ms is enough to achieve 99% conversion in a water gas shift microchannel reactor. However, a conventional reactor needs about 3–9 s because of heat and mass transfer. The difference between millisecond and second time scales indicates that a conventional system still has room to improve if one can remove the limitations. Introducing a bluff or blunt body can increase the local velocity without increasing the space velocity, which can result in reducing the heat and mass transfer limitations as well as improving the chemical kinetics by allowing higher temperatures.

Packed Bed. For the case when mass transfer (diffusion) is the limiting reaction, using a steady-state mole balance, reactant conversion (X) has a logarithmic dependence on the mass transfer coefficient (k_c), velocity (U), and the reactor length (L) as shown in Eq. (8) [10]

$$\ln \frac{1}{1-X} = \frac{k_c a_c}{U} L \tag{8}$$

Equation (8) indicates that for a constant molar average velocity U (related to space velocity), increasing the reactor length L (or the effective path length) can raise the conversion (X).

The above theory indicates the benefit of increasing the length, local velocity, and decreasing the particle diameter for a packed bed.

Flow Disturbance. For a cylindrical reactor packed with catalyst pellets, when reacting species flow through the reactor, they do not flow uniformly through the catalyst bed. On the contrary, the fluid flows through some specific channels inside the reactor, which offer less resistance resulting in a channeling effect inside the catalyst bed as shown in Fig. 6.

Consequently, some molecules spend less time flowing through these pathways than others flowing through ones with higher resistance. When the reforming reaction occurs inside a nonobstructed catalyst bed, the reformate flows away from the reaction site. Since the temperature near the outer radial region is higher than that near the centerline, the reaction rate is larger than that near the centerline. From Eq. (1), one can see how the reacting species expand in steam reformation.

As the total molar number at the product side (4 moles) is greater than that at the reactant side (2 moles), the increase in volume pushes the species flow toward the relatively colder central direction as shown in Fig. 7. This phenomenon theoretically increases the downstream velocity near the centerline and increases the channeling effect in this colder region.

Introducing ring disk obstructions inside the packed bed forces all the fluid to flow by the outer hot region near the wall and draws it back to the cold region at centerline, as shown in Fig. 8. This passive flow disturbance brings the cold centerline fluid to the hot region near the wall. In other words, it enlarges the ΔT term in Eq. (5), thus increasing the heat transfer. It also spreads out the flow more uniformly inside the packed bed thus decreasing the centerline channeling effect and gives the potential to provide better mixing of the reactants to improve mass transfer in the catalyst bed.

For a given pipe length L, a reactor with flow obstruction has a longer effective fluid pathway as compared to a nonobstructed reactor. This longer effective pathway is expected to help create a more fully developed thermal state, hence elevating the mean temperature or increasing the conversion of fuel to hydrogen.

Experimental Approach and Facility

The experimental facility was constructed at the University of California, Davis, for the research of steam reforming [15]. Figure 9 is a simplified schematic of the facility. In this reforming system, liquid premix composed of 1.5:1 water-to-methanol molar ratio was stored in a reservoir and pumped into a three-stage electric powered vaporizer via a pump. After the liquid premix had been vaporized, it was routed into a superheater to stabilize its temperature before being directed to the reactor (catalyst bed housing) for the steam-reforming reaction. Inside the reactor, bluff body obstructions were placed to disturb the reactant flow. After the endothermic steam-reforming reaction inside the catalyst bed, the reacted products could be routed into a condensing unit.

The liquid water and unreacted methanol were collected inside a trap for conversion calculation and the dry gas was introduced into a gas analyzer for concentration analysis. Reduction gas composed of nitrogen and hydrogen could be introduced into the system for the catalyst reduction procedure. Carbon dioxide gas could be purged directly before the superheater subassembly to

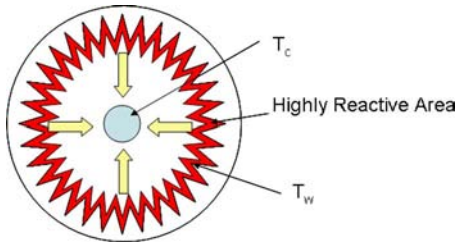

Fig. 7 Schematic of reaction in pipe cross section, $T_w > T_c$

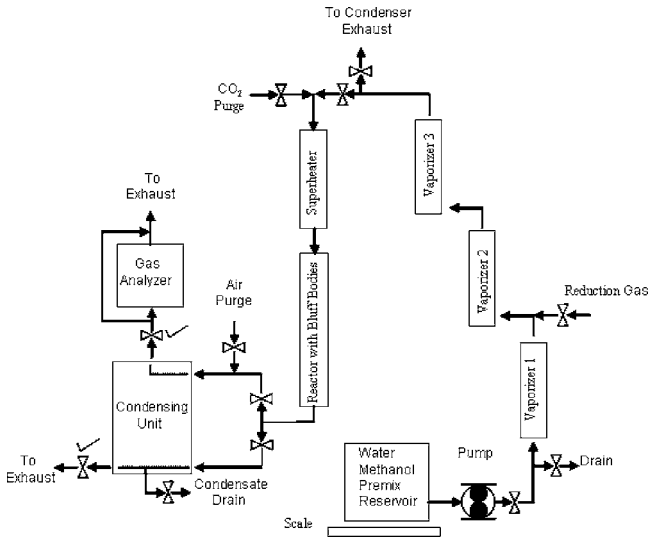

Fig. 9 General schematic of the methanol reforming system

Table 2 Kinematic viscosity (m^2/s) of species existing in a reactor

Species T °C	$CH_3OH \times 10^{-6}$	$H_2O \times 10^{-6}$	$CO_2 \times 10^{-6}$	$H_2 \times 10^{-6}$	$CO \times 10^{-6}$	$N_2 \times 10^{-6}$
250 °C	12.16	42.53	23.54	277.52	40.10	41.29

isolate the reduced catalyst from atmospheric oxygen. Directly after the reactor, an air purge unit was adapted to the analysis pathway to assure all the liquid condensate in the pipeline was collected into the trap.

The main body of the reactor is a 25.4 cm (10 in.) stainless-steel pipe (nominal 1 1/4 in. diameter, schedule 40) threaded at both ends for caps. Two caps were both machined with a 0.635 cm (0.25 in.) tube for connection to the system. At both sides of the pipe, an array of ten 0.32 cm (0.125 in.) national pipe taper threads (NPT) to 0.32 cm (0.125 in.) tube fittings were machined. These ten ports were designed for attaching ten 0.159 cm (0.0625 in.) diameter stainless-steel-sheathed, ungrounded *K*-type thermocouples to monitor the temperatures inside the catalyst bed. The reactor was divided into four zones. Four band heaters with a 3.8 cm (1.5 in.) i.d. and 3.8 cm (1.5 in.) width were used as external heating sources to heat these four zones. The four band heaters were monitored by four 0.025 cm (0.010 in.) diameter, ungrounded *K*-type thermocouples attached between the external wall and the band heaters. Highly conductive aluminum tape was wrapped between the external wall and the band heaters for better heat distribution. Inside the reactor, bluff body packages were placed in the catalyst bed to disturb the flow. The bluff body was made of 316 stainless steel with thickness of 0.06 mm (0.024 in.). One set or package of bluff bodies was composed of a ring (i.d. of 1.91 cm (3/4 in.), and o.d. of 3.47 cm (1.368 in.)) and a disk (diameter of 2.54 cm (1.000 in.)). The arrangement of two bluff body packages inside the catalyst bed was shown in Fig. 3. At the bottom of the reactor, a stainless-steel mesh (40 squares/cm^2, 0.38 mm wire diameter) was installed to support the catalyst bed.

A commercially available copper–zinc type catalyst of proprietary composition was chosen for the steam-reforming reaction in this study. The operating temperature for this catalyst was recommended at the range between 250 °C and 280 °C (482 °F–536 °F). Reduction is needed before it is used for reformation. Both as purchased pelletized and crushed catalysts were used in this study. A pelletized catalyst has a 0.47 cm (0.187 in.) diameter and 0.25 cm (0.1 in.) thickness in cylindrical shape. This pelletized catalyst was also crushed into a dimension with an average side length of 0.25 cm (0.098 in.). This catalyst is referred to as crushed catalyst in this study. These two sizes of catalyst were chosen to demonstrate the mass transfer effect as coupled with bluff body enhancement. Further study of catalyst geometry is important but beyond the scope of the present study. The mass of catalyst used was fixed at 250 g.

The methanol conversion (%) used in this study is defined in Eq. (9). As the methanol is determined on a mass basis, measuring the three parameters of premix mass, consumed, mass, and density of the condensate allows calculation of the fuel conversion

$$\mathrm{Conv}_{\cdot CH_3OH} = \frac{CH_3OH_{input} - CH_3OH_{output}}{CH_3OH_{input}} \times 100\% \tag{9}$$

LHSV-M specie was used throughout the study as the flow rate input to the reactor, as defined in Eq. (10)

$$\text{LHSV-M} = \left(\frac{m^3/h \text{ liquid methanol input}}{m^3 \text{ reactor volume}} \right) \tag{10}$$

The unit of LHSV-M is L/h. This is an alternative form of flow rate, or inverse residence time.

Results and Discussion

The experiment was carried out with a 2^3 factorial experimental design based on three independent variables of space velocity, catalyst dimension, and number of bluff bodies. Table 2 shows the kinematic viscosity of possible species existing inside the reactor at atmosphere pressure.

Based on a 1.5:1 steam to methanol molar ratio, the reactant fluid viscosity is 30.38×10^{-6} m^2/s. Defining the crushed catalyst side length (2.5 mm) as the characteristic length, the Reynolds number for unreacted fluid in this pipe is about 32, which lies in the laminar regime of pipe flow. While species do change throughout the reactor with resultant velocity and viscosity changes, this low Reynolds number implies that forced mixing due to turbulent structures would be minimized in this laminar flow regime. The drag coefficient of a laminar flow regime will also contribute to the pressure drop across the reactor.

Figures 10 and 11 show plots of methanol conversion as a function of space velocity (LHSV-M). The conversion was measured by operating experimental conditions with different numbers of bluff body packages (0–8 obstruction packages). One package represents a ring and a disk in this notation. The notations of 0*P*, 2*P* up to 8*P* in the figures represent the number of ring-disk sets for a pelletized catalyst bed. 0*C*, 2*C*, up to 8*C* represent the same meaning for a crushed catalyst bed.

In the figures above, the conversion decreases as space velocity (LHSV-M) increases. This is because for a high flow rate, more reactant enters into a reactor resulting in less reacting time for reactant, thus decreasing the fuel conversion. The conversion enhancement can be seen by increasing the number of obstructions from zero to eight bluff body packages. Based on the factorial experiment design, the conversion results show a statistical significance with a 95% confidence. Three replications were taken for each conversion data point. Pooled standard deviation (S_P, average standard deviation) Eq. (11) was calculated based on all the data collected to get the standard error Eq. (12)

$$S_P = \sqrt{\frac{\sum_i^n (S_i)^2}{n}} \tag{11}$$

where n_f is the total number of factorial points, which means the total replications of all the data (n_f=120 for total replications)

$$S_E = \frac{2 \cdot S_P}{\sqrt{n_f}} \tag{12}$$

Standard error was 0.16% in reactant conversion. Four space velocities were investigated in this study. Space velocity values were based on the gear pump's reading and confirmed by the premix mass used in each run. All the space velocities are within a small standard deviation (0.04 LHSV-M). Figure 11 shows that an increase of up to 14% conversion was achieved running with crushed catalyst at 4.2 LHSV-M with the flow obstructions.

Examining the improvement of the reformer capacity, for a given conversion of 95% or greater, the allowable space velocity increased from 1.5 h^{-1} to 2.5 h^{-1} by introducing eight packages of bluff bodies. This represents a remarkable 67% increase in hydro-

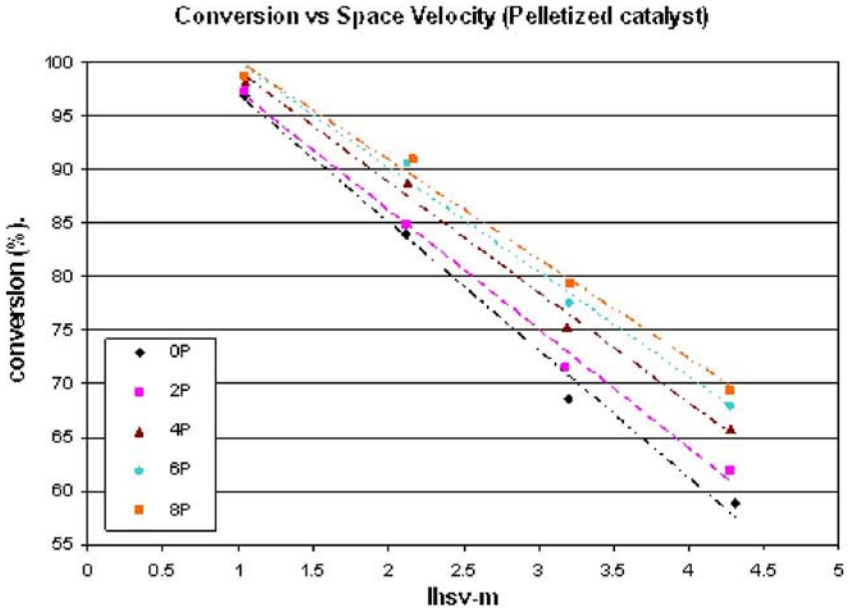

Fig. 10 Methanol conversion as a function of space velocity (lhsv m, h^{-1}) with pelletized catalyst

gen generating capacity (31.8–53.1 g/h based on actual flow rates) or similarly a reduction in reactor volume over the nonflow-obstructed case.

Comparing Figs. 10 and 11, the expected improvement of conversion with smaller particle diameter by crushing the catalyst is obvious. For a constant space velocity of 2.0 LHSV-M, the crushed catalyst reactor (8*C*) can achieve 98.66% conversion while using pelletized catalyst (8*P*) one achieves 90.89%. This enhancement shows that reducing the particle diameter effectively decreases the diffusion limitation as discussed above.

To examine the heat transfer enhancement inside the catalyst bed, the centerline temperature profiles along the axial direction inside the catalyst beds are shown in Figs. 12 and 13. Each temperature point in the figures was an average value over a 22.5 min run time at steady state. Average standard deviation was less than 1.4 °C. These temperature profiles were taken at a 2.0 h^{-1} space velocity with different numbers of bluff bodies as shown. By placing the bluff body packages within the flow, the centerline temperatures were raised. A 30 °C temperature increase was achieved at Zone 3 running six packages of bluff bodies with crushed catalyst. A step drop at Zone 1 for all experimental conditions indicates the endothermic reaction mostly took place near the upstream portion of the packed bed. Some unexpected spatial fluctuations in temperature using the higher number of bluff bodies could be a result of the placement of the ring and disk structures close to the thermocouple locations and resultant conduction to and/or away from the thermocouples. Notwithstanding, centerline temperatures are generally higher when using higher numbers of bluff bodies. Even though some locally higher temperatures were not enhanced by using the highest number (eight packages) of bluff bodies, the conversion for the eight package condition was still larger than those running at lower numbers of bluff bodies. This indicates that a longer effective path length may dominate the conversion when coupled with the temperature increase at the centerline.

From the temperature profiles and the increase in conversion, it

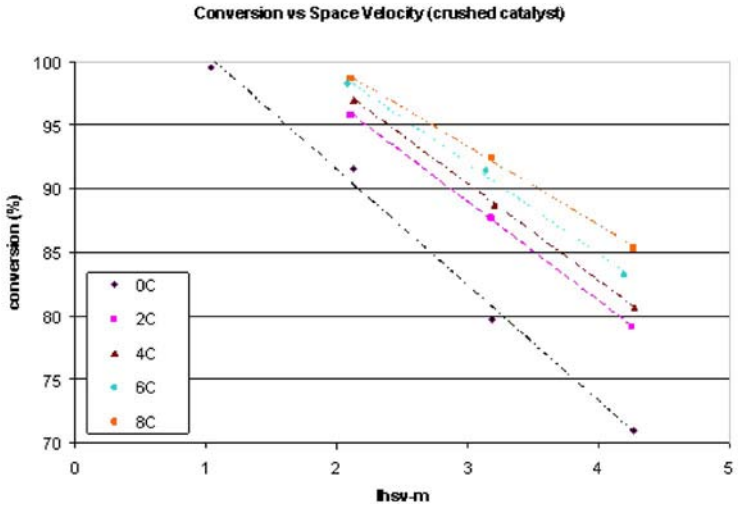

Fig. 11 Methanol conversion as a function of space velocity (lhsv m, h^{-1}) with crushed catalyst

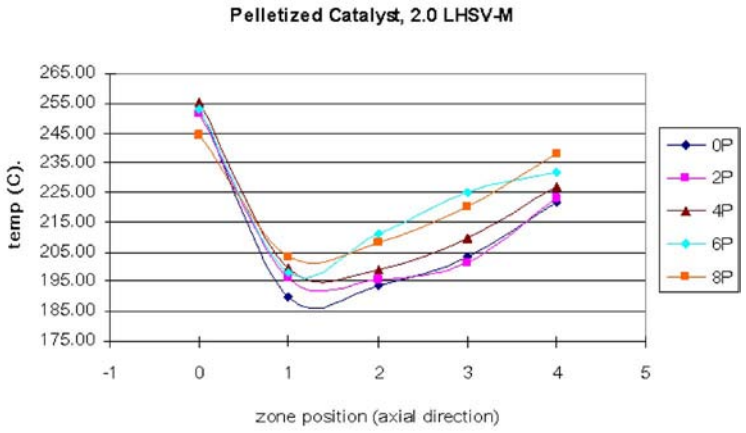

Fig. 12 Temperature profile along the axial direction inside a pelletized catalyst bed

is demonstrated that introducing flow obstruction effectively enhances the heat transfer. Due to the increase of reaction temperature, the chemical kinetics and the resultant fuel conversion is also markedly improved. Compared to the acoustic field enhancement and internal corrugated metal heater enhancement, this passive enhancing methodology has the following advantages:

1. It is simple to apply in existing conventional fixed bed steam reformers;
2. No complicated controlling device is needed to drive the acoustic field or change the heating resource system; and
3. There is a large fuel conversion increase.

A penalty of pressure drop will occur by introducing the bluff bodies inside a catalyst bed. According to the Ergun equation, Eq. (13) [10], dP/dz has a negative value. By controlling proper experimental conditions, the value at the right hand side of Eq. (13) can be fixed. Therefore the bluff body packages which elongate the effective path length (z) will build up more pressure losses inside the reactor

$$\frac{dP}{dz} = -\frac{G(1-\phi)}{\rho g_c D_P \phi^3}\left[\frac{150(1-\phi)\mu}{D_P} + 1.75G\right] \tag{13}$$

This extra pressure builtup inside the reactor represents extra power needed by the fuel pump. The pressure drop across the crushed catalyst bed with zero and eight bluff body packages was measured at different upstream pressures (corresponding to different space velocities) by purging CO_2 gas, shown in Fig. 14. With increasing space velocity, the mass flow rate, G, increases resulting in more pressure drop inside the reactor. From Fig. 14, about 1.2 kPa more pressure drop was introduced by the bluff body packages running at 2.0 LHSV-M and 2.5 kPa for 4.2 LHSV-M. Even though the fuel pump might need more power to sustain the pressure drop for the system, the energy used to raise the pressure occurs with fluid in liquid phase and is very small compared to that required for compression in gas phase. From this current experimental setup, there is no significant extra power draw increase by the gear pump. Therefore, this extra power for the liquid fuel pump is negligible.

According to a previous thermodynamic evaluation [20], higher reaction pressure will not decrease the methanol conversion when temperature is above 150 °C. However, the reaction rate does decrease under a high-pressure environment [7] because steam reformation is a reaction where the total mole number increases. When a reforming system is combined with a palladium membrane reactor to produce pure hydrogen, a higher reaction pressure can potentially increase the methanol conversion through increased hydrogen permeation [21,22]. With the system at UC Davis, the effect of pressure change on the overall efficiency has not yet been quantified.

Because introducing bluff body packages into a catalyst bed increases the catalyst usage, catalyst degradation may result. A continuously run 30 h experiment was run with and without the

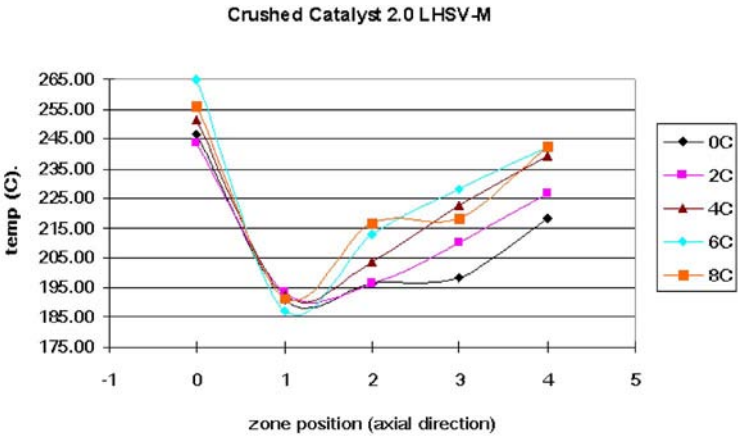

Fig. 13 Temperature profile along the axial direction inside a crushed catalyst bed

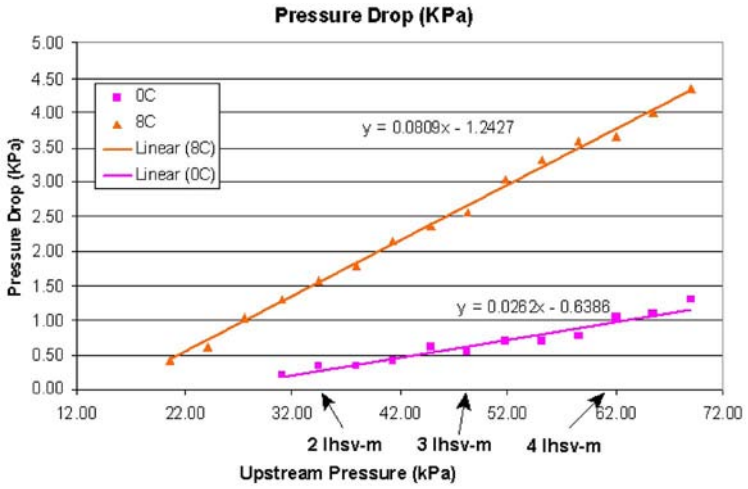

Fig. 14 Pressure drop at different upstream pressures (flow rates)

enhancement strategy to compare the degradation rates. As seen in Fig. 15, the degradation rate at 2.5 LHSV-M (slope) for the bluff body experiment (8*C*) is −0.1449 (% per hour) as compared to −0.1503 (% per hour) for the same experiment without bluff body packages (0*C*). The results show that for a 30 h experiment, no significant degradation rate change was found.

Conclusion

In this study, a preliminary test using bluff bodies to create a passive disturbance within the catalyst bed was investigated. The temperature profile and fuel conversion data prove that the flow obstruction method can significantly enhance heat transfer in a methanol-steam reformation process. The simplicity of this method and the effective results show promise for use in hydrogen generating processes. Optimization and further study of this method continues at the Hydrogen Production and Utilization Laboratory at UC Davis.

Acknowledgment

The authors would like to thank the researchers at the UC Davis Hydrogen Production and Utilization Laboratory for supporting this work. This research project was partially funded by the U.S. Dept. of Energy under DOE Grant No. DE-PS26-02NT41613-06. The views and opinions of authors expressed herein do not necessarily state or reflect those of the United States Government or any agency thereof.

Nomenclature

A = heat transfer surface area
C_A = concentration of species A
D = characteristic diameter
D_p = diameter of particle
E_a = activation energy
G = superficial mass velocity
L = reactor length

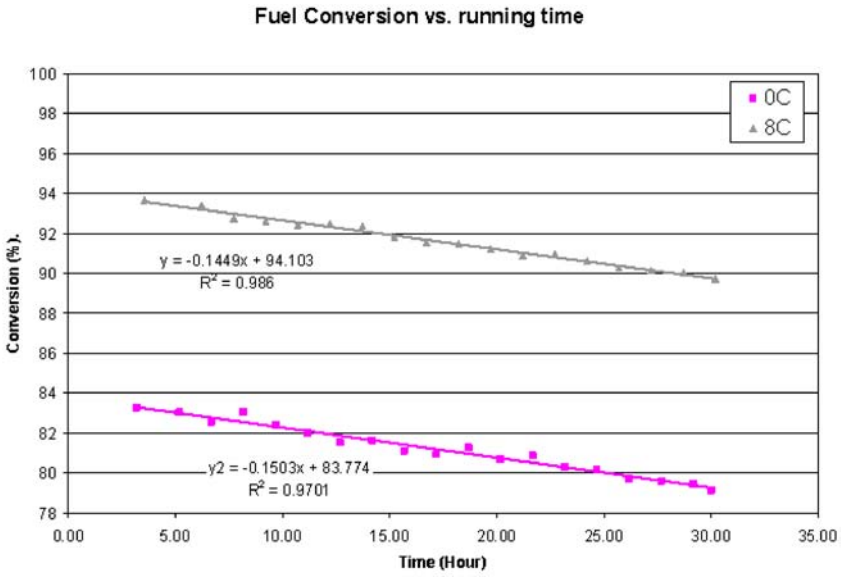

Fig. 15 Catalyst degradation rate comparison of crushed catalyst bed with eight sets of bluff body and without bluff body

Nu = Nusselt number
Q = heat transfer rate
Re = Reynolds number
R_u = universal gas constant
T = temperature
U = superficial velocity
V = velocity of fluid
W_A = molar flux of species A
X = reactant conversion
a = preexponential coefficient
a_c = external surface area of catalyst per volume of catalytic bed, (m^2/m^3) $a_c=6(1-\Phi)/d_p$, is inversely proportional to particle diameter
d_p = catalyst diameter
dP = $P_{out}-P_{in}<0$
g_c = conversion factor=1.0
h = heat transfer coefficient
k = thermal conductivity of fluid
k_c = mass transfer coefficient, analogous to heat transfer coefficient "h"
k_{eff} = effective transport coefficient x positive exponential value
k_f = reaction rate constant
r''_{As} = rate of reaction on the surface
z = length down the packed bed of pipe
μ = viscosity of gas passing through the bed
ρ = gas density
ϕ = porosity; volume of solid/total bed volume

References

[1] Docter, A., and Lamm, A., 1999, "Gasoline Fuel Cell Systems," J. Power Sources, **84**, pp. 194–200.
[2] Joensen, F., and Rostrup-Nielsen, J. R., 2002, "Conversion of Hydrocarbons and Alcohols for Fuel Cells," J. Power Sources, **105**(2), pp. 195–201.
[3] Simmons, T. C., Erickson, P. A., Heckwolf, M. J., and Roan, V. P., 2002, "The Effects of Start-up and Shutdown of a Fuel Cell Transit Bus on the Drive Cycle," SAE Technical Paper Series, Paper No. 2002-01-0101.
[4] Ledjeff-Hey, K., Formanski, V., Kalk, T., and Roes, J., 1998, "Compact Hydrogen Production Systems for Solid Polymer Fuel Cells," J. Power Sources, **71**, pp. 199–207.
[5] Peppley, B. A., Amphlett, J. C., Kearns, L. M., Mann, R. F., and Roberge, P. R., 1997, "Hydrogen Generation for Fuel Cell Power Systems by High-Pressure Catalytic Methanol-Steam Reforming," *Proceedings of the Intersociety Energy Conversion Engineering Conference*, Honolulu, July 27-August 1, Paper No. IECEC 97093.
[6] Erickson, P. A., and Roan, V., 2003, "Enhancing Hydrogen Production for Fuel Cell Vehicles by Superposition of Acoustic Fields on the Reformer: A Preliminary Study," SAE Technical Paper Series, Paper No. 2003-01-0806.
[7] Nakagaki, T., Ogawa, T., Murata, K., and Nakata, Y., 2001, "Development of Methanol Steam Reformer for Chemical Recuperation," ASME J. Eng. Gas Turbines Power, **123**, pp. 727–733.
[8] Usami, Y., Fukusako, S., and Yamada, M., 2003, "Heat and Mass Transfer in a Reforming Catalyst Bed: Analytical Prediction of Distributions in the Catalyst Bed," Heat Transfer Asian Res., **32**(4), pp. 367–380.
[9] Wakao, N., and Kaguei, S., 1982, *Heat and Mass Transfer in Packed Beds*, Gordon and Breach Science, New York, p. 161.
[10] Fogler, H. S., 1999, *Elements of Chemical Reaction Engineering*, 3rd ed., Prentice–Hall ECS Professional, Upper Saddle River, NJ, p. 768.
[11] Zhang, X. R., Shi, P., Zhao, J., Zhao, M., and Liu, C., 2003, "Production of Hydrogen for Fuel Cells by Steam Reforming of Methanol on $Cu/ZrO_2/Al_2O_3$ Catalyst," Fuel Process. Technol., **83**, pp. 183–192.
[12] Sapre, A. V., 1997, "Catalyst Deactivation Kinetics From Space-Velocity Experiments," Chem. Eng. Sci., **52**(24), pp. 4615–4623.
[13] Takeda, K., Baba, A., Hishinuma, Y., and Chikahisa, T., 2002, "Performance of a Methanol Reforming System for a Fuel Cell Powered Vehicle and System Evaluation of a PEFC System," JSAE Rev., **23**(2), pp. 183–188.
[14] Erickson, P. A., 2002, "Enhancing the Steam-Reforming Process With Acoustics: An Investigation for Fuel Cell Vehicle Application," Ph.D. dissertation, University of Florida, Gainesville, FL.
[15] Davieau, D. D., 2004, "An Analysis of Space Velocity and Aspect Ratio Parameters in Steam-Reforming Hydrogen Production Reactors," M.S. thesis, University of California, Davis, CA.
[16] DeWitt, D. P., 2001, *Introduction to Heat Transfer*, 4th ed., Wiley, New York, p. 447.
[17] Nagano, S., Miyagawa, H., Azegami, O., and Oshawa, K., 2001, "Heat Transfer Enhancement in Methanol Steam Reforming for a Fuel Cell," Energy Convers. Manage., **42**, pp. 1817–1829.
[18] Li, C. H., and Finlayson, B. A., 1977, "Heat Transfer in Packed Beds," Chem. Eng. Sci., **32**(9), pp. 1055–1066.
[19] Tonkivich, A. Y., Zilka, J. L., LaMont, M. J., Wang, J., and Wegeng, R. S., 1999, "Microchannel Reactors for Fuel Processing Applications I. Water Gas Shift Reactor," Chem. Eng. Sci., **54**, pp. 2947–2951.
[20] Faungnawakij, K., Kikuchi, R., and Eguchi, K., 2006, "Thermodynamic Evaluation of Methanol Steam Reformation for Hydrogen Production," J. Power Sources, in press.
[21] Gallucci, F., and Basile, A., 2006, "Co-current and Counter-Current Modes for Methanol Steam Reforming Membrane Reactor," Int. J. Hydrogen Energy, in press.
[22] Lin, Y.-M., and Rei, M.-H., 2001, "Study on the Hydrogen Production From Methanol Steam Reforming in Supported Palladium Membrane Reactor," Catal. Today, **67**, pp. 77–84.

The Effect of Compressive Load on Proton Exchange Membrane Fuel Cell Stack Performance and Behavior

N. Fekrazad

T. L. Bergman[1]
e-mail: tberg@engr.uconn.edu

Department of Mechanical Engineering,
Connecticut Global Fuel Cell Center,
University of Connecticut,
191 Auditorium Road,
Unit 3139,
Storrs, CT 06269

A two-dimensional model of a proton exchange membrane fuel cell stack is developed. Taking advantage of the geometrical periodicity of the stack, the model is used to predict the detailed thermal and electrochemical characteristics of the fuel cell. Using recently reported as well as new experimental results, the electrical and thermal contact resistances and modifications in the gas diffusion layer transport properties that develop within the stack in response to changes in the compressive force used to assemble the stack are accounted for. The fuel cell stack performance, reported in terms of its power output and internal temperature distributions, is very sensitive to the compressive load. [DOI: 10.1115/1.2728909]

Keywords: fuel cell, PEM fuel cell, contact resistance

Introduction

Several models of proton exchange membrane (PEM) fuel cells have been developed. Initially, the models described one-dimensional behavior for a single fuel cell membrane, and include the classic studies of Springer et al. [1] and Bernardi and Vebrugge [2]. Two- and three-dimensional models, such as those of Zhou and Liu [3] and Siegel et al. [4] followed. In general, model predictions reported in the literature examine the effects of various operating conditions on the fuel cell power output [5].

Recent experimentally determined values of contact resistances that evolve at the interface between the gas diffusion layer (GDL) and bipolar plate material [6,7] now permit the development of models that can be used to quantify the influence of the compressive forces used in the final assembly of a fuel cell stack. These effects, in terms of fuel cell performance, have been discussed to a limited degree [8,9]. Birgersson et al. [10] mention the influence of different compressive loads in their recently reported model predictions, but the influence on fuel cell stack performance and behavior was not considered in any detail.

In this study, a fuel cell stack's power output, maximum temperatures that develop within the stack membranes, and maximum temperature differences within the membranes, are predicted as a function of the compressive forces applied to the stack. Changes in the stack power output in response to varying the stack compressive load is of obvious importance. However, less frequently discussed is the notion that large local temperatures or spatial temperature gradients may also affect the durability of the membrane material and, in turn, the cost of the fuel cell stack [11]. A combined computational and experimental approach is taken.

Mathematical Model

The model takes advantage of the repetition in the geometrical structure that is inherent in most fuel cell stacks. A stack, shown schematically in Fig. 1(*a*), arbitrarily consists of five single cells and six current collector (bipolar) plates. In the interior regions of the stack, the structure of individual fuel cells repeats in the horizontal direction, and a cross-sectional view of a repeating element is highlighted by the control volume of Fig. 1(*a*).

An expanded view of the control volume of Fig. 1(*a*) is presented in Fig. 1(*b*). For fuel and oxidant flow channels that are arranged unidirectionally, geometrical repetition also occurs in the vertical direction, and a magnification of the dashed control volume of Fig. 1(*b*) (that extends from the centerline of a flow channel to the centerline of a land) is shown in Fig. 1(*c*). Finally, the membrane electrode assembly (MEA) and GDL structure within the dashed control volume of Fig. 1(*c*) is magnified and presented in Fig. 1(*d*). Nomenclature associated with relevant dimensions is included.

The computational domain utilized in this study is represented by the outermost solid lines of Fig. 1(*c*). With specification of appropriate boundary conditions, the predicted behavior for this domain may be scaled to the entire interior regions of the fuel cell stack of Fig. 1(*a*). Obviously, this modeling approach cannot be applied to stacks that have three-dimensional behavior, as would be the case if the anode- and cathode-side flow channels were arranged in an orthogonal manner.

The water vapor-saturated hydrogen that is fed to the anode side of each MEA is transferred through the GDL on the upper left-hand side (LHS) of Fig. 1(*d*) in the region marked "anode channel." Within the anode-side catalyst layer, hydrogen is decomposed into electrons and protons via an electrochemical reaction. The electrons flow through an external circuit (not shown), providing electrical power. Meanwhile, protons migrate through the membrane toward the cathode side, right-hand side (RHS), of the single cell. The oxygen contained in the air that is carried in the cathode gas stream (in the region marked "cathode channel") is transferred through the GDL to the RHS catalyst layer, and combines with the protons and electrons to form liquid water.

Several assumptions are made beyond those pertaining to the stack geometry. Steady-state behavior is assumed, while the air and hydrogen are both considered to be ideal gases, fully saturated with water vapor. Flow is assumed to be laminar everywhere because of the small physical dimensions of the gas channels. The membrane is assumed to be fully saturated with liquid water, therefore, its ionic conductivity is a function only of temperature. Water is assumed to exist in the liquid and vapor phases within the MEA, and in the vapor phase within other regions of the computational domain (excluding, of course, within the impermeable

[1]Corresponding author.

Contributed by the Heat Transfer Division of ASME for publication in the JOURNAL OF HEAT TRANSFER. Manuscript received May 25, 2006; final manuscript received October 24, 2006. Review conducted by Ben Q. Li.

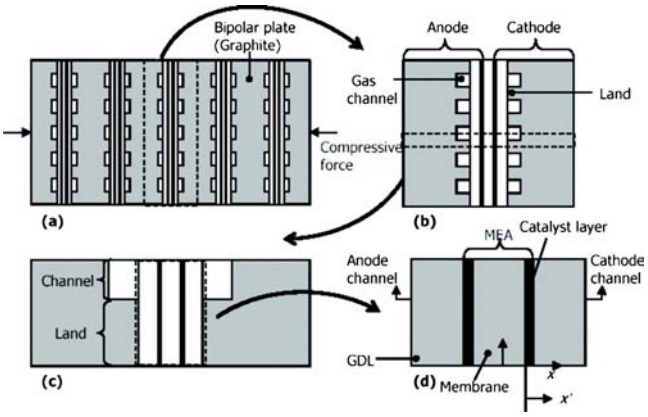

Fig. 1 Schematic diagram of: (*a*) a fuel cell stack; (*b*) a single cell within the stack; (*c*) the computational domain; and (*d*) geometric parameters of the fuel cell elements

bipolar plates). The proton concentration within the membrane is assumed to be constant, and equal to the concentration of sulfonic acid groups, which is taken as $c_f = 1200\ \text{mole/m}^3$ for Nafion [2,12]. Properties are assumed to be constant except as noted. Despite the simplifications associated with not modeling the detailed evaporation and condensation and dropwise two-phase flow, the model is capable of predicting the influence of the compressive force on the fuel cell power output, as will become evident.

Governing equations and boundary conditions may be written for the various regions of the computational domain, shown in more detail in Fig. 2.

Bipolar Plates. The thermal energy equation applied to the bipolar plate is

$$k_B\left(\frac{\partial^2 T_B}{\partial x^2}+\frac{\partial^2 T_B}{\partial y^2}\right)=0 \tag{1}$$

The potential equation represents the transport of electrons and is

$$\kappa_B\left(\frac{\partial^2 \varphi_s}{\partial x^2}+\frac{\partial^2 \varphi_s}{\partial y^2}\right)=0 \tag{2}$$

Gas Diffusion Layers. Hydrogen, water vapor, and the oxygen (contained in the air) enter the MEA through the GDLs. The GDLs also form the electrical contact between the two catalyst layers and the bipolar plates. Expressions for the conservation of mass, momentum, thermal energy, chemical species, and electronic charge are therefore applied. The conservation of mass equation is

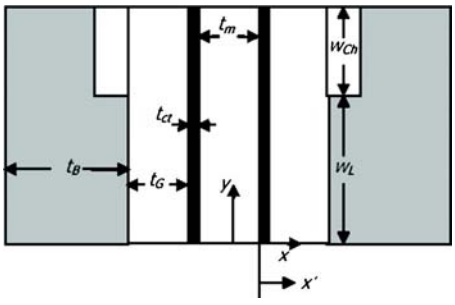

Fig. 2 Computational domain and definition of geometrical parameters

$$\frac{\partial}{\partial x}(\rho u)+\frac{\partial}{\partial y}(\rho v)=0 \tag{3}$$

The density of the fluid is calculated as a function of the local temperature, pressure, and species concentrations. The momentum equation for fluid flow through the porous GDLs is described by Darcy's equation [2], where u and v are superficial (apparent) velocity components

$$u=-\frac{K_p}{\mu}\frac{\partial P}{\partial x},\quad v=-\frac{K_p}{\mu}\frac{\partial P}{\partial y} \tag{4}$$

Combining Eqs. (3) and (4) yields

$$\frac{\partial}{\partial x}\left(-\rho\frac{K_p}{\mu}\frac{\partial P}{\partial x}\right)+\frac{\partial}{\partial y}\left(-\rho\frac{K_p}{\mu}\frac{\partial P}{\partial y}\right)=0 \tag{5}$$

The temperature distribution within each GDL is obtained by solving the energy equation including the effects of conduction and advection

$$\rho c_p\left(u\frac{\partial T}{\partial x}+v\frac{\partial T}{\partial y}\right)=k_{\text{eff}}\left(\frac{\partial^2 T}{\partial x^2}+\frac{\partial^2 T}{\partial y^2}\right) \tag{6}$$

where the effective thermal conductivity of the GDL is expressed as [13]

$$k_{\text{eff}}=-2k_s+\left(\frac{\varepsilon}{2k_s+k_f}+\frac{1-\varepsilon}{3k_s}\right)^{-1} \tag{7}$$

The fluid's thermal conductivity, k_f, is calculated based upon local species concentrations while the species conservation equation is applied to the oxygen, hydrogen, and water vapor. No chemical reaction occurs in the GDLs, and the species distributions evolve due to the combined effects of diffusion and advection

$$u\left(\frac{\partial x_i}{\partial x}\right)+v\left(\frac{\partial x_i}{\partial y}\right)=D_i^{\text{eff}}\left(\frac{\partial^2 x_i}{\partial x^2}+\frac{\partial^2 x_i}{\partial y^2}\right) \tag{8}$$

Electron transfer in the GDLs is described by the charge equation

$$\kappa_G\left(\frac{\partial^2 \varphi_s}{\partial x^2}+\frac{\partial^2 \varphi_s}{\partial y^2}\right)=0 \tag{9}$$

Membrane. Transport within the membrane is governed by conservation of mass, thermal energy, ionic charge, and species principles. Mass conservation is expressed as

$$\frac{\partial}{\partial x}(\rho u)+\frac{\partial}{\partial y}(\rho v)=0 \tag{10}$$

where the density of the fluid is calculated as a function of the local temperature, pressure, and species concentrations. The actual velocity of water vapor inside the membrane is described by Schlögl's equation [2]

$$u^*=\frac{K_\varphi}{\mu}z_f c_f F\left(\frac{\partial \varphi}{\partial x}\right)-\frac{K_P}{\mu}\left(\frac{\partial P}{\partial x}\right) \tag{11}$$

The two terms on the RHS of the preceding equation account for the electro-osmotic drag by hydrogen protons migrating through the membrane, and pressure-driven flux, respectively [12]. Since the membrane is assumed to be fully saturated, water backdiffusion is negligible [12]. The actual velocity in Eq. (11) is converted to the apparent velocity through the relationship $u^*=u/\varepsilon$.

Thermal energy is transferred by conduction and advection described by

$$\rho c_p\left(u\frac{\partial T}{\partial x}+v\frac{\partial T}{\partial y}\right)=k_{\text{eff}}\left(\frac{\partial^2 T}{\partial x^2}+\frac{\partial^2 T}{\partial y^2}\right)+S_T \tag{12}$$

where the density is based upon the local temperature, pressure, and species concentration and k_{eff} is evaluated using Eq. (7). The source term, S_T, accounts for ohmic heating

$$S_T = \frac{i_m^2}{\sigma_m} \tag{13}$$

The variable i_m is the total current density given as

$$i_m = \sqrt{i_{m,x}^2 + i_{m,y}^2} \tag{14}$$

where

$$i_{m,x} = -\sigma_m\left(\frac{\partial \varphi_m}{\partial x}\right); \quad i_{m,y} = -\sigma_m\left(\frac{\partial \varphi_m}{\partial y}\right) \tag{15}$$

Species transport in the membrane is due to advection and diffusion and is described by

$$u\left(\frac{\partial x_i}{\partial x}\right) + v\left(\frac{\partial x_i}{\partial y}\right) = D_i^{\text{eff}}\left(\frac{\partial^2 x_i}{\partial x^2} + \frac{\partial^2 x_i}{\partial y^2}\right) \tag{16}$$

The ionic charge distribution is found from

$$\frac{\partial}{\partial x}\left(-\sigma_m \frac{\partial \varphi_m}{\partial x}\right) + \frac{\partial}{\partial y}\left(-\sigma_m \frac{\partial \varphi_m}{\partial y}\right) = 0 \tag{17}$$

where the ionic conductivity is, in general, a function of water content and temperature. The following empirical expression is used for the membrane ionic conductivity

$$\sigma_m(T) = (0.5139\lambda - 0.326)\exp\left[1268\left(\frac{1}{303} - \frac{1}{T}\right)\right] \tag{18}$$

where λ is the ratio of the number of water molecules to the number of sulfonic charge sites [1] and is dependent on the local temperature expressed in Kelvin, and the water activity at the interface between the membrane and catalyst layers, a, expressed as [14]

$$\lambda = 0.043 + 17.81a - 3985a^2 + 36a^3 \quad 0 < a \leqslant 1$$

$$\lambda = 14 + 1.4(a-1) \quad 1 \leqslant a \leqslant 3 \tag{19}$$

The water activity is

$$a = \frac{P_{\text{H}_2\text{O}}}{P^{\text{sat}}} \tag{20}$$

Based on the assumption of a fully saturated membrane, $a=1$ and $\lambda=14$, so the membrane ionic conductivity is solely a function of temperature.

Catalyst Layers. Reduction of hydrogen and oxygen occurs within the catalyst layers. Equation (11) describes the conservation of momentum. A source term appears in the conservation of mass equation and accounts for: (a) the depletion of oxygen and generation of water vapor at the cathode and (b) the depletion of hydrogen at the anode by the electrochemical reaction

$$\frac{\partial}{\partial x}(\rho u) + \frac{\partial}{\partial y}(\rho v) = S_m \tag{21}$$

where the source term S_m is expressed by an equation of the form [4]

$$S_m = -\frac{M_{\text{H}_2} j_a}{2F} \tag{22}$$

At the cathode-side catalyst layer the source term, S_m, is

$$S_m = \frac{M_{\text{O}_2} j_c}{4F} - \frac{M_W j_c}{2F} \tag{23}$$

Heat transfer in the catalyst layers is described by the energy equation accounting for conduction, advection, and generation

$$\rho c_p\left(u\frac{\partial T}{\partial x} + v\frac{\partial T}{\partial y}\right) = k_{\text{eff}}\left(\frac{\partial^2 T}{\partial x^2} + \frac{\partial^2 T}{\partial y^2}\right) + S_T \tag{24}$$

where the source term, S_T, in the anode-side catalyst layer is due to (a) ohmic heating; (b) reversible chemical reaction; and (c) activation losses expressed as

$$S_T = E_\Omega + E_{\text{rev}} + E_{\text{act}} \tag{25}$$

where the individual terms are

$$E_\Omega = \frac{i_m^2}{\sigma_{\text{ct}}} \tag{26}$$

$$E_{\text{rev}} = \frac{j_a T}{2F}\sum_{p-r} s_{f,a}^o \tag{27}$$

$$E_{\text{act}} = j_a \eta_a \tag{28}$$

Similarly, in the cathode-side catalyst layer, the source term is due to; (a) ohmic heating, (b) reversible chemical reaction, (c) phase change, and (d) activation losses

$$S_T = E_\Omega + E_{\text{rev}} + E_{\text{latent}} + E_{\text{act}} \tag{29}$$

where

$$E_\Omega = \frac{i_m^2}{\sigma_{\text{ct}}} \tag{30}$$

$$E_{\text{rev}} = \frac{j_c T}{4F}\sum_{p-r} s_{f,c}^o \tag{31}$$

$$E_{\text{latent}} = \frac{M_W j_c}{2F} h_{fg} \tag{32}$$

$$E_{\text{act}} = j_c \eta_c \tag{33}$$

In each catalyst layer, the transported species are oxygen, hydrogen, and water vapor, the distributions of which are governed by the species conservation equation

$$u\left(\frac{\partial x_i}{\partial x}\right) + v\left(\frac{\partial x_i}{\partial y}\right) = D_i^{\text{eff}}\left(\frac{\partial^2 x_i}{\partial x^2} + \frac{\partial^2 x_i}{\partial y^2}\right) + S_i \tag{34}$$

The species source terms, S_i, are [4]

$$S_{\text{H}_2} = -\frac{j_a}{2FC_{\text{tot}}} \tag{35}$$

$$S_{\text{O}_2} = \frac{j_c}{4FC_{\text{tot}}} \tag{36}$$

$$S_W = -\frac{j_c}{2FC_{\text{tot}}} \tag{37}$$

Since the sum of the mole fractions is unity, the mole fraction of nitrogen can be determined from the relation $\Sigma x_i = 1$.

Two charge equations are solved for the proton and electron transfer within the catalyst layers. They are

$$\frac{\partial}{\partial x}\left(-\sigma_{\text{ct}}\frac{\partial \varphi_m}{\partial x}\right) + \frac{\partial}{\partial y}\left(-\sigma_{\text{ct}}\frac{\partial \varphi_m}{\partial y}\right) = S_\varphi \tag{38}$$

$$\kappa_{\text{ct}}\left(\frac{\partial^2 \varphi_s}{\partial x^2} + \frac{\partial^2 \varphi_s}{\partial y^2}\right) = S_\varphi \tag{39}$$

where the electronic and ionic conductivities of the catalyst layers (κ_{ct} and σ_{ct}, respectively) are expressed as

$$\kappa_{\text{ct}} = (1 - \varepsilon_{\text{ct}})^{1.5}\kappa \tag{40a}$$

Table 1 Boundary conditions[a]

x	y	T	φ_m	φ_s	x_{O_2}	x_{H_2}	x_W	u	v	P
$-A \le x \le +A$	0, C	zgy	zgy	zgy	zgy	zgy	zgy	0	0	—
$+t_m/2$	$0 \le y \le C$	cab	cab	zgx	cab	zgx	cab	cab	cab	cab
$-t_m/2$	$0 \le y \le C$	cab	cab	zgx	zgx	cab	cab	cab	cab	cab
$+(t_m/2+t_{ct})$	$0 \le y \le C$	cab	zgx	cab	Eq. (47)	N.A.	cab	cab	cab	cab
$-(t_m/2+t_{ct})$	$0 \le y \le C$	cab	zgx	cab	N.A.[b]	Eq. (47)	cab	cab	cab	cab
$+(t_m/2+t_{ct}+t_G)$	$0 \le y \le w_L$	$-k_G \partial T/\partial x = (T_G - T_B)/R''_{T,c}$	N.A.[b]	$F1$	zgx	N.A.[b]	zgx	0	0	—
$-(t_m/2+t_{ct}+t_G)$	$0 \le y \le w_L$	$-k_G \partial T/\partial x = (T_B - T_G)/R''_{T,c}$	N.A.[b]	$F2$	N.A.[b]	zgx	zgx	0	0	—
$+(t_m/2+t_{ct}+t_G)$	$w_L \le y \le C$	$-k_G \partial T/\partial x = h_A(T - T_{m,A})$	N.A.[b]	zgx	$X1$	N.A.[b]	$X2$	—	—	P_c
$-(t_m/2+t_{ct}+t_G)$	$w_L \le y \le C$	$-k_G \partial T/\partial x = h_{H_2}(T_{m,H_2} - T)$	N.A.[b]	zgx	N.A.[b]	$X3$	$X4$	—	—	P_a
A	$0 \le y \le C$	$\partial T/\partial x\|_{x=+A} = \partial T/\partial x\|_{x=-A}$	N.A.[b]	V_{cell}	N.A.[b]	N.A.[b]	N.A.[b]	N.A.[b]	N.A.[b]	N.A.[b]
$-A$	$0 \le y \le C$	$T\|_{x=+A} = T\|_{x=-A}$ $\partial T/\partial x\|_{x=-A} = \partial T/\partial x\|_{x=+A}$	N.A.[b]	0	N.A.[b]	N.A.[b]	N.A.[b]	N.A.[b]	N.A.[b]	N.A.[b]
B	$w_L \le y \le C$	$T\|_{x=-A} = T\|_{x=+A}$ $-k_B \partial T/\partial x =$	N.A.[b]	zgx	N.A.[b]	N.A.[b]	N.A.[b]	N.A.[b]	N.A.[b]	N.A.[b]
$-B$	$w_L \le y \le C$	$h_A(T_{m,A} - T) = -k_B \partial T/\partial x =$	N.A.[b]	zgx	N.A.[b]	N.A.[b]	N.A.[b]	N.A.[b]	N.A.[b]	N.A.[b]
$B \le x \le B - d_{Ch}$	w_L	$h_{H_2}(T - T_{m,H_2}) = -k_B \partial T/\partial y =$	N.A.[b]	zgy	N.A.[b]	N.A.[b]	N.A.[b]	N.A.[b]	N.A.[b]	N.A.[b]
$-B \le x \le -B + d_{Ch}$	w_L	$h_A(T - T_{m,A}) = -k_B \partial T/\partial y = h_{H_2}(T - T_{m,H_2})$	N.A.[b]	zgy	N.A.[b]	N.A.[b]	N.A.[b]	N.A.[b]	N.A.[b]	N.A.[b]

[a]Zero gradient in the x direction is denoted as zgx; zero gradient in the y direction is denoted as zgy; boundaries with continuous distributions across interfaces separating different materials are denoted as cab; x locations are: $A = t_m/2 + t_{ct} + t_G + t_B$; $B = t_m/2 + t_{ct} + t_G + d_{Ch}$; y location is: $C = w_L + w_{Ch}$; $F1$: $\kappa \partial \varphi_s/\partial x = (\varphi_{s,G} - \varphi_{s,B})|_x / R''_{e,c}$; $F2$: $\kappa \partial \varphi_s/\partial x = (\varphi_{s,B} - \varphi_{s,G})|_x / R''_{e,c}$; $X1$: $-D^{eff}_{O_2} \partial x_{O_2}/\partial x = h_m(x - x_{m,O_2})$; $X2$: $-D^{eff}_w \partial x_W/\partial x = h_m(x - x_{m,W})$; $X3$: $-D^{eff}_{H_2} \partial x_{H_2}/\partial x = h_m(x_{m,H_2} - x)$; $X4$: $-D^{eff}_w \partial x_W/\partial x = h_m(x_{m,W} - x)$.
[b]N.A. = not applied.

$$\sigma_{ct} = \varepsilon_{ct}^{1.5} \sigma_m \tag{40b}$$

The source term, S_φ, in Eqs. (38) and (39) represents volumetric transfer current density and is expressed as

$$S_\phi = \begin{cases} -j_a & \text{anode} \\ -j_c & \text{cathode} \end{cases} \tag{41}$$

The volumetric source terms associated with the catalyst layers are determined based upon the transfer currents using the Butler–Volmer equation [3]

$$j_a = a j^{ref}_{o,a} \left(\frac{x_{H_2}}{x^{ref}_{H_2}} \right)^{0.5} \left\{ \exp\left(\alpha^a_a \frac{F}{RT} \eta_a \right) - \exp\left(-\alpha^a_c \frac{F}{RT} \eta_a \right) \right\} \tag{42}$$

$$j_c = a j^{ref}_{o,c} \left(\frac{x_{O_2}}{x^{ref}_{O_2}} \right) \left\{ \exp\left(\alpha^c_a \frac{F}{RT} \eta_c \right) - \exp\left(-\alpha^c_c \frac{F}{RT} \eta_c \right) \right\} \tag{43}$$

The activation losses, η_a or η_c, which appear in Eqs. (28), (33), (42), and (43) are potential differences between the solid phase and the electrolyte membrane at the anode and cathode catalyst layers defined as [15]

$$\eta_{a,c} = \varphi_s - \varphi_m - E_o \tag{44}$$

where the open circuit potential, E_o, is set to a value of zero at the anode side and is equal to the cell open circuit potential at the cathode side. The cell open circuit potential can be determined by the Nernst equation [16]

$$E_o = 1.482 - 0.000845T + \frac{RT}{2F} \ln \left(\frac{\left(\frac{P_{H_2}}{P^o} \right) \left(\frac{P_{O_2}}{P^o} \right)^{0.5}}{\left(\frac{P_{H_2O}}{P^o} \right)} \right) \tag{45}$$

The ionic and electronic potentials appearing in Eq. (44) are evaluated using Eqs. (38) and (39).

In all the porous materials (membrane, GDLs, and catalyst layers), the molecular species diffusivity is corrected using [2]

$$D^{eff}_i = \varepsilon^{1.5} D_i \tag{46}$$

where D_i is the species diffusivity of an individual gas within a mixture of water vapor and air at the cathode side, and water vapor, nitrogen, and hydrogen at the anode side [15].

Boundary Conditions. The governing equations are solved to determine $T(x,y)$, $\varphi_m(x,y)$, $\varphi_s(x,y)$, $x_{O_2}(x,y)$, $x_{H_2}(x,y)$, $x_W(x,y)$, $u(x,y)$, $v(x,y)$, and $P(x,y)$ subject to the boundary conditions presented in Table 1. Note that the spatial distributions of several parameters within some subdomains of Fig. 2 are not predicted (e.g., $u(x,y)=0$ within the bipolar plates) and, for these cases, boundary conditions are not applied (N.A.). In some other subdomains, the field variable and associated flux is continuous across a physical boundary between materials (cab; e.g., $T(x,y)$ across the interface between the GDL and the catalyst layers).

The same temperature and temperature gradient exists at the LHS and RHS boundaries of the control volume shown in Fig. 2. Hence, periodic boundary conditions are applied at these locations. The mean temperatures of the humidified hydrogen and air within the flow channels are specified, and the convection coefficients within the flow channels are calculated based upon the di-

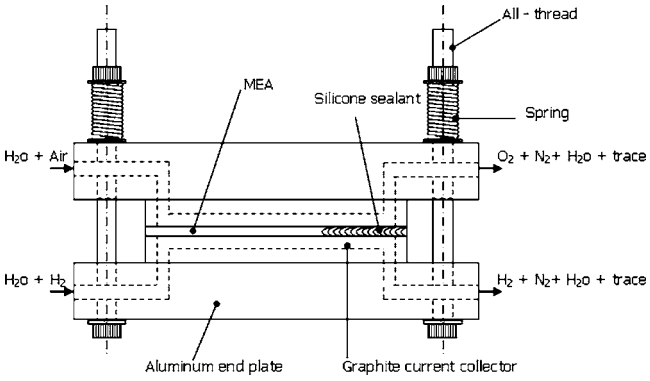

Fig. 3 Schematic of the fuel cell experiment

mensions of the flow channel, assuming constant temperature conditions along the walls of the flow channels and laminar conditions [17]. Zero gradient temperature boundary conditions are specified at the top and bottom of the domain of Fig. 2 to account for the vertical periodicity of the problem. There is a discontinuity in the oxygen (hydrogen) concentration at the interface between the RHS (LHS) GDL and catalyst layer. The oxygen and hydrogen mole fractions at the interfaces between GDLs and catalyst layers can be found from the solubility of gases in liquid water using Henry's law [2,17]

$$x_i^m = \frac{x_i P}{H} \quad \text{at } x = \pm\left(\frac{t_m}{2} + t_{\text{ct}}\right) \tag{47}$$

The mean mole fraction of all species in the flow channels is specified. At the GDL–flow channel interface, the molar flux of the species from the flow channel is equal to the molar flux associated with species transfer by diffusion into the GDL.

Thermal and electrical contact resistances are specified at the interface between the GDLs and the bipolar plates, and will be discussed later. The governing equations, subject to the applied boundary conditions, were solved using a commercially available finite element package and equation solver (FEMLAB). A grid-size sensitivity study showed that the predictions are, for all practical purposes, independent of the size of the grid (approximately 20,000 nodes) used here. Details are included in the Appendix.

Experiments

Experiments were conducted to measure the sensitivity of a fuel cell's power output to the clamping pressure. For experiments involving parallel anode- and cathode-side flow channels, a single 100 mm $\times$ 100 mm MEA with a 5000 mm^2 active area (Fuelcellstore Model 597210) was sandwiched between two custom-fabricated graphite current collectors, each consisting of 43 parallel 1.02 mm deep $\times$ 0.83 mm wide channels separated by 0.83 mm lands in the geometrical arrangement of Fig. 1(*b*). The clamping pressure was controlled by placing the current collectors and MEA between two aluminum end plates, and compressing the entire assembly with eight all-threaded rods, each equipped with a spring of known spring constant (Fig. 3). The very thin gap between the graphite plates was sealed with a pliable bead of silicone applied about the periphery of the test cell to: (a) prevent gas leakage while (b) allowing for accurate determination of the clamping force based upon a straightforward calculation using the spring constant, number of springs, and compression of each spring.

To ensure that measured changes in the cell performance were not affected by possible changes in gas leakage from the periphery of the fuel cell, a preliminary experiment with no power output was performed in which the entire assembly was submerged in liquid water while anode and cathode gases were supplied to the cell at the same rate and inlet pressure as was used in the experiment. Using a simple, visual bubble-counting method at the smallest clamping pressure, it was determined that gas leakage was less than 0.004% of the entire gas flow rate. Therefore, gas leakage is negligible even at the lowest compressive force; any change in fuel cell performance must be due to changes in compression of the MEA and/or modification of the thermal and electrical contact resistances.

Table 2 Physical parameters of fuel cell elements

Parameter	Value
Channel width	0.4 mm
Channel depth	0.5 mm
Land area width	0.3 mm
Gas diffusion layer thickness	0.26 mm
Gas diffusion layer porosity	0.4
Gas diffusion layer electronic conductivity	570 $\Omega^{-1}\,m^{-1}$
Gas diffusion layer effective thermal conductivity	1.3 W/m K
Membrane thickness	0.23 mm
Membrane porosity	0.25
Membrane thermal conductivity	0.25 W/m K
Membrane hydraulic permeability	$1.58\times10^{-18}\,m^2$
Membrane electrokinetic permeability	$1.13\times10^{-19}\,m^2$
Catalyst layer thickness	0.01 mm
Volume fraction of membrane in catalyst layer	0.5
Catalyst layer thermal conductivity	1 W/m K

Experiments were performed using anode and cathode flow rates of 1 L/min, a controlled cell temperature of 80°C, and inlet relative humidity of 70% for both the hydrogen and air. The flow rates, cell temperature, inlet humidity, and current density (1400 A/m^2 and 400 A/m^2 for the parallel- and orthogonal-channel cases, respectively) were controlled using a Teledyne Energy System, Inc., Model MEDUSA RD-890CR-50150/100250 test stand. The cell voltage and power were continuously monitored, with data logged every 30 s. After conditioning the MEA, the test was initiated at the minimum clamping pressure ($\approx$1.35 bar) the output power was allowed to reach a quasi-steady state (slight fluctuations in output power were noted at each clamping pressure and were attributed to liquid water droplet formation and movement in the cathode flow channels). The output power was monitored at each clamping pressure for approximately 2 h. After a quasi-steady state was attained, a larger clamping pressure was applied. Note that once the MEA is compressed at a higher load, the experiments could not be repeated at lower clamping pressures since the MEA is permanently deformed from its previous state with increased clamping pressure. Experiments were repeated, using fresh MEAs for orthogonal flow channel configurations.

Results and Discussion

After validating the model (below), it was used to quantify the effects of the compressive force. The dimensions and operating parameters of the simulations (except as noted otherwise) are listed in Table 2; base case conditions are provided in Table 3.

Model Validation. The model was validated to the extent possible by: (a) comparing its predictions to results in Ref. [15], incorporating the physical properties and operating conditions used in that study; (b) examining predicted temperature distributions within the fuel cell to assess the plausibility of the predictions; and (c) comparing the predictions to the experimental results.

As evident in Fig. 4, the predicted fuel cell performance is in excellent agreement with that of Ref. [15]. The temperature distribution within the fuel cell, for the base case operating conditions of Table 3, is illustrated in Fig. 5. As shown in Fig. 5(*a*), the bipolar plates are relatively cool and of nearly uniform temperature. This result is also evident in Figs. 5(*b*) and 5(*c*). The highest

Table 3 Base case operating conditions

Parameter	Value
Air inlet temperature	353 K
Air inlet pressure	3 atm
Air viscosity	1.85×10^{-5} kg/m s
Air thermal conductivity	0.03 W/m K
Air specific heat	1009 J/kg K
Air relative humidity at inlet	100%
Oxygen/nitrogen ratio in air at inlet	0.21/0.79
Oxygen diffusivity in the gas mixture	5.2197×10^{-6} m^2/s
Hydrogen inlet temperature	353 K
Hydrogen inlet pressure	3 atm
Hydrogen viscosity	1.3×10^{-5} kg/m s
Hydrogen thermal conductivity	0.182 W/m K
Hydrogen specific heat	14.43×10^{3} J/kg K
Hydrogen diffusivity in the gas mixture	2.63×10^{-6} m^2/s
Hydrogen relative humidity at inlet	100%
Number of electrons transferred for oxygen	4
Number of electrons transferred for hydrogen	2
Cathodic charge transfer coefficient for cathode reaction	2
Cathodic charge transfer coefficient for anode reaction	2
Anodic charge transfer coefficient for cathode reaction	0.5
Anodic charge transfer coefficient for anode reaction	0.5
Cathode reference exchange current density	500 A/m^3
Anode reference exchange current density	5×10^{8} A/m^3
Clamping pressure	11 bar
Henry's constant for oxygen	$0.1\exp(-666/T+14.1)P/R/T$ Pa
Henry's constant for hydrogen	4.5×10^{3} $P/R/T$ Pa
Entropy of reaction for the anode, $\Sigma_{p-r}s_f^{0}$ [a]	126.8 J/mol K
Entropy of reaction for the cathode $\Sigma_{p-r}s_{f,c}^{0}$ [a]	42.5 J/mol K

[a]See Ref. [4].

local temperature occurs inside the MEA at the interface between the cathode catalyst layer and the membrane (Fig. 5(*d*)). The cathode side temperature of the MEA is higher than the anode side, as expected, due to the larger source terms in the energy equation, and the condensation of water at that location. The minimum local temperature in the GDL–MEA assembly occurs on the anode side, and is associated with the proximity to the cool, high thermal conductivity hydrogen in the flow channel.

Of particular interest is the dependence of the fuel cell performance and membrane temperature distributions on the clamping pressure (force per unit active area of MEA) used to assemble the stack components. Both electrical and thermal contact resistances will decrease with increasing clamping pressure. Transport internal to the porous membrane and GDLs will also be affected by changes in compression.

The dependence of the thermal and electrical contact resistances to the clamping pressure for two different bipolar plate (flat and smooth graphite)–GDL combinations (Sigracet GDL 10-BC and Carbel CL GDLs) is provided in Ref. [6]. The base case GDL material considered here is arbitrarily specified to be Sigracet. The following expressions are curve fits to the Sigracet-based experimental data of Ihonen (P is expressed in bars)

$$R_{T,c} = (-2.1P_{\mathrm{CL}}^{2} + 86P_{\mathrm{CL}} + 407)^{-1} \tag{48}$$

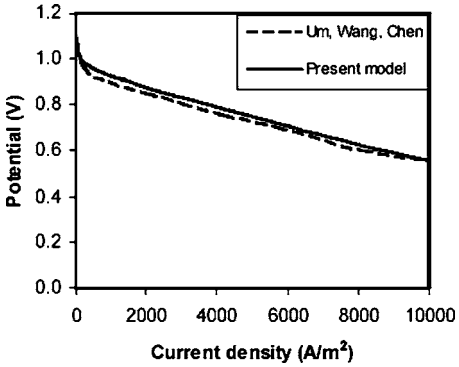

Fig. 4 Comparison of the predicted fuel cell performance with that of Ref. [15]

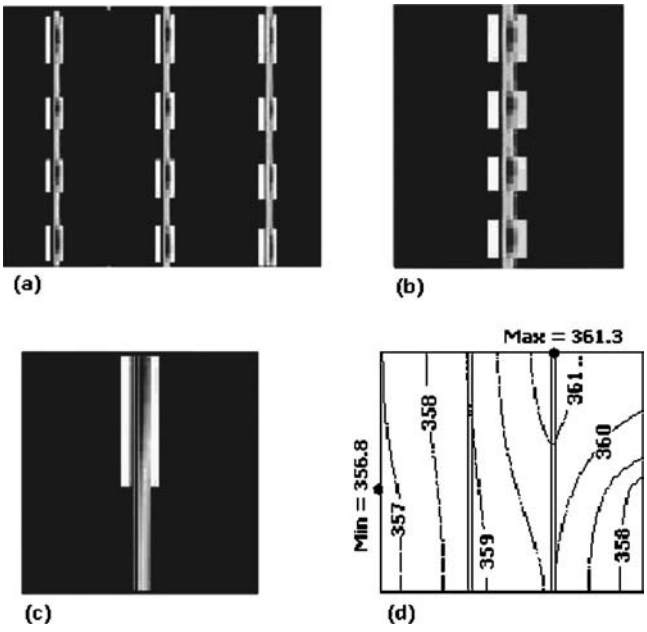

Fig. 5 Internal temperature distribution (K) for the base case operating conditions and V_{cell}=0.6 V. Results are for: (*a*) internal regions of a stack; (*b*) a single cell; (*c*) the entire computational domain; and (*d*) the GDL and MEA.

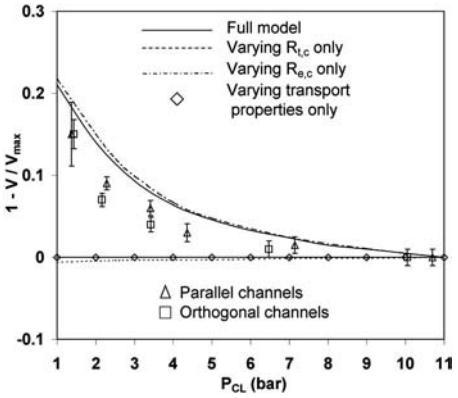

Fig. 6 Measured and predicted fuel cell performance

$$R_{e,c} = (-2.1 \times 10^3 P_{\mathrm{CL}}^2 + 9.7 \times 10^4 P_{\mathrm{CL}} + 10^5)^{-1} \quad (49)$$

The relationship between $R_{T,c}$ (and $R_{e,c}$) and P_{CL} for Carbel is [6]

$$R_{T,c} = (-4.44 P_{\mathrm{CL}}^2 + 144.2 P_{\mathrm{CL}} + 387)^{-1} \quad (50)$$

$$R_{e,c} = (-3.65 \times 10^3 P_{\mathrm{CL}}^2 + 1.3 \times 10^5 P_{\mathrm{CL}} + 1.3 \times 10^5)^{-1} \quad (51)$$

The dependence of the in-plane and through-plane permeability on the clamping pressure for two different GDLs (Sigracet 10-BC and Carbel CL) is also reported in Ref. [6]. A curve fit to the reported data for the in-plane permeability of Sigracet 10-BC is

$$K_p = -2 \times 10^{-13} P_{\mathrm{CL}}^2 - 9 \times 10^{-13} P_{\mathrm{CL}} + 2.1 \times 10^{-11} \quad (52)$$

The ratio of the in-plane to the through-plane permeability for Sigracet is 66. The in-plane permeability and clamping pressure relationship for Carbel is [6]

$$K_p = 1.3 \times 10^{-14} P_{\mathrm{CL}}^2 - 3.1 \times 10^{-12} P_{\mathrm{CL}} + 2.15 \times 10^{-11} \quad (53)$$

The ratio of the in-plane to through-plane permeability for Carbel CL is 1.6.

Other transport properties associated with the two GDL materials are assumed to be the same as those listed in Table 2, due to lack of data.

The model, including Eqs. (48)–(53), was used to predict experimental results. However, because: (a) the MEA used in the experiments was not the same as that of Ref. [6]; (b) previous investigators [6] did not report fuel cell performance results for a similar two-dimensional geometry; and (c) contact resistance information is not available for the MEA used in the experiments, a *direct* comparison of the predicted and measured effect of the clamping pressure is not possible. Therefore, the ratio of the predicted (or measured) cell voltage to the maximum cell voltage (it is assumed that the measured cell voltage at $P_{\mathrm{CL}} \approx 10.7$ bar is $V_{\max}$) as a function of the clamping pressure is reported in Fig. 6. The experimental results and numerical predictions are considered to be in remarkable agreement. The cell voltage (power) is most sensitive to P_{CL} at the smallest clamping pressures, and changes in the cell power asymptotically approach zero as the clamping pressure is increased. Simulations were performed in which only the electrical (or thermal) contact resistance dependence on the clamping pressure, or only the GDL transport property variation with clamping pressure, was taken into account. The results are also shown in Fig. 6 and indicate that electrical contact resistance has the dominant effect on the fuel cell power output. The influence of changes in the thermal contact resistance and GDL transport properties is minor and negligible, respectively. For purposes of comparison, the measured performance associated with orthogonal flow channels is also shown, exhibiting similar sensitivity to the clamping pressure as for the parallel channel configuration.

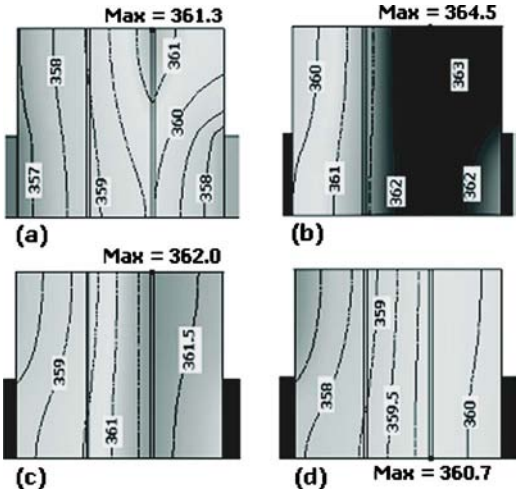

Fig. 7 Temperature distributions (K) in the MEA and GDLs, $V_{\mathrm{cell}}=0.6$ V: (*a*) $P_{\mathrm{CL}}=11$ bar, no contact resistances, $T_{\max}=361.3$ K at $x'=0$, $y=w_L+w_{\mathrm{Ch}}$; (*b*) $P_{\mathrm{CL}}=11$ bar, with contact resistances, $T_{\max}=364.5$ K at $x'=0$, $y=w_L+w_{\mathrm{Ch}}$; (*c*) $P_{\mathrm{CL}}=1$ bar, $T_{\max}=362.0$ K at $x'=0$, $y=w_L+w_{\mathrm{Ch}}$; and (*d*) $P_{\mathrm{CL}}\approx 0$, $T_{\max}=360.7$ K at $x'=0$, $y=0$

Parametric Simulations. As will become evident, the predicted temperature distribution inside the fuel cell is highly sensitive to P_{CL}. Local evaporation and condensation rates would be similarly affected. High temperatures may induce drying of the membrane or weakening of the Nafion as its glass transition temperature is approached [11]. High clamping pressures will deform the GDLs and the membrane, potentially causing cell leakage and electrical shorting [7]. Furthermore, large spatial temperature *gradients* within the Nafion, along with potentially large clamping forces exerted by the bipolar plates, may lead to large moisture gradients and excessive stresses in the material. Presumably, then, an isothermal and relatively cool membrane will exhibit greater durability than a nonisothermal, hot membrane. Since measurement of local temperatures, electrical and ionic potentials, and species distributions within operating fuel cells is difficult, the model was used to estimate the sensitivity of various distributions to the clamping pressure.

Temperature distributions inside the MEA and GDLs for various clamping pressures are shown in Fig. 7. (The geometry of Fig. 7 corresponds to that of Fig. 5(*d*).) As evident, the temperature distribution is highly sensitive to the clamping pressure. For no contact resistances and transport properties evaluated at $P_{\mathrm{CL}}=11$ bar, the minimum and maximum local temperatures in the MEA and GDLs are 356.7 K and 361.3 K, respectively. Values of $T_{\min}$ and $T_{\max}$ increase to 359.0 K and 364.5 K as P_{CL} is reduced to 11 bar (with contact resistances; Fig. 7(*b*)). Values of $T_{\min}$ and $T_{\max}$ drop to 357.7 K and 362.0 K at $P_{\mathrm{CL}}=1$ bar (Fig. 7(*c*)), and then decrease further to 357.0 K and 360.7 K at $R_{e,c}=10^{-5}\ \Omega\ \mathrm{m}^2$ ($P_{\mathrm{CL}}\approx 0$; Fig. 7(*d*)). Temperature differences between the GDL and the bipolar plates increase as P_{CL} is reduced, as expected. Overall temperatures decrease as P_{CL} is reduced due to the lower current density that is associated with higher electrical contact resistance. Interestingly, the *location* of $T_{\max}$ shifts from the top to the bottom of the computational domain as P_{CL} is reduced (but is consistently located at the left face of the RHS GDL, $x'=0$). The shift in the location of $T_{\max}$ is attributed to the fact that at low clamping pressures (Fig. 7(*d*)), the gases become more effective in cooling the membrane than the bipolar plates.

The effect of the clamping pressure on the temperature differences ($\Delta T \equiv T_{\max} - T_{\min}$) along the centerline of the membrane ($x=0$) for different operating conditions is shown in Fig. 8. Note that the results of Fig. 8(*a*) were generated by holding the current

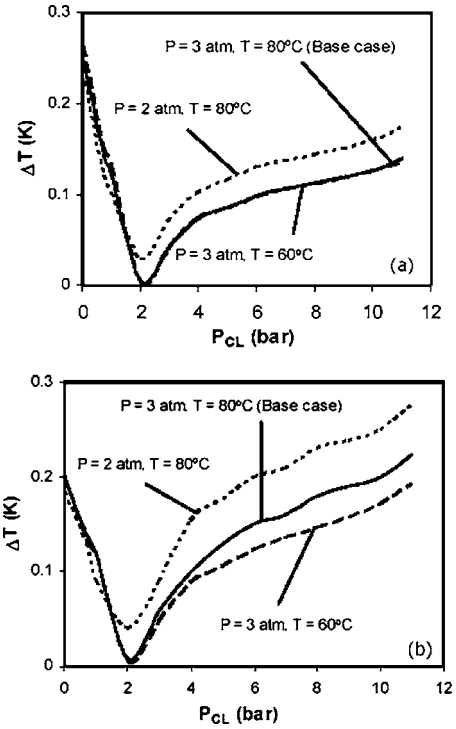

Fig. 8 (*a*) Temperature difference along the membrane centerline as a function of the clamping pressure for different operating conditions, I=7050 A/m^2; and (*b*) temperature difference along the membrane as a function of the clamping pressure for different operating conditions, V_{cell}=0.6 V

density constant while the cell potential is predicted, whereas in Fig. 8(*b*) the cell potential is held constant and the current density is predicted. The results of Figs. 7(*b*)–7(*d*) correspond to the solid line of Fig. 8(*a*).

Remarkably, regardless of the operating conditions considered here, the value of ΔT is minimized in the vicinity $P_{CL} \approx 2$ bar. At lower clamping pressures, the maximum temperature exists in the middle of the bipolar plate land region (bottom of the computational domain) for every case. At higher clamping pressures, the maximum temperature exists in the middle of the side of the gas channel (top of the computational domain) for every case. The value of ΔT exhibits modest dependence upon the gas temperatures and pressures (for the ranges of pressure and temperature considered here), and this dependence is brought about by a complicated interplay between the various transport phenomena within the fuel cell.

The effect of P_{CL} on ΔT for different flow channel dimensions is shown in Fig. 9. As less of the GDL is exposed to the relatively cool gases in the channels (smaller w_{Ch}), less area is available for the gases to cool the internal regions of the fuel cell and average temperatures (as will become evident in Fig. 11) increase. In addition, more of the GDL is exposed to the relatively isothermal bipolar plate, leading to smaller values of ΔT. These general observations are independent of whether the simulations are performed by holding either the cell potential (V_{cell}=0.6 V) or current density (I=7050 A/m^2) constant. As was observed in Fig. 8, temperature differences within the membrane are minimized at $P_{CL} \approx 2$ bar, regardless of the flow channel dimensions, or manner in which the fuel cell performance is simulated. Minimum values of ΔT correspond to the sudden shift of maximum temperatures from midchannel to midland as P_{CL} is reduced.

The fuel cell's power density (W/m^2) and the maximum temperature inside the MEA are other important factors that vary with the clamping pressure. The power density and temperature difference along the membrane are both shown as a function of P_{CL} in Fig. 10 for the two different channel dimensions. Figure 10(*a*) shows the relationship for Sigracet and Fig. 10(*b*) is associated with Carbel. The results reveal that optimum clamping pressures exist and are nearly independent of the channel dimensions, for both GDL materials. Carbel (Fig. 10(*b*)) exhibits a slightly smaller value of P_{CL} corresponding to the minimum value of ΔT. Relative changes in the power density are minor (approximately 20%) compared to the relative changes in ΔT (factor of 20) over the clamping pressure range considered here. The fuel cell power density and maximum temperature inside the MEA, and their dependence on the clamping pressure, are shown in Fig. 11 for different channel dimensions and different GDLs. The detrimental increases in the maximum temperature are considered to be minor, and are offset by desired increased power densities at higher

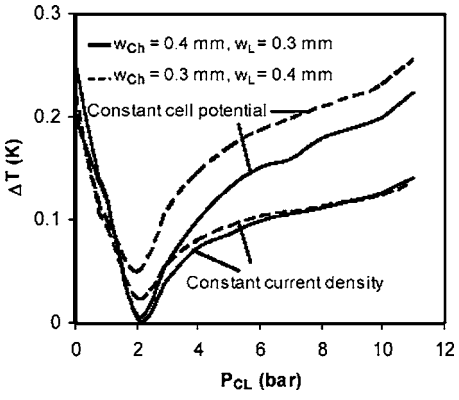

Fig. 9 Temperature difference along the membrane centerline as a function of the clamping pressure for different channel dimensions, constant current density (I=7050 A/m^2), and constant cell potential (V_{cell}=0.6 V)

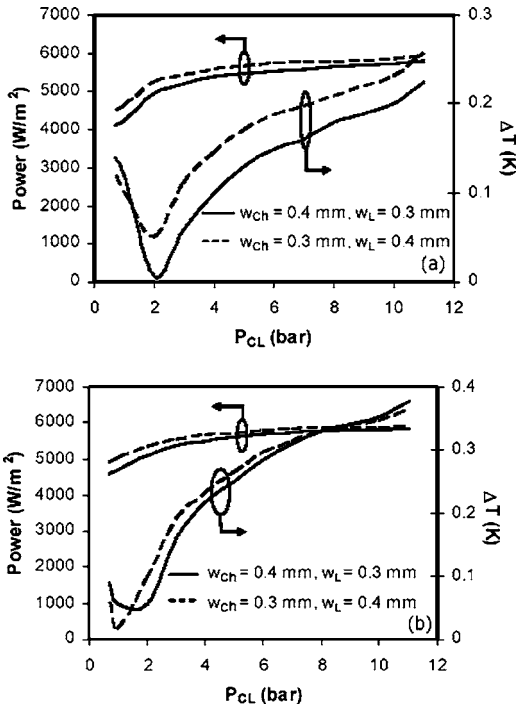

Fig. 10 Power density and temperature difference along membrane as a function of the clamping pressure for different channel dimensions and different GDL materials, V_{cell}=0.6 V: (*a*) Sigracet; and (*b*) Carbel

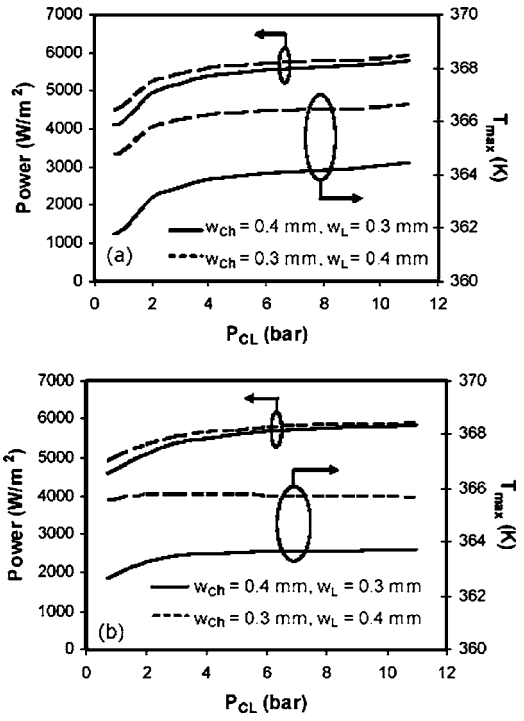

Fig. 11 Power density and maximum temperature of MEA as a function of the clamping pressure for different channel dimensions and different GDLs, V_{cell}=0.6 V: (*a*) Sigracet; and (*b*) Carbel

clamping pressures. The minor increases in the MEA temperature may become important as the Nafion's glass transition temperature is approached.

Summary and Conclusions

A two-dimensional, steady-state model of a PEM fuel cell stack has been developed. The model incorporates periodic boundary conditions that are enabled by the geometry of the internal regions of a fuel cell stack. The unique feature of the model is incorporation of thermal and electrical contact resistance effects at the interfaces separating the bipolar plates and the GDLs, as well as permeabilities that vary with changes in the compressive load applied to the stack. The model was validated by comparing its predictions with independent predictions from the literature, as well as to experiments reported here.

Increased clamping pressure reduces the contact resistances and permeabilities of the GDLs which, in turn, increases the performance of the stack and changes the stack's internal temperature distribution. The average temperature within the stack reaches a maximum at an intermediate clamping pressure. Localized condensation and evaporation rates would be similarly affected. The location of maximum membrane temperatures, and the temperature differences within the membrane, are highly dependent on the clamping pressure. Temperature differences within the membrane are minimized at clamping pressures of $P_{CL} \approx 2$ bar for a relatively wide range of operating conditions, gas channel geometries, and GDL materials.

Experimental measurements are needed to validate the predictions of local internal temperatures, species concentrations, and electronic as well as ionic current densities. The model does not account for three-dimensional or transient effects or detailed two-phase flow modeling.

Nomenclature

C_{tot} = total concentration, mol/m^3
D_i^{eff} = effective diffusion coefficient, m^2/s
E_{act} = energy due to activation loss
E_{latent} = energy due to phase change
E_Ω = energy due to ohmic heating
E_{rev} = energy due to reversible chemical reaction
F = Faraday constant, 96,485 C/mol
H = Henry's constant, Pa
K_p = hydraulic permeability of the porous media, m^2
K_φ = electronic permeability, m^2
M_{H_2} = hydrogen molar weight, kg/mol
M_{O_2} = oxygen molar weight, kg/mol
M_W = water molar weight, kg/mol
P = pressure, Pa
P^o = reference pressure, 101.3 kPa
P_{CL} = clamping pressure, bar
P_{H_2O} = water vapor pressure, Pa
R = universal gas constant, 8.314 kJ/kmol K
$R_{e,c}$ = electric contact resistance, Ω m^2
$R_{T,c}$ = thermal contact resistance, m^2 K/W
S_i = source term in species conservation equation
S_m = source term in mass equation
S_φ = source term in charge equation
S_T = source term in energy equation
T = temperature, K
V = voltage, V
$aj_{o,a}^{ref}$ = reference exchange current density times area at anode, A/m^3
$aj_{o,c}^{ref}$ = reference exchange current density times area at cathode, A/m^3
c_f = proton concentration in Nafion, mol/m^3
c_p = specific heat, J/kg K
d = depth, m
h_{fg} = latent heat, J/kg
h_m = convection mass transfer coefficient, m/s
i_m = total ionic current density, A/m^2
$i_{m,x}, i_{m,y}$ = ionic current density components
j = transfer current density, A/m^3
k = thermal conductivity, W/m K
n = number of electrons transferred
s_f^o = entropy
t = thickness, m
u^* = actual velocity, m/s
u, v = velocity components, m/s
w = width, m
x, y = coordinates, m
x' = coordinate, m
x_i = mole fraction of ith component
z_f = charge of proton, =−1

Greek Symbols

α_a^a = anodic transfer coefficient at anode
α_c^a = cathodic transfer coefficient at anode
α_a^c = anodic transfer coefficient at cathode
α_c^c = cathodic transfer coefficient at cathode
ρ = density, kg/m^3
φ_m = ionic potential, V
φ_s = electronic potential, V
κ = electronic conductivity, Ω^{-1} m^{-1}
η = overpotential, V
σ = ionic conductivity, Ω^{-1} m^{-1}
μ = viscosity, kg/m s
ε = porosity

Subscripts

A = air
B = bipolar plate
Ch = channel

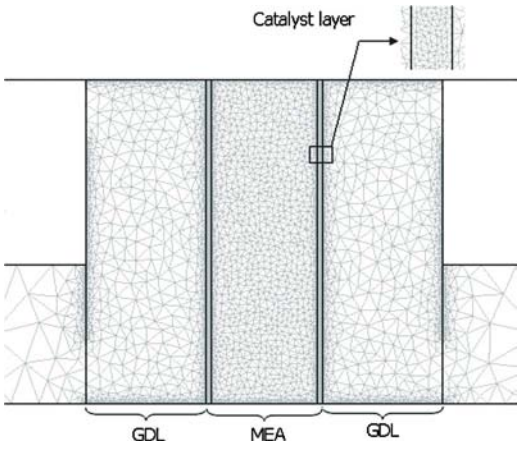

Fig. 12 Computational mesh

eff = effective
f = fluid
G = gas diffusion
H_2 = hydrogen
L = land area
O_2 = oxygen
W = water
a = anode
c = cathode
ct = catalyst
i = ith component
m = membrane, mean
s = solid

Superscripts

m = interface between GDL and catalyst layers
ref = reference
sat = saturated

Appendix

The computational mesh in the vicinity of the GDL and MEA is shown in Fig. 12 (the entire bipolar plates are not shown). The grid size is reduced in regions with relatively large gradients. For the base case, a grid size sensitivity analysis was performed by increasing the number of elements in the MEA and GDLs by 50%. Predicted temperatures at all locations within the domain changed by less than 0.01 K, and the fuel cell's power output remained constant to within six figures.

References

[1] Springer, T. E., Zawodzinski, T. A., and Gottesfeld, S., 1991, "Polymer Electrolyte Fuel Cell Model," J. Electrochem. Soc., **138**(8), pp. 2334–2342.
[2] Bernardi, D. M., and Vebrugge, M. W., 1992, "A Mathematical Model of the Solid-Polymer-Electrolyte Fuel Cell," J. Electrochem. Soc., **139**(9), pp. 2477–2491.
[3] Zhou, T., and Liu, H., 2001, "A General Three-Dimensional Model for Proton Exchange Membrane Fuel Cells," Int. J. Transp. Phenom., **3**(3), pp. 177–198.
[4] Siegel, N. P., Ellis, M. W., Nelson, D. J., and Spakovsky, M. R., 2004, "A Two-Dimensional Computational Model of a PEMFC With Liquid Water Transport," J. Power Sources, **128**, pp. 173–184.
[5] Faghri, A., and Gue, Z., 2005, "Challenges and Opportunities of Thermal Management Issues Related to Fuel Cell Technology and Modeling," Int. J. Heat Mass Transfer, **48**(19–20), pp. 3891–3920.
[6] Ihonen, J., Mikkola, M., and Lindbergh, G., 2004, "Flooding of Gas Diffusion Backing in PEFCs," J. Electrochem. Soc., **151**(8), pp. A1152–A1161.
[7] Mishra, V., Yang, F., and Pitchumani, R., 2004, "Measurement and Prediction of Electrical Contact Resistance Between Gas Diffusion Layers and Bipolar Plate for Applications to PEM Fuel Cells," ASME J. Fuel Cell Sci. Technol., **1**, pp. 1–8.
[8] Barbir, F., Braun, J., and Neutzler, J., 1999, "Properties of Molded Graphite Bi-Polar Plates for PEM Fuel Cell Stacks," J. New Mater. Electrochem. Syst., **2**, pp. 197–200.
[9] Mathias, M. F., Roth, J., Fleming, J., and Lehnert, W., 2003, "Diffusion Media Materials and Characterisation," *Handbook of Fuel Cells—Fundamentals, Technology and Applications*, Vol. 3, Wiley, New York, pp. 517–537.
[10] Birgersson, E., Noponen, M., and Vynnycky, M., 2005, "Analysis of a Two-Phase Non-Isothermal Model for a PEFC," J. Electrochem. Soc., **152**(5), pp. A1021–A1034.
[11] Uan-Zo-li, J. T., 2001, "The Effects of Structure, Humidity and Aging on the Mechanical Properties of Polymeric Ionomers for Fuel Cell Applications," M.S. thesis, The Virginia Polytechnic Institute and State University, Blacksburg, VA.
[12] Berning, T., Lu, D. M., and Djilali, N., 2002, "Three-Dimensional Computational Analysis of Transport Phenomena in a PEM Fuel Cell," J. Power Sources, **106**, pp. 284–294.
[13] Dagan, G., 1989, *Flow and Transport in Porous Formations*, Springer, New York.
[14] Wang, L., Husar, A., Zhou, T., and Liu, H., 2003, "A Parametric Study of PEM Fuel Cell Performances," Int. J. Hydrogen Energy, **28**, pp. 1263–1272.
[15] Um, S., Wang, C. Y., and Chen, K. S., 2000, "Computational Fluid Dynamics Modeling of Proton Exchange Membrane Fuel Cells," J. Electrochem. Soc., **147**(12), pp. 4485–4493.
[16] Barbir, F., 2005, *PEM Fuel Cells*, Elsevier Academic, New York, Chap. 2.
[17] Incropera, F. P., DeWitt, D. P., Bergman, T. L., and Lavine, A. S., 2007, *Fundamentals of Heat and Mass Transfer*, Wiley, Hoboken, NJ, Chaps. 8 and 14.

Porosity Formation and Prevention in Pulsed Laser Welding

Jun Zhou
Department of Mechanical and Electrical Engineering Technology,
Georgia Southern University,
Engineering Technology Bldg., Room 1126,
232 Forest Drive,
Statesboro, GA 30460
e-mail: jzhou@georgiasouthern.edu

Hai-Lung Tsai
Department of Mechanical and Aerospace Engineering,
University of Missouri-Rolla,
207 Mechanical Engineering,
1870 Miner Circle,
Rolla, MO 65409
e-mail: tsai@umr.edu

Porosity has been frequently observed in solidified, deep penetration pulsed laser welds. Porosity is detrimental to weld quality. Our previous study shows that porosity formation in laser welding is associated with the weld pool dynamics, keyhole collapse, and solidification processes. The objective of this paper is to use mathematical models to systematically investigate the transport phenomena leading to the formation of porosity and to find possible solutions to reduce or eliminate porosity formation in laser welding. The results indicate that the formation of porosity in pulsed laser welding is caused by two competing factors: one is the solidification rate of the molten metal and the other is the backfilling speed of the molten metal during the keyhole collapse process. Porosity will be formed in the final weld if the solidification rate of the molten metal exceeds the backfilling speed of liquid metal during the keyhole collapse and solidification processes. Porosity formation was found to be strongly related with the depth-to-width aspect ratio of the keyhole. The larger the ratio, the easier porosity will be formed, and the larger the size of the voids. Based on these studies, controlling the laser pulse profile is proposed to prevent/eliminate porosity formation in laser welding. Its effectiveness and limitations are demonstrated in the current studies. The model predictions are qualitatively consistent with reported experimental results. [DOI: 10.1115/1.2724846]

Keywords: laser welding, modeling, heat transfer, fluid flow, pulse control, porosity formation, prevention

1 Introduction

Joining of components with high precision and small heat-affected zone has recently made laser welding more prevalent in industry. Especially, with large depth-to-width aspect ratio and high welding efficiency, keyhole mode laser welding is more promising when compared with conventional welding processes. However, in deep penetration laser welds, porosity is frequently observed [1–4]. Porosity deteriorates the strength of the welded part. In order to optimize the laser welding process and to ensure high weld quality and strength, it is necessary to understand how porosity is formed in the welding process and, subsequently, to find methods to reduce or eliminate porosity defects.

Over the years, some researchers have conducted experiments to investigate porosity formation in laser welding. Katayama et al. [5] studied porosity formation in welding A5083 alloy and 304 steel with a high power YAG laser. They reported that alot of pores/voids were formed due to the evaporation of metal from the bottom tip of the keyhole, with the vapor being trapped by the solidifying front. They also discovered that shielding gas was trapped in those pores/voids. Seto and co-workers [6] took x-ray transmission images of the keyhole dynamics during laser welding using a high-speed video camera. As shown in their images, the rear side of the molten metal was depressed near the bottom when the keyhole front was inclined in the rear direction at the root. The reflected laser beam can superheat the molten metal near the bottom, resulting in a depression due to the high recoil pressure acting on the molten metal. They concluded that the shape of the keyhole front had a significant influence on porosity formation. Katayama et al. [7] observed the fusion and solidification behavior of a molten puddle during laser spot welding of 316S steel. They found that the formation of porosity had a close correlation with the collapse of the keyhole right after the irradiation termination. Once the laser beam was terminated, the melt in the upper part of the keyhole flowed downward to fill the keyhole. Some gas seems to have been trapped in the lower part of the keyhole. At the same time, the upper part of the melt rapidly solidified, which prevented the melt from flowing to fill the keyhole. Thus porosity was formed in the weld.

Based on these experimental observations, several methods have been proposed to prevent porosity formation for keyhole mode laser welding. The first method [8] focused on preventing the invasion of shielding gas during the welding process by welding in a vacuum. The experimental results showed that in vacuum welding, evaporation of metals was intensive so that the metallic vapors swelled the middle and the bottom rear wall of the keyhole, but no pores or voids were generated in the rear or bottom part of the molten pool. However, welding in a vacuum environment is not feasible in most industrial situations because of its inflexibility and high cost. The second method is to use a particular kind of shielding gas that can be dissolved in the molten metal. In YAG and CO_2 laser welding of 304S steels [5,9], reduced porosity formation was found using the shielding gas N_2, compared to that using other shielding gases, due to the high solubility of N_2 in metals with a high Cr content. The use of CO_2 shielding gas to suppress porosity formation was also reported in YAG laser welding of mild steels [10]. However, this approach is only suitable for certain welding cases in which the shielding gas "matches" the weld metal, limiting its applications.

The last method is to control the flow of molten metal during the keyhole collapse process, allowing the lower part of the keyhole to be filled up by molten metal. This can be achieved by increasing the backfilling speed of the molten metal or by delaying the solidification of the molten metal. Delaying the solidification process can be realized by optimizing the pulse shape of the laser beam [7]. From experimental results, it was revealed that by adding a tailing power to the laser pulse, a deep keyhole weld without porosity could be produced. Since this method can be

Contributed by the Heat Transfer Division of ASME for publication in the JOURNAL OF HEAT TRANSFER. Manuscript received January 19, 2006; final manuscript received September 5, 2006. Review conducted by Ben Q. Li.

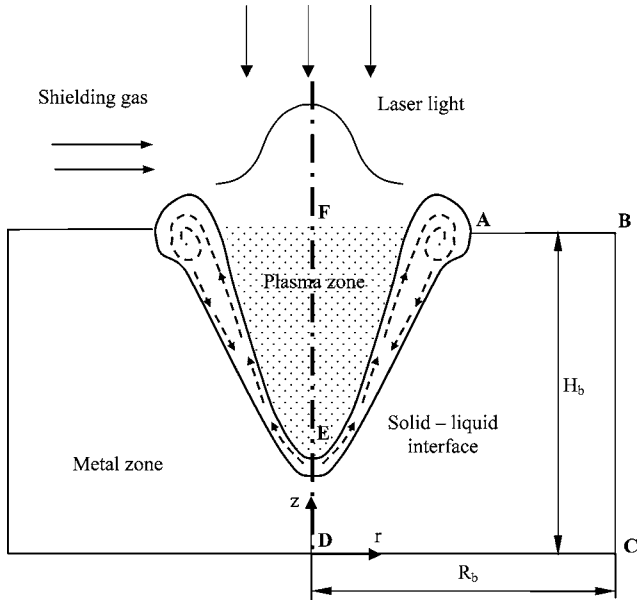

Fig. 1 Schematic sketch of a pulsed laser welding process

easily achieved compared with the aforementioned other methods, it is more practical to be adopted in industrial applications to prevent porosity formation.

So far, all reported research of porosity formation and prevention are based on experimental studies. Although experimental results such as the observations through microfocused x-ray transmission imaging can provide useful information about porosity formation, the underlying physics, such as temperature and velocity evolutions during the keyhole formation and collapse cannot be revealed. This is especially true for the phenomena that occur inside the keyhole. However, the temperature and velocity evolutions during the keyhole collapse and solidification processes have a significant influence on porosity formation. Hence, numerical simulation of keyhole mode laser welding is needed to study what happens during porosity formation. Until recently, a comprehensive numerical model was developed by Zhou et al. [11] to simulate the keyhole formation and collapse in the laser welding process. This work included the calculation of temperature field distributions, pressure balance, melt flow, free surface, laser-induced plasma, and multiple reflections. The model predictions are in good agreement with the experimental results. In this paper, this model is employed to systematically investigate the porosity formation mechanisms and the effectiveness of the prevention approach by optimizing the pulse shape in pulsed laser welding.

2 Mathematical Models

Figure 1 is a schematic sketch of stationary keyhole mode pulsed laser welding. The base metal is assumed to be 304S steel containing 100 ppm of sulfur. A finite difference model employing the volume of fluid (VOF) technique [12] and the continuum formulation [13] was used to calculate the momentum and energy transport in the keyhole and welding coupon. The VOF technique can handle a transient deformed weld pool surface, while the continuum formulation can handle fusion and solidification for the liquid region, the mush zone, and the solid region. Laser-induced plasma is often present in laser welding processes and it is a key factor affecting the keyhole dynamics. Due to the different energy transport mechanisms in the solid/liquid metal zone and the plasma zone, two submodels are developed to handle the transport phenomena in these two zones.

2.1 Metal Zone Simulation. The governing differential equations used to describe heat and mass transfer and fluid flow in a cylindrical coordinate (r-z system) given by Chiang and Tsai [13] are modified and used in the current study:

Continuity

$$\frac{\partial}{\partial t}(\rho) + \nabla \cdot (\rho \boldsymbol{V}) = 0 \tag{1}$$

Momentum

$$\frac{\partial}{\partial t}(\rho u) + \nabla \cdot (\rho \boldsymbol{V} u) = \nabla \cdot \left(\mu_l \frac{\rho}{\rho_l} \nabla u \right) - \frac{\partial p}{\partial r} - \frac{u_l}{K} \frac{\rho}{\rho_l}(u - u_s) - \frac{C\rho^2}{K^{0.5}\rho_l}|u - u_s|(u - u_s) - \nabla \cdot (\rho f_s f_l \boldsymbol{V}_r u_r) + \nabla \cdot \left(\mu_s u \nabla \left(\frac{\rho}{\rho_l} \right) \right) \tag{2}$$

$$\frac{\partial}{\partial t}(\rho v) + \nabla \cdot (\rho \boldsymbol{V} v) = \rho g + \nabla \cdot \left(\mu_l \frac{\rho}{\rho_l} \nabla v \right) - \frac{\partial p}{\partial z} - \frac{u_l}{K} \frac{\rho}{\rho_l}(v - v_s) - \frac{C\rho^2}{K^{0.5}\rho_l}|v - v_s|(v - v_s) - \nabla \cdot (\rho f_s f_l \boldsymbol{V}_r v_r) + \nabla \cdot \left(\mu_s v \nabla \left(\frac{\rho}{\rho_l} \right) \right) + \rho g \beta_T (T - T_0) \tag{3}$$

Energy

$$\frac{\partial}{\partial t}(\rho h) + \nabla \cdot (\rho \boldsymbol{V} h) = \nabla \cdot \left(\frac{k}{c_p} \nabla h \right) - \nabla \cdot \left(\frac{k}{c_p} \nabla (h_s - h) \right) - \nabla \cdot (\rho(\boldsymbol{V} - \boldsymbol{V}_s)(h_l - h)) \tag{4}$$

The physical meaning of each term appearing in the above equations can be found in Ref. [13]. In Eqs. (1)–(4), the continuum density, specific heat, thermal conductivity, solid mass fraction, liquid mass fraction, velocity, and enthalpy are defined in Ref. [13].

2.2 Track of Free Surface. The algorithm of volume-of-fluid (VOF) is used to track the dynamic free surface [12]. The fluid configuration is defined by a volume of fluid function, $F(r,z,t)$, which tracks the location of the free surface. The function F takes the value of one for the cell full of fluid and the value of zero for the empty cell. Cells with F values between zero and one are partially filled with fluid and identified as surface cells. The function F is governed by the following equation:

$$\frac{dF}{dt} = \frac{\partial F}{\partial t} + (\boldsymbol{V} \cdot \nabla) F = 0 \tag{5}$$

2.3 Plasma Zone Simulation. Plasma inside the keyhole can be treated as the vapor of the weld material. Although the velocity and pressure change dramatically across the Knudsen layer, the generic translation vapor flow along the keyhole is not significant [14]. Meanwhile, the pressure along the keyhole can be considered to be approximately constant [15]. Since the keyhole is open to the atmosphere, the pressure will be comparable to the atmospheric pressure. Therefore, in the present study, the fluid flow of plasma in the keyhole is neglected and only the temperature field is considered. Since the heat production by viscous dissipation is rather small in laser welding, the energy equation can be simplified as [16]

Table 1 Thermophysical properties of 304 stainless steel and process parameters

Nomenclature	Value
Specific heat of solid phase, c_s (J kg^{-1} K^{-1})	700
Specific heat of liquid phase, c_l (J kg^{-1} K^{-1})	780
Thermal conductivity of solid phase, k_s (W m^{-1} K^{-1})	22
Thermal conductivity of liquid phase, k_l (W m^{-1} K^{-1})	22
Density of solid phase, ρ_s (kg m^{-3})	7200
Density of liquid phase, ρ_l (kg m^{-3})	6900
Dynamic viscosity, μ_l (kg m^{-1} s^{-1})	0.006
Latent heat of fusion, H (J kg^{-1})	2.47×10^5
Solidus temperature, T_s (K)	1670
Liquidus temperature, T_l (K)	1727
Thickness of substrate metal, H_b (mm)	3.0
Radius of substrate metal, R_b (mm)	20.0

$$\frac{\partial}{\partial t}(\rho_{\mathrm{pl}}h_{\mathrm{pl}}) = \nabla\cdot\left(\frac{k_{\mathrm{pl}}}{c_{\mathrm{pl}}}\nabla h_{\mathrm{pl}}\right) + K_{\mathrm{pl}}I_c\exp\left(-\int_0^s K_{\mathrm{pl}}ds\right) + \sum_{m=1}^{n} K_{\mathrm{pl}}I_{r,m}(r,z)\exp\left(-\int_0^{s_m} K_{\mathrm{pl}}ds\right) \quad (6)$$

where h_{pl} and ρ_{pl} represent the enthalpy and density of the plasma, k_{pl} and c_{pl} represent the thermal conductivity and specific heat of the plasma, s is the penetration depth of laser light in the plasma, K_{pl} denotes the inverse Bremsstrahlung (iB) absorption coefficient. When an intense laser pulse interacts with the vapor in the keyhole, a significant amount of laser radiation is absorbed by the ionized particles through iB absorption. For the laser-induced plasma inside the keyhole, the scattering effect is not significant compared with the absorbing and emitting effects. For simplicity, the plasma is assumed to be an absorbing-emitting medium and the laser intensity is exponentially attenuated inside the keyhole plasma.

More details including the assumptions and simplifications about the model and the corresponding boundary conditions can be found in our previous paper [11] and will not be included here.

3 Numerical Method

In computation, the evaluation of the transport equations in the metal and plasma zones is coupled. That is, simulations of the metal and plasma zones provide boundary conditions for each other. However, there are large spatial and physical differences between them. For a compromise between the result convergence and calculation times, different time resolutions were used for these simulations. The governing equations (Eqs. (1)–(6)) and all related supplemental equations and boundary conditions are solved through the following iterative scheme:

1. Equations (1)–(4) are solved iteratively to obtain velocity, pressure, and temperature distributions under the associated boundary conditions for the metal zone.
2. Equation (6) is solved iteratively to obtain the temperature field of the plasma in the keyhole under the associated boundary conditions.
3. Iteration between step (1) and (2).
4. Solve the VOF algorithm Eq. (5) to obtain the new domain for the metal and plasma zones.
5. Update the boundary conditions for the metal and plasma zones.
6. Advance to the next time step until the desired time is reached.

The technique for solving the partial differential equations is given by Wang and Tsai [17]. Following the MAC scheme, the r- and z-velocity components are located at cell face centers on lines of constant r and z respectively, while the pressures, VOF function, temperature, and absorbed laser flux are located at cell centers. Since the temperature and pressure field change more dramatically near the keyhole, a nonuniform grid system with 202 $\times$252 points is used for the total computational domain of 5.0 mm$\times$6.25 mm, in which smaller grids are arranged near the keyhole and larger grids for other parts. Due to the y-axis-symmetry of the domain, only half of the grid points were used in the actual calculation. Due to the large spatial and physical differences between the solid/liquid metal and plasma zones, for a compromise between the result convergence and calculation time, different time resolutions must be used for these simulations. Calculations were executed on the DELL OPTIPLEX GX270 workstations with LINUX-REDHAT 9.0 OS and took 6 h of CPU time

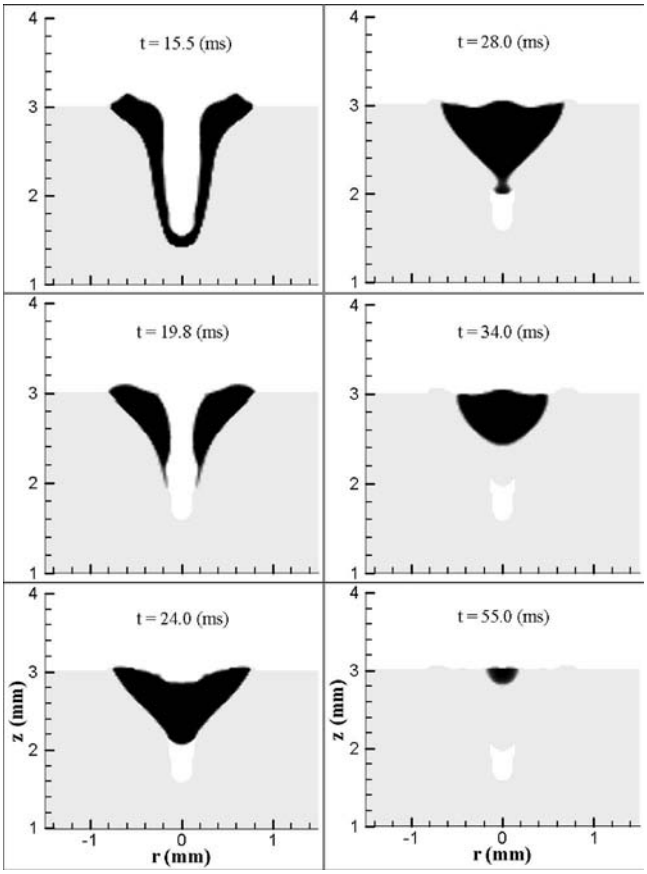

Fig. 2 A sequence of liquid metal evolution showing porosity formation

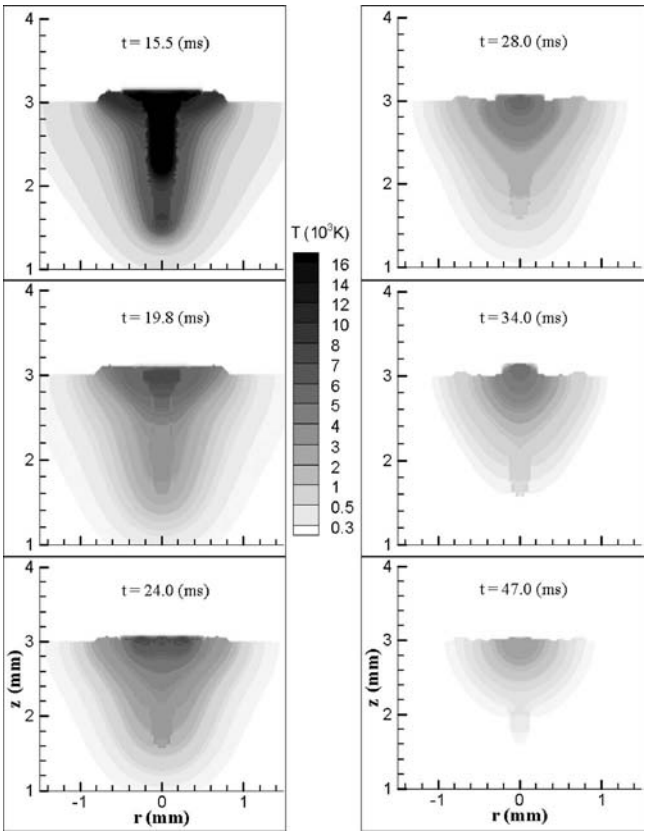

Fig. 3 The corresponding temperature distributions for the case as shown in Fig. 2

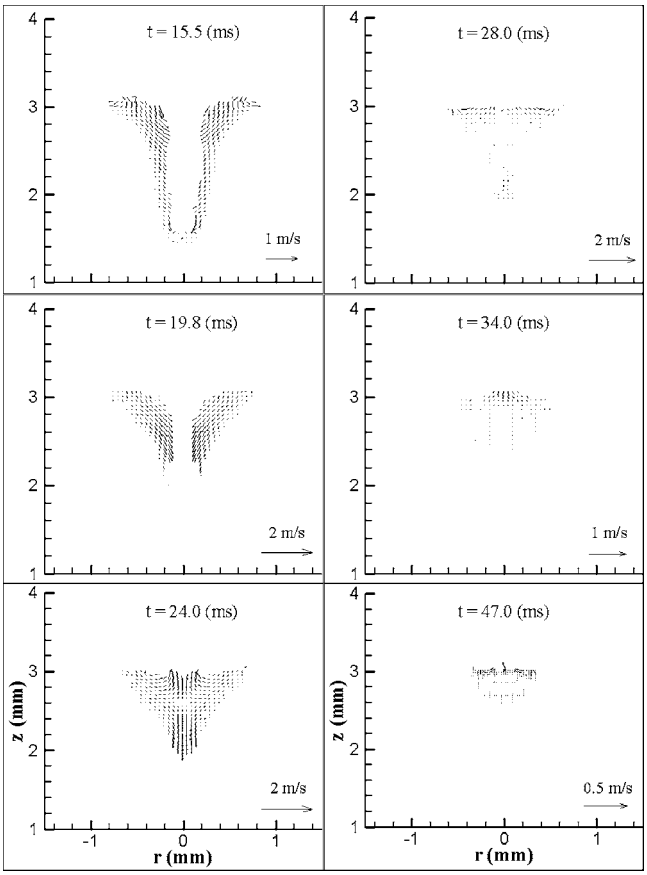

Fig. 4 The corresponding velocity distributions for the case as shown in Fig. 2

to simulate about 100 ms of real-time welding. The average time step is 10^{-4} s and the smallest time step is about 10^{-6} s.

4 Results and Discussion

The thermophysical properties and welding conditions used in the present study are summarized in Table 1. The following welding conditions are assumed in the model: the radius of the laser beam at focus is 0.25 mm, the laser beam energy is a Gaussian distribution, and the laser beam energy and pulse shape vary according to different study cases. The divergence of the laser beam is assumed to be negligible for a 3.0 mm metal thickness.

4.1 Porosity Formation. Since the keyhole formation process has been discussed before [11], the following discussions will be focused on the keyhole collapse process. Figure 2 shows a typical keyhole collapse and solidification process in pulsed laser welding with laser power at 1.7 kW and pulse duration time at 15.0 ms. The corresponding temperature and velocity evolutions are given in Figs. 3 and 4, respectively.

As shown in Fig. 2, once the laser is shut off at $t=15.0$ ms, the hot plasma is the only heat input source to irradiate the keyhole wall. Since the heat capacity of the plasma is very small, the temperature of the plasma drops very quickly after the laser is turned off, as shown at $t=15.5$ ms in Fig. 3. At $t=19.8$ ms, the keyhole plasma almost completely disappears. Furthermore, due to the large aspect ratio of the keyhole and the high temperature gradient, the heat loss conducted from the hot keyhole wall to the surrounding metal is very strong. Hence, as shown in Fig. 3, the temperature of the keyhole wall drops very quickly, especially for the lower part of the keyhole having only a thin layer of the liquid metal. Due to this quick temperature drop, the thin layer of liquid metal on the bottom of the keyhole solidifies very quickly after the shut-off of the laser power, as shown at $t=19.8$ ms in Fig. 2.

As shown in Fig. 3, after the laser beam is shut off, the temperature on the bottom surface of the keyhole drops faster than that on the upper surface, so the temperature gradient along the

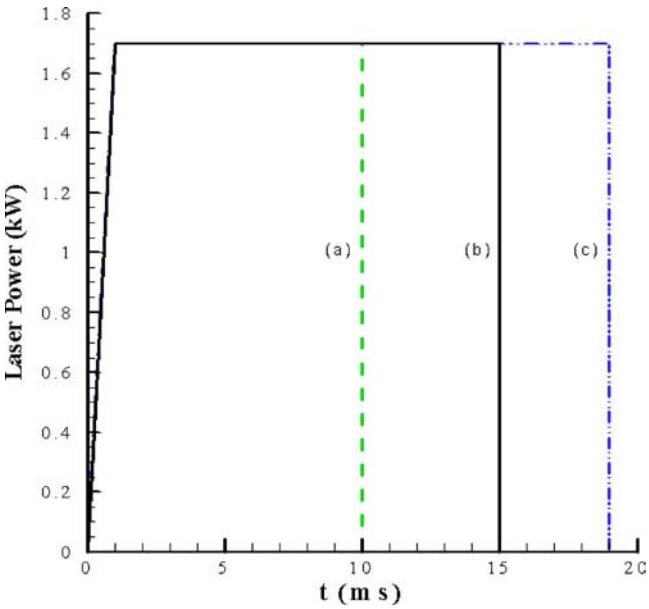

Fig. 5 Laser pulse profile used to generate (*a*) a small depth-to-width ratio keyhole; (*b*) a medium depth-to-width ratio keyhole; and (*c*) a large depth-to-width ratio keyhole

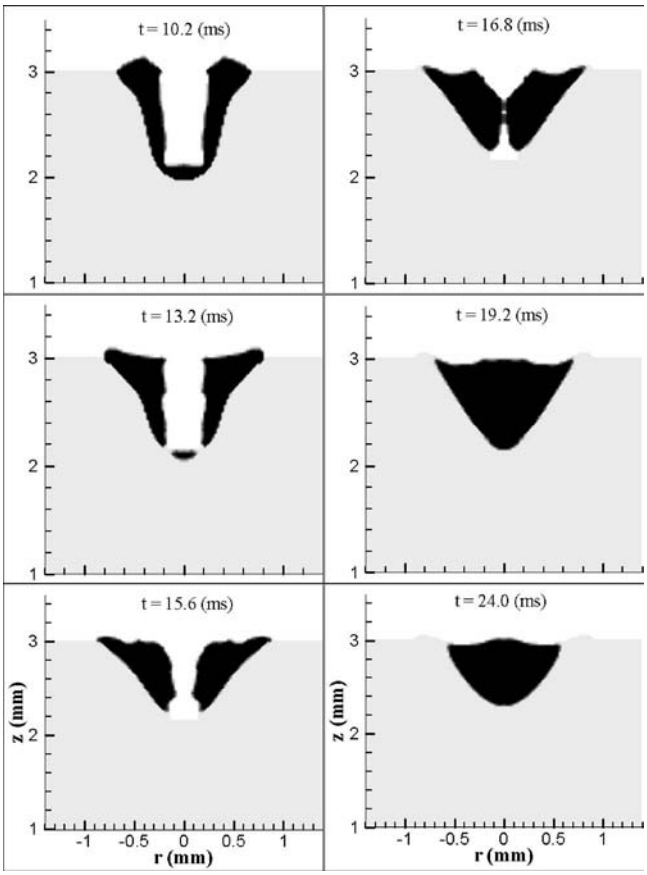

Fig. 6 A sequence of liquid metal evolution during the keyhole collapse and solidification in a small depth-to-width ratio keyhole welding process

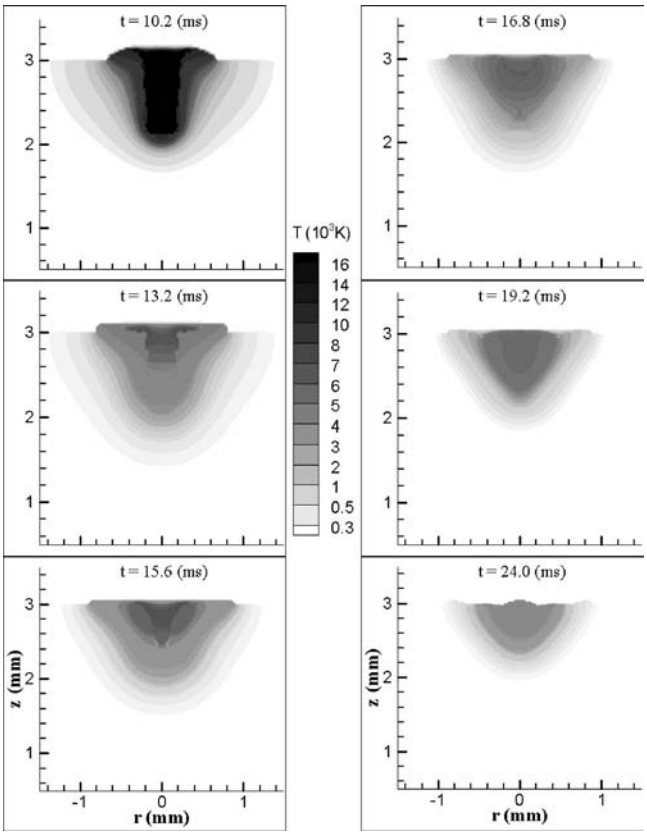

Fig. 7 The corresponding temperature distributions for the case as shown in Fig. 6

keyhole wall decreases. This causes the temperature-dependent Marangoni shear stress to decrease accordingly. Meanwhile, with the removal of the recoil pressure due to the shut-off of the laser, the recoil pressure-driving hydrodynamic pressure of the squeezed liquid metal also decreases very quickly. Consequently, surface tension and hydrostatic pressure become dominant and drive the liquid metal to have a tendency to fill back the keyhole. As shown in Fig. 4 at $t=15.5$ ms, the liquid metal located on the upper part of the keyhole starts to flow inward and downward under the hydrostatic pressure and surface tension. Since the liquid metal layer is thicker on the top and the flow friction along the liquid-solid interface is larger for a thinner liquid layer, the backfilling velocity for the liquid metal on the upper part is accelerated more quickly than those on the lower part of the keyhole. As shown in Fig. 2, the keyhole is closed on the top first. After the keyhole is closed on the top, the liquid metal continues to flow downward along the keyhole wall. When the liquid metal flows downward along the solidified keyhole wall, its velocity is decreased by the friction force of the cool keyhole wall. Meanwhile the solid-liquid interface moves inward to the centerline of the keyhole because of the strong heat conduction loss to the surrounding metal along the keyhole wall. As shown in Fig. 2 from $t=24.0$ ms to $t=28.0$ ms, the liquid region shrinks as the liquid refills the keyhole, especially for the liquid metal at the bottom because of higher conduction heat loss and lower heat capacity there. Finally the bottom of the downward flowing liquid metal completely solidified before it can reach the bottom of the keyhole as shown at $t=28.0$ ms. From then on, although there is still a certain amount of liquid metal on the top, this part of liquid metal cannot continue to flow downward, which leaves a pore or void at the root of the keyhole.

4.2 Aspect Ratio of Keyhole Versus Size of the Pore. The aspect ratio is the ratio of keyhole depth to its width. In laser welding, especially in keyhole mode laser welding, the aspect ratio can be very large, which is one of the main advantages of laser welding. However, porosity is frequently found in a deep keyhole laser weld. The following studies are addressed toward investigating the effect of keyhole aspect ratio on porosity formation. In the studies, the laser power and keyhole width are fixed and the keyhole depth is determined by the laser pulse duration. By changing the pulse duration of the laser beam, different aspect ratio keyholes can be obtained in different study cases. In the following discussions, small aspect ratio means the ratio is less than 0.6, while the medium aspect ratio means the ratio is larger than 0.6 and less than 1.0. If the ratio is larger than 1.5, it is considered as a large aspect ratio.

4.2.1 Small Aspect Ratio Keyhole. The laser power used in this study was 1.7 kW and the radius of the laser beam at the focus was 0.2 mm. As shown in Fig. 5(*a*), the laser power was set at 1.7 kW within 1.0 ms and was turned off at $t=10.0$ ms. Figure 6 shows the keyhole collapse and solidification processes. The corresponding temperature and velocity distributions are given, respectively, in Figs. 7 and 8.

As shown in Fig. 6 at $t=10.2$ ms, alot of liquid metal was squeezed from the bottom of the keyhole to its shoulder by the laser-induced recoil pressure during the keyhole formation process. After the laser beam was turned off at $t=10.0$ ms, the laser-induced recoil pressure very quickly disappeared. Hence, there was no strong driving force to push the liquid metal to flow toward the top of the keyhole. Meanwhile, as shown in Fig. 7 from $t=10.2$ ms to $t=13.2$ ms, the temperature of the keyhole plasma and liquid metal very quickly drops due to the shut-off of the laser power. Once the liquid metal temperature drops below 2150 K, the surface tension gradient coefficient $\partial\gamma/\partial T$ will turn positive.

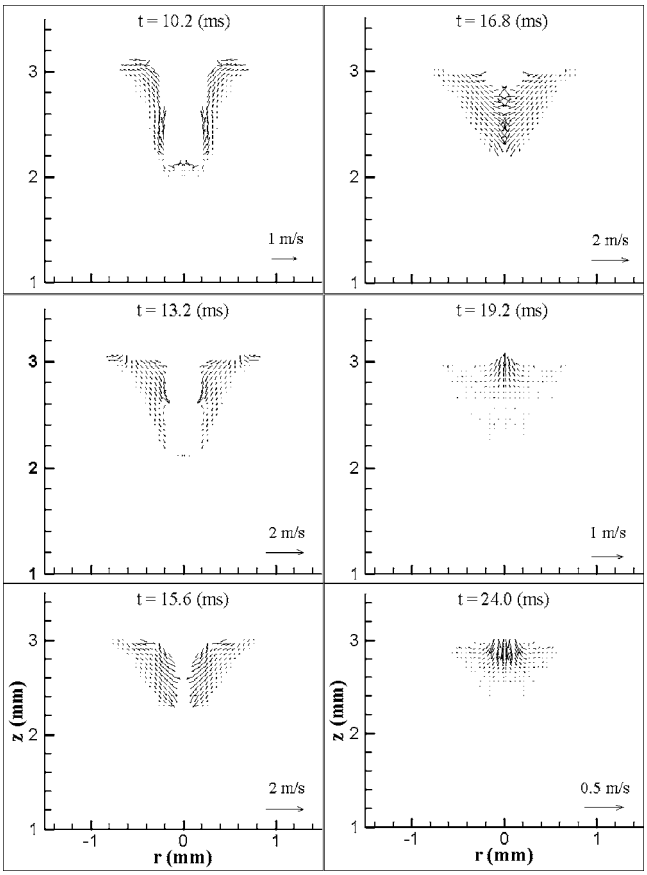

Fig. 8 The corresponding velocity distributions for the case as shown in Fig. 6

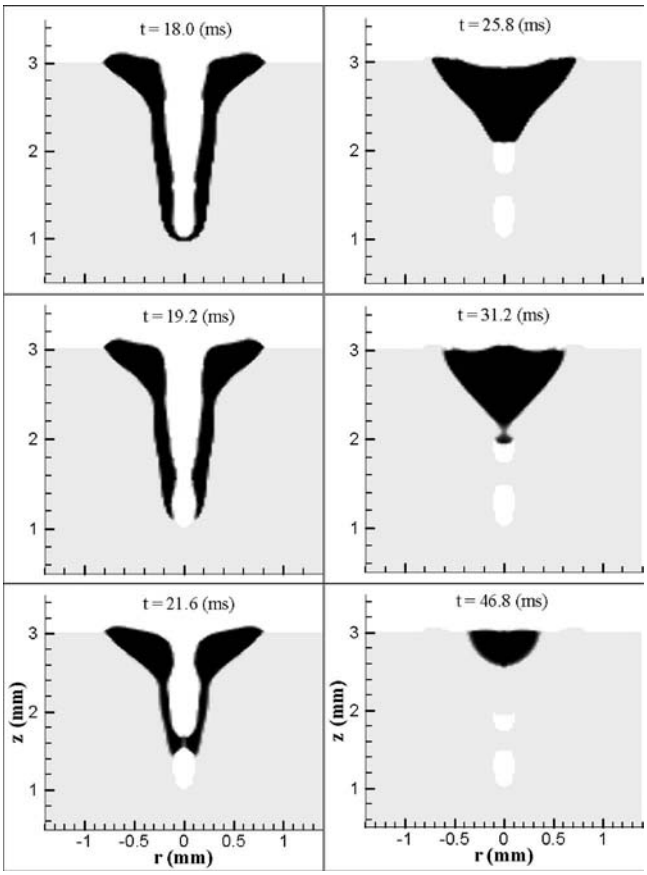

Fig. 9 A sequence of liquid metal evolution during the keyhole collapse and solidification in a large depth-to-width ratio keyhole welding process

Since at this time the temperature gradient from the center to the shoulder is still positive, it will cause the temperature-dependent surface tension force to change its direction to negative along the weld pool surface. This will drive the liquid metal to flow inward. This surface tension force combined with the hydrostatic pressure will drive the accumulated liquid metal on the top to have a tendency to fill back the keyhole. As shown in Fig. 6 at $t=13.2$ ms, the keyhole starts to collapse from the top under these forces. Since it takes time for the liquid metal flow to change its direction, the liquid metal is still flowing outward and upward at $t=10.2$ ms in Fig. 8. With the continuous acceleration of the surface tension force and hydrostatic pressure, the liquid metal finally flows downward and inward at $t=13.2$ ms.

In Fig. 6 at $t=10.2$ ms, after the shut-off of the laser, since there is no heat input, the solidification process quickly becomes dominant. Comparing the figures at $t=10.2$ ms, $t=13.2$ ms, and $t=15.6$ ms in Fig. 6, it is easy to find the liquid metal on the bottom of the keyhole almost completely solidifies at $t=15.6$ ms due to the solidification process. As indicated by previous discussions of the porosity formation process, it is known that porosity formation is determined by two competing processes: the backfilling process and the solidification process. Since the keyhole depth is small in this case, it requires shorter time for the liquid metal on the top to fill back the bottom of the keyhole. As shown in Fig. 6, although the liquid metal on the bottom of the keyhole almost completely solidifies at $t=15.6$ ms, since the keyhole is shallow, the liquid metal flowing downward from the top can still reach the keyhole bottom at $t=19.2$ ms and fill up the keyhole before complete solidification. Hence, no porosity is found in the final weld in this case.

4.2.2 Medium Aspect Ratio Keyhole. The laser power density and the radius of the laser beam at the focus are kept the same as those in the previous case to ensure the same width of the keyhole. As shown in Fig. 5(*b*), the laser beam is held for a longer time to 15.0 ms to get a deeper keyhole. The keyhole collapse process after shut-off of the laser power is shown in Fig. 2. The corresponding temperature and velocity distributions are given, respectively, in Figs. 3 and 4. As discussed in the previous porosity formation section, a pore/void is found at the root of the keyhole in this case since the solidification process exceeds the backfilling process.

4.2.3 Large Aspect Ratio Keyhole. In this case, the laser power and the radius of the laser beam are still kept the same as those in the previous two cases to ensure the same keyhole width. As shown in Fig. 5(*c*), the laser beam is held for a longer time to 19.0 ms to produce an even deeper keyhole. Figure 9 shows the keyhole collapse and solidification processes. The corresponding temperature and velocity distributions are given, respectively, in Fig. 10 and 11. As shown in Fig. 9 at $t=18.0$ ms, since the keyhole is deeper, only a small amount of laser beam energy can reach the bottom of the keyhole and there is only a very thin layer of liquid metal on the bottom of the keyhole. After the shutoff of the laser beam, due to less heat capacity and strong heat loss on the bottom of the keyhole, the thin layer of liquid metal on the bottom of the keyhole quickly solidifies at $t=19.2$ ms. Meanwhile, with the actions of hydrostatic pressure and surface tension force, the liquid metal in the upper and middle part of the keyhole is flowing downward along the keyhole wall. While flowing along the solidified keyhole wall, since there is not too much liquid metal there and its heat capacity is small, the downward flowing liquid metal quickly cools down and its downward velocity rap-

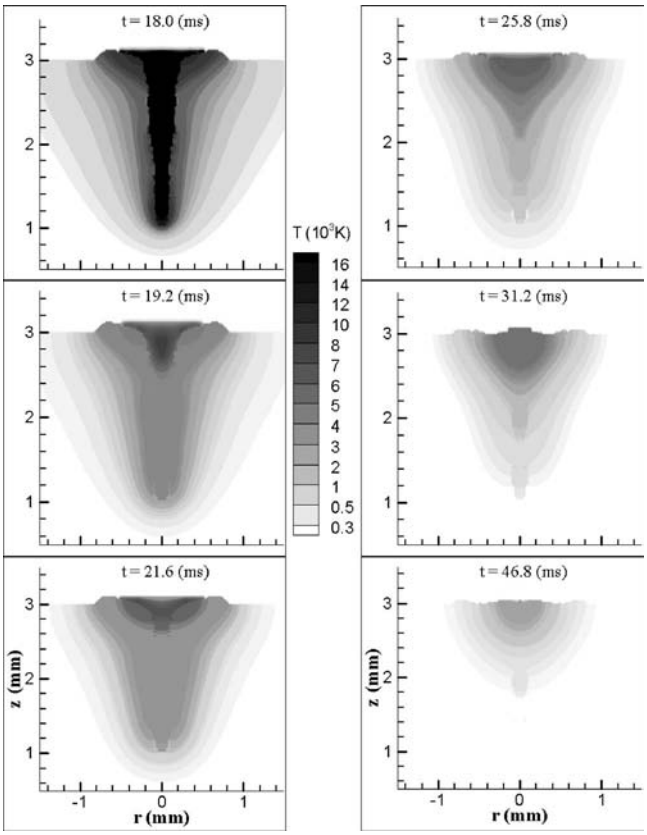

Fig. 10 The corresponding temperature distributions for the case as shown in Fig. 9

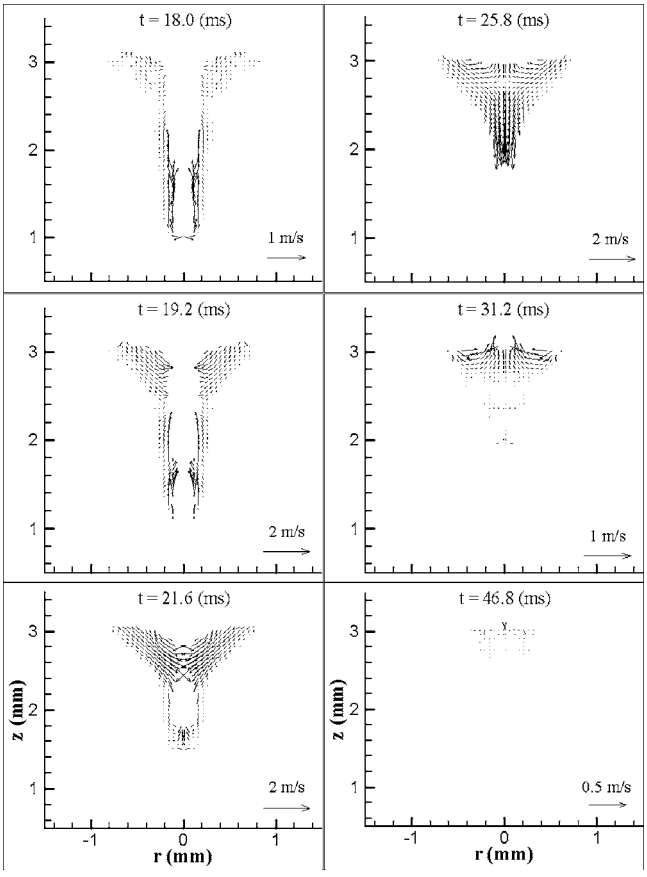

Fig. 11 The corresponding velocity distributions for the case as shown in Fig. 9

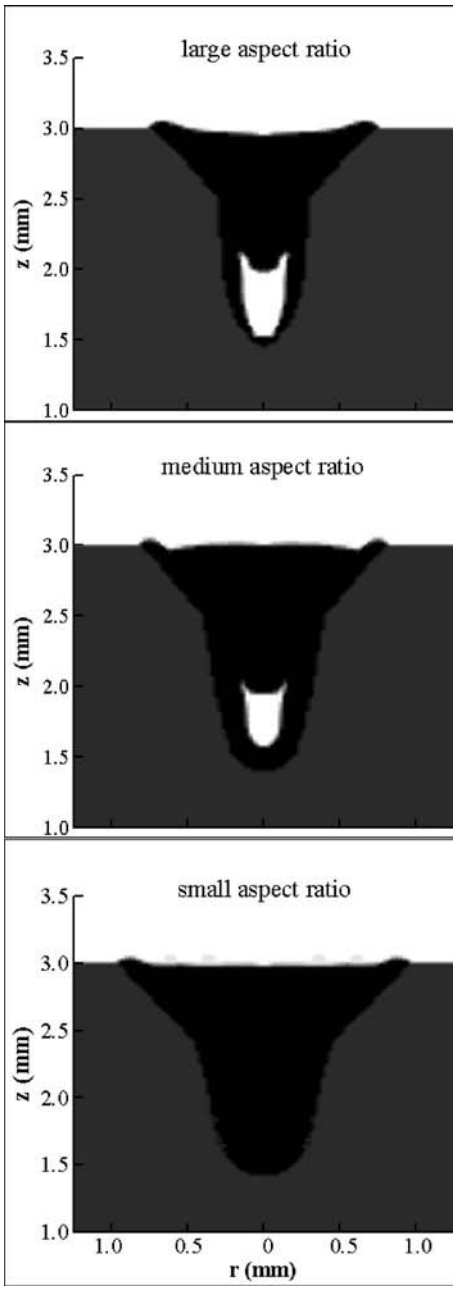

Fig. 12 The effect of depth-to-width ratio on pore formation for constant keyhole depth

idly decreases due to the friction force of the cool keyhole wall. After a very short period of time, when the downward flowing liquid metal reaches a certain depth (z=1.5 mm in Fig. 9), the bottom velocity of this downward flowing liquid metal decreases to almost zero and its bottom completely solidifies. Although, at this time, there is still some liquid metal on the top (z>1.5 mm in Fig. 9), this amount of liquid metal is blocked by the solidified metal and cannot flow downward any farther. At t=25.8 ms, this small amount of liquid metal completely solidifies in the middle of the keyhole. So, a pore/void is formed at the root of the keyhole.

Meanwhile, with the combined actions of surface tension force and hydrostatic pressure, the liquid metal on the top of the keyhole is still flowing downward and inward to fill back the keyhole. It takes a while for the liquid metal in the middle of the keyhole wall to change its flow direction as shown in Fig. 11, when t

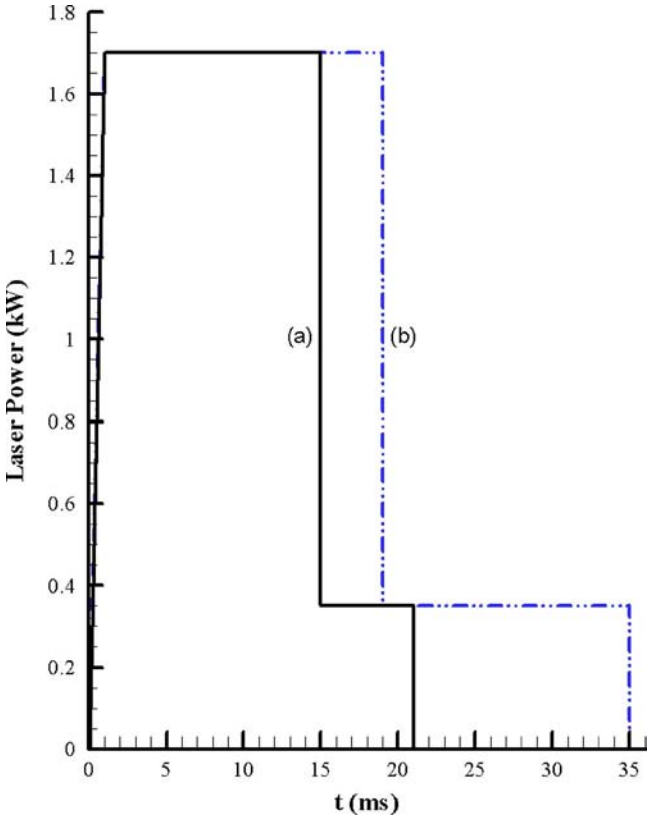

Fig. 13 Laser pulse profiles used to reduce/eliminate pore/void formation for a keyhole with (*a*) a medium depth-to-width ratio and (*b*) a large depth-to-width ratio

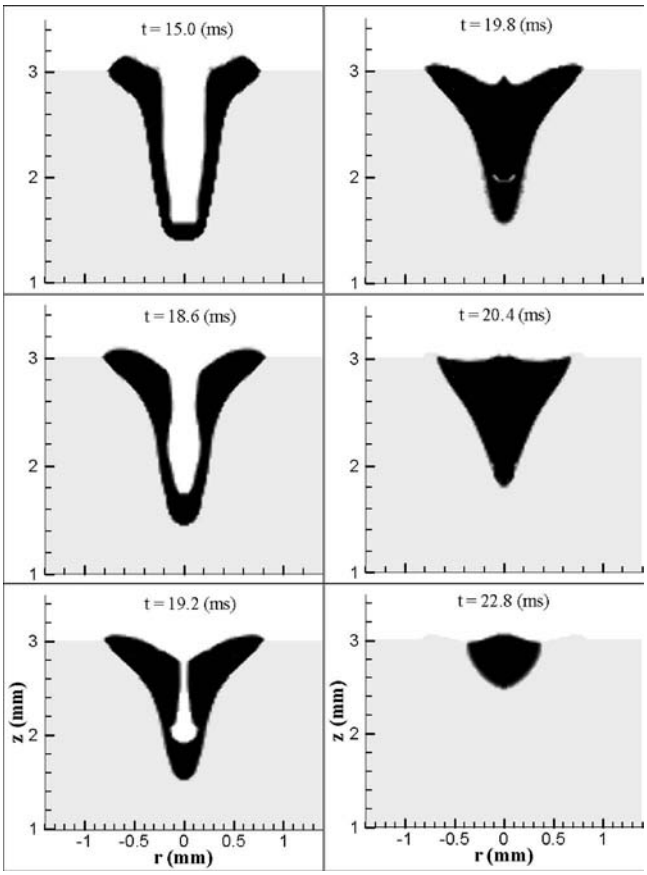

Fig. 14 A sequence of liquid metal evolution during pore/void reduction/elimination for a medium depth-to-width ratio keyhole welding process by using the pulse profile in Fig. 13(*a*)

>21.6 ms, the liquid metal changes its direction to flow downward. The magnitude of the velocity is relatively small and the amount of liquid metal in the middle of the keyhole wall is small, so the solidification process becomes dominant. Compared to that at $t=19.2$ ms, the liquid metal region in the middle part of the keyhole shrinks at $t=21.6$ ms due to the solidification process. At $t=25.8$ ms, the keyhole is closed from the top and the downward flowing liquid metal very quickly cooled down. The whole liquid region shrinks from outside to inside and from bottom to top and its velocity is decreased by the friction forces. At $t=31.2$ ms, when the downward flowing liquid metal reaches the middle of the keyhole (at $z=2.0$ mm in Fig. 9), the bottom part almost completely solidifies. Hence, the remaining liquid metal on the top cannot flow downward farther. Another pore/void was formed in the middle of the keyhole in the final weld. In the previous three case studies, the keyhole width was fixed and the change of the aspect ratio was controlled by changing the keyhole depth. It was found that for a small depth-to-width keyhole, there was no porosity found in the final weld. For a medium and large depth-to-width aspect ratio keyhole, porosity was found and for a large aspect ratio keyhole, the porosity size was larger. In the following, the porosity formation process was further studied using a fixed keyhole depth and varying keyhole width conditions. Results are shown in Fig. 12 and similar phenomena are found. For a small depth-to-width aspect ratio keyhole, there was no porosity found in the final weld bead. For a medium and large aspect ratio keyhole, porosity was found. This can also be explained through investigation of the porosity formation process. As the keyhole width increases, the backfilling time (the time from laser light removal to when the liquid metal stops filling back) will correspondingly increase due to the increasing amount of liquid metal on the top and decreasing solidification rate. This gives more time for the liquid metal to flow downward to fill the keyhole. Moreover, larger keyhole diameter leads to a smaller wall friction, which also increases backfilling speed of the liquid metal. Both factors help to reduce porosity formation in the final welds.

4.3 Porosity Prevention/Elimination by Laser Pulse Control. From the aforementioned studies, it is clear that if the downward flowing liquid metal can fill up the bottom of the keyhole before complete solidification, there will be no porosity in the final weld. This can be achieved in two ways: (1) delaying the solidification process to increase the backfilling time; (2) increasing the backfilling speed of the liquid metal. The following studies will be focused on studying the effectiveness of the first method for delaying the solidification process. This can be realized by controlling the laser pulse shape and power density.

4.3.1 Medium Aspect Ratio Keyhole. As inspired by the previous studies, at $t=15.0$ ms if the laser is not completely shut off, but reduced to a moderate power level, whose density is not large enough to produce a recoil pressure, but large enough to provide additional heat for the weld pool. Then the solidification process will be delayed by this additional heat input and, consequently, the backfilling time will be increased. This increased backfilling time can allow the downward flowing liquid metal to fill up the keyhole. As shown in Fig. 13(*a*) at $t=15.0$ ms, the laser power is reduced to 0.35 kW, one-fifth of its peak value, and lasts for another 6.0 ms. This reduced laser power is small enough to prevent the recoil pressure effect on the keyhole wall while it can provide enough heat to delay the solidification process. Figure 14 shows the keyhole collapse and solidification processes. The corresponding temperature and velocity evolutions are shown in Figs. 15 and 16.

As shown in Fig. 14, with the removal of the main laser power

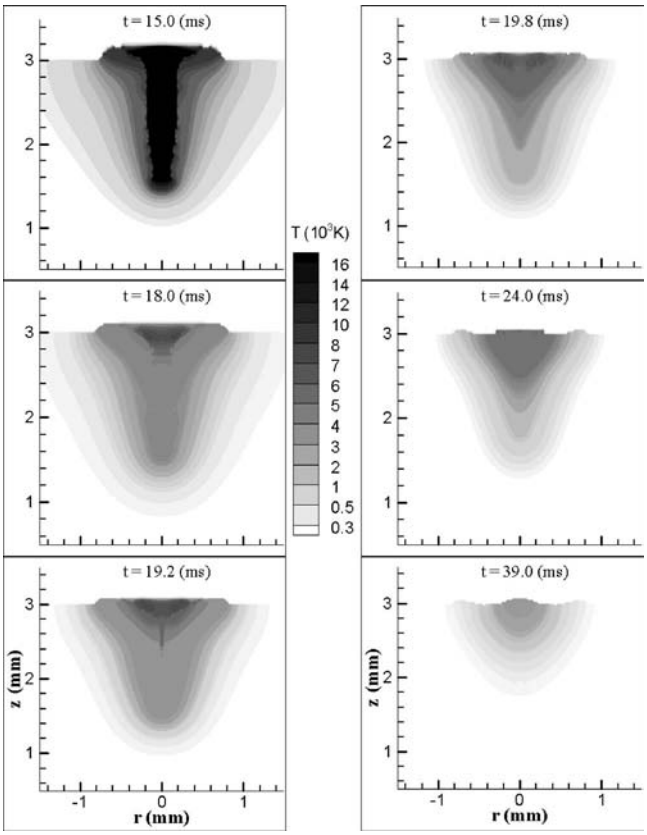

Fig. 15 The corresponding temperature distributions for the case as shown in Fig. 14

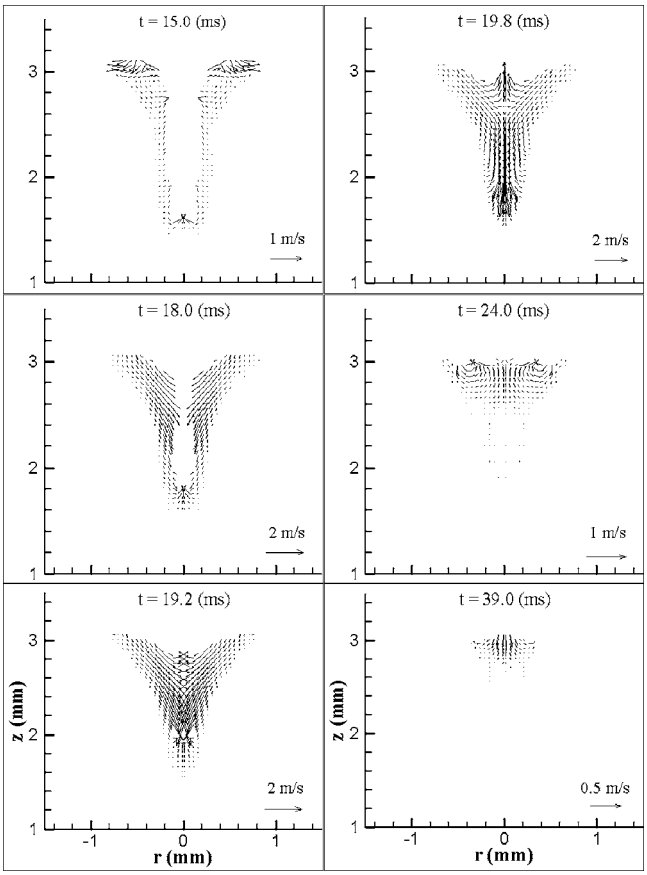

Fig. 16 The corresponding velocity distributions for the case as shown in Fig. 14

at $t=15.0$ ms, the keyhole begins to collapse. Meanwhile the reduced laser power continues to heat the keyhole surface, which allows liquid metal at the bottom of the keyhole to remain liquid at $t=18.6$ ms as compared to what occurred in Fig. 2. As the liquid metal from the shoulder of the keyhole approaches the center, it prevents part of the laser light from reaching the bottom surface of the keyhole. This will lead to a temperature decrease on this part of the keyhole wall. However, the multiple reflections on the keyhole wall will reflect some laser energy to the keyhole wall where laser light cannot radiate directly. This helps to delay the solidification process along the keyhole wall. At $t=19.2$ ms, the keyhole is almost completely closed from the top and from then on only a very small portion of the laser light can reach the bottom of the keyhole. However, as shown in Fig. 15, the temperature on the bottom of the keyhole wall is still hot enough to allow the metal to stay liquid. At this time, most of the laser energy is used to heat the liquid metal on the top, which can help the liquid metal on the top to flow downward. As shown in Fig. 16 at $t=19.2$ ms, the downward momentum of the liquid metal is strong. Hence, within a short period of time, the downward flowing liquid metal almost completely fills up the keyhole at $t=19.8$ ms and the porosity which was found in Fig. 2 has been eliminated. Although some gas is enclosed, the gas is surrounded by liquid metal, which can continue to flow into the gas region. During the backfilling process, the hydrostatic pressure continues to accelerate the melt flow, which facilitates the backfilling process. The downward flowing liquid metal makes the gas region smaller and smaller. In addition, since the gas is a mixture of shielding gas and metal vapor, some of it will be dissolved in the liquid metal during the compression process and eventually the gas region will completely disappear in the metal liquid, as shown at $t=20.4$ ms in Fig. 14. This result is consistent with the experimental observations by Katayama and Matsunawa [3].

4.3.2 Large Aspect Ratio Keyhole. As shown above, through providing additional heat to increase the backfilling time, controlling the laser pulse shape is a very effective way to eliminate porosity formation for a medium aspect ratio keyhole laser weld. In the following study, the effectiveness of this method is investigated for a large aspect ratio keyhole. As shown in Fig. 13(*b*) at $t=19.0$ ms, the laser power density is reduced to 0.35 kW. Since the keyhole is deeper, this reduced laser power is held for a longer time (35.0 ms) to provide more additional heat. Figure 17 shows the keyhole collapse and solidification processes and the corresponding temperature and velocity distributions are shown in Figs. 18 and 19, respectively.

As shown in Fig. 18, due to the additional heat input after the removal of the main laser power, the plasma temperature drops slower from $t=18.0$ ms to $t=19.2$ ms as compared to that in Fig. 10. This is helpful to keep the liquid metal on the bottom of the keyhole and to delay the solidification process of the liquid metal on the side of the keyhole. This is clearly indicated at $t=19.2$ ms in Fig. 17, due to irradiation from the hot plasma and the additional heat input from the laser, the metal on the keyhole bottom is still a liquid and the amount of the liquid metal on the side of the keyhole is almost the same as that at $t=18.0$ ms.

However, since the keyhole aspect ratio is larger in this case, more liquid metal is located on the shoulder, which leaves a larger crater on the top of the keyhole. Meanwhile, the reduced laser energy can keep the temperature of the liquid metal on the top high, which facilitates the melt flow there. Hence, at $t=19.0$ ms, after the removal of the main laser power, with the action of surface tension force and hydrostatic pressure, this large crater will drive the hot liquid metal on the top to move inward easily to close the keyhole and shorten the time for keyhole closure. When the liquid metal from the shoulder of the keyhole approaches the

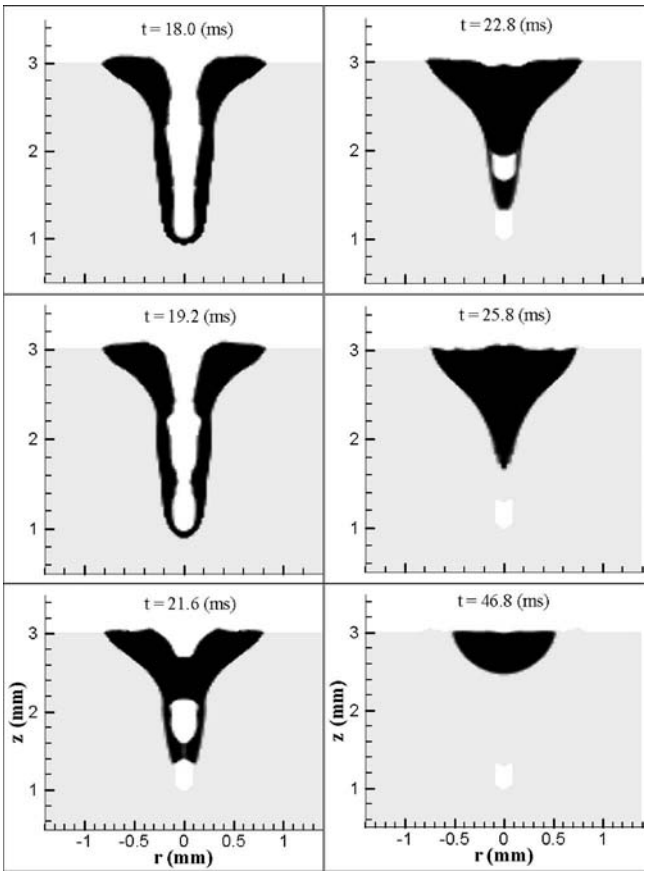

Fig. 17 A sequence of liquid metal evolution during pore reducing/elimination for a large depth-to-width ratio keyhole welding process by using the pulse profile in Fig. 13(*b*)

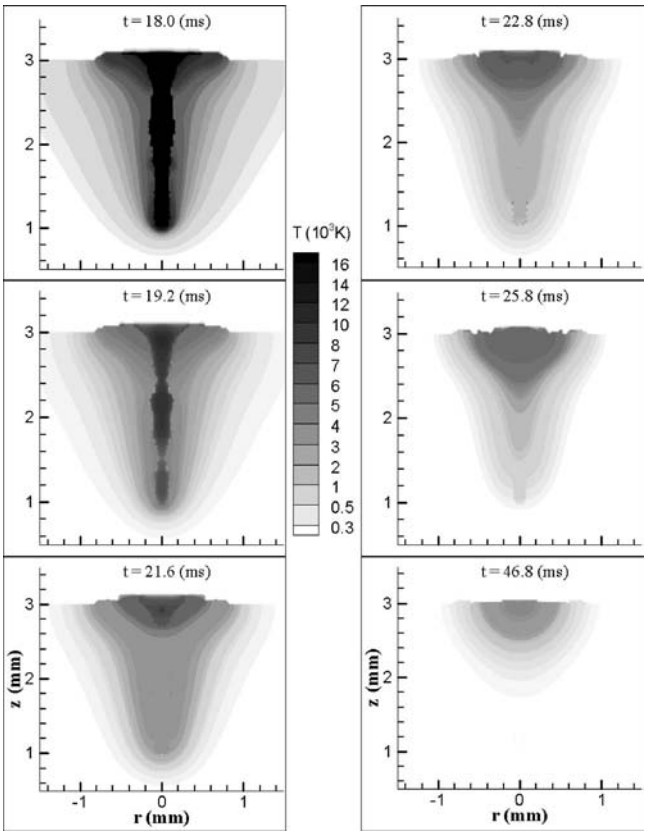

Fig. 18 The corresponding temperature distributions for the case as shown in Fig. 17

keyhole center, the amount of the laser beam energy entering the keyhole becomes smaller and smaller. Although the multiple reflections can still bring some laser light to heat the keyhole wall where the laser light cannot radiate directly, the total area is relatively large compared with that in a medium aspect ratio keyhole, the heat input per unit area is reduced for a high aspect ratio keyhole. This facilitates the solidification process on the keyhole wall and bottom. As shown in Fig. 18, at $t=19.2$ ms, the temperature of the liquid on the bottom quickly decreases due to the heat loss to the surrounding metal and the reduced incoming heat input caused by the keyhole collapse from the top. At $t=21.6$ ms in Fig. 17, the keyhole is completely closed on the top, then laser light cannot enter the keyhole and the liquid metal on the bottom of the keyhole quickly solidifies. Although, with the action of hydrostatic pressure, the liquid metal on the upper and middle part of the keyhole flows downward to fill the keyhole, due to the fast solidification rate, at $t=22.8$ ms the bottom part of the downward flowing liquid metal completely solidifies at $z=1.65$ mm in Fig. 17. After that, no liquid metal can reach the bottom of the keyhole and a pore/void shown in Fig. 9 is still found at the root of the keyhole.

However, there is no pore or void found in the upper part of the keyhole in this case, which is different from that shown in Fig. 9. This is easy to understand. As shown in Fig. 17 at $t=21.6$ ms, the keyhole is fully closed on the top. From then on, although the laser light cannot penetrate into the keyhole any more, it still can heat the liquid metal on the top and keep the temperature of the liquid metal high, which facilitates the liquid metal to flow downward against small friction force. Although, at this time, part of the liquid metal solidifies along the keyhole wall due to the solidification process. Since there is a considerable amount of liquid metal with high temperature on the top as shown in Fig. 18 and the downward momentum of the liquid metal is strong as shown in Fig. 19, this hot downward flowing liquid metal can eventually reach the top of the previously solidified metal (at $z=1.4$ mm) and fill up the keyhole there at $t=25.8$ ms. Hence, the pore/void shown in the middle part of the keyhole in Fig. 9 has been eliminated.

5 Conclusions

Porosity formation is investigated in a keyhole mode laser welding process using mathematical models. The influence of depth-to-width aspect ratio of the keyhole on porosity formation is discussed. Based on these investigations, the prevention/elimination of porosity through laser pulse control is put forward. The conclusions obtained are listed as follows.

Porosity is formed during the keyhole collapse and solidification process. The formation of porosity has a close relationship with two competing factors: (1) the solidification rate of the liquid metal, and (2) the backfilling speed of the liquid metal. If the backfilling speed of the liquid metal is not large enough to make the downward flowing liquid metal completely fill up the keyhole before its complete solidification, a pore/void will be found in the final weld. Aspect ratio of the keyhole has major influence on porosity formation. For a small depth-to-width aspect ratio keyhole welding process, there is no pore/void found in the final weld. For a medium or large aspect ratio keyhole welding process, porosity is found in the final weld. The larger the aspect ratio, the easier the porosity is formed and the larger the size of the pore/void.

The mechanism of preventing porosity formation through laser pulse shape control is to delay the solidification process, which allows the liquid metal in the weld pool to have enough time to flow downward to fill up the keyhole. This method is very effec-

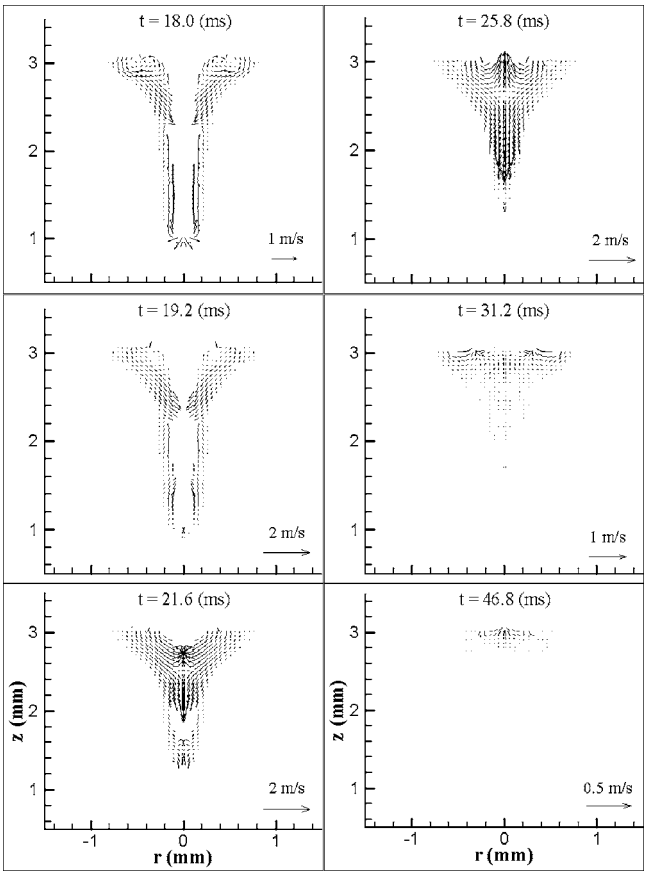

Fig. 19 The corresponding velocity distributions for the case as shown in Fig. 17

tive in eliminating porosity formation for a medium aspect ratio keyhole. But for a large aspect ratio keyhole, it has its limitations. The pore/void in the middle of the keyhole can be eliminated, but it cannot eliminate porosity formation at the root of the keyhole. Other porosity prevention methods, such as increasing the backfilling speed of the liquid metal via application of electromagnetic force to eliminate the porosity in large aspect ratio keyhole laser welding will be investigated in future studies.

Acknowledgment

It is gratefully acknowledged that this research is partially supported by the General Motors Corporation. Also, special thanks go to Professor Terry F. Lehnhoff for his guidance in writing and for beneficial discussions with him.

Nomenclature

c_p = specific heat for metal
c_{pl} = specific heat for keyhole plasma
C = coefficient defined in Eq. (2)
f = mass fraction
F = volume of fluid function
g = gravitational acceleration
h = enthalpy for metal
h_{pl} = enthalpy for plasma
H_b = thickness of base metal
I = laser beam intensity
k = thermal conductivity for metal
K = permeability function defined in Eqs. (2) and (3)
K_{pl} = plasma laser absorption coefficient
p = pressure for metal zone simulation
r-z = cylindrical coordinate system
R_b = radius of base metal
s = penetration depth of laser light in plasma
t = time
T = temperature
u = velocity in the r-direction
v = velocity in the z-direction
$\boldsymbol{V}$ = velocity vector

Greek symbols

β_T = thermal expansion coefficient
μ = dynamic viscosity
ρ = density for metal

Subscripts

0 = initial value
c = original incident laser light
l = liquid phase
r = relative to solid velocity
(r,m) = mth reflected laser beam
pl = plasma
s = solid phase

References

[1] Ishide, T., Tsubota, S., Nayama, M., Shimokusu, Y., Nagashima, T., and Okimura, K., 1999, "10 kW Class YAG Laser Application for Heavy Components," *SPIE High-Power Lasers in Manufacturing*, Osaka, Vol. 3888, pp. 543–550.
[2] Katayama, S., Seto, N., Kim, J., and Matsunawa, A., 1997, "Formation Mechanism and Reduction Method of Porosity in Laser Welding of Stainless Steel," in *Proceedings of ICALEO*, Sec. G, pp. 83–92.
[3] Katayama, S., and Matsunawa, A., 1998, "Formation Mechanism and Prevention of Defects in Laser Welding of Aluminum Alloys," in *Proceedings of CISFFEL 6*, Vol. 1, pp. 215–222.
[4] Katayama, S., Seto, N., Kim, J., and Matsunawa, A., 1998, "Formation Mechanism and Suppression Procedure of Porosity in High Power Laser Welding of Aluminum Alloys," in *Proceedings of ICALEO*, Sec. C, pp. 24–33.
[5] Katayama, S., Seto, N., Mizutani, M., and Matsunawa, A., 2000, "Formation Mechanism of Porosity in High Power YAG Laser Welding," in *Proceedings of ICALEO*, Sec. C, pp. 16–25.
[6] Seto, N., Katayama, S., and Matsunawa, A., 1999, "A High – Speed Simultaneous Observation of Plasma and Keyhole Behavior during High Power CO_2 Laser Welding," in *Proceedings of ICALEO*, Sec. E, pp. 17–19.
[7] Katayama, S., Kohsaka, S., Mizutani, M., Nishizawa, K., and Matsunawa, A., 1993, "Pulse Shape Optimization for Defect Prevention in Pulsed Laser Welding of Stainless Steels," in *Proceedings of ICALEO*, pp. 487–497.
[8] Katayama, S., Kobayashi, Y., Seto, N., Mizutani, M., and Matsunawa, A., 2000, "Effect of Vacuum on Penetration and Defects in Laser Welding," in *Proceedings of ICALEO*, Sec. C, pp. 182–191.
[9] Tsukamoto, S., Kawaguchi, I., and Arakane, G., 2000, "Suppression of Welding Defects in Deep Penetration CO2 Laser Welding," in *Proceedings of ICALEO*, Sec. C, pp. 7–15.
[10] Todate, A., Ueno, Y., Katsuki, M., Katayama, S., and Matsunawa, A., 2000, "YAG Laser Weldability of Carbon Steel in CO_2 Shielding Gas," in *Proceedings of the National Meeting of JWS*, No. 66, pp. 144–145.
[11] Zhou, J., Tsai, H. L., and Wang, P. C., 2006, "Transport Phenomena and Keyhole Dynamics During Pulsed Laser Welding," ASME J. Heat Transfer, **128**(7), pp. 680–690.
[12] Kothe, D. B., Mjolsness, R. C., and Torrey, M. D., 1991, "Ripple: A Computer Program for Incompressible Flows With Free Surfaces," LA-12007-MS, Los Alamos National Laboratory.
[13] Chiang, K. C., and Tsai, H. L., 1992, "Shrinkage-Induced Fluid Flow and Domain Change in Two-Dimensional Alloy Solidification," Int. J. Heat Mass Transfer, **35**, pp. 1763–1769.
[14] Miyamoto, I., Ohmura, E., and Maede, T., 1997, "Dynamic Behavior of Plume and Keyhole in CO_2 Laser Welding," in *Proceedings of the ICALEO*, Sec. G, pp. 210–218.
[15] Dowden, J., Postacioglu, N., Davis, M., and Kapadia, P., 1987, "A Keyhole Model in Penetration Welding WIth a Laser," J. Phys. D, **20**, pp. 36–44.
[16] Siegel, R., and Howell, J. R., 1992, *Thermal Radiation Heat Transfer*, 3rd ed., Hemisphere, NY, Chap. 13.
[17] Wang, Y., and Tsai, H. L., 2001, "Impingement of Filler Droplets and Weld Pool Dynamics During Gas Metal Arc Welding Process," Int. J. Heat Mass Transfer, **44**, pp. 2067–2080.

Metal Transfer and Arc Plasma in Gas Metal Arc Welding

J. Hu[1]

H. L. Tsai[2]
e-mail: tsai@umr.edu

Department of Mechanical and Aerospace Engineering,
University of Missouri-Rolla,
Rolla, MO 65409

This article analyzes the transient complex heat transfer and fluid flow in molten metal and arc plasma during the gas metal arc welding process. The model predicts the formation, growth, detachment, and transfer of droplets from the tip of a continuously fed electrode under the influences of several competing forces including gravity, electromagnetic force, arc pressure, plasma shear stress, and surface tension. Simulations were conducted for five different current levels to study the effects of current on the distributions of temperature, velocity, pressure, and current density in the droplet and/or the arc plasma. Agreement between the simulated results and published experimental data was obtained. [DOI: 10.1115/1.2724847]

Keywords: gas metal arc welding, metal transfer, arc plasma, droplet formation, free surface

1 Introduction

Gas metal arc welding (GMAW) is an arc welding process that uses a plasma arc between a continuous, consumable filler-metal electrode and the weld pool, as shown in Fig. 1. The high temperature plasma arc melts the electrode and forms a droplet at the electrode tip. The droplet is detached and transferred in the arc to the workpiece. A weld pool forms under the influences of the arc plasma and the periodical impingement of droplets. In gas metal arc welding, metal transfer describes the process of the molten metal's movement from the electrode tip to the workpiece, which includes droplet formation, detachment, and transfer in the arc. The transport of droplets into the weld pool is largely responsible for the finger penetration commonly observed in the fusion zone [1]. A better understanding of the metal transfer process is important for improvements in the quality and productivity of welding. The influence of droplet impingement on the weld pool varies with the droplet size, the impingement frequency, and the impingement velocity. The welding voltage, current, arc length, shielding gas, and wire feed rate can all affect the metal transfer process [2]. Among them, current is most often studied for its influence on the droplet size, frequency, and acceleration in the arc. There are various modes of metal transfer including short-circuit, globular, spray, and streaming. Globular transfer occurs at low currents with the droplet diameter being larger than the electrode diameter. Spray transfer occurs at higher current with the droplet diameter being smaller than the electrode diameter and the droplet generation being more frequent. Experimental results [2–6] have shown that a sharp transition in the droplet detachment frequency and size occurs when the mode changes between the globular and spray transfer modes in argon shielded environment. This paper will focus on the study of the transport phenomena of globular transfer to avoid numerical error that may be caused by simulating small droplets in the spray transfer mode.

Droplet formation [6–28] has been widely investigated to obtain the droplet size and frequency under different current levels. However, many of these models [6–12] neglected the complex fluid flow and thermal phenomena during droplet formation. These models include the static force balance theory (SFBT) [7–10], magnetic pinch instability theory (PIT) [10], and the dynamic models calculating the dynamic growth of the droplet with force balance [6,11,12]. The SFBT considers the balance between gravity, axial electromagnetic force, plasma shear stress, and surface tension. The PIT considers perturbation due to the radial magnetic force acting on an infinite column of liquid metal. Recently, several numerical models have been developed to predict droplet formation and detachment by calculating the fluid flow only [13–18], heat transfer only [19], or both the fluid flow and heat transfer [20–28] in the electrode. However, the current density and heat flux distributions were assumed at the electrode surface and the arc was not included in most of the models [13–21]. Haider and Lowke [22], Haider [23–26], Zhu et al. [27], and Fan and Kovacevic [28] have included the arc in their models to predict droplet formation. However, the droplet shapes [22–27] or arc plasma distribution [27,28] obtained in those models matched experimental results [6] poorly. Droplet detachment and further acceleration in the arc were not addressed in Refs. [22–26].

Droplet acceleration in the arc has been calculated by many authors [1,21,28–31] using the empirical formulation presented by Lancaster [10]. To calculate the plasma drag force exerted on the droplet using this formulation, the droplet was assumed to have a spherical shape and was accelerated to the workpiece with a constant acceleration. The physical properties of the arc plasma, the drag coefficient, and the plasma velocity also had to be assumed. Given the range of temperature found in a welding arc, the appropriate value of the arc plasma properties is difficult to determine. There is also much uncertainty in the drag coefficient and the plasma flow velocity changes dramatically during the welding process. Furthermore, the shape of the droplet changes along the way as it is transported to the workpiece [32]. An effective method is needed to simulate droplet acceleration without assuming the droplet shape, the plasma properties, the drag coefficient, and the plasma velocity.

To accurately model the dynamic metal transfer process, the fluid flow and heat transfer in both the electrode and arc and the interaction of the droplet with the arc have to be considered. In this paper, a transient unified model, which includes the electrode, droplet, weld pool, arc, and their interactions, is developed to model the metal transfer process. The dynamic growth of the droplet at the electrode tip is simulated by integrating the heat transfer and the fluid flow in the electrode with the momentum and heat transfer from the arc. The heat flux from the arc plasma and current density distribution in the droplet are calculated in the unified model, thus no assumption of these terms need to be made as in the previous models. The changes of droplet shape and temperature, and droplet acceleration in the arc are also modeled by

[1]Present address: Department of Mechanical Engineering, University of Bridgeport, Bridgeport, CT 06604.

[2]Corresponding author.

Contributed by the Heat Transfer Division of ASME for publication in the JOURNAL OF HEAT TRANSFER. Manuscript received January 24, 2006; final manuscript received October 12, 2006. Review conducted by Ben Q. Li.

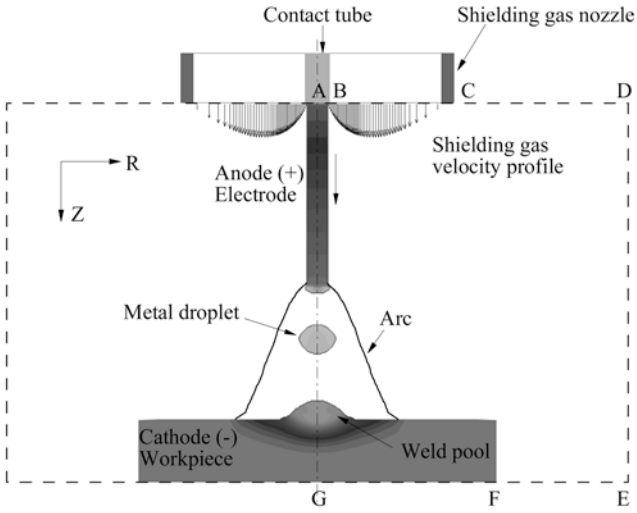

Fig. 1 A schematic representation of a GMAW system including the electrode, the arc, and the weld pool (not to scale)

simulating the fluid flow and heat transfer inside the droplet. The heat exchange between the arc and droplet and the momentum transfer from the arc to the droplet are obtained through the direct results obtained in the arc calculation at each time step. No assumptions of the arc plasma temperature, properties and velocity and the drag coefficient are needed. The simulated results are then compared with published experimental data and reasonable agreement is found.

2 Mathematical Model

2.1 Governing Equations. Figure 1 is a schematic sketch of a stationary axisymmetric GMAW system. In this system, a constant current is applied to the electrode through the contact tube at the top of the computational domain. An arc plasma is struck between the electrode and the workpiece. The electrode is continuously fed downward and then melted at the tip by the high temperature arc. Droplets are formed at the molten electrode tip, and are then detached and transferred to the workpiece. A weld pool is formed by the continuous impingement of droplets and dynamic interaction with the high temperature and high pressure arc plasma at the workpiece. Inert shielding gas is provided through the shielding gas nozzle to prevent the molten metal from oxidation.

The computational domain has an anode region, an arc region and a cathode region. For GMAW, the anode region is the electrode, and the cathode region is the workpiece. The differential equations governing the arc, the electrode, and the workpiece can be included in a single set. The differential equations governing the conservation of mass, momentum, and energy based on the continuum formulation given by Chiang and Tsai [33] are employed in the present study, and the current continuity equation is used to calculate the current density distribution. The equations are given below

Mass continuity

$$\nabla \cdot (\rho \boldsymbol{V}) = 0 \tag{1}$$

Momentum

$$\frac{\partial}{\partial t}(\rho u) + \nabla \cdot (\rho \boldsymbol{V} u) = \nabla \cdot \left(\mu_l \frac{\rho}{\rho_l} \nabla u \right) - \frac{\partial p}{\partial r} - \frac{\mu_l}{K} \frac{\rho}{\rho_l}(u - u_s) - \frac{C\rho^2}{K^{1/2}\rho_l}|u - u_s|(u - u_s) - \nabla \cdot (\rho f_s f_l \boldsymbol{V}_r u_r) - J_z \times B_\theta \tag{2}$$

$$\frac{\partial}{\partial t}(\rho v) + \nabla \cdot (\rho \boldsymbol{V} v) = \nabla \cdot \left(\mu_l \frac{\rho}{\rho_l} \nabla v \right) - \frac{\partial p}{\partial z} - \frac{\mu_l}{K} \frac{\rho}{\rho_l}(v - v_s) - \frac{C\rho^2}{K^{1/2}\rho_l}|v - v_s|(v - v_s) - \nabla \cdot (\rho f_s f_l \boldsymbol{V}_r v_r) + \rho g \beta_T (T - T_0) + J_r \times B_\theta \tag{3}$$

Energy

$$\frac{\partial}{\partial t}(\rho h) + \nabla \cdot (\rho \boldsymbol{V} h) = \nabla \cdot \left(\frac{k}{c_s} \nabla h \right) + \nabla \cdot \left(\frac{k}{c_s} \nabla (h_s - h) \right) - \nabla \cdot (\rho (\boldsymbol{V} - \boldsymbol{V}_s)(h_l - h)) - \Delta H \frac{\partial f_l}{\partial t} + \frac{J_r^2 + J_z^2}{\sigma_e} - S_R + \frac{5k_b}{e} \left(\frac{J_r}{c_s} \frac{\partial h}{\partial r} + \frac{J_z}{c_s} \frac{\partial h}{\partial z} \right) \tag{4}$$

Current continuity

$$\nabla^2 \phi = \frac{1}{r} \frac{\partial}{\partial r} \left(r \frac{\partial \phi}{\partial r} \right) + \frac{\partial^2 \phi}{\partial z^2} = 0 \tag{5}$$

Ohm's law

$$J_r = -\sigma_e \frac{\partial \phi}{\partial r} \quad J_z = -\sigma_e \frac{\partial \phi}{\partial z} \tag{6}$$

Maxwell's equation

$$B_\theta = \frac{\mu_0}{r} \int_0^r J_z r dr \tag{7}$$

In Eqs. (1)–(4), u and v are the velocities in the r and z directions, respectively. $\boldsymbol{V}_r = \boldsymbol{V}_l - \boldsymbol{V}_s$ is the relative velocity vector between the liquid phase and the solid phase in the mushy zone. The subscripts s and l refer to the solid and liquid phases, respectively, and the subscript 0 represents the initial condition. f is the mass fraction of the liquid or solid; K is the permeability function; C is the inertial coefficient; p is the pressure; T is the temperature; h is the enthalpy; Φ is the electrical potential; ρ is the density; μ is the viscosity; k is the thermal conductivity; g is the gravitational acceleration; β_T is the thermal expansion coefficient; c is the specific heat; σ_e is the electrical conductivity; J_r and J_z are current densities, in the respective r and z directions; B_θ is the self-induced electromagnetic field; S_R is the radiation heat loss; μ_0 is the magnetic permeability; k_b is the Stefan-Boltzmann constant; and e is the electronic charge.

The third and fourth terms on the right-hand side of Eqs. (2) and (3) represent the respective first- and second-order drag forces for the flow in the mushy zone. The fifth term on the right-hand side of Eqs. (2) and (3) represents an interaction between the solid and the liquid phases. The second term on the right-hand side of Eq. (4) represents the net Fourier diffusion flux. While the third term represents the energy flux associated with the relative phase motion, and the forth term is used to consider the latent heat of fusion. All the terms mentioned in this paragraph are zero, except in the mushy zone. When Eqs. (2)–(4) are used to calculate the arc plasma, these terms associated with the mushy zone are set to zero and all the thermal physical properties are replaced with those of the arc plasma. In GMAW, as the arc is concentrated, the resulting weld pool is small and the solidification time is short (relative to, for example a casting process), the solid phase velocity is as-

sumed to be zero in the present study.

The second-to-last term on the right-hand side of Eq. (3) is the thermal expansion term. The last term of Eq. (2) and Eq. (3) is the electromagnetic force term. The last three terms in Eq. (4) are Ohmic heating, radiation loss, and electron enthalpy flow, respectively.

Continuum density, specific heat, thermal conductivity, solid mass fraction, liquid mass fraction, velocity, and enthalpy are defined as follows:

$$\rho = g_s\rho_s + g_l\rho_l c = f_s c_s + f_l c_l k = g_s k_s + g_l k_l$$

$$f_s = \frac{g_s\rho_s}{\rho} \quad f_l = \frac{g_l\rho_l}{\rho}$$

$$\boldsymbol{V} = f_s\boldsymbol{V}_s + f_l\boldsymbol{V}_l \quad h = h_s f_s + h_l f_l \tag{8}$$

Assuming constant phase specific heats, the phase enthalpy for the solid and liquid can be expressed as

$$h_s = c_s T \quad h_l = c_l T + (c_s - c_l)T_s + H \tag{9}$$

where H is the latent heat of fusion for the alloy.

The assumption of permeability function in the mushy zone requires consideration of the growth morphology specific to the alloy under study. In the present study, the permeability function analogous to fluid flow in porous media is assumed, employing the Carman-Kozeny equation [34,35]

$$K = \frac{g_l^3}{c_1(1-g_l)^2} \quad c_1 = \frac{180}{d^2} \tag{10}$$

where d is proportional to the dendrite dimension, which is assumed to be a constant and is on the order of 10^{-2} cm. The inertial coefficient, C, can be calculated from [36]

$$C = 0.13 g_l^{-3/2} \tag{11}$$

2.2 Arc Region. In the arc region, the plasma is assumed to be in local thermodynamic equilibrium (LTE) [37], implying the electron and the heavy particle temperatures are equal. On this basis, the plasma properties, including enthalpy, specific heat, density, viscosity, thermal conductivity, and electrical conductivity, are determined from an equilibrium composition calculation [37]. Note the metal vaporized from the metal surface may influence plasma material properties, but this effect is omitted in the present study. It is also assumed that the plasma is optically thin, thus the radiation may be modeled in an approximate manner by defining a radiation heat loss per unit volume [37].

2.3 Anode Sheath Region. At the plasma-electrode interface, there exists an anode sheath region [37]. In this region, the mixture of plasma and metal vapor departs from LTE, thus it no longer complies with the model presented above. The anode sheath region has been neglected in many arc models [7,22,23,32], which leads to a more constricted arc distribution at the bottom of the droplet. This paper adopts the anode sheath formulation of Haidar [24] by including a noncollisional sheath region for the anode. Formulation of the noncollisional zone is based on the Langmuir sheath model. Heat transfer from the plasma to the electrode is determined by charged particle fluxes across the sheath. These fluxes are due to the electrons and the ions from the plasma, and also to a limited number of electrons emitted from the anode surface due to the thermionic emission. The corresponding current densities of these electrons and ions flow are J_e, J_i, and J_R. As J_R is several orders of magnitude lower than J_e and J_i, it is omitted in the calculation for simplification. The following formulations [24] are used to calculate the anode voltage drop across the sheath V_s

$$J = J_e - J_i$$

$$J_e = en_{e,s}\left(\frac{k_b T_{e,s}}{2\pi m_e}\right)^{0.5}\exp\left(\frac{eV_s}{k_b T_{e,s}}\right)$$

$$J_i = \tfrac{1}{4}en_{e,s}v_B$$

$$V_s \le 0 \tag{12}$$

where J is the total current density at the arc-anode interface calculated from the current density equation (5), J_i and J_e are calculated from the electron number density as charge neutrality is assumed valid through the transition zone; $T_{e,s}$ is the electron temperature at the sheath edge, which is taken as the local plasma temperature calculated from LTE; $n_{e,s}$ is the electron number density at the sheath edge, which is taken as the equilibrium electron number density at the local plasma temperature; v_B is the Bohm velocity given by $v_B=(k_b T_{e,s}/m_i)^{0.5}$; e is the electronic charge; k_b is the Stefan-Boltzmann constant; m_e is the electron mass; and m_i is the ion mass for the plasma gas.

The energy balance equation at the anode surface is modified to include a source term, S_a, expressing the heating effects due to conduction by neutral particles, charge transport across the sheath through J_e and J_i, and cooling effects due to evaporation and blackbody radiation,

$$S_a = \frac{k_{\text{eff}}(T_{e,s} - T_a)}{\delta} + J_i\left(V_i - V_s + \frac{5k_b}{2e}T_a\right) + J_e\left(\phi_w + \frac{5k_b}{2e}T_{e,s}\right) - q_{\text{ev}}H_{\text{ev}} - \epsilon k_b T_a^4 \tag{13}$$

where k_{eff} is the thermal conductivity taken at the arc plasma temperature; T_a is the anode surface temperature; δ is the mesh size adjacent to the anode surface; V_i is the ionization energy of the plasma gas; ϕ_w is the work function of the anode material; ε is the emissivity of the surface; q_{ev} is the evaporation mass rate of metal vapor, and H_{ev} is the latent heat of vaporization. For metal such as steel, q_{ev} can be written as [38]

$$\log(q_{\text{ev}}) = A_v + \log P_{\text{atm}} - 0.5\log T \tag{14}$$

$$\log P_{\text{atm}} = 6.121 - \frac{18836}{T} \tag{15}$$

The energy balance equation for the plasma in the transition zone is also modified to include a source term, S_{ap}, expressing the cooling effects due to conduction by neutral particles and charge transport across the sheath through J_e and J_i

$$S_{\text{ap}} = -\frac{k_{\text{eff}}(T_{e,s} - T_a)}{\delta} - J_i\left(V_i + \frac{5k_b}{2e}T_a\right) - J_e\left(\frac{5k_b}{2e}T_{e,s} - V_s\right) \tag{16}$$

2.4 Cathode Sheath Region. Similar to the anode region, there exists a cathode sheath region between the plasma and the cathode. However, the physics of the cathode sheath and the energy balance at the nonthermionic cathode for GMAW are not well understood [10,22–26]. The thermal effect due to the cathode sheath has been omitted in many models but reasonable results were obtained [22–26,37]. Thus, the source term of the energy balance equation at the cathode surface will only consider conduction, radiation, and evaporation

$$S_c = \frac{k_{\text{eff}}(T_{\text{arc}} - T_c)}{\delta} - q_{\text{ev}}H_{\text{ev}} - \epsilon k_b T_c^4 \tag{17}$$

where k_{eff} is the effective thermal conductivity at the arc-cathode surface taken as the thermal conductivity of the arc plasma; δ is the length of the cathode sheath region; and T_c is the cathode surface temperature.

In additional to the heat loss by conduction, another positive term is included in the energy source term for the plasma at the cathode surface. This positive term is used to approximate the

energy used in the cathode boundary layer to ionize the plasma [39] and it can also eliminate the unreasonable cooling effect of the electron flow term in the cathode region [37]. The energy source term for the plasma at the cathode surface is given by

$$S_{\mathrm{cp}} = -\frac{k_{\mathrm{eff}}(T_{\mathrm{arc}} - T_c)}{\delta} + \frac{5k_b(T_{\mathrm{arc}} - T_c)}{2e} \tag{18}$$

2.5 Metal Region (Electrode, Droplet, and Workpiece). In this model, the anode region and cathode region change their shapes with time. Together with free droplets in the arc, they consist of the metal region, which is occupied by metal. The temperature distribution within the metal region is at an energy balance of conduction, Ohmic heating, and convection in the metal and the heat transferred from the arc plasma. Considerations are also given to energy gains and losses due to latent heat resulting from melting and solidification at the solid-liquid interface. Changes in the shape of the electrode tip and the weld pool surface result in changes in the current distribution, the heat generated due to Ohmic heating, and the heat transferred from the arc to the metal surface.

2.6 Tracking of Solid-Liquid Interface. The solid/liquid phase-change boundary is handled by the continuum model [33]. The third, fourth, and fifth terms on the right-hand side of Eqs. (2) and (3) vanish at the solid phase because $u=u_s=v=v_s=0$ and $f_l=0$. For the liquid region, since K goes to infinity due to $g_l=1$ in Eq. (7) and $f_s=0$, all the aforementioned terms also vanish. These terms are only valid in the mushy zone, where $0<f_l<1$ and $0<f_s<1$. Therefore, there is no need to explicitly track the phase-change boundaries, and the liquid region, mushy zone, and solid region all are calculated by the same Eqs. (2) and (3). During the fusion and solidification processes, the latent heat is absorbed or released in the mushy zone, which is handled through the use of enthalpy defined in Eq. (9).

2.7 Tracking of Free Surfaces. Precise tracking of the free surface of the droplet and the welding pool are essential to correctly predicting the shape of the droplet and the weld pool as a function of time. The algorithm of volume-of-fluid (VOF) is used to track the moving free surface [40,41]. The fluid configuration is defined by a volume of fluid function, $F(r,z,t)$, which tracks the location of the free surface. This function represents the volume of fluid per unit volume and satisfies the following conservation equation:

$$\frac{dF}{dt} = \frac{\partial F}{\partial t} + (\boldsymbol{V}\cdot\nabla)F = 0 \tag{19}$$

When averaged over the cells of a computing mesh, the average value of F in a cell is equal to the fractional volume of the cell occupied by the metal. A unit value of F corresponds to a cell full of metal, whereas a zero value indicates the cell contains no metal. Cells with F values between zero and one are partially filled with metal.

2.8 Forces at the Arc Plasma and Metal Interface. The molten part of the metal is subjected to body forces such as gravity and electromagnetic force. It is also subjected to surface forces such as surface tension due to surface curvature, Marangoni shear stress due to temperature difference, and arc plasma shear stress and arc pressure at the arc plasma and metal interface. For cells containing a free surface, surface tension pressure normal to the free surface can be expressed as [41]

$$p_s = \gamma\kappa \tag{20}$$

where γ is the surface tension coefficient and κ is the free surface curvature given by

$$\kappa = -\left[\nabla\cdot\left(\frac{\boldsymbol{n}}{|\boldsymbol{n}|}\right)\right] = \frac{1}{|\boldsymbol{n}|}\left[\left(\frac{\boldsymbol{n}}{|\boldsymbol{n}|}\cdot\nabla\right)|\boldsymbol{n}| - (\nabla\cdot\boldsymbol{n})\right] \tag{21}$$

where $\boldsymbol{n}$ is a vector normal to the local free surface which equals the gradient of the VOF function

$$\boldsymbol{n} = \nabla F \tag{22}$$

The temperature-dependent Marangoni shear stress at the free surface in a direction tangential to the local free surface is given by [21]

$$\tau_{\mathrm{Ms}} = \frac{\partial\gamma}{\partial T}\frac{\partial T}{\partial \boldsymbol{s}} \tag{23}$$

where $\boldsymbol{s}$ is a vector tangential to the local free surface.

The arc plasma shear stress is calculated at the free surface from the velocities of arc plasma cells immediately adjacent the metal cells

$$\tau_{\mathrm{ps}} = \mu\frac{\partial \boldsymbol{V}}{\partial \boldsymbol{s}} \tag{24}$$

where μ is the viscosity of arc plasma.

The arc pressure at the metal surface is obtained from the computational result in the arc region. The surface forces are included by adding source terms to the momentum equations according to the CSF (continuum surface force) model [41,42]. Using F of the VOF function as the characteristic function, the surface tension pressure, Marangoni shear stress, arc plasma shear stress, and arc pressure are all transformed to the localized body forces and added to the momentum transport equations as source terms at the boundary cells.

2.9 Boundary Conditions

2.9.1 External Boundary Conditions. The calculation domain, as shown in Fig. 1, is ABCDEFGA. Only half of the entire physical domain is calculated due to the cylindrical symmetry along the centerline AG. The corresponding external boundary conditions for the entire domain are listed in Table 1. Symmetrical boundary conditions are used along the centerline AG. The wire feed rate is incorporated through a boundary condition on v along AB. The imposed shielding gas flow is set through a boundary condition on v along BC. For the inflow of gas from the nozzle, the radial velocity component is omitted and the axial velocity component is determined from the formula for pipe flow as shown in the following [43]:

$$v(r) = \frac{2Q}{\pi}\frac{\left\{R_n^2 - r^2 + (R_n^2 - R_w^2)\dfrac{\ln(r/R_n)}{\ln(R_n/R_w)}\right\}}{\left\{R_n^4 - R_w^4 + \dfrac{(R_n^2 - R_w^2)^2}{\ln(R_n/R_w)}\right\}} + V_w\frac{\ln\dfrac{R_n}{r}}{\ln\dfrac{R_n}{R_w}} \tag{25}$$

where Q is the inflow rate of the shielding gas, R_w is the radius of the electrode, R_n is the internal radius of the shielding gas nozzle, and V_w is the wire feed rate. A constant mass flow boundary condition is used for the open boundaries CD and DE.

The temperature boundaries along AD, DE, and EG are determined by the ambient condition, which is set as room temperature 300 K. Uniform current density is specified along AB as $J_z = -\sigma_e(\partial\phi/\partial z) = (I/\pi R_w^2)$. The voltage, ϕ, is set to zero at the bottom of the workpiece FG.

2.9.2 Internal Boundary Conditions. Within the computational domain, the moving surface of the electrode, droplet, and weld pool forms a moving inner boundary condition for the arc region. VOF Eq. (19) is solved in the metal domain to track the moving free surface with free boundary conditions set at the metal free surface. Additional body force source terms are added to the momentum transport equations at the metal free surface to consider the effects of surface tension, Maragoni shear stress, arc plasma

Table 1 Boundary conditions on the outer boundaries

	AB	BC	CD	DE	EF	FG	GA
u	0	0	0	$\frac{\partial(\rho u)}{\partial r}=0$	0	0	0
v	v_w	Eq. (25)	$\frac{\partial(\rho v)}{\partial z}=0$	0	0	0	$\frac{\partial v}{\partial r}=0$
h	T=300 K	T=300 K	T=300 K	T=300 K	T=300 K	T=300 K	$\frac{\partial T}{\partial r}=0$
ϕ	$-\sigma\frac{\partial \phi}{\partial z}=\frac{I}{\pi R_c^2}$	$\frac{\partial \phi}{\partial z}=0$	$\frac{\partial \phi}{\partial z}=0$	$\frac{\partial \phi}{\partial r}=0$	ϕ=0	ϕ=0	$\frac{\partial \phi}{\partial r}=0$

shear stress, and arc pressure. Additional source terms described in Eqs. (13) and (17) are added to the energy equation for the special treatment of the anode sheath and the cathode sheath.

A fixed computational domain is used to solve the equations in the arc region. The metal region is used as the inner boundary for the arc region. As the velocity of the metal domain is much smaller than the velocity of the arc plasma, the metal region serves as an inner obstacle in the arc domain. The temperature at the metal free surface is considered as the temperature boundary for the arc domain. Additional source terms described in Eqs. (16) and (18) are added to the energy equation for the arc near the anode and cathode.

3 Numerical Considerations

In the present study, the transport phenomena in the arc plasma and the metal are calculated separately in the corresponding metal domain and arc domain, and the two domains are coupled through interfacial boundary conditions in each time step. The current distribution is greatly influenced by the temperature in the arc column and the shape of the metal domain, but it is only slightly influenced by the temperature distribution in the metal domain as the electrical conductivity of metal varies slightly with temperature. Therefore, the current continuity equation and its associated boundary conditions are solved in the entire domain, while other primary variables, including p, u, v, and T, are calculated separately in the metal domain and the arc domain. The current continuity equation is iterated with the transport equations in the arc domain to obtain the current density distribution for both the arc domain and the metal domain. Iterations are required to assure convergence of each domain and then the boundary conditions are calculated from each domain for the coupling between the two domains.

For the metal domain, the method developed by Torrey et al. [40] was used to solve p, u, v, and T. This method is Eulerian and allows for an arbitrary number of segments of free surface with any reasonable shape. The basic procedure for advancing the solution through one time step, Δt, consists of three steps. First, at the beginning of the time step, explicit approximations to the momentum equations (2) and (3) are used to find provisional values of the new time velocities. Second, an iterative procedure is used to solve for the advanced time pressure and velocity fields that satisfy Eq. (1) to within a convergence criterion at the new time. Third, the energy equation is solved.

For the arc plasma domain, a fully implicit formulation is used for the time-dependent terms, and the combined convection/diffusion coefficients are evaluated using an upwind scheme. The SIMPLE algorithm [44] is applied to solve the momentum and continuity equations to obtain the velocity field. At each time step, the current continuity equation is solved first, based on the updated parameters. Current density and electromagnetic force are then calculated for the momentum and energy equations. The momentum equations and the continuity equation are then solved in the iteration process to obtain pressure and velocity. The energy equation is solved to get the new temperature distribution. Next, the temperature-dependent parameters are updated, and the program goes back to the first step to calculate the current continuity equation. This process is repeated for each time step until the convergence criteria are satisfied.

The governing differential equations (Eqs. (1)–(5) and Eq. (19)) and all related supplemental and boundary conditions are solved through the following iterative scheme:

1. At t=0, the electrode is set up at an initial position and initial temperature distribution is given to the metal domain. Based on the initial fixed metal domain and temperature distribution, the initial distribution of temperature, velocity, pressure, and current are obtained by solving the steady state equations in the arc domain (this procedure is similar to the steps from 5–7 for the steady state).
2. Surface tension, Marangoni shear stress, electromagnetic force, plasma shear stress, and arc pressure are calculated, and other associated boundary conditions are evaluated for the metal domain.
3. Equations (1)–(4) are solved iteratively to obtain pressure, velocity and temperature in the metal domain.
4. VOF Eq. (19) is solved to obtain the new free surface profile for the metal domain. The physical properties of cells and the boundary conditions within the computing domain are updated.
5. The current continuity equation, Eq. (5), is solved in the whole domain with updated parameters. Current density and electromagnetic force are calculated.
6. Equations (1)–(3) and the associated boundary conditions are solved iteratively to get the velocity and pressure distributions of the arc plasma. When solving these equations, the electrode, droplet and the workpiece are treated as fixed inner obstacles.
7. Energy equation, Eq. (4), is solved in the arc domain to get the new temperature distribution. Thermal physical properties of the arc plasma are updated. From here, the iteration goes back to step 5 to repeat the process for new distribution of current density, velocity pressure and temperature, until convergence criteria are satisfied.
8. Advance to the next time step and back to step 2 until the desired time is reached.

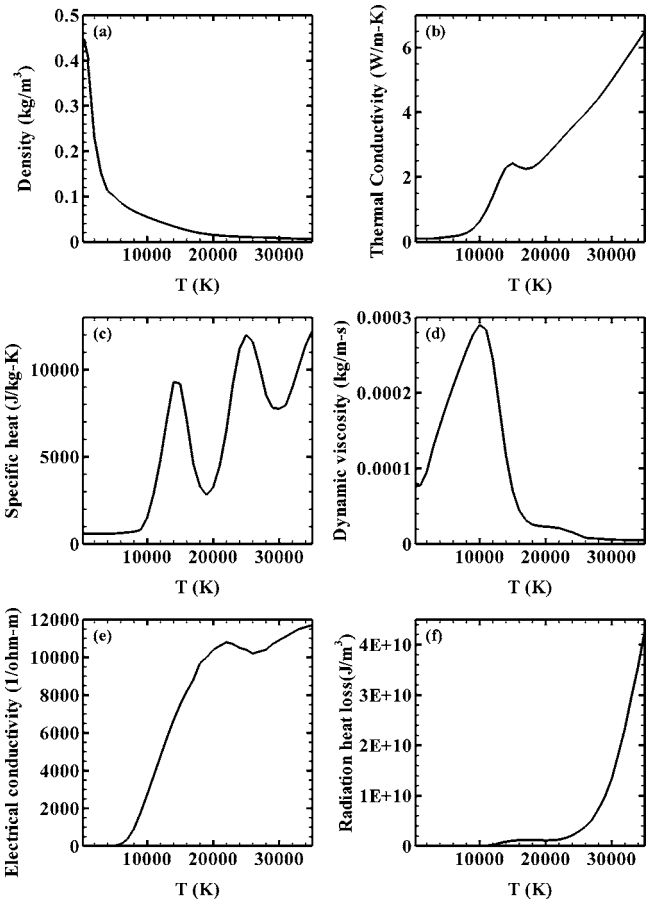

Fig. 2 Temperature-dependant material properties of argon and the volume radiation heat loss taken from [10]

A nonuniform grid point system is employed with finer grid sizes near both the cathode and anode regions. The mesh sizes near the anode and cathode center are set as 0.01 cm. Extensive tests using different grid sizes and time step sizes have been conducted to assure consistent results, and the final grid and time step sizes used can be considered the compromised between computational time and numerical accuracy. The calculation domain is half of the cylinder of 5.0 cm radius and 3.04 cm in length. Time step size is set as 5×10^{-6} s.

4 Results and Discussion

The electrode is mild steel with a 0.16 cm diameter. The workpiece is also a mild steel disk with a 3 cm diameter and a 0.5 cm thickness. The shielding gas is argon and flows out of a 1.91 cm gas nozzle at a rate of 24 l/min. The contact tube is set flush with the bottom of the gas nozzle and is 2.54 cm above the workpiece. The initial arc length is set as 0.8 cm. Five cases are studied in this paper and the current for each case is set to a constant during the calculation. Temperature-dependant material properties of argon and the volume radiation heat loss are taken from [10] and drawn in Fig. 2. The thermophysical properties of the solid and liquid mild steel are taken from [21], and are listed in Table 2 with other parameters used in the computation.

Five current levels in the range of 200–280 A, with 20 A increases, are chosen to study the effects of current on droplet formation, detachment, and acceleration in the arc. Current is a very important factor which influences the droplet formation time, size, droplet impingement velocity onto the weld pool, and thus weld pool size and penetration. Many researchers [10,21,30,31] have investigated the weld pool dynamics by assuming the droplet size, the impingement frequency, and velocity because there is little understanding of the metal transfer process. The direct and accurate measurement of droplet velocity and acceleration is also difficult to conduct due to the complicated welding process of high speed and high temperature arc plasma. A unified model which simulates the heat transfer and fluid flow in both the droplet and arc plasma and their interaction can provide insights into how the current influences the metal transfer process. For each of the five current levels, the temperature, velocity, arc pressure, and current density distributions are obtained by solving Eqs. (1)–(7), but only a full set of data is drawn for the current level of 200 A in Figs. 3–8. The temperature and velocity distributions in the metal domain are shown in Figs. 3 and 4, respectively. The arc plasma temperature, velocity, and pressure distributions are drawn in Figs. 5–7 and current density distributions are drawn in Fig. 9 with the results for two other current levels.

Table 2 Thermophysical properties of mild steel and other parameters

Nomenclature	Symbol	Value (unit)
Constant in Eq. (14)	A_v	2.52
Specific heat of solid phase	c_s	700 (J kg^{-1} K^{-1})
Specific heat of liquid phase	c_l	780 (J kg^{-1} K^{-1})
Thermal conductivity of solid phase	k_s	22 (W m^{-1} K^{-1})
Thermal conductivity of liquid phase	k_l	22 (W m^{-1} K^{-1})
Density of solid phase	ρ_s	7200 (kg m^{-3})
Density of liquid phase	ρ_l	7200 (kg m^{-3})
Thermal expansion coefficient	β_T	4.95×10^{-5}(K^{-1})
Radiation emissivity	ε	0.4
Dynamic viscosity	μ_l	0.006 (kg m^{-1} s^{-1})
Latent heat of fusion	H	2.47×10^{5} (J kg^{-1})
Latent heat of vaporization	H_{ev}	7.34×10^{6} (J kg^{-1})
Solidus temperature	T_s	1750 (K)
Liquidus temperature	T_l	1800 (K)
Vaporization temperature	T_{ev}	3080(K)
Ambient temperature	T_∞	300 (K)
Surface tension coefficient	γ	1.2 (N m^{-1})
Surface tension temperature gradient	$\partial\gamma/\partial T$	10^{-4} (N m^{-1} K^{-1})
Electrical conductivity	σ_e	7.7×10^{5} (Ω^{-1} m^{-1})
Magnetic permeability	μ_0	1.26×10^{-6} (H m^{-1})
Work function	ϕ_ω	4.3(V)
Argon ionization energy	V_i	15.76 (V)

The solid electrode tip is melted by the heat flux from the surrounding high temperature arc and the melted metal forms a

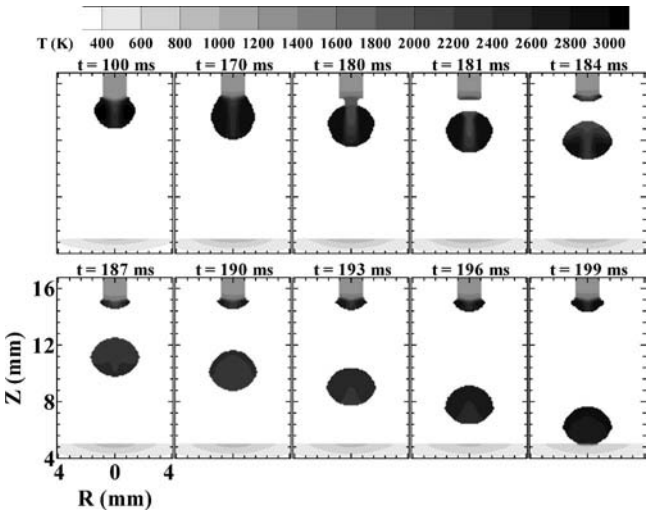

Fig. 3 Temperature distributions in the metal domain for *I* =200 A

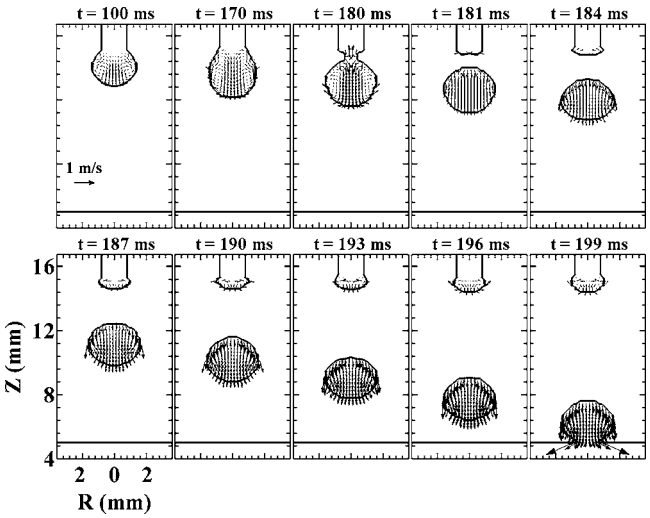

Fig. 4 Velocity distributions in the metal domain for *I*=200 A

droplet at the electrode tip under the influence of surface tension. The droplet is subjected to electromagnetic force, gravity, arc pressure, plasma shear stress, and surface tension. Arc pressure at the bottom of the droplet and surface tension are attaching forces which sustain the droplet at the electrode tip. The gravity and plasma shear stress are detaching forces which separate the droplet from the electrode tip. The radial component of the electromagnetic force has a pinch effect on the droplet and thus it is a detaching force. In argon shielded gas metal arc welding, the axial component of the electromagnetic force is also a detaching force [45]. Arc plasma has been observed to cover the entire droplet for current above 140 A [10]. From the arc coverage around the droplet, the current is hypothesized by researchers [5,10,45] to flow outside from the entire droplet surface. The radially outward current flow causes a downward detaching electromagnetic force in the droplet. The model in this paper includes the heat effect of the anode sheath and predicts a wider spread of the arc root at the droplet surface than the previous models did [22,23,32]. As seen in Fig. 5, the high temperature arc covers almost the entire droplet

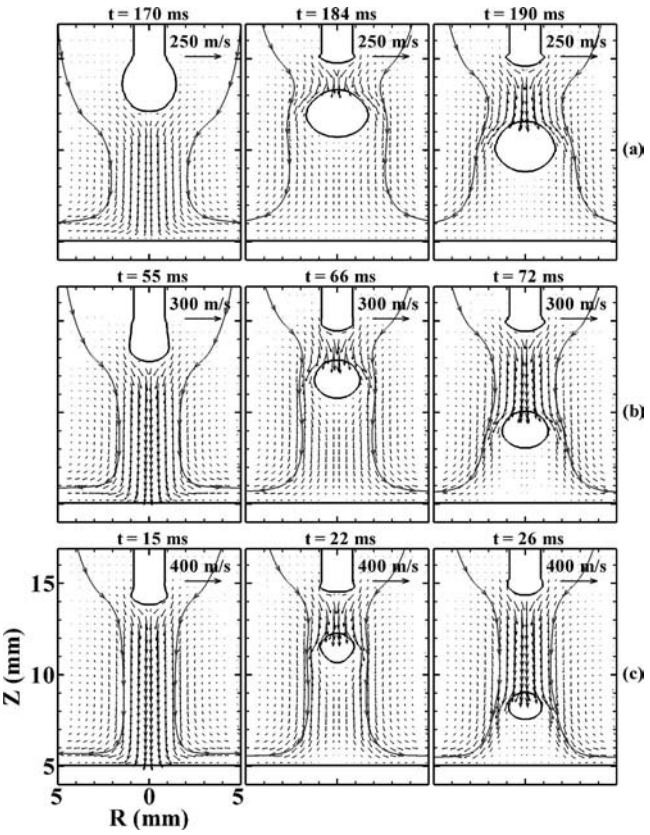

Fig. 6 Arc plasma velocity distributions for (*a*) *I*=200 A, (*b*) *I*=240 A, (*c*) *I*=280 A

surface and the current flows outward. However, compared with that of the radial component of the electromagnetic force, the detaching effect of the axial component of the electromagnetic force is small, as the current is almost parallel to the axis and only flows slightly outward. At the balance of these attaching and detaching forces, the droplet grows bigger at the electrode tip with

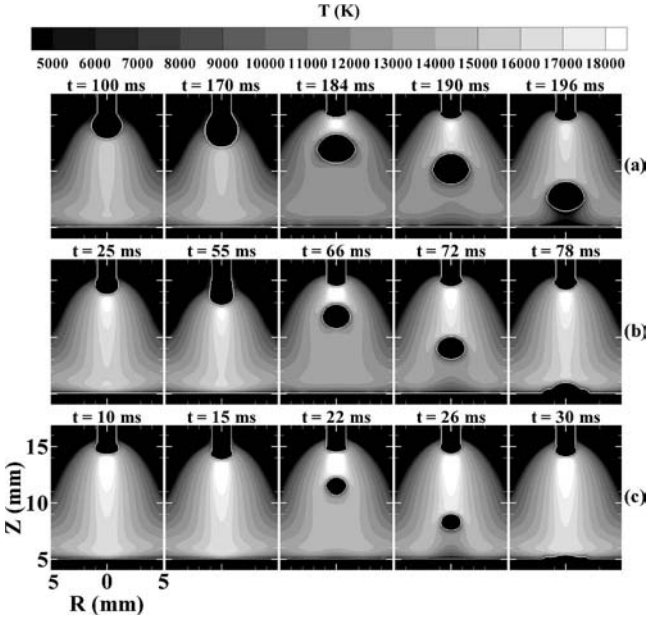

Fig. 5 Arc plasma temperature distributions for (*a*) *I*=200 A, (*b*) *I*=240 A, (*c*) *I*=280 A

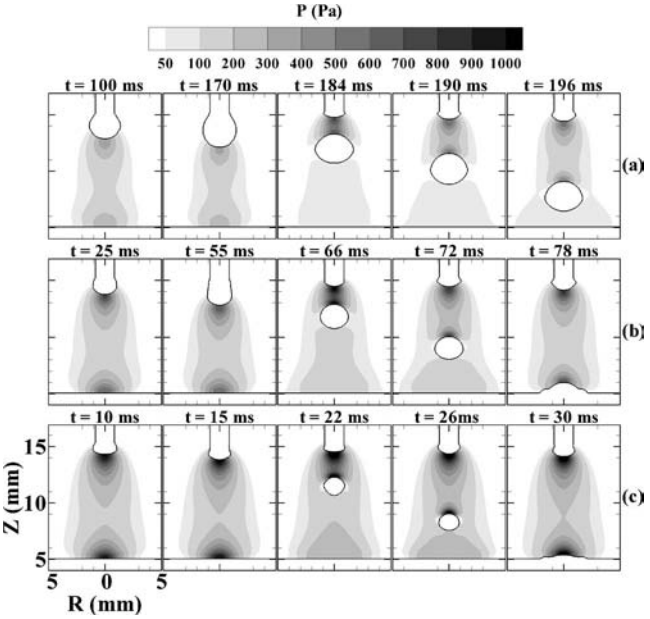

Fig. 7 Arc pressure distributions for (*a*) *I*=200 A, (*b*) *I*=240 A, (*c*) *I*=280 A

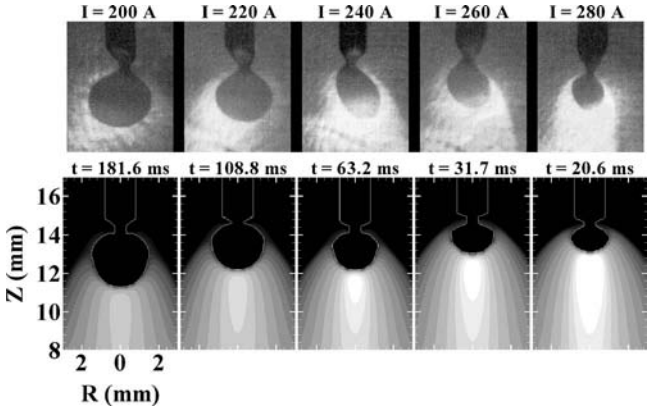

Fig. 8 Comparison of experimental results (the first row) and computational results (the second row) for droplets at the moment before detachment

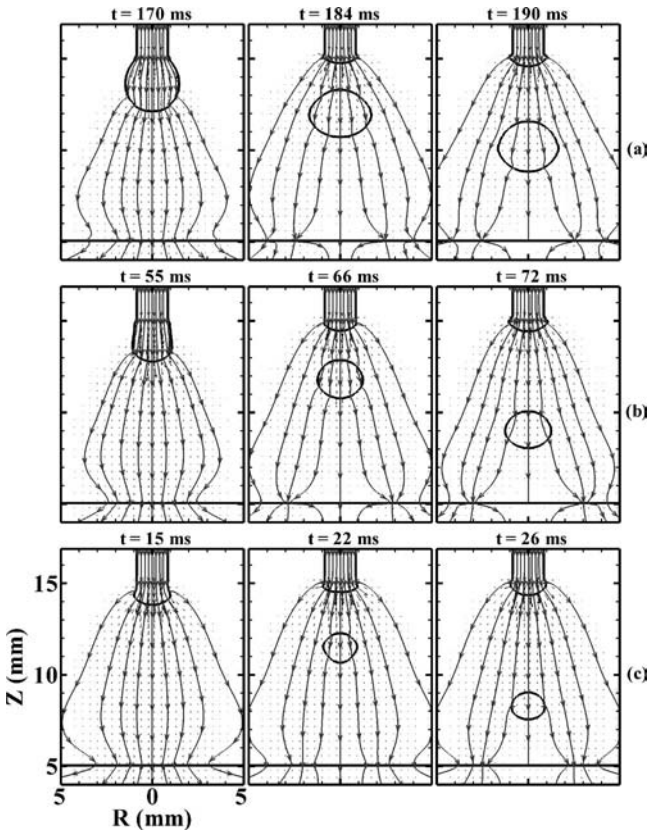

Fig. 9 Current density distributions for (*a*) *I*=200 A, (*b*) *I* =240 A, (*c*) *I*=280 A

complex flows formed inside the droplet as seen in the velocity distributions of Fig. 4. When the droplet is growing bigger, the arc pressure and surface tension becomes smaller. The droplet is detached from the electrode tip when the sustaining forces are no longer able to hold the increasing weight of the droplet. Assuming a constant surface tension coefficient in this model, the surface tension is only determined by the curvature of the droplet. Therefore, among the forces the droplet is subjected to, the changes of current will only affect the electromagnetic force, arc pressure, and plasma shear stress.

A higher current induces a higher magnetic field and thus a bigger electromagnetic force in both the metal and the arc. The bigger electromagnetic force in the arc causes a stronger arc plasma flow. As can be seen in Fig. 6, the velocity in the arc plasma becomes bigger when current increases. From Fig. 7, it can also be seen that a higher arc pressure field is formed at the electrode tip for a higher current. The bigger arc plasma velocity can also lead to a bigger plasma shear stress at the droplet surface. As the arc plasma flow is mainly drawn to the bottom of the droplet, the velocity at the arc plasma around the droplet is small. Thus, the detaching effect of the plasma shear stress is not very significant on the droplet, except at high current levels. The detaching electromagnetic force in the droplet increases faster than the attaching arc pressure with current, thus, smaller droplets are formed and detached from the electrode tip. As can be seen in Figs. 5–7, the droplet size is smaller when the current increases from 200 A to 280 A. The droplets at the moment of detachment are also compared with the experimental results of Jones et al. [4–6] in Fig. 8. It can be seen that the simulated droplet size and arc distribution around the droplet are in fair agreement with the experimental results. Only the first droplet is drawn in all the figures. However, it still can be seen that the droplet formation time is less for higher currents. As listed in Table 3, the droplet frequency obtained from several droplet formation intervals increases with higher currents. The temperature in the droplet is high near the bottom surface surrounded by the arc and low at the center where cool metal flows down from the droplet root. The temperature of the droplet only increases slightly with the current, which is mainly due to the metal evaporation effect considered in the model.

After the droplet is detached, the temperature distribution in the droplet becomes more uniform through the mixing of fluid flow inside the droplet at the beginning of the separation. The detached droplet is then heated by the surrounding high temperature arc. The detached droplet is also subjected to the electromagnetic force, gravity, arc pressure, plasma shear stress, and surface tension. At the balance of these forces, the droplet is accelerated to the workpiece. These forces are also responsible for the shape change of the droplet during the flight in the arc. The arc pressure is higher at the top surface of the detached droplet than at its bottom surface. The pressure difference does not cause the droplet to be flattened, because of the effect of surface tension, which tries to maintain a round droplet shape. The oscillation of droplet shape from oblate to prolate is mainly the work of surface tension. However, the electromagnetic force also helps the droplet to resist

Table 3 Comparison of the droplet size, frequency, and acceleration at different current levels[a]

Current (A)	Wire feed rate (cm/s)	Droplet radius (mm)	Droplet frequency (Hz)	Droplet acceleration (m/s^2)
200	4.0 (3.8)	1.49 (1.47)	5.5 (5.0)	20.6 (21.0)
220	4.5 (4.3)	1.32 (1.34)	9.2 (8.8)	25.0 (22.4)
240	5.0 (4.8)	1.13 (1.17)	16.8 (13.8)	30.4 (24.5)
260	5.5 (5.3)	0.95 (0.97)	31.5 (23.8)	38.0 (43.8)
280	6.0 (5.8)	0.82 (0.81)	65.0 (59.0)	52.4 (55.8)

[a]The experimental results shown in the parentheses are from Jones et al. [6]. The experiment was a continuous constant current welding for the 1.6 mm mild steel electrode shielded by Ar-2% O_2. The shielding gas flow rate was 24 l/min and the inner diameter of the nozzle was 19.1 mm. The contacted tube was mounted flush with the bottom of the gas nozzle and was 25.4 mm above the workpiece.

being flattened to oblate by the arc pressure. From the current streamlines drawn in Figs. 9, it can be seen that current flows around the detached droplet. Except at the place where the droplet is close to the electrode tip, only a small amount of current flows through the detached droplet. When the droplet moves farther away from the electrode tip, less current flows through it and the electromagnetic force in the droplet also becomes smaller. As it is seen in Figs. 5–7, the detached droplets have a more flattened shape near the workpiece than when they are near the electrode tip. At higher currents of 260 A and 280 A, the higher electromagnetic pinch force even elongates the detached droplets when they are near the electrode tip.

The arc pressure difference between the top and bottom surfaces of the detached droplet propels the droplet down to the workpiece. The effect of the plasma shear stress is also remarkable in bringing down the detached droplet. From the plasma velocity distributions in Fig. 6, it can be seen that the plasma flow around the detached droplet is significant. At higher currents, the plasma flow around the droplet is stronger and the arc pressure difference between the top and bottom surfaces of the droplet is greater. Therefore, a stronger acceleration of the detached droplet is found with a higher current. As shown in Figs. 5–7, the detached droplet at higher current level takes less time to reach the workpiece.

The acceleration of the droplet is found to be near constant by Jones et al. [6] and assumed to be constant by many authors in their calculations [10,21,30,31]. Jones et al. [6] have taken video images of droplets from the moment they were detached to the time they contacted the workpiece. Taken from the video images, the center positions of the droplets were then drawn with time as the flight trajectories. It was found that the flight trajectories could be fitted with quadratic curves within error limits. The first derivatives of these fitted curves were taken as the droplet velocities and the second derivatives were taken as the droplet accelerations. The droplet center positions from the computational results are compared with the fitted curves of the flight trajectories of Jones et al. [6] at each current level in Fig. 10(*a*). The solid lines are the fitted curves of the droplet trajectories from Jones et al. [6] and the symbols are the center positions of droplets from the computation. As can be seen, the calculated droplet center positions match the fitted curve well, except at some points near the electrode tip. The computational results show the droplets have a bigger acceleration at the early stage of the flight when they are near the electrode tip. While this bigger acceleration could not be shown in the fitted curve, as a constant acceleration was assumed, it was shown in the original flight trajectories made from the video images [6]. The bigger acceleration can also be explained by the computational results. From Figs. 6 and 7, it can be seen that the plasma flow between the electrode tip and the droplet is stronger and the arc pressure at the top surface of the droplet is higher when the distances between them are shorter. From the axial velocity distributions at the droplet center, which is drawn in Fig. 10(*b*) with only symbols, the trend of higher acceleration at the early stage is more obvious. The droplet velocities calculated by taking the first derivatives from both the fitted curves of the experimental and computational trajectories are drawn in Fig. 10(*b*). The droplet velocities calculated from the experimental trajectories are drawn with a solid line for each current level. The droplet velocities calculated from the computational trajectories are drawn with a dotted line and the symbol for each current level. The droplet velocities calculated from the trajectories match well for each current level. However, the velocities at the droplet center from the computational results do not fit well with them, especially at higher current levels. This is because the acceleration of the droplet is higher at the early stage. The droplet size, frequency and acceleration at different current levels are summarized in Table 3 with the corresponding experimental results.

Shielding gas flow rate is very important for the gas metal arc welding process. The flow rate should be high enough for the shielding gas to protect the weld pool, but it can not be so high that it will disturb the weld pool. A constant shielding gas flow rate is used in the computations for all the current levels. The effect of the current changes on the requirement of shielding gas flow rate is demonstrated in Fig. 6. The streamlines in all the figures start from the same point at the entrance of the shielding gas. As can be seen clearly, the streamlines are drawn more toward the center when the current increases. A higher shielding gas flow rate is required to protect the weld pool for a higher current, which is supported by the Welding Handbook [2]. However, the shielding gas can still cover the weld pool for all the current levels as the current range is not very wide in this computation.

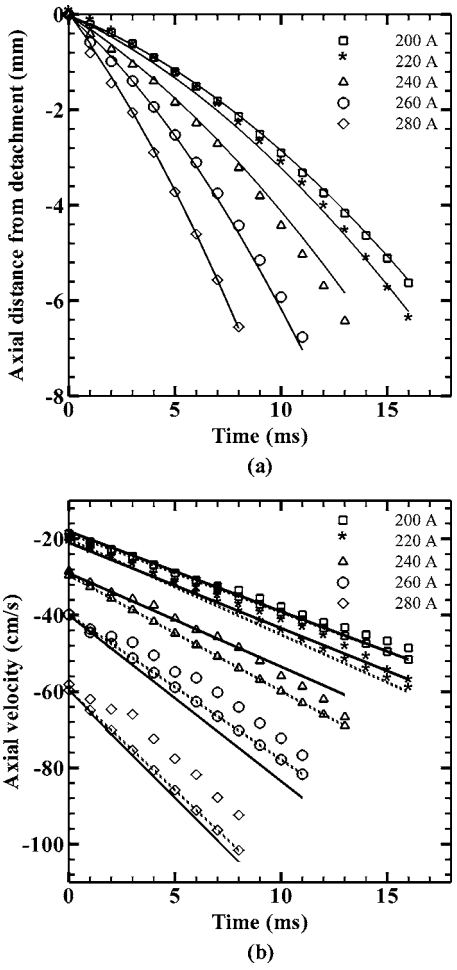

Fig. 10 Computational droplet positions and axial velocities compared with the experimental results at different currents. (*a*) Droplet flight trajectories; (*b*) axial droplet velocities.

5 Conclusions

A unified model has been used to study the droplet formation, detachment, and transfer in the arc during a gas metal arc welding process. Five current levels in the range of the globular transfer mode have been used to study the current effect on the droplet size, temperature, and acceleration. Smaller droplet size, and thus higher frequency, was found for higher currents. The temperature of the droplet at higher currents was found to be only slightly higher than at lower currents. The detached droplet was further heated by the high temperature arc during the flight in the arc. The shape of the detached droplet changes in the arc at the balance of electromagnetic force, arc pressure, plasma shear stress, and surface tension. More flattened droplets were found near the workpiece than near the electrode tip, due to the smaller electromag-

netic force further away from the electrode tip. The acceleration of the detached droplets was higher at the early stage of the flight and was near constant at the later stage. Higher acceleration was found for higher currents. The higher plasma flow driven by the electromagnetic force at higher current also showed that higher shielding flow rates were required to cover the weld pool at higher currents. The calculated results were compared with the experimental results and agreement was found.

Acknowledgment

This work was partially supported by GM R&D Center which is gratefully acknowledged.

Nomenclature

A_v = constant, defined in Eq. (14)
B_θ = self-induced azimuthal magnetic field
c = specific heat
C = coefficient, defined in Eq. (11)
c_1 = permeability coefficient, defined in Eq. (10)
d = dendrite arm spacing
e = electronic charge
F = volume of fluid function
f = mass fraction
g = volume fraction or gravitational acceleration
h = enthalpy
h_c = convective heat-transfer coefficient between the base metal and its surroundings
H = latent heat of fusion
H_{ev} = latent heat of vaporization
I = welding current
J_e = electron current density
J_i = ion current density
J_r = radial current density
J_R = current density due to electron emission
J_z = axial current density
k = thermal conductivity
K = permeability, defined in Eq. (10)
k_b = Stefan-Boltzmann constant
k_{eff} = effective thermal conductivity at arc-metal interface
m_e = electron mass
m_i = ion mass
$\boldsymbol{n}$ = vector normal to the local free surface
$n_{e,s}$ = electron number density at the sheath edge
p = pressure
P_{atm} = atmospheric pressure
p_s = surface tension pressure
Q = shielding gas flow rate
q_{ev} = evaporation mass rate of metal vapor
r-z = cylindrical coordinate system
R = gas constant
R_n = internal radius of the shielding gas nozzle
R_w = radius of the electrode
$\boldsymbol{s}$ = vector tangential to the local free surface
S_a = anode sheath energy heat flux for the metal
S_{ap} = anode sheath energy heat flux for the arc plasma
S_c = cathode sheath energy heat flux for the metal
S_{cp} = cathode sheath energy heat flux for the arc plasma
S_R = radiation heat loss
t = time
T = temperature
T_{arc} = arc plasma temperature close to the anode and cathode
T_a, T_c = anode, cathode surface temperature
$T_{e,s}$ = electron temperature at the sheath edge
T_l = liquidus temperature
T_s = solidus temperature
T_∞ = ambient temperature
u = velocity in the r direction
v = velocity in the z direction
$\boldsymbol{V}$ = velocity vector
v_B = Bohm velocity
V_i = ionization energy of plasma
V_s = anode sheath voltage drop
$\boldsymbol{V}_r$ = relative velocity vector $(\boldsymbol{V}_l - \boldsymbol{V}_s)$
V_w = wire feed rate

Greek Symbols

β_T = thermal expansion coefficient
γ = surface tension coefficient
$\partial\gamma/\partial T$ = surface tension temperature gradient
ε = surface radiation emissivity
κ = free surface curvature
μ_l = dynamic viscosity
μ_0 = magnetic permeability
ϕ = electric potential
ϕ_w = work function of the anode material
σ_e = electrical conductivity
ρ = density
τ_{ps} = plasma shear stress
τ_{Ms} = Marangoni shear stress
δ = mesh size near the anode or cathode sheath surface
Δt = time interval

Subscripts

0 = initial value
l = liquid phase
r = relative to solid phase velocity
s = solid phase
w = wire

References

[1] Kim, C. H., Zhang, W., and DebRoy, T., 2003, "Modeling of Temperature Field and Solidified Surface Profile During Gas-Metal Arc Fillet Welding," J. Appl. Phys., **94**, pp. 2667–2679.
[2] AWS, 1983, *Welding Handbook*, 7th ed., American Welding Society, Vol. 2.
[3] Lin, Q., Li, X., and Simpson, S. W., 2001, "Metal Transfer Measurements in Gas Metal Arc Welding," J. Phys. D, **34**, pp. 347–353.
[4] Jones, L. A., Eagar, T. W., and Lang, J. H., 1998, "Images of Steel Electrode in Ar-2%O_2 Shielding during Constant Current Gas Metal Arc Welding," Weld. J. (Miami, FL, U.S.), **77**, pp. 135–141s.
[5] Jones, L. A., Eagar, T. W., and Lang, J. H., 1998, "Magnetic Forces Acting on Molten Drops in Gas Metal Arc Welding," J. Phys. D, **31**, pp. 93–106.
[6] Jones, L. A., Eagar, T. W., and Lang, J. H., 1998, "A Dynamic Model of Drops Detaching from a Gas Metal Arc Welding Electrode," J. Phys. D, **31**, pp. 107–123.
[7] Simpson, S. W., and Zhu, P. Y., 1995, "Formation of Molten Droplets at a Consumable Anode in an Electric Welding Arc," J. Phys. D, **28**, pp. 1594–1600.
[8] Nemchinsky, V. A., 1994, "Size and Shape of the Liquid Droplet at the Molten Tip of an Arc Electrode," J. Phys. D, **27**, pp. 1433–1442.
[9] Choi, J. H., Lee, J., and Yoo, C. D., 2001, "Dynamic Force Balance Model for Metal Transfer Analysis in Arc Welding," J. Phys. D, **34**, pp. 2658–2664.
[10] Lancaster, J. F., 1986, *The Physics of Welding*, 2nd ed., Pergamon, Oxford.
[11] Zhang, Y. M., and Liguo, E., 2000, "Numerical Analysis of the Dynamic Growth of Droplets in Gas Metal Arc Welding," Proc. Inst. Mech. Eng., Part C: J. Mech. Eng. Sci., **214** Part C, pp. 1247–1258.
[12] Zhang, Y. M., and Li, P. J., 2001, "Modified Active Control of Metal Transfer and Pulsed GMAW of Titanium," Weld. J. (Miami, FL, U.S.), **80**, pp. 54–61s.
[13] Fan, H. G., and Kovacevic, R., 1998, "Dynamic Analysis of Globular Metal Transfer in Gas Metal Arc Welding: A Comparison of Numerical and Experimental Results," J. Phys. D, **31**, pp. 2929–2941.
[14] Choi, S. K., Yoo, C. D., and Kim, Y. S., 1998, "The Dynamic Analysis of Metal Transfer in Pulsed Current Gas Metal Arc Welding," J. Phys. D, **31**, pp. 207–215.
[15] Choi, S. K., Kim, Y. S., and Yoo, C. D., 1999, Dimensional Analysis of Metal Transfer in GMA Welding," J. Phys. D, **32**, pp. 326–334.
[16] Choi, S. K., Yoo, C. D., and Kim, Y. S., 1998, "Dynamic Simulation of Metal Transfer in GMAW, Part 1: Globular and Spray Transfer Modes," Weld. J. (Miami, FL, U.S.), **77**, pp. 38–44s.

[17] Choi, S. K., Yoo, C. D., and Kim, Y. S., 1998, "Dynamic Simulation of Metal Transfer in GMAW, Part 2: Short-Circuit Transfer Mode," Weld. J. (Miami, FL, U.S.), **77**, pp. 45–51s.
[18] Wang, G., Huang, P. G., and Zhang, Y. M., 2003, "Numerical Analysis of Metal Transfer in Gas Metal Arc Welding under Modified Pulsed Current Conditions," Metall. Mater. Trans. B, **35B**, pp. 857–866.
[19] Zhu, P., Rados, M., and Simpson, S. W., 1995, "A Theoretical Study of Gas Metal Arc Welding System," Plasma Sources Sci. Technol., **4**, pp. 495–500.
[20] Wang, F., Hou, W. K., Hu, S. J., Kannatey-Asibu, E., Schultz, W. W., and Wang, P. C., 2003, "Modelling and Analysis of Metal Transfer in Gas Metal Arc Welding," J. Phys. D, **36**, pp. 1143–1152.
[21] Fan, H. G., and Kovacevic, R., 1999, "Droplet Formation, Detachment, and Impingement on the Molten Pool in Gas Metal Arc Welding," Metall. Mater. Trans. B, **30B**, pp. 791–801.
[22] Haidar, J., and Lowke, J. J., 1996, "Predictions of Metal Droplet Formation in Arc Welding," J. Phys. D, **29**, pp. 2951–2960.
[23] Haidar, J., 1998, "An Analysis of the Formation of Metal Droplets in Arc Welding," J. Phys. D, **31**, pp. 1233–1244.
[24] Haidar, J., 1998, "A Theoretical Model for Gas Metal Arc Welding and Gas Tungsten Arc Welding. I," J. Appl. Phys., **84**, pp. 3518–3529.
[25] Haidar, J., 1998, "Prediction of Metal Droplet Formation in Gas Metal Arc Welding II," J. Appl. Phys., **84**, pp. 3530–3540.
[26] Haidar, J., 1998, "An Analysis of Heat Transfer and Fume Production in Gas Metal Arc Welding. III.," J. Appl. Phys., **85**, pp. 3448–3459.
[27] Zhu, F. L., Tsai, H. L., Marin, S. P., and Wang, P. C., 2004, "A Comprehensive Model on the Transport Phenomena during Gas Metal Arc Welding Process," Prog. Comput. Fluid Dyn., **4**, pp. 99–117.
[28] Fan, H. G., and Kovacevic, R., 2004, "A Unified Model of Transport Phenomena in Gas Metal Arc Welding including Electrode, Arc Plasma and Molten Pool," J. Phys. D, **37**, pp. 2531–2544.
[29] Subramaniam, S., White, D. R., Scholl, D. J., and Weber, W. H., 1998, "In Situ Optical Measurement of Liquid Drop Surface Tension in Gas Metal Arc Welding," J. Phys. D, **31**, pp. 1963–1967.
[30] Wang, Y., and Tsai, H. L., 2001, "Impingement of Filler Droplets and Weld Pool Dynamics During Gas Metal Arc Welding Process," Int. J. Heat Mass Transfer, **44**, pp. 2067–2080.
[31] Wang, Y., and Tsai, H. L., 2001, "Effects of Surface Active Elements on Weld Pool Fluid Flow and Weld Penetration in Gas Metal Arc Welding," Metall. Mater. Trans. B, **32B**, pp. 501–515.
[32] Hu, J., 2005, "Heat and Mass Transfer in the Gas Metal Arc Welding Process," Ph.D. dissertation, University of Missouri-Rolla, Rolla, MO.
[33] Chiang, K. C., and Tsai, H. L., 1992, "Shrinkage Induced Fluid Flow and Domain Change in Two-Dimensional Alloy Solidification," Int. J. Heat Mass Transfer, **35**, pp. 1763–1770.
[34] Carman, P. C., 1937, "Fluid Flow Through Granular Beds," Trans. Inst. Chem. Eng., **15**, pp. 150–166.
[35] Kubo, K., and Pehlke, R. D., 1985, "Mathematical Modeling of Porosity Formation in Solidification," Metall. Trans. A, **16A**, pp. 823–829.
[36] Beavers, G. S., and Sparrow, E. M., 1969, "Non-Darcy Flow through Fibrous Porous Media," ASME J. Appl. Mech., **36**, pp. 711–714.
[37] Lowke, J. J., Kovitya, P., and Schmidt, H. P., 1992, "Theory of Free-Burning Arc Columns Including the Influence of the Cathode," J. Phys. D, **25**, pp. 1600–1606.
[38] Zacharia, T., David, S. A., and Vitek, J. M., 1992, "Effect of Evaporation and Temperature-Dependent Material Properties on Weld Pool Development," Metall. Trans. B, **22B**, pp. 233–241.
[39] Jonsson, P. G., Westhoff, R. C., and Szekely, J., 1993, "Arc Characteristics in Gas-Metal Arc Welding of Aluminum Using Argon as the Shielding Gas," J. Appl. Phys., **74**, pp. 5997–6006.
[40] Torrey, M. D., Cloutman, L. D., Mjolsness, R. C., and Hirt, C. W., 1995, "NASA-VOF2D: A Computer Program for Incompressible Flows with Free Surfaces," LA-10612-MS, Los Alamos National Laboratory.
[41] Brackbill, J. U., Kothe, D. B., and Zemach, C., 1992, "A Continuum Method for Modeling Surface Tension," J. Comput. Phys., **100**, pp. 335–354.
[42] Celic, A., and Zilliac, G. G., 1997, "Computational Study of Surface Tension and Wall Adhesion Effects on an Oil Film Flow Underneath an Air Boundary Layer," Nasa Ames Research Center.
[43] Granger, R. A., 1995, *Fluid Mechanics*, CBS College, New York, Chap. 10.
[44] Patanka, S. V., 1980, *Numerical Heat Transfer and Fluid Flow*, McGraw-Hill, New York.
[45] Nemchinsky, V. A., 1996, "The Effect of the Type of Plasma Gas on Current Constriction at the Molten Tip of an Arc Electrode," J. Phys. D, **29**, pp. 1202–1208.

Characterization of Variable Thermal Contact Resistance in Rapid Contact Solidification Utilizing Novel Ultrasound Technique

F. J. Hong
School of Mechanical and Power Engineering,
Shanghai Jiao Tong University,
Shanghai, China

H.-H. Qiu[1]
Department of Mechanical Engineering,
Hong Kong University of Science and Technology,
Kowloon, Hong Kong, SAR China
e-mail: meqiu@ust.hk

A method based on a novel ultrasound technique and inverse heat transfer analysis was developed to study the transient thermal contact resistance (TCR) at the early stage of a rapid contact solidification process. This promising technique is nonintrusive and, therefore, provides no distortion to the contact surface as well as the heat transfer process. The effects of impact velocity and initial molten metal temperature on TCR were investigated in detail. An empirical equation that correlates the variable TCR with the initial and interfacial conditions was introduced utilizing the experimental data.
[DOI: 10.1115/1.2724848]

Keywords: ultrasound, heat transfer, rapid contact solidification, thermal contact resistance

Introduction

The interfacial heat transfer between the melt and the substrate is a critical issue for many industrial applications based on molten droplet impact, such as thermal spray coating, splat quenching [1], solder jet printing [2], high precision net-form manufacturing [3], and shape deposition manufacturing (SDM) with microcasting [4]. During a melt spread over a solid surface, a perfect thermal contact between the solidifying metal and the solid substrate can hardly be achieved because of the roughness of the solid surface, the surface tension of the melt, the impurities on the surfaces and the gas entrapment. This imperfection leads to TCR that reduces the heat transfer rate. Numerical simulations [5–14] demonstrated that TCR plays an important role in these molten droplet impact processes. It has been found that TCR varies with the impact conditions. It is no longer kept constant during the impact and solidification processes [15,16]. Therefore, the numerical simulations using a constant value of thermal contact resistance, however, sacrifice the prediction power because an appropriate value of it has to be assumed with a posteriori calibration for different initial conditions. A correlation of variable thermal contact conductance was introduced into the numerical simulation of a molten alloy158 droplet impacting onto a copper substrate [15,16]. Therefore, the prerequisite for assuming and estimating an appropriate constant TCR can be removed.

The knowledge on the formation of TCR between a solidifying molten metal and a substrate is still very limited due to lack of experimental data. Most of work was focused on the systems with large dimensions such as in conventional metal mold casting, die casting, and continuous casting [17,18].

Recently, much attention was paid on the early stage of rapid solidification when an intimate contact exists. One technique to estimate TCR in molten droplet impact is matching the measured temperatures at the substrate interface [1,19] or at the top surface of the splat [20–23] with those from 1D numerical models. This method, however, can hardly be used to determine the variation of TCR which, in fact, varies with time and space. Measurement techniques that can be used to track the variation of TCR in situ are needed. The dynamic behavior of TCR was also investigated by solving an inverse heat transfer problem [24,25]. The transient variation of TCR when a molten droplet impacting onto a substrate was estimated through comparing the measured temperature by the semi-intrinsic thermocouples buried inside the substrate and the calculated temperature from a 1D heat conduction model [24,25]. However, no model or empirical correlation equation of variable TCR was achieved. Furthermore, due to the low response speed of the thermocouples and the large heat capacity of the metal substrate, it is difficult to estimate the variable TCR under a rapid contact condition. To improve the response speed of the measurement system, instead of measuring the temperature inside the substrate, the substrate interface temperature measured by a microfabricated semi-intrinsic thermocouple integrated on the substrate surface was used to estimate the transient TCR during the rapid contact solidification of molten alloy158 contacting with copper substrate [26]. The advantage of this method is that it avoids the complexity in using the inverse heat transfer technique and also improves the response speed of the measurement system. An empirical correlation of variable TCR with interfacial heat flux was also developed [15]. Unfortunately, the correlation did not reveal the effects of initial impact velocity and interfacial conditions on thermal contact resistance. Furthermore, the microfabricated semi-intrinsic thermocouple integrated on the substrate surface may change the surface properties, such as the surface wetting and roughness, of the substrate, which limits its application to other substrate materials.

In this study, a one-dimensional rapid contact solidification experiment is performed by impacting a substrate onto a thin layer of molten metal, where the local contact heat transfer and solidification in molten droplet impact process is simulated. The effect of existence of the lateral flow on TCR during molten droplet impact is assumed to be negligible with current experiments. This assumption is reasonable because in most of the molten droplet impact processes, the droplet impact velocity is small ($\sim$1 m/s) and the viscosity of the molten metal is high. As a result, the lateral velocity of the molten metal adjacent to the contact inter-

[1]Corresponding author.

Contributed by the Heat Transfer Division of ASME for publication in the JOURNAL OF HEAT TRANSFER. Manuscript received April 6, 2006; final manuscript received September 21, 2006. Review conducted by Suresh V. Garimella.

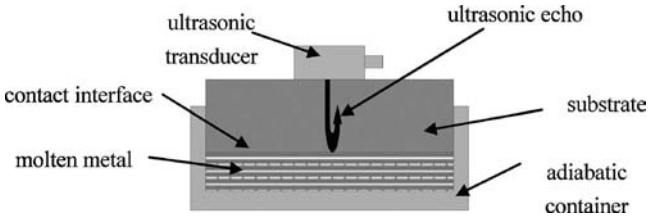

Fig. 1 The schematic diagram of a one-dimensional solidification problem

face is small. The variable TCR is estimated by solving an inverse heat transfer problem utilizing a novel ultrasound technique.

Inverse Heat Transfer Problem Using Ultrasound

Considering a one-dimensional contact solidification problem as shown in Fig. 1, given the geometric size of the materials and the initial temperatures of the molten metal and the substrate, the only unknown condition for solving this heat transfer problem is TCR at the contact interface. To determine the thermal contact resistance, the inverse heat transfer method is calculated which is based on the measurements of the delay time of ultrasound echoes from the contact interface. Because the speed of sound in a material is a function of temperature, the delay time measured will carry the temperature information along the ultrasound path which can be used to determine the variation of thermal contact resistance. Normally, the relationship between the speed of sound and the temperature can be expressed linearly as

$$c(T) = c_0 + \gamma T \tag{1}$$

where c_0 is the speed of sound at 0 °C (m/s); γ is the temperature coefficient (m/s/ °C), and T is the material temperature (°C). As for the present problem, on the one hand, the substrate is heated up continuously after contact with the molten metal, correspondingly, the measured time delay of ultrasonic echoes from the contact interface increases continuously. The change of the measured time delay of the echo (*UM*) after contact can be derived by subtracting the initial time delay of the last echo before contact from the time delay of the echo after contact. On the other hand, supposing the variation of TCR with time is known, the temperature distribution inside the substrate can be computed by solving the heat transfer problem. The computed time delay change (*UC*) of the echo can then be calculated as

$$UC = 2\int_0^a \frac{dz}{c(T(z))} - \frac{2a}{c(T_{s,0})} \tag{2}$$

where, $T(z)$ is the temperature along the sound path, $T_{s,0}$ is the initial substrate temperature, and a is the thickness of the substrate. If the variation of TCR is properly estimated by using the iteration method, the difference between *UC* and *UM* can be minimized. Therefore, by comparing *UM* with *UC*, the variable TCR can be estimated using the inverse heat transfer method.

Compared with traditional inverse methods using the thermocouple to measure temperature, the present ultrasonic method has some advantages. First, it does not affect the heat transfer process inside the substrate, because no thermocouple is buried inside the substrate. Therefore, this method is workable for thin layer molten liquid and substrate impact processes. Secondly, the time delay of the ultrasonic echo actually reflects the integration of the temperature field along the sound path, revealing the temperature change at any location of the substrate, therefore the well-known problem of the lagged temperature response in the interior point of the substrate with respect to the heat flux excitation at the contact interface does not exist.

Figure 2 shows the schematic diagram of the heat transfer problem. Because the molten metal undergoes phase change after contact with the substrate, in the following text, the molten metal is also called the phase change material (PCM). The consideration of TCR is realized by inserting a thin massless contact interface layer with a tunable thermal conductivity [27]. Since TCR is often quantified by the interfacial heat transfer coefficient, h_{cr}, which is the reciprocal of the thermal contact resistance, in the following text, the two terms are both used for convenience. The effective thermal conductivity of the interfacial layer, k_2, is related to h_{cr} by

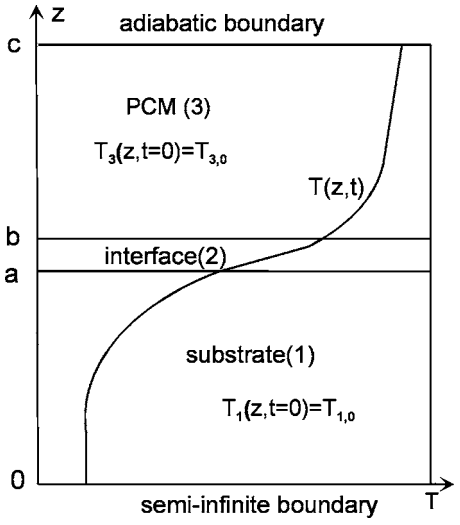

Fig. 2 The geometry, initial, and boundary conditions of the heat transfer problem

$$k_2(\tau) = (b-a)h_{cr}(\tau) \tag{3}$$

where b-a is the thickness of the interface layer as shown in Fig. 2. Therefore, there are three physical domains: the substrate (1), the contact interface layer (2), and the phase change material (PCM) (3). Using enthalpy formulation, the numerical computation can be conducted in one computational domain. The mathematical formulation is given by

$$\rho_j \frac{\partial h_j}{\partial \tau} = \frac{\partial}{\partial z}\left(k_j \frac{\partial T_j}{\partial z}\right) \tag{4}$$

where the subscript $j=1$, 2, 3 stands for substrate (1), interface (2), and PCM (3), respectively. In order to close the formulation, the enthalpy h is related to the temperature T via

$$h = \begin{cases} c_{p,s}(T - T_{\mathrm{m}}) & T < T_m \\ c_{p,l}(T - T_{\mathrm{m}}) + h_{sl} & T \geq T_m \end{cases} \tag{5}$$

where the subscripts s and l stand for solid and liquid phases, respectively, and h_{sl} is the latent heat of fusion. The substrate and the PCM are initially at the uniform temperature of $T_{1,0}$ and $T_{3,0}$, respectively. The thermal conductivities and capacities of the solid and the liquid are assumed to be different, while their densities are considered to be the same. The bottom surface of the PCM is assumed to be adiabatic with the consideration of good thermal insulation of the container material. The substrate is supposed to be thick enough to guarantee the validity of the semi-infinite boundary condition within the short time duration of experiments (several seconds). Therefore, the initial and boundary conditions of the heat transfer problem are given by

$$\begin{aligned} &T = T_{1,0} \quad 0 < z \leq a \quad \tau = 0 \\ &T = T_{3,0} \quad b < z \leq c \quad \tau = 0 \\ &T = T_{1,0} \quad z = 0 \quad \tau > 0 \end{aligned} \tag{6}$$

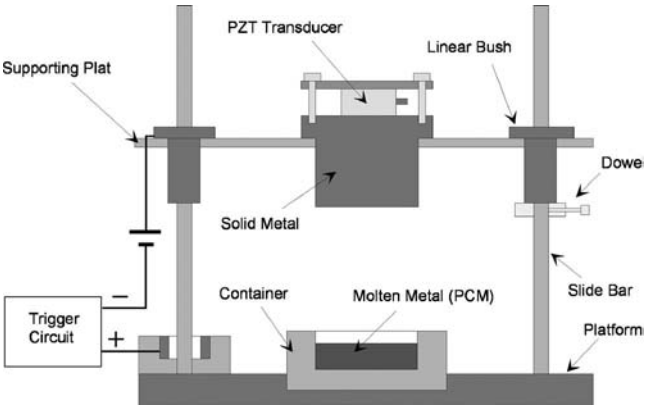

Fig. 3 The schematic diagram of the experimental setup

$$\left.\frac{\partial T}{\partial z}\right|_{z=c} = 0$$

The Levenberg-Marquardt method for parameter estimation is adopted for solving the present inverse heat transfer problem. For the inverse problem, $h_{cr}(\tau)$ is regarded as unknown. The change of the time delay of the echoes from the contact interface, $UM(\tau)$, measured at time τ_i, i=1,2,...,I, is considered available for analysis. $h_{cr}(\tau)$ is assumed to consist of a series of basic function, $\varphi_i^k(\tau)$, as

$$h_{cr}(\tau) = \sum_{i=1}^{M} P_i \varphi_i^k(\tau) \tag{7}$$

Following the previous research [24], the B-spline function with the order $k=4$ is adopted as the basic function. The detailed characteristics of the B-spline function can be found in Ref. [28]. The inverse problem is then reduced to minimize the residual function $S(P)$, which is defined as

$$S(P) = [UM - UC]^T [UM - UC] \tag{8}$$

where UC is the calculated time delay change of the echoes from the contact interface defined by Eq. (2) at time, τ_i, $i=1,2,\ldots,I$, and $\boldsymbol{P}$ is the parameter vector to be determined. The algorithm of solving this inverse heat transfer problem can be found in Ref. [29].

Experimental Setup and Procedure

The materials of both the substrate and the molten metal are alloy158, a eutectic alloy with a melting point of 70°C. Figure 3 shows the schematic diagram of the one-dimensional contact solidification setup, which includes a cylindrical container, a substrate supporting plate, a translation system, and a platform. The container is made of Teflon® (FEP) with an inner diameter of 25 mm. Because of its low thermal conductivity (0.25 W/m/°C), Teflon is considered as an ideal thermal insulator. The translation system consisting of four stainless steel rods and four linear bushes is to realize a sudden falling impact of the substrate with the molten metal once the dowel released. The impact velocity can be regulated by changing the falling height. Figure 4 shows the block diagram of the measurement system. In this experiment, Panametrics V110-RM fingertip contact PZT transducer with a nominal frequency of 5 MHz is selected to transmit and receive ultrasonic signals, taking both the measurement resolution and the energy attenuation issues into account. The contact surface of the substrate is polished with abrasive papers (USA320) using polishing machines. The solid alloy158 is melted in an oven before pouring it into the Teflon container. The temperature measured just before the contact of the substrate with molten metal is considered as the initial temperature of the molten metal. As shown in

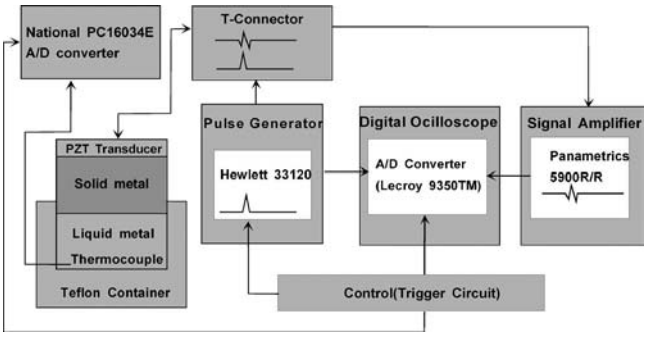

Fig. 4 The block diagram of the measurement system

Fig. 3, when the substrate contacts with the molten metal, a voltage will be fed to the trigger circuit that immediately starts the trigger circuit to produce transistor-transistor logic (TTL) signals, which are connected to the external trigger input ports of Hewlett 33120A and Lecroy 9350TM. Once Hewlett 33120A receives the external trigger, it emits an excitation pulse to the PZT transducer. The reflected echo signal from the contact interface is received by the same PZT transducer and transferred to an electrical signal. The signal is filtered and amplified by PR5900 and then converted to a digital signal saved in the memory of 9350TM. The excitation pulse is also acquired by Lecroy 9350TM at the same time using another input channel. After a while (pulse repetition interval, which is determined by the TTL circuit), another pulse is emitted and the measurement is repeated. The measurement stops automatically when the set record number is reached. The length of the sampling window and the sampling trigger delay are determined according to the testing experiment to guarantee both the echo signal and excitation pulse are included in the window. The typical measurement setup for the present experiment is: (1) 16 cycles burst sine wave (5 MHz, 3.2 μs duration) for Hewlett 33120A; (2) 250 MS/s sampling rate, 20 μs signal window length and 199 record segments for Lecroy 9350TM; (3) the pulse repetition interval of 13 ms for TTL circuit. The initial molten metal temperature and the substrate temperature were measured by thermocouples with an uncertainty of 0.1°C.

Ultrasonic Signal Processing

The signal processing is to get the time delay change of each echo, UM. Figure 5 shows a sample of the recorded signals. Figure 5(a) is the ultrasonic signal from PR5900, including the excitation pulse and the echo signal from the contact interface. The excitation pulse is clipped, since PR5900 has a limit on the maximum output voltage. Figure 5(b) is the excitation pulse directly

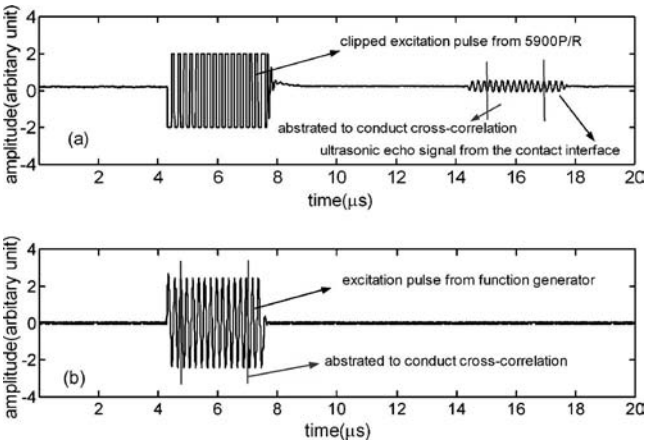

Fig. 5 Typical recorded signals

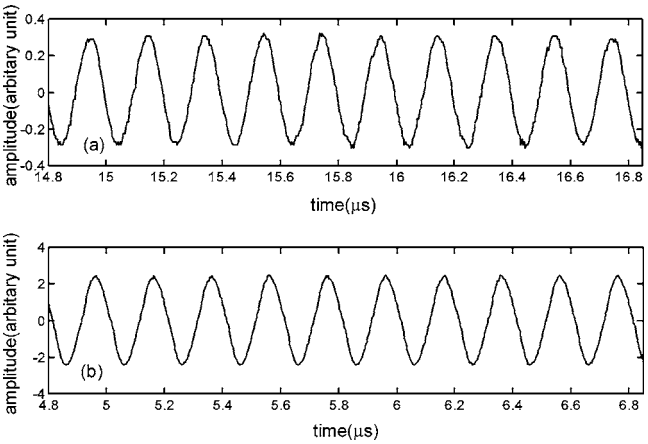

Fig. 6 Abstracted signals to do cross-correlation

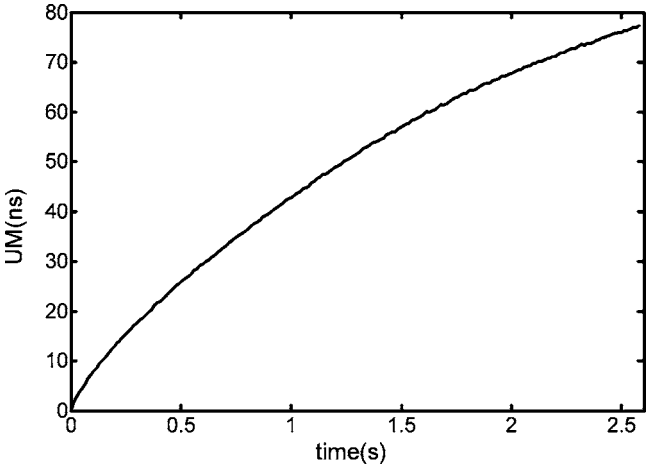

Fig. 8 Typical time delay change as a function of time

from Hewlett 33120A. Because the excitation pulse in Fig. 5(*b*) and the echo signal in Fig. 5(*a*) are strictly synchronized, they can be used to calculate time delay of the echo. To measure the time delay change of the echo, *UM*, the resolution of *UM* is important for the inverse heat transfer problem. Therefore, a high resolution cross-correlation method based on the five point fitting method for FFT [30] was adopted to calculate the phase difference between the excitation wave and the echo signal. In order to reduce the error induced by the signal damping at the edge, the central segment of the signal as shown in Figs. 6(*a*) and 6(*b*) are abstracted to conduct the cross-correlation. By subtracting the initial phase difference before the contacting of the substrate with the molten metal, the phase difference change as a function of echo sequence number can be obtained, as shown in Fig. 7. Because the ultrasonic pulse repetition rate and the ultrasonic frequency are both known (13 ms and 5 MHz for the present experiments), from Fig. 7, the ultrasonic time delay change (*UM*) of the echo as a function of time can be derived as shown in Fig. 8. Validation experiments were conducted by repeating the measurement of the echo from the back wall of the substrate before contacting with the molten metal for 1000 times. It was found that for the current measurement setup (5 MHz ultrasonic wave, 250 MS/s sampling rate, 512 points FFT), the signal noise ratio (SNR) of the back wall echo is about 25 dB and the standard deviation of the phase difference is about 0.06 deg, corresponding to the time resolution of 0.033 ns.

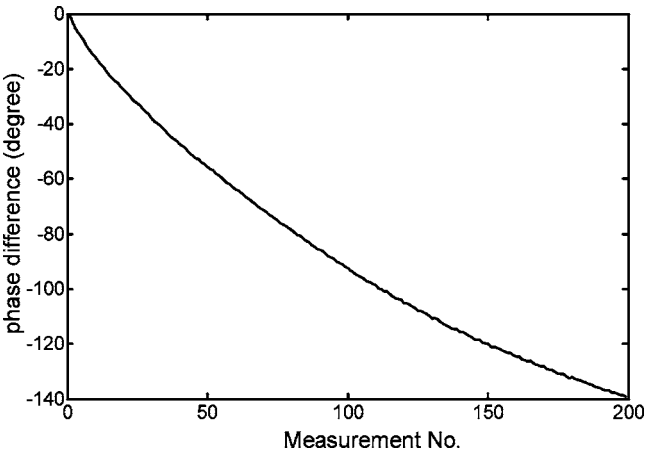

Fig. 7 Typical phase difference change as a function of measurement number

Results and Discussions

The acoustic properties of solid alloy158 are indispensable to calculate the ultrasonic time delay. According to the characterization experiments, $c_0=2400$ m/s and $\gamma=1.95$ m/s/K, respectively, which are very close to those of Wood's metal [31]. This is reasonable because the components of alloy158 and Wood's metal are very similar (alloy158: 50% Bi, 26.7% Pb, 13.3% Sn, 10% Cd; Wood's metal: 50% Bi, 25% Pb,12.5% Sn, 12.5 Cd). The material properties of alloy158 summarized by Wang and Qiu [26] were used in the mathematical computation (see Table 1).

General Experimental Results

Figure 9 shows the variation of interfacial heat transfer coefficient h_{cr} with time for experiment 1. The experimental conditions are: the initial PCM temperature, $T_{d,0}=135\,^{\circ}$C, the initial substrate temperature, $T_{s,0}=21\,^{\circ}$C; the thickness of PCM, $L_d=3.0$ mm, the thickness of substrate, $L_s=12.0$ mm, and the impact height, $H=12.0$ mm. It clearly indicates that h_{cr} at first decreases very quickly and the decreasing rate then slows down. Figure 10 shows the variation of ultrasonic time delay change with time from both

Table 1 The thermophysical properties of alloy158

Property	Units	Solid	Liquid
ρ	kg/m^3	9400	9400
c_p	kJ/kg/K	0.167	0.167
k	W/m/K	19.0	5.499
L	kJ/kg	32.6	…
T_m	°C	70.0	…
v	m^2/s	…	0.331×10^{-6}

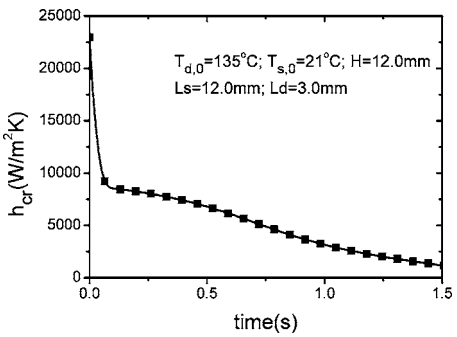

Fig. 9 The variation of h_{cr} with time for experiment 1

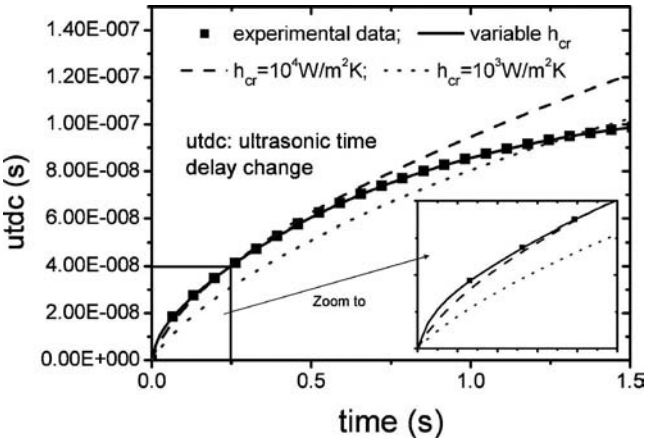

Fig. 10 The variation of UTDC with time for experiment 1

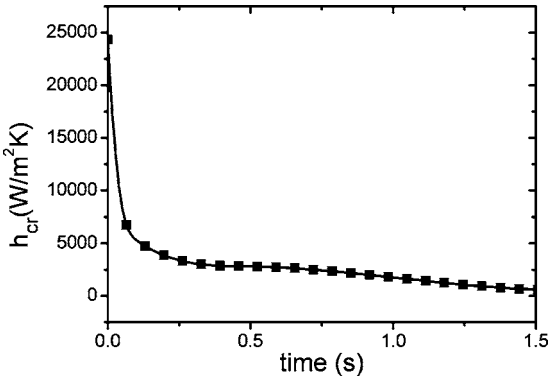

Fig. 12 The variation of h_{cr} with time for experiment 2

the experimental measurement and the numerical computation utilizing variable and constant thermal contact resistances h_{cr}, respectively. It shows that a constant h_{cr} cannot lead to the computed result agreeing with the experiment. Figure 11 shows the calculated interface temperatures of the PCM and the substrate as well as the measured and the calculated temperature at the bottom of PCM as a function of time. It indicates that the numerically estimated temperature agrees very well with the measured temperature. Since the PCM interface temperature is always above the melting point (70°C) in this experiment during the period of analysis, the contact type is liquid/solid contact. It has been reported that there is a peak in the variation of h_{cr} with time during the solidification of molten metal on a substrate [18,26,32] and the time to achieve the peak varies from less than 1 s to more than 30 s according to the experimental conditions. The plausible explanation was that the wetting ability of substrate increases with the increase of substrate temperature due to the heating by PCM, causing a better contact between the PCM and the solid substrate. No such peak, however, is observed in the present experiment (see Fig. 9). Nevertheless, it does not mean that the present experimental result is contradictory to the previous research. The reason is that the experimental conditions are different. In the previous experiments [18,26,32], the materials of substrate and PCM are not the same, the superheats of PCM are relatively small, and the thicknesses of PCM are large (more than 15 mm). In this kind of experimental condition, the drop of the PCM temperature is small at the early stage of contact, but the substrate interface temperature increases very quickly, causing the increase of h_{cr}. It however should be noted that while the increase of substrate temperature improves the wetting ability of substrate, the decrease of PCM temperature increases the surface tension of the PCM, resulting in the deterioration of the wetting at the contact interface. Under the present experimental conditions, the superheat is high ($T_{d,0}=135°C$, $T_m=70°C$) and the thickness of PCM is only about 3 mm. As a result, as we can see from Fig. 11, the PCM temperature at the contact interface drops dramatically at the first stage of contact within 0.1 s, causing the increase of the surface tension. Although the increase of the substrate temperature to some degree can compensate for the deterioration of the wetting condition, the combination effect is negative for wetting. Therefore, there is a dramatic drop of h_{cr} at the first stage of contact. During the period from $t=0.1$ s to $t=0.5$ s, the PCM interface temperature continues to decrease and the substrate interface temperature continues to increase. Because the temperature change rate is much smaller within this period, although h_{cr} is still decreasing, the decreasing rate is much smaller compared to the first period (see Fig. 9). After $t=0.5$ s, the interfacial heat flux is not enough to sustain the substrate interface temperature, and the substrate interface temperature starts to decrease. As a result, the decreasing rate of h_{cr} becomes larger again. With the decrease of the interfacial heat flux q, the PCM interface temperature starts to increase due to the accumulation of the heat transferred from the PCM, and the decreasing rate of h_{cr} slows down again. From the above analysis, we can see the variation of h_{cr} is always corresponding to the variation of interfacial temperatures. It should also be noted that, theoretically, there must be a period, during which, h_{cr} increases from zero to a certain value, because the contact area before contact is zero and the TCR is considered to be infinite. The time scale of this period however is extremely small and no experiment until now has the ability to resolve it. Therefore, this period is neglected and it is assumed that it takes no time to establish the initial contact of substrate and PCM.

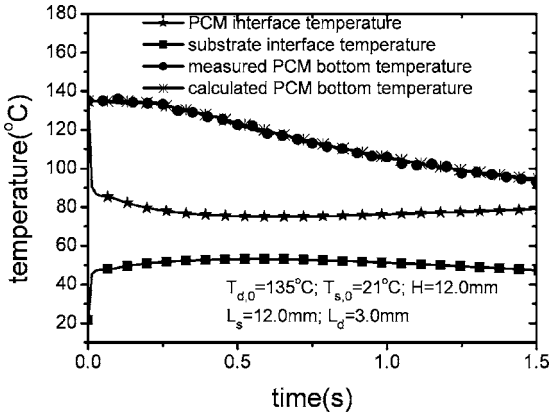

Fig. 11 The variation of temperatures with time for experiment 1

The conditions of experiment 2 are: $T_{d,0}=105°C$, $T_{s,0}=21°C$; $L_d=3.25$ mm; $L_s=12.0$ mm, and $H=18.0$ mm. Figures 12 and 13 shows h_{cr} and the temperatures as a function of time, respectively. The variation curve of h_{cr} for experiment 2 is basically similar to experiment 1. Comparing experiment 1 with experiment 2, it is found that h_{cr} of experiment 2 reaches a low value in a shorter time than that in experiment 1. This is because the PCM interface temperature drops more quickly (comparing Fig. 11 and Fig. 13) for experiment 2 due to the lower $T_{d,0}$. The larger impact height causing the better initial contact between PCM and substrate is also a reason for the quicker PCM interface temperature drop for experiment 2. From Fig. 12, it can be seen that there is a plenum (very small slope) during the period of from about $t=0.3$ s to $t=0.75$ s, corresponding to the PCM interfacial temperature close to melting point (see Fig. 13). That means at that time, the phase change is happening at the contact interface. It should also be pointed out that at the later stage of experiment 2 (from about $t=0.75$ s to $t=1.5$ s), the contact type becomes solid/solid contact

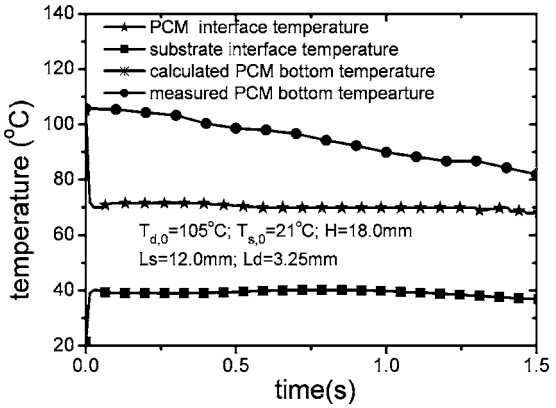

Fig. 13 The variation of temperatures with time for experiment 2

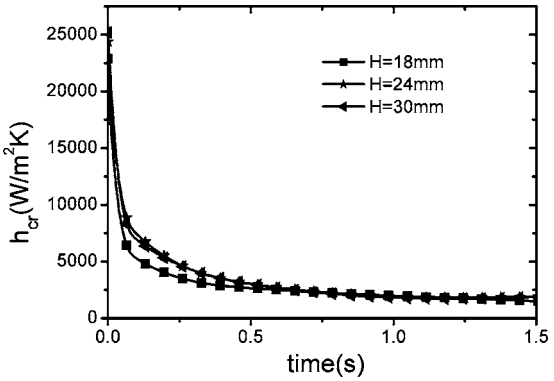

Fig. 15 The effect of impact height on h_{cr}

because the PCM interface temperature is lower than its melting point. During this period, a relatively stable contact forms, resulting in a very slow decrease of h_{cr} with the decrease of the PCM interface temperature.

The Effect of Initial PCM Temperature and Impact Height on h_{cr}

The effect of PCM temperature on h_{cr} was studied by changing $T_{d,0}$ while keeping other parameters constant. Figure 14 shows the experimental results for H=18 mm, L_s=12 mm, L_d=3.0 mm, $T_{s,0}$=21°C and $T_{d,0}$=105°C, 110°C, and 125°C, respectively. It indicates that with the increase of $T_{d,0}$, h_{cr} increases. This is because the larger the initial PCM temperature, the larger the interface temperatures. As explained previously, it increases the wetting ability of the substrate, resulting in a smaller TCR (a larger h_{cr}). The smaller surface tension of PCM in the case of higher $T_{d,0}$, causing a better initial contact during the impact process, is another reason.

The effect of impact height on h_{cr} was studied by changing H while keeping other parameters constant. Figure 15 shows the experimental results for L_s=12 mm, L_d=3.0 mm, $T_{s,0}$=21°C, $T_{d,0}$=115°C and H=18 mm, 24 mm, and 30 mm, respectively. It indicates that with the increase of H, the interfacial heat transfer coefficient increases. However, this effect becomes less obvious with the increase of H, as we can see that the difference between h_{cr} in the case of H=24 mm and H=30 mm is smaller than that between H=18 mm and H=24 mm. The increase of $h_{cr}$with impact height can be attributed to the better initial contact under a higher impact velocity.

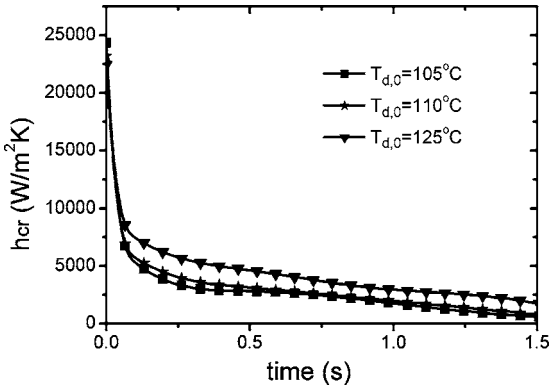

Fig. 14 The effect of initial PCM temperature on h_{cr}

Empirical Correlation of Variable Thermal Contact Resistance

The experimental data of variable h_{cr} with time cannot be used in the mathematical computation, because different initial conditions such as impact velocity and initial PCM temperature cause the different variation profiles of h_{cr} with time. Experiments of rapid contact solidification were performed under the conditions of different impact heights and initial PCM temperatures. The purpose was to build an empirical correlation equation, in which h_{cr} is related to initial and interfacial conditions. To analyze the experimental data, we first define a dimensionless interfacial heat transfer coefficient

$$C_{cr} = \frac{R_a h_{cr}}{k_c} \tag{9}$$

In Eq. (9), $k_c = 2k_s k_d/(k_s + k_d)$ is the effective interface thermal conductivity, where k_s and k_d are the thermal conductivities of the substrate and the PCM, respectively. R_a is a reference thickness of the interface layer, which can be the average roughness and oxidation layer of the substrate surface. In this study, we assume R_a=10 μm. Then, we define a dimensionless heat flux,

$$C_q = \frac{R_a}{\Delta T_{\max}} \frac{q}{k_c} \tag{10}$$

where $\Delta T_{\max} = T_m - T_{s,0}$ and heat flux q,

$$q = h_{cr}(T_{d,i} - T_{s,i}) \tag{11}$$

In Eq. (11), $T_{d,i}$ and $T_{s,i}$ denote the interface temperatures of the PCM and the substrate, respectively. According to the detailed analysis of experimental data, by defining an additional dimensionless number,

$$C_{qt} = \frac{C_q}{\left(1 - \exp\left(\frac{T_m - T_{s,i}}{T_m + 273}\right)\right)\left(\frac{T_{d,0}}{T_m}\right)} \tag{12}$$

the relation of dimensionless TCR C_c (the reciprocal of C_{cr}) with C_{qt} for different $T_{d,0}$ (regardless of L_d) can be fitted as

$$C_c = \frac{1 + \left(\frac{a2}{C_{qt} + a3}\right)^{a4}}{a1} \tag{13}$$

for the fixed impact height. For example, Figs. 16(*a*) and 16(*b*) show the experimental data and the fitting curves for the cases of H=18 mm and H=6 mm, respectively. We can see that the fitting curves fit the experimental data very well. The values of a1, a2, a3, and a4 are found to be related to impact height, as summarized in Table 2. In order to convert H to impact velocity, the charac-

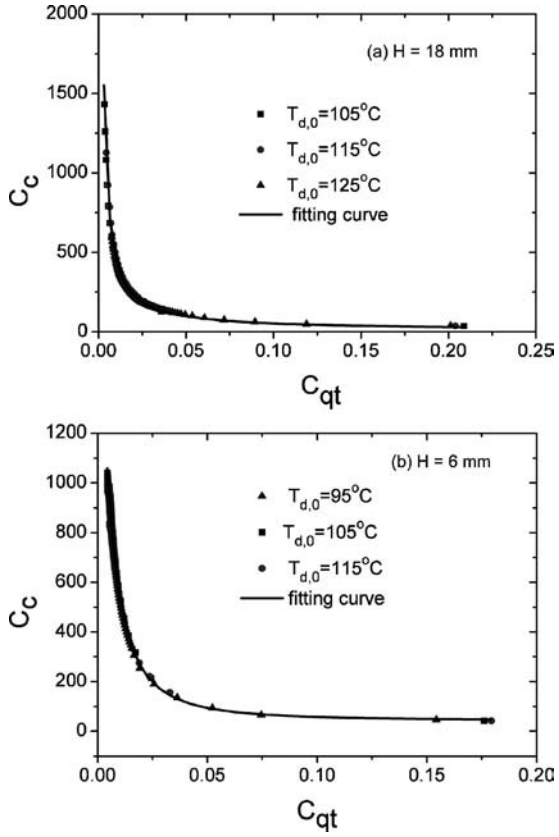

Fig. 16 The variation of C_c with C_{qt}

terization experiment of the acceleration of the impact system was conducted by recording the falling process of the substrate using a high speed CCD camera (Redlake 100k) with 5000 frames/s. The acceleration of impact system is determined to be 8.94 m/s^2, a little lower than gravity acceleration due to the friction between linear bush and slide bar (see Fig. 3). According to the value of acceleration, impact velocity (V_c) can be calculated from impact height with an uncertainty of ±1%. The variations of a1, a2, a3, and a4 with impact velocity are also graphed in Fig. 17. As shown in Fig. 17, when V_c is large, the variation of a1, a2, a3, and a4 become very small. That means the effect of V_c on the TCR become less important. This is reasonable because when impact velocity is very large, the initial contact of PCM and substrate being already good, it is difficult to further improve the contact by further increasing impact velocity. It is found that a1 and a2 can be fitted using sigmodial function and a3 and a4 can be fitted using first order exponential decay function as

$$a1 = 0.357 + \frac{0.304 - 0.357}{1 + \exp\left(\frac{V_c - 0.527}{0.0372}\right)}$$

Table 2 The values of a1, a2, a3, and a4

H (mm)	V_c (m/s)	a1	a2	a3	a4
6	0.328	0.03125	0.0110	0.00745	1.80
12	0.464	0.08333	0.2811	0.0012	1.10
14	0.502	0.13698	0.5727	0.00013	1.03
18	0.568	0.27777	1.3501	−0.00062	0.98
24	0.657	0.34482	1.8317	−0.00115	0.95
30	0.734	0.35714	1.8660	−0.00112	0.945

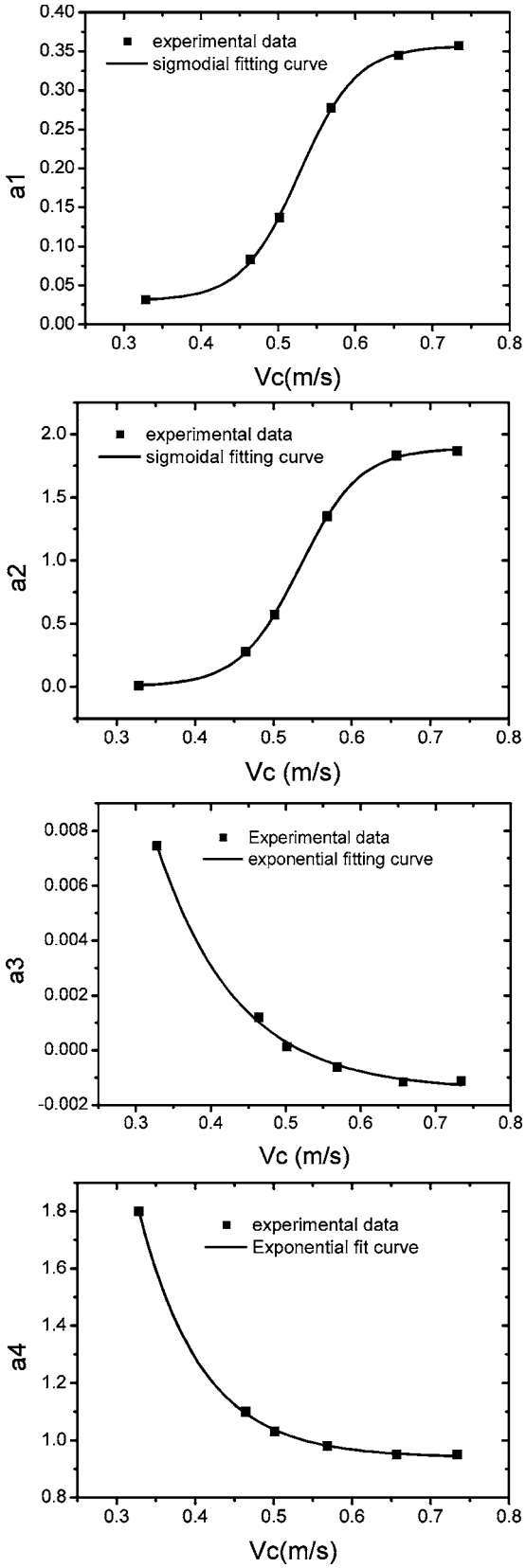

Fig. 17 a1, a2, a3, and a4 as a function of impact velocity

$$a2 = 1.889 + \frac{0.0061 - 1.889}{1 + \exp\left(\frac{V_c - 0.533}{0.0383}\right)}$$

$$a3 = 0.00146 + 0.198 \exp\left(\frac{-V_c}{0.106}\right)$$

$$a4 = 0.940 + 54.29 \exp\left(\frac{-V_c}{0.0792}\right) \tag{14}$$

To further discuss the meaning of Eq. (13), we transfer it back to dimensional form by combining Eqs. (10)–(13) and substituting a1, a2, a3, a4 with the functions of V_c as illustrated in Eq. (14). It is found that the interfacial heat transfer coefficient is actually determined by an implicit function,

$$h_{cr} = \frac{k_c\left(\frac{a1}{R_a}\right)}{\left[1 + \frac{k_c\left(\frac{a2}{R_a}\right)\left(1 - \exp\left(\frac{T_m - T_{s,i}}{T_m + 273}\right)\right)\left(\frac{T_{d,0}}{T_m}\right)}{\frac{h_{cr}(T_{d,i} - T_{s,i})}{(T_m - T_{s,0})} + k_c\left(\frac{a3}{R_a}\right)\left(1 - \exp\left(\frac{T_m - T_{s,i}}{T_m + 273}\right)\right)\left(\frac{T_{d,0}}{T_m}\right)}\right]^{a4}}$$

$$= \frac{k_c a1'}{\left[1 + \frac{k_c a2'\left(1 - \exp\left(\frac{T_m - T_{s,i}}{T_m + 273}\right)\right)\left(\frac{T_{d,0}}{T_m}\right)}{\frac{h_{cr}(T_{d,i} - T_{s,i})}{(T_m - T_{s,0})} + k_c a3'\left(1 - \exp\left(\frac{T_m - T_{s,i}}{T_m + 273}\right)\right)\left(\frac{T_{d,0}}{T_m}\right)}\right]^{a4}} = f(h_{cr}, T_{d,0}, T_{s,0}, T_{d,i}, T_{s,i}, V_c) \tag{15}$$

where $a1' = a1/R_a$, $a2' = a2/R_a$, and $a3' = a3/R_a$, respectively. That means h_{cr} is related to the initial conditions ($T_{d,0}$, $T_{s,0}$, and V_c) and the contact interface temperatures ($T_{d,i}$ and $T_{s,i}$). Because the temperatures of contact interfaces can be determined by the heat transfer problem itself and the initial conditions are known, h_{cr} can be calculated using the iteration method.

To analyze the sensitivity of the present inverse heat transfer method to the measurement results, the method was tested using the following method: First, we assume a parameter vector P to get a variable thermal contact resistance h_{cr}

(1) Then solve the direct heat transfer problem, to get the predicted temperature fields and consequently calculated ultrasonic time delay change (UC);
(2) Then, we add a random error (with a certain level of deviation) to the calculated ultrasonic time delay change (UC) to simulate the "measured" ultrasonic time delay change (UM);
(3) UM is then used to solve the inverse heat transfer problem to get P' and the variable thermal contact resistance h'_{cr};
(4) The difference between h'_{cr} and h_{cr} is used to determine the estimation sensitivity of the inverse heat transfer method.

Two validation examples are shown below:

(1) Constant thermal contact resistance: In this case, a constant thermal contact resistance is considered. The given parameters are h_{cr}=5000 W/m^2/°C, the measurement No.=150, the liquid layer thickness=3 mm and 135°C, and the solid substrate thickness is 12 mm and 23°C, and the measurement interval is equal to 13 ms. It was found that with the "measurement error" of ±0.05 ns for UM (the measurement error in the actual experiment is within ±0.033 ns), the interfacial heat transfer coefficient predicted by inverse heat transfer will be within 5090 W/m^2/°C–4920 W/m^2/°C (about ±1.8%). Therefore, the inverse heat transfer can correctly predict the interfacial heat transfer coefficient.
(2) Variable thermal contact resistance: In this case, a variable thermal contact resistance is given as shown in Fig. 18. The other conditions are the same as that in the case of constant thermal contact resistance. The interfacial heat transfer coefficient predicted by the inverse heat transfer is also shown in Fig. 18. It is hardly to distinguish the difference between curves and the variation of the inversed h_{cr} is about ±1.2%.

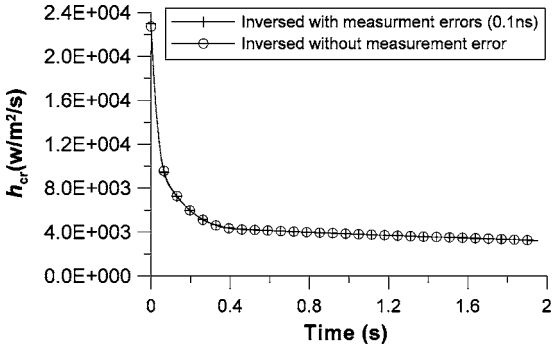

Fig. 18 The given and predicted variable thermal contact resistance (assuming ultrasound measurement errors with a standard deviation of 0.1 ns)

Conclusions

The experimental study of the variable TCR during the solidification of molten alloy158 on the substrate of the same material was performed. A novel inverse heat transfer method based on the ultrasonic measurements was developed to estimate the thermal contact resistance. There is no peak in the variation profile of the interfacial heat transfer coefficient under the present experimental conditions. The interfacial heat transfer coefficient decreases rapidly at the first stage after the contact, then the decrease becomes less noticeable. The effects of impact velocity and initial molten metal temperature on TCR were investigated. An empirical correlation equation of variable thermal contact resistance, which can be used in the numerical simulation of molten droplet impact, has been developed utilizing the experimental data.

Acknowledgment

This research was supported by the Hong Kong Government under RGC (Research Grants Council) Grant Nos. HKUST6043/99E and HKUST6230/02E.

Nomenclature

a = substrate thickness, m
c = speed of sound, m/s
c_p = specific heat, kJ/kg/°C
C_c = dimensionless thermal contact resistance
C_{cr} = dimensionless interfacial heat transfer coefficient
C_q = dimensionless heat flux
C_{qt} = dimensionless number
f = frequency, Hz
h = specific enthalpy, kJ/kg
h_{sl} = latent heat of fusion, kJ/kg
h_{cr} = interfacial heat transfer coefficient, W/m^2/K
H = impact height, m
k = thermal conductivity, W/m/°C
k_c = effective thermal conductivity, W/m/°C
L = thickness of molten metal, m
$\boldsymbol{P}$ = parameters vectors
q = heat flux, W/m^2
R_a = reference thickness of the interfacial layer, m
S = residual function
SDM = shape deposition manufacturing
T = temperature, K, °C
TCR = thermal contact resistance
t = time, s
UM = measured ultrasonic time delay change, s
UC = calculated ultrasonic time delay change, s
V_c = substrate impact velocity, m/s

Greek symbols

α = thermal diffusivity, m^2/s
γ = temperature coefficient of speed of sound, m/s/°C
ρ = density, m^3/kg
φ_i = basic functions of interfacial heat transfer coefficient

Subscripts

0 = initial state
d = molten metal region
i = contact interface
m = melting point
max = maximum
s = substrate region; solid phase
l = liquid phase

References

[1] Bennett, T., and Poulikakos, D., 1994, "Heat Transfer Aspects of Splat-Quench Solidification: Modeling and Experiment," J. Mater. Sci., **29**, pp. 2025–2039.
[2] Hayes, D. J., Wallace, D. B., and Hayes, M. T., 1992, "Picoliter Solder Droplet Dispensing," *Proceedings of the ISHM'92*, San Francisco, pp. 316–321.
[3] Liu, Q., and Orme, M., 2001, "On Precision Droplet-Based Net-Form Manufacturing Technology," Proc. Inst. Mech. Eng., Part B, **215**, pp. 1333–1355.
[4] Amon, C. H., Beuth, J. L., Merz, R., Prinz, F. B., and Weiss, L. E., 1998, "Shape Deposition Manufacturing With Microcasting: Processing, Thermal and Mechanical Issues," ASME J. Manuf. Sci. Eng., **120**, pp. 656–665.
[5] Tong, A. Y., and Holt, B. R., 1997, "Numerical Study on the Solidification of a Liquid Metal Droplets Impacting Onto a Substrate," Numer. Heat Transfer, Part A, **31**, pp. 797–817.
[6] Waldvogel, J. M., and Poulikakos, D., 1997, "Solidification Phenomena in Picoliter Size Solder Droplet Deposition on a Composite Substrate," Int. J. Heat Mass Transfer, **40**, pp. 295–309.
[7] Trapaga, G., Matthys, E. F., Valencia, J. J., and Szekely, J., 1992, "Fluid Flow, Heat Transfer and Solidification of Molten Metal Droplets Impinging on Substrate: Comparison of Numerical and Experimental Results," Metall. Trans. B, **23B**, pp. 701–718.
[8] Pasandideh-Fard, M., and Mostaghimi, J., 1996, "On the Spreading and Solidification of Molten Particles in a Plasma Spray Process: Effect of the Thermal Contact Resistance," Plasma Chem. Plasma Process., **16**, pp. 83–98.
[9] Pasandideh-Fard, M., Bhola, R., Chandra, S., and Mostaghimi, J., 1998, "Deposition of Tin Droplets on a Steel Plate: Simulations and Experiments," Int. J. Heat Mass Transfer, **41**, pp. 2929–2945.
[10] Rangel, R. H., and Bian, X., 1998, "Undercooling and Contact Resistance in Stagnation—Flow Solidification on a Semi-Infinite Substrate," Int. J. Heat Mass Transfer, **41**, pp. 1645–1653.
[11] Hong, F. J., and Qiu, H.-H., 2005, "Modeling of Remelting, Flow, and Resolidification of a Substrate in Microcasting," Numer. Heat Transfer, Part A, **48**, pp. 987–1008.
[12] Attinger, D., and Poulikakos, D., 2001, "Melting and Resolidification of a Substrate Caused by Molten Microdroplet Impact," ASME J. Heat Transfer, **123**, pp. 1110–1122.
[13] Sivakumar, D., and Nishiyama, H., 2004, "Numerical Analysis on the Impact Behavior of Molten Metal Droplets Using a Modified Splat-Quench Solidification Model," ASME J. Heat Transfer, **126**, pp. 1014–1022.
[14] Mehdizadeh, N. Z., Raessi, M., Chandra, S., and Mostaghimi, J., 2004, "Effect of Substrate Temperature on Splashing of Molten Tin Droplets," ASME J. Heat Transfer, **126**, pp. 445–452.
[15] Wang, W., Hong, F. J., and Qiu, H.-H., 2006, "Prediction of Solder Bump Formation in Solder Jet Packaging Process," IEEE Trans. Compon. Packag. Technol., **29**(3), pp. 486–493.
[16] Wang, W., Hong, F. J., and Qiu, H.-H., 2006, "The Impact of Thermal Contact Resistance on the Spreading and Solidification of a Droplet on a Substrate," Heat Transfer Eng., **27**(9), pp. 68–80.
[17] Ho, K., and Pehlke, R. D., 1985, "Metal-Mold Interfacial Heat Transfer," Metall. Trans. B, **16B**, pp. 585–596.
[18] El-Mahallawy, N. A., and Assar, A. M., 1991, "Effect of Melt Superheat on Heat Transfer Coefficient for the Aluminium Solidifying Against Copper Chill," J. Mater. Sci., **261**, pp. 729–1733.
[19] Heichal, Y., and Chandra, S., 2005, "Predicting Thermal Contact Resistance Between Molten Metal Droplets and a Solid Surface," ASME J. Heat Transfer, **127**, pp. 1269–1275.
[20] Liu, W., Wang, G. X., and Matthys, E. F., 1992, "Determination of the Thermal Contact Coefficient for a Molten Metal Droplet Impinging on a Substrate," *Transport Phenomena in Materials Processing and Manufacturing*, ASME, New York, Vol. HTD-196, pp. 111–118.
[21] Liu, W., Wang, G. X., and Matthys, E. F., 1995, "Thermal Analysis and Measurement for a Molten Drop Impacting on a Substrate: Cooling, Solidification, and Heat Transfer Coefficient," Int. J. Heat Mass Transfer, **38**, pp. 1387–1395.
[22] Wang, G. X., and Matthys, E. F., 1996, "Experimental Investigation of Interfacial Thermal Conductance for Molten Metal Solidification on a Substrate," ASME J. Heat Transfer, **118**, pp. 157–163.
[23] Wang, G. X., and Matthys, E. F., 2002, "Experimental Determination of the Interfacial Heat Transfer During Cooling and Solidification of Molten Metal Droplet Impacting on a Metallic Substrate: Effect of Roughness and Superheat," Int. J. Heat Mass Transfer, **45**, pp. 4967–4981.
[24] Loulou, T., Artyukhin, E. A., and Bardon, J. P., 1999, "Estimation of Thermal Contact Resistance During the First Stages of Metal Solidification Process: I—Experiment Principle," Int. J. Heat Mass Transfer, **42**, pp. 2119–2127.
[25] Loulou, T., Artyukhin, E. A., and Bardon, J. P., 1999, "Estimation of Thermal Contact Resistance During the First Stages of Metal Solidification Process: II—Experimental Setup and Results," Int. J. Heat Mass Transfer, **42**, pp.

2129–2142.
[26] Wang, W., and Qiu, H.-H., 2002, "Interfacial Thermal Conductance in Rapid Contact Solidification Process," Int. J. Heat Mass Transfer, **45**(10), pp. 2043–2053.
[27] Waldvogel, J. M., and Poulikakos, D., 1997, "Solidification Phenomena in Picoliter Size Solder Droplet Deposition on a Composite Substrate," Int. J. Heat Mass Transfer, **40**, pp. 295–309.
[28] Boor, C. de, 1981, *A Practical Guide to Splines*, 1st ed., Springer-Verlag, Berlin.
[29] Ozisik, M. Necati, 2000, *Inverse Heat Transfer*, Taylor & Francis, New York.
[30] Qiu, H.-H., Sommerfeld, M., and Durst, F., 1991, "High Resolution Data Processing for Phase Doppler Measurement in a Complex Two-Phase Flow," Meas. Sci. Technol., **2**, pp. 455–463.
[31] Parker, R. L., Manning, J. R., and Peterson, N. C., 1985, "Application of Pulsed-Echo Ultrasonic to Locate the Solid/Liquid Interface During the Solidification and Melting of Steel and Other Metals," J. Appl. Phys., **58**(11), pp. 4150–4164.
[32] Muojekwu, C. A., Samarasekera, I. V., and Brimacombe, J. K., 1995, "Heat Transfer and Microstructure During the Early Stages of Metal Solidification," Metall. Mater. Trans. B, **26B**, pp. 361–382.

E. G. Colgan
e-mail: ecolgan@us.ibm.com

B. Furman

M. Gaynes

N. LaBianca

J. H. Magerlein

R. Polastre

IBM Watson Research Center,
1101 Kitchawan Road,
Yorktown Heights, NY 10598

R. Bezama

K. Marston

IBM East Fishkill,
2070 Route 52,
Hopewell Junction, NY 12533

R. Schmidt
IBM Poughkeepsie,
2455 South Road,
Poughkeepsie, NY 12601

High Performance and Subambient Silicon Microchannel Cooling

High performance single-phase Si microchannel coolers have been designed and characterized in single chip modules in a laboratory environment using either water at 22 °C *or a fluorinated fluid at temperatures between 20 and* −40 °C *as the coolant. Compared to our previous work, key performance improvements were achieved through reduced channel pitch (from 75 to 60 microns), thinned channel bases (from 425 to 200 microns of Si), improved thermal interface materials, and a thinned thermal test chip (from 725 to 400 microns of Si). With multiple heat exchanger zones and 60 micron pitch microchannels with a water flow rate of* 1.25 lpm*, an average unit thermal resistance of* 15.9 C mm^2/W *between the chip surface and the inlet cooling water was demonstrated for a Si microchannel cooler attached to a chip with Ag epoxy. Replacing the Ag epoxy layer with an In solder layer reduced the unit thermal resistance to* 12.0 C mm^2/W. *Using a fluorinated fluid with an inlet temperature of* −30 °C *and 60 micron pitch microchannels with an Ag epoxy thermal interface layer, the average unit thermal resistance was* 25.6 C mm^2/W. *This fell to* 22.6 C mm^2/W *with an In thermal interface layer. Cooling* >500 W/cm^2 *was demonstrated with water. Using a fluorinated fluid with an inlet temperature of* −30 °C*, a chip with a power density of* 270 W/cm^2 *was cooled to an average chip surface temperature of* 35 °C. *Results using both water and a fluorinated fluid are presented for a range of Si microchannel designs with a channel pitch from 60 to 100 microns.* [DOI: 10.1115/1.2724850]

Keywords: microchannel cooling, high power density, single phase liquid cooling

Introduction

The problem of cooling high power processor chips becomes even more difficult as chip geometries are scaled down and operating speeds are increased, resulting in increased power density. At the same time, reduced chip operating temperatures are desired in order to improve device performance and reliability. In some applications, operation at cryogenic temperatures may be a possibility to take advantage of greater CMOS device performance reported at such temperatures [1,2]. In recent work [3], it has been demonstrated that a CMOS performance gain equivalent to more than one technology generation can be achieved with minimal manufacturing process changes by lowering the operating temperature from 100 °C to −50 °C. Microchannel liquid cooling is attractive for high power density and low junction temperature applications because it offers very low thermal resistance between the chip surface and the coolant and it allows further reduction in chip temperature by lowering the coolant temperature.

Twenty five years ago, Tuckerman and Pease first described the use of microchannel cooling for very high power densities [4]. They demonstrated cooling of 790 W/cm^2 with a temperature increase of 71 °C for a flow rate of 0.52 lpm with a pressure drop of 214 kPa where the 0.3 mm deep channels were fabricated on the opposite side of a 0.4 mm thick wafer from a 1×1 cm thin film resistor. However, the coolers could not be fabricated easily and pressure drops were very high. Given the cost of high-performance processor chips, it is not practical to form the microchannels directly on the back surface of the chip. It is preferable to instead bond a separate microchannel cooler to the back of the chip with a material having as low a thermal resistance as possible.

Since the pioneering work by Tuckerman and Pease [4] extensive literature has developed on microchannel cooling, and a number of reviews are available [5–7]. Only a few recent publications though discuss integration of microchannel coolers with packaged silicon chips [8–10]. In the work by Zhang et al. [8], an aluminum microchannel heat sink with 0.21 mm wide, 15 mm long, and 2 mm deep channels was formed and assembled onto the back of a 12×12 mm thermal test chip using a thermal interface material. The finned area was 12.2 mm wide and the thermal test chip was mounted in a flip chip ball grid array package. With a flow rate of 1 lpm of water and 60 W of input power, the measured thermal resistance (chip junction to inlet fluid) was 0.317 °C/W. For a chip junction to inlet fluid temperature difference of 60 °C, this would correspond to a power dissipation of 189 W or 131 W/cm^2. Ignoring spreading, and using the whole chip area, the unit thermal resistance from the chip junction to the inlet can be estimated as about 46 C mm^2/W. In the work by Chang et al. [9], 100 microchannels 61 μm wide, 272 μm deep, 15 mm long on a 100 μm pitch were fabricated on the back of a 680 μm thick silicon wafer where heaters and temperature sensors were formed on the opposite side over a 10 mm $\times$ 12 mm area. With a flow rate of 0.098 lpm and 70 W of input power to the main heater, the measured thermal resistance from the inlet to the maximum chip junction temperature was 0.22 °C/W and between the outlet to the maximum chip junction temperature was 0.08 °C/W. The pressure drop, with a flow rate of 0.098 lpm, was 44.1 kPa. Ignoring spreading, and using the heater area, the unit thermal resistance

Contributed by the Heat Transfer Division of ASME for publication in the JOURNAL OF HEAT TRANSFER. Manuscript received April 26, 2006; final manuscript received October 17, 2006. Review conducted by Satish G. Kandlikar. Paper presented at the 4th International Conference on Nanochannels, Microchannels and Minichannels (ICNMM2006), Limerick, Ireland, June 19–21, 2006.

from the maximum chip junction to the inlet can be estimated as about 26 C mm^2/W and from the maximum chip junction to the outlet as about 10 C mm^2/W.

In a previous publication [10], we addressed a number of the practical issues for implementing microchannel cooling in a single chip module (SCM). Recent progress in high-rate reactive ion etching (DRIE) of Si [11] has greatly simplified the fabrication of microchannel coolers from silicon. Also, a number of methods of reducing the pressure drop have been reported including subdividing the flow into multiple heat exchanger zones with shorter channel lengths [12] and manifold designs with large cross-sectional area (i.e. equal, or larger than, the channel cross-sectional area) [13]. In addition, staggered fins in microchannel coolers have been found to increase the heat transfer coefficient compared to continuous fins [10,14], though there is also a slight increase in pressure drop with staggered fins compared to equivalent continuous fins [10]. For the center of the thermal chip, an average total unit resistance between the inlet water and the chip surface of 20.7 C mm^2/W was reported [10] for a flow of 1.25 lpm where the thermal chip was 725 microns thick and Ag epoxy was used to attach the Si microchannel cooler. The silicon microchannel coolers were 20×20 mm in size, used staggered fins, had six heat exchanger zones, and the channels were fabricated in a 675 micron thick wafer and were 45 micron wide, 254 micron deep, and had a 75 micron pitch. Cooling of more than 300 W/cm^2 was demonstrated in a SCM where the temperature was about 60°C above the inlet temperature at the chip center and the heated area was 3 cm^2.

The thermal resistance of silicon microchannel coolers can be reduced by optimizing the channel pitch, increasing the fluid flow rate, reducing the thickness of the silicon between the base of the fins and the bottom of the cooler, reducing the thermal resistance of the material used to join the microchannel cooler to the chip being cooled, and reducing the thickness of the chip being cooled. The minimum practical channel pitch is determined by the fluid flow resistance, fabrication difficulty, and fin efficiency. The fluid flow rate is limited by the acceptable pressure drop and design of the fluid circulating system.

In a recent publication [15], we demonstrated a SCM with an average unit resistance of 16.2 C mm^2/W between the chip surface and the inlet along with cooling a power density of greater than 400 W/cm^2, by using a silicon microchannel cooler with a 450 micron thick channel chip joined to a 400 micron thick thermal chip with an Ag epoxy layer. For silicon microchannel coolers attached to a chip in an SCM with an Ag epoxy layer, very good uniformity from SCM to SCM, ±2% standard deviation, and within an SCM, ±5% standard deviation, was achieved.

Once the design of the silicon microchannel cooler has been optimized to minimize the thermal resistance, one means of further reducing the chip junction temperature is to reduce the coolant temperature. Circulating a fluid at temperatures below the dew point presents significant system design challenges to avoid condensation on the components in contact with the coolant. For this work, we used a fluorinated fluid since it is not conductive, and did not reduce the inlet temperature below −40°C as the power required to cool the fluid increases significantly if a two stage vapor-compression cycle is needed.

In the first portion of this paper, the structure of the silicon microchannel coolers and the single chip modules will be briefly described. Results are then presented for microchannel coolers with channel pitches between 60 and 100 microns joined to 400 micron thick thermal chips using either Ag epoxy or In solder where 22°C water was used as the cooling fluid. The next section includes results where a fluorinated fluid was used as the coolant and the inlet temperature was varied between −40°C and 20°C.

Microchannel and SCM Design

The general configuration of the microchannel coolers and single chip modules (SCMs) used in this work has been described previously [10]. The microchannel coolers used were each 20 $\times$ 20 mm in size, with a 0.7 mm seal region around the perimeter, so the actively cooled area was 18.6×18.6 mm in size. The manifold chip contained zig-zagged rows of fluid vias through the chip and distribution channels were etched about 250 microns deep on the side of the manifold chip bonding to the channel chip to help redistribute the flow to, or from, the fluid vias. Also, the fin segments were removed from the regions under the fluid vias on the channel chip to further aid in the redistribution of the flow at the fluid vias. A 3D rendering of part of an assembled microchannel cooler is shown in Fig. 1, where the manifold chip is on top and is shown semitransparent. In operation, alternate zig-zagged rows of fluid vias are used as inlets and outlets, so the microchannel cooler is divided into six parallel-fed heat exchanger zones and the flow length between the inlets and outlets is about 3.1 mm. The fluid vias in the manifold chip were formed as zig-zagged arrays of circular openings instead of elongated slots to reduce the likelihood of the manifold wafers breaking during fabrication and assembly. The microchannel coolers were fabricated using photolithography and deep Si reactive ion etching (DRIE) on 150 mm wafers where the channel wafers were either 450 or 525 microns thick and the manifold wafers were 675 microns thick. The manifold and channel wafers were fusion bonded together and then diced to produce the completed Si microchannel coolers. Five different microchannel designs were fabricated, with channel pitches between 60 and 100 microns and channel widths between 35 and 60 microns. The channel depth varied slightly with the channel width, from about 243 microns for the 35 micron wide channels to about 269 microns for the 60 micron wide channels. Cross-sectional images of representative microchannel coolers used in this work are shown in Fig. 2 and the dimensions are indicated. The microchannel designs are designated as *Pxx/Cyy* where *xx* is the pitch and *yy* is the channel width in microns. In all cases, staggered fins with a length of 500 microns were used; 250 micron long fins are shown in Fig. 1.

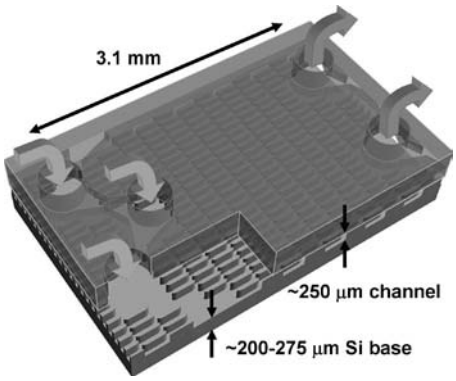

Fig. 1 3D rendering of a portion of an assembled microchannel cooler have six heat exchanger zones

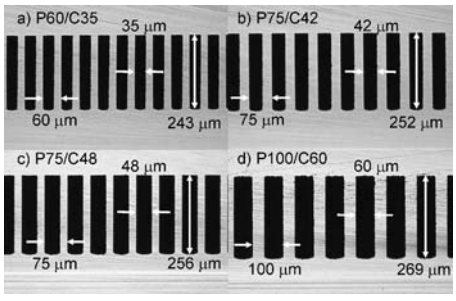

Fig. 2 Cross-sectional images of microchannel coolers perpendicular to the fin segments

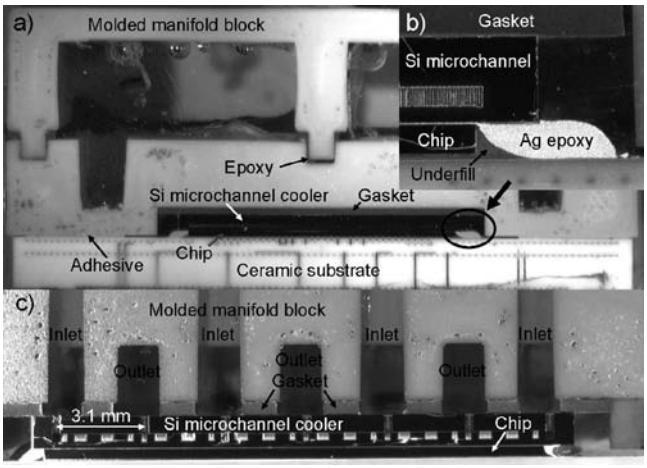

Fig. 3 Cross-sectional images of complete microchannel single chip module

Cross-sectional images of an SCM assembly containing a Si microchannel cooler are shown in Fig. 3(*a*). From top to bottom, the first component is a two piece manifold block to transform a single inlet and outlet into alternating inlet and outlet zones. Next is a flexible gasket between the manifold block and the Si microchannel cooler. In the detailed image in Fig. 3(*b*), the channels are visible. The 18.5×18.6 mm thermal test chip was mounted with solder balls onto a ceramic module and underfilled. The microchannel cooler was bonded to the thermal chip using a Ag epoxy (white in Fig. 3(*b*)). The bottom perimeter of the manifold block was bonded to the ceramic package with an adhesive. The cross section in Fig. 3(*c*) is perpendicular to those in Figs. 3(*a*) and 3(*b*) and shows the alternating inlet/outlet zones and the staggered fins on the channel chip. Further details on the molded manifold block and the SCM components can be found in an earlier publication [10].

Single Chip Module Results Using Water

The thermal chip used had six temperature sensor resistors, two near the chip center, two near the chip edges, and two near mid-diagonal positions. The sensor resistors were calibrated by varying the water inlet temperature while measuring the sensor resistor values. The samples were measured using a test station where the water flow rate could be varied while measuring the differential pressure across the SCM, the inlet and outlet water temperatures, the sensor resistor values, and the power applied to the heater resistor. The thermal chip heated area was 3 cm^2, which is about 87% of the total chip area. The thermal chip size is nearly identical with the active area of the microchannel cooler, 18.6×18.6 mm. The differential pressure measurements were not corrected for the ~0.4 kPa pressure drop measured in the test station when the SCM was replaced with a short hose segment. For water, the uncertainty in the flow measurements was about ±0.05 lpm, the uncertainty in the pressure measurements was about ±0.15 kPa, and the uncertainty in the inlet and outlet temperature measurements was about 0.5°C. The uncertainty in the measured thermal resistance is ≤5% and is due mainly to the uncertainty in the sensor calibration and the small amount of heat which does not flow through the microchannel cooler. Based on the measured temperature rise in the water, the flow rate, and applied power, the amount of heat which was not removed by the water was typically less than or equal to 1% of the applied power.

The total unit thermal resistance versus flow rate is plotted for seven SCMs and five different microchannel designs in Fig. 4(*a*). The reported thermal resistance values are relative to the inlet water temperature; the measured thermal resistance (°C/W), is calculated as the chip junction temperature minus the inlet water

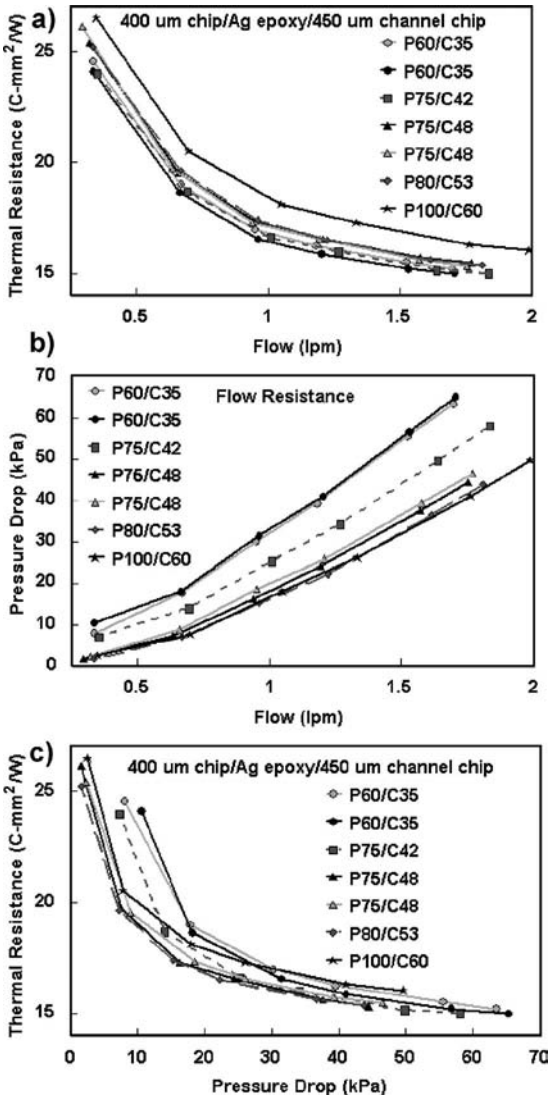

Fig. 4 Single chip module results using water

temperature divided by the total applied power. Since only about 87% of the thermal chip area was powered, the thermal transport of the complete structure was simulated numerically using a commercially available CFD code to relate the measured thermal resistance (°C/W) to the unit thermal resistance (C mm^2/W) indicated in Fig. 4(*a*). The correlation between the measured thermal resistance and the unit thermal resistance from the simulations resulted in an average unit thermal resistance about 5% larger than if just the powered chip area of 300 mm^2 was multiplied by the measured thermal resistance and about 10% smaller than if the full chip area of 344 mm^2 was multiplied by the measured thermal resistance. The total unit thermal resistance includes the thermal chip, the Ag epoxy thermal interface material (TIM) and the microchannel cooler and is based on the average of the six temperature sensors. The measurements were made with four inlets and three outlets where the chip sensors were on average closer to the fluid inlets than to the outlets. With a flow of 1.25 lpm, reversing the flow direction causes the measured thermal resistance to increase by 3%. Note that two samples were measured for both the P60/C35 and the P75/C48 configurations. At a fixed flow rate, the finer pitch channels had a lower thermal resistance than wider pitch channels. The differential pressure of the SCMs versus the flow rate for these samples is plotted in Fig. 4(*b*). The pressure drop was less at a fixed flow with wider channels. The total ther-

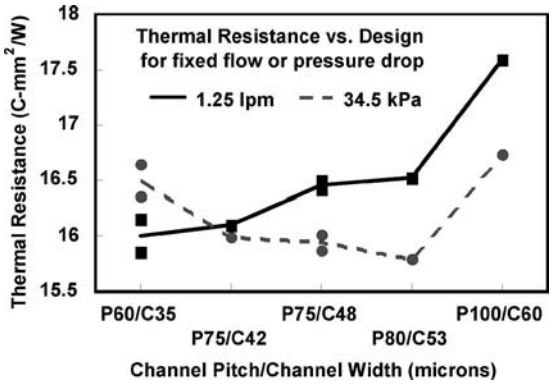

Fig. 5 Total thermal resistance versus channel design for a flow of 1.25 lpm or a pressure drop of 34.5 kPa

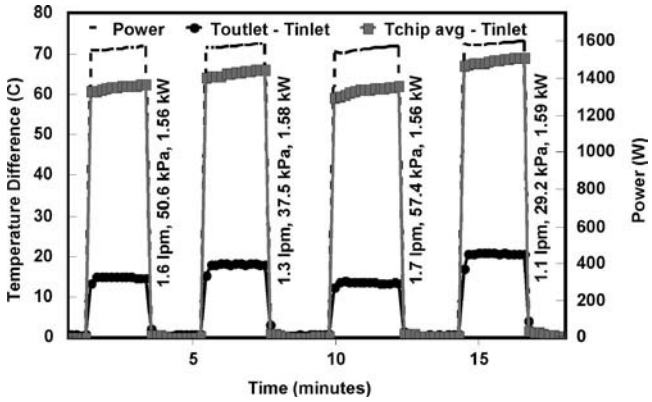

Fig. 7 P60/C35 microchannel SCM with In solder attach for various flows and about 1.6 kW applied power

mal resistance is plotted against the differential pressure drop of the SCMs in Fig. 4(*c*). For differential pressures less than about 40 kPa, the 80 micron pitch microchannel has the lowest total thermal resistance.

The optimum silicon microchannel design will depend on the application and what water flow rate, or differential pressure drop, is available. The total thermal resistance corresponding to a flow rate of 1.25 lpm, or to a differential pressure drop of 34.5 kPa was interpolated from the results in Fig. 4 and plotted against the microchannel designs in Fig. 5. For a fixed flow rate of 1.25 lpm, the P60/C35 design, with a pressure drop of 42.1 kPa, provides the lowest thermal resistance but with a fixed pressure drop of 34.5 kPa, the P80/C53 design, with a flow rate of 1.5 lpm, provides the lowest thermal resistance.

The total thermal resistance versus flow rate is plotted in Fig. 6 for three SCMs all using 400 micron thick thermal chips and P60/C35 microchannel coolers, but two used Ag epoxy and one used In solder as the TIM to attach the microchannel coolers to the thermal chips. The pressure drops versus flow rates for the three SCMs were nearly identical. At a given flow rate, the total thermal resistance was reduced by about 4.0 C mm^2/W using In solder instead of Ag epoxy for attaching the microchannel cooler to the thermal chip. With In solder, the total thermal resistance was 12.0 C mm^2/W with a flow rate of 1.25 lpm and 12.5 C mm^2/W with a pressure drop of 34.5 kPa. Even though a separate cooler was used, these values are close to the 9.0 C mm^2/W unit thermal resistance value reported by Tuckerman and Pease [4] where the silicon substrate below the channels was only 0.1 mm thick and the pressure drop was much higher. Since the exact value of the TIM thermal resistance is not known, the average apparent heat transfer coefficient can only be estimated, and is approximately 200,000 W/m^2 K with a flow rate of 1.25 lpm.

The high power performance of a P60/C35 microchannel attached with In solder [16] was also measured. Figure 7 shows the results for various flow conditions when about 1.6 kW was applied to the heater resistors. The powered area was 3 cm^2, so the power density was >500 W/cm^2. The temperature difference between the chip (determined from the average of the six chip sensors) and the inlet water is plotted with square symbols. The temperature difference between the outlet and inlet water is plotted with circular symbols and indicated on the left axis. The power (dashed line without symbols and right hand axis) was turned off while stabilizing different flow conditions and to allow the chiller to recover. The applied power exceeded the cooling capacity of the recirculating chiller being used, so with time the inlet water temperature increased. This resulted in the thermal chip heater resistors values increasing with time, and hence the total power increased slightly with time, as a constant current was being applied.

Subambient Single Chip Module Results

An image of the test station used for the subambient measurements is shown in Fig. 8. The test station was similar to that used for the measurements with water, but a nitrogen purged enclosure was used to avoid condensation and an ultralow temperature recirculating chiller was also used. The coolant used was a fluorinated compound with approximately the following properties at −40°C; heat capacity of 1210 J/kg K, density of 1770 kg/m^3, and thermal conductivity of 0.096 W/m K. Fluorinated com-

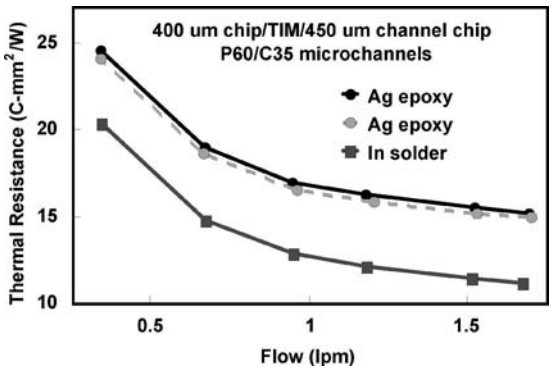

Fig. 6 Total thermal resistance versus flow for Ag epoxy and In solder between the microchannel and the chip

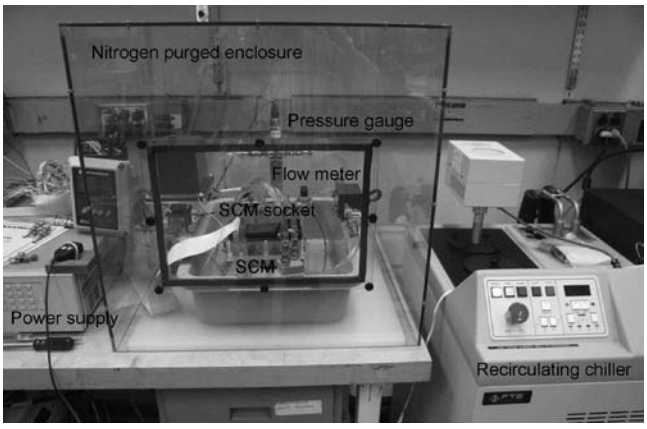

Fig. 8 Subambient microchannel SCM test station

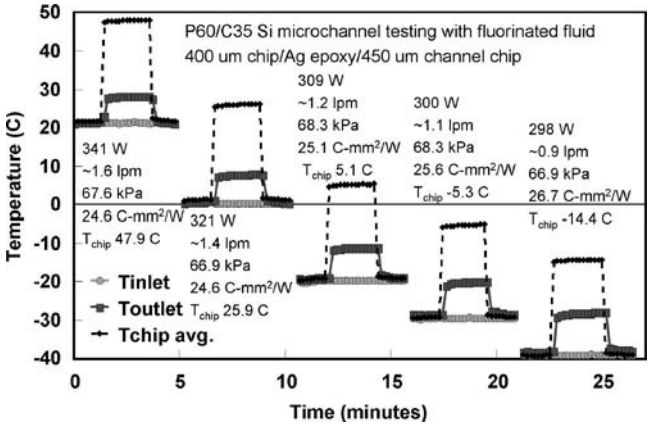

Fig. 9 P60/C35 microchannel SCM with Ag epoxy TIM for various inlet temperatures and about 300 W applied power

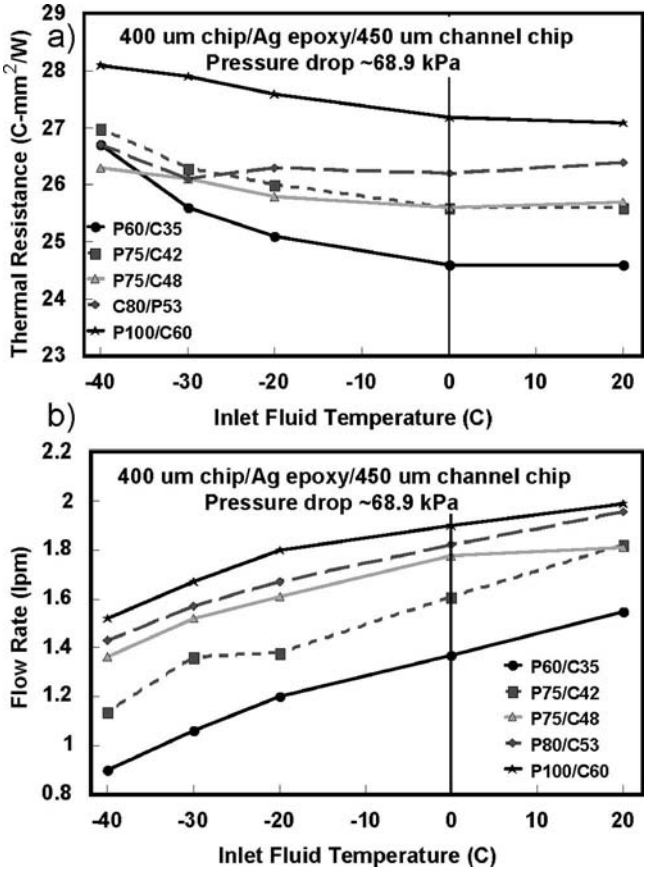

Fig. 10 Single chip module subambient results

pounds are dielectric, nonflammable and nontoxic, but are expensive and lower performance than some aqueous based fluids. Aqueous based fluids though are conductive and could cause system failure if there was a leak near electrical components.

The subambient performance of a P60/C35 cooler attached with Ag epoxy was measured for fluid inlet temperatures between 20°C and −40°C, as shown in Fig. 9. The measured inlet, outlet, and chip temperatures are plotted versus time for the different inlet temperatures. The applied power was around 300 W and the pressure drop was about 68.9 kPa for each inlet temperature. The actual power and pressure drops are indicated in Fig. 9 along with the approximate flow rate, unit thermal resistance, and average chip temperature. The unit resistance is again between the inlet and the average of the six sensors on the chip. As the fluid inlet temperature decreased, the unit thermal resistance increased slightly. The use of a fluorinated fluid increases the unit thermal resistance at room temperature by about 9 C mm^2/W compared to using water. This means that to cool a chip with a power density of 100 W/cm^2 to the same chip temperature as can be achieved with 20°C water, the fluorinated compound inlet temperature would need to be about 11°C.

The subambient performance of the other four microchannel designs were also characterized, using the same conditions as were used for P60/C35 in Fig. 9, and the results are summarized in Fig. 10. For fluid inlet temperatures between −30°C and 20°C, with a constant pressure drop of about 68.9 kPa, the P60/C35 design had the lowest unit thermal resistance, Fig. 10(*a*). With a −40°C inlet temperature, the P75/C48 design had the lowest unit thermal resistance. The wider channels provided the best performance with a −40°C inlet temperature because of the increased viscosity of the coolant. The approximate flow rates are shown in Fig. 10(*b*) for a pressure drop of about 68.9 kPa. As expected, the flow rates were lower for the finer pitch channels and the flow rates decreased as the inlet temperature was reduced due to the increase in the viscosity of the fluorinated compound used as the coolant. The scatter for some of the samples in Fig. 10 could be due to variations in the pressure drop, which ranged from 66.9 to 71.7 kPa. The pressure was adjusted before power was applied, but the coolant viscosity decreased due to the increased temperature when power was applied during the measurements, resulting in the variations.

The subambient performance of a P75/C42 cooler with a 525 micron channel chip, attached with Ag epoxy, was characterized for a variety of applied power levels. Figure 11 shows the results where the inlet temperature was −28°C, the flow rate was about 1.4 lpm, and the differential pressure drop was about 70 kPa, for power levels between 320 and 815 W. The powered area was 3 cm^2, so the maximum power density was >270 W/cm^2. The applied power is indicated by the dashed line without symbols, temperature difference between the chip (determined from the average of the six chip sensors), and the inlet fluid is plotted with square symbols, and the temperature difference between the outlet and inlet fluid is plotted with circular symbols. With over 100 W/cm^2, the chip temperature was −4°C, with over 200 W/cm^2, the chip temperature was 21°C, and with over 270 W/cm^2, the chip temperature was 35°C.

The total thermal resistance versus inlet temperature is plotted in Fig. 12 for two SCMs, both using 400 micron thick thermal chips, 450 micron thick channel chips, and P60/C35 microchannel coolers, but one used Ag epoxy and other used In solder as the TIM to attach the microchannel cooler to the thermal chip. The

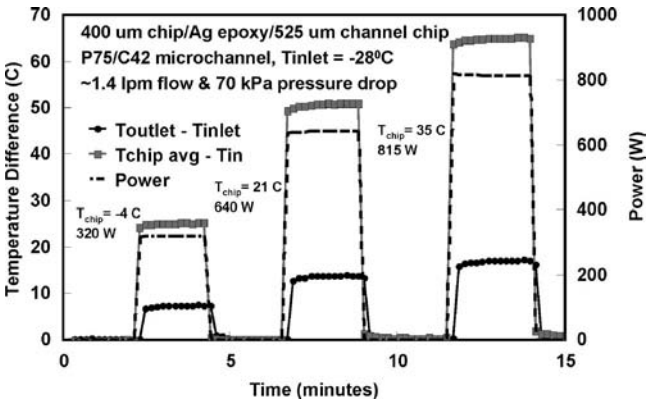

Fig. 11 P75/C42 microchannel SCM with Ag epoxy attach and an inlet temperature of −28°C for various power levels

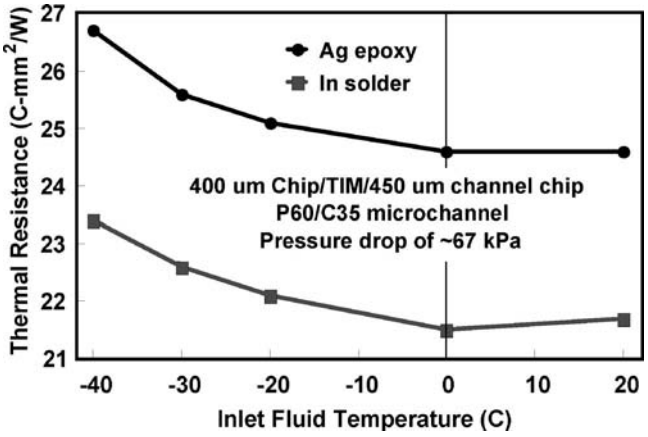

Fig. 12 Total thermal resistance versus inlet temperature for Ag epoxy and In solder as the TIM between the microchannel cooler and the chip

pressure drops versus flow rates for the two samples were nearly identical. At a given inlet temperature, the total thermal resistance was reduced by about 3.1 C mm^2/W when using In solder instead of Ag epoxy for attaching the microchannel cooler to the thermal chip. With In solder as the TIM layer, for an inlet temperature of $-40°C$, with a power density of 100 W/cm^2, the average chip temperature was $-17°C$.

Conclusions

High performance single-phase Si microchannel coolers have been designed and characterized in single chip modules in a laboratory environment using either water at $22°C$ or a fluorinated fluid at temperatures between 20 and $-40°C$ as the coolant. With a water flow rate of 1.25 lpm, total average unit thermal resistances as low as 12.0 C mm^2/W have been demonstrated for P60/C35 microchannel coolers built from 450 micron thick channel chips attached to 400 micron thick thermal chips using an In solder TIM. Cooling over 500 W/cm^2 has been demonstrated using such a single chip module. Replacing the In solder TIM layer with an Ag epoxy layer increased the unit thermal resistance to 15.9 C mm^2/W between the chip surface and the inlet cooling water for a similar SCM configuration.

Using a fluorinated fluid with an inlet temperature of $-30°C$, for 60 micron pitch microchannels with an Ag epoxy layer, the average unit thermal resistance was 25.6 C mm^2/W and with a In solder layer, the unit thermal resistance was 22.6 C mm^2/W. Cooling of 270 W/cm^2 using a fluorinated compound with an inlet temperature of $-30°C$ resulted in an average chip surface temperature of $35°C$. For a fixed pressure drop, the optimum microchannel design depended on the inlet temperature, with wider channels performing better at $-40°C$.

Improved cooling, either through the introduction of direct liquid cooling of the chips with a low total thermal resistance, or by using a subambient fluid, has the potential to enable significant increases in CMOS performance. There are, however, significant system level challenges in the use of subambient cooling fluids.

Acknowledgment

We are deeply indebted to C. Jahnes, B. White, D. Patsey, D. Posillico, W. Lam, D. Lisounenko, B. Kane, M.T. Robson, J. Moore, and J. Wilson in the IBM Yorktown Microelectronics Research Laboratory for fabrication of the thermal chips, to E. Sprogis and A. Wirsing of for wafer thinning and bumping, and to S. Bradley and F. Pompeo for chip joining. We would also like to thank J. Cai, L. Campbell, M. Ellsworth, D. Frank, and R. Guernsey for helpful discussions.

Nomenclature

$T_{\text{chip avg.}}$ = average chip temperature, °C
T_{inlet} = fluid inlet temperature, °C
T_{outlet} = fluid outlet temperature, °C

References

[1] Sun, J.Y-C., Taur, Y., Dennard, R. H., and Klepner, S. P., 1987, "Submicrometer Channel CMOS for Low-Temperature Operation," IEEE Trans. Electron Devices, **34**(1), pp. 19–27.
[2] Wind, S. J., Shi, L., Lee, K-L., Roy, R. A., Zhang, Y., Sikorski, E., Kozlowski, P., D'emic, C., Bucchignano, J. J., Winn, H-J., Viswanathan, R. G., Cai, J., and Taur, Y., 1999, "Very High Performance 50 nm CMOS at Low Temperature," Tech. Dig. - Int. Electron Devices Meet., pp. 928–930.
[3] Dennard, R. H., Cai, J., and Kumar, A., 2007, "A Perspective on Today's Scaling Challenges and Possible Future Directions," Solid-State Electron., **51**, pp. 518–525.
[4] Tuckerman, D. B., and Pease, R. F. W., 1981, "High Performance Heat Sink for VLSI," IEEE Electron Device Lett., **EDL-2**(5), pp. 126–129.
[5] Phillips, R. J., 1990, "Micro-Channel Heat Sinks," *Advances in Thermal Modeling of Electronics*, A. Bar-Cohen and A. D. Kraus, eds., ASME, New York, Vol. 2, pp. 109–184.
[6] Sobhan, C. B., and Garimella, S. V., 2001, "A Comparative Analysis of Studies on Heat Transfer and Fluid Flow in Microchannels," Microscale Thermophys. Eng., **5**, pp. 293–311.
[7] Kandlikar, S., Garimella, S., Li, D., Colin, S., and King, M., 2005, *Heat Transfer and Fluid Flow in Minichannels and Microchannels*, Elsevier, New York, Chap. 3, pp. 87–136.
[8] Zhang, H. Y., Pinjala, D., Wong, T. N., and Joshi, Y. K., 2005, "Development of Liquid Cooling Techniques for Flip Chip Ball Grid Array Packages With High Heat Flux Dissipations," IEEE Trans. Compon. Packag. Technol., **28**(1), pp. 127–135.
[9] Chang, J-Y., Prasher, R., Chau, D., Myers, A., Dirner, J., Prstic, S., and He, D., 2005, "Convective Performance of Package Based Single Phase Microchannel Heat Exchanger," IPACK2005-73126, *Proceedings of ASME InterPACK '05*, July 17–22, San Francisco, CA.
[10] Colgan, E. G., Furman, B., Gaynes, M., Graham, W., LaBianca, N., Magerlein, J. H., Polastre, R. J., Rothwell, M. B., Bezama, R. J., Choudhary, R., Marston, K., Toy, H., Wakil, J., Zitz, J., and Schmidt, R., 2005, "Practical Implementation of Silicon Microchannel Coolers for High Power Chips," *Proceedings of the 21st Annual IEEE Semiconductor Thermal Measurement and Management Symposium*, San Jose CA, March 15–17, pp. 1–7.
[11] Laermer, F., and Urban, A., 2003, "Challenges, Developments and Applications of Silicon Deep Reactive Ion Etching," Microelectron. Eng., **67–68**, pp. 349–355, and references therein.
[12] Harpole, G. M., and Eninger, J. E., 1991, "Micro-Channel Heat Exchanger Optimization," *Proceedings of the Seventh IEEE Semi-Therm Symposium*, pp. 59–63.
[13] Webb, R. L., 2003, "Effect of Manifold Design on Flow Distribution in Parallel Micro-Channels," *Proceedings of IPACK03, International Electronic Packaging Technology Conference*, Paper No. 35251.
[14] Kishimoto, T., and Sasaki, S., 1987, "Cooling Characteristics of Diamond-Shaped Interrupted Cooling Fins for High Power LSI Devices," Electron. Lett., **23**(9), pp. 456–457.
[15] Colgan, E. G., Furman, B., Gaynes, M., LaBianca, N., Magerlein, J. H., Polastre, R. J., Bezama, R. J., Choudhary, R., Marston, K., Toy, H., Wakil, J., and Schmidt, R., 2006, "Silicon Microchannel Cooling for High Power Chips," HVAC&R Res., **12**(4), pp. 1031–1045.
[16] Furman, B. K., Lauro, P. A., Shih, D. Y., Van Kessel, T., Martin, Y., Colgan, E. G., Zou, W., Iruvanti, S., Wakil, J., Schmidt, R., and Iyengar, M. K., 2005, "Metal TIMs for High Power Cooling Applications," IMAPS Advanced Technology Workshop on Thermal Management, Palo Alto, CA, Oct. 23–26.

Spray Cooling of High Aspect Ratio Open Microchannels

Johnathan S. Coursey

Jungho Kim[1]
e-mail: kimjh@umd.edu

Kenneth T. Kiger

Department of Mechanical Engineering,
University of Maryland,
College Park, MD 20742

Direct spraying of dielectric liquids has been shown to be an effective method of cooling high-power electronics. Recent studies have illustrated that even higher heat transfer can be obtained by adding extended structures, particularly straight fins, to the heated surface. In the current work, spray cooling of high-aspect-ratio open microchannels was explored, which substantially increases the total surface area and allows more residence time for the incoming liquid to be heated by the wall. Five such heat sinks were constructed, and their thermal performance was investigated. These heat sinks featured a projected area of 1.41×1.41 cm^2*, channel width of* 360 μm*, a fin width of* 500 μm*, and fin lengths of* 0.25 mm*,* 0.50 mm*,* 1.0 mm*,* 3.0 mm*, and* 5.0 mm*. The five enhanced surfaces and a flat surface with the same projected area were sprayed with a full cone nozzle using PF-5060 at* 30°C *and nozzle pressure differences from* 1.36–4.08 atm (69–121 ml/min)*. In all cases, the enhanced surfaces improved thermal performance compared to the flat surface. Longer fins were found to outperform shorter ones in the single-phase regime. Adding fins also resulted in the onset of two-phase effects (and higher-heat transfer) at lower wall temperatures than the flat surface. The two-phase regime was characterized by a balance between added area, changing flow flux, flow channeling, and added conduction resistance. Spray efficiency calculations indicated that a much larger percentage of the liquid sprayed onto the enhanced surface evaporated than with the flat surface. Fin lengths between* 1 mm *and* 3 mm *appeared to be optimum for heat fluxes as high as* 124 W/cm^2 *(based on projected area) and the range of conditions studied.* [DOI: 10.1115/1.2737476]

Keywords: spray cooling, thermal management, fins, heat sink, evaporation

Introduction

With chip heat fluxes predicted to continue to rise past what is practical for air-cooling, advanced liquid immersion cooling techniques are likely to play a more prominent role. Two-phase systems utilizing boiling or liquid evaporation have long been recognized as having the potential to carry large thermal loads at low temperature difference. One such system is spray cooling, in which an atomizing nozzle provides a flow of liquid droplets directed at a hot chip or the entire circuit board. Some disadvantages of spray cooling include the need for pumps, filters, and nozzles that can potentially clog, and a sensitivity to nozzle-to-surface distances. However, very high heat transfer rates over large areas can be achieved because vapor removal from the surface is much easier than with other two-phase systems. Heat fluxes as high as 1000 W/cm^2 have been observed in gas-assisted spray cooling with water [1,2]. Over 100 W/cm^2 has been observed when using dielectric FC-72, which is compatible with direct cooling of electronics [3–6]. Spray cooling technology has been applied in the cooling of supercomputers and commercial off-the-shelf (COTS) electronics for military applications.

Because of the complexity of the spray cooling process and the inability to independently control drop size, drop velocity, and mass flux, the mechanisms by which heat is removed during spray cooling are not well understood. One proposed mechanism is that the spray produces a thin film on the surface through which thermal conduction occurs. Mixing caused by impinging droplets increases the effective conductance of this layer and promotes evaporation from the free surface [2]. In another proposed mechanism (commonly referred to as secondary nucleation), boiling is thought to occur in the liquid film; however, the incoming droplets puncture the growing bubbles before they can grow to appreciable size. The incoming droplets which serve as nucleation sites for new bubbles, can also trap vapor nuclei within the liquid film. The growth and collapse of many small rapidly growing bubbles is proposed to be the dominant heat transfer mechanism [1,7]. In yet another proposed mechanism, heat is primarily transferred from the surface to the liquid convectively through sensible heating. Pautsch and Shedd [8] have shown that the best performance is obtained when liquid is not used efficiently but is in great supply, thus avoiding phase change and the ultimate dewetting of the surface. Horacek et al. [5,6] found that the phase-change component of the heat flux varied directly with the three-phase contact line length but not the wetted area fraction. It was not known if the heat transfer was due to evaporation at the contact line through the mechanism suggested by Potash and Wayner [9] or by an alternate mechanism, such as transient conduction into the liquid as it moves over the surface as proposed by Demiray and Kim [10].

Although some research has been performed on the effects of flow rate, liquid subcooling, spray angle, droplet parameters, and dissolved gas on cooling performance [3–6,11–15], few studies are available on spray cooling of enhanced surfaces. In fact, it has been argued that increasing the surface roughness decreases the heat transfer by increasing the thickness of the liquid film on the surface [16]. However, recent studies have indicated that enhanced surfaces with large-scale roughness elements (greater than the liquid film thickness) have the potential to transfer much more heat than comparable flat surfaces. Silk et al. [17,18] investigated spraying gassy (1 atm) PF-5060 on a flat surface and enhanced surfaces, including straight fins, square pin fins, and pyramidal fins. They used a 2×2 Parker Hannefin nozzle array with a volumetric flux of 0.016 $m^3/(m^2\,s)$. All of their enhanced surfaces significantly increased the critical heat flux (CHF). They also found that straight fins outperformed the other two types of surface enhancements and resulted in a CHF of 156 W/cm^2 (based

[1]Corresponding author.

Contributed by the Heat Transfer Division of ASME for publication in the JOURNAL OF HEAT TRANSFER. Manuscript received July 21, 2006; final manuscript received January 18, 2007. Review conducted by Satish G. Kandlikar.

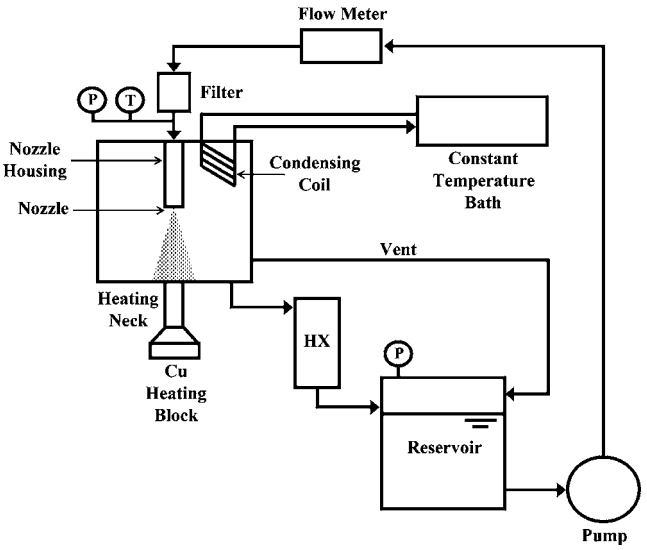

Fig. 1 Schematic diagram of the experimental apparatus

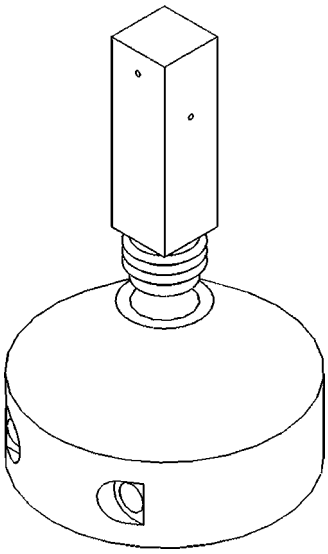

Fig. 2 OFHC copper heating base and a detachable heating neck with four thermocouple holes, each positioned through a different face

on the projected area), an enhancement of 47% compared to the flat surface. They speculated that this enhancement was due to channeling of the liquid into the space between the fins, resulting in much higher CHF. These straight fins were 1 mm in height, width, and spacing, and the projected base was a 2 cm^2 circle. Sodtke and Stephan [19] investigated microstructured surfaces with a full-cone pressure-atomized water spray. They studied micro grooves and pyramids (height=75 μm, width=pitch =150 μm) and a porous surfaces made from aluminum powder, methyl ethyl ketone (MEK), and epoxy. The porous surface failed to improve performance, likely because of the increased conduction resistance of the epoxy binder. The microgrooves and micropyramids improved the heat transfer by up to five times compared to the unstructured surface. The authors speculated that the enhancement was caused by an increase in the three-phase contact line length following the rupture of the liquid film.

The present study was designed to further investigate the mechanisms behind the performance enhancement provided by spray cooling heat sinks with straight fins. The heat sinks used in this study were electric discharge machined (EDM) to have a channel width of 0.36 mm, fin width of 0.50 mm, and lengths of 0.25 mm, 0.50 mm, 1.0 mm, 3.0 mm, and 5.0 mm. The high aspect ratio of these channels provided an increase in surface area of up to 13 times the comparable flat (smooth) surface. With such a large increase in area, the spray can be utilized more effectively. Furthermore, varying only the fin length provided an opportunity to study the relative spray utilization provided by the increased area. The effect of increased fin length is discussed in detail along with its pronounced effect on the spray efficiency.

Experimental Setup

A schematic diagram of the experimental setup and flow loop is shown in Fig. 1.

Spray Chamber. An acrylic and polycarbonate spray chamber was formed by attaching polycarbonate disks to a large diameter acrylic tube. The top plate included feedthroughs for the nozzle and a condensing coil. A brass spray nozzle from Isothermal Systems Research (ISR) was insulated with 5 mm of neoprene to minimize temperature increases due to vapor condensation on the nozzle housing. The copper coil (with 30°C water flowing inside) provided the primary condensation location. The chamber base featured a drain and another opening which allowed the insertion of the test surfaces. Each test surface was surrounded by ceramic insulation (OD=10 cm, 6 mm thick, Cotronics 914 machinable glass ceramic), which was sealed to the chamber base with a neoprene o-ring.

Heat Source and Test Surfaces. Heat was provided by two 250 W cartridge heaters (0.635 cm OD, 3.8 cm long) embedded within an oxygen-free high-conductivity (OFHC) copper heating block (k=391 W/m K). The top of the heating block featured a female threaded hole into which different heating necks could be screwed (see Fig. 2). The necks were surrounded by air, which provided sufficient insulation to effectively create a one-dimensional heat flux along their axes. This was verified by the measurement of a linear temperature gradient along their length. This heat flux and the wall temperature were determined using sheathed thermocouple probes (type K) dryfit into each of four close-fit holes (1.2 mm diam, 7.1 mm deep, 10 mm separation) located in the heating necks. Heat losses from the thermocouple probes were negligible due to large insertion depth and small diameter. Heat losses from the neck in the instrumented region were also negligible, as indicated by the good agreement between the electric power input (after accounting for losses from the base) and the heat flux calculated using one-dimensional conduction through the neck of the heater; see the Uncertainty Analysis section. Six different heaters with 1.41×1.41 cm^2 profiles were used. Square rather than circular profiles were used to better simulate the cooling of an electronic device. One heater featured a simple flat surface for baseline comparisons. Five heaters featured EDM wire machined straight fins with a channel width (C) of 360 μm, fin width (W) of 500 μm, and fins lengths (L) of 0.25 mm, 0.50 mm, 1.0 mm, 3.0 mm, and 5.0 mm (see Table 1). These heat-

Table 1 Channel aspect ratios and surface areas of test surfaces

Fin length (L) (mm)	Channel aspect ratio (L/C)	Total surface area (mm^2)	Area enhancement
0	—	200	1
0.25	0.7	320	1.6
0.5	1.4	440	2.2
1	2.8	681	3.4
3	8.3	1642	8.2
5	13.9	2604	13

ers were then bonded to the ceramic insulation described above using an electronic grade silicone (GE RTV162). Losses from the heater to the insulation were estimated with a commercial finite element code and found to be about 1–2% depending on the experimental data point being modeled. This heat loss was subtracted from the heat flux predicted by Fourier's law in all data presented.

Spray Characteristics. PF-5060 (3M performance fluid composed of perfluoro compounds with primarily six carbons) was chosen as the working fluid because its chemical stability and dielectric nature make it suitable for direct cooling of electronics. Furthermore, its boiling point of 56°C at 1 atm is low enough to allow for two-phase cooling at a temperature that is appropriate for high reliability electronics. Flow was provided by a magnetically coupled gear pump (Cole Palmer 75211-10), and the flow rate through the nozzle was measured with a digital turbine flow meter (Omega FLR1000BR). The working fluid was filtered using a 2 μm borosilicate glass filter. The pressure immediately upstream of the nozzle housing was measured with a Bourdon tube gage (Omega PGS-25L-160). The chamber pressure was maintained at 1 atm through use of a vent on the fluid reservoir. The fluid was not degassed and had a dissolved gas concentration that was estimated using Henry's law for ideal solutions

$$C_{\text{gas}} = H(P_T - P_{\text{sat}}) \tag{1}$$

where H is Henry's constant and the gas concentration C_{gas} was found to be 3420 ppm. Nozzle pressure differences ranged from 1.36 to 4.08 atm (20–60 psig).

The upstream spray temperature was measured with a type T thermocouple inside the nozzle housing body. The temperature directly upstream of the nozzle was 29.6±0.8°C. The temperature of the droplets actually striking the heater was measured with four separate downstream thermocouples (OD=500 μm) that were placed within and around the spray cone. Repeated trials indicated that the addition of the downstream thermocouples had a negligible impact on thermal performance, and therefore, they were included in all data presented in this work. Although the upstream spray temperature, copper cooling coil, and external heat exchanger were all maintained at nominally 30°C, hot spent gas leaving the heated surface resulted in an increase in the downstream temperature. The downstream temperature ranged from 30.6°C (for the bare surface at its lowest heat flux) to 40.8°C (for the 3 mm long fins at its highest spray efficiency). This downstream thermocouple within the spray cone is considered the most accurate measure of the average spray temperature and is used in all calculations below.

A nominally full cone spray nozzle was used. This pressure atomizing nozzle had an orifice diameter of 404±14 μm. The nozzle was fixed 18±1 mm above the heated wall (i.e., the base of the fins for the finned surfaces), which resulted in a spray that appeared to approximately inscribe the square test surface at the smooth-wall elevation. The nominal flow rate through the nozzle ranged from 69 ml/min to 123±1 ml/min; however, the amount of fluid incident on the test surface was less due to some overspray. Since the nozzle height was fixed with respect to the heated wall, the incident flux on the top of the fins increased with fin length due to decreased overspray. The amount of fluid incident on the top of the fins was measured by removing the heaters and replacing them with rapid prototyped collection funnels that were shaped as hollow, truncated, square pyramids. The top lip of the funnel was placed at the same height as the upper surface of the finned heat sinks and featured a 2 cm^2 opening that allowed incident fluid to be collected into a graduated cylinder. The collection system (shown schematically in Fig. 3) was sealed from the ambient and vented to the spray chamber to prevent evaporation. The amount of fluid incident on each of the heat sinks is given in Table 2.

The Sauter mean diameter of the droplets was estimated using

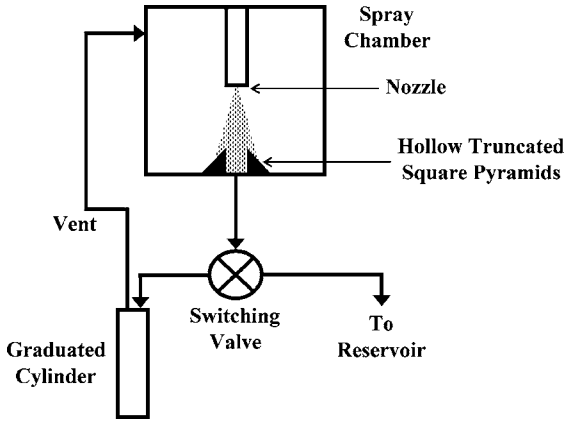

Fig. 3 Schematic of incident flow measurement system

the correlation of Estes and Mudawar [4], which was developed using data from three full cone nozzles spraying FC-72 and water,

$$\frac{d_{32}}{d_0} = 3.07\left(\frac{\rho_v^{1/2}\Delta P d_0^{3/2}}{\sigma^{1/2}\mu_l}\right)^{-0.259} \tag{2}$$

Equation (2) estimates the Sauter mean diameter to vary from 54 μm to 72 μm over the range of pressure used. The droplet breakup velocity can be estimated using the expression given by Ghodbane and Holman [20] based on a control volume energy balance

$$v_{\text{drop}} = \left(v_{\text{upstream}}^2 + \frac{2\Delta P}{\rho_l} - \frac{12\sigma}{\rho_l d_{\text{MMD}}}\right)^{1/2} \tag{3}$$

The large nozzle pressure differences used in this study ensure that the breakup velocity is dominated by the ΔP term. The droplet velocity was estimated to range from 13 to 22 m/s.

Control System and Data Acquisition. Data acquisition and heating control were provided by a custom Visual C++ program implemented through a general programing interface bus (GPIB) on a Pentium III personal computer. An HP6675A DC power supply provided a controllable power source, while a Fluke Hydra data acquisition unit acquired data from the flow and temperature channels every 6 s. Power was initially set at 30 W, and thermocouple temperatures were monitored to determine when steady state occurred. Once the time- and space-averaged temperature in the heater neck changed by <0.1°C over a 60 s period, 60 s of steady-state data were recorded. Power was then incremented and system monitoring resumed. Experiments were concluded when the temperature of the heating block (monitored with two separate thermocouple probes) reached a temperature limit of 260°C, set to ensure safe operation of the test apparatus or when the surface temperature increased rapidly indicating CHF.

Uncertainty Analysis

All standard deviations given below are stated with 95% confidence. The thermocouples and thermocouple reader used to mea-

Table 2 Fluid flow rate incident on top surface of heat sinks

Fin length (mm)	Fraction of total flow rate incident on top surface (±0.02)
0	0.75
0.25	0.76
0.5	0.77
1	0.78
3	0.85
5	0.91

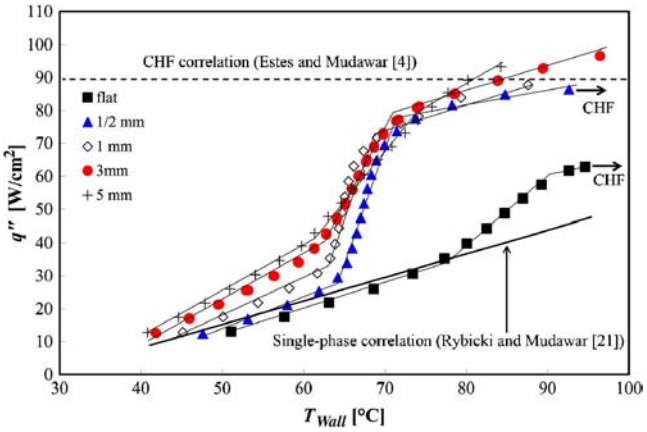

Fig. 4 Spray cooling curves for 1.36 atm (20 psig) nozzle pressure where solid lines indicate single-phase, two-phase, and drying-out regimes. Heat fluxes are based on the 2 cm² projected area.

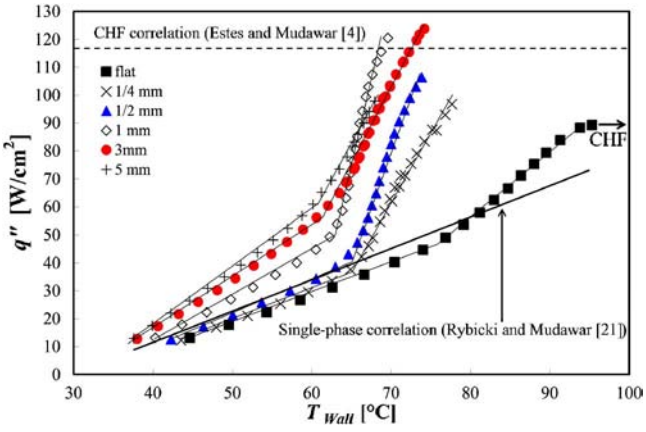

Fig. 6 Spray cooling curves for 4.08 atm (60 psig) nozzle pressure where solid lines indicate single-phase and two-phase regimes. Heat fluxes are based on the 2 cm² projected area.

sure the heat flux, wall temperature, and nozzle temperature were calibrated with mercury-in-glass thermometers to ±0.25°C for $T \leq 100$°C and ±0.5°C for $T > 100$°C. The experimental error was estimated using the square root sum-of-squares method applied to the Fourier conduction law

$$\sigma_{q''} = \sqrt{\left(\frac{\partial q''}{\partial(dT/dx)}\sigma_{dT/dx}\right)^2 + \left(\frac{\partial q''}{dk}\sigma_k\right)^2} \tag{4}$$

In this manner, the largest error in the heat flux was calculated to be 7% at the lower heat fluxes and as little as 5% error for the highest, assuming a 5% error in the thermal conductivity. Heat fluxes calculated assuming one-dimensional conduction were generally ~12% (and never more than 15%) less than the power supplied to the cartridge heaters, depending on ambient conditions and the contact resistance of the threaded heating neck. This is consistent with losses expected due to natural convection from the base.

Results and Discussion

Spray cooling curves for the six test surfaces at three nozzle pressures are shown in Figs. 4–6. A significant performance enhancement over the flat surface is observed for each of the five enhanced surfaces at all nozzle pressures. As expected, increasing the nozzle pressure (and mass flux) resulted in higher heat transfer. Furthermore, there were also distinctly different trends in the single-phase and two-phase regimes (shown by solid lines). In particular, the finned surfaces showed a significant enhancement in the total heat flux once two-phase effects became dominant. Although CHF was observed for the flat surface, CHF was not reached for most of the finned surfaces due to the heating block reaching temperatures greater than the safe temperature limit of the test apparatus. The correlation of Estes and Mudawar [4] for spray cooling CHF is indicated in Figs. 4–6 and shown to consistently overpredict the observed flat-plate CHF magnitude. The uncertainty in their correlation was ±30%, however.

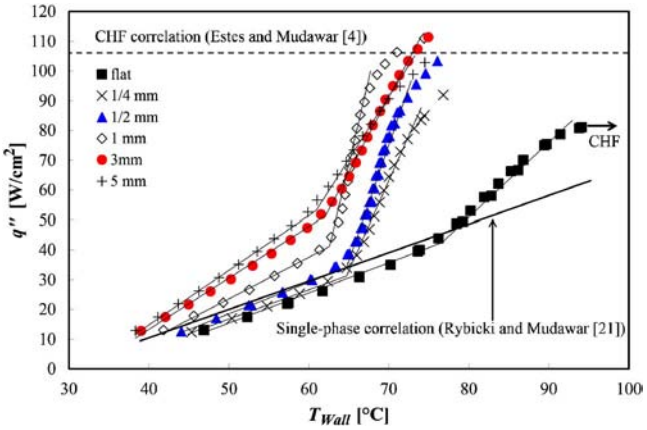

Fig. 5 Spray cooling curves for 2.72 atm (40 psig) nozzle pressure where solid lines indicate single-phase and two-phase regimes. Heat fluxes are based on the 2 cm² projected area.

Single-Phase Results. The single-phase regime is defined as the linear portion of the cooling curve where the wall temperature is not high enough to cause any significant amount of boiling, which would cause the heat transfer coefficient to increase dramatically as it does in nucleate pool boiling. The bare surface performance was typical and a comparison to the single-phase correlation of Rybicki and Mudawar [21] is shown in Figs. 4–6. This correlation was developed from two data sets using PF-5050 and water, and the claimed error in the correlation is 13.1%. The current data are found to lie just outside of this expected error with a mean deviation of −15% with respect to the predicted value. The slight deviation from linearity in the present data that were observed in the "single-phase" regime is due to at least some evaporation from the top of the liquid film. The relatively low temperature of the spray, spray chamber, and coiling coil promote evaporation from the wall even when its temperature is below the saturation temperature (56°C). Although the evaporative effect is significant, as will be discussed below in greater detail, the heat transfer coefficient is nearly constant within this region of the spray cooling curve and drastically different from within the two-phase or boiling regime. In this single-phase regime, longer fins always provided more enhancement than shorter ones.

The effect of nozzle pressure difference on heat transfer over the range of conditions explored is illustrated in Fig. 7. As expected, a larger ΔP resulted in significant improvement in heat transfer, most likely due to the higher mass flow rate, finer droplets, and higher droplet velocity that accompany an increasing ΔP.

The relative performance enhancement as a function of fin length is shown on Fig. 8. While the total surface area increases linearly with fin length, the heat transfer enhancement appears to be asymptotically approaching an optimum value. The dependence of heat transfer enhancement on fin length is rather insensitive to changes in flow rate and well within the experimental uncertainty. The results observed in the single-phase regime were due to a number of competing mechanisms. Adding fin length not only increased the wetted area, but also increased the amount of

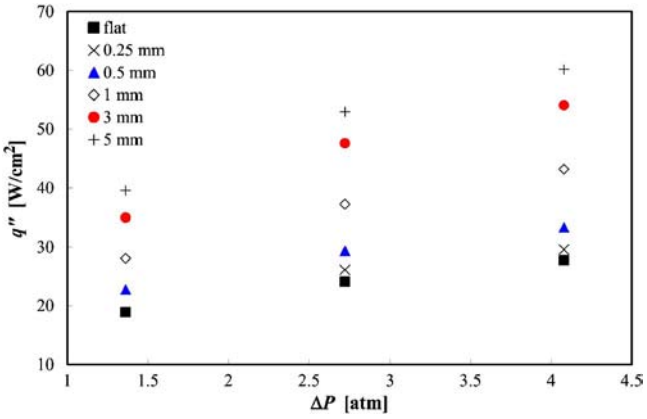

Fig. 7 Heat flux as a function of nozzle pressure difference for $T_{wall}=60°C$ (similar results are obtained at other wall temperatures). Heat fluxes are based on the 2 cm² projected area.

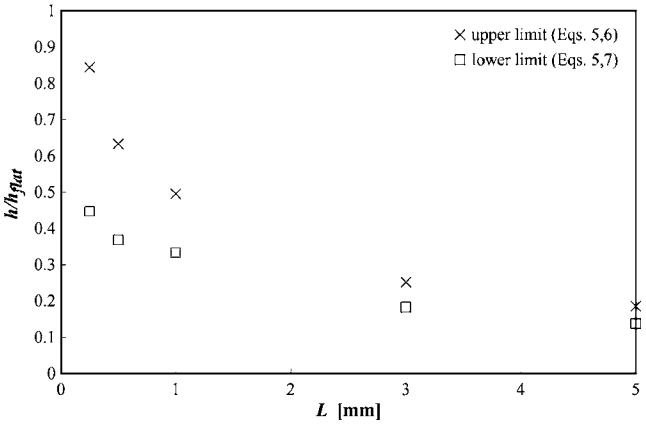

Fig. 9 One-dimensional model results as a function of fin length for $T_{wall}=60°C$, $\Delta P=4.08$ atm (60 psig) normalized by $h_{flat}=9784$ W/m² K

fluid incident on the surface (note Table 2). These two positive effects were offset by the addition of conduction resistance within the fin, less uniform distribution of liquid due to increased channeling, and heating of the fluid as it traveled down the fins (thus lower local ΔT near the bottoms of the fins). While longer fins showed improvement, the addition of conduction resistance should eventually decrease performance by adding a temperature drop between the base of the fins and the top of the fins where the liquid is the coolest.

One-Dimensional Model for the Single-Phase Regime. A simple, one-dimensional fin model is proposed to gain better understanding of the underlying mechanisms. The heat transfer coefficient on a typical fin was determined by solving the convection tip fin equation [22], Eq. (5), using one of two different values for the fin heat transfer

$$q_{\text{sides+tip}} = \sqrt{hPkA_c}\,\theta_w \frac{\sinh(mL) + \frac{h}{mk}\cosh(mL)}{\cosh(mL) + \frac{h}{mk}\sinh(mL)} \tag{5}$$

In the first case, the heat transfer from the bottom of the channels was neglected. The entire heat transfer observed in the experiment was then attributed to the sides and tip of the fin according to Eq. (6), where $n=17$ is the number of fins on the heat sink.

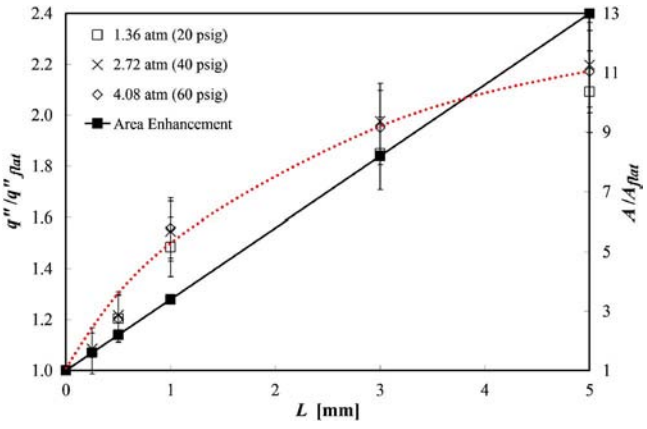

Fig. 8 Area and heat flux enhancement as a function of fin length for $T_{wall}=60°C$ (similar results are obtained at other wall temperatures). Heat fluxes are based on the 2 cm² projected area.

Since heat transfer from the bottom of the channels was neglected, this method yielded an upper limit for the average heat transfer coefficient for the sides and tip

$$\frac{q_{\text{heatsink}}}{n} = q_{\text{sides+tip}} \tag{6}$$

In the second case, the heat transfer from the bottom of the channels was assumed to be unchanged from the flat surface experimental result. Since the model assumes the flat surface was impacted by fresh cold liquid (the liquid is actually preheated by the upstream area), the bottom surface heat transfer is overestimated yielding a lower limit for the heat transfer coefficient on the sides/tip. The average sides/tip heat transfer is then given by Eq. (7), where the 1/2 factor on the last term is required because the bottom surface has a total area of 1 mm², whereas the flat surface has an area of 2 mm²

$$\frac{q_{\text{heatsink}}}{n} = q_{\text{sides+tip}} + \frac{q_{\text{flat}}}{2n} \tag{7}$$

These two cases were used to determine the heat transfer coefficient with Eq. (5), which is then used to predict the temperature profile with Eq. (8) [22]

$$\frac{\theta}{\theta_w} = \frac{\cosh[m(L-x)] + \frac{h}{mk}\sinh[m(L-x)]}{\cosh(mL) + \frac{h}{mk}\sinh(mL)} \tag{8}$$

Note that while Figs. 4–8 show heat fluxes based on the 2 cm² projected area, the heat transfer coefficient discussed here is based on the wetted area. Figure 9 shows the lower- and upper-limit heat transfer coefficients (normalized by the bare surface heat transfer coefficient) calculated using the above method. The heat transfer coefficients are significantly lower than the bare surface heat transfer coefficient, which is expected since the enhancement in heat transfer observed with the channeled surfaces is not as great as the area enhancement (Fig. 8). Furthermore, both the lower and upper limits predict similar heat transfer coefficients for the sides/tip as the fins become long, indicating the decreasing significance of the troughs. In both cases, the temperature profile is qualitatively similar (Fig. 10). The temperature profile predicted by the model shows a modest temperature drop along the length of the fin, suggesting that heat transfer is not limited by the fin temperature. Given the increased area of the channeled surfaces and the modest temperature drop along the fin suggested by this model, it is more likely that heat transfer is limited by an increase in liquid temperature which lowers the local ΔT.

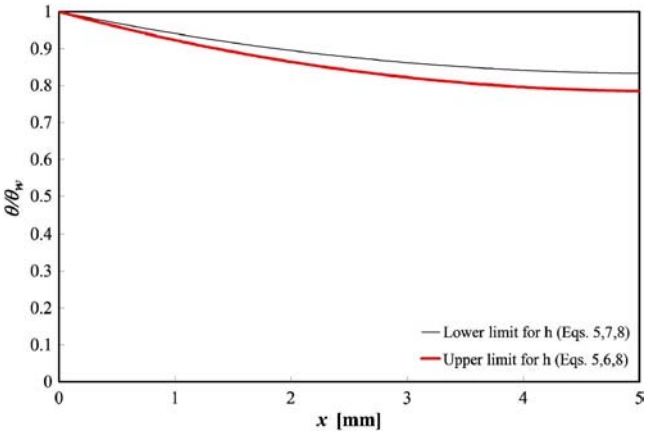

Fig. 10 Predicted temperature profile on 5 mm fins using one-dimensional model for T_{wall}=60°C, ΔP=4.08 atm (60 psig)

Spray Efficiency in the Single-Phase Regime. Calculating the spray efficiency as defined in Eq. (9) yields further support for the notion of an increasing liquid temperature

$$\eta = \frac{q}{\dot{m}[c_{p,l}(T_{\text{wall}} - T_{\text{spray}}) + h_{fg}]} \tag{9}$$

The latent heat term is included in the denominator of Eq. (9) despite its application in the single-phase regime because evaporation occurs when the environment surrounding the heater is at a lower temperature than the heater itself. In fact, during the experiment, condensation was observed on the 30°C copper coiling coil at all reported wall temperatures. Additionally, a spray efficiency calculation that excludes the latent heat term results in efficiencies of >100% for much of the data, indicating the importance of the latent heat term. The spray efficiency as defined in Eq. (9) is shown as a function of fin length in Fig. 11. Lower nozzle pressure resulted in a higher spray efficiency, most likely due to a reduced impact velocity generating an increased residence time of the droplets on the surface. This increased the evaporative heat transfer despite any reduction in the convective heat transfer due to lower droplet velocity. The spray efficiency also shows the same trend at a wall temperature of 50°C as at 60°C, which further supports the notion that boiling had yet to begin, even though the wall temperature had elevated past the saturation temperature of 56°C. Furthermore, the spray efficiency, like the heat transfer enhancement, is seen to asymptotically approach an optimum for a given wall temperature and nozzle pressure difference.

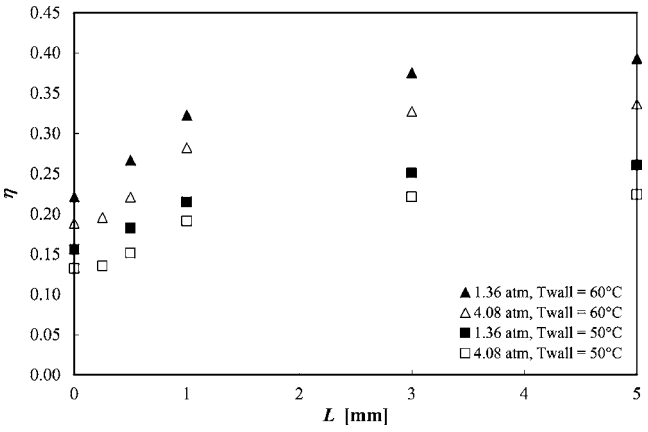

Fig. 11 Spray efficiency as a function of fin length in the single-phase regime

Table 3 Temperatures required for dominant two-phase effects

Fin length (mm)	Approx. temp. at onset of boiling (°C)
0	77
0.25	66
0.5	65
1	63
3	62
5	61

Two-Phase Effects. In many spray cooling studies, heat transfer has been found to be primarily a single-phase phenomenon [8]. Usually, the supply of cold liquid is so high (in order to maximize heat transfer) that there is little time for the heater to increase the local liquid temperature. Liquid is swept away by fresh cold liquid before it can heat up enough to generate a bubble. This suppression of nucleation due to the convective effect of liquid sweeping across a flat surface has also been observed in flow boiling by many researchers [23]. As a result, very high wall temperatures are required to begin significant bubble nucleation. This phenomenon was observed in this study—the flat surface remains essentially single-phase up to almost 20°C above the saturation temperature of 56°C.

The finned surfaces entered the two-phase regimes at temperatures closer to the saturation temperature (note lines in Figs. 4–6 and see Table 3). This may have been due to: (i) an increase in the number of potential nucleation sites due to increased area, (ii) a longer residence time (the liquid must travel down the fin and out of the channel before leaving the hot structure), or (iii) channeling of the liquid by the fins leaving the inner channels with sufficient liquid but the outer channels partially starved. Furthermore, liquid pooling may have occurred on portions of the fin that were shaded from the impinging droplets. These shaded regions would have seen no cool drops and are cooled by preheated liquid that might form thicker pools, allowing nucleation to occur more easily. It is also noteworthy that this sharp transition to the two-phase regime occurred at a temperature that was independent of nozzle pressure difference. This may indicate that geometry rather than residence time was responsible for the earlier onset of boiling with the addition of microchannels.

Another interesting aspect of the two-phase regime was the delayed transition toward CHF observed in the ΔP=1.36 atm (20 psig) tests. The finned surfaces began to show a decrease in their heat transfer coefficients around 71°C even though CHF is not reached until over 90°C, indicating that dryout occurred gradually. This may have been due to channeling of the spray, which allowed the outer channels with less liquid to begin drying out before the fluid-rich center channels.

Greater insight into the significance of the two-phase regime can be gained by considering the spray efficiency. Typically, the spray efficiency is defined as in Eq. (10); however, this makes no allowance for superheating of the liquid or vapor.

$$\eta = \frac{q}{\dot{m}[c_{p,l}(T_{\text{sat}} - T_{\text{spray}}) + h_{fg}]} \tag{10}$$

Our experimental data indicate significant vapor production within the confines of the microchannels, and this vapor may have been heated by dry portions of the channels as it escapes. A more appropriate definition of spray efficiency would include the sensible heat required to increase the vapor temperature from the saturation temperature to the wall temperature as follows:

$$\eta' = \frac{q}{\dot{m}[c_{p,l}(T_{\text{sat}} - T_{\text{spray}}) + c_{p,v}(T_{\text{wall}} - T_{\text{sat}}) + h_{fg}]} \tag{11}$$

The vapor specific heat was estimated using the Yoneda method [24,25] for organic compounds in the ideal gas state. This estimate

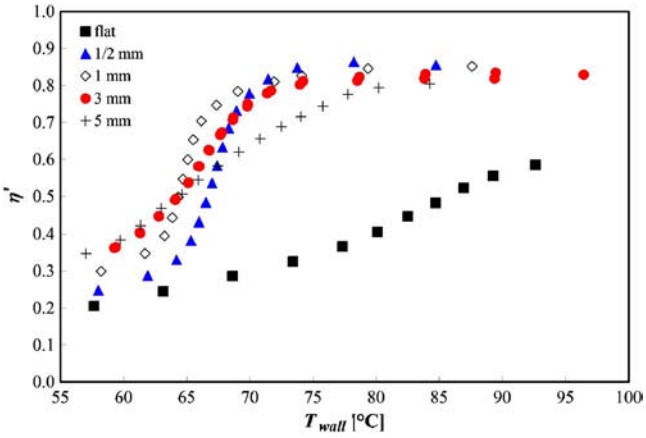

Fig. 12 Spray efficiency as a function of wall temperature for 1.36 atm (20 psig) nozzle pressure difference

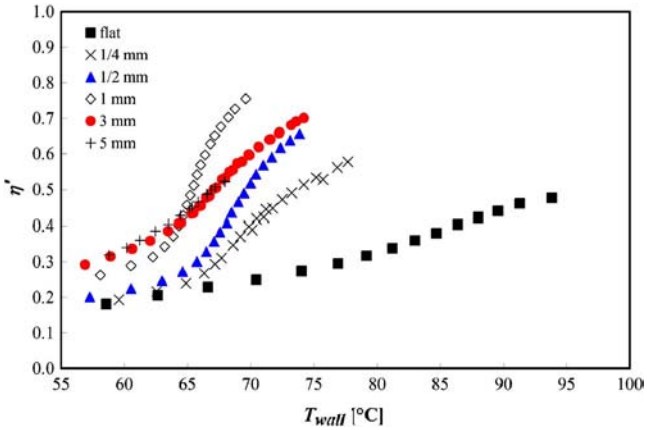

Fig. 14 Spray efficiency as a function of wall temperature for 4.08 atm (60 psig) nozzle pressure difference

is based on the principle of group contribution in which the molecule (e.g., PF-5060 or C_6F_{14}) is decomposed into atom groups, called functional groups. The inclusion of each functional group results in a contribution to the specific heat, which is then estimated by summing all group contributions. Only the effects of nearest-neighbor atoms and geminal effects (the effects of atoms separated by one atom) are included since more complicated molecular interactions are usually insignificant. The method results in an expression of the specific heat as a function of temperature

$$c_{p,v} = 229.38 + 2.4998T - 0.0013041T^2 \quad (12)$$

The Yoneda method estimates a 4% standard deviation for the specific heat estimation of fluorine compounds. Following this procedure for C_5F_{12} and comparing to NIST Standard Reference Database 69 [26] resulted in agreement within 2.1%. Also note that the liquid and vapor specific heats are similar ($c_{p,l}$ = 1102 J/kg K, $c_{p,v}$ = 912 J/kg K at T_{sat}), so the state of the fluid being superheated is of little importance as long as a superheating term is included in the efficiency definition.

The spray efficiencies are shown as a function of temperature in Figs. 12–14. The mass flow rates used are based on the flow incident on the top surface of the finned structure (see Table 2). Although the spray efficiencies of the flat surface are characteristically low, the efficiencies with microchannels appear to approach an asymptote slightly less than the theoretical limit of unity. This trend is particularly evident in the 1.36 atm data, while data at higher temperatures are required at higher nozzle pressure differences. In the single-phase regime, spray efficiencies are low and monotonically increase along with fin length. The onset of boiling corresponds to a large increase in the spray efficiency, and since the onset occurs at different temperatures for different channel heights, the optimum fin length varies with temperature.

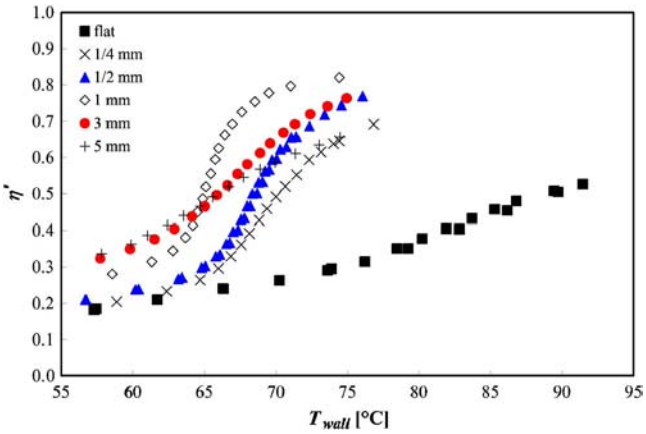

Fig. 13 Spray efficiency as a function of wall temperature for 2.72 atm (40 psig) nozzle pressure difference

These findings indicate some important results. The efficiencies of the finned surfaces for the 1.36 atm pressure difference collapse onto a single curve as CHF is approached, and this single curve indicates almost total evaporation of the incident spray. By channeling the spray and forcing liquid to travel down the fins and through the microchannels, it has sufficient residence time to heat up to the wall temperature in the single-phase regime, or to the saturation temperature and completely evaporate in the two-phase regime. The very high spray efficiencies observed in this study are likely due to the small scale of the microchannels along with the relative sparseness of the spray. It may likely be confirmed that given a greater flow rate, the heat transfer could be improved at the expense of a decreased spray efficiency as shown by Pautsch and Shedd [8] with flat surfaces and Silk et al. [17,18] with enhanced surfaces. However, spraying microchannels with a sparse spray may be one way of improving thermal performance without merely increasing the mass flow rate, which can be expensive in terms of pump power, cost, and weight.

Conclusions

The addition of open microchannels has been shown to be a very effective way of enhancing the thermal performance of a spray cooled system. Performance was evaluated for 1.41 $\times$ 1.41 cm^2 heat sinks featuring a channel width of 360 μm, a fin width of 500 μm, and fin lengths of 0.25 mm, 0.50 mm, 1.0 mm, 3.0 mm, and 5.0 mm. In the single-phase regime, where boiling is nonexistent or negligible, longer fins had the best performance. The relative performance enhancement decreased with increasing fin length indicating that the optimal fin length would be only slightly longer than 5 mm for the single-phase regime. A one-dimensional fin model has been proposed to explain that the apparent decrease in the heat transfer coefficient is likely due to an increase in the local liquid temperature. This rise in the liquid temperature was enough to promote at least some evaporation at wall temperatures below T_{sat}. The addition of fins served to promote the onset of boiling at lower wall temperatures than for the flat surface, leading to improved heat transfer coefficients at lower wall temperatures. As two-phase effects became dominant, the performance of the 5 mm fins decreased relative to the 1 mm fins, which may be due to evaporation of the spray near the fin tips and the addition of a conduction resistance. Finally, the microchannel surfaces approached CHF gradually, as shown in the 1.36 atm

(20 psig) data, since dry out likely first occurred near the perimeter of the heater and moved from areas of low liquid flux to regions with plentiful supply.

Acknowledgment

The authors would like to thank the Office of Naval Research, and specifically Dr. Mark Spector, for their support of this project (Grant No. N000140410315). We would also like to thank Isothermal Systems Research for supplying the spray nozzle, Dr. Hitoshi Sakamoto for his insight and review of this paper, and William Michie for help with test equipment design and drafting.

Nomenclature

A = area (surface unless specified) (m^2)
C = channel width (mm)
C_{gas} = gas concentration
$c_{p,l}$ = specific heat (J/kg K)
d_0 = nozzle orifice diameter (m)
d_{32} = Sauter mean diameter (m)
d_{MMD} = mass median diameter (m)
h = heat transfer coefficient (W/m^2 K)
H = Henry's constant (Pa^{-1})
h_{fg} = latent heat of vaporization (J/kg)
k = thermal conductivity (W/m K)
L = fin length (m)
m = fin constant=$(hP/k\text{-}A_c)^{1/2}$ (m^{-1})
$\dot{m}$ = mass flow rate (kg/s)
n = number of fins on heatsink=17
P = fin perimeter (m)
P_{sat} = saturation pressure (Pa)
P_T = total pressure (Pa)
q = heat transfer (W)
q'' = heat flux (W/cm^2)
T = temperature (K)
T_{sat} = saturation temperature (°C)
T_{spray} = downstream spray temperature (°C)
T_{wall} = wall temperature (°C)
v_{drop} = droplet breakup velocity (m/s)
$v_{upstream}$ = upstream liquid velocity (m/s)
W = fin width (mm)
x = position along fin or between thermocouples (m)
ΔP = nozzle pressure difference (Pa)
ΔT = temperature difference (K)
η = spray efficiency
η' = spray efficiency including vapor sensible heating
θ = $T\text{-}T_{spray}$ (K)
θ_w = $T_{wall}\text{-}T_{spray}$ (K)
μ = dynamic viscosity (N s/m^2)
ρ = density (kg/m^3)
σ = surface tension (N/m), error (various)

Subscripts

c = cross-sectional
dT/dx = temperature gradient
flat = flat surface without microchannels
l = liquid
v = vapor

References

[1] Yang, J. D., Chow, L. C., and Pais, M. R., 1996, "Nucleate Boiling Heat Transfer in Spray Cooling," ASME J. Heat Transfer, **118**, pp. 668–671.
[2] Chow, L. C., Sehmbey, M. S., and Pais, M. R., 1997, "High-Heat-Flux Spray Cooling," Annu. Rev. Heat Transfer, **8**, pp. 291–318.
[3] Estes, K. A., and Mudawar, I., 1995, "Comparison of Two-Phase Electronic Cooling Using Free Jets and Sprays," ASME J. Electron. Packag., **117**, pp. 323–332.
[4] Estes, K. A., and Mudawar, I., 1995, "Correlation of Sauter Mean Diameter and Critical Heat Flux for Spray Cooling of Small Surfaces," Int. J. Heat Mass Transfer, **38**(16), pp. 2985–2996.
[5] Horacek, B., Kim, J., and Kiger, K., 2004, "Spray Cooling Using Multiple Nozzles: Visualization and Wall Heat Transfer Measurements," IEEE Trans. Device Mater. Reliab., **4**(4), pp. 614–625.
[6] Horacek, B., Kiger, K., and Kim, J., 2005, "Single Nozzle Spray Cooling Heat Transfer Mechanisms," Int. J. Heat Mass Transfer, **48**(8), pp. 1425–1438.
[7] Chen, R.-H., Tan, D. S., Lin, K.-C., Chow, L. C., Griffin, A. R., and Rini, D. P., 2005, "Droplet and Bubble Dynamics in Saturated FC-72 Spray Cooling," *Proc. of 2005 ASME International Mechanical Engineering Congress and Exposition*, Orlando, Nov. 5–11, FL, Paper No. IMECE2005-80456.
[8] Pautsch, A. G., and Shedd, T. A., 2005, "Spray Impingement Cooling With Single- and Multiple-Nozzle Arrays. Part I: Heat Transfer Data Using FC-72," Int. J. Heat Mass Transfer, **48**, pp. 3167–3175.
[9] Potash, Jr., M., and Wayner, Jr., P. C., 1972, "Evaporation From a Two-Dimensional Extended Meniscus," Int. J. Heat Mass Transfer, **15**, pp. 1851–1863.
[10] Demiray, F., and Kim, J., 2004, "Microscale Heat Transfer Measurements During Pool Boiling of FC-72: Effect of Subcooling," Int. J. Heat Mass Transfer, **47**, pp. 3257–3268.
[11] Tilton, D. E., Tilton, C. L., Pais, M. R., and Morgan, M. J., 1992, "High-Flux Spray Cooling in a Simulated Multichip Module," Proc. of 1992 ASME Heat Transfer Conference, ASME, New York, HTD-Vol. 206-2, pp. 73–79.
[12] Ortiz, L., and Gonzalez, J. E., 1999, "Experiments on Steady-State High Heat Fluxes Using Spray Cooling," Exp. Heat Transfer, **12**, pp. 215–233.
[13] Kendall, C. M., and Holman, J. P., 1996, "Spray Cooling Heat-Transfer With Subcooled Trichlorotrifluoroethane (Freon-113) for Vertical Constant Heat Flux Surfaces," Proc. of ASME Heat Transfer Division, Vol. 2, HTD-Vol. 333, ASME, New York, pp. 159–179.
[14] Chen, R. C., Chow, L. C., and Navedo, J. E., 2002, "Effects of Spray Characteristics on Critical Heat Flux in Subcooled Water Spray Cooling," Int. J. Heat Mass Transfer, **45**, pp. 4033–4043.
[15] Lin, L., and Ponnappan, R., 2003, "Heat Transfer Characteristics of Spray Cooling in a Closed Loop," Int. J. Heat Mass Transfer, **46**, pp. 3737–3746.
[16] Pais, M. R., Chow, L. C., and Mahefkey, E. T., 1992, "Surface Roughness and Its Effects on the Heat Transfer Mechanism in Spray Cooling," ASME J. Heat Transfer, **114**(1), pp. 211–219.
[17] Silk, E. A., Kim, J., and Kiger, K., 2005, "Spray Cooling Trajectory Angle Impact Upon Heat Flux Using a Straight Finned Enhanced Surface," *Proc. of HT2005: ASME 2005 Heat Transfer Summer Conference*, July 17–22, San Francisco, ASME, New York, ASME Paper No. HT2005-72634.
[18] Silk, E. A., Kim, J., and Kiger, K., 2006, "Spray Cooling of Enhanced Surfaces: Impact of Structure Surface Geometry and Spray Axis Inclination," Int. J. Heat Mass Transfer, **49**, pp. 4910–4920.
[19] Sodtke, C., and Stephan, P., 2005, "Spray Cooling Heat Transfer on Micro Structured Surfaces," *Proc. of 6th World Conference on Experimental Heat Transfer, Fluid Mechanics, and Thermodynamics*, April 17–21, Matsushima, Miyagi, Japan.
[20] Ghodbane, M., and Holman, J. P., 1991, "Experimental Study of Spray Cooling With Freon-113," Int. J. Heat Mass Transfer, **34**, pp. 1163–1174.
[21] Rybicki, J. R., and Mudawar, I., 2006, "Single-Phase and Two-Phase Cooling Characteristics of Upward-Facing and Downward-Facing Sprays," Int. J. Heat Mass Transfer, **49**, pp. 5–16.
[22] Incropera, F. P., and DeWitt, D. P., 2002, *Fundamentals of Heat and Mass Transfer*, 5th ed., Wiley, New York, p. 133.
[23] Chen, J. C., 1966, "Correlation for Boiling Heat Transfer to Saturated Fluids in Convective Flow," Ind. Eng. Chem. Prod. Res. Dev., **5**(3), pp. 322–339.
[24] Yoneda, Y., 1979, "An Estimation of the Thermodynamic Properties of Organic Compounds in the Ideal Gas State. I. Acyclic Compounds and Cyclic Compounds With a Ring of Cyclopentane, Cyclohexane, Benzene, or Naphthalene," Bull. Chem. Soc. Jpn., **52**(5), pp. 1297–1314.
[25] Reid, R. C., Prausnitz, J. M., and Poling, B. E., 1989, *The Properties of Gases & Liquids*, 4th Ed., McGraw-Hill, New York, pp. 157–167.
[26] Lemmon, E. W., McLinden, M. O., and Friend, D. G., 2005, "Thermophysical Properties of Fluid Systems," *NIST Chemistry WebBook*, NIST Standard Reference Database Number 69, Linstrom, P. J., and Mallard, W. G., eds. June, National Institute of Standards and Technology, Gaithersburg MD, http://webbook.nist.gov.

Aspect Ratio Effect on Natural Convection Flow in a Cavity Submitted to a Periodical Temperature Boundary

Nader Ben Cheikh
e-mail: nader_bc@yahoo.fr

Brahim Ben Beya

Taieb Lili

Faculté des Sciences de Tunis,
Département de Physique,
University of El-Manar II,
Tunis 2092, Tunisia

The effect of aspect ratio on natural convection flow in a cavity submitted to periodic temperature boundary, is investigated numerically. The temperature of the heated wall is either maintained constant or varied sinusoidally with time while the temperature of the opposite vertical wall is maintained constant. The results are given for a range of varied parameters as Rayleigh number ($5\times10^3\leqslant \mathrm{Ra}\leqslant 10^6$), *cavity aspect ratio* ($1/6\leqslant A\leqslant 8$), *and period of the sinusoidally heated wall* ($1\leqslant\tau\leqslant 1600$). *The amplitude of oscillation* ($a=0.8$) *and the Prandtl number* ($\mathrm{Pr}=0.71$) *were kept constant. The results obtained in the steady state regime show that the heat transfer averaged over the cold wall is maximum when the aspect ratio is in the range* $1\leqslant A\leqslant 2$. *In the case of a periodic temperature boundary, it is shown that the deviation between the mean heat transfer and the heat transfer of the constant heated case is larger for shallow cavities.*
[DOI: 10.1115/1.2728908]

Keywords: natural convection, heat transfer, sinusoidal heating, aspect ratio

1 Introduction

During these last years, numerous theoretical and experimental studies on natural convection in enclosures have been carried out. From practical and industrial points of view, the interest is justified by its many applications which include heating and cooling of buildings, grain storage, energy drying processes, etc. Representative reviews of these applications and other convective heat transfer applications may be found in the recent books by Bejan and Kraus [1], Ingham and Pop [2], and Vafai [3]. Most of the published works in natural convection in enclosures considers steady-state flows. However, in many applications such as bioengineering, chemical engineering, solar energy collectors, or cooling of electronic equipment, the thermal boundary conditions vary with time. Time-dependent boundary conditions are also present in building heat transfer due to the changing ambient conditions and the intermittent usage of the heating system.

Patterson and Imberg [4] studied the unsteady natural convection in an enclosure whose left and right wall temperatures are suddenly changed by $+\Delta T$ and $-\Delta T$, respectively. The transient behavior of a rectangular enclosure in which the temperature of one side wall is changed suddenly, while the remaining walls are adiabatic, was studied by Nicolette et al. [5] and Hall et al. [6]. In the same topic, Vasseur and Robillard [7] investigated the case of a transient natural convection in a rectangular enclosure with end walls submitted to a continuous decreasing temperature at a constant rate. The works of Schladow et al. [8], who studied the case of an enclosure in which the driving wall temperature is ramped in a linear fashion, revealed that such a changing wall temperature had a negligible effect on the predicted flow and temperature fields.

In 1991, Kazmierczak and Chinoda [9] studied numerically the effect of a periodically changing wall temperature in a square cavity. Their investigation showed that the time-averaged heat transfer across the enclosure is insensitive to the time-dependent boundary condition. Lage and Bejan [10] investigated the case of natural convection in a square enclosure with one side cold and isothermal, and the other side heated with pulsating heat flux. They showed that the buoyancy induced circulation resonates to a certain frequency of the pulsating heat input, a frequency which depends on the Rayleigh and Prandtl numbers.

Recently, a comparative study of a transient natural convection in a square cavity was conducted by Lakhal et al. [11]. They showed that the mean heat transfer is more efficient in the case where the temperature of the hot wall varied with a pulsating manner than sinusoidally. Abourida et al. [12] investigated the case of a square cavity where the temperature of the heated wall varied sinusoidally with time while the temperature of the opposite vertical wall is either maintained constant or varied sinusoidally with time. They concluded that the case of the two temperatures varying in opposition of phase, favors the heat transfer through the cold wall.

More recently, Semma et al. [13] studied numerically the effect of thermal fluctuations on a vertical Bridgman configuration containing a fluid with a low Prandtl number. They showed that the velocity and temperature oscillations are very sensitive to the hot temperature fluctuations for low frequencies. They also identified the existence of a critical frequency for which the heat transfer from the cold wall reached a minimum value. Saeid and Mohamad [14] investigated numerically the free convection from a vertical heated plate in a porous medium and studied the effect of the sinusoidal plate temperature oscillation. They reported that increasing the amplitude and the frequency of the oscillating surface temperature decreased the free convection heat transfer from the plate. Many other interesting papers which also deal with oscillation-induced heat transport and sinusoidal thermal boundaries may be found in Refs. [15–23].

The majority of the studies cited above on transient natural convection submitted to variable thermal boundaries, considered enclosures with a fixed aspect ratio and generally considered the case $A\geqslant 1$. The aim of this paper is to study numerically natural convection in a cavity submitted to a periodic temperature boundary for a wide range of aspect ratios including the case $A<1$ (shallow cavities). The temperature of the heated wall is either

Contributed by the Heat Transfer Division of ASME for publication in the JOURNAL OF HEAT TRANSFER. Manuscript received May 9, 2006; final manuscript received September 30, 2006. Review conducted by Jay M. Khodadadi.

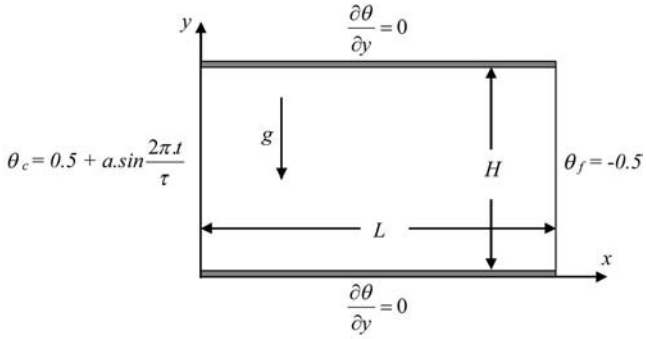

Fig. 1 Schematic diagram of the physical model and coordinate system

maintained constant or varied sinusoidally with time while the temperature of the opposite vertical wall is maintained constant. The study is conducted for different values of the Rayleigh number. The flow patterns, the temperature distributions, and the heat transfer rates are analyzed and discussed.

2 Mathematical Formulation

A schematic representation of the system under investigation is shown in Fig. 1, where W is the width and H the height of the enclosure. The enclosure aspect ratio is $A=H/W$ and takes on the range $1/6 \leqslant A \leqslant 8$. The gravity vector is directed in the negative y coordinate direction, and the Boussinesq approximation is assumed to be valid.

The nondimensional governing equations for the time-dependent thermal convection problem are the incompressible Navier–Stokes equations, conservation of mass, and the energy equation

$$\frac{\partial u_i}{\partial x_i} = 0 \quad (i = 1,2) \tag{1}$$

$$\frac{\partial u_i}{\partial t} + \frac{\partial (u_j u_i)}{\partial x_j} = -\frac{\partial p}{\partial x_i} + \sqrt{\frac{\mathrm{Pr}}{\mathrm{Ra}}}\frac{\partial^2 u_i}{\partial x_j \partial x_j} + \theta\delta_{i2} \quad (i = 1,2) \tag{2}$$

and

$$\frac{\partial \theta}{\partial t} + \frac{\partial (u_i \theta)}{\partial x_i} = \frac{1}{\sqrt{\mathrm{Ra}\,.\,\mathrm{Pr}}}\frac{\partial^2 \theta}{\partial x_i \partial x_i} \quad (i = 1,2) \tag{3}$$

where $u_i=(u,v)$, p, and θ are the velocity, the deviation from the hydrostatic pressure, and temperature, respectively; and $\delta_{i,j}$ the Krönecker symbol. These nondimensional equations where obtained using the characteristic length W, velocity scale $u_0 = \sqrt{g\beta W \Delta T}$, time scale $t_0=W/u_0$, and pressure scale $p_0=\rho u_0^2$. Here, ρ is the mass density, g the gravitational acceleration, and β the coefficient of thermal expansion. The nondimensional temperature is defined in terms of the wall temperature difference and a reference temperature as

$$\theta = \frac{T - T_r}{\overline{T_h} - T_c} \tag{4}$$

where

$$T_r = \frac{\overline{T_h} + T_c}{2} \tag{5}$$

$\overline{T_h}$ is the averaged temperature of the hot wall, and T_c is that of the cold wall. The Rayleigh number and Prandtl number are, respectively

$$\mathrm{Ra} = \frac{g\beta\Delta T W^3}{\nu\alpha} \tag{6}$$

and

$$\mathrm{Pr} = \frac{\nu}{\alpha} \tag{7}$$

where α is the thermal diffusivity; ν the kinematic viscosity; and $\Delta T=\overline{T_h}-T_c$ the temperature difference between the hot and cold walls.

The enclosure boundary conditions consist of no-slip and no-penetration walls, i.e., $u=v=0$ on all four walls. The thermal boundary conditions on the left and right walls are

$$\theta|_{x=0} = \theta_h = 0.5 + a\,\sin\left(\frac{2\pi t}{\tau}\right) \tag{8}$$

$$\theta|_{x=1} = \theta_c = -0.5 \tag{9}$$

where a is the amplitude and τ the period of the thermal excitation. The top and bottom horizontal walls are adiabatic as shown in Fig. 1.

At each instant, the heat flux averaged over the cold wall is defined by

$$\mathrm{Nu}_c = -\frac{1}{A}\int_0^A \left.\frac{\partial\theta(x,y,t)}{\partial x}\right|_{x=1} dy \tag{10}$$

For the established periodical regime, the mean heat transfer through the cold wall is evaluated on one period by the expression

$$\overline{\mathrm{Nu}_c} = \frac{1}{\tau_e}\int_0^{\tau_e} \mathrm{Nu}_c(t)\,dt \tag{11}$$

where τ_e is the period of the excited flow.

Streamlines are adopted here to study the mass transport principle. According to the continuity equation, the corresponding dimensionless streamfunction, ψ, is defined by

$$\frac{\partial\psi}{\partial x} = -v, \quad \frac{\partial\psi}{\partial y} = u \tag{12}$$

with $\psi=0$ on the cavity boundary.

3 Numerical Method

The unsteady Navier–Stokes and energy equations are discretized by a second-order time stepping of finite difference type. The nonlinear terms in Eq. (2) are treated explicitly with a second-order Adams–Bashforth scheme. The convective terms in Eq. (3) are treated semi-implicitly while viscous terms in both Eqs. (2) and (3) are treated implicitly.

A fractional step method (or projection method) [24], is used to solve the Navier–Stokes equations. An intermediate velocity is first computed and later updated for satisfaction of mass continuity. In the intermediate velocity field the old pressure is used. A Poisson equation, with the divergence of the intermediate velocity field as the source term, is then solved to obtain the pressure correction and the real velocity field.

A finite-volume method [25] is used to discretize the Navier–Stokes and energy equations. The advective terms are discretized using a QUICK third-order scheme [26] in Eq. (2) and a second-order central differencing one in Eq. (3).

The discretized momentum and energy equations are resolved using the red and black successive over relaxation method (RB-SOR), while the Poisson pressure correction equation is solved using a multigrid method [27]. The convergence of thenumerical results is established at each time step according to the following criterion

Table 1 Convergence of average Nusselt number with grid refinement

	Grid size		
	32×32	40×40	52×52
$\overline{\mathrm{Nu}_c}$	5.118	5.049	4.998

$$\sqrt{\left(i,j\sum X_{i,j}^{k}-i,j\sum X_{i,j}^{k-1}\right)^2}\leq 10^{-6} \tag{13}$$

where X stands for u, v, p, or θ and k is the iteration level.

In order to ensure grid-independent solutions, a series of trial calculations for the case $A=1$, $a=0.8$, $\tau=10$, and $\mathrm{Ra}=10^5$ were conducted for different uniform grid distributions, i.e., 32×32, 40×40, and 52×52. Table 1 shows the convergence of the time averaged Nusselt number, $\overline{\mathrm{Nu}_c}$, at the cold wall with grid refinement. It is observed that difference between the results of grid 40×40 and that of grid 52×52 is less than 1.02%. Consequently, to optimize appropriate grid refinement with computational efficiency, grid 40×40 was chosen for all computations related to the sinusoidal heating case for $A=1$. For the other aspect ratios, a proportionately larger number of grids are used as shown in Table 2. According to the Rayleigh number and the aspect ratio, the time step was taken in the interval $0.01\leq\Delta t\leq0.04$.

The present numerical model was checked for accuracy against the published numerical solution of Kazmierczak and Chinoda [9] and Abourida et al. [12] for natural convection of water ($\mathrm{Pr}=7$) in a square cavity heated sinusoidally from the vertical wall. A comparison of the time averaged Nusselt number $\overline{\mathrm{Nu}_c}$ is given in Table 3 (Test 1), with the results of Refs. 9 and 12. As seen, our results are in good agreement with those of the literature. It should be noted that the scaling is different in the present investigation, so that appropriate conversions are used for comparison. Our code was also validated (on a relatively fine grid (96×480)) against the benchmark solution of Xin and LeQuéré [28] for the case of a time dependent natural convection in a differentially heated tall enclosure ($A=8$) at $\mathrm{Ra}=3.4\times10^5$. The relative differences in the mean Nusselt number, $\overline{\mathrm{Nu}_c}$, the amplitude of $\overline{\mathrm{Nu}_c}$, $\Delta\overline{\mathrm{Nu}_c}$, and the period of the flow are reported in Table 3 (Test 2) and shows excellent agreement.

Table 2 Grid sizes for the different aspect ratios

A	8	6	4	2
Grid nodes	48×240	40×176	40×120	40×80
A	1	1/2	1/4	1/6
Grid nodes	40×40	80×40	120×40	176×40

Table 3 Comparison of the present results with those of Refs. [9,12,28]

Test 1				
a	τ	Present work	Published work[a]	Published work[b]
0.4	0.01	5.43	5.41	5.48
0.8	0.01	5.61	5.58	5.67
0.4	0.005	5.38	5.36	5.43

Test 2			
	Present work	Published work[c]	Difference (%)
$\overline{\mathrm{Nu}_c}$	4.58179	4.57946	0.05
$\Delta\overline{\mathrm{Nu}_c}$	0.007104	0.007100	0.05
Period	3.41600	3.41150	0.13

[a]See Ref. [9].
[b]See Ref. [12].
[c]See Ref. [28].

4 Results and Discussion

4.1 Constant Heating. As a representative case, streamlines and isotherms at a Rayleigh number of 10^4 and for various aspect ratios are presented in Figs. 2 and 3. For all investigated aspect ratios, the flow structure is dominated by a primary negative cell rotating in a clockwise direction and located in the center of the enclosure. The intensity of these cells increases with aspect ratio but remains relatively weak for $A\leq1/4$. For these aspect ratios and for moderate values of Rayleigh number ($\mathrm{Ra}=10^4$), conduction is the principal mode of heat transfer. Indeed, in the isotherm contours related to $A=1/6$ and $1/4$, equal horizontal thermal gradients may be observed. For bigger values of A, the isotherm plots become more concentrated toward the active walls indicating the presence of big temperature gradients there.

The Nusselt number Nu_c defined in Eq. (10), has been numerically calculated for different values of Rayleigh number, $5\times10^3\leq\mathrm{Ra}\leq10^5$. It should be noted here that the considered Rayleigh numbers are chosen lower than 2×10^5 in order to ensure a steady state for all aspect ratios. It was observed that Nu_c increases with A until reaching a peak, and then decreases again. For $4\times10^4\leq\mathrm{Ra}\leq10^5$, the maximum heat transfer rate is obtained at $A=1$, while for $5\times10^3\leq\mathrm{Ra}\leq3\times10^4$, this maximum is obtained at $A=2$. This phenomenon is in good agreement with the results given by Frederick [29] who reported that the maximum heat transfer was located at values of A between 1 and 2 and occurs at higher values of A when the Rayleigh number decreases.

The numerical results obtained for the average Nusselt numbers Nu_c are expressed through correlations put in the form

$$\mathrm{Nu}_c=0.095\times A^{-0.47}\times(\log_{10}\mathrm{Ra})^{(2.86-0.64\times0.7^A)} \tag{14}$$

for aspect ratios in the range $4\leq A\leq8$ and Rayleigh numbers in the range $5\times10^3\leq\mathrm{Ra}\leq10^5$. For lower values of A, simple monomial correlations were obtained

$$\mathrm{Nu}_c=0.195\times\mathrm{Ra}^{0.27}\quad\text{for } A=2 \text{ and } 5\times10^3\leq\mathrm{Ra}\leq10^5 \tag{15}$$

$$\mathrm{Nu}_c=0.127\times\mathrm{Ra}^{0.31}\quad\text{for } A=1 \text{ and } 5\times10^3\leq\mathrm{Ra}\leq10^5 \tag{16}$$

$$\mathrm{Nu}_c=0.018\times\mathrm{Ra}^{0.46}\quad\text{for } A=1/2 \text{ and } 10^4\leq\mathrm{Ra}\leq10^5 \tag{17}$$

Note that Eq. (14) was obtained by a combination of three equations in a similar form of Eqs. (15)–(17).

4.2 Sinusoidal Heating. In this section, we study the case where the left wall is sinusoidally heated. We remind that the thermal signal imposed on the left wall is defined by

$$\theta_h=0.5+a\sin\left(\frac{2\pi t}{\tau}\right)$$

As a representative case, streamlines and isotherms plots related to $A=1/2$ will be presented on a cycle in order to illustrate the behavior of the flow against the imposed thermal excitation. Numerical solutions are obtained for $\mathrm{Ra}=10^4$ and 10^5 and one fixed amplitude $a=0.8$, for periods included between 1 and 1600, and for aspect ratios in the range $1/6\leq A\leq8$. An additional Rayleigh number of $\mathrm{Ra}=10^6$ is investigated for shallow cavities corresponding to $1/6\leq A\leq1/2$. All results were obtained from an initial steady state related to the corresponding Rayleigh number.

4.2.1 Effect of Period. As a representative case, results related to $A=8$ and $\mathrm{Ra}=10^4$ are presented in this section. Figures 4(a1),

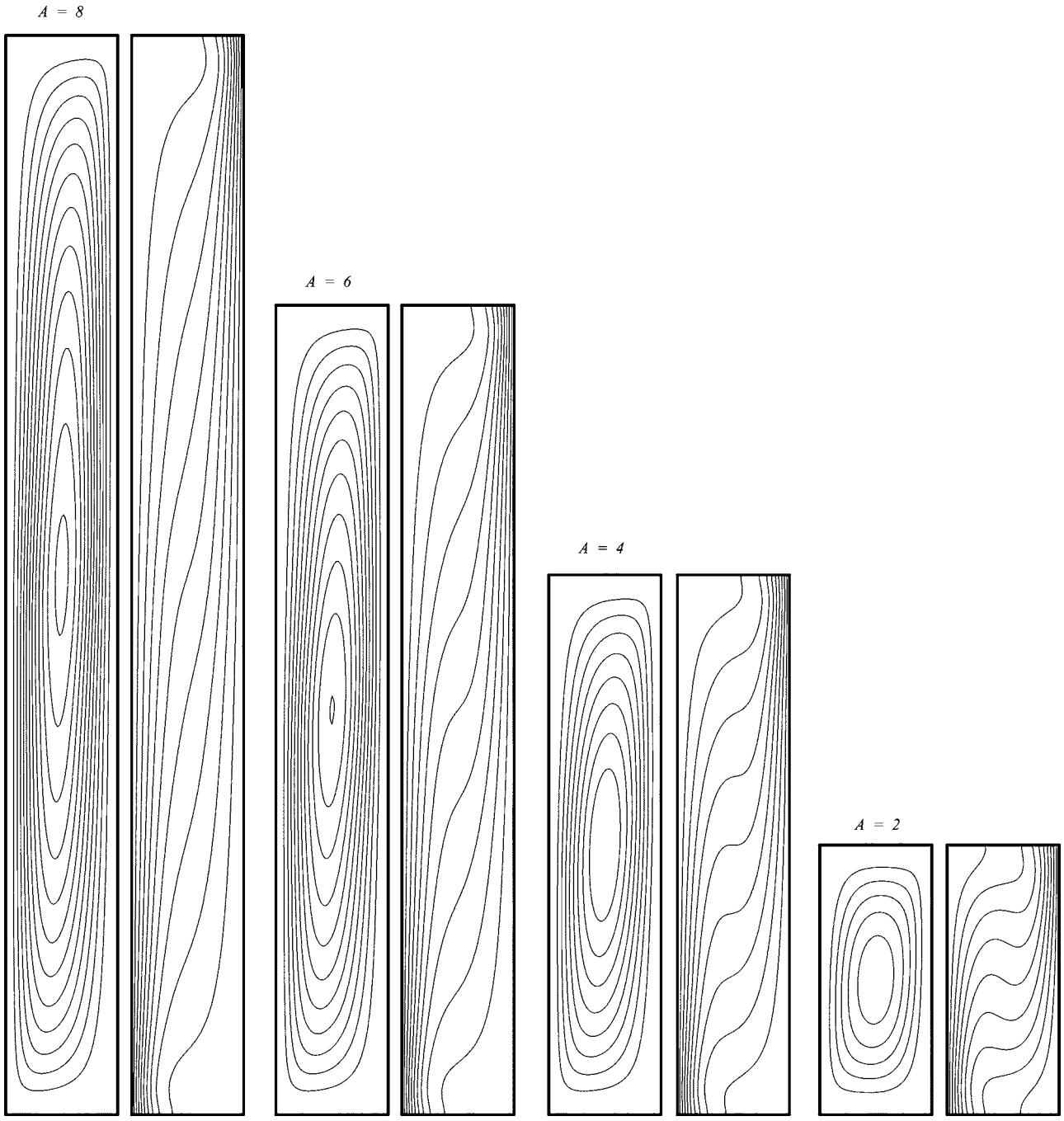

Fig. 2 Streamlines (left) and isotherms (right) for Ra=10^4, for aspect ratios A=8, A=6, A=4, and A=2

4(b1), and 4(c1) show the time evolution of the extreme stream functions ($\psi_{\min}$ and $\psi_{\max}$) and Nu_c as a function of period τ, ($30 \leqslant \tau \leqslant 120$). These figures show that the plotted lines have a periodical response with the same period τ imposed on the hot wall, and confirm the same phenomenon observed by Abourida et al. [12]. The sinusoidally oscillations behavior is preserved in the evolution of Nu_c and $\psi_{\min}$ but not in $\psi_{\max}$ evolution. In fact, the presence of the periodical boundary condition generates the apparition of a secondary positive recirculation cell ($\psi_{\max} \neq 0$) during a part of the cycle. The apparition and disappearance of this cell during a cycle modify meaningfully the global structure of the flow and particularly the extreme stream functions fluctuations.

The amplitude of Nu_c, (Fig. 4(a2)), increases in a monotonous manner for periods included between 7 and 100. Beyond the period τ=100, an asymptotic behavior is observed. Figure 4(b2) shows that the amplitude of $\psi_{\max}$ presents a peak for a period close to 10. This amplitude is relatively weak for periods lower than 5 and greater than 100. Otherwise, the amplitude of $\psi_{\min}$, (Fig. 4(c2)), increases with the period in a considerable manner, reaching a maximum value when τ=24 and then tends toward a limit value.

4.2.2 Flow Structure. We analyze now the flow structure at Ra=10^4 related to a thermal fluctuation of period τ=20 and an aspect ratio A=1/2. Figure 5 shows the streamlines evolution plotted at ten different times over the duration of one cycle. Time increases from Fig. 5(a) to Fig. 5(j) in equal increments (1/10 cycle). It is to be noted that this sequence repeats itself, and

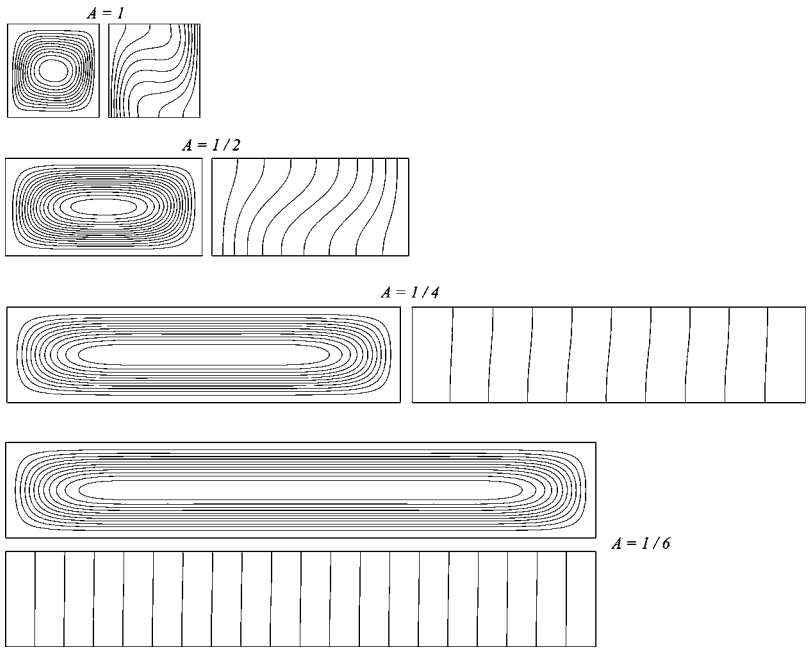

Fig. 3 Streamlines and isotherms for Ra=10^4, for aspect ratios $1/6 \leq A \leq 1$

the very next streamline plots generated following Fig. 5(*j*) are identical to Fig. 5(*a*). The apparition of a secondary recirculation cell rotating in the counter clockwise direction may be observed during a part of the cycle (Figs. 5(*f*)–5(*i*)). The intensity of this cell increases, remaining secondary in comparison to the primary large cell which rotates in a clockwise direction. A similar behavior has been reported by Kazmierczak and Chinoda [9] who studied the transient natural convection in a square cavity submitted to a sinusoidal boundary condition on the hot wall. As explained by these authors, the apparition of the positive cell is attributed to the existence of a portion of fluid, near the hot wall, warmer than the hot wall temperature, which provokes a heat transfer toward the outside of the enclosure via the hot wall. This phenomenon of back heat flow is confirmed by the isotherms plots (Figs. 6(*f*)–6(*i*)). During the remaining part of the cycle (Figs. 5(*j*) and 5(*a*)–5(*c*)), the positive secondary cell disappears and yields its

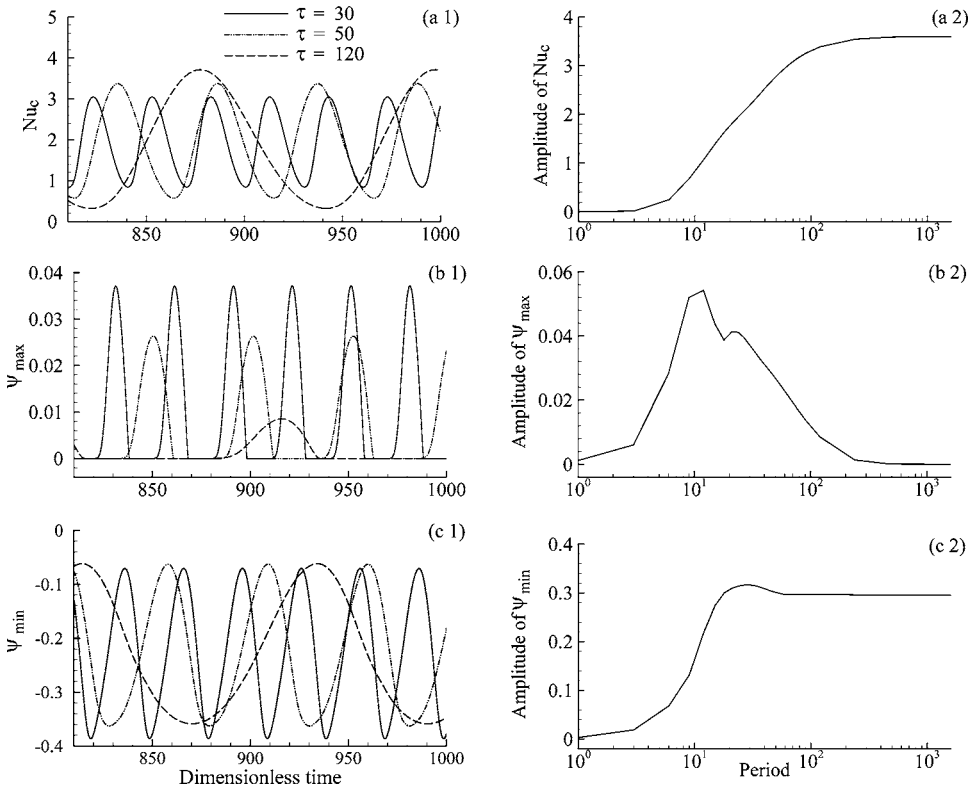

Fig. 4 Evolution and amplitude of Nu_c, ψ_{min}, and ψ_{max} related to aspect ratio $A=8$

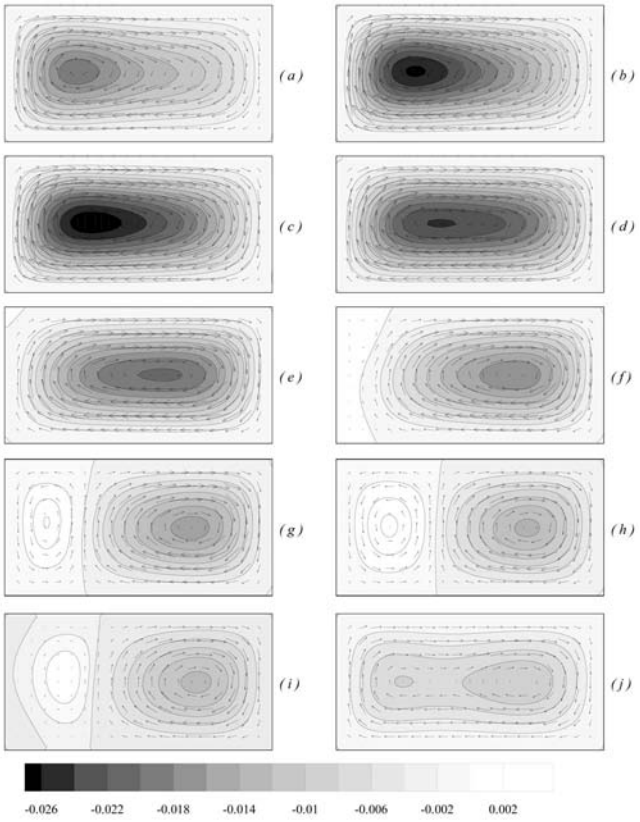

Fig. 5 Streamlines for Ra=10^4, A=1/2, and τ=20 at ten equal increments

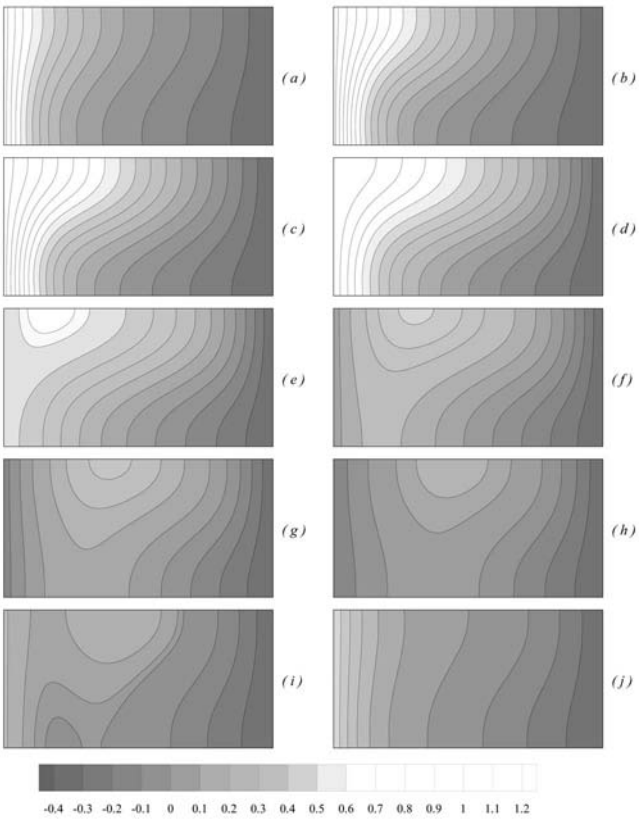

Fig. 6 Isotherms for Ra=10^4, A=1/2, and τ=20 at ten equal increments

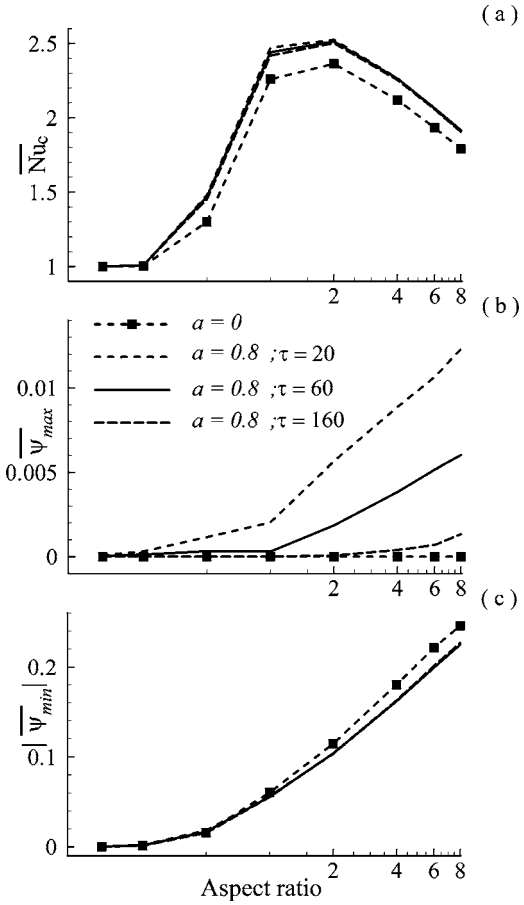

Fig. 7 Time-averaged values: $\overline{Nu_c}$, $\bar{\psi}_{max}$, and $|\bar{\psi}_{min}|$ according to aspect ratio A for $20 \leqslant \tau \leqslant 160$ and Ra=10^4

place to two negative cells that fuse at the end of the cycle. This phenomenon of back heat transfer is also observed at other aspect ratios and for a higher value of Rayleigh number (Ra=10^5).

4.2.3 Time-Averaged Values. The time-averaged quantities $\overline{Nu_c}$, $\bar{\psi}_{max}$, and $|\bar{\psi}_{min}|$ according to the aspect ratio A for different periods $20 \leqslant \tau \leqslant 160$ and a Rayleigh number of Ra=10^4 are presented in Fig. 7. We remark (Fig. 7(*a*)) that the periodical heating case causes an increase of the mean heat transfer in comparison to the constant heating case, and this for the different considered aspect ratios as well as the different considered periods. The maximum deviation from the steady-state regime will be discussed in detail in the next paragraph. Figure 7(*b*) shows variations of $\bar{\psi}_{max}$ according to the aspect ratio and reveals that the intensity of the positive cells increases with the aspect ratio. These intensities are as much smaller as the exciting period τ is greater. In an analogous manner, Fig. 7(*c*) shows that the periodical heating case decreases slightly the negative cell intensities in comparison to the constant heating case for all considered aspect ratios.

Time-averaged values of Nu_c are presented in Figs. 8(*a*)–8(*d*) as a function of period τ for Ra=10^4 and 10^5 for two representative cases of aspect ratios, A=2 and A=1/2. It is observed that the mean heat transfer, $\overline{Nu_c}$, increases with τ until reaching a peak, then decreases tending asymptotically toward a constant value. This peak corresponds to a resonance phenomenon which appears at period, τ_r.

The determination of the critical period τ_r was performed as follows. Large values of period step, $\Delta\tau$, were first used to detect an approximate value of the critical period τ_r, $\tilde{\tau}_r$. Once that value was obtained, a period step of $\Delta\tau$=2 was used around all periods

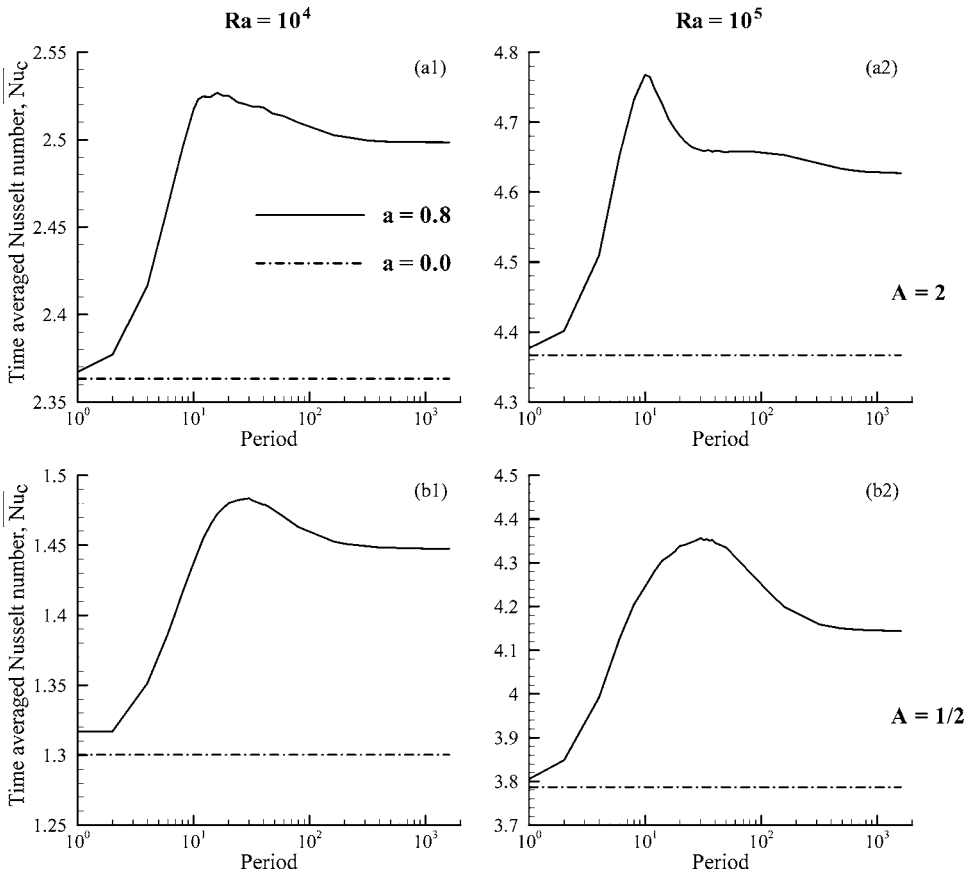

Fig. 8 Time-averaged Nusselt number according to period, τ, for aspect ratios $A=1/2$ and $A=2$ related to $Ra=10^4$ and $Ra=10^5$

close to $\tilde{\tau}_r$. Most of the different values of the period were considered in the range $8 \leqslant \tau \leqslant 80$ (approximately 22 values). For $100 \leqslant \tau \leqslant 1600$, and according to the asymptotic behaviors of $\overline{Nu}_c$ in that range, only 5–7 periods were generally considered.

The value of τ_r strongly depends on the aspect ratio and the Rayleigh number. Indeed, for $A=2$, $\tau_r(Ra=10^4)=16$ and $\tau_r(Ra=10^5)=10$, while for $A=1/2$, $\tau_r(Ra=10^4)=\tau_r(Ra=10^5)=30$. Values of τ_r are reported in Table 4 for all the simulations along with the maximum values of $\overline{Nu}_c$, $\overline{Nu}_{cmax}$, the asymptotic values of $\overline{Nu}_c$, $\overline{Nu}_{c\infty}$, and the maximum percentage increase above the constant heating solution, P_{inc}. Results show that for tall cavities, i.e., $A>1$, the percentage increase is rather weak and does not exceed 10% while for shallow cavities ($A<1$), the percentage increase may reach 20%. For a low Rayleigh number ($Ra=10^4$) and for

Table 4 Resonance period, maximum time averaged Nusselt number, asymptotic time averaged Nusselt number, and percentage increase above the constant heating case for $Ra=10^4$ and $Ra=10^5$

	$Ra=10^4$			$Ra=10^5$		
Aspect ratio, A	τ_r	$\overline{Nu}_{cmax}$ ($\overline{Nu}_{c\infty}$)	P_{inc} (%)	τ_r	$\overline{Nu}_{cmax}$ ($\overline{Nu}_{c\infty}$)	P_{inc} (%)
1/6	—	1.000 (1.000)	0.00	34	1.040 (1.025)	2.66
1/4	16	1.049 (1.006)	4.66	54	1.517 (1.429)	21.07
1/2	30	1.483 (1.447)	14.10	30	4.356 (4.143)	15.05
1	17	2.472 (2.413)	9.38	9	5.066 (4.937)	9.79
2	16	2.527 (2.498)	6.91	10	4.767 (4.627)	9.15
4	30	2.269 (2.250)	7.03	19	4.227 (4.127)	7.97
6	38	2.067 (2.053)	6.97	24	3.897 (3.818)	7.44
8	44	1.918 (1.906)	7.13	28	3.585 (3.560)	6.15

Table 5 Same quantities as in Table 4 for Ra=10^6

	Ra=10^6		
Aspect ratio A	τ_r	$\overline{Nu_{cmax}}$ ($\overline{Nu_{c\infty}}$)	P_{inc} (%)
1/6	82	2.779 (2.510)	41.96
1/4	46	6.934 (6.407)	24.44
1/2	62	9.955 (9.625)	11.15

$A=1/6$, the sinusoidal heating has no effect on heat transfer rate through the cold wall. Indeed, for all the values of τ_r considered in the interval $1 \leqslant \tau_r \leqslant 1600$, $\overline{Nu_c}$ values oscillated around values very close to that of the steady-state case and no particular resonance period could be detected. By increasing the Rayleigh number at 10^5, a difference of 2.66% was observed for $A=1/6$. For cavities of aspect ratio $2 \leqslant A \leqslant 8$ and for both Rayleigh numbers (Ra=10^4 and 10^5), a correlation is detected between τ_r and the aspect ratio A. The resonance period τ_r is expressed as a function of the aspect ratio through the simple correlation equation in the form

$$\tau_r = b \log_{10}(A) + c \tag{18}$$

The dimensionless correlation equations obtained for Ra=10^4 and 10^5 are, respectively

$$\tau_r = 46.50 \times \log_{10}(A) + 2.00 \tag{19}$$

and

$$\tau_r = 29.89 \times \log_{10}(A) + 1.00 \tag{20}$$

For aspect ratios equal to or lower than 1, no obvious correlation between τ_r and A has been detected. However, it is in these ranges of aspect ratios that maximum values of P_{inc} were reached. Indeed, for $A=1/2$ at Ra=10^4, $P_{inc}=14.1\%$ and for $A=1/4$ at Ra=10^5, $P_{inc}=21.07\%$. For aspect ratios $\leqslant 1/2$, P_{inc} may reach some even more higher values. Indeed, for Ra=10^6, the percentage increase above the constant heating case reached 41.96% at $A=1/6$ and was obtained for a resonance period of $\tau_r=82$. Quantities, τ_r, $\overline{Nu_{cmax}}$, $\overline{Nu_{c\infty}}$, and P_{inc} for $1/6 \leqslant A \leqslant 1/2$ at Ra=10^6 are summarized in Table 5.

Hence, the maximum heat transfer enhancement moves to lower aspect ratios as the Rayleigh number increases. This may be explained by the fact that for lower aspect ratios, the maximum size of the secondary positive cell (MaxSPC) becomes flatter, thus dragging more heat closer to the cold wall. By comparison to higher aspect ratios, the MaxSPCs are less flattened against the hot wall and thus less heat is dragged by convection to the cold wall (see Fig. 9). Notice that by increasing the Rayleigh number (Figs. 9(*a*) and 9(*b*)), the intensity of both positive and negative eddies and the MaxSPC also increased, entraining an increase of the mean heat transfer in the enclosure.

Finaly, it is observed (see Table 4 and 5) that values of $\overline{Nu_{c\infty}}$ are very close to that of $\overline{Nu_{cmax}}$ whatever the considered aspect ratio or Rayleigh number. This means that for periods greater than τ_r, the time averaged heat transfer does not change significantly and keeps a value relatively close to that obtained at the critical period, τ_r.

5 Conclusions

Natural convection in a differentially heated enclosure, where the temperature of the heated wall is either constant or varied sinusoidally with time, was investigated and analyzed numerically for a range of Rayleigh number, cavity aspect ratio, and period of the sinusoidally heated wall. The flow and thermal fields and minimum/maximum values of the stream function and the time-averaged Nusselt number have been presented for several representative cases. In the case of constant heating, the heat transfer rate through active walls was maximum for $A=1$ when $4 \times 10^4 \leqslant Ra \leqslant 10^5$ and $A=2$ when $5.10^3 \leqslant Ra \leqslant 3 \times 10^4$. Some correlations between Nusselt number and both aspect ratio and Rayleigh number have been presented and showed good agreement with previous numerical results.

For the case of sinusoidal heating, it was observed that the flow varied with the same period of the hot wall. A secondary cell periodically appeared near the hot wall of the enclosure and the negative cell intensities decreased in comparison to the constant heating case. The secondary cell is situated in the upper left corner

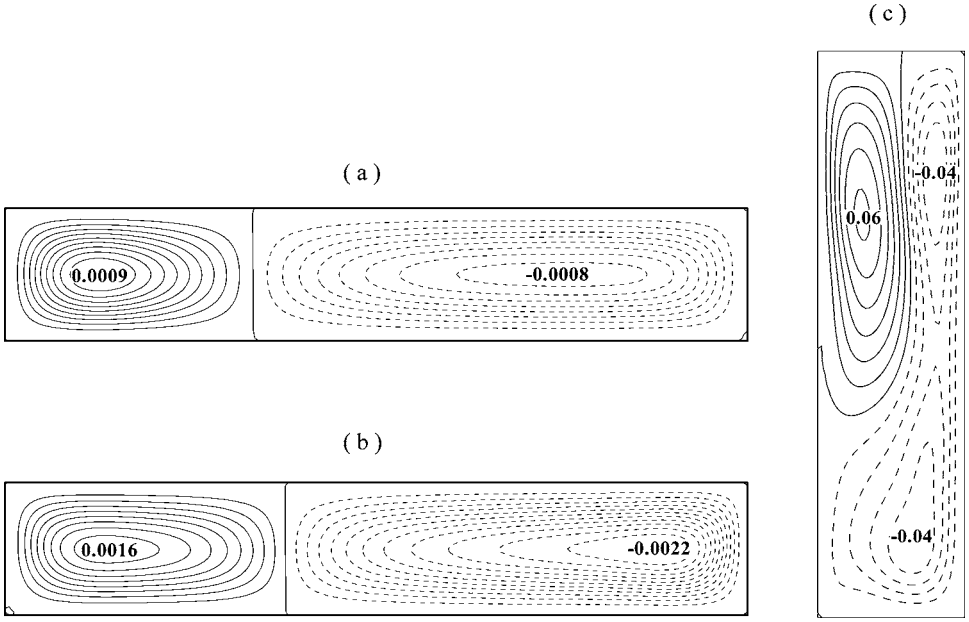

Fig. 9 Maximum secondary positive cell sizes (solid lines) at $\tau=\tau_r$: (a) Ra=10^5 and $A=1/6$; (b) Ra=10^6 and $A=1/6$; and (c) Ra=10^5 and $A=4$

for tall cavities and in the center left side for shallow ones. Its intensity strongly depends on the exciting temperature period and the aspect ratio. As far as the space-averaged Nusselt number is concerned, the amplitude of its oscillation decreased with distance into the enclosure. For low values of period of the hot wall temperature, the amplitude became nearly constant at the cold wall. By increasing the period, the amplitude of the Nusselt number at the cold wall also increased until reaching the same value as the one at the hot wall. For an intermediate value of the period, the time-averaged Nusselt number reached a maximum value corresponding to a resonance period. The increase of the time-averaged heat transfer through the cold wall, in comparison to the constant heating case, was in the range of 10% for cavities of aspect ratio $A \geqslant 1$. For shallow cavities, this percentage was enhanced and reached a value of 40% for $A=1/6$ and for $\mathrm{Ra}=10^6$.

Acknowledgment

The authors thank the three referees who contributed to the improvement of this work. The financial support from the FST is gratefully acknowledged.

Nomenclature

A = cavity aspect ratio, $=H/W$
a = dimensionless amplitude of the hot wall temperature variation
g = gravitational acceleration
H = cavity height
Nu_c = instantaneous Nusselt number
p = nondimensional pressure
Pr = Prandtl number, $=\nu/\alpha$
Ra = Rayleigh number, $=g\beta\Delta TW^3/\nu\alpha$
t = nondimensional time
Δt = nondimensional time step
T = fluid temperature
T_h = temperature of the hot wall
T_c = temperature of the cold wall
ΔT = temperature difference
(u,v) = non-dimensional velocity components along (x,y) axes
W = cavity width
(x,y) = non-dimensional Cartesian coordinates

Greek Letters

α = effective thermal diffusivity
β = coefficient of thermal expansion
δ_{ij} = Krönecker symbol
θ = nondimensional temperature
ν = kinematic viscosity
ρ = fluid density
τ = nondimensional period
τ_r = nondimensional critical period
ψ = nondimensional stream function

Subscripts

c = cold wall
h = hot wall
i,j = nodal location
max = maximum
min = minimum

Superscript

$\overline{}$ = denoting a quantity averaged over time

References

[1] Bejan, A., and Kraus, A. D., eds., 2003, *Heat Transfer Handbook*, Wiley, New York.
[2] Ingham, D. B., and Pop, I., eds., 2002, *Transport Phenomena in Porous Media*, Pergamon, Oxford, UK, Vol. II.
[3] Vafai, K., ed., 2000, *Handbook of Porous Media*, Marcel Dekker, New York.
[4] Patterson, J., and Imberger, J., 1980, "Unsteady Natural Convection in a Rectangular Cavity," J. Fluid Mech., **100**, pp. 65–86.
[5] Nicolette, V. F., Yang, K. T., and Lloyd, J. R., 1985, "Transient Cooling by Natural Convection in a Two-Dimensional Square Enclosure," Int. J. Heat Mass Transfer, **28**, pp. 1721–1732.
[6] Hall, J. D., Bejan, A., and Chaddock, J. B., 1988, "Transient Natural Convection in a Rectangular Enclosure With One Heated Side Wall," Int. J. Heat Fluid Flow, **9**, pp. 396–404.
[7] Vasseur, P., and Robillard, L., 1982, "Natural Convection in a Rectangular Cavity With Wall Temperature Decreasing at a Uniform Rate," Waerme- Stoffuebertrag., **16**, pp. 199–207.
[8] Schladow, S. G., Patterson, J. C., and Street, R. L., 1989, "Transient Flow in a Side-Heated Cavity at High Rayleigh Number: A Numerical Study," J. Fluid Mech., **200**, pp. 121–148.
[9] Kazmierczak, M., and Chinoda, Z., 1992, "Buoyancy-Driven Flow in an Enclosure With Time Periodic Boundary Conditions," Int. J. Heat Mass Transfer, **35**, pp. 1507–1518.
[10] Lage, J. I., and Bejan, A., 1993, "The Resonance of Natural Convection in an Enclosure Heated Periodically From the Side," Int. J. Heat Mass Transfer, **36**, pp. 2027–2038.
[11] Lakhal, E. K., Hasnaoui, M., and Vasseur, P., 1999, "Numerical Study of Transient Natural Convection in a Cavity Heated Periodically With Different Types of Excitations," Int. J. Heat Mass Transfer, **42**, pp. 3927–3941.
[12] Abourida, B., Hasnaoui, M., and Douamna, S., 1998, "Convection Naturelle dans une Cavité Carrée avec des Parois Verticales Soumises à des Températures Périodiques," Rev. Gen. Therm., **37**, pp. 788–800.
[13] Semma, E., Timchenko, V., El Ganaoui, M., and Leonardi, E., 2005, "The Effect of Wall Temperature Fluctuations on the Heat Transfer and Fluid Flow Occurring in a Liquid Enclosure," Int. J. Heat Fluid Flow, **26**, pp. 547–557.
[14] Saeid, N. H., and Mohamad, A. A., 2005, "Periodic Free Convection From a Vertical Plate in a Saturated Porous Medium, Non-Equilibrium Model," Int. J. Heat Mass Transfer, **48**, pp. 3855–3863.
[15] Kuhn, D., and Oosthuizen, P. H., 1987, "Unsteady Natural Convection in a Partially Heated Rectangular Cavity," ASME J. Heat Transfer, **109**, pp. 789–801.
[16] Antohe, B. V., and Lage, J. L., 1996, "Experimental Investigation on Pulsating Horizontal Heating of an Enclosure Filled With Water," ASME J. Heat Transfer, **118**, pp. 889–896.
[17] Kwak, H. S., and Hyun, J. M., 1996, "Natural Convection in an Enclosure Having a Vertical Wall With Time-Varying Temperature," J. Fluid Mech., **329**, pp. 65–88.
[18] Chung, K. H., Kwak, H. S., and Hyun, J. M., 2001, "Finite-Wall Effect on Buoyant Convection in an Enclosure With Pulsating Exterior Surface Temperature," Int. J. Heat Mass Transfer, **44**, pp. 721–732.
[19] Kim, G. B., Hyun, J. M., and Kwak, H. S., 2002, "Enclosed Buoyant Convection With Internal Heat Generation under Oscillating Sidewall Temperature," ASME J. Heat Transfer, **124**, pp. 577–580.
[20] Bae, J. H., and Hyun, J. M., 2004, "Time-Dependent Buoyant Convection in an Enclosure With Discrete Heat Sources," Int. J. Therm. Sci., **43**, pp. 3–11.
[21] Saeid, N. H., 2004, "Periodic Free Convection From Vertical Plate Subjected to Periodic Surface Temperature Oscillation," Int. J. Therm. Sci., **43**, pp. 569–574.
[22] Dalal, A., and Das, M. K., 2006, "Natural Convection in a Cavity With a Wavy Wall Heated From Below and Uniformly Cooled From the Top and Both Sides," ASME J. Heat Transfer, **128**, pp. 717–725.
[23] Zhang, X., Maruyama, S., and Yamaguchi, H., 2005, "Laminar Natural Convection Heat Transfer From a Vertical Baffled Plate Subjected to a Periodic Oscillation," ASME J. Heat Transfer, **127**, pp. 733–739.
[24] Fortin, M., Peyret, R., and Temam, R., 1971, "Résolution Numérique des Équations de Navier–Stokes pour un Fluide Incompressible," J. Mec., **10**(3), pp. 357–390.
[25] Patankar, S. V., 1980, *Numerical Heat Transfer and Fluid Flow*, McGraw–Hill, New York.
[26] Leonard, B. P., 1979 "A Stable and Accurate Convective Modelling Procedure Based on Quadratic Upstream Interpolation," Comput. Methods Appl. Mech. Eng., **19**, pp. 59–98.
[27] Hortmann, M., Peric, M., and Scheuerer, G., 1990, "Finite Volume Multigrid Prediction of Laminar Natural Convection: Bench-mark Solutions," Int. J. Numer. Methods Fluids, **11**, pp. 189–207.
[28] Xin, S., and Le Quéré, P., 2002, "An Extended Chebyshev Pseudo-Spectral Benchmark for the 8:1 Differentially Heated Cavity," Int. J. Numer. Methods Fluids, **40**, pp. 981–998.
[29] Frederick, R. L., 1999, "On the Aspect Ratio for Which the Heat Transfer in Differentially Heated Cavities is Maximum," Int. Commun. Heat Mass Transfer, **26**, pp. 549–558.

Discontinuous Finite Element Approach for Transient Radiative Transfer Equation

L. H. Liu[1]
e-mail: lhliu@hit.edu.cn

L. J. Liu

School of Energy Science and Engineering,
Harbin Institute of Technology,
92 West Dazhi Street,
Harbin 150001, P.R. China

A discontinuous finite element method based on the discrete ordinates equation is extended to solve transient radiative transfer problems in absorbing, emitting, and scattering media. The fully implicit scheme is used to discretize the transient term. Three numerical examples are studied to illustrate the performance of this discontinuous finite element method. The numerical results are compared to the other benchmark approximate solutions. By comparison, the results show that the discontinuous finite element method is efficient, accurate, and stable, and can be used for solving transient radiative transfer problems in participating media. Because the continuity at interelement boundaries is relaxed in discontinuous finite element discretization so that field variable is considered discontinuous across the element boundaries. This feature makes the discontinuous finite element method able to predict the correct propagation speed within medium and accurately capture the sharp drop in the incident radiation and the radiative heat flux at the penetration front. [DOI: 10.1115/1.2737477]

Keywords: transient radiative transfer, semitransparent medium, discontinuous finite element method

1 Introduction

In the past decade, due to the availability of short-pulse lasers, transient radiative transfer (TRT) in participating media has received considerable attention in many emerging applications. The recent developments in microscale systems [1], pulsed laser interaction with materials [2,3], optical tomography [4,5], laser therapy [6], and other applications have indicated that TRT is an important process which requires rigorous study. A detailed review dealing with various aspects of the TRT caused by the irradiation of short-pulse lasers was given by Kumar and Mitra [7].

Recently, many numerical methods for solving TRT have been developed. Brewster and Yamada [8] reported a computational and experimental investigation regarding the feasibility of determining optical properties of turbid media from picosecond time-resolved light-scattering measurements in conjunction with diffusion theory predictions and Monte Carlo (MC) simulations. Guo et al. [9] simulated three-dimensional TRT for short pulse laser transport in scattering and absorbing media by the MC method. The simulation results were compared to the experimental values of 60 ps pulsed laser transmission in scattering media. Good agreement between the MC simulation and experimental measurement was found. In order to reduce the computational time, Lu and Hsu [10] employed the reverse (backward) MC method to solve a one-dimensional TRT problem in participating media. Wu and Wu [11], Wu [12], Wu and Wu [13], Tan and Hsu [14], and Tan et al. [15] used a time-dependent integral equation (IE) formulation to develop a modeling method of TRT. At present, the MC and the IE methods are two of the most accurate solution methods available to date for TRT, and often taken as the benchmark to develop or validate new methods for solving TRT. However, they are found to be computational time and memory intensive, especially for the case of complex geometry.

The discrete ordinates method (DOM) and the finite volume method (FVM), because of their general applicability and their ability to treat complex geometry, are, today, probably two of the most popular methods to solve steady-state radiative transfer in semitransparent medium. Very recently, the DOM and FVM were extended to solve TRT. Chai [16,17] and Chai et al. [18] used the FVM to calculate transient radiative transfer within a semitransparent media. Because of hyperbolic wave characteristics of the TRT equation, the propagation speed of light within medium is predicted with some inaccuracies with the traditional DOM and the FVM. A special high-order upwind difference scheme, for example, piecewise parabolic scheme, or total variation diminishing scheme is needed to handle the discontinuity at the wave front. Following this way, Sakami et al. [19,20] developed a time-dependent DOM with a piecewise parabolic scheme to analyze ultrashort light pulse propagation in a two-dimensional anisotropically scattering medium.

Recently, Cui and Li [21–23] introduced a discontinuous finite element method (DFEM) to solve steady-state radiative heat transfer in semitransparent medium with uniform refractive index. Their numerical results show that the DFEM has good accuracy and excellent numerical behavior. The DFEM was originally introduced by Reed and Hill [24] for the solution of the neutron transport, in which the continuity at interelement boundaries is relaxed so that field variable is considered discontinuous across the element boundaries. This feature makes the DFEM being a local method (no global matrix needs to be assembled) with higher-order accuracy and geometric flexibility [25,26]. Therefore, the DFEM is particularly powerful for convection-dominated problems, in which the solutions develop sharp fronts, and also for hyperbolic type of problems. In this paper, we extend the DFEM to solve transient radiative heat transfer problems in semitransparent medium. Three numerical examples are studied in order to illustrate the performance of the DFEM in solving transient radiative transfer problems.

2 Mathematical Formulation

2.1 Transient Radiative Transfer Equation. Consider transient radiative transfer in an enclosure filled with a semitranspar-

[1]Corresponding author.

Contributed by the Heat Transfer Division of ASME for publication in the JOURNAL OF HEAT TRANSFER. Manuscript received September 3, 2006; final manuscript received January 17, 2007. Review conducted by Walter W. Yuen.

ent media. By the linearization of source term [27], the discrete ordinates equation of transient radiative transfer can be written as

$$\frac{1}{c}\frac{\partial I^m}{\partial t} + \mathbf{s}^m \nabla I^m + \left(\kappa_a + \kappa_s - \frac{\kappa_s}{4\pi}\Phi^{m,m} w^m\right) I^m = \kappa_a I_b + \frac{\kappa_s}{4\pi} \sum_{m'=1, m' \neq m}^{M} I^{m'} \Phi^{m',m} w^{m'} \tag{1}$$

with boundary conditions

$$I_w^m = \varepsilon_w I_{bw} + \frac{1-\varepsilon_w}{\pi} \sum_{\mathbf{n}_w \cdot \mathbf{s}^{m'} > 0} I_w^{m'} |\mathbf{n}_w \cdot \mathbf{s}^{m'}| w^{m'} \tag{2}$$

Here, c is the propagation speed of light in medium, I is the radiative intensity, I_b is the blackbody radiative intensity at the temperature of the medium, κ_a and κ_s are the absorption and the scattering coefficients, respectively, Φ is the scattering phase function, ε_w is the emissivity of boundary, $\mathbf{s}$ is the unit vector of the discrete direction m, and $\mathbf{n}_w$ is the unit outer normal vector of boundary. Using the fully implicit scheme to discretize the transient term, Eq. (1) can be rewritten as

$$\frac{I^m}{c\Delta t} + \mathbf{s}^m \nabla I^m + \beta'^m I^m = S^m + \frac{\tilde{I}^m}{c\Delta t} \tag{3}$$

where

$$\beta'^m = \kappa_a + \kappa_s - \frac{\kappa_s}{4\pi}\Phi^{m,m} w^m \tag{4a}$$

$$S^m = \kappa_a I_b + \frac{\kappa_s}{4\pi} \sum_{m'=1, m' \neq m}^{M} I^{m'} \Phi^{m',m} w^{m'} \tag{4b}$$

Here, $\tilde{I}$ is the radiative intensity value of the last time step calculation and Δt is the time step.

2.2 Discontinuous Finite Element Discretization. Similar to the standard Galerkin finite element method, the computational domain is discretized into a collection of finite elements. By using the shape function, an approximate solution of I^m over an element e can be assumed in the form

$$I^{m,n} = \sum_j I_j^{m,n} \phi_j \tag{5}$$

where I_j^m is the values at the node j and ϕ_j is the shape function. Taking shape function ϕ_i as the weight function, Eq. (1) is weighted over the element e and its integrated residuals are set to zero

$$\frac{1}{c\Delta t}\int_{V_e} \phi I^m dV + \mathbf{s}^m \cdot \int_{V_e} \phi \nabla I^m \mathrm{d}V + \int_{\Gamma_e} \phi [I^m]_{\Gamma_e} (\mathbf{n}_{\Gamma_e} \cdot \mathbf{s}^m) \mathrm{d}\Gamma + \int_{V_e} \phi \beta'^m I^m \mathrm{d}V = \int_{V_e} \phi S^m \mathrm{d}V + \frac{1}{c\Delta t}\int_{V_e} \phi \tilde{I}^m dV \tag{6}$$

where V_e and Γ_e are volume and boundary of element e, respectively. As shown in Fig. 1, the jump of I^m across the element e may be modeled using the upwind scheme as following [23,26]

$$[I^m]_{\Gamma_e^{Bj}} = \begin{cases} I^m_{\Gamma_e^{Bj+}} - I^m_{\Gamma_e^{Bj}}, & \text{if } \mathbf{n}_{\Gamma_e^{Bj}} \cdot \mathbf{s}^m < 0 \\ 0, & \text{if } \mathbf{n}_{\Gamma_e^{Bj}} \cdot \mathbf{s}^m > 0 \end{cases} \tag{7}$$

where Γ_e^{Bj+} and Γ_e^{Bj} denote the element boundaries outside and inside the element e, respectively. Introduction of jump term into Eq. (6) makes that the DFEM can predict the correct propagation speed within medium and easily handle the discontinuity at the wave front.

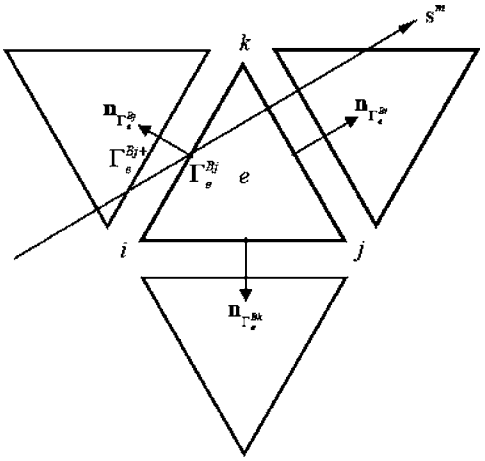

Fig. 1 Element boundary, its unit outward normal vectors, and the neighboring elements

Following the standard procedures for element calculations, we obtain the matrix equation for each element as

$$\mathbf{KI} = \mathbf{F} \tag{8}$$

where the matrices $\mathbf{K}$ and $\mathbf{F}$ are given as follows:

$$K_{ij} = \frac{1}{c\Delta t}\int_{V_e} \phi_i \phi_j dV + \mathbf{s}^{m,n} \cdot \int_{V_e} \phi_i \nabla \phi_j \mathrm{d}V + \int_{V_e} \phi_i \phi_j \beta'^m \mathrm{d}V + \sum_{k=1}^{N_{\Gamma_e}} \max(0, -\mathbf{n}_{\Gamma_e^{Bk}} \cdot \mathbf{s}^m) \int_{\Gamma_e^{Bk}} \phi_i \phi_j \mathrm{d}\Gamma \tag{9a}$$

$$F_i = \int_{V_e} \phi_i \phi_j S_j^m dV + \sum_{k=1}^{N_{\Gamma_e}} \max(0, -\mathbf{n}_{\Gamma_e^{Bk}} \cdot \mathbf{s}^m) \int_{\Gamma_e^{Bk}} \phi_i \phi_j I^m_{\Gamma_e^{Bj+}} \mathrm{d}\Gamma + \frac{1}{c\Delta t}\int_{V_e} \phi_i \phi_i \tilde{I}_j^m dV \tag{9b}$$

Here, N_{Γ_e} is the number of boundaries associated with the element e, and $I^m_{\Gamma_e^{Bj+}}$ is the radiative intensity at the element boundaries outside the element e. The solution of Eq. (8) can be carried out element by element until the entire computational domain and all discretized directions are covered. The global iterations similar to that used in the discrete ordinates method are necessary to include the source term and the boundary conditions. In addition, similar to the finite difference approaches, time step Δt and element size in the DFEM are also subjected to the Courant-Friedrich-Levy (CFL) criteria.

3 Results and Discussion

To verify the accuracy of the DFEM approach for solving transient radiative transfer problems in absorbing, emitting and scattering media, three particular test examples are examined. A computer code based on the preceding formulation was written. Grid-refinement studies are also performed for solutions to ensure that the solutions of the problems are independent of grid size. The maximum relative error, 10^{-5}, of the radiative heat flux and the incident radiation is taken as the stopping criterion of iteration. For the sake of comparison, the integrated mean relative error based on the data in references is defined as

$$\text{Integrated mean relative error} = 100\frac{\left[\int_0^L [\text{data obtained by DFEM-data in references}]^2 dx\right]^{1/2}}{\int_0^L \text{data in references } dx} \tag{10}$$

3.1 One-Dimensional Semitransparent Slab With Diffuse Pulse Radiation. We consider a transient radiative transfer problem in an absorbing, nonemitting, and isotropically scattering medium bounded by two parallel black plates. The plates and the medium are initially at absolute zero (0 K). The thickness of the medium is L. At time $t=0$, the temperature of the left boundary ($x/L=0$) is suddenly raised to provide an emissive power of $\sigma T_{w_0}^4=\pi$ for all subsequent time. The optical thickness $\tau_L=\beta L$ and the scattering albedo ω of medium are 1 and 0.5, respectively.

The DFEM approach is used to solve for the dimensionless incident radiation and radiative heat flux in the medium. The slab is divided uniformly into 200 elements. Direction cosine μ ($-1 \leqslant \mu \leqslant 1$) is divided uniformly into 80 discrete direction. In the case of a one-dimensional linear isoparametric element, Eq. (8) can be given in detail as follows:

$$\begin{aligned}
&\left\{\frac{\Delta x_e}{6c\Delta t}\begin{bmatrix}2,1\\1,2\end{bmatrix}+\frac{\mu^m}{2}\begin{bmatrix}-1,1\\-1,1\end{bmatrix}+\frac{\Delta x_e}{6}\begin{bmatrix}2,1\\1,2\end{bmatrix}\begin{bmatrix}\beta'_{e,1},0\\0,\beta'_{e,2}\end{bmatrix}\right.\\
&\quad\left.+\max(0,\mu^m)\begin{bmatrix}1,0\\0,0\end{bmatrix}+\max(0,-\mu^m)\begin{bmatrix}0,0\\0,1\end{bmatrix}\right\}\begin{bmatrix}I^m_{e,1}\\I^m_{e,2}\end{bmatrix}\\
&=\frac{\Delta x_e}{6c\Delta t}\begin{bmatrix}2,1\\1,2\end{bmatrix}\begin{bmatrix}\tilde{I}^m_{e,1}\\\tilde{I}^m_{e,2}\end{bmatrix}+\left\{\max(0,\mu^m)\begin{bmatrix}1,0\\0,0\end{bmatrix}+\max(0,-\mu^m)\right.\\
&\quad\left.\times\begin{bmatrix}0,0\\0,1\end{bmatrix}\right\}\begin{bmatrix}I^m_{e,1+}\\I^m_{e,2+}\end{bmatrix}+\frac{\Delta x_e}{6}\begin{bmatrix}2,1\\1,2\end{bmatrix}\begin{bmatrix}S^m_{e,1}\\S^m_{e,2}\end{bmatrix}
\end{aligned} \tag{11}$$

The corresponding relationships of node, boundary, and upwind radiative intensity in one-dimensional linear elements are shown in Fig. 2. For all computations in this case, the dimensionless time step is taken as $\Delta t^*=\beta c\Delta t=0.0001$.

The profiles of dimensionless incident radiation and radiative heat flux are shown in Figs. 3 and 4, respectively, and compared to the exact values obtained by Tan and Hsu [14] using the IE method. The DFEM results agree with the data obtained by Tan and Hsu [14] very well. No observable difference could be detected between the results of the DFEM and the IE method. Theoretically the wave front of the pulse radiation will arrive at the dimensionless positions $x/L=0.3$, 0.6, and 0.9 at the dimensionless time $t^*=0.3$, 0.6, and 0.9, respectively, and strike the right boundary at and after the dimensionless time $t^*=1.0$. As shown in Figs. 3 and 4, the DFEM predicted the correct propagation speed within medium. The effects of the dimensionless time step on the solutions of dimensionless incident radiation are shown in Fig. 5. The comparison is quite good, even with a dimensionless time step of $\Delta t^*=0.001$.

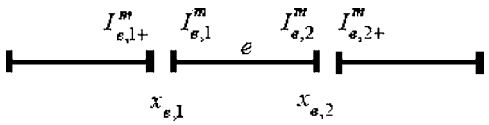

Fig. 2 Relationship of node, boundary, and upwind radiative intensity in one-dimensional linear elements

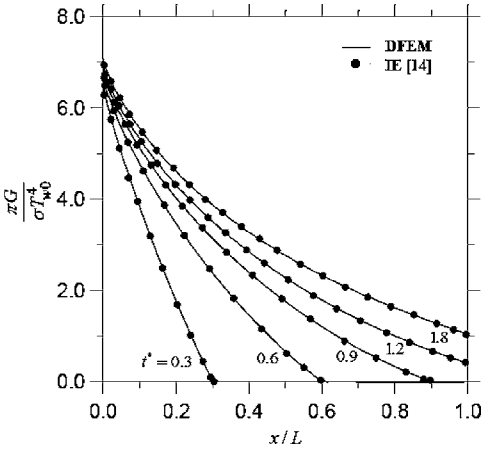

Fig. 3 Dimensionless incident radiation distributions at different dimensionless times

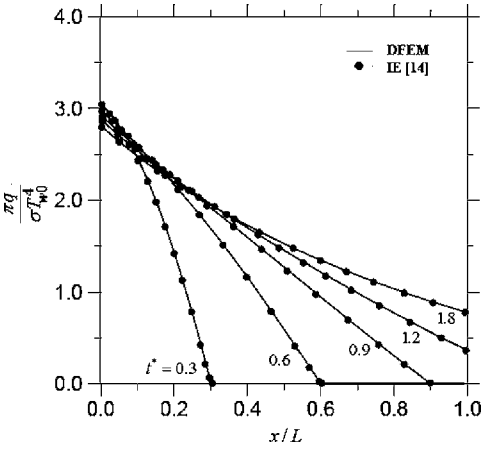

Fig. 4 Dimensionless radiation heat flux distributions at different dimensionless times

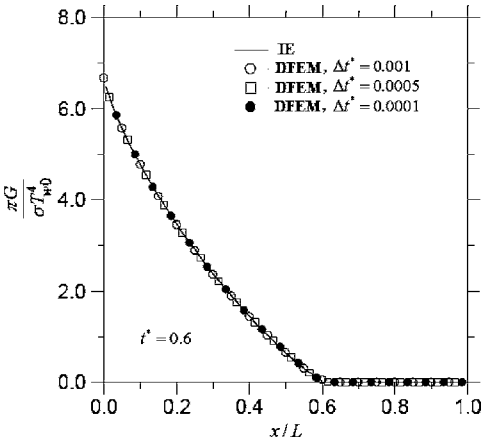

Fig. 5 Effects of dimensionless time step on the solution accuracy for incident radiation

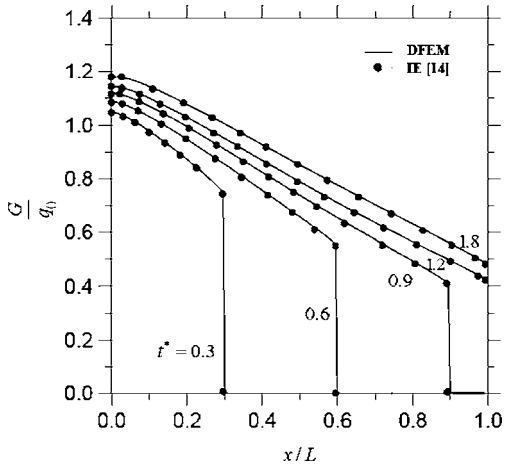

Fig. 6 Dimensionless incident radiation distributions in medium with collimated irradiation at boundary

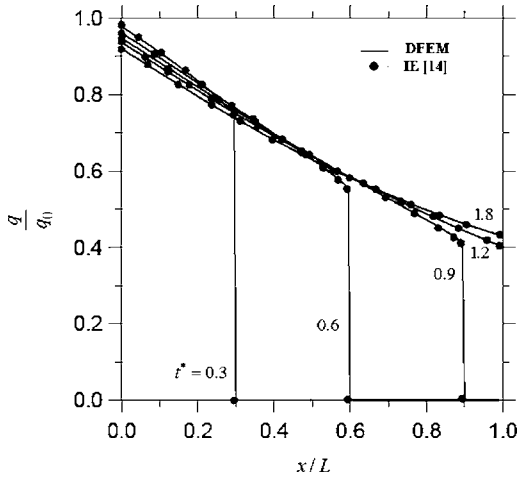

Fig. 7 Dimensionless radiative heat flux distributions in medium with collimated irradiation at boundary

3.2 One-Dimensional Semitransparent Slab With Collimated Pulse Irradiation. In this problem, the walls are nonparticipating and the left ($x/L=0$) wall is subjected to a collimated beam directed perpendicularly to the wall. The other conditions and parameters are identical to those described in previous problem. For the sake of computation, we separate collimated radiation within the medium into two parts, namely, the remnant of the collimated beam after partial extinction and the fairly diffuse part. The collimated remnant of the irradiation obeys Beer's law as

$$q^c(x,t) = q_0 e^{-\beta ct} \tag{12}$$

where q_0 is the total radiative flux of the collimated irradiation directed perpendicularly to the wall. The noncollimated radiation can be obtained by solving Eq. (1) using the DFEM after modifying the source term as

$$S^m = \kappa_a I_b + \frac{\kappa_s}{4\pi} \sum_{m'=1, m' \neq m}^{M} I^{m'} \Phi^{m',m} w^{m'} + q_0 e^{-\beta ct} \Phi(0, \mu^m) \tag{13}$$

The radiative heat flux and the incident radiation can be computed by

$$q(x,t) = q_0 e^{-\beta ct} + \sum_{m=1}^{M} I^m \mu^m w^m \tag{14}$$

$$G(x,t) = q_0 e^{-\beta ct} + \sum_{m=1}^{M} I^m w^m \tag{15}$$

The DFEM approach is used to solve for the dimensionless incident radiation and radiative heat flux in the medium. The profiles of dimensionless incident radiation and radiative heat flux are shown in Figs. 6 and 7, respectively, and compared to the exact values obtained by Tan and Hsu [14] using the IE method. The DFEM results agree with the data obtained by Tan and Hsu [14] very well. As shown in Figs. 6 and 7, the DFEM accurately captures the sharp drop in the dimensionless incident radiation and radiative heat flux at the penetration front.

3.3 Two-Dimensional Absorbing and Emitting Medium in Irregular Quadrilateral Enclosure. As shown in Fig. 8, we consider an irregular quadrilateral enclosure (all dimensions are in meters). The enclosure is filled with an absorbing and emitting medium. The absorption coefficient is taken to be 1 m^{-1}. The medium and black enclosure walls are initially kept at 0 K. At time $t=0$, the medium is suddenly increased to a constant temperature of T_g.

The DFEM approach is used to solve for the transient evolution of radiative heat fluxes on the bottom wall. As shown in Fig. 8, the irregular quadrilateral enclosure is discretized into 800 triangular elements and the equal weight even quadrature S_8 is selected to discretize the angular space. By using linear isoparametric elements, the shape function can be written as [26]

$$\phi_i(x,y) = \frac{1}{2A_e}(a_i + b_i x + c_i y), \quad i = 1,2,3 \tag{16}$$

where A_e is the area of element e. In this case, Eq. (8) can be given in detail as follows:

$$\left[\frac{A_e}{12c\Delta t}\mathbf{B} + \frac{A_e}{3}\mathbf{D} + \frac{A_e}{12}\mathbf{B}\boldsymbol{\beta} + \sum_{k=1}^{3}\frac{L_{Bk}}{6}\max(0, -\mathbf{n}_{\Gamma_e^{Bk}} \cdot \mathbf{s}^m)\mathrm{Cof}B_{(k,k)}\right] \times \begin{bmatrix} I_{e,1}^m \\ I_{e,2}^m \\ I_{e,3}^m \end{bmatrix} = \frac{A_e}{12c\Delta t}\mathbf{B}\begin{bmatrix} \tilde{I}_{e,1}^m \\ \tilde{I}_{e,2}^m \\ \tilde{I}_{e,3}^m \end{bmatrix} + \frac{A_e}{12}\mathbf{B}\begin{bmatrix} S_{e,1}^m \\ S_{e,2}^m \\ S_{e,3}^m \end{bmatrix} + \sum_{k=1}^{3}\frac{L_{Bk}}{6}\max(0, -\mathbf{n}_{\Gamma_e^{Bk}} \cdot \mathbf{s}^m)\mathrm{Cof}B_{(k,k)}\begin{bmatrix} I_{e,1}^m \\ I_{e,2}^m \\ I_{e,3}^m \end{bmatrix}_{\Gamma_e^{Bk+}} \tag{17}$$

where

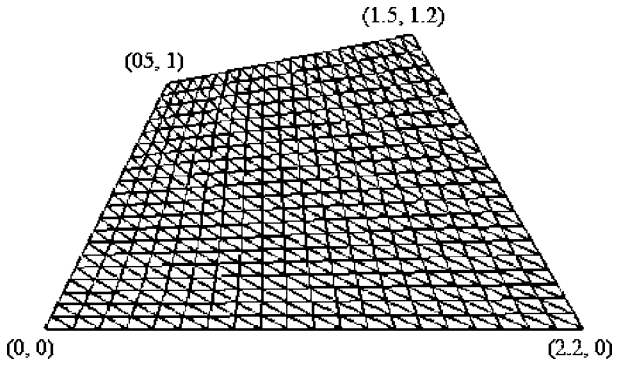

Fig. 8 Schematic and grid system of an irregular quadrilateral enclosure (dimensions in meters)

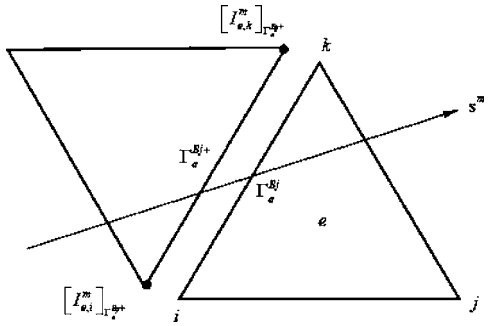

Fig. 9 Relationship of node, boundary, and upwind radiative intensity in triangular elements

$$\mathbf{B} = \begin{bmatrix} 2 & 1 & 1 \\ 1 & 2 & 1 \\ 1 & 1 & 2 \end{bmatrix} \tag{18a}$$

$$\boldsymbol{\beta} = \begin{bmatrix} \beta'_{e,1} & 0 & 0 \\ 0 & \beta'_{e,2} & 0 \\ 0 & 0 & \beta'_{e,3} \end{bmatrix} \tag{18b}$$

$$\mathbf{D} = \begin{bmatrix} \mathbf{s}^m \cdot \nabla\phi_1 & \mathbf{s}^m \cdot \nabla\phi_2 & \mathbf{s}^m \cdot \nabla\phi_3 \\ \mathbf{s}^m \cdot \nabla\phi_1 & \mathbf{s}^m \cdot \nabla\phi_2 & \mathbf{s}^m \cdot \nabla\phi_3 \\ \mathbf{s}^m \cdot \nabla\phi_1 & \mathbf{s}^m \cdot \nabla\phi_2 & \mathbf{s}^m \cdot \nabla\phi_3 \end{bmatrix} \tag{18c}$$

$$\mathbf{s}^m \cdot \nabla\phi_i = (\mu^m \mathbf{i} + \eta^m \mathbf{j}) \cdot \left(\frac{b_i}{2A_e}\mathbf{i} + \frac{c_i}{2A_e}\mathbf{j} \right) = \frac{\mu^m b_i}{2A_e} + \frac{\eta^m c_i}{2A_e} \tag{18d}$$

Here, $\mathrm{Cof}B_{(k,k)}$ means the matrix $\mathbf{B}$ whose kth row and kth column are changed to zero, and L_{Bk} is the length of boundary Γ_e^{Bk} of the element e. The corresponding relationships of node, boundary, and upwind radiative intensity in triangular elements are shown in Fig. 9. Equation (17) is the natural extension of Eq. (11) for one-dimensional cases to two-dimensional problems. For steady-state radiative transfer problems, Cui and Li [22,23] and Li [26] have given very detailed derivation of the DFEM discretization for multidimensional problems. Readers can refer to Refs. [22,23,26].

For all computations in this case, the dimensionless time step is taken as $\Delta t^* = 0.001$. The dimensionless radiative heat fluxes on the bottom wall at four different dimensionless times, namely, 0.025, 0.5, 1.0, and 2.0, are shown in Fig. 10 and compared to the solution obtained by Chai [17] using the FVM. The DFEM results agree with the data obtained by Chai [17] very well. The maximum integrated mean relative error is $<2.0\%$.

4 Conclusion

A discontinuous finite element method based on the discrete ordinates equation is extended to solve transient radiative transfer problems in absorbing, emitting, and scattering media. The fully implicit scheme is used to discretize the transient term. Three numerical examples are studied to illustrate the performance of this discontinuous finite element method. The numerical results are compared to the other benchmark approximate solutions in references. The results show that the discontinuous finite element method is efficient, accurate, and stable, and can be used for solving transient radiative transfer problems in participating media. The discontinuous finite element method can predict the correct propagation speed within medium and accurately capture the sharp drop in the incident radiation and the radiative heat flux at the penetration front.

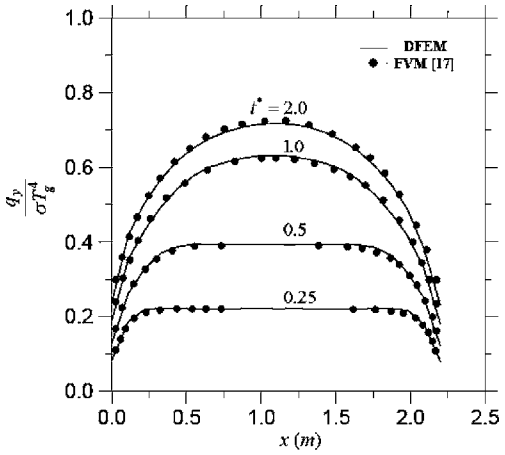

Fig. 10 Transient evolution of dimensionless radiative heat fluxes on the bottom wall

Acknowledgment

The support of this work by the National Natural Science Foundation of China (Grants No. 50425619, No. 50636010, No. 50336010) is gratefully acknowledged.

Nomenclature

A_e = area of element e
$\mathbf{B}$ = matrix defined in Eq. (18a)
c = propagation speed of radiant energy, m/s
$\mathbf{D}$ = matrix defined in Eq. (18c)
$\mathbf{F}$ = matrix defined in Eqs. (8) and (9b)
G = incident radiation, $\mathrm{W/m^3}$
I = radiative intensity, $\mathrm{W/m^2\ sr}$
$\mathbf{I}$ = vector of radiative intensity
I_b = blackbody radiative intensity, $\mathrm{W/m^2\ sr}$
$\tilde{I}$ = radiative intensity value of the last time step calculation, $\mathrm{W/m^2\ sr}$
$\mathbf{K}$ = coefficient matrix defined in Eqs. (8) and (9a)
L = slab thickness, m
L_{Bk} = the length of boundary Γ_e^{Bk} of the element e, m
M = number of discrete ordinates
$\mathbf{n}_w$ = outward unit normal vector of boundary surface
$\mathbf{n}_{\Gamma_e^{Bk}}$ = outward unit normal vector of element boundary
N_{Γ_e} = number of boundaries associated the element e
q = radiative heat flux, $\mathrm{W/m^2}$
q_0 = total radiative flux of the collimated irradiation, $\mathrm{W/m^2}$
$\mathbf{s}$ = unit vector in the discrete ordinate direction
S = source term of radiation defined in Eq. (4b)
t = time, s
Δt = time step, s
t^* = dimensionless time, $t^* = \beta c t$
Δt^* = dimensionless time step, $\Delta t^* = \beta c \Delta t$
T_g = medium temperature, K
T_{w_0} = temperature of plate at $x=0$, K
V_e = volume of element e
w^m = weight corresponding to the direction m
β = extinction coefficient, $\beta = \kappa_a + \kappa_s$, $\mathrm{m^{-1}}$
β' = modified extinction coefficient defined in Eq. (4a), $\mathrm{m^{-1}}$
$\boldsymbol{\beta}$ = matrix defined in Eq. (18b)
ε_w = wall emissivity
κ_a = absorption coefficient, $\mathrm{m^{-1}}$

κ_s = scattering coefficient, m^{-1}
μ, η = direction cosines of discrete ordinates
σ = Stefan-Boltzmann constant, $W/m^2 K^4$
τ_L = optical thickness of slab, $\tau_L = \beta L$
ϕ = shape function
Φ = scattering phase function
ω = single scattering albedo, $= \kappa_s / \beta$

Subscripts

w = value at boundary wall
Γ_e^{Bk-} = value at element boundary inside the element e
Γ_e^{Bk+} = value at element boundary outside the element e

Superscript

m, m' = discrete ordinates direction

References

[1] Tien, C. L., Majumdar, A., and Gerner, F., 1998, *Microscale Energy Transport*, Begell House, New York, Redding, CT, pp. 1–93.
[2] Longtin, J. P., and Tien, C. L., 1996, "Saturable Absorption During High Intensity Laser Heating of Liquids," ASME J. Heat Transfer, **118**(4), pp. 924–930.
[3] Qiu, T. Q., and Tien, C. L., 1992, "Short Pulse Laser Heating in Metals," Int. J. Heat Mass Transfer, **35**(3), pp. 719–726.
[4] Yamada, Y., and Tien, C. L., 1995, "Light-Tissue Interaction and Optical Imaging in Biomediacine," Annu. Rev. Fluid Mech., **6**, pp. 1–59.
[5] Liu, F., Yoo, K. M., and Alfano, R. R., 1993, "Ultrafast Laser-Pulse Transmission and Imaging Through Biological Tissues," Appl. Opt., **32**(4), pp. 554–558.
[6] Grant, M. J. C., and Welch, A. J., 1989, "Clinical Use of Laser-Tissue Interaction," IEEE Eng. Med. Biol. Mag., **8**(4), pp. 10–13.
[7] Kumar, S., and Mitra, K., 1999, "Microscale Aspects of Thermal Radiation and Laser Applications," Adv. Heat Transfer, **33**, pp. 187–294.
[8] Brewster, M. Q., and Yamada, Y., 1995, "Optical Properties of Thick, Turbid Media From Picosecond Time-Resolved Light Scattering Measurements," Int. J. Heat Mass Transfer, **38**(14), pp. 2569–2581.
[9] Guo, Z. X., Aber, J., Garetz, B. A., and Kumar, S., 2002, "Monte Carlo Simulation and Experiments of Pulsed Radiative Transfer," J. Quant. Spectrosc. Radiat. Transf., **73**(2–5), pp. 159–168.
[10] Lu, X. D., and Hsu, P.-F., 2004, "Reverse Monte Carlo Method for Transient Radiative Transfer in Participating Media," ASME J. Heat Transfer, **126**(4), pp. 621–627.
[11] Wu, C. Y., and Wu, S. H., 2000, "Integral Equation Formulation for Transient Radiative Transfer in an Anisotropically Scattering Medium," Int. J. Heat Mass Transfer, **43**(11), pp. 2009–2020.
[12] Wu, C. Y., 2000, "Propagation of Scattered Radiation in a Participating Planar Medium With Pulse Irradiation," J. Quant. Spectrosc. Radiat. Transf., **64**(5), pp. 537–548.
[13] Wu, S. H., and Wu, C. Y., 2001, "Time-Resolved Spatial Distribution of Scattered Radiative Energy in A Two-Dimensional Cylindrical Medium With a Large Mean Free Path for Scattering," Int. J. Heat Mass Transfer, **44**(14), pp. 2611–2619.
[14] Tan, Z. M., and Hsu, P.-F., 2001, "An Integral Formulation of Transient Radiative Transfer," ASME J. Heat Transfer, **123**(3), pp. 466–475.
[15] Tan, Z. M., Hsu, P.-F., and Chai, J. C., 2002, "Transient Radiative Transfer in Three-Dimensional Homogeneous and Non-Homogeneous Participating Media," J. Quant. Spectrosc. Radiat. Transf., **73**(2–5), pp. 181–194.
[16] Chai, J. C., 2003, "One-Dimensional Transient Radiation Heat Transfer Modeling Using a Finite-Volume Method," Numer. Heat Transfer, Part B, **44**(2), pp. 187–208.
[17] Chai, J. C., 2004, "Transient Radiative Transfer Modeling in Irregular Two-Dimensional Geometries," J. Quant. Spectrosc. Radiat. Transf., **84**(3), pp. 281–294.
[18] Chai, J. C., Hsu, P.-F., and Lam, Y. C., 2004, "Three-Dimensional Transient Radiative Transfer Modeling Using the Finite-Volume Method," J. Quant. Spectrosc. Radiat. Transf., **86**(3), pp. 299–313.
[19] Sakami, M., Mitra, K., and Hsu, P.-F., 2000, "Transient Radiative Transfer in Anisotropically Scattering Media Using Monotonicity-Preserving Schemes," ASME Int. Mechanical Engineering Congress & Exposition, Orlando, Nov, ASME HTD-Vol. 366-1, pp. 135–143.
[20] Sakami, M., Mitra, K., and Hsu, P.-F., 2002, "Analysis of Light Pulse Transport Through Two-Dimensional Scattering and Absorbing Media," J. Quant. Spectrosc. Radiat. Transf., **73**(2–5), pp. 169–179.
[21] Cui, X., and Li, B. Q., 2004, "A Discontinuous Finite Element Formulation for Internal Radiation Problems," Numer. Heat Transfer, Part B, **46**(3), pp. 223–242.
[22] Cui, X., and Li, B. Q., 2004, "A Discontinuous Finite Element Formulation for Multidimensional Radiative Transfer in Absorbing, Emitting, and Scattering Media," Numer. Heat Transfer, Part B, **46**(5), pp. 399–428.
[23] Cui, X., and Li, B. Q., 2005, "Discontinuous Finite Element Solution of 2-D Radiative Transfer With and Without Axisymmetry," J. Quant. Spectrosc. Radiat. Transf., **96**(3–4), pp. 383–407.
[24] Reed, W. H., and Hill, T. R., 1973, "Triangular Mesh Methods for the Neutron Transport Equation," Los Alamos Scientific Laboratory Technical Report No. LA-UR-73–479, Los Alamos, NM.
[25] Chen, Z. X., 2005, *Finite Element Methods and Their Applications*, Springer-Verlag, Berlin.
[26] Li, B. Q., 2006, *Discontinuous Finite Elements in Fluid Dynamics and Heat Transfer*, Springer-Verlag, Berlin.
[27] Chai, J. C., Lee, H. S., and Patankar, S. V., 1994, "Improved Treatment of Scattering Using the Discrete Ordinates Method," ASME J. Heat Transfer, **116**(1), pp. 260–263.

Determination of the Sensitivity of Heat Transfer Systems Using Global Sensitivity and Gaussian Processes

A. F. Emery
e-mail: emery@u.washington.edu

D. Bardot

Department of Mechanical Engineering,
University of Washington,
Seattle, WA 98195-2600

A critical aspect of the design of systems or experiments is a sensitivity analysis to determine the effects of the different variables. This is usually done by representing the response by a Taylor series and evaluating the first-order derivatives at a nominal operating point. When there is uncertainty about the operating point, the common approach is the construction of a response surface and Monte Carlo sampling based on the probability distribution of these uncertain variables. Because of the expense of Monte Carlo sampling, it is important to restrict the analysis to those variables to which the response is most sensitive. Identification of the most sensitive parameters can be conveniently done using Global sensitivity, which both defines the most critical variables and also quantifies the effects of interacting variables. This also can be a computationally expensive process and, for complex models, is generally prohibitively expensive. A solution is the use of Gaussian processes that allows one to create a response surface using easy-to-evaluate functions. This paper describes the use of these ideas for a heat transfer problem.
[DOI: 10.1115/1.2737478]

Keywords: sensitivity, global sensitivity, Gaussian processes, parameter estimation, variability, uncertainty

Introduction

The responses, whether measured in real systems or predicted by simulation, are sensitive to the environment, as characterized by boundary conditions, and to intrinsic characteristics, i.e., component behavior or material properties.

We will refer to all of these factors as parameters. Predicting the sensitivity of the responses to these parameters is important. For the designer, a goal is often to minimize the sensitivity so as to reduce the need to accurately characterize the variability. For engineers interested in determining parameters from experiments, the goal is to increase the sensitivity in order to achieve high-precision estimates.

Most sensitivity analyses [1] are based on local estimates of sensitivity, typically by expanding the response in a Taylor series about some specific values of the parameters to give, for example, for two parameters

$$R(X+\delta X)=\left[R(X)+\underbrace{\frac{\partial R}{\partial x_1}\delta x_1+\frac{\partial R}{\partial x_2}\delta x_2}_{1st}+\underbrace{\frac{\partial^2 R}{\partial x_1^2}\frac{\delta x_1^2}{2}+\frac{\partial^2 R}{\partial x_1\partial x_2}\delta x_1\delta x_2+\frac{\partial^2 R}{\partial x_2^2}\frac{\delta x_2^2}{2}}_{2nd}+\cdots\right]\Bigg|_{X^*} \tag{1}$$

where R is the response, x_1 and x_2 are the parameters whose influences are sought, X represents the set (x_1,x_2), and $|X^*$ represents the values of these parameters at which the terms are evaluated.

The local sensitivity is defined as the coefficients of the first-order effects evaluated at X^*, i.e.,

$$S^*_{x_i}\equiv \left.\frac{\partial R}{\partial x_i}\right|_{X^*} \tag{2}$$

Figure 1 depicts the response as a function of the two parameters, x_1 and x_2 at different locations, X^*. We see that at point X^*= (a), the slopes are very small and the system is insensitive to both x_1 and x_2. At point (b), it is sensitive primarily to x_1, whereas at point (c) it is sensitive to both x_1 and x_2. Clearly, different conclusions about the sensitivity of the system would be drawn, depending on the point at which the sensitivity were evaluated.

The problem is that, in general, designers are not always sure of the values of the parameters that will exist during the operation of the system. Although those interested in estimating parameters often have a reasonably good estimate of the parameters, there are conditions in which some parameters, usually associated with boundary conditions, are poorly known or controlled. What one needs is a metric that reasonably describes the effects of imprecision in the set of parameters.

Example Problem

To illustrate an approach to quantifying the effects, let us consider the following problem schematically shown in Fig. 2. It is desired to install a thermal protection system (TPS) to prevent the temperature at the surface of an object from exceeding a specific value. The TPS will be modeled as a thin layer of insulation whose temperature can be computed by assuming one-dimensional conduction. The temperature at a point A, at the interface between the insulation and the object to be protected, is chosen as the quantity of interest. If it exceeds a certain value, then the attachment between the TPS and the object will degrade and the object will be at risk. T(A) will be a function of the

Contributed by the Heat Transfer Division of ASME for publication in the JOURNAL OF HEAT TRANSFER. Manuscript received March 21, 2006; final manuscript received September 26, 2006. Review conducted by Ben Q. Li. Paper presented at the 2005 ASME Heat Transfer Summer Conference (HT2005), San Francisco, CA, July 15–22, 2005.

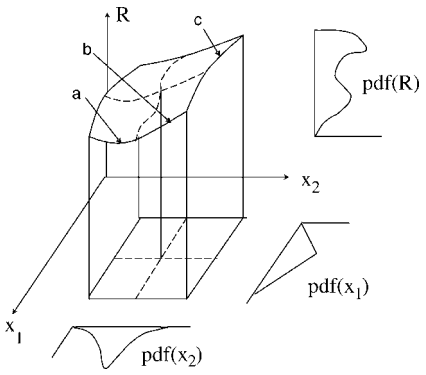

Fig. 1 Representative response surface

thermal conductivity of the TPS, the convective heat transfer coefficient at the exposed surface, and the attachment resistance, all of which contain uncertainty. The attachment resistance will be expressed in terms of an effective Biot number, $\mathrm{Bi}=h_0L/k$, where $h_0=1/R$, L is the thickness of the layer. In solving for the temperature at A, we will nondimensionalize in terms of a temperature in the object of $T=0$, in the environment of $T=1$ and with surface convective coefficient of h_L.

For the designer, the question is "how sensitive is the temperature" to uncertainties in k, h_0 and h_L? For an investigator seeking to estimate the conductivity from a transient experiment, the question is" how will the estimate of k be degraded by the uncertainties in h_0 and h_L?

Both individuals will probably look at the sensitivity in drawing their conclusions. The temperature histories can be characterized in terms of the thermal diffusivity, κ and the Biot moduli $\mathrm{Bi}_0=h_0L/k$ and $\mathrm{Bi}_L=h_LL/k$. The nondimensional sensitivities computed at the nominal values of $\kappa=1$, $\mathrm{Bi}_0=10$, and $\mathrm{Bi}_L=100$ are shown in Fig. 3.

It is important to recall that sensitivities should always be nondimensionalized in terms of the parameters, i.e., the sensitivity to k should be presented as $k_{\mathrm{nom}}\partial T/\partial k$, where k_{nom} is a nominal value of k. Such sensitivities, termed "scaled" sensitivities have the dimensions of temperature and can be directly compared. Of course, there is the complication of choosing a nominal value, but since the sensitivities are being derived from mathematical models (simulations) the most obvious choices are the values used in the simulation.

Although h_L contains uncertainty, the sensitivity of $T(\mathrm{A})$ to h_L is approximately 1/100 of the sensitivity to h_0 and k and we will ignore its effects. We see that $S_k^*>S_{h_0}^*$ at early times, but they become almost equal at steady state. For parameter estimation, the sensitivities of the parameters should be as different as possible. For estimating k and h_0, from Fig. 3 we see that this means that measurements should be taken during the times, $0\leqslant Fo\leqslant 0.4$, during which S_k^* differs from $S_{h_0}^*$. For both designing and parameter estimation, the near equality of the two sensitivities indicates that uncertainty in h_0 will have a strong effect on the final conclusions about the estimated value of k.

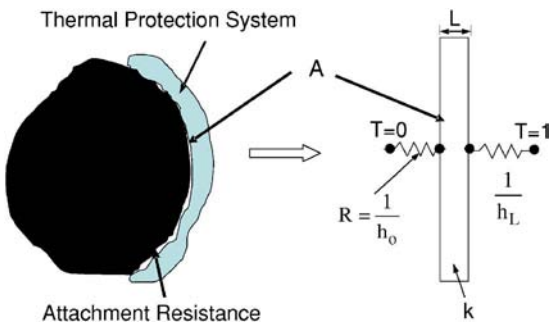

Fig. 2 Schematic of thermal protection of an object

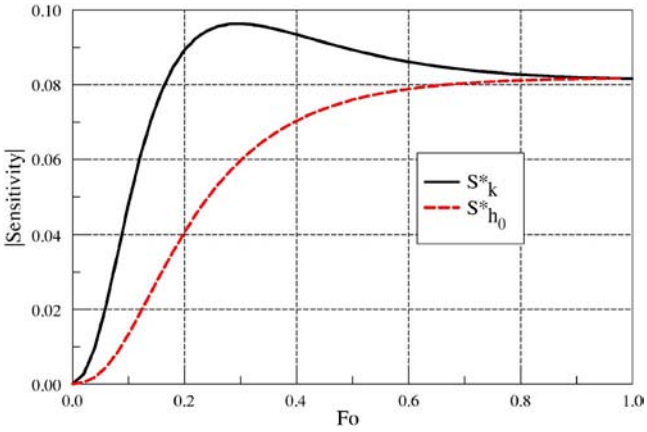

Fig. 3 Time histories of sensitivity S^* to k and to h_0 evaluated at k^{nom} and h_0^{nom}

Because of the uncertainty in k and h_0, we need to examine the sensitivities at several different combinations of these parameters. Let us assume a coefficient of variation of $\sigma[x]/x_{\mathrm{nom}}=0.125$ and a Gaussian distribution for which the range of $\pm 3\sigma[x]$ will encompass more than 99% of the probable values. Figures 4(*a*) and 4(*b*) show how the sensitivity is affected by different parameter values. The range of sensitivities is quite large, but more importantly, it is possible for $S_{h_0}^*$ to exceed S_k^* for certain combinations. When h_0 = minimum and k = maximum, the sensitivity to h_0 is approximately twice the sensitivity to k for h_0 = maximum and k = maximum.

Measures of Sensitivity and Variance

When estimating parameters, experimental design usually focuses on sensitivity. For example, if the conductivity is to be estimated by measuring temperatures at different times, the uncertainty in the estimate can be expressed by

$$\sigma^2[\hat{k}]=\frac{\sigma^2[\epsilon]}{\sum_{t_i}[(\partial T/\partial k|_{t_i})]^2} \tag{3}$$

where $\hat{k}$ is the estimate of k and $\sigma[\epsilon]$ is the standard deviation of the measurement noise. From Eq. (3), it is clear that the greatest precision is obtained when the temperatures are measured at times of maximum sensitivity. When some of the other parameters of the experiment are uncertain, e.g., h_0 or the specific heat c_p, then the situation is more complicated. One approach is to either infer both k and c_p. Unfortunately, doing so often leads to inverse problems with excessive imprecision in both parameters or instabilities in the estimation process when the response is strongly nonlinear in the parameters. The other approach is to use Bayesian inference [2], which leads to joint probability density distributions for both parameters, and then to regard c_p as a nuisance variable and integrate out its effect to obtain a marginal probability distribution for k alone. Regardless of the approach taken, the result will be a degradation in the precision of $\hat{k}$ unless the experimental design has maximized the information [3,4].

On the other hand, the designer is likely to be more interested in minimizing the sensitivity to the uncertain parameters. In fact, the more important metric is likely to be how much the response varies as the uncertain parameters vary. Thus to the designer, the

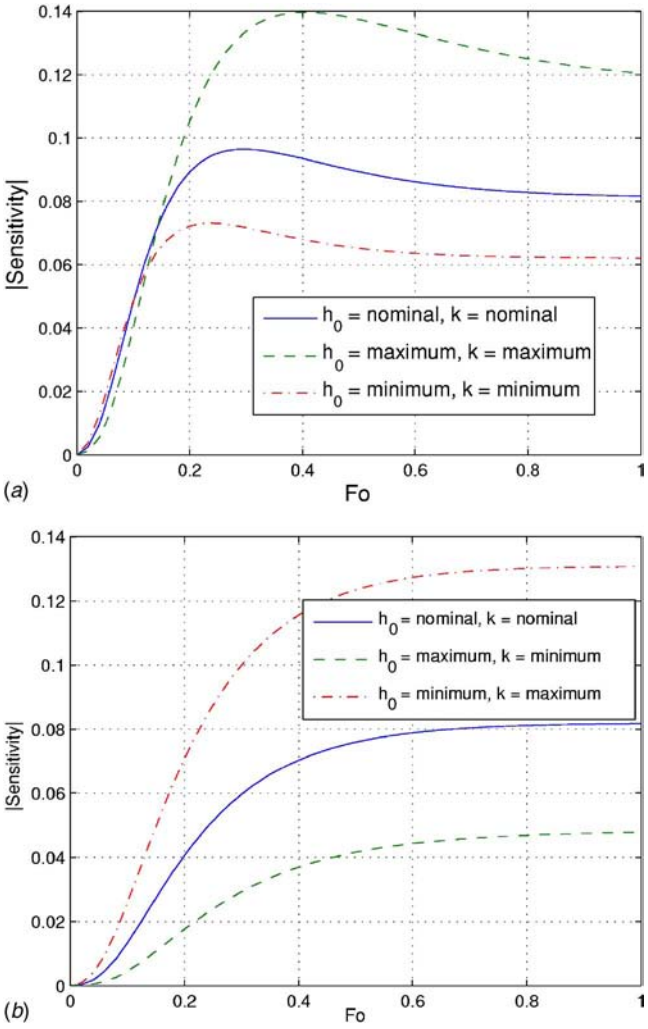

Fig. 4 (*a*) Sensitivity to k (S_k^*) over the range of k and h_0 and (*b*) sensitivity to h_0 ($s_{h_0}^*$) over the range of k and h_0

standard deviation, $\sigma[T]$, or its equivalent the variance, is a better indication of how important the uncertainty of the parameters is.

In reality, it is unusual to be able to specify a local point that characterizes the sensitivity in a general sense. If we have some idea of the probability distributions of the parameters, we can determine a *generalized* sensitivity, defined as the average sensitivity found by integrating the sensitivity over the range of the parameters weighted by the probability of the occurrence of any specific value of the parameter.

$$\bar{S}_i = \int_X S_i(X) f(X) dX \tag{4}$$

where $S_i(X)$ is the sensitivity to parameter x_i over the entire space of the n parameters, $x_1, x_2, \ldots, x_n$, and $f(X)$ is the joint probability density distributions of the parameters. $\bar{S}_i$ is the expected (average) value of the sensitivity.

Creation of the Approximate Response Surface

Let the m uncertain parameters be denoted by x_i, $1 \leq i \leq m$ and the assemblage of parameters be denoted by X. If $R(X)$ is easy to compute, then the differentiations to determine $S_i(X)$ and the integrations to compute $\bar{S}_i(X)$ can be performed analytically or numerically. If $R(X)$ is expensive or difficult to compute, then the common way is to create an approximation to the response surface that is easy to compute. This is usually done by least-squares fitting. For a given probability distribution of the variables, the integrated sensitivity is found either by integrating numerically or by sampling the surface by Monte Carlo techniques.

For more than one or two variables, the expense of computing the response surface (either the exact or its approximation) for the typical nonlinear thermal system model can be daunting and it is important to consider only the most critical parameters and then to construct the most accurate fit. The optimum process is in two steps:

1. Choosing the critical parameters using global sensitivity
2. Defining the response surface using a Gaussian process

Using Global Sensitivity to Define the Critical Parameters. Global sensitivity analysis is an outgrowth of Sobol's [5] approach to representing a function by an additive model. *Additive* models of system responses are composed of the sum of functions, each of which is a function of only one variable,

Additive model:

$$R(x_1, x_2, \ldots, x_m) = g_0 + g_1(x_1) + g_2(x_2) + \cdots + g_m(x_m) \tag{5}$$

where the constituent functions, $g_i(x_i)$, may be nonlinear functions of the single parameter, x_i. Additive models have several very desirable characteristics, among the most important are

a. the behavior of the model with respect to any single parameter, x_j, can be determined without specifying any of the other parameters
b. the maximum/minimum response is simply the sum of the maximum/minimum values of each of the constituent functions
c. the sensitivities and the confidence intervals of estimated parameters are easily determined
d. error analyses are simple to conduct

Unfortunately, models of engineering systems are rarely additive. Instead, the model is usually a function of several parameters that often occur in groups, e.g., Reynolds or Nusselt numbers. When this happens, cross derivative terms appear in the Taylor series. As a result of these cross derivatives, parameter estimation problems may become much more complex, depending on the magnitude and the character of the interactions.

Sobol' [5] showed that a function could be decomposed into the unique form

$$g(X) = g_0 + \sum_i^m g_i(x_i) + \sum_i^m \sum_{j>i}^m g_{i,j}(x_i, x_j) + \sum_i^m \sum_{j>i}^m \sum_{k>j}^m g_{i,j,k}(x_i, x_j, x_k) \ldots \tag{6}$$

where $g(X)$ is either the exact response $R(X)$ or an approximation to it, $g_i, g_{i,j}$, et seq. are orthogonal functions with zero means. $g_i(x_i)$ are termed first-order effects and $g_{i,j}(x_i, x_j)$, and higher-order terms represent the interactions. The sum of g_0 and the first-order effects comprise the additive model. If the additive model is a good fit to the surface, then the sensitivity to x_i is given by $\partial g_i(x_i)/\partial x_i$ and is only a function of x_i and can be found independently of the values of the other parameters. If the additive model is not a good fit, then interactions are important and finding the sensitivity to x_i alone is more difficult and its interpretation is less clear. In this case, (i) individual parameters will be hard to estimate with precision and (ii) designers will have difficulty in understanding how the individual parameters affect the design.

Since variances are always positive, a naturally explicit measure of the effect of any one of the functions is its variance. The total variance of the system response is given by

$$V[R(X)] = \int_X \{R(X) - E_X[R(X)]\}^2 f(X)dX \tag{7}$$

where $E_X[R(X)]$ is the expected value of $R(X)$, i.e., the average of $R(X)$ with respect to all of the uncertain parameters. We use subscripts on V and E to make it very clear what parameter space we are integrating over.

Sobol also showed that that the variances for independent parameters could be decomposed in the same fashion.

$$V[g(X)] = \sum_i^m V_i[g_i(x_i)] + \sum_i^m \sum_{j>i}^m V_{i,j}[g_{i,j}(x_i,x_j)] + \sum_i^m \sum_{j>i}^m \sum_{k>j}^m V_{i,j,k}[g_{i,j,k}(x_i,x_j,x_k)] \tag{8a}$$

where

$$V_{i,j}[g_{i,j}(x_i,x_j)] = \int_{x_i} \int_{x_j} [g_{i,j}(x_i,x_j)]^2 f(x_i,x_j)dx_i dx_j \tag{8b}$$

$$E_{i,j}[g_{i,j}(x_i,x_j)] = \int_{x_i} \int_{x_j} g_{i,j}(x_i,x_j) f(x_i,x_j)dx_i dx_j \tag{8c}$$

Now suppose that x_i is known, then the variance considering all parameters except x_i to be uncertain is given by

$$V_{-i}[R(X)[x_i)] = \int_{X_{-i}} \{R(X|x_i) - E_{-i}[R(X|x_i)]\}^2 f(X_{-i})dX_{-i} \tag{9}$$

where the subscript $-i$ on V_{-i} denotes the variance with respect to all parameters except x_i (i.e., we integrate over all parameters, but x_i and $R(X|x_i$ indicates that $R(X)$ is a function of all parameters), but with x_i held fixed. Since x_i is not known precisely, being itself uncertain, the best that we can do is to compute its expected value

$$E_i\{V_{-i}[R(X|x_i)]\} = \int_{x_i} V_{-i}[R(X|x_i)]f(x_i)dx_i \tag{10}$$

Now the total variance is related to $E_i\{V_{-i}[R(X|x_i)]\}$ by [2]

$$V_i\{E_{-i}[R(X|x_i)]\} + E_i\{V_{-i}[R(X|x_i)]\} = V[R(X)] \tag{11a}$$

or transposing terms

$$V_i\{E_{-i}[R(X|x_i)]\} = V[R(X)] - E_i\{V_{-i}[R(X|x_i)]\} \tag{11b}$$

and we see that $V_i\{E_{-i}(R(X|x_i)]\}$ represents how much the total variance is reduced by knowing x_i. That is, it represents the contribution of x_i to the total variance. Consequently, Saltelli et al. [6] defined the sensitivity as

$$\mathcal{S}_i \equiv \frac{V_i\{E_{-i}[R(X|x_i)]\}}{V[R(X)]} \tag{12a}$$

calling it the *sensitivity index* or *first-order effect* that represents the importance of the parameter x_i. When more than one parameter is uncertain the second-order effects can be defined as

$$\mathcal{S}_{i,j} = \frac{V_{i,j}\{E_{-i,j}[R(X|x_{i,j})]\}}{V[R(X)]} \tag{12b}$$

Returning to Eq. (11*b*), we can transpose it to the form

$$V_{-i}\{E_i[R(X|x_{-i})]\} = V[R(X)] - E_{-i}\{V_i[R(X|x_{-i})]\} \tag{13}$$

where $V_{-i}\{E_i[R(X|x_{-i})]\}$, represents the expected resulting variance that would be left if all parameters except x_i were known. That is, it represents the effect of the parameter x_i and all of its interactions.

Saltelli et al. defined the *total effect sensitivity* for x_i to be

$$\mathcal{S}_i^T \equiv 1 - \frac{V_{-i}\{E_i[R(X|x_{-i})]\}}{V[R(X)]} \tag{14}$$

These two sensitivities, $\mathcal{S}_i$ and $\mathcal{S}_i^T$ give a complete picture of the effect of x_i on the response of the system. Both are scaled to be between 0 and 1. For $\mathcal{S}_i$, a value of 0 means that x_i has no effect and a value of 1 means that it constitutes the entire variability of the response. The difference $\mathcal{S}_i^T - \mathcal{S}_i$ is a measure of the effects of all of the interactions involving x_i.

Unfortunately for m parameters, there will be $2^m - 1$ such interaction terms and it is not feasible to construct them for more than three parameters. More importantly, even given $g_{i,\ldots,m}(x_1,\ldots,x_m)$, it is not possible to estimate their effects on the fit. From the definition of the sensitivities, using Eq. (8*a*), we have

$$1 = \underbrace{\sum_i \mathcal{S}_i}_{1st} + \underbrace{\sum_i \sum_{j>i} \mathcal{S}_{i,j}}_{2nd} + \underbrace{\sum_i \sum_{j>i} \sum_{k>j} \mathcal{S}_{i,j,k}}_{3rd} + \cdots \tag{15}$$

and we see that the sum of $\mathcal{S}_i$ is always <1 by the totality of the effects of all of the interactions between the parameters. Thus, this sum can be used as a convenient measure of the interaction effects. When it differs from 1 by more than a few percent, substantial interactions exist.

Example 1: Nonreacting Foam Insulation. Consider a protection system composed of a nonreacting foam. Taking the temperature at A as the response, i.e., $R(X)=T(t,k,h_0,h_l,\rho c_p)=T(t,X)$, Fig. 5(*a*) shows the time history of this sum when $\sigma[k]/k = \sigma[h_0]/h_0 = \sigma[\rho c_p]/\rho c_p = 0.20$. These values are relatively large, but chosen to illustrate the effects. Although conductivity is often presumed to be known with relative accuracy, uncertainties in the convective heat transfer coefficients and the specific heats often approach this level.

At early times, T(A) is constant at 0 until the heat flux reaches $x=0$. The time at which T(A) is first affected is a function of $k/\rho c$, and consequently, almost all of the variance is due to k and ρc, as shown on Fig. 5(*b*). Once the heat has reached $x=0$, then the value of T(A) is affected by h_0 and we see that its sensitivity rises while that of ρc drops. Note that as steady state is approached, sensitivity to ρc vanishes, that to h_0 exceeds that of k and a small interaction effect remains. Because of the high value of h_L, the temperature at $x=L$ is essentially prescribed at $T(L)=1$ for all times, and there is essentially no effect on T(A). Although at longer times a knowledge of k and h_0 is sufficient to fully define T(A), at early times ρc must be known.

In evaluating the expected values and variances, one must know the joint probability density distributions of the parameters, $f(X)$. Assuming that the parameters are independent, we have $f(X) = f(x_1)f(x_2),\ldots,f(x_n)$. Probably the most common distributions are a Gaussian distribution with a specified mean and standard deviation or a uniform distribution over a range, x_i(min) to x_i(max). If the two distributions have the same standard deviation, we have found that the resulting sensitivities are very similar in both their magnitude and their temporal behavior. The integrations needed to evaluate the integrals Eq. (8)–(14) were done numerically using Gauss-Hermite quadrature for Gaussian distributions and Gauss-Legendre quadrature for uniform distributions. In Figs. 5(*d*) and 6, five to seven Gaussian quadrature points were found to be sufficient.

Of course the ultimate desiderata is the expected change in T(A), which is shown on Figs. 5(*c*). We see that the expected value of the temperature is slightly different from the nominal value, i.e., $T(t,k_0,h_0)$, because of symmetry of the probability distributions. The 20% coefficient of variation has produced a substantial uncertainty in the temperature as indicated by the $\pm 1\sigma$ curves ($\sigma(T)$ was computed from Eq. (8).

Figure 5(*d*) compares the standard deviation computed from

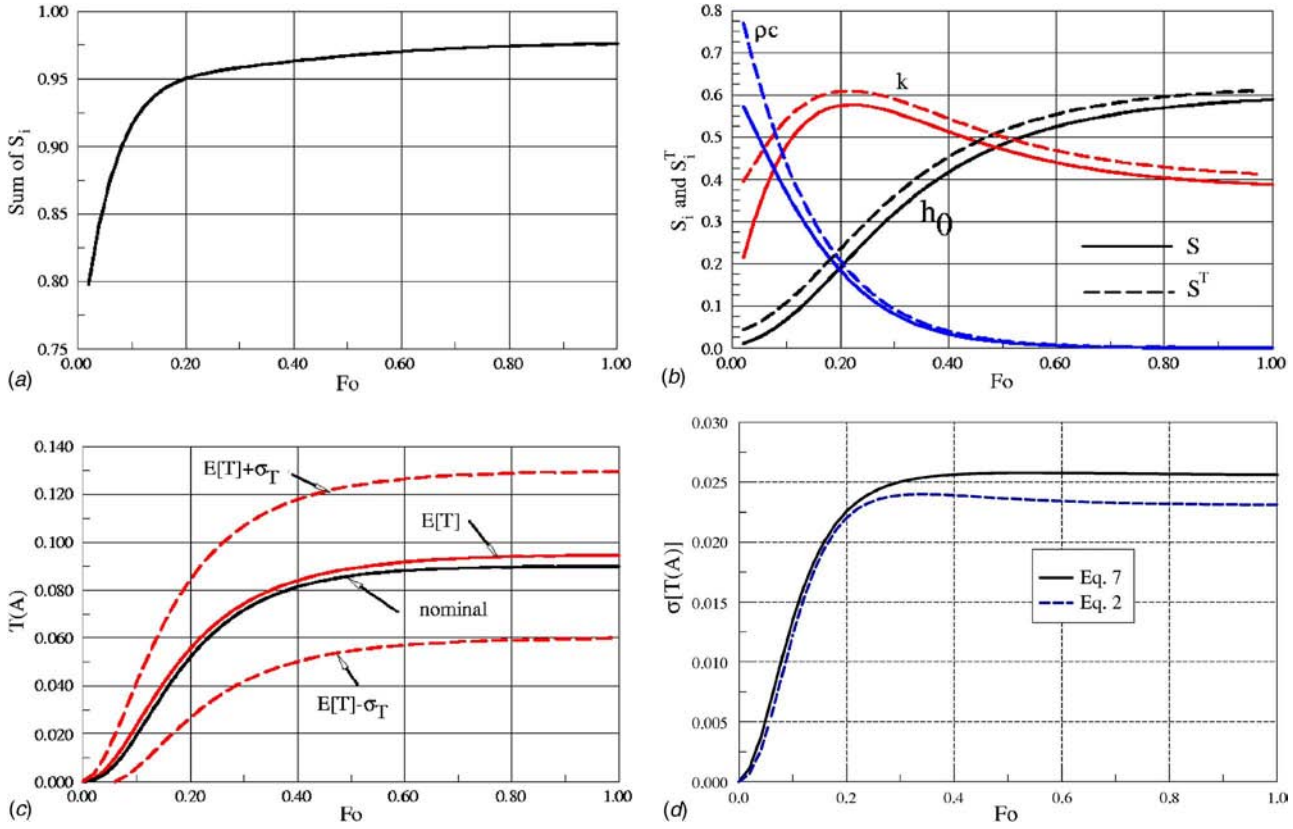

Fig. 5 Time histories for (*a*) $\Sigma \mathcal{S}_i$ for $T(\mathbf{A})$ and (*b*) for $\mathcal{S}_i[T(\mathbf{A})]$ and $\mathcal{S}_i^T[T(\mathbf{A})]$, (*c*) effect of uncertain parameters on $T(\mathbf{A})$ and (*d*) standard deviation of $T(\mathbf{A})$ based on Eqs. (7) and (2)

Eq. (7) and using the local sensitivities, Eq. (2). For this problem, the interactions are small enough that the additive model is a good representation and the standard deviation obtained using the local sensitivity, Eq. (2), is sufficient.

Example 2: Reacting Foam Insulation. The insulation is taken to be a foam that undergoes a chemical reaction when exposed to a high-temperature radiant flux. Two first-order reactions are involved. In the first the foam decomposes into a gas G_1 and a solid S, Eq. (16*a*); in the second, the solid S decomposes into a gas G_2, Eq. (16*b*),

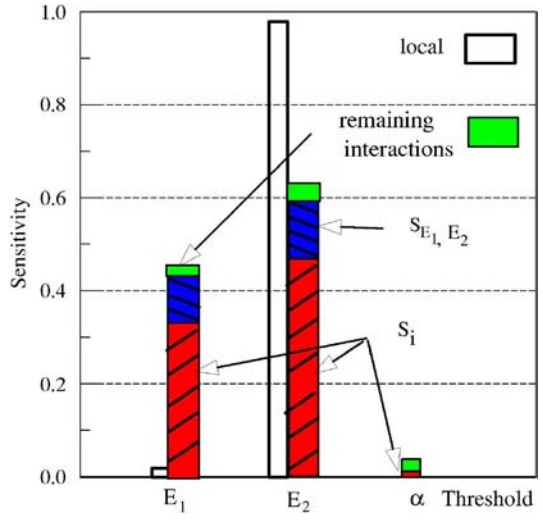

Fig. 6 Sensitivities of regression time based on Eqs. (7) and (2)

$$\text{Foam} \rightarrow \alpha G_1 + (1-\alpha)S \tag{16a}$$

$$S \rightarrow G_2 \tag{16b}$$

The activation energies, E_1 and E_2, of the two reactions and the coefficient α are the uncertain parameters. The metric of interest is the time it takes for the front surface of the foam to regress one centimeter (details are given in [7]). Figure 6 compares the sensitivities. The unfilled bars represent the fraction of the variance computed using local sensitivities and equal coefficients of variation for all parameters of 10%. Based on local sensitivity, only E_2 had any effect, all others were $<1\%$. The difference between global and local results is dramatic and underscores the need to use local sensitivity to understand the behavior of a system when there are several strongly interacting parameters.

Constructing the Response Surface Using Gaussian Processes. Having calculated the sensitivities, $\mathcal{S}_i$ and $\mathcal{S}_i^T$ it would appear that we have achieved our aim. However with only a modest effort, we can extend our capabilities by constructing an accurate representation of the response surface. Using this, we can investigate the effects of different parameter ranges and distributions and compute local sensitivities at any point in the parameter space.

The construction of an "easy-to-evaluate" approximation to the response surface is usually done by least-squares fitting or similar techniques. This involves evaluating the model at a number of points in the parameter space. However, this has already been done in evaluating the integrals associated with the evaluation of Eq. (12)–14.

Unfortunately, the usual approach of least-squares fitting is often not acceptable because the fitted surface does not pass through the values produced by the computational model. An alternative is to use what is called a Gaussian process. The idea is to fit the

exact model results with an approximation that goes through each of the points, yet is smoothly behaved between them, and most importantly is a linear combination of easy to compute basis functions. In geostatistics, the method is termed "kriging" and Emery [8] has used this approach to estimate properties in the presence of uncertain parameters. Oakley and O'Hagan [9] and Haylock and O'Hagan [10] have adapted this approach to model expensive-to-compute models. The approach is based on Bayesian inference and consists of first assuming a very simple prior model, getting a few computed points from the expensive model, and then modifying the prior using these points to produce a posterior model.

Let **y** be the responses computed from the expensive simulation model and $\eta(X)$ be the response surface to be fitted to **y**. We assume that $\eta(X)$ is correlated to $\eta(X')$ by a correlation function $c(X,X')$. A typical correlation is

$$c(X,X') = \sigma_\eta^2 \exp\left(-\frac{(X-X')^2}{\lambda^2}\right) \tag{17}$$

where λ is the correlation length. σ_η and λ are hyperparameters to be estimated. The kriging literature is replete with descriptions of the acceptable form of the correlation and methods for estimating them. The prior model is expressed in terms of a linear combination of simple-to-evaluate basis functions, $h_i(X)$ with

$$\eta(X) = \sum_i h_i(X)\beta_i = h(X)^T\beta \tag{18}$$

Using Bayesian inference, it can be shown that the fitted $\eta(X)$ has a Gaussian distribution with a mean of $m(X)$ given by

$$m(x) = h(x)^T\hat{\beta} + t(x)^T A^{-1}(y - H\hat{\beta}) \tag{19}$$

The matrix A has components $A_{i,j}=c(X_i,X_j)$, the vector $t(x)$ has components $t_i=c(X,X_i)$ and the vector H has components $H_i = h(X_i)^T$. Details of the computation of $\hat{\beta}$ and the hyperparameters and implementing the method are given in a forthcoming paper [11].

Here we point out that once the expensive simulation has been run to obtain **y** and the matrix A inverted, it is easy to evaluate $t(X)$ and $H(X)$ and to solve for $m(X)$ for any point X on the design surface.

To illustrate the effect, we chose the simple prior model, $\eta(X)=$const. This prior model is about as far from the true response surface as one can imagine. The data **y** were obtained at ten times from $0.1 \leq Fo \leq 1$ and for three sets of k, h_0, and h_L equal to $k-3\sigma[k]$, k, $k+3\sigma[k]$ and similarly for h_0 and h_L. These points are referred to as the *design* points. A total of 270 design points were used to obtain **y**. Contours of the temperatures from the exact model and $m(x)$ the Gaussian process are shown in Fig. 7. The calculation of $m(X)$ is extremely fast, and the reduction in the overall computational time was more than an order of magnitude when compared to solving the heat conduction equation in evaluating the integrals.

Even with this grossly simplified model and with the relatively few design points, the agreement of the contours is very good. Using the values of $m(X)$ in the equations for the expected values and the variances gives the results shown in Fig. 8(*a*) and compared to the exact values shown in Fig. 8(*b*). Comparing Figs. 8(*a*) and 8(*b*), we see that the Gaussian process has performed very well. Sacks et al. [12] give a good description of choosing the design points. We have made no attempt to optimize the design, wishing to apply the simplest design and prior model to illustrate the value of the method.

Computational Issues

A valid concern is the computational costs associated with the global sensitivities. Our experience has been that for uniformly and normally distributed parameters, Gaussian quadrature with

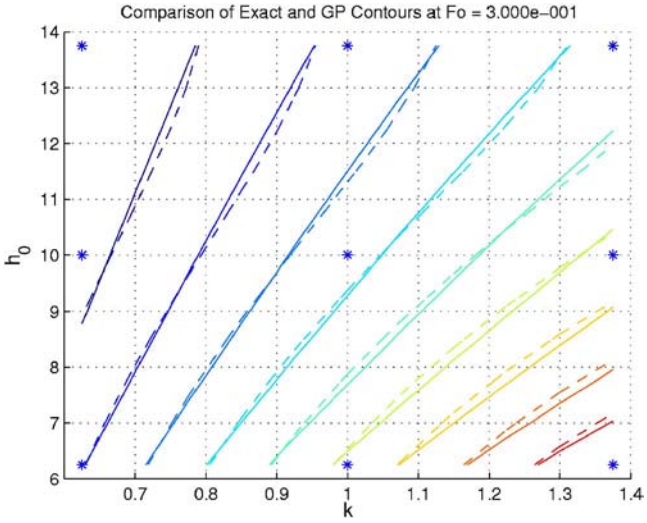

Fig. 7 Comparing the contours of the exact temperatures (solid lines) and $m(x)$ from the Gaussian process (dashed lines); * denotes the design points (for κ=1, Bi_0=10, Bi_L=100)

three points is quite acceptable. For problems in which discontinuities are present, e.g., phase change fronts, five-point quadrature is sufficient. m parameters and G quadrature points mean evaluating the response at $G^{m-1}+1$ parameter values. For the four parameters considered here, this is 28 or 126 evaluations for $G=3$ or 5, respectively.

Local sensitivities, involving first- or second-order cross derivatives requires, for the lowest level of precision using finite differences, four points per pair of parameters, a minimum of 2^m evalu-

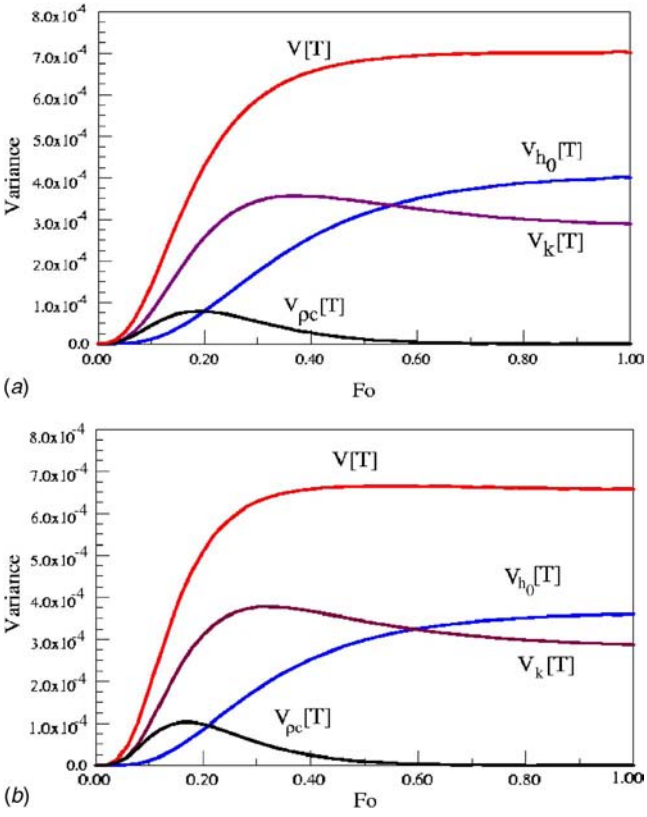

Fig. 8 Variances computed from (*a*) the Gaussian process and (*b*) the exact model (Eq. (12*a*))

ations. To get the global effect, Eq. (4), requires integration over the parameter space, i.e., at G^m points, thus, requiring at least or generally more points than the evaluation of the global sensitivities using Eq. (12). More importantly, second-order interactions need not be dominant and the evaluation of the total interaction effects is not possible by using local derivatives unless one is willing to evaluate all 2^m+1 terms in Eq. (6).

Conclusions

Although local sensitivity is widely used, it suffers from several serious deficiencies, as follows:

1. Since it represents only the linear (first-order) terms in the Taylor series, it is not an adequate representation of the effects of the parameters unless $R(X)$ is linear in the parameters. Otherwise, the higher-order terms must be considered.
2. Because it looks at each parameter independently, it ignores the effects of any interaction between the parameters.
3. It is often applied linearly, that is $\sigma[R] \propto (\sigma[x_1]/x_1)\ S_i^*$ and thus ignores the nature of the parameter variability, e.g., that conductivity must be positive, that emissivity must range between 0 and 1

The average sensitivity, $\bar{S}$, resolves deficiency (3), but because it is only the first-order term in Eq. (1) it does not consider any interaction between the parameters. Global sensitivity is an effective way to determine both the first-order sensitivities and the interactions while taking parameter variability into account.

It is important to realize and that even for highly nonlinear problems, if the uncertainty of a parameter is small, then the integrations, Eq. (8*b*) and (8*c*), will cover a small range of the parameter. In this case, except for unusual circumstances, such as found at the near discontinuous behavior near melting or solidification fronts, the response will be well represented by a linear model and local sensitivities will suffice.

The importance of using Gaussian processes is that an approximate model with easy-to-evaluate responses has been constructed. From this model, first- and higher-order sensitivities and the interactions can be efficiently (quickly) computed. This model can then be used to investigate the effects for a wide variety of conditions.

The development presented here progressed from the point of view of additive surfaces to the Gaussian processes, pointing out that the same computed responses are utilized in both. Given that the approximate response surface is of more value, particularly to those interested in parameter estimation, than simply knowing the global sensitivity, a more practical approach is to generate the Gaussian process first. However, this requires the determination of the hyperparameters, which for some problems may be difficult or expensive [11]. In this case, one would have to be content with the computation of the global sensitivities. One must keep in mind that the idea behind Gaussian processes is to produce an easy-to-evaluate model. It is useful only when the original model is expensive to compute.

Acknowledgment

This work was supported by Sandia National Laboratories, Albuquerque, NM, under the technical direction of Dr. Kevin Dowding. The authors would like to acknowledge his assistance and the helpful comments of his associates. We would also like to thank Dr. O'Hagan, Dr. Oakley, and Dr. Murray-Smith for their help in answering our questions and the reviewers whose suggestions materially improved the paper.

Nomenclature

$E[\ ]$ = expectation
$f(X)$ = probability density distribution
$g_i(X_i)$ = decomposition functions
h = heat transfer coefficient
h_0 = heat transfer coefficient at x=0
h_L = heat transfer coefficient at x=L
k = thermal conductivity
m = number of parameters
R = response
S_i^* = local sensitivity to x_i
$\mathcal{S}_i$ = global sensitivity to x_i
$\mathcal{S}_i^T$ = total sensitivity to x_i
T = temperature
x = parameter, x coordinate
X = space of all parameters
X^* = point of evaluation
$V[\ ]$ = total variance
V_i = variance with respect to x_i
ϵ = measurement noise
$\sigma[x]$ = standard deviation of x
β = coefficients in the Gaussian process
σ_n, λ = hyperparameters in the Gaussian process

References

[1] Beck, J. V., and Arnold, K. J., 1977, *Parameter Estimation in Engineering and Science*, Wiley, New York.
[2] Gelman, A., Carlin, J. B., Stern, H. S., and Rubin, D. B., 2004, *Bayesian Data Analysis*, Chapman and Hall, New York.
[3] Emery, A. F., 2001, "Using the Concept of Information to Optimally Design Experiments With Uncertain Parameters," ASME J. Heat Transfer, **123**(3), pp. 593–600.
[4] Emery, A. F., Blackwell, B. F., and Dowding, K. J., 2003, "The Relationship Between Information, Sampling Rates, and Parameter Estimation Models," ASME J. Heat Transfer, **124**(6), pp. 1192–1199.
[5] Sobol, I. M., 1990, "Sensitivity Estimates for Nonlinear Mathematical Models," MMCE, **1**(4), pp. 407–414.
[6] Saltelli, A., Tarantola, S., Campolongo, F., and Ratto, M., 2004, *Sensitivity Analysis in Practice*, Wiley, New York.
[7] Emery, A. F., and Bardot, D., 2006, "The Design of a Thermal Protection System Using Global Sensitivity," *13th International Heat Transfer Conference*, Sydney.
[8] Emery, A. F., 2003, "The Use of Kriging and Nuisance Variables in Parameter Estimation," *Proc. of 4th International Conference on Inverse Problems, Identification, Design, and Control*, O. M. Alifanov et al., Moscow, pp. 81–88.
[9] Oakely, J. E., and O'Hagan, A., 2004, "Probabilistic Sensitivity Analysis of Complex Models: A Bayesian Approach," J. R. Stat. Soc. Ser. B (Stat. Methodol.), **66**, pp. 751–769.
[10] Haylock, R. G., and O'Hagan, A., 1996, "On Inference for Outputs of Computationally Expensive Algorithms with Uncertainty on The Inputs," *Bayesian Statistics 5*, Oxford University Press, London, pp. 629–637.
[11] Bardot, D., and Emery, A. F., 2006, "Capturing Real Life Variability in Virtual Testing," *ASME Int. Mech. Eng. Conf. and Exposition*, Chicago.
[12] Sacks, J., Welch, W. J., Mitchell, T. J., and Wynn, H. P., 1989, "Design and Analysis of Computer Experiments," Stat. Sci., **4**, pp. 409–435.

Journal of Heat Transfer

Technical Briefs

A New Finite-Conductivity Droplet Evaporation Model Including Liquid Turbulence Effect

M. S. Balasubramanyam

C. P. Chen[1]
e-mail: cchen@che.uah.edu

Department of Chemical and Materials Engineering,
University of Alabama in Huntsville,
Huntsville, Huntsville, AL 35899

H. P. Trinh
Engineering Directorate
NASA-Marshall Space Flight Center,
Huntsville, AL 35812

*A new approach to account for finite thermal conductivity and turbulence effects within atomizing droplets of an evaporating spray is presented in this paper. The model is an extension of the T-blob and T-TAB atomization/spray model of Trinh and Chen [Atomization and Sprays, **16**(8), pp. 907–932]. This finite conductivity model is based on the two-temperature film theory in which the turbulence characteristics of the droplet are used to estimate the effective thermal diffusivity for the liquid-side film thickness. Both one-way and two-way coupled calculations were performed to investigate the performance of this model against the published experimental data.* [DOI: 10.1115/1.2737481]

Keywords: evaporation, spray, numerical modeling

Introduction

Spray vaporization and combustion studies are of primary importance in the prediction and improvement of systems utilizing spray injection. In liquid fueled combustion systems, such as industrial boilers, gas turbines, direct ignition diesel engines, and rocket and air-breathing engine applications, the combustion performance is highly dependent on effective liquid fuel atomization and its subsequent evaporation processes. The recent review by Sazhin [1] had summarized the development of various droplet heat-up and evaporation models with different levels of complexity. As also pointed out in [1], to numerically simulate evaporating spray using CFD (computational fluid dynamics) methodologies, detailed droplet heating and evaporation models based on single-droplet analysis have to be simplified to be CPU efficient (also see [2,3]). Although the film-theory-based evaporation models had been extensively used, most of the developments were done on the gas-side heat and mass transfer [4,5]. On the other hand, the importance of convection-diffusion process in the liquid side was also shown in various studies [5–8]. Within the liquid droplet, the two-temperature formulations, in which the finite-conductivity (F-C) effect was modeled by the temperature difference between the droplet surface temperature and a droplet "core" temperature have been proposed recently. In the model of Renksizbulut et al. [9], the difference between the surface and core temperature was related to the heat flux at the droplet surface by a constant Nusselt number. Zeng and Lee [10] developed a zero-dimensional model, in which the difference between surface and core temperature was traced by an ordinary differential equation (ODE) to account for the nonuniform distribution of temperature inside the droplet. The ODE two-temperature model was also used by Miller et al. [11] to account for the nonequilibrium Langmuir-Knudsen mass transfer effect. Ra and Reitz [12] used a thermal boundary layer within the droplet to account for the finite-conductivity effect. The thermal boundary layer thickness was calculated using the thermal diffusivity model of Abramzon and Sirignano [13] to account for the droplet internal circulation.

In this paper, a new finite-conductivity model is developed based on the two-temperature formulation. The finite-conductivity effect is phenomenologically modeled through a thermal boundary layer within the droplet. The thermal diffusivity is calculated based on the turbulent characteristics within the droplet. The current study is an extension of a recently developed atomization/spray model [14,15], the T-blob/T-TAB model, to include spray evaporation effects. Because of the unique feature of T-blob/T-TAB, in which the turbulence characteristics is accounted for within the droplet phase, extension of this model to include finite conductivity effect in the evaporating droplet can be made naturally. The model development will be described in this paper. Validations for one-way one-dimensional and two-way coupled multi-dimensional evaporating sprays will be presented.

Model Development

The current vaporization model is developed for computational analysis based on the Eulerian-Lagrangian numerical approach. In this formulation, the spray/droplets dynamics is described in a Lagrangian coordinate such that numerical droplets are tracked within the Eulerian gas dynamics. Liquid phase is tracked from the injector plane, and the primary atomization as well as the subsequent secondary breakup is modeled using the T-blob/T-TAB hybrid model of Trinh and Chen [14]. Both primary and secondary droplet break-up processes are modeled and the transition from primary to secondary breakup is modeled based on an energy balance. In addition to the droplets position and velocity, liquid turbulence is accounted for through the injector characteristics by the two-equation k-ε turbulence model formulation using

[1]Corresponding author.

Contributed by the Heat Transfer Division of ASME for publication in the JOURNAL OF HEAT TRANSFER. Manuscript received March 30, 2006; final manuscript received December 7, 2006. Review conducted by Raj M. Manglik.

the T-blob/T-TAB model. The inherent turbulence in the injected fuel spray affects the heat and mass transfer rates of the vaporization process. The effects of these changes in the rates have to be accounted for in the numerical models for spray evaporation. Detailed model description and validations can be found in [14,15], and it is suffice to say that within each numerical droplet, turbulence characteristics, such as fluctuating velocity level, length, and time scales, are supplied by the model.

To utilize the T-blob/T-TAB model liquid jet atomization, turbulence characteristics need to be specified as the inlet boundary conditions. Based on integral analysis of straight injector [14], liquid turbulent kinetic energy and its dissipation rate at the injector nozzle exit are estimated from

$$k_l^o = \frac{U^2}{8L/D_{\text{nozzle}}}\left[\frac{1}{C_d^2} - K_c - (1-s^2)\right] \tag{1}$$

$$\varepsilon_l^o = K_\varepsilon \frac{U^3}{2L}\left[\frac{1}{C_d^2} - K_c - (1-s^2)\right] \tag{2}$$

where L is the length of the injector nozzle, D_{nozzle} is the nozzle diameter, and the jet injection velocity U. A set of ODEs were derived to track the evolution of k_l and ε_l within the droplet according to the T-blob/T-TAB model. The values obtained from the evolution of k_l and ε_l are used in the heat transfer calculations of the evaporation droplet.

To relax the infinite-conductivity assumption, and thus perfect mixing within the liquid droplet, a "two-temperature" model is formulated. In the two-temperature model, the core (or bulk) temperature (T_d), is assumed to be well mixed by convection/turbulence transport. To be consistent with the "film theory," heat resistance exists at the near surface region and the droplet surface temperature (T_s) differs from the droplet core temperature. The heat transfer coefficient across this thin film (or boundary layer) is then formulated through the turbulence characteristics supplied from the T-blob/T-TAB model, to account for the finite conductivity effect. In the Lagrangian coordinate, the heat-up of the droplet core is formulated as

$$m_d C_p \frac{dT_d}{dt} = h_l (T_s - T_d) A_d \tag{3}$$

where, h_l is the liquid-side heat transfer coefficient and A_d is the droplet surface area. The heat transfer coefficient is determined from the thermal conductivity and a thermal boundary layer formulation [16] as:

$$h_l = \frac{\lambda_l}{\delta_e} \tag{4}$$

where λ_l is the liquid thermal conductivity. Using an unsteady equivalent boundary layer thickness, the film thickness δ_e is given by $\sqrt{\pi \alpha_{\text{eff}} t}$. The time scale t is estimated based on the heat transfer-limited integration time step and should be independent of the global time step used in numerical calculations (see the results in Fig. 1). In this study, we adopted the evaporation subcycle time step based on the formulation described in Amsden et al. [17]. This time step is computed by the relation given by

$$t = \frac{\rho_g \, dV}{\mu_g \, \text{Sh}_g (4\pi r_d) N_p} \tag{5}$$

where dV is the volume of the computational cell, ρ_g is density, μ_g is the viscosity of gas mixture within the cell, and N_p is the number of droplets for each computational particle p. The effective thermal diffusivity (α_{eff}), based on the turbulence characteristics within the droplet, is estimated from: $\alpha_{\text{eff}} = \alpha_{\text{lam}} + \alpha_{\text{turb}}$, in which the turbulent thermal diffusivity is calculated from the two-equation turbulence model diffusivity formulation:

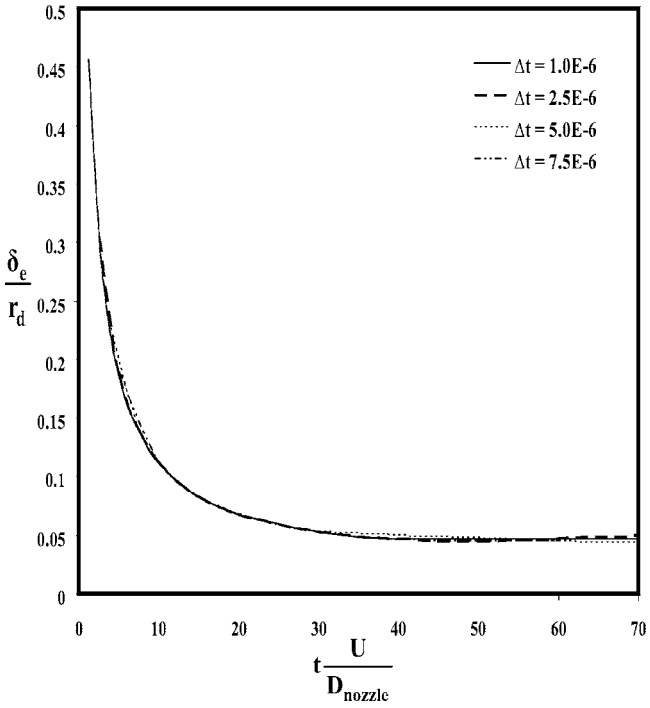

Fig. 1 History of effective film thickness within the evaporating droplet using various integration time steps

$$\alpha_{\text{turb}} = \frac{C_\mu k_l^2}{\text{Pr}_t \, \varepsilon_l} \tag{6}$$

here, Pr_t is the turbulent Prandtl number and is set to be 0.9. The liquid droplet turbulence quantities k_l and ε_l are obtained from the T-blob/T-TAB atomization/spray model. In cases where gas phase diffusivities are much larger than liquid diffusivities, as in diesel engine sprays [1], the time scale of liquid drop heating is longer when compared to the gas phase heating time scale. Thus, the droplet core heating will be rate controlling and the gas-side heat/mass transfer will respond in a quasi-steady manner. The surface temperature of the droplet is determined from a heat and mass transfer balance at the interface between the droplet and the surrounding gas, assuming no heat accumulation at the droplet surface such that

$$L_v \dot{m}_d = q_g - q_l \tag{7}$$

where L_v is the latent heat of the fuel at the surface temperature and q_g is the heat transfer rate from the environmental gas to the surface. In this paper, the classical Spalding evaporation model is used to model the gas-phase transport; thus, the gas heat transfer rate was calculated as

$$q_g = 2\pi r_d \lambda_g \, \text{Nu}_g (T_g - T_s) \frac{\ln(1+B_T)}{B_T} \tag{8}$$

q_l in Eq. (7) is the heat transfer rate from the droplet interior to droplet surface and is calculated from

$$q_l = \frac{\lambda_l (T_s - T_d)}{\delta_e} A_d \tag{9}$$

The evaporation rate at the droplet surface is given as

$$\dot{m}_d = \frac{dm_d}{dt} = 2\pi r_d (\rho_g \bar{D}) \text{Sh}_g \ln(1+B_m) \tag{10}$$

In Eq. (10), B_m is the Spalding mass transfer number, Sh_g is the Sherwood number, and $\bar{D}$ is the binary diffusivity. The Sherwood

and Nusselt numbers were calculated using the classical correlations given by

$$\mathrm{Nu}_g = 2 + 0.6\ \mathrm{Re}_p^{0.5}\mathrm{Pr}^{0.333} \tag{11}$$

$$\mathrm{Sh}_g = 2 + 0.6\ \mathrm{Re}_p^{0.5}\mathrm{Sc}^{0.333} \tag{12}$$

The solution algorithm used in this study starts with an estimated surface temperature T_s at a new time step. The Clausius-Clayperon equation and the Raoult's law are then used to calculate the fuel vapour molar fraction followed by the calculation of the evaporation rate. An estimation of T_d is also required to simultaneously satisfy Eqs. (3) and (7). More detailed iterative procedure can be found in Balasubramanyam [18].

Results and Discussion

One-Way Evaporating Atomizing Spray. In one-way simulation, the gas flow field was prescribed and the droplets were tracked in time domain. This case is an extension of the one-way T-blob/T-TAB testing case described in Trinh and Chen [14]. Iso-octane fuel similar to the fuel used in reference [12] was issued through a long injector tube at 300 K. The length of the injector nozzle L is 0.8 mm, and the nozzle diameter D_{nozzle} is 0.3 mm. A jet injection velocity U of 102-m/s was used for the test case. The environment is quiescent nitrogen at a temperature of 600 K. The gas properties were calculated based on the reference state determined from the "1/3" rule [16]. In this calculation, a "blob" of numerical droplet was injected at the orifice plane with orifice diameter. The droplet then went through the primary and secondary breakup processes; thus, its diameter decreased with time. The variation of the thermal boundary layer within the droplet also changed with time. The purpose here is to investigate the concept of boundary layer film thickness within liquid droplets involving two temperatures. In the course of study, it was found that in the secondary breakup regime (i.e., the T-TAB regime) the droplets were so small they were heated up rapidly. Thus, the current model was only implemented within the T-blob (i.e., the primary breakup) model. Figure 1 shows the history of the normalized effective film thickness within the liquid droplets. The results indicate that the normalized thermal boundary layer thickness is rather thick in the initial stage and then decreases quickly to a small value exhibiting a reasonable physical trend. It should be noted that the current model gives thinner thermal boundary layer thickness when compared to the limiting thermal layer thickness based on internal vortex convection model. Utilizing the model of Abramzon and Sirignano [13], Ra and Reitz [12] suggested that the value of thermal layer thickness be limited to 1/2.257 of the droplet radius. It was also observed that, based on the current model, the turbulent diffusivity within the droplet was at least one order of magnitude greater than the laminar thermal diffusivity. The turbulent thermal diffusivity decreased in tandem with the decrease in the kinetic energy experienced by the drop. The variation of the drop surface temperature T_s and the bulk temperature of the drop T_d for the finite-conductivity (F-C) model in comparison to the bulk temperature calculated using the infinite-conductivity (I-C) model is shown in Fig. 2. The temperature profiles for T_d and T_s were in close comparison to the results obtained by Ref. [12] for iso-octane evaporation. The variation of the normalized parent drop radius with time for a one-way coupled test case, with iso-octane fuel evaporating in a quiescent environment is shown in Fig. 3. The present F-C model predicted higher rate of change in the droplet radius (i.e., shorter droplet lifetime) when compared to the ones using the I-C model. This is due to the higher droplet surface temperature predicted by the current model, as seen from Fig. 2. The higher surface temperature produced higher fuel molar fraction and thus gave higher evaporation rate according to Eq. (10). The results of this comparison indicated that the droplet lifetimes predicted by the finite conductivity model are shorter than the prediction by the infinite

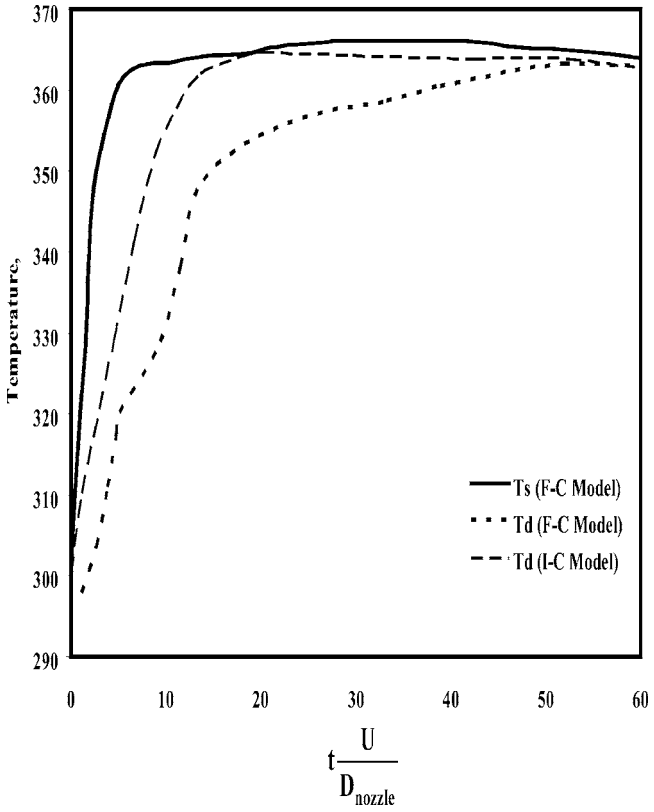

Fig. 2 Droplet temperature history comparisons using the current finite-conductivity (F-C) and the infinite-conductivity (I-C) models

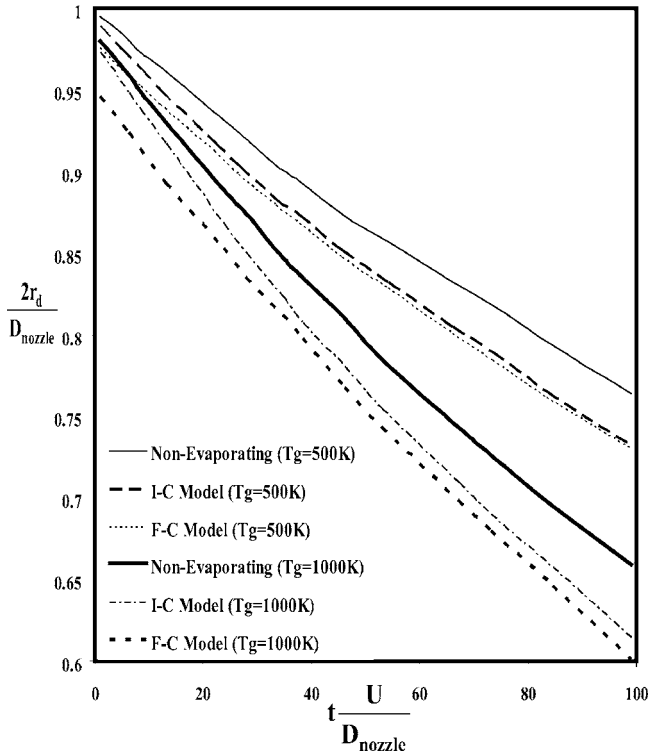

Fig. 3 Comparative change in drop size for the F-C and I-C models (nonevaporating-atomization without vaporization model)

Table 1 Test conditions for the measurements of Yokota et al. [21]

Case	P_{inj}	P_{gas}	T_{amb}	M_{inj}	Gas Environment
Evap. spray	30 Mpa	3 Mpa	900 K	0.00326 kg/s	N_2

conductivity model. The difference in rates increases with increase in ambient temperature. It should be noted that this one-way coupling simulation case involves droplet (blob) evaporation with primary breakup; thus, the droplet size decreases quite rapidly in the initial region. The nonevaporating one-way results using the T-blob/T-TAB model is also shown in Fig. 3 for comparison. The current model compares favorably with the models of Refs. [8,10,12]. The next step in the numerical development of the model was to validate its efficiency for applications in practical situations. To this effect, the model was then incorporated into the finite volume CFD code ACE+ [19] for two-way coupled validation study using the stochastic Eulerian-Lagrangian methodology [20]. In the two-way simulation, mutual interaction between the gas phase and the evaporating spray were accounted for by extra source terms in the equations of change for mass and momentum. Detailed numerical implementation, as well as grid size and time step issues, can be found in Balasubramanyam [18].

Two-Way Coupled Evaporating Spray Validation. To evaluate the current evaporation model, the two-dimensional (2D) axissymmetric subsonic low-evaporating spray of Yokota et al. [21] was tested for a two-way coupling CFD calculation since a similar nonevaporating test case was used for the T-blob/T-TAB validation study [15]. Liquid fuel (Tridecane, $C_{13}H_{28}$) is injected through a single-hole nozzle into a pressurized, high-temperature ambient N_2 environment. The test conditions for the evaporating spray are summarized in Table 1. The nozzle diameter was 0.16 mm. Eqs. (1) and (2), with the same values for nozzle parameters except for nozzle diameter and jet velocity, were used to estimate the initial liquid turbulence quantities. A computational domain of 20 mm in radius and 100 mm in length discretized by a 50 radial $\times$ 75 axial grid was used. The mesh spacing was nonuniform with refinement on the centreline and close to the injector. A constant time step of 2.5×10^{-6} s was used with an injection period of 4 μs. The properties of liquid fuel Tridecane were taken from the NIST/JANAF database.

Estimating the penetration of a fuel jet into an airstream is an important global property for model validation and is presented first. In Fig. 4, the predicted tip penetration results using the current finite-conductivity (F-C) evaporation model coupled with the T-blob/T-TAB atomization model are compared to the measured data. For reference, predictions using classical Blob/TAB/infinite-conductivity (I-C) model, as well as using T-blob/T-TAB/infinite-conductivity model are also shown in the same figure. As indicated in [8], the infinite-conductivity evaporation models tend to

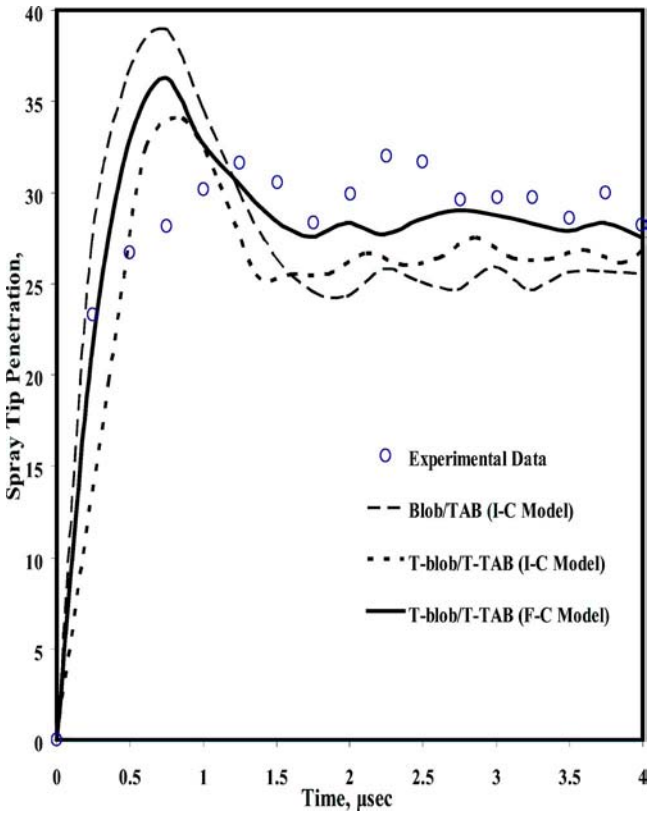

Fig. 4 Spray tip penetration with time comparisons using the current F-C model and the infinite-conductivity (I-C) model

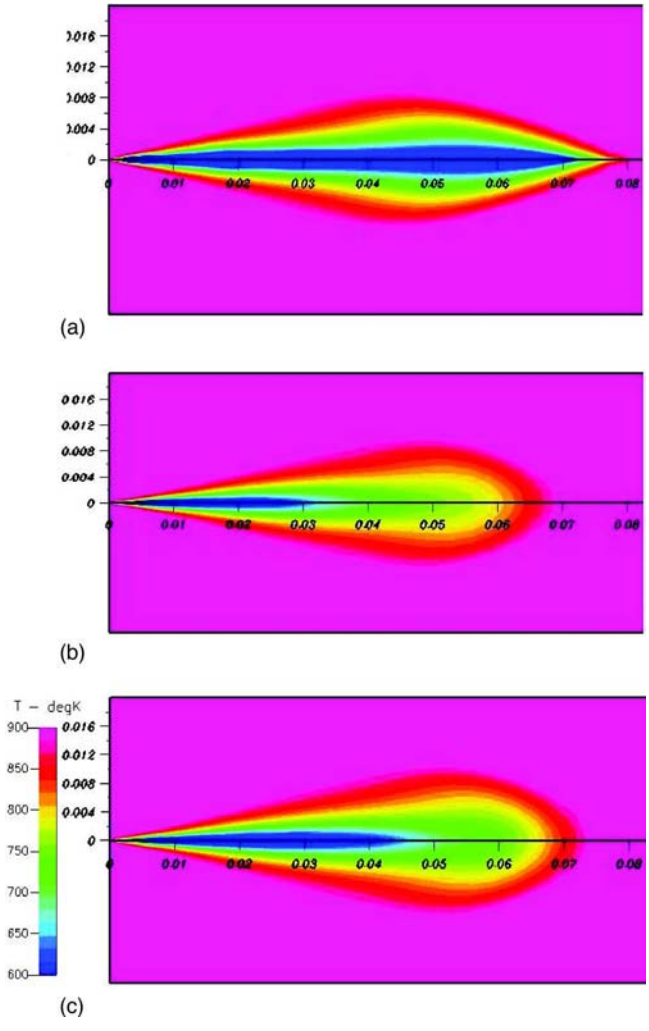

Fig. 5 Temperature contours (*X*, *Y* direction in meters) at 4 μs: (*a*) I-C with Blob/TAB, (*b*) I-C with T-blob/T-TAB, and (*c*) F-C with T-blob /T-TAB

overpredict the evaporation rate for multidimensional two-way coupled calculations, thus, gave shorter tip penetration. On the other hand, the finite-conductivity model slows down the evaporation process, and produce larger droplets and longer penetration. It should be noted that the coalescence model [15] was used for all two-way coupling calculation cases. The coalescence model is responsible for the calculated overshoot phenomena observed in the initial period of injection for all simulated cases. In the downstream region, the current model gives much better comparison to the experimental data. The heat transfer aspects of the evaporating jet are shown in Fig. 5 at time of 4 μs after injection. As can be observed, the models incorporating the turbulence effects in the primary and secondary atomization processes give more reasonable qualitative pictures when compared to the classical atomization model without liquid turbulence effect. Comparing Figs. 5(*b*) and 5(*c*), the surface temperature contours predicted by the current finite-conductivity model show the effect of slowing down the rate of evaporation, and qualitatively compared well to the more sophisticated droplet heat-up model of Bertoli and Migliaccio [8].

Concluding Remarks

Based on the two-temperature film theory, a new finite-conductivity model accounting for droplet internal turbulence effect is developed for evaporating spray numerical calculations. The model is an extension of the existing T-blob/T-TAB atomization/spray model that provides the turbulence characteristics for estimating an effective thermal diffusivity within the droplet. Based on the one-way simple spray results, the model exhibits reasonable physical trends in terms of droplet evaporation features. The current model can be efficiently incorporated into practical spray combustion CFD codes. In two-way Eulerian-Lagrangian multidimensional full CFD simulations utilizing CFD-ACE+ code, the current finite-conductivity model coupled with the T-blob/T-TAB model shows superior performance to the conventional infinite-conductivity evaporation model, by comparison to evaporating spray experimental data.

Acknowledgment

This study was partially supported by NASA Grant No. NCC8-200 through the UAH Propulsion Research Centre. The authors would also like to acknowledge the use of the CFD-ACE+ code under an educational agreement with CFD Research Corporation.

Nomenclature

A_d = droplet surface area (m^2)
B_m = gas phase mass transfer number
C_d = discharge coefficient of injector nozzle (0.07 in this study)
C_p = specific heat capacity of mixture (KJ/kg K)
C_μ = turbulence constant
$\bar{D}$ = binary diffusivity (m^2/s)
K_c = loss coefficient due to nozzle inlet geometry (0.45)
K_ε = proportionality constant (0.23)
k_l = turbulent kinetic energy of the liquid (m^2/s^2)
L_v = latent heat of the fuel at surface temperature (KJ/kg)
m_d = droplet mass (kg)
Nu_g = gas phase Nusselt number
Pr_t = turbulent Prandtl number (0.9)
P_{atm} = atmospheric pressure (Pa)
P_{gas} = gas phase pressure (Pa)
q_l = heat transfer rate from droplet surface to droplet core
q_g = heat transfer rate from gas phase to droplet surface
r_d = droplet radius (m), D_p is diameter
Sh_g = gas phase Sherwood number
T_b = fuel boiling temperature (K)
T_d = bulk temperature of droplet (K)
T_g = ambient gas temperature (K)
T_s = droplet surface temperature (K)
s = area ratio at nozzle contraction, (0.0 in this study)
U = droplet injection velocity (m/s)
α_{eff} = effective thermal diffusivity (m^2/s)
α_{lam} = laminar thermal diffusivity (m^2/s)
α_{turb} = turbulent thermal diffusivity (m^2/s)
λ_l = liquid thermal conductivity
λ_g = gas thermal conductivity (KW/m K)
ε_l = turbulent dissipation rate (m^2/s^3)
δ_e = equivalent thickness of thermal boundary layer

References

[1] Sazhin, S. S., 2006, "Advanced Models of Fuel Droplet Heating and Evaporation," Prog. Energy Combust. Sci., **32**, pp. 162–214.
[2] Dombrovsky, L. A., and Sazhin, S. S., 2003, "A Parabolic Temperature Profile Model for Heating of Droplets," ASME J. Heat Transfer, **125**, pp. 535–537.
[3] Mukhopadhyay, A., and Sanyal, D., 2005, "A Semi-Analytical Model for Evaporating Fuel Droplets," ASME J. Heat Transfer, **127**, pp. 199–203.
[4] Yao, G. F., 2006, "A Film-Theory-Based Model for a Multicomponent Droplet Evaporation at Both Low and High-Pressure Environments," ASME J. Heat Transfer, **128**, pp. 290–294.
[5] Aggarwal, S. K., 1987, "Modeling of Dilute Vaporizing Multicomponent Fuel Spray," Int. J. Heat Mass Transfer, **30**, pp. 1949–1961.
[6] Aggarwal, S. K., Tong, A., and Sirignano, W. A., 1984, "A Comparison of Vaporization Models for Spray Calculations," AIAA J., **22**, pp. 1448–1457.
[7] Tolpadi, A. K., Aggarwal, S. K., and Mongia, H., 2000, "An Advanced Spray Model for Application to the Prediction of Gas Turbine Combustor Flowfields," Numer. Heat Transfer, Part A, **38**, pp. 325–340.
[8] Bertoli, C., and Migliaccio, M., 1999, "A Finite Conductivity Model for Diesel Spray Evaporation Computations," Int. J. Heat Fluid Flow, **20**, pp. 552–561.
[9] Renksizbulut, M., Bussmann, M., and Li, X., 1992, "A Droplet Vaporization Model for Spray Calculations," Part. Part. Syst. Charact., **9**, 59–65.
[10] Zeng, Y., and Lee, C. F., 2002, "A Model for Multicomponent Spray Vaporization in a High-Pressure and High-Temperature Environment," ASME J. Eng. Gas Turbines Power, **124**, pp. 717–724.
[11] Miller, R. S., Harstad, K., and Bellan, J., 1998, "Evaluation of Equilibrium and Non-Equilibrium Evaporation Models for Many-Droplet Gas-Liquid Flow Simulations," Int. J. Multiphase Flow, **24**, pp. 1025–1055.
[12] Ra, Y., and Reitz, R. D., 2003, "The Application of a Multicomponent Droplet Vaporization Model to Gasoline Direct Injection Engines," Int. J. Energy Res., **4**, pp. 193–218.
[13] Abramzon, B., and Sirignano, W. A., 1989, "Droplet Vaporization Model for Spray Combustion Calculations," Int. J. Heat Mass Transfer, **32**, 1605–1618.
[14] Trinh, H. P., and Chen, C. P., 2006, "Modeling of Turbulence Effects on Liquid Jet Atomization and Breakup," Atomization Sprays **16**(8), pp. 907–932.
[15] Trinh, H. P., Chen, C. P., and Balasubramanyam, M. S., 2007, "Numerical Simulation of Liquid Jet Atomization Including Turbulence Effects," ASME J. Eng. Gas Turbines Power(accepted).
[16] Sirignano, W. A., 1999, *Fluid Dynamics and Transport of Droplets and Sprays*, Cambridge University Press, Cambridge, UK.
[17] Amsden, A. A., O'Rourke, P. J., and Butler, T. D., 1989, "KIVA-II: A Computer Program for Chemically Reactive Flows With Sprays," KIVA LA-11560-MS.
[18] Balasubramanyam, M. S., 2006, Modeling Turbulence Effects on the Heat and Mass Transfer of Evaporating Sprays, Ph. D. dissertation, Department of Mechanical and Aerospace Engineering, University of Alabama in Huntsville.
[19] CFD-ACE+, 2004, *ACE+ Theory Manual*, CFD Research Corporation.
[20] Chen, C. P., Shang, H. M., and Jiang, Yu, 1992, "An Efficient Pressure-Velocity Coupling Method for Two-Phase Gas-Droplet Flows," Int. J. Numer. Methods Fluids, **15**, pp. 233–245.
[21] Yokota, H., Kamimoto, T., and Kobayashi, H., 1988, "A Study of Diesel Spray and Flame by an Image Processing Technique," Bull. JSME, **54**, pp. 741–748.

Mixed Convection on the Stagnation Point Flow Toward a Vertical, Continuously Stretching Sheet

A. Ishak

R. Nazar[1]
e-mail: rmn72my@yahoo.com

School of Mathematical Sciences,
Faculty of Science and Technology,
Universiti Kebangsaan Malaysia,
43600 UKM Bangi, Selangor, Malaysia

I. Pop
Faculty of Mathematics,
University of Cluj,
R-3400 Cluj CP 253, Romania

The stagnation point flow toward a stretching vertical sheet is investigated in this study. The temperature and velocity of the sheet as well as the velocity of the external flow are assumed to vary in a power law with the distance from the stagnation point. The governing system of equations is first transformed into a dimensionless form, and then the resulting equations are solved numerically by a finite-difference method. The features of the flow and heat transfer characteristics for different values of the governing parameters are analyzed and discussed. Both assisting and opposing flows are considered. It is found that, for opposing flow, dual solutions exist in the neighborhood of the separation region, whereas for assisting flow the solution is unique.
[DOI: 10.1115/1.2737482]

Keywords: mixed convection, stagnation point, stretching sheet, dual solutions

1 Introduction

The flow near a stagnation point has wide industrial and technical applications, such as cooling of electronic devices by fans, cooling of nuclear reactors during emergency shutdown, heat exchangers placed in a low-velocity environment, solar central receivers exposed to wind currents, and many hydrodynamic processes. The combined forced and free convection (mixed convection) flow is important when the buoyancy forces due to the temperature difference between the surface and the freestream become large, which in turn significantly affected the flow and the thermal fields. The study of free (natural) convection, forced convection or the combination of both convections has attracted many investigations until recently (see e.g. [1,2]). Ramachandran et al. [3] studied laminar mixed convection in two-dimensional stagnation flows around heated surfaces at rest. They found that a reverse flow develops in the buoyancy opposing flow region, and dual solutions are found to exist for a certain range of the buoyancy parameter.

In this note, we present an analysis that may be regarded as the extension of Chen [4], by considering external flow impinging normally toward the stretching vertical surface. The boundary and external flow velocities as well as the surface temperature are assumed to vary in a power law with the distance from the stagnation point.

2 Mathematical Formulation

Consider the steady, two-dimensional stagnation flow normal to a stretching sheet immersed in an incompressible viscous fluid. The temperature and velocity of the sheet as well as the velocity of the external flow are assumed to vary in a power law with the distance from the stagnation point, i.e., $T_w(x)=T_\infty+ax^n$, $u_w(x)=bx^m$ and $u_e(x)=cx^m$, respectively, where a, b, and c are constants and m and n are the exponents. Under these assumptions along with the Boussinesq and boundary layer approximations, the equations that model the problem under consideration are

$$\frac{\partial u}{\partial x}+\frac{\partial v}{\partial y}=0 \tag{1}$$

$$u\frac{\partial u}{\partial x}+v\frac{\partial u}{\partial y}=u_e\frac{du_e}{dx}+\nu\frac{\partial^2 u}{\partial y^2}+g\beta(T-T_\infty) \tag{2}$$

$$u\frac{\partial T}{\partial x}+v\frac{\partial T}{\partial y}=\alpha\frac{\partial^2 T}{\partial y^2} \tag{3}$$

subject to the boundary conditions

$$u=u_w(x),\quad v=0,\quad T=T_w(x)\quad \text{at}\quad y=0$$

$$u\to u_e(x),\quad T\to T_\infty\quad \text{as}\quad y\to\infty \tag{4}$$

The continuity equation can be satisfied by introducing a stream function ψ, such that $u=\partial\psi/\partial y$ and $v=-\partial\psi/\partial x$. The momentum and energy equations can be transformed into the corresponding ordinary differential equations by the following dimensionless similarity variables (see [4]):

$$\eta=\left[\frac{u_w(x)}{\nu x}\right]^{1/2}y$$

$$f(\eta)=\frac{\psi(x,y)}{[\nu x u_w(x)]^{1/2}}$$

$$\theta(\eta)=\frac{T-T_\infty}{T_w-T_\infty} \tag{5}$$

The transformed ordinary differential equations are

$$f'''+\frac{m+1}{2}ff''-mf'^2+m\epsilon^2+\lambda\theta=0 \tag{6}$$

$$\frac{1}{\mathrm{Pr}}\theta''+\frac{m+1}{2}f\theta'-nf'\theta=0 \tag{7}$$

Here, primes denote differentiation with respect to η, $\epsilon=c/b$ is the velocity ratio parameter, $\mathrm{Pr}=\nu/\alpha$ is the Prandtl number, $\mathrm{Gr}_x=g\beta(T_w-T_\infty)x^3/\nu^2$ is the local Grashof number, and $\mathrm{Re}_x=u_w x/\nu$ is the local Reynolds number. It can be shown that λ is independent of x if $n=2m-1$. Thus, when $\lambda\neq 0$, the similarity solutions are obtained under this limitation. Now, Eq. (7) becomes

$$\frac{1}{\mathrm{Pr}}\theta''+\frac{m+1}{2}f\theta'-(2m-1)f'\theta=0 \tag{8}$$

The transformed boundary conditions are

$$f(0)=0,\quad f'(0)=1,\quad \theta(0)=1$$

$$f'(\eta)\to 0,\quad \theta(\eta)\to 0\quad \text{as}\quad \eta\to\infty \tag{9}$$

Furthermore, $\lambda>0$ and $\lambda<0$ correspond to the assisting (aiding) and opposing flows, respectively. It is worth mentioning that for

[1]Corresponding author.

Contributed by the Heat Transfer Division of ASME for publication in the JOURNAL OF HEAT TRANSFER. Manuscript received September 4, 2006; final manuscript received December 19, 2006. Review conducted by Ranga Pitchumani.

Table 1 Values of the local Nusselt number $-\theta'(0)$ for various values of Pr and n when $\lambda=0$, $\epsilon=0$, and $m=1$

	Chen [4]			Grubka and Bobba [6]			Present results		
n	Pr=1	Pr=3	Pr=10	Pr=1	Pr=3	Pr=10	Pr=1	Pr=3	Pr=10
−2	−1.00003	−3.00046	−10.0047	−1.0000	−3.0000	−10.0000	−1.0000	−3.0000	−10.0000
−1	—	—	—	0.0	0.0	0.0	0.0	0.0	0.0
0	0.58199	1.16523	2.30796	0.5820	1.1652	2.3080	0.5820	1.1652	2.3080
1	—	—	—	1.0000	1.9237	3.7207	1.0000	1.9237	3.7207
2	1.33334	2.509972	4.79686	1.3333	2.5097	4.7969	1.3333	2.5097	4.7969

$\lambda=0$, Eqs. (6) and (8) are decoupled and this case corresponds to the forced convection flow past a stretching sheet.

We note that in the absence of the external flow ($c=0$), Eqs. (6) and (8) reduce to those of Chen [4], while when both external flow and buoyancy force are absent, the analytical solution of Eq. (6) for $m=1$ is given by Crane [5], and the analytical solution of Eq. (8) can be found in Grubka and Bobba [6]. On the other hand, when $\lambda=0$ and $\epsilon=1$, the solution of Eq. (6) subjected to (9) is given by

$$f(\eta)=\eta \tag{10}$$

Integrating Eq. (8) subject to the boundary conditions (9) gives

$$-\theta'(0)=\frac{5m-1}{2}\mathrm{Pr}\int_0^\infty f'\,\theta d\eta \tag{11}$$

which represents the heat transfer rate at the surface. From Eq. (11), $m=1/5$ represents a stretching surface subject to an adiabatic situation, i.e., $-\theta'(0)=0$.

3 Results and Discussion

Equations (6) and (8) subject to the boundary conditions (9) have been solved numerically for some values of parameters using the Keller-box method. For simplicity, we considered Prandtl number unity throughout the paper, except for comparisons to the previously investigated cases from open literature. The comparisons of the values of the local Nusselt number and the skin friction coefficient in terms of $-\theta'(0)$ and $f''(0)$ are shown in Tables 1 and 2, respectively. The results are found to be in very good agreement.

Figure 1 shows the numerical results of the dimensionless skin friction coefficient as a function of λ for various values of the velocity exponent parameter m when Pr=1 and $\epsilon=1$, while the respective local Nusselt number is presented in Fig. 2. It is seen from Fig. 1 that the values of $f''(0)$ are positives for the assisting flow, whereas they are negatives for the opposing flow. Physically, positive sign of $f''(0)$ implies that the fluid exerts a drag force on the sheet and negative sign implies the opposite. Moreover, all curves intersect at a point where $\lambda=0$, i.e., when the buoyancy force is lacking. The value of $f''(0)$ at this point is zero. This is not surprising since Eqs. (6) and (8) are decoupled when $\lambda=0$, and the stretching velocity is equal to the external velocity when $\epsilon=1$, which implies zero skin friction. This result is in agreement with the exact solution (10), which implies $f''(\eta)=0$, for all η. The zero skin friction here does not mean separation, but corresponds to the situation when the sheet and the fluid move with the same velocity. In contrast, Fig. 2 shows that there are heat transfers from the sheet to the fluid even when the skin friction is zero for $m\neq 0.2$, because the sheet and the fluid are at different temperatures. An interesting result is found when $m=0.2$; that is, $-\theta'(0)=0$, which indicates no local heat transfer at the surface of the stretching sheet for all $x>0$ even they are at different temperatures. This result is in agreement with Eq. (11). The paradox is resolved by recalling that the similarity solution requires a singular behavior of the temperature at $x=0$, cf. $T_w(x)=T_\infty+bx^{2m-1}$. Nevertheless, although dissipation has been neglected, the temperature of the fluid keeps changing during the flow process. Thus, all the necessary heat to change the fluid temperature must be transferred at the singular point $x=0$ [11,12].

Figures 1 and 2 show the existence of dual solutions in the neighborhood of the separation region. The solution for a particular value of m exists up to a critical value of λ (λ_c say). Beyond this value, the boundary layer separates from the surface; thus, we are unable to get the solution using the boundary layer approximations. To obtain further solution, the full Navier-Stokes equation has to be used. It is evident from Figs. 1 and 2 that larger values of m delay the boundary layer separation. The curve for a particular value of m bifurcates at $\lambda=\lambda_c$, and the lower branch solution continues further and terminates at a certain value of λ. It should be remarked that the computations have been performed until the point where the solution does not converge, and the calculations were terminated at that point. Figures 3 and 4 present the velocity and temperature profiles for selected values of parameters, which support the dual nature of the solutions presented in Figs. 1 and 2. Furthermore, Fig. 3 shows that there exist a region of reversed flow located away from the sheet.

Figures 5 and 6 present the numerical solutions of the skin friction coefficient and the local Nusselt number for various values of the velocity ratio parameter ϵ. The results for $\epsilon=0$ are qualitatively in good agreement with those obtained by Chen [4]. It is evident from Figs. 5 and 6 that the boundary layer separation can be delayed by increasing the velocity of the external flow in comparison with the velocity of the stretching sheet. As mentioned previously, dual solutions are found to exist in the neighborhood of the separation region, which gives an early sign that the flow is unstable and in transition to become turbulent.

Table 2 Values of the skin friction coefficient $f''(0)$ for various values of ϵ when $\lambda=0$ and $m=0$

ϵ	Mahapatra and Gupta [7]	Nazar et al. [8]	Nazar et al. [9]	Ishak et al. [10]	Present results
0.1	−0.9694	−0.9694	−0.9694	−0.9694	−0.9694
0.2	−0.9181	−0.9181	−0.9181	−0.9181	−0.9181
0.5	−0.6673	−0.6673	−0.6673	−0.6673	−0.6673
2	2.0175	2.0176	2.0176	2.0175	2.0175
3	4.7293	4.7296	4.7296	4.7294	4.7294

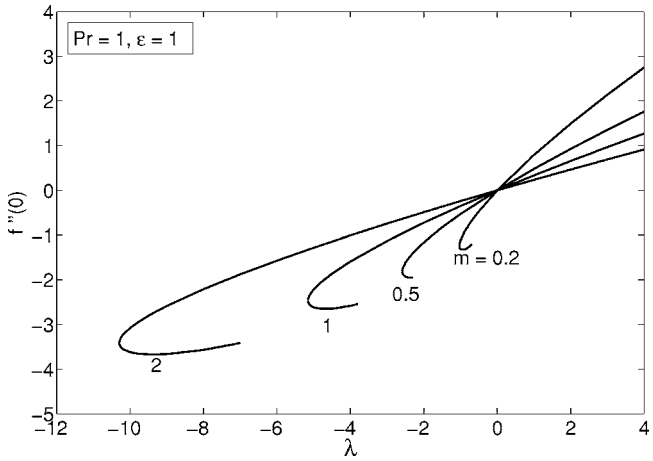

Fig. 1 Plot of $f''(0)$ versus λ for Pr=1 and ϵ=1

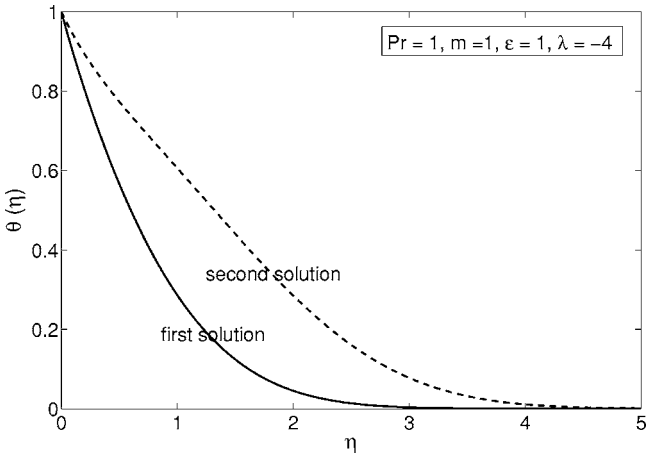

Fig. 4 Plot of $\theta(\eta)$ versus η for Pr=1, m=1, ϵ=1 and λ=–4

4 Conclusions

The effects of governing parameters such as m, n, ϵ, and λ on the flow and heat transfer characteristics are examined for a fixed value of Pr, namely, Pr=1. Similarity solutions are obtained in the presence of buoyancy force if $n=2m-1$. Dual solutions are found to exist in the neighborhood of the separation region. Boundary layer separation for the case of opposing flow can be delayed by increasing the value of m or ϵ. Both the skin friction coefficient and the local Nusselt number increase as the buoyancy parameter λ increases. For m=0.2 (i.e., n=–0.6), although the surface temperature is different from the freestream temperature, there is no local heat transfer at the surface except at the singular point, i.e., stagnation point.

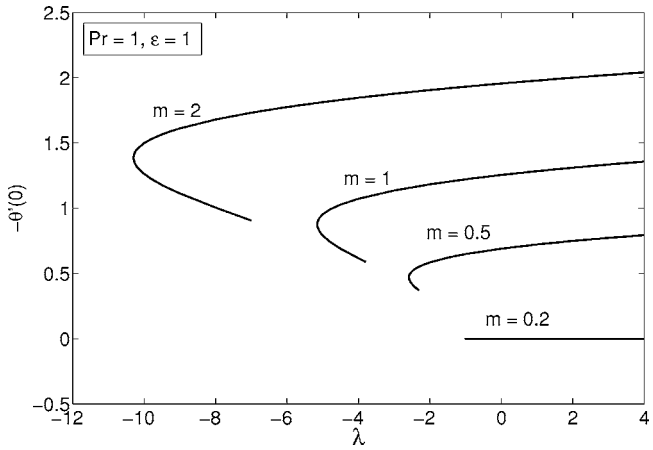

Fig. 2 Plot of $-\theta'(0)$ versus λ for Pr=1 and ϵ=1

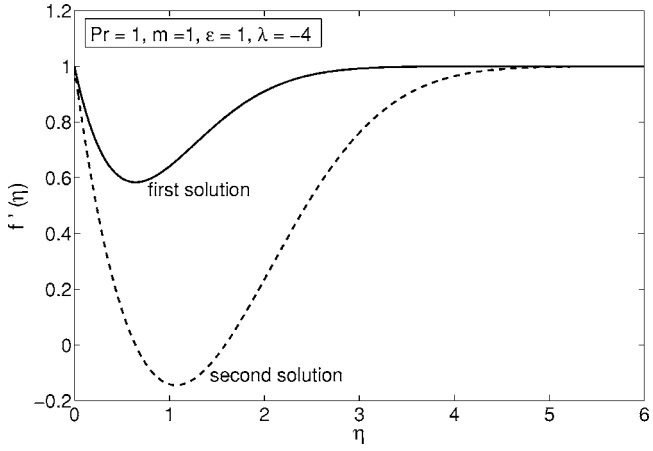

Fig. 3 Plot of $f'(\eta)$ versus η for Pr=1, m=1, ϵ=1 and λ=–4

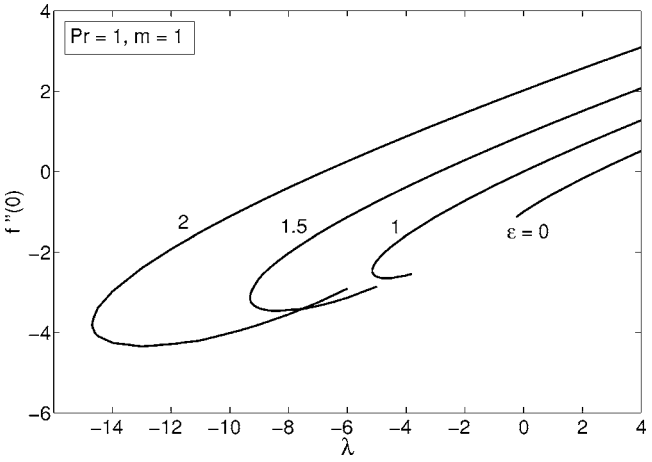

Fig. 5 Plot of $f''(0)$ versus λ for Pr=1 and m=1

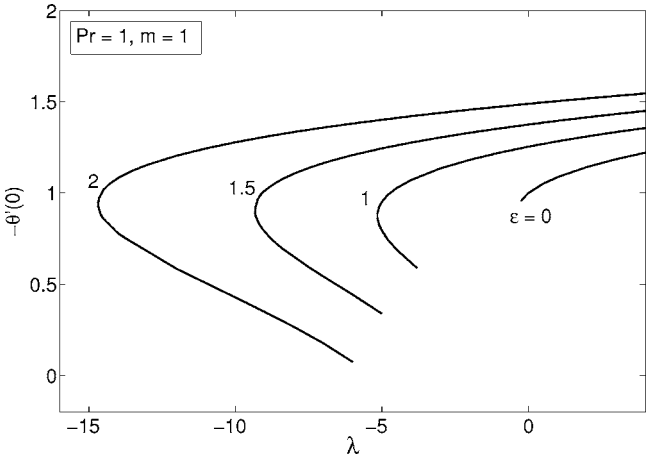

Fig. 6 Plot of $-\theta'(0)$ versus λ for Pr=1 and m=1

Acknowledgment

The authors wish to express their very sincere thanks to the reviewers for their valuable time spent reading this paper and for their valuable comments. This work is supported by a research grant (IRPA Project Code No. 09-02-02-10038-EAR) from the Ministry of Science, Technology and Innovation (MOSTI), Malaysia.

Nomenclature

a, b, c = constants
f = dimensionless stream function
g = acceleration due to gravity
Gr_x = local Grashof number
m = velocity exponent parameter
n = temperature exponent parameter
Nu_x = local Nusselt number
Pr = Prandtl number
Re_x = local Reynolds number
T = fluid temperature
$T_w(x)$ = temperature of the stretching sheet
T_∞ = ambient temperature
u, v = velocity components along the x and y directions, respectively
$u_e(x)$ = velocity of the external flow
$u_w(x)$ = velocity of the stretching sheet
x, y = Cartesian coordinates along the surface and normal to it, respectively

Greek Symbols

α = thermal diffusivity
β = thermal expansion coefficient
ϵ = velocity ratio parameter
η = similarity variable
θ = dimensionless temperature
λ = buoyancy or mixed convection parameter
μ = dynamic viscosity
ν = kinematic viscosity
ρ = fluid density
ψ = stream function

Subscripts

w = condition at the stretching sheet
∞ = condition far from the stretching sheet

Superscript

$'$ = differentiation with respect to η

References

[1] Saeid, N. H., 2006, "Natural Convection From Two Thermal Sources in a Vertical Porous Layer," ASME J. Heat Transfer, **128**, pp. 104–109.
[2] Roy, S., and Anilkumar, D., 2006, "Unsteady Mixed Convection From a Moving Vertical Slender Cylinder," ASME J. Heat Transfer, **128**, pp. 368–373.
[3] Ramachandran, N., Chen, T. S., and Armaly, B. F., 1988, "Mixed Convection in Stagnation Flows Adjacent to Vertical Surfaces," ASME J. Heat Transfer, **110**, pp. 373–377.
[4] Chen, C.-H., 1998, "Laminar Mixed Convection Adjacent to Vertical, Continuously Stretching Sheets," Heat Mass Transfer, **33**, pp. 471–476.
[5] Crane, L. J., 1970, "Flow Past a Stretching Plane," Z. Angew. Math. Phys., **21**, pp. 645–647.
[6] Grubka, L. G., and Bobba, K. M., 1985, "Heat Transfer Characteristics of a Continuous Stretching Surface With Variable Temperature," ASME J. Heat Transfer, **107**, pp. 248–250.
[7] Mahapatra, T. R., and Gupta, A. S., 2002, "Heat Transfer in Stagnation-Point Flow Towards a Stretching Sheet," Heat Mass Transfer, **38**, pp. 517–521.
[8] Nazar, R., Amin, N., Filip, D., and Pop, I., 2004, "Stagnation Point Flow of a Micropolar Fluid Towards a Stretching Sheet," Int. J. Non-Linear Mech., **39**, pp. 1227–1235.
[9] Nazar, R., Amin, N., Filip, D., and Pop, I., 2004, "Unsteady Boundary Layer Flow in the Region of the Stagnation Point on a Stretching Sheet," Int. J. Eng. Sci., **42**, pp. 1241–1253.
[10] Ishak, A., Nazar, R., and Pop, I., 2006, "Magnetohydrodynamic Stagnation-Point Flow Towards a Stretching Vertical Sheet," Magnetohydrodynamics, **42**, pp. 17–30.
[11] Schneider, W., 1979, "A Similarity Solution for Combined Forced and Free Convection Flow Over a Horizontal Plate," Int. J. Heat Mass Transfer, **22**, pp. 1401–1406.
[12] Ishak, A., Nazar, R., and Pop, I., 2006, "The Schneider Problem for a Micropolar Fluid," Fluid Dyn. Res., **38**, pp. 489–502.

Mixed Convection in a Vertical Parallel Plate Microchannel With Asymmetric Wall Heat Fluxes

Mete Avcı

Orhan Aydın[1]
e-mail: oaydin@ktu.edu.tr

Department of Mechanical Engineering,
Karadeniz Technical University,
61080 Trabzon, Turkey

In this study, exact analytical results are presented for fully developed mixed convective heat transfer of a Newtonian fluid in an open-ended vertical parallel plate microchannel with asymmetric wall heating at uniform heat fluxes. The velocity slip and the temperature jump at the wall are included in the formulation. The effects of the modified mixed convection parameter, $\mathrm{Gr}_q/\mathrm{Re}$*, the Knudsen number, Kn, and the ratio of wall heat flux,* $r_q=q_1/q_2$*, on the microchannel hydrodynamic and thermal behaviors are determined. Finally, a* $\mathrm{Nu}=f(\mathrm{Gr}_q/\mathrm{Re},\mathrm{Kn},r_q)$ *expression is developed. For, the limiting case of* $\mathrm{Kn}=0$*, the results are found to be in an excellent agreement with those in the existing literature.*
[DOI: 10.1115/1.2737483]

Keywords: microfluidics, vertical microchannel, mixed convection, temperature jump, velocity slip

1 Introduction

With the rapid growth of novel techniques applied in microelectromechanical systems (MEMS) and biomedical applications, such as drug delivery, DNA sequencing, and bio-MEMS, the microfluidics become an important research area in recent years. Aydın and Avcı [1–4] theoretically studied forced convective heat transfer in two different microgeometries, mainly microtube and microduct between two parallel plates, both for the fully developed and for the developing cases.

Although there are many studies on forced convection in microchannels, there are only a few studies regarding natural or mixed convection. Chen and Weng [5] analytically studied the fully developed natural convection in an open-ended vertical parallel plate microchannel with asymmetric wall temperature distributions. The effects of rarefaction and fluid-wall interaction were shown to increase the volume flow and to decrease the heat transfer rate. Khadrawi et al. [6] analytically investigated the transient hydrodynamics and thermal behaviors of fluid flow in an open-ended vertical parallel-plate microchannel under the effect of the hyperbolic heat conduction model. Haddad et al. [7] numerically investigated the developing hydrodynamical behaviors of free convection gas flow in a vertical open-ended parallel-plate microchannel filled with porous media.

In a recent study, the present authors [8] studied mixed convection of rarefied gas in a vertical asymmetrically heated microchannel between two parallel plates. In that study, isothermal boundary conditions at walls were considered. In the present attempt, it is aimed at extending that study to the case at which constant wall heat fluxes are considered at walls. The effects of the modified mixed convection parameter, $\mathrm{Gr}_q/\mathrm{Re}$, the Knudsen number, Kn, and the ratio of wall heat flux, $r_q=q_1/q_2$, on the temperature profile and subsequently on the Nusselt, Nu, number are determined.

2 Analysis

Figure 1 illustrates the geometry considered, a microchannel between two parallel plates having asymmetric heat fluxes. Both hydrodynamically and thermally fully developed flow is assumed. Steady, laminar flow having constant properties is considered. The axial heat conduction in the fluid and in the wall is assumed to be negligible. In a similar manner followed in Ref. [8], the usual continuum approach is applied by the continuum equations with the two main characteristics of the microscale phenomena, the velocity slip and the temperature jump. Velocity slip is defined as [9]

$$u_s = -\frac{2-F}{F}\lambda \left.\frac{\partial u}{\partial y}\right|_{y=W} \tag{1}$$

where u_s is the slip velocity, λ is the molecular mean free path, and F is the tangential momentum accommodation coefficient, and the temperature jump is defined as [9]

$$T_s - T_w = -\frac{2-F_t}{F_t}\frac{2\gamma}{\gamma+1}\frac{\lambda}{\mathrm{Pr}}\left.\frac{\partial T}{\partial y}\right|_{y=W} \tag{2}$$

where T_s is the temperature of the gas at the wall, T_w is the wall temperature, and F_t is the thermal accommodation coefficient, which depends on the gas and surface material. Particularly for air, it assumes typical values near unity. For the rest of the analysis, F and F_t will be shown by F.

In a sufficient long channel, the velocity and the temperature profiles will cease to change with distance along the channel, i.e., a fully developed flow will exist [10]. Assuming hydrodynamically fully developed flow, the transverse velocity becomes equal to zero. Then, the continuity equation drops to $\partial u/\partial x=0$. Using the Boussinesq approximation, ignoring viscous dissipation (assuming a low-speed flow of a low-Pr fluid [5]) and substituting the above condition into the governing equations of the heat and fluid flow, we obtain

$$0 = -\frac{dp}{dx} + \mu\frac{\partial^2 u}{\partial y^2} \pm \beta g\rho(T - T_{s,1}) \tag{3}$$

$$u\frac{\partial T}{\partial x} = \frac{k}{\rho c_p}\frac{\partial^2 T}{\partial y^2} \tag{4}$$

The pressure p is thus measured relative to that which would exist at the same elevation in the stagnant fluid if it were at a uniform temperature of T_0 The positive sign in front of the buoyancy term applies to the buoyancy-assisted flow and the negative one applying to the buoyancy-opposed flow [10].

The boundary conditions for these equations are

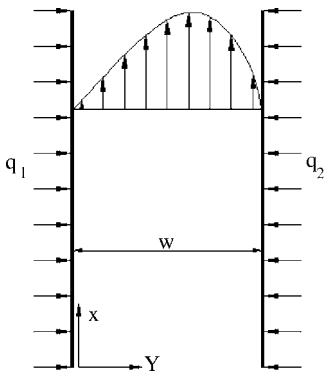

Fig. 1 Schematic diagram of the flow domain

[1]Corresponding author.

Contributed by the Heat Transfer Division of ASME for publication in the JOURNAL OF HEAT TRANSFER. Manuscript received May 29, 2006; final manuscript received October 26, 2006. Review conducted by Jay M. Khodadadi.

$$u = u_{s1} \quad \text{at} \quad y = 0$$

$$u = u_{s2} \quad \text{at} \quad y = W$$

$$\frac{\partial T}{\partial y} = -\frac{q_1}{k} \quad \text{at} \quad y = 0$$

$$\frac{\partial T}{\partial y} = \frac{q_2}{k} \quad \text{at} \quad y = W \tag{5}$$

For thermally developed flow,

$$\frac{\partial T}{\partial x} = \frac{q_1 + q_2}{\rho c_p u_m W} \tag{6}$$

By introducing the following nondimensional quantities,

$$X = \frac{x}{D_h \,\mathrm{Re}}, \quad Y = \frac{y}{D_h}, \quad r_q = \frac{q_1}{q_2}, \quad P = \frac{p + \rho g x}{\rho u_0^2},$$

$$\theta = \frac{T - T_{s,1}}{q_2 D_h / k}, \quad U = \frac{u}{u_0}$$

$$\mathrm{Kn} = \frac{\lambda}{D_h}, \quad \mathrm{Pr} = \frac{\mu c_p}{k}, \quad \mathrm{Gr}_q = \frac{g\beta q_2 D_h^4}{k\nu^2}, \quad \mathrm{Re} = \frac{u_0 D_h}{\nu}, \tag{7}$$

$$\beta_v = \frac{2 - F}{F}, \quad \beta_t = \frac{2 - F_t}{F_t}\frac{2\gamma}{\gamma + 1}\frac{1}{\mathrm{Pr}}$$

Equations (3) and (4) can be written as

$$-\frac{dP}{dX} + \frac{d^2U}{dY^2} + \frac{\mathrm{Gr}_q}{\mathrm{Re}}\theta = 0 \tag{8}$$

$$\frac{d^2\theta}{dY^2} = 2\left(1 + \frac{q_1}{q_2}\right) \tag{9}$$

In terms of the dimensionless variables introduced in Eq. (7), the boundary conditions given in Eq. (5) can be shown as

$$U = \beta_v \,\mathrm{Kn}\frac{dU}{dY} \quad \text{at} \quad Y = 0$$

$$U = -\beta_v \,\mathrm{Kn}\frac{dU}{dY} \quad \text{at} \quad Y = 0.5$$

Table 1 Typical values of constants C_1, C_2, C_3, and C_4

		$r_q = 0.0$			
$\mathrm{Gr}_q/\mathrm{Re}$	Kn	C_1	C_2	C_3	C_4
	0.00	3.56532	−3.56532	−13.38252	20.51316
1	0.02	2.97156	−2.77816	−10.78692	16.53665
	0.06	2.28121	−1.86303	−7.76875	11.91299
	0.10	1.89216	−1.34734	−6.06755	9.30705
	0.00	1.29901	−1.29901	−0.94282	3.54083
50	0.02	1.13344	−0.94733	−0.72772	2.80849
	0.06	0.94099	−0.54284	−0.47635	1.96018
	0.10	0.83253	−0.31800	−0.33367	1.48420
	0.00	1.05750	−1.05750	−0.41937	2.53437
100	0.02	0.93062	−0.75168	−0.29550	1.97780
	0.06	0.78272	−0.40403	−0.14962	1.33636
	0.10	0.69901	−0.21364	−0.06600	0.97864
			$r_q = 0.5$		
	0.00	3.14584	−3.14584	−10.56372	17.16560
1	0.02	2.61851	−2.42500	−8.50416	13.85787
	0.06	2.00538	−1.58690	−6.10936	10.01184
	0.10	1.65983	−1.11458	−4.75956	7.84418
	0.00	1.00047	−1.00047	−0.60638	3.43220
50	0.02	0.85921	−0.66729	−0.45242	2.80379
	0.06	0.69508	−0.28235	−0.27305	2.07535
	0.10	0.60259	−0.06705	−0.17163	1.66614
	0.00	0.76537	−0.76537	−0.21609	2.72778
100	0.02	0.65912	−0.46864	−0.13323	2.24193
	0.06	0.53554	−0.12801	−0.03637	1.68086
	0.10	0.46578	0.06109	0.01867	1.36697
			$r_q = 1.0$		
	0.00	2.87634	−2.87634	−8.90402	15.15670
1	0.02	2.39220	−2.19857	−7.16036	12.25113
	0.06	1.82928	−1.41051	−5.13293	8.87272
	0.10	1.51201	−0.96634	−3.99024	6.96858
	0.00	0.82091	−0.82091	−0.42563	3.39702
50	0.02	0.69563	−0.49796	−0.30682	2.82999
	0.06	0.55026	−0.12322	−0.16895	2.17201
	0.10	0.46847	0.08763	−0.09137	1.80179
	0.00	0.59553	−0.59553	−0.11637	2.88858
100	0.02	0.50312	−0.30136	−0.05680	2.44242
	0.06	0.39610	0.03930	0.01218	1.92576
	0.10	0.33599	0.23064	0.05093	1.63556

$$\frac{d\theta}{dY} = -\frac{q_1}{q_2} = -r_q \quad \text{at} \quad Y = 0$$

$$\frac{d\theta}{dY} = 1 \quad \text{at} \quad Y = 0.5 \tag{10}$$

Equation (8) can be rewritten to give θ as

$$\theta = \frac{\mathrm{Re}}{\mathrm{Gr}_q}\left(\frac{dP}{dX} - \frac{d^2U}{dY^2}\right) \tag{11}$$

By double-differentiating Eq. (8) with respect to Y and using Eq. (9), one obtains the fourth-order differential equation

$$\frac{d^4U}{dY^4} = -2\frac{\mathrm{Gr}_q}{\mathrm{Re}}\left(1 + \frac{q_1}{q_2}\right)U \tag{12}$$

or

$$\frac{d^4U}{dY^4} = -4\xi^4 U \quad \text{where} \quad \xi = \left[\frac{\mathrm{Gr}_q}{2\ \mathrm{Re}}\left(1 + \frac{q_1}{q_2}\right)U\right]^{1/4} \tag{13}$$

The parameter ξ is real since $q_2 \geq |q_1|$ (i.e., the net heating effect is positive). The general solution of Eq. (13), therefore, leads to the following velocity profile:

$$U = C_1 e^{\xi Y}\cos(\xi Y) + C_2 e^{-\xi Y}\cos(\xi Y) + C_3 e^{\xi Y}\sin(\xi Y) + C_4 e^{-\xi Y}\sin(\xi Y) \tag{14}$$

By applying the boundary conditions given in Eq. (10), the four unknown constants C_1, C_2, C_3, and C_4 can be obtained. Some typical values of these constants for different values of $\mathrm{Gr}_q/\mathrm{Re}$, Kn and r_q are tabulated in Table 1.

Once the velocity profile is obtained, Eq. (3) is applied at $Y = 0$ and yields the pressure gradient

$$\frac{dP}{dx} = 2\xi^2(C_3 - C_4) \tag{15}$$

Substituting Eqs. (14) and (15) into the energy equation, Eq. (11), gives

$$\theta = -\frac{\mathrm{Re}}{\mathrm{Gr}_q}\{2\xi^2 e^{-\xi Y}[(C_4 - C_3)e^{\xi Y} + (C_3 e^{2\xi Y} - C_4)\cos(\xi Y) + (C_2 - C_1 e^{2\xi Y})\sin(\xi Y)]\} \tag{16}$$

Taking the temperature jump into consideration, Eq. (16) becomes

$$\theta^* = \frac{T - T_1}{q_2 D_h/k} = \frac{(T - T_{s,1})}{q_2 D_h/k} + \frac{(T_{s,1} - T_1)}{q_2 D_h/k} = \frac{\mathrm{Re}}{\mathrm{Gr}_q}\{2\xi^2 e^{-\xi Y}[(C_4 - C_3)e^{\xi Y} + (C_3 e^{2\xi Y} - C_4)\cos(\xi Y) + (C_2 - C_1 e^{2\xi Y})\sin(\xi Y)]\} - \beta_t\,\mathrm{Kn}(q_1/q_2) \tag{17}$$

Using Eq. (17), the dimensionless mean/bulk temperature is defined as

$$\theta_m^* = \frac{T_m - T_1}{(q_2 D_h/k)} = \frac{\int_0^{0.5} U\theta^* dY}{\int_0^{0.5} U dY} \tag{18}$$

The convective heat transfer coefficients at the left-hand side and right-hand side walls can be obtained as follows:

$$h_1 = \frac{-k\,(\partial T/\partial y)\big|_{y=0}}{T_1 - T_m} = -\frac{1}{\theta_m^*}\frac{k(q_1/q_2)}{D_h}$$

$$h_2 = \frac{k\,(\partial T/\partial y)\big|_{y=W}}{T_2 - T_m} = -\frac{k\,(\partial T/\partial y)\big|_{y=W}}{(T_m - T_1) - (T_{s,2} - T_1) + (T_{s,2} - T_2)} = -\frac{k/D_h}{\theta_m^* - \theta^*(0.5) - \beta_t\,\mathrm{Kn}} \tag{19}$$

Similarly, the Nusselt numbers at the left-hand side and right-hand side walls can be written as, respectively,

$$\mathrm{Nu}_1 = -\frac{(q_1/q_2)}{\theta_m^*} \tag{20}$$

$$\mathrm{Nu}_2 = -\frac{1}{\theta_m^* - \theta^*(0.5) - \beta_t\,\mathrm{Kn}} \tag{21}$$

3 Results and Discussion

In this study, we investigate the interactive effects of the modified mixed convection parameter, $\mathrm{Gr}_q/\mathrm{Re}$, the Knudsen number, Kn, and the ratio of wall heat flux, q_1/q_2, on heat and fluid flow in a microchannel between two parallel plates with asymmetrical heating for both hydrodynamically and thermally fully developed case. The Knudsen number is the ratio of the gas mean free path λ to the characteristic dimension in the flow field D_h and determines the degree of rarefaction and the degree of the validity of the continuum approach. As Kn increases, rarefaction become more

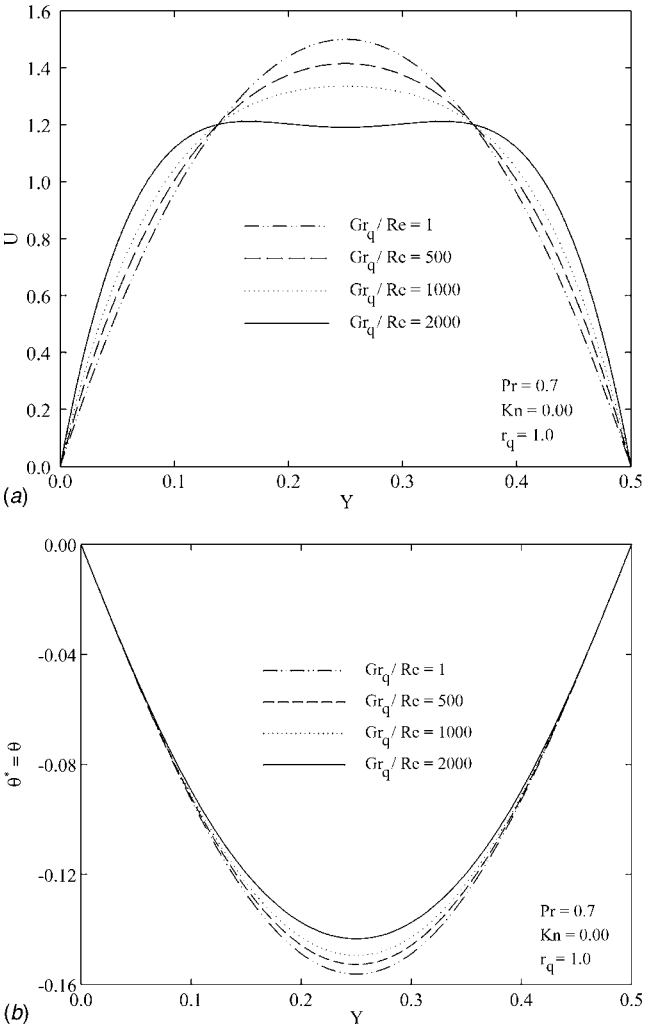

Fig. 2 Velocity (*a*) and temperature (*b*) distributions as a function $\mathrm{Gr}_q/\mathrm{Re}$ for Kn=0 and r_q=1

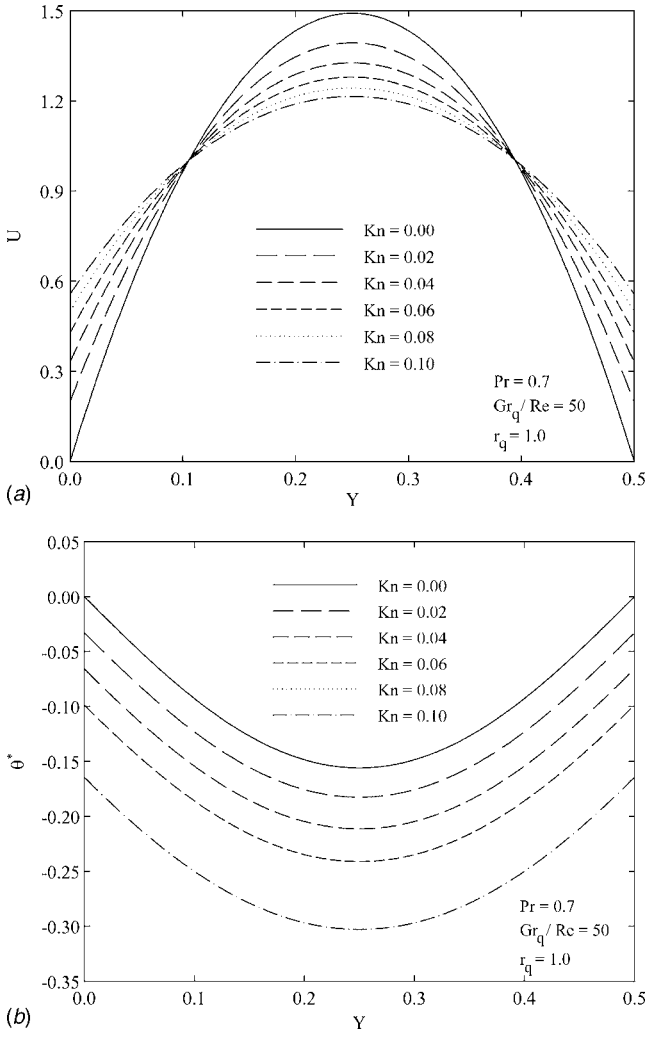

Fig. 3 Velocity and temperature distributions as a function Kn for $Gr_q/Re=50$ at $r_q=1$

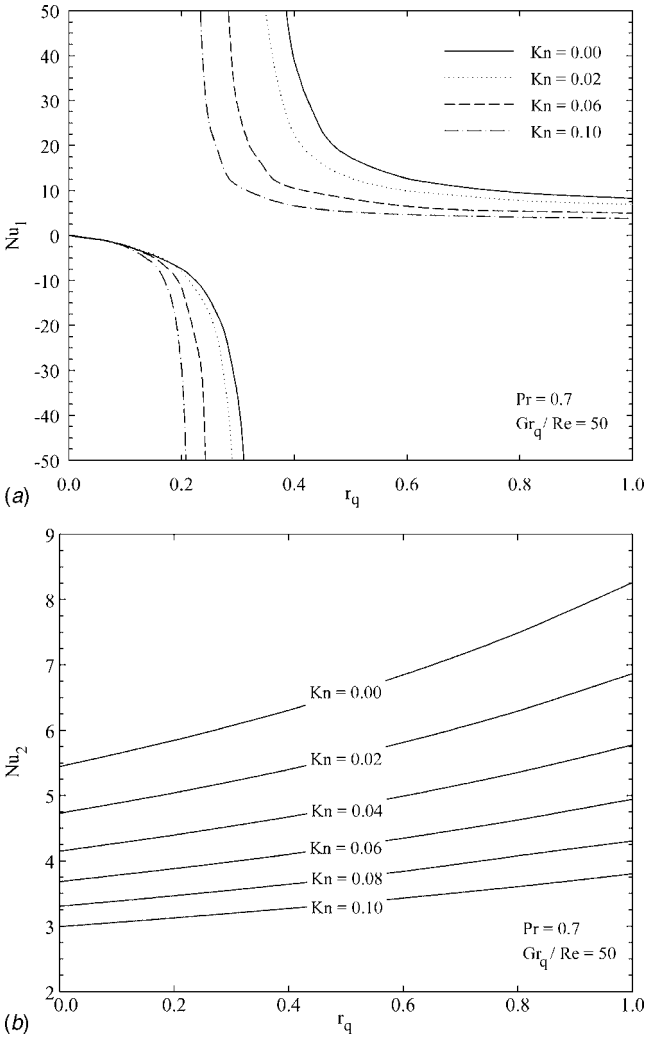

Fig. 5 The variation of the Nu_1 (*a*) and Nu_2 (*b*) with the r_q at different values of Kn for $Gr_q/Re=50$

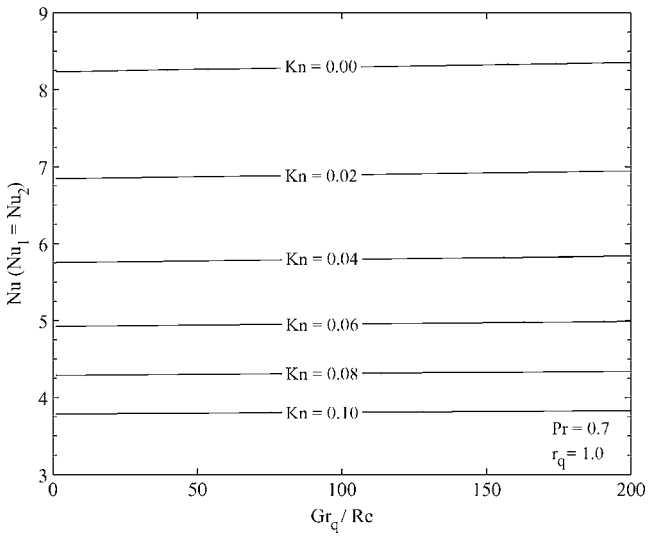

Fig. 4 The variation of the Nu with the Gr_q/Re at different values of Kn for $r_q=1$

important, and eventually the continuum approach breaks down. In this study, we examined Knudsen number values in the range of $0 \leqslant Kn \leqslant 0.1$. In the range of $0.001 \leqslant Kn \leqslant 0.1$, the slip-flow regime (slightly rarefied) is disclosed to exist. We covered the following values of the modified mixed convection parameter: $Gr_q/Re=1$, 50, 100, 200, 1000, and 2000. The working fluid is considered as air with a Prandtl number of 0.7. The regarding value of β_i is calculated to be 1.667.

At first, we validated our analysis by comparing limiting results for the case of Kn=0 to those available in the existing literature. For $r_q=1$, Fig. 2 shows velocity and temperature profiles for Kn =0, which are exactly identical to those given by Boulama and Galanis [11]. As expected, for $r_q=1$, both velocity and temperature profiles are symmetrical. An increase in Gr_q/Re results in flow acceleration near the walls and consequently flow deceleration in the centerline of the channel. In addition, for $r_q=1$, the Nusselt numbers are obtained for $Gr_q/Re=1000$ and 2000 as 8.819 and 9.377, respectively. These two values agree excellently with those obtained in [11].

At microscale, for $Gr_q/Re=50$, the influence of Kn on the velocity and temperature profiles is illustrated for $r_q=1$ in Fig. 3. It can be seen that increasing Kn increases velocity slips at the walls and decreases the maximum velocity.

At $r_q=1$, the variation of Nu with Gr_q/Re is plotted for different values of Kn in Fig. 4. As expected, increasing Gr_q/Re in-

creases Nu, whereas increasing Kn decreases Nu. Because of the lower values of the Gr_q/Re present at microscale, the aiding effect of the buoyancy forces on the inertia forces are not much. Therefore, increasing Gr_q/Re in this limited range will not have a profound effect on Nu. For example, at Kn=0.02, increasing Gr_q/Re from 1 to 200 will lead to an increase of ~2% in Nu. Similarly, at $Gr_q/Re=50$, the variation of Nu with r_q is shown for different values of Kn at each wall in Fig. 5. For Nu at the left-hand side wall, we observe a singular point at r_q (Fig. 5(*a*)). At this singular value of r_q, the temperature at the left-hand side wall is equal to that of the bulk fluid. The singular value of r_q decreases with increasing Kn. From Fig. 5(*b*), it is observed that Nu at the right-hand side wall increases with increasing r_q, as expected, since the temperature at the right-hand side-wall is always higher than the temperature of the bulk fluid ($q_2 > q_1$).

Acknowledgment

The authors greatly acknowledge the financial support of this work by the Scientific and Technological Research Council of Turkey (TUBITAK) under Grant No. 104M436.

Nomenclature

c_p = specific heat at constant pressure (J/kg K)
D_h = hydraulic diameter=2 W (m)
g = gravitational acceleration (m/s^2)
Gr_q = Grashof number, Eq. (7)
F = tangential momentum accommodation coefficient
F_t = thermal accommodation coefficient
h = convective heat transfer coefficient (W/m^2 K)
k = thermal conductivity (W/m K)
Kn = Knudsen number=λ/D_h
Nu = Nusselt number=hD_h/k
p = static pressure (Pa)
P = dimensionless pressure=$(p+\rho gx)/\rho u_0^2$
Pr = Prandtl number
r_q = ratio of wall heat flux=q_1/q_2
Re = Reynolds number=$u_m D_h/\nu$
q = imposed heat flux (W/m^2)
T = temperature (K)
u = axial velocity (m/s)
U = dimensionless axial velocity
W = channel width (m)
x, y = axial and transverse coordinates (m)
X, Y = dimensionless axial and transverse coordinates $X=x/(D_h \mathrm{Re})$ and $Y=y/D_h$

Greek Symbols

β = thermal expansion coefficient (1/K)
β_{iv}, β_t = dimensionless variables, Eq. (7)
γ = specific heat ratio
λ = molecular mean free path
μ = dynamic viscosity (Pa s)
ρ = density (kg/m^3)
ν = kinematic viscosity (m^2/s)
θ = dimensionless temperature, Eq. (7)
θ^* = dimensionless temperature, Eq. (17)

Subscripts

0 = inlet properties of the fluid (i.e., at $x=0$)
1 = value on left wall (i.e., at $y=0$)
2 = value on right wall (i.e., at $y=W$)
m = mean value
s = fluid properties on wall
$s,1$ = fluid properties on left wall
$s,2$ = fluid properties on right wall
w = wall

References

[1] Aydın, O., and Avcı, M., 2006, "Heat and Fluid Flow Characteristics of Gases in Micropipes," Int. J. Heat Mass Transfer, **49**, pp. 1723–1730.
[2] Aydın, O., and Avcı, M., 2006, "Analsysis of Micro-Graetz Problem in a Microtube," Nanoscale Microscale Thermophy. Eng., **10**(4), pp. 345–358.
[3] Aydın, O., and Avcı, M., 2007, "Analysis of Laminar Heat Transfer in Micro-Poiseuille Flow," Int. J. Therm. Sci., **46**(1), pp. 30–37.
[4] Aydın, O., and Avcı, M., 2006, "Thermally Developing Flow in Microchannels," J. Thermophys. Heat Transfer, **20**(3), pp. 628–631.
[5] Chen, C. K., and Weng, H. C., 2005, "Natural Convection in a Vertical Microchannel," ASME J. Heat Transfer, **127**, pp. 1053–1056.
[6] Khadrawi, A. F., Othman, A., and Al-Nimr, M. A., 2005, "Transient Free Convection Fluid Flow in a Vertical Microchannel as Described by the Hyperbolic Heat Conduction Model," Int. J. Thermophys., **26**(3), pp. 905–918.
[7] Haddad, O. M., Abuzaid, M. M., and Al-Nimr, M. A., 2005, "Developing Free-Convection Gas Flow in a Vertical Open-Ended Microchannel Filled With Porous Media," Numer. Heat Transfer, Part A, **48**, pp. 693–710.
[8] Avcı, M., and Aydın, O., 2007, "Mixed Convection in a Vertical Parallel Plate Microchannel," ASME J. Heat Transfer, **129**(2), pp. 162–166.
[9] Gad-el-Hak, M., (ed.), 2001, *The MEMS Handbook*, CRC Press, New York.
[10] Oosthuizen, P. H., and Naylor, D., 1999, *Introduction to Convective Heat Transfer Analysis*, McGraw-Hill, New York, pp. 158–167.
[11] Boulama, K., and Galanis, N., 2004, "Analytical Solution for Fully Developed Mixed Convection Between Parallel Vertical Plates With Heat and Mass Transfer," ASME J. Heat Transfer, **126**, pp. 381–388.

Thermal Conductivity of Single-Walled Carbon Nanotube/PMMA Nanocomposites

Csaba Guthy
Materials Science and Engineering,
University of Pennsylvania,
3231 Walnut Street,
Philadelphia, PA 19104-6272

Fangming Du
Chemical and Biomolecular Engineering,
University of Pennsylvania,
220 South 33rd Street,
Philadelphia, PA 19104-6393

Stijn Brand
Materials Science and Engineering,
University of Pennsylvania,
3231 Walnut Street,
Philadelphia, PA 19104-6272

Karen I. Winey
Materials Science and Engineering,
University of Pennsylvania,
3231 Walnut Street,
Philadelphia, PA 19104-6272;
Chemical and Biomolecular Engineering,
University of Pennsylvania,
220 South 33rd Street,
Philadelphia, PA 19104-6393

John E. Fischer[1]
Materials Science and Engineering,
University of Pennsylvania,
3231 Walnut Street,
Philadelphia, PA 19104-6272
e-mail: fischer@seas.upenn.edu

Single-walled carbon nanotubes (SWNTs) are considered as promising filler materials for improving the thermal conductivity of conventional polymers. We carefully investigated the thermal conductivity of SWNT poly(methylmethacrylate) (PMMA) nanocomposites with random SWNT orientations and loading up to 9 vol % *using the comparative technique. The composites were prepared by coagulation and exhibit* ~250% *improvement in the thermal conductivity at* 9 vol %. *The experimental results were analyzed using the versatile Nielsen model, which accounts for many important factors, including filler aspect ratio and maximum packing fraction. In this work, the aspect ratio was determined by atomic force microscopy (AFM) and used as an input parameter in the Nielsen model. We obtained good agreement between our results and the predictions of the Nielsen model, which indicates that higher aspect ratio fillers are needed to achieve further enhancement. Our analysis also suggests that improved thermal contact between the SWNT network and the matrix material would be beneficial.* [DOI: 10.1115/1.2737484]

Keywords: heat transfer, SWNT/PMMA nanocomposites, Nielsen model, coagulation method, comparative method

Introduction

The exceptional thermal and mechanical properties of single walled carbon nanotubes (SWNTs) make them a promising filler material for polymer composites. Theoretically, the thermal conductivity κ of a (10,10) SWNT is 6000, W/mK higher than that of diamond [1]. In addition, due to the very large aspect ratio (of order 2000 [2]), the percolation threshold (the concentration at which the dispersed nanotubes start to form interconnected paths) for nanotube composites can be as low as 1% by volume. Based on this, theoretical models predict that an addition of even a small volume fraction of SWNTs would result in a significant increase of composite κ. However, experimental values for SWNT-polymer composites are generally lower than those predicted [2–5]. Several studies [6,7] suggested that large thermal resistance at the nanotube-polymer interface, and between the nanotubes themselves, limits κ. Experimental investigations of heat transport in these systems are still scarce, especially those with rigorous characterization of the nanotubes incorporated into the composites.

Significantly, an atomic force microscopy (AFM) study [8] showed that large SWNT aspect ratios are not preserved during composite processing. Our analysis based on the Nielsen model confirms that composite κ depends very sensitively on aspect ratio. Thus, κ measurements combined with complete characterization of nanotubes processed in the same way as for the composites is very important for understanding thermal transport in nanotube composites.

Sample Fabrication and Experimental Method

SWNT-PMMA composites with random SWNT orientations were prepared by coagulation [9]. Purified SWNTs are dispersed in dimethylformamide (DMF) using a sonication bath. In the next step, the quantity of PMMA needed to obtain the desired composition is dissolved in the SWNT/DMF suspension, which is then mixed with a large amount of distilled water in a blender. Due to insolubility of PMMA in the DMF/water mixture, the PMMA chains precipitate and trap the SWNT, preserving the dispersion of SWNT in the composite. The final raw SWNT/PMMA nanocomposites are obtained after filtration and drying in vacuum. Molded samples were cut to $2\times2\times1.7$ mm^3 using a diamond saw. The nanotubes were synthesized by the high-pressure CO (HiPCO) method at Rice University [10]. Composite samples were fabricated with SWNT loading as high as 9 vol %.

We used the comparative method [11] to measure κ. A heat flow Q passes through a constantan rod, then the sample, and finally a second constantan rod, to a heat sink. A chip resistor is used as a heater in order to establish a temperature gradient. Three differential type-E thermocouples using 0.0005 in. diam wire measure the temperature drops across the sample and the standards. The sample thermal conductance can be obtained by comparison to either of the two standards. Averaging of the two results approximately accounts for radiation losses, since one of the two standards is hotter or colder than the sample.

AFM Characterization of SWNT Suspension

We characterized the SWNT/DMF suspension with a Nanoscope III Multimode AFM in tapping mode in air. A silicon wafer with a layer of 3-aminopropyl triethoxy silane on top was used as substrate; the amine groups make the surface attractive to nanotubes [12]. To deposit the nanotubes, the wafer was dipped into

[1]Corresponding author.
Contributed by the Heat Transfer Division of ASME for publication in the JOURNAL OF HEAT TRANSFER. Manuscript received June 28, 2006; final manuscript received March 5, 2007. Review conducted by Yogesh Jaluria.

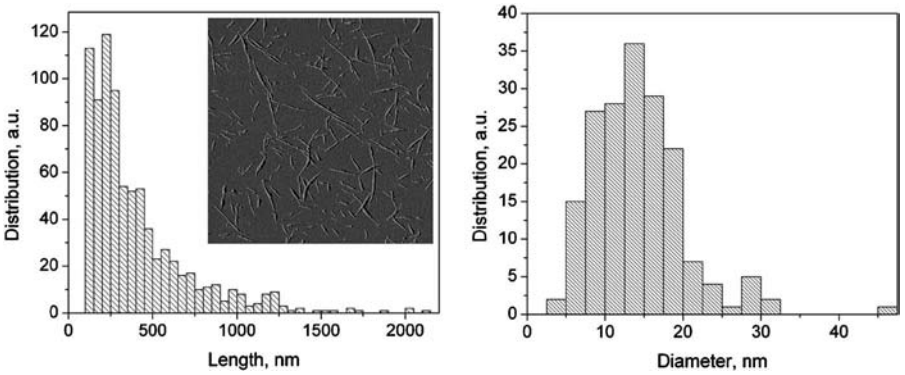

Fig. 1 Bundle length and diameter distributions of SWNT/DMF suspension used in the preparation of the composites. The length distribution was compiled from several 5 μm×5 μm AFM scans of surface treated Si wafers dipped into the SWNT/DMF solution. The diameter distribution is derived from a large number of line scans. The mean bundle diameter and length are 14.2 and 372 nm, respectively, giving an estimated aspect ratio of 26.

the prepared nanotube suspension in DMF. Dipping time was one second or less and the surface was immediately washed with methanol and blown dry with dry air. The short preparation time minimized nanotube reaggregation. Scans 5 μm×5 μm were taken with 512 pixels per scan line. This choice of the image size was a trade-off between undersampling of single tubes (due to resolution) and underestimating the true length distribution (due to small scan size). Length measurements were done in Adobe Photoshop (5.0.2) with the Measure Tool with an error of ±40 nm. The measurements of bundle diameter were done with Nanoscope (v5.12r2) software with an error of ±0.2 nm. Only tubular objects over 100 nm in length were measured. Figure 1 shows a scan and the corresponding length and diameter distributions. The mean bundle diameter is 14.2±6 nm. The mean length is 372 nm. Thus, we estimate the aspect ratio as 26. Assuming a circular cross section and the ideal hexagonal close packing, one can estimate that an average bundle consists of ~92 single tubes of 1.3 nm in diameter. In reality there are fewer tubes per cross section because of less than ideal packing. On the other hand, a bundle probably has a total of more than 92 tubes because they are not continuous from one end of a bundle to the other. This means that the effective κ of the filler (bundles) can be much lower than that for a single tube.

The Nielsen Model

Numerous models have been developed to predict κ of two-phase composites. The most basic models are the rule of mixtures and the inverse rule of mixtures. The rule of mixtures model (or series model) is the weighted average of matrix and filler thermal conductivities. This model works well for unidirectional composites with continuous fibers. The inverse rule of mixtures (parallel model) usually underestimates κ of short fiber composites. The more sophisticated heat transfer models can be categorized either as heat flux law models, where the temperature field is solved for an assumed geometry, or Ohm's law models based on electrical series resistance analogy.

We analyzed our experimental results based on the Nielsen model [13], which is one of the Ohm's law models. The Nielsen model is one of the most versatile for conductive short fiber/particulate systems. It accounts for almost all important factors including the constituent κ's, volume fraction, aspect ratio, orientation, and packing of the filler material. The model is based on the analogy of equations describing the elastic moduli of a composite, and the version for κ uses the versatile Halpin-Tsai equations as its basis. The equations for the two-phase systems are

$$\frac{\kappa_c}{\kappa_m} = \frac{1 + AB\phi_f}{1 - B\psi\phi_f} \tag{1}$$

$$A = k_E - 1 \tag{2}$$

$$B = \frac{\kappa_f/\kappa_m - 1}{\kappa_f/\kappa_m + A} \tag{3}$$

$$\psi = 1 + \left(\frac{1 - \phi_{\max}}{\phi_{\max}^2}\right)\phi_f \tag{4}$$

where the subscripts c, m, and f refer to composite, matrix, and filler, respectively. The constant A is related to the generalized Einstein coefficient k_E and depends on the shape of the dispersed filler and its orientation with respect to the heat flow. The factor B takes into account the relative thermal conductivity of the filler and matrix materials. The factor ψ determines the shape of the thermal conductivity curve versus filler volume fraction ϕ_f.

κ of a two-phase system should increase rapidly in the concentration range near the maximum packing fraction $\phi_{\max}$ due to the large number of filler-filler contacts. However, in the original Nielsen model, $\phi_{\max}$ for randomly oriented rods is 0.52 regardless of the aspect ratio. This is a reasonable choice for fillers with relatively small aspect ratio (<10). However, nanotubes usually have much larger aspect ratios. Milewski studied the three-dimensional packing of wooden rods and glass fibers of various aspect ratios. Based on these experiments, he developed a relationship between the maximum packing fraction and aspect ratio for fibers. We included in our calculations the dependence of $\phi_{\max}$ on the aspect ratio according to Milewski [14].

Comparison of Experimental Results With the Model

Figure 2 shows the dependence of room temperature κ as a function of nanotube volume fraction. Based on numerous measurements of control polymer samples, we estimate the error as less than ±15% including dimensional errors. For each chosen composition, we measured several nominally identical samples. Our average value for the PMMA control samples is 0.18 W/mK, in very good agreement with a handbook value of 0.19 W/mK [15]. The increase in κ is relatively modest up to about 4.5 vol %, followed by a more significant increase (more than 240%) in the 4.5–6 vol % range. Above 6 vol %, κ_c saturates at 0.45 W/mK at 9 vol %, possibly due to poorly dispersed nanotubes at higher loadings.

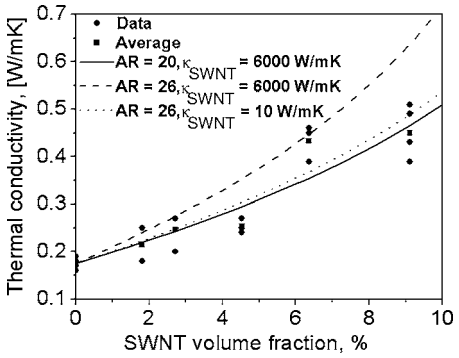

Fig. 2 Experimental thermal conductivities of SWNT-PMMA composites as a function of nanotube loading, and comparison with the predictions of the Nielsen model. The circles represent the experimental data; squares are the average values for nominally identical nanotube loadings. Dashed and solid curves are the predictions of the Nielsen model for aspect ratios of 26 and 20, respectively, assuming SWNT thermal conductivity=6000 W/mK. To obtain better agreement using the measured aspect ratio ~26, an effective SWNT κ of 10 W/mK must be chosen (dotted curve).

We include in Fig. 2 the Nielsen model predictions for aspect ratios 20 and 26, assuming the SWNT κ is 6000 W/mK (solid and dashed curves, respectively). The simulation that best reproduces the data corresponds to an aspect ratio of 20. From AFM we obtained a value of 26 for nanotubes subjected to the same processing steps as in the composites. As Fig. 1 illustrates, this aspect ratio is not unique but rather a distribution. To obtain better agreement with this aspect ratio, we need to ascribe an *effective* SWNT κ value of 10 W/mK (dotted curve). The rationale for this ad hoc procedure is to include within the Nielsen formalism the effect of interfacial thermal resistance. While this procedure is not at all precise, it does imply a significant interfacial thermal resistance between polymer matrix and nanotubes. As noted previously, the diminishing quality of nanotube dispersion at higher loadings (9 vol %) may also contribute to the lower than expected κ.

Discussion

Overall, the predictions of the Nielsen model are in good agreement with the thermal conductivity values for our composites (see Fig. 2). However, at 9 vol % the thermal conductivity of the composite is slightly lower than the prediction of the Nielsen model. This can be caused by large interfacial thermal resistance between the polymer matrix and SWNTs, bad dispersion, and intrinsically low thermal conductivity of the filler. Among these factors, the large interfacial thermal resistance seems to be the most likely reason. Picosecond transient measurements [6] on carbon nanotubes suspended in micelles in water indicate a very small interface conductance ($12\ \mathrm{MW\,m^{-2}\,K^{-1}}$). Similar results were obtained from molecular dynamics simulations of heat flow between a carbon nanotube and octane liquid [7]. This high value of interfacial thermal resistance is caused by weak matrix-filler adhesion and significant acoustic mismatch at the nanotube-polymer interface. The large Young's modulus is largely responsible for high SWNT κ; it also means that high frequency phonons have a large contribution in heat transport. However, in a composite the nanotubes are only weakly coupled with polymer chains. This means that only a few low frequency phonon modes of a SWNT contribute to heat transport across the interface. This is also supported by a molecular dynamics simulation [7]. Therefore, in order to improve the interfacial thermal transport, the polymer-SWNT adhesion has to be improved and/or larger diameter SWNTs having a high density of low frequency phonon states should be used in the composites.

The Nielsen model results show that the increase of composite κ is very sensitive to the filler aspect ratio. Choi et al. [2] demonstrated a significant increase in κ of MWNT/oil suspensions at volume fractions below 1%. Their filler material had an average aspect ratio of 2000 before dispersion, which is probably responsible for the significant increase in κ. The importance of aspect ratio can be understood physically from two viewpoints. First, at a given volume fraction, the number of nanotube-polymer-nanotube contacts decreases with increasing aspect ratio, which in turn reduces the influence of high interfacial thermal resistance. In addition, the study in Ref. [7] showed that increasing nanotube length (or aspect ratio for constant diameter) shifts the phonon dispersion towards lower frequencies, a "softening" of the tube with increasing length. Again, large aspect ratio nanotubes should improve the thermal transport across a nanotube-polymer interface.

Another approach to improved composite κ is to covalently bond the nanotubes to the matrix, for example, by functionalization. However, most functionalization methods require treatments that reduce the aspect ratio and/or create defects that limit the phonon mean free path. Thus, there exists a trade-off between increasing interfacial conductance and reducing the effective SWNT κ. The aspect ratio of the SWNT used in this work is unusually small. The AFM study shows that the aspect ratio of bundles is reduced significantly for sonication times required to achieve good dispersion [16]. AFM also revealed that our filler is not dispersed down to the single tube level, but are bundles consisting on average of 92 tubes. Thus, the effective κ of the bundles could be much smaller than the intrinsic value. The ideal scenario would be a process which efficiently disperses *and* functionalizes the nanotubes while preserving a large aspect ratio.

Conclusions

We have fabricated SWNT-PMMA composites by the coagulation method with nanotube loadings as high as 9 vol % and measured their effective thermal conductivity. We demonstrated a 240% increase in κ with nanotube loading as low as 6 vol %. Further increase in nanotube loading does not result in significant increase in κ. This saturation can be attributed to poor nanotube dispersion at high concentration. Our experimental results are slightly lower than the predictions of the Nielsen model. This discrepancy is most likely caused by the contact resistance of nanotube-polymer-nanotube interfaces. We conclude that nanotubes with larger aspect ratios are needed to obtain further improvement in thermal transport, and that care must be taken to preserve the large aspect ratio of nanotubes during processing.

Acknowledgment

This work was supported by ONR Grant Nos. N00014-01-10657 and N00014-03-10890.

References

[1] Berber, S., Kwon, Y. K., and Tomanek, D., 2000, "Unusually High Thermal Conductivity of Carbon Nanotubes," Phys. Rev. Lett. **84**(20), pp. 4613–4616.
[2] Choi, S. U. S., Zhang, Z. G., Yu, W., Lockwood, F. E., and Grulke, E. A., 2001, "Anomalous Thermal Conductivity Enhancement in Nanotube Suspensions," Appl. Phys. Lett. **79**(14), pp. 2252–2254.
[3] Biercuk, M. J., Llaguno, M. C., Radosavljevic, M., Hyun, J. K., Johnson, A. T., and Fischer, J. E., 2002, "Carbon Nanotube Composites for Thermal Management," Appl. Phys. Lett. **80**(15), pp. 2767–2769.
[4] Choi, E. S., Brooks, J. S., Eaton, D. L., Al-Haik, M. S., Hussaini, M. Y., Garmestani, H., Li, D., and Dahmen, K., 2003, "Enhancement of Thermal and Electrical Properties of Carbon Nanotube Polymer Composites by Magnetic Field Processing," J. Appl. Phys. **94**(9), pp. 6034–6039.
[5] Xie, H. Q., Lee, H., Youn, W., and Choi, M., 2003, "Nanofluids Containing Multiwalled Carbon Nanotubes and their Enhanced Thermal Conductivities," J. Appl. Phys. **94**(8), pp. 4967–4971.
[6] Huxtable, S. T., Cahill, D. G., Shenogin, S., Xue, L. P., Ozisik, R., Barone, P., Usrey, M., Strano, M. S., Siddons, G., Shim, M., and Keblinski, P., 2003, "Interfacial Heat Flow in Carbon Nanotube Suspensions," Nat. Mater. **2**(11), pp. 731–734.
[7] Shenogin, S., Xue, L. P., Ozisik, R., Keblinski, P., and Cahill, D. G., 2004, "Role of Thermal Boundary Resistance on the Heat Flow in Carbon-Nanotube

Composites," J. Appl. Phys., **95**(12), pp. 8136–8144.
[8] Brand, S., 2004, "The Effect of Purification, Sonication and Nitric Acid Reflux on the Length and Diameter Distribution of Single Walled Carbon Nanotubes," MS thesis, Eindhoven University of Technology, Eindhoven, The Netherlands.
[9] Du, F. M., Fischer, J. E., and Winey, K. I., 2003, "Coagulation Method for Preparing Single-Walled Carbon Nanotube/Poly(methyl Methacrylate) Composites and Their Modulus, Electrical Conductivity, and Thermal Stability," J. Polym. Sci., Part B: Polym. Phys. **41**(24), pp. 3333–3338.
[10] Nikolaev, P., Bronikowski, M. J., Bradley, R. K., Rohmund, F., Colbert, D. T., Smith, K. A., and Smalley, R. E., 1999, "Gas-Phase Catalytic Growth of Single-Walled Carbon Nanotubes From Carbon Monoxide," Chem. Phys. Lett., **313**(1–2), pp. 91–97.
[11] Llaguno, M. C., Hone, J., Johnson, A. T., and Fischer, J. E., 2001, "Thermal Conductivity of Single Wall Carbon Nanotubes: Diameter and Annealing Dependence," in *Molecular Nanostructures*, H. Kuzmany, J. Fink, M. Mehring, and S. Roth, eds., AIP Conf. Proc. No. 591, New York, pp. 384–387.
[12] Liu, J., Casavant, M. J., Cox, M., Walters, D. A., Boul, P., Lu, W., Rimberg, A. J., Smith, K. A., Colbert, D. T., and Smalley, R. E., 1999, "Controlled Deposition of Individual Single-Walled Carbon Nanotubes on Chemically Functionalized Templates," Chem. Phys. Lett., **303**(1–2), pp. 125–129.
[13] Nielsen, L. E., 1974, "The Thermal and Electrical Conductivity of Two-Phase Systems," Ind. Eng. Chem. Fundam. **13**(1), pp. 17–20.
[14] Milewski, J. V., 1978, "Combined Packing of Rods and Spheres in Reinforcing Plastics," Ind. Eng. Chem. Prod. Res. Dev. **17**(4), pp. 363–366.
[15] Brandrup, J., Immergut, E. H., and Grulke, E. A., 1999, *Polymer Handbook*, John Wiley & Sons, Inc., New York, V/88.
[16] We cannot distinguish between the release of short tubes present in the initial material during sonication/exfoliation, versus cutting of tubes during sonication and dispersion.

Nusselt Number Correlations for Turbulent Natural Convection Flows Using Asymptotic Analysis of the Near-Wall Region

C. Balaji[1]
Alexander Von Humboldt Fellow

M. Hölling
Research Scholar

H. Herwig
Professor and Head

Institute of Thermo-Fluid Dynamics,
Hamburg University of Technology,
Denickestrasse 17, D-21073 Hamburg, Germany

In this paper, we propose a general methodology by which a universal temperature profile, derived by matching temperature gradients in the overlap region of the wall layer and the core layer, that is valid for high Rayleigh number flows, can be recast into a correlation for the Nusselt number. We then evaluate its adequacy for three types of flows: (a) fully developed flows (e.g., the infinite channel), (b) developing flows (e.g., the vertical flat plate boundary layer), and (c) complex flows (e.g., Rayleigh-Bénard convection and the differentially heated square cavity). The correlation for the Nusselt number, in general, contains a logarithmic term, usually missing in earlier studies, with which we are able to match existing direct numerical simulations or experimental data very well for both fully developed and complex flows.
[DOI: 10.1115/1.2737485]

Keywords: turbulent flow, natural convection, Nusselt number, correlations, asymptotic analysis

1 Introduction

Several studies are available on turbulent natural convection from basic geometries such as the infinite channel and the vertical flat plate. Even so, scarce are the studies that provide high quality experimental or direct numerical simulation (DNS) data of local quantities such as velocity and temperature, particularly near the wall. These are crucial if one attempts to develop wall functions, using asymptotic analysis or otherwise, not only to determine the model constants but also to validate the hypothesis. Wall functions can be successfully used to reduce the number of grid points required to perform computations and their use in problems involving forced convection flow and/or heat transfer is well known and is considered as a standard practice. Such an approach is referred to as wall treatment. Even so, an "exclusive" wall treatment for natural convection flows, with a possible extension to mixed convection, remains largely elusive to date.

The few studies that provide us with data that can be used for developing wall functions for turbulent natural convection fall into three categories: (a) fully developed flows, (b) boundary layer type of flows, and (c) complex flows. Under category (a), the geometry for which either DNS or experimental data are available is the infinite vertical channel. The infinite channel geometry consists of two vertical plates of infinite extent in which one wall is cooled and the other wall is heated. This geometry has been numerically investigated by Boudjemadi et al. [1], Versteegh and Nieuwstadt [2], Wang et al. [3], and experimentally by Betts and Bokhari [4].

For the case of boundary layer flows (category (b)), turbulent natural convection from a vertical hot plate standing in a quiescent environment has been studied by Tsuji and Nagano [5] and Cheesewright [6]. George and Capp [7] proposed the first ever wall functions for turbulent natural convection from vertical surfaces, by performing an analysis of the near-wall region using scaling arguments and the method of matched asymptotics for the inner and outer layers. Henkes [8] performed an extensive numerical study of turbulent natural convection from a vertical hot flat plate and a square cavity (category (c)) and compared the performance of various turbulence models. The square enclosure consists of differentially heated side walls and "adiabatic" top and bottom walls. This geometry is considered to be a "benchmark," at least for laminar natural convection (see, for example, deVahl Davis and Jones [9]). However, the adiabatic conditions are hard to realize in the laboratory, particularly if the medium inside the enclosure has a low thermal conductivity, as for example, air. As a consequence, experimental studies on turbulent natural convection from a square enclosure are scarce. Among the few studies reported are the ones by Ampofo and Karayiannis [10] for a differentially heated cavity, and Cheesewright et al. [11] for a tall cavity. However, in [10] adiabatic conditions on the top and bottom walls could not be realized. Recently, Dixit and Babu [12] have used the Lattice-Boltzmann method to solve the problem of turbulent natural convection from a square cavity ab initio; i.e., without using a turbulence model. The two asymptotic limits for natural convection from an enclosure, namely (1) $\mathrm{Ra}\rightarrow\infty$ and (2) aspect ratio $\rightarrow\infty$, correspond to the categories of developing and fully developed flows, respectively, though the flows near the corners even at very high values of Ra for the enclosure will cause some deviation from true boundary layer behavior.

As a category (c) flow, the problem of turbulent Rayleigh-Bénard convection has been investigated experimentally among others by Castaing et al. [13], Shraiman and Siggia [14], Wu and Libchaber [15], and recently by Chavanne et al. [16], Nikolaenko and Ahlers [17], Niemala and Sreenivasan [18], and Roche et al. [19]. The same problem has been investigated using DNS by Kerr [20], Grötzbach [21], Wörner [22], and Hartlep [23]. Hölling and Herwig [24] performed an asymptotic analysis of the near-wall region for the above problem and proposed a correlation for the Nusselt number that involved a logarithmic term.

From a careful review of the literature, it is clear that while several studies are available for turbulent natural convection in a class of geometries, a systematic approach to obtain a universal velocity and temperature profile by studying the near-wall behavior along the lines of the approach followed for turbulent forced convection (see for example Schlichting and Gersten [25]) is hard to find, save the study of George and Capp [7] and the very recent study of Hölling and Herwig [26] that showed excellent agreement with existing experimental and DNS studies. In these references, a rigorous derivation of the temperature and velocity profile for the viscous sublayer and the overlap layer are presented. In this paper, we discuss a general methodology by which the temperature profile thus obtained can be converted into a general expression for Nusselt number and evaluate its adequacy for a class of flows.

2 Universal Temperature Profile

Following [24] the energy equation for the near-wall region of turbulent natural convection flows is given by

[1]Corresponding author.
Contributed by the Heat Transfer Division of ASME for publication in the JOURNAL OF HEAT TRANSFER. Manuscript received February 14, 2006; final manuscript received December 1, 2006. Review conducted by Jay M. Khodadadi.

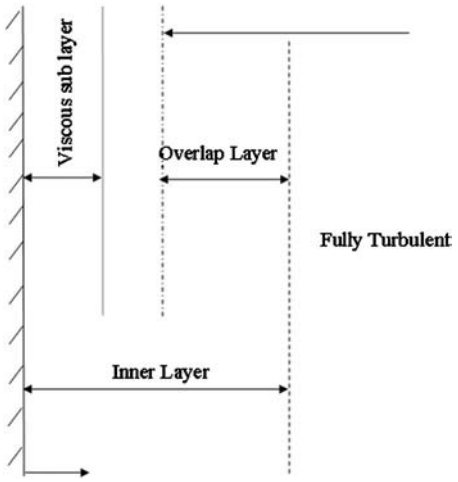

Fig. 1 Two layer structure of the near wall region of high Rayleigh number flows showing the viscous sub-layer, overlap, and the fully turbulent outer layers

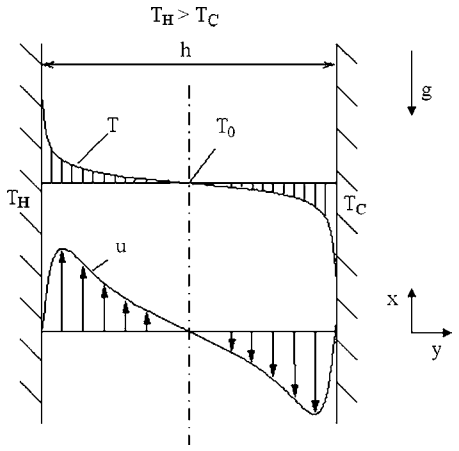

Fig. 2 Schematic showing turbulent natural convection from an infinite vertical channel with the left wall being heated and the right wall being cooled. Also shown are typical velocity and temperature distributions across the channel.

$$0 = \frac{\partial}{\partial y}\left(\alpha\frac{\partial \bar{T}}{\partial y} - \overline{v'T'}\right) \Leftrightarrow \alpha\frac{\partial \bar{T}}{\partial y}\bigg|_w = \alpha\frac{\partial \bar{T}}{\partial y} - \overline{v'T'} = \text{const} \quad (1)$$

The "0" appearing on the left hand side of Eq. (1) denotes that the leading neglected terms in the energy equation are the convection terms whose order is small compared to the terms retained in the equation, as long as one is close to the wall.

We can now define a characteristic temperature T_c as

$$T_c \equiv \left(\frac{\alpha\nu}{g\beta}\left|\frac{\partial \bar{T}}{\partial y}\right|_w^3\right)^{1/4} \quad (2)$$

The above can be interpreted as a form of "turbulent Rayleigh number." With this characteristic temperature, a dimensionless temperature Θ^x is introduced as

$$\Theta^x \equiv \frac{T_H - \bar{T}}{T_c} \quad (3)$$

The temperature field consists of an inner layer and fully turbulent outer layer; see Fig. 1. In the inner layer, both molecular and turbulent heat fluxes are present. The thickness of the wall layer scales as $\delta = T_c|\partial\bar{T}/\partial y|_W^{-1}$. With increasing Rayleigh numbers, the thickness of the inner layer decreases and for $\mathrm{Ra}\to\infty$ it vanishes ($\delta\to 0$), and in view of this, there exists a singularity of the temperature profile at the wall.

The dimensionless wall distance for the inner layer is now defined as

$$y^x \equiv \frac{y}{T_c}\left|\frac{\partial \bar{T}}{\partial y}\right|_w = \frac{y}{\delta} \quad (4)$$

so that $y^x = O(1)$ for all y within the wall layer. In the fully turbulent outer layer only the turbulent heat flux exists. There, the non-dimensional wall distance of $O(1)$ is

$$\eta \equiv \frac{y}{H} \quad (5)$$

If we define a dimensionless wall distance as $H^x = H/\delta$ (where H is the geometrical length scale for the temperature field), this would go to infinity for $\mathrm{Ra}\to\infty$, and hence H^x is not an appropriate length scale for the outer layer, forcing us to introduce the second dimensionless wall distance $\eta = y/H$. Using a third dimensionless wall distance that is valid in the overlap layer and the above definitions, an asymptotic matching of the temperature gradients in the inner and outer layers leads to a universal temperature profile in the overlap layer. This is

$$\Theta^x = C\ln(y^x) + D \quad (6)$$

C and D are constants that are, in general, functions of Ra.

Viscous Sublayer. For the viscous sublayer, the dimensional temperature profile can be shown to be

$$\Theta^x = y^x \quad (7)$$

3 Nusselt Number Correlations From the Universal Temperature Profile

Once the temperature field in a flow is known, one can find the Nusselt number, and for this the temperature gradient at the wall and a characteristic temperature difference of the field as a whole are required.

Our approach is: *Once the asymptotic structure of the temperature field in any turbulent natural convection flow is known, we basically can get the information on the Nusselt number. Certain constants remain undetermined, but the mathematical form and the parameters involved in the Nusselt number correlation are enlightened.*

3.1 Category (a): Fully Developed Flows. Under this category, we take up the problem of turbulent natural convection from an infinite channel. The details of the problem geometry are given in Fig. 2. The left wall is isothermal at T_H, the right wall is isothermal at T_C and $T_H > T_C$, and the two walls are infinite in extent (henceforth, we drop the overbar on the temperature as we will be dealing with only the mean temperatures in the rest of the paper). This is a frequently studied geometry because it is simple both from the viewpoint of conducting experiments and carrying out DNS investigations. Another equally important reason is that many studies on turbulent natural convection look at a possible extension to mixed convection and the infinite channel geometry can be very useful. This is because of the fact that if a vertical velocity is imposed at the bottom of the channel, one can simultaneously have aiding and opposing flows. The general procedure by which the universal temperature profile (Eq. (6)) can be converted into an expression for the Nusselt number using some algebraic manipulations is discussed below.

The first step is the assumption that the universal temperature profile is approximately valid up to the center of the channel. This is a good approximation in a problem like this where the flow is fully developed, consequent upon the infinite extent of the plates.

That the temperature profile is valid all the way up to the middle is also supported by several studies, both experimental and DNS (cf. [26]).

At this location

$$T = (T_H + T_C)/2 \tag{8}$$

Therefore, Eq. (6) becomes

$$\frac{\Delta T}{2T_C} = C \ln(H/2\delta) + D \tag{9}$$

In the above equation, $\Delta T = T_H - T_C$. Substituting for δ from Eq. (4), we have

$$\frac{\Delta T}{2T_C} = C \ln\left(\frac{H}{2T_c}\left|\frac{\partial T}{\partial y}\right|_w\right) + D \tag{10}$$

Now we define the Nusselt number Nu as

$$\mathrm{Nu} = \frac{H}{\Delta T}\left|\frac{\partial T}{\partial y}\right|_w \tag{11}$$

and the Rayleigh number Ra as $g\beta\Delta T H^3/\nu\alpha$, where H is the width of the channel and β is the cubic expansivity of the medium. Using these definitions, and substituting for T_c from Eq. (2) and some mathematical manipulation, we get

$$\mathrm{Nu} = \frac{\mathrm{Ra}^{1/3}}{\left[\frac{C}{2}\ln\left(\frac{1}{16}\mathrm{Ra\,Nu}\right) + 2D\right]^{4/3}} \tag{12}$$

The constants C and D in the above equation can be determined from highly accurate DNS or experimental data. In this study, we use the DNS results of [2] and using curve fitting based on the method of least squares, we obtain C as 0.153 and D as 3. With improved computational resources in the future, one will have DNS data for higher values of Ra, and with these data the constants can be fine tuned.

Therefore, Eq. (12) can be rewritten with the newly obtained constants as

$$\mathrm{Nu} = \frac{\mathrm{Ra}^{1/3}}{\left[0.0765\ln\left(\frac{1}{16}\mathrm{Ra\,Nu}\right) + 6.7148\right]^{4/3}} \tag{13}$$

Equation (13) is cumbersome to use in view of the fact that it is implicit in Nu, consequent upon which Nu has to be iteratively determined. In order to circumvent this, we can replace Nu in the denominator of Eq. (13) by a power law form say, $\mathrm{Nu} = a\,\mathrm{Ra}^b$. This is not expected to cause significant error as the Nu appears within the logarithm term (we will demonstrate this shortly) and more importantly, further developments actually do not need the values of a and b, as they can be readily absorbed in the constant that multiplies the logarithmic term.

Equation (13) can now be written as

$$\mathrm{Nu} = \frac{\mathrm{Ra}^{1/3}}{\left[C_1\ln\left(\frac{a}{16}\mathrm{Ra}^{1+b}\right) + D_1\right]^{4/3}} \tag{14}$$

This can again be simplified as

$$\mathrm{Nu} = \frac{\mathrm{Ra}^{1/3}}{[C_2\ln(\mathrm{Ra}) + D_2]^{4/3}} \tag{15}$$

Using least squares, C_2 and D_2 (with the same data given in [2]) were determined to be 0.101 and 6.3063, respectively.

Hence, the final, "explicit" form of the Nusselt number is

$$\mathrm{Nu} = \frac{\mathrm{Ra}^{1/3}}{[0.101\ln(\mathrm{Ra}) + 6.3063]^{4/3}} \tag{16}$$

Table 1 Nusselt number predictions for the infinite channel

No	Ra	Nu (DNS [2])	Nu (Eq. (16))
1	5.4×10^5	5.35	5.41
2	8.2×10^5	6.26	6.18
3	2.0×10^6	8.19	8.18
4	5×10^6	10.9	10.93

The excellent agreement between the values of Nu predicted by Eq. (16) and the raw data (DNS) of [2] can be seen in Table 1, and confirms that the assumption for Nu in the denominator of Eq. (12) is justified.

The fundamental question before us is whether the logarithmic correction is needed or not. To answer this question, we look at Eq. (16) and can see that in the range of Ra considered, the logarithmic term can contribute to around 25% to the denominator. In a previous study [26], the existence of the logarithmic variation of the near-wall temperature was firmly established and the correlation for Nu corroborates this.

3.2 Category (b): Developing Flows. The extension of the arguments presented in Sec. 3.1 to a developing flow, as for example, turbulent natural convection from a vertical flat plate, is not so straightforward, as the problem is now two dimensional and the boundary layer scales become functions of the axial distance x. A schematic of the vertical plate geometry is given in Fig. 3. The vertical wall is heated and is at a temperature, T_H standing in quiescent air at T_O. The starting point for obtaining the Nusselt number correlation is again the "universal temperature profile." The next step would be to relate the temperature and the normal distance from the wall at a station (x,y) in the near-wall region. The general near-wall temperature profile is given by Eq. (6) and is reproduced here

$$\Theta^x = C\ln(y^x) + D \tag{17}$$

We now focus our attention on some distance within the outer layer where $T - T_\infty$ is say, $0.8\Delta T$, and let this be $y_{0.8}$. For high Rayleigh number flows ($\mathrm{Ra}\to\infty$), $y_{0.8}$ can be written, with the help of scaling analysis (see for example [27]), for most fluids (except for those with $\mathrm{Pr}\ll 1$) as

$$\frac{y_{0.8}}{x} = a_1\,\mathrm{Ra}_x^{b1} \tag{18}$$

Where a_1 and b_1 are constants and Ra_x is the local Rayleigh number based on axial distance x, and as discussed before, neither will this assumption cause significant error nor do we have to actually

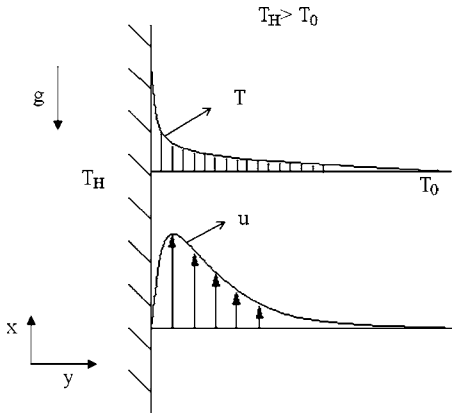

Fig. 3 Schematic depicting turbulent natural convection from a hot vertical flat plate losing heat to quiescent air. Also shown are velocity and temperature profiles at an axial location *x*.

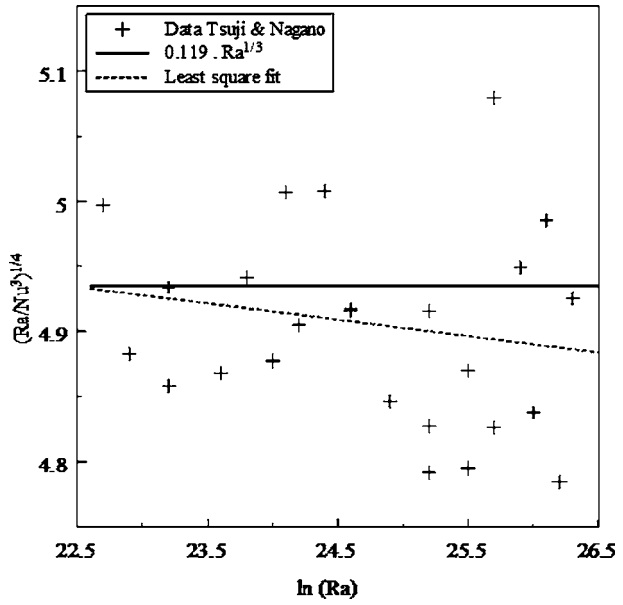

Fig. 4 High resolution plot demonstrating the procedure to determine the constants in the Nusselt number correlation for the vertical flat plate

determine the two constants. On substituting for the temperature and y^x in Eq. (17), we get

$$\frac{0.8\Delta T}{T_c} = C \ln\left(\frac{a_1 \mathrm{Ra}_x^{1+b1}}{T_c} \left| \frac{\partial T}{\partial y} \right|_w \right) + D \tag{19}$$

Using the arguments presented in Section 3.1, Eq. (19) can be recast as

$$\mathrm{Nu}_x = \frac{\mathrm{Ra}_x^{1/3}}{[C_3 \ln(\mathrm{Ra}_x) + D_3]^{4/3}} \tag{20}$$

where Nu_x is the local Nusselt number based on x, the axial distance along the plate, as is the local Rayleigh number Ra_x.

The basic difference between Eqs. (16) and (20) is that the former was for the average Nusselt number, while the latter gives the local Nusselt number. Using the benchmark experimental data of [5], we can determine the constants C_3 and D_3 using the procedure detailed out in the previous section, and they turn out to be −0.0126 and 5.2189, respectively (see Fig. 4). Inserting these values in Eq. (19), the local Nusselt number for the vertical flat plate may be written as

$$\mathrm{Nu}_x = \frac{\mathrm{Ra}_x^{1/3}}{[5.219 - 0.126 \ln(\mathrm{Ra}_x)]^{4/3}} \tag{21}$$

A comparison of the predictions of Eq. (21) with those obtained from the best fit 1/3 power law for the data of [17] (that turns out to be $\mathrm{Nu}_x = 0.119 \mathrm{Ra}_x^{1/3}$) shows that both the power law and the log-power law (Eq. (21)) represent the data very well (both have R^2 values over 99%) and one may at first sight conclude that there is "little" to choose between the two. However, it is instructive to mention here that the data of [5] are for a narrow range of $10^9 \leqslant \mathrm{Ra}_x \leqslant 10^{11}$ and hence data at higher values of Ra_x are required to answer the fundamental question of the need for the logarithmic correction. For this purpose, we now look at the values of Nu reported in Henkes [8] for the same geometry wherein fine grids were used along with the two "best performing low Reynolds number k-ε models" (cf. [8]), namely those of Jones and Launder and Chien. Details of these models can be found in the original papers and also in [8]. The results for turbulent natural convection from a vertical flat plate standing in air are summarized in Table 2.

From Table 2, it is clear that the predictions using two models,

Table 2 Nusselt number predictions for the vertical flat plate (fluid–air)

S.No	Ra_x	Nu (Chien)	Nu (Jones and Launder)	$\mathrm{Nu}=0.119\ \mathrm{Ra}_x^{1/3}$
1	5×10^{10}	256	242	256
2	10^{11}	627	539	522
3	10^{12}	1535	1305	1190[a]
4	10^{13}	3654	3357	2564[a]
5	10^{14}	7873	7873	5524[a]

[a]extrapolated beyond the range of measured Nusselt numbers.

widely recommended for buoyant flows give good agreement with the experimental results (last column of Table 2, first two lines) while predicting higher values of the Nusselt number, if one speculatively extrapolates the experimental correlation beyond its validity. Now, one can argue that while in the range of Ra_x numbers for which experiments have been done, a correlation without the logarithmic correction performs as good as the one with it, in the region outside of this, or more explicitly, in the range $\mathrm{Ra} \to \infty$, a correlation with a logarithmic correction that is based on asymptotic correctness should be able to adequately capture the Nusselt number behavior seen in Table 2. This of course, remains to be proved. In order to do this, the numerical data from one of the two models, say for example, the Jones and Launder model can be taken to recalibrate the constants C_3 and D_3 in Eq. (20). For the sake of clarity, we rewrite Eq. (20) but with the constants replaced by the notation C_∞ and D_∞ to denote that these are asymptotic constants

$$\mathrm{Nu}_x = \frac{\mathrm{Ra}_x^{1/3}}{[C_\infty \ln(\mathrm{Ra}_x) + D_\infty]^{4/3}} \tag{22}$$

The constants C_∞ and D_∞ are evaluated using the Nu_x versus Ra_x data given in Table 2 (column 4, Jones and Launder) for the range $10^{11} \leqslant \mathrm{Ra}_x \leqslant 10^{14}$ and these turn out to be −0.1869 and 9.742, respectively. Using these values, the asymptotically correct form of the local Nusselt number can be given as

$$\mathrm{Nu}_x = \frac{\mathrm{Ra}_x^{1/3}}{[9.742 - 0.1869 \ln(\mathrm{Ra}_x)]^{4/3}} \tag{23}$$

Figure 5 shows the data obtained using the Jones and Launder model, the predictions of Eq. (23), along with the raw data of Tsuji and Nagano [5]. The plot confirms that Eq. (23), with an R^2 value of 99.9% performs very well for all values of Ra_x, including those below 10^{11} that were not used for obtaining the constants of the correlation. More importantly, it is evident that while the data of Tsuji and Nagano may be reliable, the 1/3 power law is an adequate representation of the Nusselt number behavior only for the range of Rayleigh numbers for which the experiments were done, as the Rayleigh numbers are not "asymptotically high enough." The next logical question is," How high is "high enough?" This question can be easily answered if one looks at Table 2. For $\mathrm{Ra} > 10^{12}$, it is clear that the 1/3 power law fails to accurately predict the Nusselt numbers obtained by using reliable models, and so we can conclude that the experimental data of Tsuji and Nagano are not in the "high enough" range of Rayleigh numbers, from an asymptotic viewpoint.

3.3 Category (c): Complex Flows. The geometry of interest here is a square cavity. The left wall is hot at T_H and the right wall is cold at T_C. The top and bottom walls are adiabatic. The medium inside is air (Pr=0.7) for which realising adiabatic conditions on the horizontal walls is very difficult in experiments. The problem is also complex because of the flow being recirculating. In view of the above reasons, both experimental and DNS data are scarce. The only experimental results for a square cavity are those of Ampofo and Karayiannis [10]. However, in this study, the top and

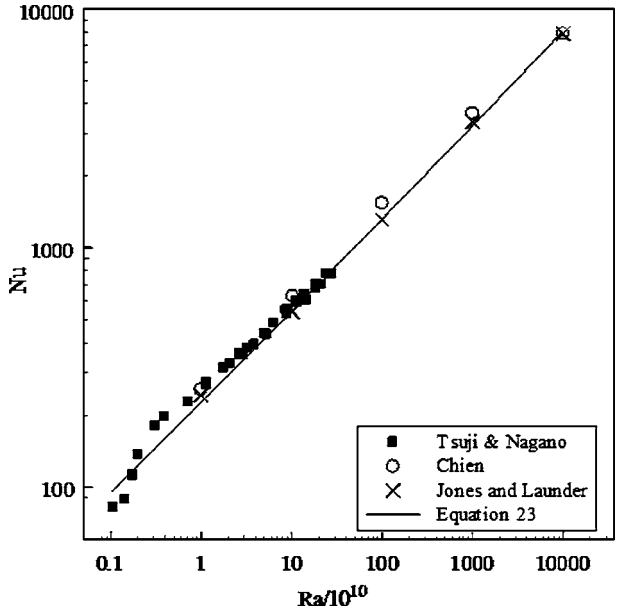

Fig. 5 Nusselt-Rayleigh plot for the vertical flat plate at high Rayleigh numbers showing comparison of Eq. (23) with the results reported in the literature

bottom walls were not adiabatic and results are reported for a single Rayleigh number ($Ra=1.58\times10^9$). Hence, evaluating the constants of the Nusselt number correlation with the approach proposed in this study, using the results of [10] is not feasible. In view of this, we have generated our own solutions with the help of a commercially available software package FLUENT 6.2.

Mathematical Formulation and Solution Procedure. The governing equations for the flow and heat transfer in the geometry under consideration are the well known Reynolds averaged Navier-Stokes equations and the equation of energy. For this study, the standard k-ε model (where k is the turbulent kinetic energy and ε is the dissipation) with "enhanced wall treatment" is used to model the turbulence. The "enhanced wall treatment" is actually a two layer wall treatment, based on the one equation model of Wolfstein [28]. Details of (i) the model and the constants employed and (ii) the near wall treatment are available in [29]. This approach has also been tried for the problem of turbulent natural convection from a rectangular cavity with an aspect ratio (height/spacing) of 5 by Tieszen et al. [30]. The boundary conditions for the problem are straightforward with the no-slip condition being applied on all the walls, as far as the momentum equations are concerned. Regarding the energy equation, $T=T_H$ and $T=T_C$ on the left and right walls and $\partial T/\partial x=0$ on the top and bottom walls.

The flow is assumed to be steady, incompressible and the fluid has constant properties outside of density, for which the Boussinesq approximation is assumed to be valid. The equations are discretized using the finite volume method and the pressure velocity coupling is handled by the SIMPLE algorithm. A first-order upwinding scheme has been used for the convection terms. Relaxation factors were optimally used to ensure convergence. Nonuniform grids with grid clustering near the walls (using geometric progression) were used. The grid size varied from 220×220 to 250×250 depending upon the value of Ra, based on the spacing of the cavity. Care was taken to ensure that the value of y^+ ($y^+=yu_\tau/\nu$, u_τ is the frictional velocity given by $\sqrt{\tau_w/\rho}$ where τ_w is the wall shear stress) at the first grid point is less than 3. This is a prerequisite for using the enhanced wall treatment, as in this approach the near wall mesh has to be fine enough to be able to resolve the viscous sublayer ($y^+\approx1$ and at the maximum 5). Strict convergence criteria were applied such that the difference in heat transfer rates between the left and right walls was always less than 1%. This translated to the following convergence criteria: (a) continuity; momentum; k and ε equations: 1×10^{-4}; (b) energy equation: 1×10^{-7}. Solutions were generated for the following range of Rayleigh numbers $1\times10^{10}\leqslant Ra\leqslant2\times10^{13}$.

For $Ra=1\times10^{10}$, the average Nusselt number (Nu) turns out to be 101. This is very close to the value of 104 reported in [12] where the Lattice-Boltzmann method was employed to solve the same problem, albeit without a turbulence model.

4 Asymptotic Theory for the Nusselt Number Correlation

As before, we assume that the universal temperature profile exists and based on arguments presented in Sec. 3.2 for the vertical flat plate, we propose a correlation for the local Nusselt number (Nu_x) for the cavity as

$$Nu_x=\frac{Ra_x^{1/3}}{[C_{c,\infty}\ln(Ra_x)+D_{c,\infty}]^{4/3}} \tag{24}$$

where we have now qualified the constants with a double subscript (c, ∞), to denote that the constants are for a cavity and are asymptotic. In Eq. (24), Ra_x is the local Rayleigh number, based on axial distance x.

For a problem like the square cavity, the quantity of engineering interest is the average Nusselt number. Hence, one has to obtain the local heat flux for a differential area and then integrate it from 0 to d (where d is the spacing that equals the height for a square cavity). Equation (24) may be rewritten as

$$Nu_x=\frac{Ra_x^{1/3}}{[C'_{c,\infty}\ln(Ra_x^{1/3})+D'_{c,\infty}]^{4/3}} \tag{25}$$

Using the above equation, the general form of the integral that has to be solved when it comes to determining the Nusselt number will be non-elementary that is not easy to integrate. It would be instructive to examine if it could be approximated by a form that has the logarithmic term in the numerator such that after the integration is done, one has a form of the average Nusselt number Nu, as

$$Nu=Ra^{1/3}[C^*_{c,\infty}\ln(Ra^{1/3})+D^*_{c,\infty}] \tag{26}$$

We tested the above approximation for the problem of Rayleigh-Bénard convection with the correlation proposed in [24] and found that the approximation does not lead to any significant error (less than 0.5%).

We can now extend these arguments to the cavity problem and propose a general form of the average Nusselt number as given in Eq. (26). The constants in the correlation can be determined from accurate experimental or numerical data. For the present study, we use our own numerical solutions and using the principle of least squares again, the constants were determined and they can be seen in the correlation given below

$$Nu=Ra^{1/3}[0.0195+0.0035\ln(Ra^{1/3})] \tag{27}$$

A high resolution plot (Fig. 6) between $Nu/Ra^{1/3}$ and Ra using confirms the inadequacy of the 1/3 power law (the solid line on this plot represents the best fit line for the numerical data generated in this study which appear as filled squares on the plot). The R^2 value of Eq. (27) is 99.9%.

5 Conclusions

An asymptotic analysis of the structure of the temperature profile in the near-wall region of high Rayleigh number flows was presented. This was subsequently converted into a correlation for the Nusselt number, which in general will have undetermined con-

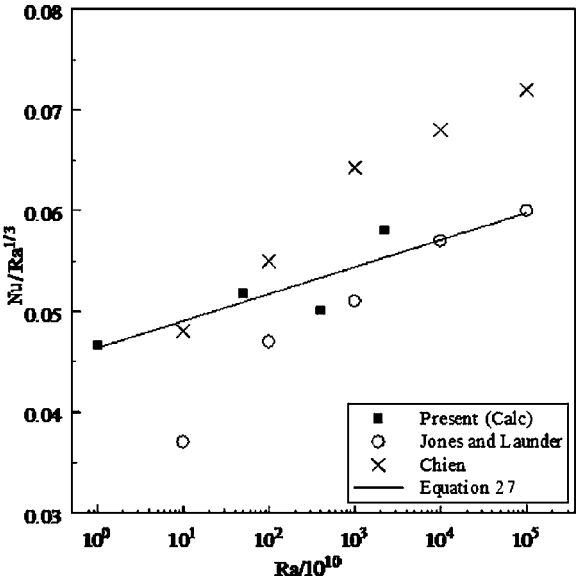

Fig. 6 Comparison of $Nu/Ra^{1/3}$ versus Ra from various studies for turbulent natural convection from a square cavity (high resolution plot)

stants. The general applicability of this method was tested for three types of flows: (a) simple, (b) developing, and (c) complex. An example was chosen from each of the categories and the procedure to determine that the constants were elucidated. For simple flows, like the infinite channel and some complex flows like the Rayleigh-Bénard convection, the asymptotic treatment gives the average Nusselt number, while for developing flows and other complex flows like natural convection in a square enclosure, one gets the local Nusselt number. For the square enclosure problem, solutions were obtained using FLUENT 6.2 and for other geometries, data from existing studies were used to calibrate the constants in the Nusselt number correlation. For all the flows considered, the Nusselt number correlation has a logarithmic correction in addition to the $Ra^{1/3}$ and one may call it a log-power law. A simple and effective way of handling the logarithmic correction approximately, when one calculates the average Nusselt number for a square cavity, has been proposed. For all the flows considered, the agreement with existing studies is excellent. The methodology proposed in this study is expected to be useful for a wide class of problems, when one correlates numerical or experimental data.

References

[1] Boudjemadi, R., Mapu, V., Laurence, D., and Le Quere, P., 1997, "Budgets of Turbulent Stresses and Fluxes in a Vertical Slot Natural Convection at Rayleigh $Ra=10^5$ and 5.4×10^5," Int. J. Heat Fluid Flow, **18**, pp. 70–79.

[2] Verseteegh, T. A. M., and Nieuwstadt, F. T. M., 1999, "A Direct Numerical Simulation of Natural Convection Between Two Infinite Vertical Differentially Heated Walls: Scaling Laws and Wall Functions," Int. J. Heat Mass Transfer, **42**, pp. 3673–3693.

[3] Wang, M., Fu, S., and Zhang, G., 2002, "Large Scale Spiral Structures in Turbulent Natural Convection Along Vertical Plates," Phys. Rev. E, **66**, pp. 066306.

[4] Betts, P. L., and Bokhari, I. H., 2000, "Experiments on Turbulent Natural Convection in an Enclosed Tall Cavity," Int. J. Heat Fluid Flow, **21**, pp. 675–683.

[5] Tsuji, T., and Nagano, Y., 1988, "Characteristics of a Turbulent Natural Convection Boundary Layer Along a Vertical Flat Plate," Int. J. Heat Mass Transfer, **31**, pp. 2101–2111.

[6] Cheesewright, R., 1968, "Turbulent Natural Convection From a Vertical Plane Surface," ASME J. Heat Transfer, **90**, pp. 1–8.

[7] George, W. K., and Capp, S. P., 1979, "A Theory for Natural Convection Turbulent Boundary Layer Next to Heated Vertical Surfaces," Int. J. Heat Mass Transfer, **22**, pp. 813–826.

[8] Henkes, R. A. W. M., 1990, "Natural Convection Boundary Layers," Ph.D. thesis, Delft University of Technology, The Netherlands.

[9] de Vahl Davis, G., and Jones, I. P., 1983, "Natural Convection in a Square Cavity: A Comparison Exercise," Int. J. Numer. Methods Fluids, **3**, pp. 249–264.

[10] Ampofo, F., and Karayiannis, T. G., 2003, "Experimental Benchmark Data for Turbulent Natural Convection in an Air Filled Square Cavity," Int. J. Heat Mass Transfer, **46**, pp. 3551–3572.

[11] Cheesewright, R., King, K. J., and Ziai, S., 1989, "Experimental Data for the Validation of Computer Codes for the Prediction of Two Dimensional Buoyant Cavity Flows," *Significant Questions in Buoyancy Affected by Cavity Flows*, J. A. C. Humphry et al., eds., ASME, New York, pp. 75–81.

[12] Dixit, H. N., and Babu., V., 2006, "Simulation of High Rayleigh Number Natural Convection in a Square Cavity Using the Lattice Boltzmann Method," Int. J. Heat Mass Transfer, **49**, pp. 727–739.

[13] Castaing, B., Gunaratne, G., Heslot, F., Kadanoff, L., Libchaber, S., Thomae, S., Wu, X., Zaleski, G., and Zanetti, G., 1989, "Scaling of Hard Thermal Turbulence in Rayleigh-Bénard Convection," J. Fluid Mech., **204**, pp. 1–30.

[14] Shraiman, B. I., and Siggia, E. D., 1990, "Heat Transport in High-Rayleigh Number Convection," Phys. Rev. A, **42**, pp. 3650–3653.

[15] Wu, X. Z., and Libchaber, A., 1992, "Scaling Relations in Thermal Turbulence: The Aspect Ratio Dependence," Phys. Rev. A, **45**, pp. 842–845.

[16] Chavanne, X., Chilla, F., Chabuad, B., and Castaing, B., 2001, "Turbulent Rayleigh Bénard Convection in Gaseous and Liquid He," Phys. Fluids, **13**, pp. 1300–1320.

[17] Nikolaenko, A., and Ahlers, G., 2003, "Nusselt Number Measurements for Turbulent Rayleigh-Bénard Convection," Phys. Rev. Lett., **91**, pp. 084501.

[18] Niemala, J. J., and Sreenivasan, K. R., 2003, "Confined Turbulent Convection," J. Fluid Mech., **481**, pp. 355–384.

[19] Roche, P. E., Castaing, B., Chabaud, B., and Hebral, B., 2004, "Heat Transfer in Turbulent Rayleigh-Bénard Convection Below the Ultimate Regime," J. Low Temp. Phys., **134**, pp. 1011–1042.

[20] Kerr, R., 1996, "Rayleigh Number Scaling in Numerical Convection," J. Fluid Mech., **310**, pp. 139–179.

[21] Grötzbach, G., 1990, "Simulation of Turbulent Flow and Heat Transfer for Selected Problems of Nuclear Thermal-Hydraulics," *Proc. First International Conference on Supercomputing in Nuclear Applications (SNA '90)*, Mito, Japan.

[22] Wörner, M., 1994, "Direkte Simulation of Turbulenter Rayleigh-Bénard Konvektion in flüssigem Natrium," Ph.D. thesis, University of Karlsruhe.

[23] Hartlep, T., 2004, "Strukturbildung and Turbulenz. Eine Numerische Studie zur Turbulenten Rayleigh-Bénard Konvektion," Ph.D. thesis, University of Göttingen.

[24] Hölling, M., and Herwig, H., 2006, "Asymptotic Analysis of Heat Transfer in Turbulent Rayleigh Bénard Convection," International Journal of Heat and Mass Transfer, to be published.

[25] Schlichting, H., and Gersten, K., 2003, *Boundary Layer Theory*, Springer Verlag, Heidelberg, Germany.

[26] Hölling, M., and Herwig, H., 2005, "Asymptotic Analysis of the Near Wall Region of Turbulent Natural Convection Flows," J. Fluid Mech., **541**, pp. 383–397.

[27] Bejan, A., 1984, *Convection Heat Transfer*, John Wiley, New York.

[28] Wolfstein, M., 1969, "The Velocity and Temperature Distribution of One-Dimensional Flow With Turbulence Augmentation and Pressure Gradient," Int. J. Heat Mass Transfer, **12**, pp. 301–318.

[29] FLUENT 6.2 Documentation, 2005, FLUENT INC, USA.

[30] Tieszen, S., Ooi, A., Durbin, P., and Behnia, M., 1998, "Modelling of Natural Convection Heat Transfer," *Proceedings of the Centre for Turbulence Research*, Stanford University, CA, pp. 287–301.

Journal of Heat Transfer

Announcement

Call for Photographs: Photogallery—Heat Transfer Visualization

2007 International Mechanical Engineering Congress and Exposition (IMECE)
[http://www.asmeconferences.org/congress07]

November 11–15, 2007, Seattle, Washington

[ENTRY DEADLINE: OCTOBER 31, 2007]

Photographs based on experimental and numerical visualizations of thermal heat and mass transport are solicited for the Photogallery of Heat Transfer Phenomena Session, sponsored by the K-22 Heat Transfer Visualization Committee, at the 2007 IMECE [http://www.asmeconferences.org/congress07].

The Photogallery will consist of photographic displays, which illustrate phenomena that are widely relevant to thermal and mass transfer problems. The purpose is to provide a forum for displaying innovative visualization techniques and their applications to heat transfer phenomena.

A subset of submitted entries, selected on the basis of originality, innovative feature of the visualization technique, the ability to convey and exchange information, and the artistic beauty of heat transfer, will be published in the ASME *Journal of Heat Transfer*.

Authors interested in presenting a photograph, please send your entry in a poster-ready format, preferably in an electronic PDF file, to the following organizer by **October 31, 2007**:

Dr. Kenneth D. Kihm
Mechanical, Aerospace and Biomedical Engineering Department
University of Tennessee
Knoxville, TN 37996
E-mail: kkihm@utk.edu

For further inquiry, please contact the Heat Transfer Division Program Representative:

Dr. Chang Oh
Idaho National Laboratory
Idaho Falls, ID 83415
E-mail: Chang.Oh@inl.gov

